DISTRIBUTION STATEMENT A
Approved for Public Release
Distribution Unlimited

MATERIALS RESEARCH SOCIETY
SYMPOSIUM PROCEEDINGS VOLUME 655

Ferroelectric Thin Films IX

Symposium held November 26–30, 2000, Boston, Massachusetts, U.S.A.

EDITORS:

Paul C. McIntyre
Stanford University
Stanford, California, U.S.A.

Stephen R. Gilbert
Agilent Laboratories
Palo Alto, California, U.S.A.

Yoichi Miyasaka
NEC Corporation
Sagamihara, Japan

Robert W. Schwartz
Clemson University
Clemson, South Carolina, U.S.A.

Dirk Wouters
IMEC
Leuven, Belgium

20020214 081

Materials Research Society
Warrendale, Pennsylvania

Single article reprints from this publication are available through
University Microfilms Inc., 300 North Zeeb Road, Ann Arbor, Michigan 48106

CODEN: MRSPDH

Copyright 2001 by Materials Research Society.
All rights reserved.

This book has been registered with Copyright Clearance Center, Inc. For further information, please contact the Copyright Clearance Center, Salem, Massachusetts.

Published by:

Materials Research Society
506 Keystone Drive
Warrendale, PA 15086
Telephone (724) 779-3003
Fax (724) 779-8313
Web site: http://www.mrs.org/

Library of Congress Cataloging-in-Publication Data

Ferroelectric thin films IX : symposium held November 26–30, 2000, Boston, Massachusetts, U.S.A. / editors, Paul C. McIntyre, Stephen R. Gilbert, Yoichi Miyasaka, Robert W. Schwartz, Dirk Wouters
p.cm.—(Materials Research Society symposium proceedings, ISSN 0272-9172 ; v. 655)
Includes bibliographical references and indexes.
ISSN 1526-2405
ISBN 1-55899-565-X
I. McIntyre, Paul C. II. Gilbert, Stephen R. III. Miyasaka, Yoichi IV. Schwartz, Robert W. V. Wouters, Dirk VI. Materials Research Society symposium proceedings ; v. 655
2001

Manufactured in the United States of America

CONTENTS

Preface xv

Acknowledgments xvii

Materials Research Society Symposium Proceedings xviii

FERROELECTRIC NON-VOLATILE MEMORIES—TECHNOLOGY AND FUNDAMENTALS I

* **An Overview of FERAM Technology for High Density Applications** CC1.1
Nicolas Nagel, Thomas Mikolajick, Igor Kasko, Walter Hartner, Manfred Moert, Cay-Uwe Pinnow, Christine Dehm, and Carlos Mazure

Scaled PLZT Thin Film Capacitors With Excellent Endurance and Retention Performance CC1.2
Fan Chu, Glen Fox, and Tom Davenport

Nanoscale Electromechanical Phenomena in Ferroelectric Thin Films CC1.5
C.S. Ganpule, A.L. Roytburd, V. Nagarajan, A. Stanishevsky, J. Melngailis, E.D. Williams, and R. Ramesh

Preparation of Sub-100 nm Thickness PZT Thin Films With Chemical Solution Deposition Method for Low Voltage Operation CC1.7
Yong Kyun Lee, June Key Lee, Chang Jung Kim, Insook Yi, and Ilsub Chung

Characterization of Ferroelectric Property of c-Axis and Non-c-Axis Oriented Epitaxially Grown Bismuth Layer-Structured Ferroelectric Thin Films With Different m-Numbers Prepared by MOCVD CC1.9
Takayuki Watanabe, Tomohiro Sakai, Atsushi Saiki, Keisuke Saito, Toyohiko Chikyo, and Hiroshi Funakubo

MOCVD of Ir and IrO_2 Thin Films for PZT Capacitors CC1.10
M. Shimizu, K. Kita, H. Fujisawa, and H. Niu

INTEGRATION AND ELECTRODES I

* **Electrodes and Barriers for DRAM and FERAM: Processing, Integration, and Fundamentals** CC2.1
K.L. Saenger, P.C. Andricacos, S.D. Athavale, J.D. Baniecki, C. Cabral, Jr., G. Costrini, K.T. Kwietniak, R.B. Laibowitz, J.J. Lian, Y. Limb, D.A. Neumayer, and M.L. Wise

*Invited Paper

Oxidation Resistance of TaSiN Diffusion Barriers for Stacked Capacitors CC2.2
F. Letendu, M.C. Hugon, B. Agius, I. Vickridge, F. Ayguavives, and A.I. Kingon

Highly Stable Ir-Ta-O Electrode for Ferroelectric Material Deposition CC2.3
Fengyan Zhang, Sheng Teng Hsu, Jer-shen Maa, Yoshi Ono, Ying Hong, Weiwei Zhuang, Shigeo Ohnishi, Wendong Zhen, and Norito Fujiwara

Etching Characteristics of Noble Metal Electrode CC2.5
St. Schneider, H. Kohlstedt, and R. Waser

* **Process Degradation of a Ferroelectric Capacitor** CC2.6
Seigen Otani and Tetsuro Tamura

Degradation of Ferroelectric Pb(Zr,Ti)O_3 Under Reducing Conditions CC2.7
Yuichi Shimakawa and Yoshimi Kubo

Degradation of Ferroelectric Capacitors During Metal Etching and Ashing Processes CC2.8
Chanro Park, O. Sung Kwon, Yeo Song Seol, Jin Woong Kim, and Hee Koo Yoon

200°C Preparation of SiN_x Passivation Films for PZT Ferroelectric Capacitors by Catalytic CVD CC2.10
Toshiharu Minamikawa, Yasuto Yonezawa, Yoshikazu Fujimori, Takashi Nakamura, Atsushi Masuda, and Hideki Matsumura

BST, GATE MATERIALS, AND DRAM: FUNDAMENTALS AND TECHNOLOGY

Investigation of Dead Layer Thickness in $SrRuO_3/Ba_{0.5}Sr_{0.5}TiO_3$/Au Thin Film Capacitors CC3.2
L.J. Sinnamon, R.M. Bowman, and J.M. Gregg

Preparation and Characterization of MFM and MFIS Structures Using $Sr_2(Ta_{1-x}, Nb_x)_2O_7$ Thin Film by Pulsed Laser Deposition CC3.5
Masanori Okuyama, Toshiyuki Nakaiso, and Minoru Noda

New Pt/$(Bi,La)_4Ti_3O_{12}/Si_3N_4$/Si MFIS Structure for FET-Type Ferroelectric Memories by the Sol-Gel Method CC3.6
Takeshi Kijima, Yoshihisa Fujisaki, and Hiroshi Ishiwara

*Invited Paper

Ferroelectric Properties of La-Doped $Bi_4Ti_3O_{12}$ Thin Films Deposited Directly on Si by Pulse-Injection MOCVD CC3.7
Joon Hyeong Kim, Jin Yong Kim, and Hyeong Joon Kim

The Properties of MFMOS and MFOS Capacitors With High k Gate Oxides for One Transistor Memory Applications CC3.10
Tingkai Li, Sheng Teng Hsu, Hong Ying, and Bruce Ulrich

Improvement of Retention Property of $YMnO_3/Y_2O_3/Si$ MFIS Capacitor CC3.11
Norifumi Fujimura, Daisuke Ito, Kousuke Kakuno, and Taichiro Ito

INTEGRATION AND ELECTRODES II

Suppression of Oxidation of an Epitaxial (100)ZrN Film on Si During the Deposition of Ir Film CC4.2
Sadayoshi Horii and Susumu Horita

Property Improvement of PLZT Capacitor Using $CaRuO_3$ Top Electrode CC4.6
Hiroshi Funakubo, Noriyuki Higashi, and Norikazu Okuda

Characterization of Conductive RuO_2 Thin Film as Bottom Electrodes for Ferroelectric Thin Films CC4.7
S. Bhaskar, P.S. Dobal, S.B. Majumder, and R.S. Katiyar

FERROELECTRIC NON-VOLATILE MEMORIES— TECHNOLOGY AND FUNDAMENTALS II

Properties of $Au/Pb(Zr_{0.52}Ti_{0.48})O_3/Bi_4Ti_3O_{12}/p\text{-}Si$ Ferroelectric Memory Diodes CC5.1
Jun Yu, Hua Wang, Xiaomin Dong, Wenli Zhou, Yunbo Wang, and Lili Zhu

Direct Comparison of Structural and Electrical Properties of Epitaxial (001)-, (116)-, and (103)-Oriented $SrBi_2Ta_2O_9$ Thin Films on $SrTiO_3$ and Silicon Substrates CC5.3
H.N. Lee, A. Pignolet, S. Senz, C. Harnagea, and D. Hesse

MOCVD Kinetics of Precursors for Ferroelectric SBT Film CC5.5
A. Baeri, G.G. Condorelli, and I.L. Fragalà

Preparation and Characterization of Ba and Nb Substituted $SrBi_2Ta_2O_9$ Compounds CC5.6
Rasmi R. Das, P.S. Dobal, A. Dixit, W. Perez, M.S. Tomar, R.E. Melgarejo, and Ram S. Katiyar

Role of the Electrode Morphology, Thickness and Orientation in the Ferroelectric Performance of Epitaxial Pb(Zr,Ti)O_3 Thin Films CC5.7
Cesar Guerrero, Florencio Sánchez, José Roldán, Frank Güell, María V. García-Cuenca, Cesar Ferrater, and Manuel Varela

BST FOR DRAM AND GATE DIELECTRICS

* **The Effect of Forming Gas Annealing on Pt/(Ba,Sr)TiO_3/Pt Thin Film Capacitors for Future DRAM Applications: Electrical Properties and Degradation Mechanisms** CC6.1
J.D. Baniecki, C. Parks, R.B. Laibowitz, T.M. Shaw, and J. Lian

Improved Deposition Process of CVD-(Ba,Sr)TiO_3 on Ru CC6.5
M. Tarutani, T. Sato, M. Yamamuka, T. Kawahara, T. Horikawa, T. Takenaga, Y. Yoneda, T. Kuroiwa, S. Matsuno, and T. Shibano

* **Manufacturability Study for Etching High-Density BST/Pt Capacitors** CC6.6
Jay Hwang

FUNDAMENTAL PROPERTIES OF FERROELECTRIC THIN FILMS I

Imaging Mechanism and Quantification of Scanning Probe Microscopies of Ferroelectric Surfaces CC7.2
Sergei V. Kalinin and Dawn A. Bonnell

Nanometer Scale Domain Measurement of Ferroelectric Thin Films Using Scanning Nonlinear Dielectric Microscopy CC7.4
Hiroyuki Odagawa, Kaori Matsuura, and Yasuo Cho

Lattice Vibrational Properties of $SrBi_2Ta_2O_9$ CC7.5
Ran Liu and Pengdi Han

* **Transient Behavior of the Polarization in Ferroelectric Thin Film Capacitors** CC7.6
Oliver Lohse, Michael Grossmann, Dierk Bolten, Ulrich Boettger, and Rainer Waser

Self-Polarization Mechanism in Textured Pyroelectric $Pb(Ti_{1-x}Zr_x)O_3$ Films CC7.7
G. Suchaneck, G. Gerlach, Yu. Poplavko, A.I. Kosarev, and A.N. Andronov

*Invited Paper

Strain-Induced Elevation of the Spontaneous Polarization in $BaTiO_3$ Thin Films CC7.8
W. Tian, J.H. Haeni, D.G. Schlom, and X.Q. Pan

DOMAINS IN FERROELECTRIC THIN FILMS

* **Nanoscale Properties of $SrBi_2Ta_2O_9$ Thin Films** CC8.5
A. Gruverman, C. Isobe, and M. Tanaka

Cellular Domain Architecture of Stress-Free Epitaxial Ferroelectric Films CC8.8
S.P. Alpay, A.L. Roytburd, V. Nagarajan, L.A. Bendersky, and R. Ramesh

Near Field Optical Second Harmonic Imaging of the Polydomain Structure of Epitaxial $PbZr_xTi_{1-x}O_3$ Thin Films CC8.9
H.Y. Liang, I.I. Smolyaninov, C.H. Lee, C.C. Davis, V. Nagarajan, and R. Ramesh

PROCESSING, PROPERTIES, AND CHARACTERIZATION

* **Orientation Selection in Sol-Gel Derived PZT Thin Films** CC9.1
G.J. Norga and Laura Fè

Surface Reaction Mechanisms in the Chemical Vapor Deposition of $(Ba,Sr)TiO_3$ Films CC9.3
M. Yamamuka, T. Kawahara, M. Tarutani, T. Horikawa, T. Oomori, and T. Shibano

Growth of $(Ba,Sr)TiO_3$ Thin Films in a Multi-Wafer MOCVD Reactor CC9.4
P. Ehrhart, F. Fitsilis, S. Regnery, C.L. Jia, H.Z. Jin, R. Waser, F. Schienle, M. Schumacher, and H. Juergensen

FUNDAMENTAL PROPERTIES OF FERROELECTRIC THIN FILMS II

Piezoresponse Measurements for $Pb(Zr,Ti)O_3$ Island Structure Using Scanning Probe Microscopy CC10.4
H. Fujisawa, K. Morimoto, M. Shimizu, H. Niu, K. Honda, and S. Ohtani

*Invited Paper

Fatigue in PZT Thin Films CC10.8
V. Shur, E. Nikolaeva, E. Shishkin, I. Baturin, D. Bolten, O. Lohse, and R. Waser

Response of the Electric Field Gradient in Ion Implanted $BaTiO_3$ to an External Electric Field CC10.11
Marc Dietrich, Jörn Bartels, Manfred Deicher, Kristian Freitag, Vyacheslav Samokhvalov, and Sepp Unterricker

Surface and Size Effects in TGS, $NaNO_2$, and DKDP Nanocrystals CC10.12
Juan D. Romero, Luis F. Fonseca, Rafael Ramos, Manuel I. Marqués, and Julio A. Gonzalo

Preparations and Characterizations of Epitaxial $SrBi_2Ta_2O_9$ Thin Films CC10.13
Keisuke Saito, Masatoshi Mitsuya, Toshimasa Suzuki, Yuji Nishi, Masayuki Fujimoto, Masanori Nukaga, Isao Yamaji, Takao Akai, and Hiroshi Funakubo

Use of an External Electric Field to Convert the Paraelectric Phase to the Ferroelectric Phase in Ultra-Thin Copolymer Films of P(VDF-TrFE) CC10.14
Matt Poulsen, S. Adenwalla, Stephen Ducharme, V.M. Fridkin, S.P. Palto, N.N. Petukhova, and S.G. Yudin

PIEZOELECTRIC, PYROELECTRIC, AND OPTICAL MATERIALS AND DEVICES

Ferroelectric and Piezoelectric Properties of Epitaxial $Pb(Yb_{1/2}Nb_{1/2})O_3$-$PbTiO_3$ Films CC11.3
Takeshi Yoshimura and Susan Trolier-McKinstry

Crystalline and Electrical Properties of Ferroelectric Silver Niobate-Tantalate Thin Films CC11.5
Jung-Hyuk Koh, S.I. Khartsev, Alex Grishin, and Vladimir Petrovsky

Dielectric and Piezoelectric Properties of PZT 52/48 Thick Films With (100) and Random Crystallographic Orientation CC11.7
Q.F. Zhou, E. Hong, R. Wolf, and S. Trolier-McKinstry

Piezoresponse Measurement and Imaging of Electromechanical PZT and PZN-BT Thin Films CC11.8
C. Morros, M.H. Corbett, G. Catalan, J.M. Gregg, and R.M. Bowman

A Dielectric Bolometer Behavior of BST Thin Film Prepared by Metal-Organic-Decomposition With Excellent Reproducibility in Thermal Cycling Test CC11.9
Minoru Noda, Hong Zhu, Huaping Xu, Tomonori Mukaigawa, Kazuhiko Hashimoto, and Masanori Okuyama

Sol-Gel Derived Pyroelectric Barium Strontium Titanate Thin Films for Infrared Detector Applications CC11.10
Jian-Gong Cheng, Jun Tang, Shao-Ling Guo, and Jun-Hao Chu

A Modified SBN System for Pyroelectric Sensors CC11.11
H. Amorín, F. Guerrero, J. Portelles, M. Venet, A. Fundora, and J.M. Siqueiros

Sensing Properties of $Ba_{1-x}La_xNb_yTi_{1-y}O_3$ (x=0.25%, y=0.25%) Thin-Film on SiO_2/Si Substrate CC11.12
B. Li, P.T. Lai, G.Q. Li, S.H. Zeng, and M.Q. Huang

The Physics of Electric Field Effect Thermoelectric Devices CC11.13
V. Sandomirsky, A.V. Butenko, R. Levin, and Y. Schlesinger

THIN FILM PROCESSING

Electrophoretic Deposition of Ferroelectric Composites for Applications in Electronic Scanning Systems CC12.8
E. Ngo, P.C. Joshi, M.W. Cole, and C.W. Hubbard

Growth and Characterization Studies of $ABi_2Ta_2O_9$ (A = Ba, Sr, and Ca) Ferroelectric Thin Films CC12.11
R.R. Das, W. Pérez, R.J. Rodríguez, P.S. Dobal, R.S. Katiyar, and S.B. Krupanidhi

Ferroelectric and Fatigue Properties of Alkoxy-Derived $CaBi_2Ta_2O_9$ Thin Films CC12.12
Kazumi Kato, Kazuyuki Suzuki, Kaori Nishizawa, and Takeshi Miki

Hydrothermal Fabrication of Barium Strontium Titanate Ceramics for High-Frequency Wireless Communication Networks CC12.13
K. Zelonka, M. Sayer, H. Hammad, and A.P. Freundorfer

Electrical Characteristics of Chemical Solution Deposited Nd^{3+} Doped PZT (53/47) Thin Films in Planar Electrode Configuration CC12.14
S.B. Majumder, B. Perez, B. Roy, A. Martinez, and R.S. Katiyar

PIEZOELECTRIC MATERIALS, CAPACITORS, AND NOVEL DEVICES

* **Oxide Films for Integrated Capacitors in Thin Film Functional Modules** CC13.1
M. Klee, D. Wissen, W. Keur, R. Kiewitt, D. Bausen, and P. Lok

Thin Film Superlattices of Lead Based Relaxors CC13.2
M.H. Corbett, J.M. Gregg, and R.M. Bowman

* **Macroscopic Actuators Using Thick Piezoelectric Coatings** CC13.6
M. Sayer, G.R. Lockwood, T.R. Olding, G. Pang, Lester M. Cohen, W. Ren, and B.K. Mukherjee

High-Frequency Thin Film Acoustic Ferroelectric Resonators CC13.7
Paul Kirby, Qing-Xin Su, Eiju Komuro, Masaaki Imura, Qi Zhang, and Roger Whatmo re

Preparation and Characterization of $(Bi,La)_4Ti_3O_{12}$ Films by the Sol-Gel Technique CC13.9
Eisuke Tokumitsu, Takeaki Isobe, Takeshi Kijima, and Hiroshi Ishiwara

Theoretical and Experimental Studies on Retention Characteristics of Metal-Ferroelectric-Insulator-Semiconductor and Metal-Insulator-Ferroelectric-Insulator-Semiconductor Structures CC13.10
Masanori Okuyama, Mitsue Takahashi, Kazushi Kodama, Toshiyuki Nakaiso, and Minoru Noda

HIGH-FREQUENCY APPLICATIONS OF FERROELECTRICS

Microstructural and Electrical Properties of La Doped $Ba_{1-x}Sr_xTiO_3$ Thin Films for Tunable Microwave Device Applications CC14.2
M.W. Cole, P.C. Joshi, E. Ngo, C.W. Hubbard, U. Lee, and M.H. Ervin

Experimental and Theoretical Investigation into the Dielectric Behavior of Ferroelectric Thin Film Superlattices CC14.9
J.M. Gregg, D. O'Neill, G. Catalan, and R.M. Bowman

*Invited Paper

Effect of Laser Energy and Laser Pulses on the Microstructure, Composition and Properties of Barium Strontium Titanate Thin Films Synthesized by Pulsed Laser Deposition **CC14.10**
Costas G. Fountzoulas, J.D. Demaree, and Steven H. McKnight

Author Index

Subject Index

PREFACE

This symposium, "Ferroelectric Thin Films IX," held November 26–30 at the 2000 MRS Fall Meeting in Boston, Massachusetts, was the ninth in a series of highly successful MRS symposia on this topic. Understanding ferroelectric thin films through use of novel and sophisticated characterization methods was an important theme in this edition of the symposium series. Both oral and poster presentations at the symposium described recent advances in scanning probe imaging methods and analysis techniques, electrical characterization methods, and x-ray and TEM-based probes of ferroelectric thin films. In addition, several presentations reviewed progress in the technology of ferroelectric thin films for use in semiconductor memories, piezoelectric devices, and other applications. The technical quality of the contributed presentations was evidenced by the awarding of Poster Awards by the 2000 Fall Meeting chairs to two posters in this symposium, a rare honor.

As has been the case in previous years, the symposium was noted for its mix of excellent presentations from academia, industry, and national laboratories, and from North America, Europe, and Asia. Both the oral and poster presentations were well-attended (approximately 200 attendees were present for many of the oral sessions), and the number of abstracts submitted (~160) was similar to past symposia in this series. Important new results on thin film ferroelectrics were also presented in symposia at this MRS Meeting on high frequency dielectrics and domain structures (Symposia DD and BB, respectively), and joint sessions were held with these two symposia.

The strong and increasing interest in ferroelectric thin films, both domestic and international, indicates the growing technological importance of these materials and the fascinating scientific problems associated with them that remain to be resolved. This proceedings volume presents the latest technical information on ferroelectric thin films reported by researchers in academia, government laboratories and industry. It also provides insight into the emerging trends of this exciting new technology.

Paul C. McIntyre
Stephen R. Gilbert
Yoichi Miyasaka
Robert W. Schwartz
Dirk Wouters

April 2001

ACKNOWLEDGMENTS

The symposium chairs are pleased to acknowledge the contributing and invited authors for the outstanding quality of their presentations and proceedings manuscripts. The invited speakers included:

J.D. Baniecki
J. Hwang
M. Klee
I. Levin
G. Norga
J. Ramdani
K.L. Saenger
S.K. Streiffer
R. Waser
A. Gruverman
A.I. Kingon
K.M. Lee
N. Nagel
S. Otani
R. Ramesh
M. Sayer
A. Tagantsev
X.X. Xu

We are also pleased to acknowledge the following poster presenters who received MRS Poster Awards from the 2000 Fall Meeting chairs:

H.N. Lee et al. (Max Planck Institute, Halle, Germany)
Y. Shimakawa et al. (NEC, Japan)

The symposium chairs are also indebted to the session chairs for their efforts in overseeing the sessions, guiding subsequent discussions, and for assisting with review of the proceedings manuscripts:

O. Auciello
C.H. Chung
D.L. Kaiser
M. Klee
P. Muralt
G. Norga
J. Ramdani
K. Saenger
S.K. Streiffer
M. Yamamuka
J.D. Baniecki
Q. Jia
A.I. Kingon
J-P. Maria
N. Nagel
S. Otani
R. Ramesh
M. Sayer
S. Trolier-McKinstry

The chairs also wish to express their gratitude to the following organizations for providing financial support, enabling us to present "Ferroelectric Thin Films IX":

Agilent Technologies
aixACCT Systems
ATMI
Inorgtech
Kojundo Chemical Laboratory
NEC Corporation
Rohm
ULVAC Japan Ltd.

Finally, we extend special thanks to the Materials Research Society staff, as well as the 2000 Fall Meeting chairs, for the development of yet another outstanding conference.

MATERIALS RESEARCH SOCIETY SYMPOSIUM PROCEEDINGS

Volume 609 Amorphous and Heterogeneous Silicon Thin Films 2000, R.W. Collins, H.M. Branz, M. Stutzmann, S. Guha, H. Okamoto, 2001, ISBN: 1-55899-517-X
Volume 610 Si Front-End Processing Physics and Technology of Dopant-Defect Interactions II, A. Agarwal, L. Pelaz, H-H. Vuong, P. Packan, M. Kase, 2001, ISBN: 1-55899-518-8
Volume 611 Gate Stack and Silicide Issues in Silicon Processing, L.A. Clevenger, S.A. Campbell, P.R. Besser, S.B. Herner, J. Kittl, 2001, ISBN: 1-55899-519-6
Volume 612 Materials, Technology and Reliability for Advanced Interconnects and Low-k Dielectrics, G.S. Oehrlein, K. Maex, Y-C. Joo, S. Ogawa, J.T. Wetzel, 2001, ISBN: 1-55899-520-X
Volume 613 Chemical-Mechanical Polishing 2000 Fundamentals and Materials Issues, R.K. Singh, R. Bajaj, M. Moinpour, M. Meuris, 2001, ISBN: 1-55899-521-8
Volume 614 Magnetic Materials, Structures and Processing for Information Storage, B.J. Daniels, T.P. Nolan, M.A. Seigler, S.X. Wang, C.B. Murray, 2001, ISBN: 1-55899-522-6
Volume 615 Polycrystalline Metal and Magnetic Thin Films 2001, B.M. Clemens, L. Gignac, J.M. MacLaren, O. Thomas, 2001, ISBN: 1-55899-523-4
Volume 616 New Methods, Mechanisms and Models of Vapor Deposition, H.N.G. Wadley, G.H. Gilmer, W.G. Barker, 2000, ISBN: 1-55899-524-2
Volume 617 Laser-Solid Interactions for Materials Processing, D. Kumar, D.P. Norton, C.B. Lee, K. Ebihara, X.X. Xi, 2001, ISBN: 1-55899-525-0
Volume 618 Morphological and Compositional Evolution of Heteroepitaxial Semiconductor Thin Films, J.M. Millunchick, A-L. Barabasi, N.A. Modine, E.D. Jones, 2000, ISBN: 1-55899-526-9
Volume 619 Recent Developments in Oxide and Metal Epitaxy Theory and Experiment, M. Yeadon, S. Chiang, R.F.C. Farrow, J.W. Evans, O. Auciello, 2000, ISBN: 1-55899-527-7
Volume 620 Morphology and Dynamics of Crystal Surfaces in Complex Molecular Systems, J. DeYoreo, W. Casey, A. Malkin, E. Vlieg, M. Ward, 2001, ISBN: 1-55899-528-5
Volume 621 Electron-Emissive Materials, Vacuum Microelectronics and Flat-Panel Displays, K.L. Jensen, R.J. Nemanich, P. Holloway, T. Trottier, W. Mackie, D. Temple, J. Itoh, 2001, ISBN: 1-55899-529-3
Volume 622 Wide-Bandgap Electronic Devices, R.J. Shul, F. Ren, W. Pletschen, M. Murakami, 2001, ISBN: 1-55899-530-7
Volume 623 Materials Science of Novel Oxide-Based Electronics, D.S. Ginley, J.D. Perkins, H. Kawazoe, D.M. Newns, A.B. Kozyrev, 2000, ISBN: 1-55899-531-5
Volume 624 Materials Development for Direct Write Technologies, D.B. Chrisey, D.R. Gamota, H. Helvajian, D.P. Taylor, 2001, ISBN: 1-55899-532-3
Volume 625 Solid Freeform and Additive Fabrication 2000, S.C. Danforth, D. Dimos, F.B. Prinz, 2000, ISBN: 1-55899-533-1
Volume 626 Thermoelectric Materials 2000 The Next Generation Materials for Small-Scale Refrigeration and Power Generation Applications, T.M. Tritt, G.S. Nolas, G.D. Mahan, D. Mandrus, M.G. Kanatzidis, 2001, ISBN: 1-55899-534-X
Volume 627 The Granular State, S. Sen, M.L. Hunt, 2001, ISBN: 1-55899-535-8
Volume 628 Organic/Inorganic Hybrid Materials 2000, R. Laine, C. Sanchez, C.J. Brinker, E. Giannelis, 2001, ISBN: 1-55899-536-6
Volume 629 Interfaces, Adhesion and Processing in Polymer Systems, S.H. Anastasiadis, A. Karim, G.S. Ferguson, 2001, ISBN: 1-55899-537-4
Volume 633 Nanotubes and Related Materials, A.M. Rao, 2001, ISBN: 1-55899-543-9
Volume 634 Structure and Mechanical Properties of Nanophase Materials Theory and Computer Simulations vs. Experiment, D. Farkas, H. Kung, M. Mayo, H. Van Swygenhoven, J. Weertman, 2001, ISBN: 1-55899-544-7
Volume 635 Anisotropic Nanoparticles Synthesis, Characterization and Applications, S.J. Stranick, P. Searson, L.A. Lyon, C.D. Keating, 2001, ISBN: 1-55899-545-5
Volume 636 Nonlithographic and Lithographic Methods of Nanofabrication From Ultralarge-Scale Integration to Photonics to Molecular Electronics, L. Merhari, J.A. Rogers, A. Karim, D.J. Norris, Y. Xia, 2001, ISBN: 1-55899-546-3

MATERIALS RESEARCH SOCIETY SYMPOSIUM PROCEEDINGS

Volume 637 Microphotonics Materials, Physics and Applications, K. Wada, P. Wiltzius, T.F. Krauss, K. Asakawa, E.L. Thomas, 2001, ISBN: 1-55899-547-1
Volume 638 Microcrystalline and Nanocrystalline Semiconductors 2000, P.M. Fauchet, J.M. Buriak, L.T. Canham, N. Koshida, B.E. White, Jr., 2001, ISBN: 1-55899-548-X
Volume 639 GaN and Related Alloys 2000, U. Mishra, M.S. Shur, C.M. Wetzel, B. Gil, K. Kishino, 2001, ISBN: 1-55899-549-8
Volume 640 Silicon Carbide Materials, Processing and Devices, A.K. Agarwal, J.A. Cooper, Jr., E. Janzen, M. Skowronski, 2001, ISBN: 1-55899-550-1
Volume 642 Semiconductor Quantum Dots II, R. Leon, S. Fafard, D. Huffaker, R. N tzel, 2001, ISBN: 1-55899-552-8
Volume 643 Quasicyrstals Preparation, Properties and Applications, E. Belin-Ferr , P.A. Thiel, A-P. Tsai, K. Urban, 2001, ISBN: 1-55899-553-6
Volume 644 Supercooled Liquid, Bulk Glassy and Nanocrystalline States of Alloys, A. Inoue, A.R. Yavari, W.L. Johnson, R.H. Dauskardt, 2001, ISBN: 1-55899-554-4
Volume 646 High-Temperature Ordered Intermetallic Alloys IX, J.H. Schneibel, S. Hanada, K.J. Hemker, R.D. Noebe, G. Sauthoff, 2001, ISBN: 1-55899-556-0
Volume 647 Ion Beam Synthesis and Processing of Advanced Materials, D.B. Poker, S.C. Moss, K-H. Heinig, 2001, ISBN: 1-55899-557-9
Volume 648 Growth, Evolution and Properties of Surfaces, Thin Films and Self-Organized Structures, S.C. Moss, 2001, ISBN: 1-55899-558-7
Volume 649 Fundamentals of Nanoindentation and Nanotribology II, S.P. Baker, R.F. Cook, S.G. Corcoran, N.R. Moody, 2001, ISBN: 1-55899-559-5
Volume 650 Microstructural Processes in Irradiated Materials 2000, G.E. Lucas, L. Snead, M.A. Kirk, Jr., R.G. Elliman, 2001, ISBN: 1-55899-560-9
Volume 651 Dynamics in Small Confining Systems V, J.M. Drake, J. Klafter, P. Levitz, R.M. Overney, M. Urbakh, 2001, ISBN: 1-55899-561-7
Volume 652 Influences of Interface and Dislocation Behavior on Microstructure Evolution, M. Aindow, M. Asta, M.V. Glazov, D.L. Medlin, A.D. Rollet, M. Zaiser, 2001, ISBN: 1-55899-562-5
Volume 653 Multiscale Modeling of Materials 2000, L.P. Kubin, J.L. Bassani, K. Cho, H. Gao, R.L.B. Selinger, 2001, ISBN: 1-55899-563-3
Volume 654 Structure-Property Relationships of Oxide Surfaces and Interfaces, C.B. Carter, X. Pan, K. Sickafus, H.L. Tuller, T. Wood, 2001, ISBN: 1-55899-564-1
Volume 655 Ferroelectric Thin Films IX, P.C. McIntyre, S.R. Gilbert, M. Miyasaka, R.W. Schwartz, D. Wouters, 2001, ISBN: 1-55899-565-X
Volume 657 Materials Science of Microelectromechanical Systems (MEMS) Devices III, M. deBoer, M. Judy, H. Kahn, S.M. Spearing, 2001, ISBN: 1-55899-567-6
Volume 658 Solid-State Chemistry of Inorganic Materials III, M.J. Geselbracht, J.E. Greedan, D.C. Johnson, M.A. Subramanian, 2001, ISBN: 1-55899-568-4
Volume 659 High-Temperature Superconductors Crystal Chemistry, Processing and Properties, U. Balachandran, H.C. Freyhardt, T. Izumi, D.C. Larbalestier, 2001, ISBN: 1-55899-569-2
Volume 660 Organic Electronic and Photonic Materials and Devices, S.C. Moss, 2001, ISBN: 1-55899-570-6
Volume 661 Filled and Nanocomposite Polymer Materials, A.I. Nakatani, R.P. Hjelm, M. Gerspacher, R. Krishnamoorti, 2001, ISBN: 1-55899-571-4
Volume 662 Biomaterials for Drug Delivery and Tissue Engineering, S. Mallapragada, R. Korsmeyer, E. Mathiowitz, B. Narasimhan, M. Tracy, 2001, ISBN: 1-55899-572-2

Prior Materials Research Society Symposium Proceedings available by contacting Materials Research Society

Ferroelectric Non-Volatile Memories—Technology and Fundamentals I

Mat. Res. Soc. Symp. Proc. Vol. 655 © 2001 Materials Research Society

An Overview of FeRAM Technology for High Density Applications

Nicolas Nagel, Thomas Mikolajick, Igor Kasko, Walter Hartner, Manfred Moert, Cay-Uwe Pinnow, Christine Dehm and Carlos Mazure

Infineon Technologies, Memory Product Division
Otto-Hahn Ring. 6, 81739 Munich, Germany

ABSTRACT

Ferroelectric random access memories (FeRAMs) are new types of memories especially suitable for mobile applications due to their unique properties such as non-volatility, small DRAM - like cell size, fast read and write as well as low voltage / low power behavior. Although standard CMOS processes can be used for frontend and backend / metallization processes, FeRAM technology development has to overcome major challenges due to new materials used for capacitor formation. In this paper, advantages and disadvantages of different ferroelectric materials and major development issues for high density applications are discussed. Results of a 0.5μm ferroelectric process using $SrBi_2Ta_2O_9$ (SBT) as ferroelectric layer, Pt as electrode material, and 2-layer tungsten / aluminum metallization are discussed.

INTRODUCTION

In recent years ferroelectric memories (FeRAMs) have attracted considerable attention as a possible next generation nonvolatile memory technology [1]. This is due to the fact that FeRAMs promise to combine DRAM benefits like small cell size, low voltage and fast access time with a nonvolatile data storage (see table I). Up to now only low density products have appeared in the market. For high density applications some major technological issues remain to be solved. An overview of these problems is given in the following sections.

Table I. Comparison of FeRAM with DRAM, Flash and SRAM

	FeRAM[a]	DRAM	Flash	SRAM
Read cycles	10^{12} (10^{15})	10^{15}	10^{15}	10^{15}
Write cycles	10^{12} (10^{15})	10^{15}	10^{6}	10^{15}
Access time	100ns (20ns)	40-70ns	40-70ns	6-70ns
Write time	100ns (20ns)	ns	μs	Ns
Relative cell size	2x-5x (1x)	1x	1x	> 4x
Data retention	10 years	None	10 years	None

[a]The numbers in parentheses refer to the prognosticated values for further generations.

Table II. Comparison of PZT and SBT as ferroelectric layer in FeRAMs

	Coercive Voltage	Read/Write Cycles	Leakage Current Density (A/cm^2)	Switched Polarization (μC/cm^2)	Processing Temperature (°C)
PZT	2V @ 50nm	10^{12}	10^{-7}-10^{-6} @ 4V and 200nm	30-60	550-700
SBT	2V @ 200nm	> 10^{14}	10^{-9}-10^{-8} @ 6V and 200nm	15-25	650-800

Either Pb(Zr,Ti)O_3 (PZT) or $SrBi_2Ta_2O_9$ (SBT) is used in current applications. SBT offers the benefits of low fatigue and low voltage operation while PZT offers seemingly easier integration scheme due to its lower processing temperature and higher polarization values (see table II for details).
Ferroelectric memories can be operated in a 2T / 2C (2 transistor / 2 capacitor) or in a 1T / 1C (1 transistor / 1 capacitor) mode. The 2T / 2C mode offers the benefit of one reference capacitor for each cell and therefore an increased reliability margin. However, for high density applications a 1T / 1C approach is essential.
The simplest way to integrate a ferroelectric capacitor is to contact top and bottom electrode via metal lines resulting in a so called offset cell (figure 1b). A smaller bitcell can be obtained when the capacitor is arranged on top of the transistor resulting in the stacked cell structure shown in figure 1a. For high density applications the stacked cell is indispensable, but introduces additional process complexity.

2. INTEGRATION OF A SBT CAPACITOR INTO A HALF MICRON CMOS PROCESS

In this work a 0.5μm, 3.3V CMOS process with 2 layers of metallization was used as a basis to integrate SBT capacitors. The base process uses LOCOS isolation, and retrograde twin wells in the frontend of line and an Al metallization with W contacts and vias as well as CMP planarization in the backend of line. The process described in the following refers to the fabrication of stacked cells. The used test chip allows the evaluation of stacked and offset cells. A summary of the process flow is given in figure 2. After the formation of the transistors and deposition and planarization of the first interlayer dielectric (BPSG), poly plugs are formed to connect the transistor to the capacitor in the stacked cells. Then the oxygen barrier is deposited and structured, followed by the deposition and structuring of the

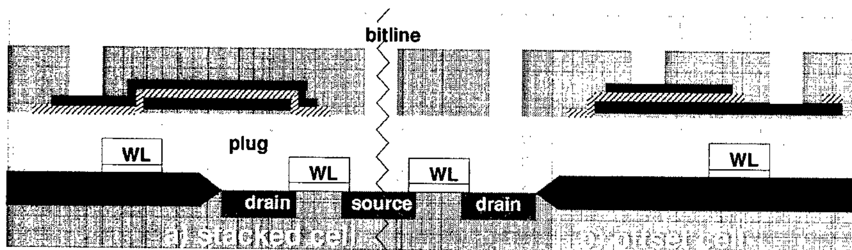

Figure 1. Principle approaches to integrate a ferroelectric capacitor a) stacked cell b) offset cell

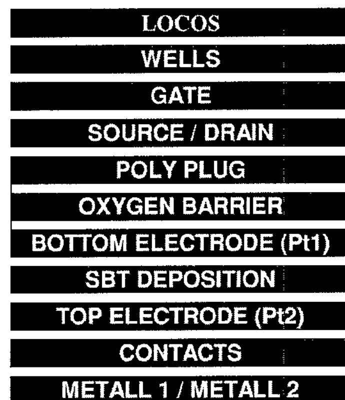

Figure 2. Process flow for the integration of a SBT capacitor into a 0.5µm CMOS process.

bottom electrode (Pt1). Subsequently SBT is deposited by CSD (chemical solution deposition) and subjected to a high temperature crystallization anneal. After deposition of the top electrode (Pt2), capacitors are formed by two mask layer lithography and RIE process for Pt2 and SBT layer respectively. In this way both offset and stacked cells can be characterized on the same chip. An isolation oxide is now deposited and planarized by CMP. After contact holes to Pt and diffusion / poly are etched, the standard BEOL processing as used in the CMOS base process can continue. In figures 3a and 3b SEM cross sections of a typical offset and a typical stacked cell are shown.

The device parameters of the CMOS base process are nearly unaffected. There is slightly increased diffusion as well as some deactivation of dopants [2] resulting from the additional anneals. For 0,5µm technology used here, these effects are negligible. As an example in figure 4, the transfer characteristics of a NMOS transistor after processing of the SBT module and metallization is compared to the transfer characteristics of a reference transistor without SBT module. Only a slight difference is seen between the two curves. For feature sizes below 0.2µm, however, these effects are expected to become more pronounced.

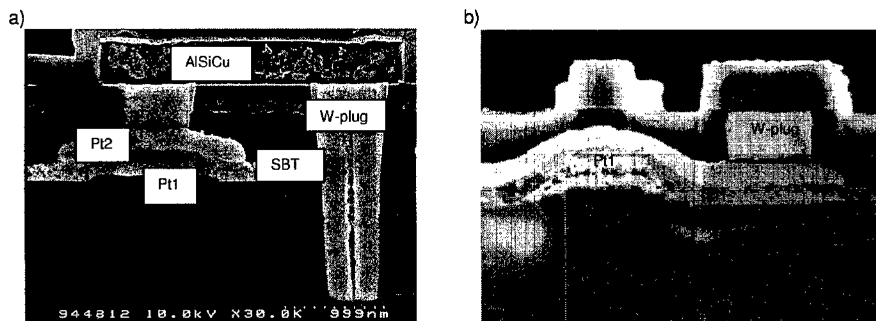

Figure 3. SEM cross section of a) offset cell and b) stacked cell)

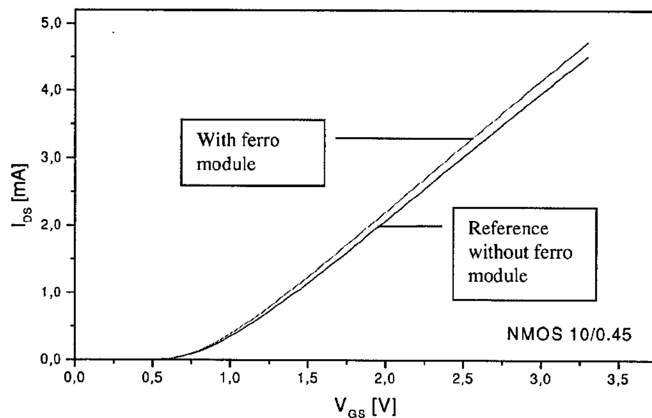

Figure 4. Transfer characteristic of NMOS device with and without ferro module

3. LOW TEMPERATURE SBT PROCESSING

In order to make the requirements for the oxygen barrier as relaxed as possible and in order to minimize the impact of ferroelectric capacitor processing on FEOL results, the processing temperature of the ferroelctric layer has to be kept as low as possible. In figure 5 the hysteresis curves and $2P_r$ values of our standard SBT process (before optimization) are given as a function of SBT annealing temperature. For temperatures below 650°C no ferroelectric behavior is observed. As can be seen from figure 5 a processing temperature of 700°C is necessary to achieve a $2P_r$ value above 10µC/cm^2. Reducing the film thickness increases the $2P_r$ value in the useful temperature regime. At low processing temperature [3] an

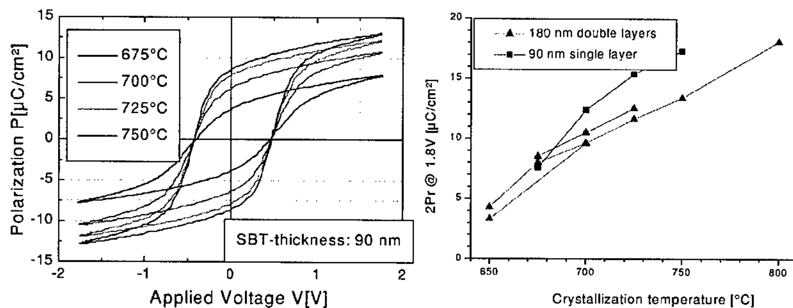

Figure 5. Hysteresis curves and $2P_r$ values of SBT as a function of processing temperature

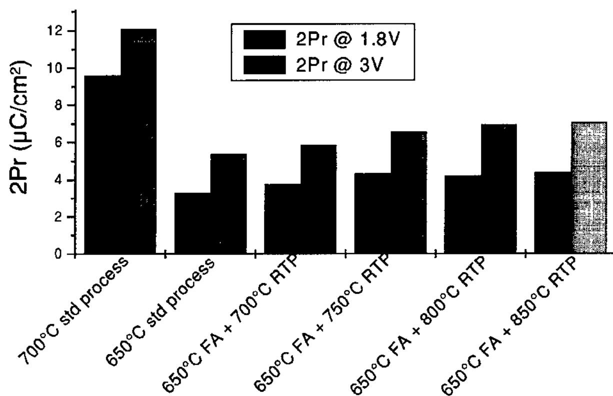

Figure 6. Results from SBT processed at 650°C with an additional RTP step in the temperature range from 700°C to 850°C compared to a 700°C result using standard SBT processing. Note that no further optimization was done in SBT processing.

optimized SBT stoichiometry also improves the $2P_r$ values a little bit. We found another helpful way to increase the $2P_r$ value by introducing an RTP step before doing the crystallization anneal. In figure 6, a 650°C process with additional RTP steps performed at different temperatures is compared to the results obtained by 700°C processing. It can be clearly seen that the higher the RTP temperature the higher is the $2P_r$ value. Since the RTP step is very short compared to the crystallization anneal, the total thermal budget is more favorable compared to a SBT process with higher crystallization temperature. Another way to increase $2P_r$ values at low processing temperatures is to use niobium doped SBT (usually referred to as SBTN). In figure 7 our best process using conventional SBT is compared to our best results using SBTN. In this experiment all SBT optimizations were combined and therefore higher $2P_r$ values are obtained as compared to the figures given earlier in this chapter. The results from the optimized SBT process are comparable to the results using SBTN were we have done no further optimization. SBTN on the other hand has the drawback of a higher coercive voltage, making this material less favorable for low voltage applications. In table III our best results using SBT and SBTN are compared to the best low temperature SBT results reported in the literature. Note that our results were obtained using a integrated process, where bottom electrode, SBT and top electrode were structured. In contrast the other results were obtained on unstructured layers using shadow masks to define the capacitor. The

Table III. Comparison of various low-temperature SBT processes

Company	Sharp	Symetrix	Infineon	Infineon
Material	SBT (200nm)	SBTN (90nm)	SBTN (90nm)	SBT (90nm)
Electrode	Pt / Ta / SiO_2 / Si	Pt / SiO_2 / Si	Pt / Ti / SiO_2 / Si	Pt / Ti / SiO_2 / Si
Process	600°C, 30min, O_2 600°C, 30min, 5 Torr O_2	650°C, 2h, O_2	Structured Electrodes and SBT RTP = 800°C, 10s, O_2 650°C, 90min, O_2	Structured Electrodes and SBT RTP = 800°C, 10s, O_2 650°C, 90min, O_2
Electrical characterization (5V)	$2P_r$ = 17μC/cm^2 V_c= 0.6V I_L= 1x10^{-7} A/cm	$2P_r$ = 15μC/cm^2 V_c = 1.2V I_L=1x10^{-7} A/cm	$2P_r$ = 12μC/cm^2 V_c = 0.9V I_L= 1x10^{-6} A/cm	$2P_r$ = 12μC/cm^2 V_c = 0.6V I_L= 1x10^{-5} A/cm
Reference	[4]	[5]		

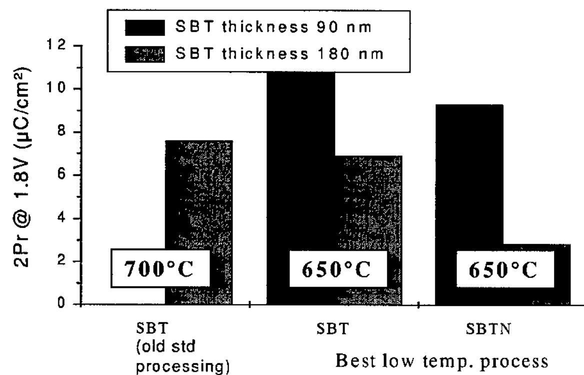

Figure 7. Best 650°C SBT process compared to a non optimized 650°C SBTN and a non optimized standard SBT process at 700°C

lowest thermal budget was reported in [4]. A 600°C process was achieved by using a low pressure SBT anneal. This results in a bismuth loss during annealing and therefore reduces the crystallization temperature of SBT. It will be interesting to see whether these results can be applied to integrated processes. Up to today the authors are not aware of any other results at such low temperatures. The results reported in [5] show higher $2P_r$ values than our results. On the other side a longer annealing time is used and the results were obtained on non integrated SBT.

4. HYDROGEN BARRIER

One of the major integration challenges for ferroelectric films is their hydrogen sensitivity [6-8]. In order to obtain sufficient ferroelectric properties after BEOL processing a barrier layer has to be introduced to avoid the direct contact of the ferroelectric with hydrogen during subsequent temperature steps. A number of barrier materials are proposed in the literature. Table IV gives an overview of these materials. We have applied a novel LPCVD (low pressure chemical vapor deposition) SiN layer to our SBT capacitor. The drawback of this approach is that LPCVD SiN deposition contains hydrogen compounds like NH_3 and SiH_4 by itself. We have used two approaches to solve this problem. First a SiO_2 buffer layer was introduced and second the SiN deposition itself was modified to give as little damage to the capacitor as possible [8]. Figure 8 shows hysteresis curves after capacitor formation, after

Table IV. Comparison of various hydrogen barrier layers

Company	Samsung	Samsung	NEC	Infineon
Material	TiO_2 (50nm)	Al_2O_3 (8 – 10nm)	O_3 – TEOS – SiO_2(300nm) / PE – SiON(60nm) / O_3 – TEOS – SiO2(200nm)	SiO_2 / SiN
Anneal in Hydrogen including ambience	300°C, 30min	450°C, 30min	400°C, 20min, ambience with 50% H_2	430°C, 30min, N_2/ H_2(5%)
Reference	[11]	[6]	[7]	[8]

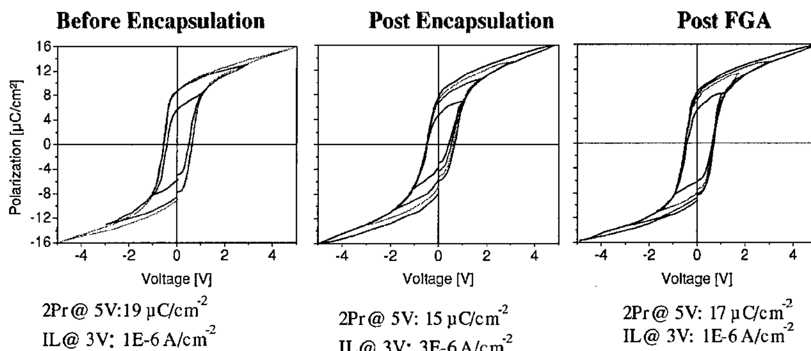

Figure 8. Hysteresis curves after capacitor formation, after hydrogen barrier deposition and after forming gas anneal.

deposition of the SiN hydrogen barrier layer and after an additional forming gas anneal. Even after the forming gas anneal only a very small damage to the capacitor remains. In contrast to other materials like TiO_2 or Al_2O_3, our approach offers the benefit of using only materials that are well established in CMOS production. The hydrogen barrier approach discussed in [7] looks similar but the SiON is deposited by PECVD (plasma enhanced chemical vapor deposition) at lower temperatures. The approach is for PZT capacitors compared to SBT capacitors in our approach [8].

5. OXYGEN BARRIER

For high density applications a stacked capacitor cell (see figure 1a and figure 3b) is necessary. In order to maintain a stable contact between the transistor and the bottom electrode after annealing of the ferroelectric layer, a barrier layer has to be introduced. This barrier layer has to prevent the oxidation of the plug material (in our case polysilicon) and has to prevent reactions between the bottom electrode material and the plug material. Also all reactions between the barrier material itself and either the plug or the bottom electrode have to be avoided. Table V gives an overview of different oxygen barriers proposed in the literature. Besides the barrier approach with Pt-Rh alloys [12], IrO_2 based barriers are used, if the annealing temperature is higher than 600°C in oxygen ambience. It will be interesting to see weather the Pt-Rh alloy results can be applied to integrated processes. In the case of IrO_2

Table V. Comparison of various oxygen barrier stacks

Company	Sharp	TI	Samsung	Infineon	Sharp / University of Virginia
Ferroelectric	SBT	PZT	PZT	SBT	PZT
Top electrode	Pt	IrO_2	IrO_2 / Ir	Pt	Pt
Barrier + bottom electrode	Poly – Si / TaSiN / Ir / IrO_2 / Pt	W / TaAlN / Ir	Ir / IrO_2 / Pt	Ir / IrO_2 / Pt	Poly – Si / Pt – Rh – O_x / Pt – Rh / Pt – Rh – O_x
Temperature	700°C	< 600°C	700°C	700°C, 45min, O_2	650°C
Contact resistance	200 - 400Ω / plug(∅0.5µm)	100 - 200Ω / plug (∅0.5µm)	100 - 200Ω / plug (∅0.5µm)	500 - 700Ω / plug (∅0.6µm)	1.5kΩ / plug (∅0.6µm)
Reference	[9]	[10]	[11]		[12]

based barriers, IrO_2 has the function of the oxygen barrier and Ir prevents the reduction of IrO_2 by the plug material during annealing. Besides the barrier layer itself we have observed that the contact layer system used between plug and barrier layer is of great importance. This is illustrated in figure 9 where yield and resistance values of contact resistance chains containing 100 plugs are given for different contact layers after 675°C anneals and after 700°C anneal respectively. A non conducting contact hole chain was considered as non yielding. The Ti contact layer already shows a largely reduced yield after a 675°C anneal. Ti does not act as a plug material diffusion barrier. As a result interdiffusion with the Ir layer occurs. Depending on time and process temperature the barrier stack is destroyed. TiN, TaN and TaSiN are well known diffusion barriers for the plug material. Low contact resistances after 45minutes at 700°C were obtained. With these results the oxygen barrier stack could be integrated into our stacked capacitor process. Figure 10 shows the results of a hysteresis measurement performed between bottom and top electrode and one performed between Plug and top electrode. This shows, that SBT capacitors can be integrated into stacked capacitor cells. In addition functional stacked capacitor cells were also obtained using this barrier[13].

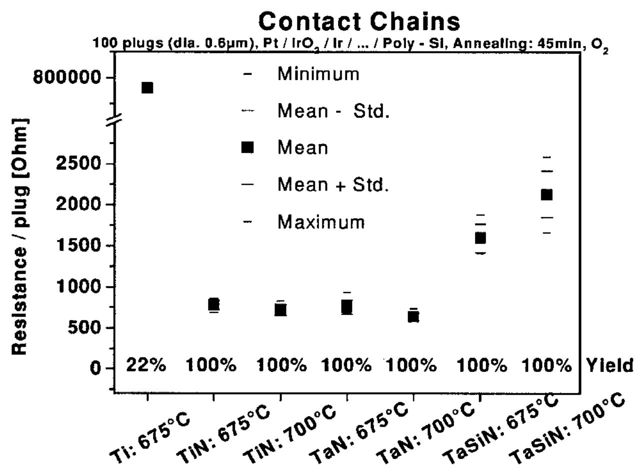

Figure 9. Oxygen barrier yield and contact resistance for different contact layers

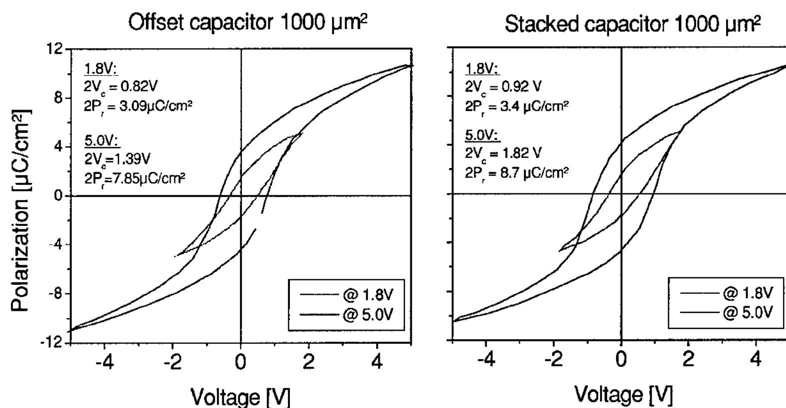

Figure 10. Hysteresis curve of offset capacitor and stacked capacitor fabricated on the same wafer

6. SUMMARY AND CONCLUSIONS

In this paper an overview of the technological issues associated with the development of high density ferroelectric memories were discussed. The three mayor issues are: low temperature processing of the ferroelectric film, hydrogen barriers and oxygen barriers for stacked capacitor cells. For all of these problem fields promising solutions were demonstrated. A low temperature SBT process with processing temperature as low as 650°C was demonstrated. A novel LPCVD SiN hydrogen barrier resulted in excellent capacitor properties after forming gas anneal and an Ir/IrO_2 based oxygen barrier shows stability for 45 minutes at 700°C in oxygen. Combining all these processes, stacked capacitors with good hysteresis curves as well as functional stack cells were demonstrated. This opens the path to the production of high density FeRAMs. If FeRAM wants to compete with DRAM and Flash technology, the technology has to rapidly scale into the sub 0,2μm region. To maintain a sufficient read signal, 3-dimensional capacitors will be necessary to achieve this goal. Additional basic development work with respect to very thin ferroelectric films as well as very thin electrodes, a conformal deposition of ferroelectrics and electrode e.g. by MOCVD processe etc. has to be carried out.

REFERENCES

1. D.J.Jung, B.G.Jeon, H.H.Kim, Y.J.Song, B.J.Koo, S.Y.Lee, S.O.Park, Y.W.Park, and K.Kim, IEDM Technical Digest, 279 (1999)
2. A.H.Perera, W.J.Taylor, and M. Orlowski, IEDM Technical Digest, 835 (1993)
3. M.Moert, G.Schindler, W.Hartner, I.Kasko, M.Kastner, T.Mikolajick C.Dehm, and R.Waser, to be published in Intergrated Ferroelectrics, Proc. 12th Int. Symp. Integrated Ferroelectrics (2000)
4. Y. Ito, M. Ushikubo, S. Yokoyama, H. Matsunaga, T. Atsuki, T. Yonezawa, and K. Ogi, Jpn. J. Appl. Phys. Vol.35, 4925 (1996)
5. V. Joshi, N. Solayappan, J. Celinska, D. McMillan, and C.A. Araujo, to be published in Intergrated Ferroelectrics, Proc. 12th Int. Symp. Integrated Ferroelectrics (2000)

6. I.S.Park, Y.K.Kim, S.M.Lee, J.H.Chung, S.B.Kang, C.S.Park, C.Y.Yoo, S.I.Lee, and M.Y.Lee, IEDM Technical Digest, 617 (1997)
7. T.Nakura, H.Mori, N. Inoue, N.Ikarashi, S.Takahashi, and N.Kasai, IEDM Technical Digest, 801 (1999)
8. W.Hartner, G.Schindler, P.Bosk, Z.Gabric, M.Kastner, G.Beitel, T.Mikolajick, C.Dehm, and C.Mazure, to be published in Intergrated Ferroelectrics, Proc. 12th Int. Symp. Integrated Ferroelectrics (2000)
9. J.Kudo, Y. Ito, S. Mitarai, N.Ogata, S.Yamazaki, H.Urashima, A. Okutoh, M.Nagata, and K.Ishihara, IEDM Technical Digest, 609 (1997)
10. T.S.Moise, S.R.Summerfelt, G.Xing, L.Colombo, T.Sakoda, S.R.Gilbert, A.Loke, S.Ma, R.Kavari, L.A.Wills, T.Hsu, J.Amano, S.T.Johnston, D.J.Vestyck, M.W.Russel, and S.M.Bilodeau, IEDM Technical Digest, 940 (1999)
11. K.Kim, Integrated Ferroelectrics, Vol. 25, 149 (1999)
12. S. Onishi, M.Nagata, S.Mitarai, Y.Ito, J.Kudo, K.Sakiyama, S.B.Desu, H.D.Bhatt, D.P.Vijay, and Y.Hwang, J.Electrochem.Soc., Vol.145, No.7, 2563 (1998)
13. C.Dehm, T.Mikolajick, G.Schindler, I.Kasko, and N.Nagel, unpublished results

Mat. Res. Soc. Symp. Proc. Vol. 655 © 2001 Materials Research Society

Scaled PLZT Thin Film Capacitors with Excellent Endurance and Retention Performance

Fan Chu, Glen Fox and Tom Davenport
Ramtron International Corporation, 1850 Ramtron Drive,
Colorado Springs, CO 80921, U.S.A.
e-mail: fchu@ramtron.com

ABSTRACT

The requirements for future ferroelectric non-volatile memories (FRAM) include lower operating voltages, higher densities and tighter design rules. In order to achieve these requirements the key component of the FRAM device, viz., the $PbZr_xTi_{1-x}O_3$ (PZT) thin film capacitor must be scaled dimensionally to obtain reduced film thickness and capacitor area. This paper presents the ferroelectric performance of RF magnetron sputtered PLZT thin films with thickness scaled down to 1000Å. The switching performance of the thickness scaled PLZT thin films meets the requirements of 1.8V FRAM device. Though PLZT ceramic thin films, of which the fatigue is often a concern, are utilized as non-volatile component, excellent fatigue performance was observed. The scaled PLZT thin film capacitors are fatigue free up to 10^{11} fatigue cycles (E=200kV/cm). The scaled 1000Å PLZT thin films also showed good imprint performance. The opposite-state charge after 10 years baking at 150°C was still above the sensing level. The thickness scaled PZT thin films, showing dramatically improved ferroelectric performance, can be applied to the manufacturing of low voltage FRAM products.

INTRODUCTION

Ferroelectric non-volatile memories (FRAM), which possess the merits of a fast write speed and low power consumption, have been mass-produced for approximately a decade. FRAM memory density has increased and the CMOS design rule for FRAM memory has decreased exponentially since 1988. The primary component for data storage in current FRAM products, such as 64kbit and 256kbit memories, is the ferroelectric capacitor. The core of this capacitor consists of doped (Pb,La)(Zr,Ti) O_3 (PLZT) deposited by RF magnetron sputtering. PLZT and doped PZT ceramic thin films exhibit properties such as high switchable polarization, crystallographically textured growth, and low processing temperatures, which facilitate scaling for higher densities and lower operating voltages. PLZT and doped PZT thin film materials provide a clear path for the development of future generations of FRAM products.

In order to meet the requirements for future ferroelectric non-volatile memories (FRAM), such as lower operating voltages, higher densities and tighter design rules, PLZT thin film capacitors must be scaled down with respect to thickness and area. Scaling in terms of thickness is one of the most interesting topics as the reduction in PLZT thin film thickness can effectively lower the ferroelectric switching voltage. To achieve higher densities and tighter design rules, a reduced capacitor stack height is also necessary in order to facilitate the etching of the PLZT thin film capacitors with smaller lateral dimension. However, scaling requires process modification otherwise degraded ferroelectric performance will be obtained.

Fatigue, defined as the loss of switchable polarization during continuous ferroelectric switching, has been a common concern for PZT based capacitors used in FRAM applications. Extensive technical literature is available on the topic of fatigue for both un-doped and doped PZT thin films [1-5]. It is well established that PZT capacitors with Pt top electrode exhibit severe fatigue [6,7,8]. Replacing the Pt top electrode with Ir metal or oxide electrodes such as IrOx, RuO_2, $SrRuO_3$ and $La_{0.5}Sr_{0.5}CoO_3$ can significantly improve the fatigue [9-12]. But a simple replacement of the electrode material cannot fully eliminate fatigue without sacrificing other performance metrics, e.g., retention, that are required for product performance. In fact the improvement of the IrOx electrode become less evident as the PZT film thickness is reduced indicating a modification on PLZT thin film processing is more important than the alternation of electrode materials.

This paper presents the ferroelectric performance of PLZT thin films with thickness downscaled to 1000 Å. Applying an improved PLZT thin film processing, the scaled PLZT thin films showed not only excellent switching, and fatigue performance but also very good retention and imprint properties.

PROCESSING AND FERROELECTRIC METRIC TERMINOLOGY

2.1 Process description

ULVAC Ceraus ZX-1000 sputtering system is utilized for electrodes and PLZT thin film deposition. The Ti adhesion layer, Pt bottom electrode (BE) and top electrode (TE) as well as IrOx top electrode were DC magnetron sputtered. The Ca and Sr doped PLZT (3/40/60) thin films were RF magnetron sputtered. Rapid thermal annealing technique (RTA) was used to crystallize PLZT thin films. The annealing temperature was 550°C ~ 750°C. The discrete (50x50μm) capacitors were formed using photolithographic/etching technique.

2.2 Ferroelectric metric terminology

Q_{SW}: The average pulse switched charge density (switachable charge), which approximately equals twice the remanent polarazation ($2P_r$) for a dynamic hysteresis loop measurement. The standard 4-pulse sequence used to measure the charge components of the capacitor consists of pulses with a 1 μs pulsewidth and 1s delay between pulses. Q_{SW} data were collected from 3 sites, top, center, and flat sites, of each 6" wafer.

$V_{90\%}$: Electrical potential applied to the capacitor that induces 90% of the saturated Q_{SW} value. $V_{90\%}$ data were collected from 3 sites, top, center and flat sites, of each 6" wafer.

Q_{SS}: Same-state charge remaining after a memory state is baked at 150°C and read at room temperature. Q_{SS} (10 years) = extrapolated same-state charge post 10 year baking at 150°C. Q_{SS} reflects the data retention capability of the thin film capacitor. Q_{SS} data were collected from 3 sites, top, center and flat sites, of each 6" wafer.

Q_{OS}: Opposite-state charge remaining after a memory state is baked at 150°C, reset to the opposite-state and read after a time delay. Q_{OS} (10 years) = extrapolated opposite state charge

post 10 years baking at 150°C. Q_{OS} reflects the imprint performance of the thin film capacitor. Q_{OS} data were collected from 3 sites, top, center and flat sites, of each 6" wafer.

RESULTS AND DISCUSSION

To achieve low operating voltage and high density, the thickness of the PZT capacitor needs to be reduced so that the ferroelectric capacitor stack height will not be too high and hopefully $V_{90\%}$ can be reduced if a simple reduction in thickness does not affect the switching characteristics such as switchable charge and coercive field. Figure 1 shows switchable charge (Q_{SW}) and $V_{90\%}$ as a function of PLZT thin film thickness. The reduction in PLZT thin film thickness involves no process modification and the structure of the PLZT thin film capacitor is Pt BE / PLZT/Pt TE. The thin film processing was optimized for 2200 Å PLZT films. It can be seen that $V_{90\%}$ does decrease with the thickness of the PZT thin film but only to certain thickness such as around 1700Å. Further reducing the thickness leads to increase in $V_{90\%}$ indicating that the switching characteristic of the PLZT thin films is changed. Therefore, a re-optimization of PLZT thin film processing is required.

Figure 2 shows the switching performance of scaled PLZT thin films prepared using an improved thin film processing. The thickness of the scaled PLZT thin film is 1000Å. Compared with 1000 Å PLZT thin film without process modification, the improved 1000Å PLZT thin films showed much better switching property. $V_{90\%}$ reduced from 3.6 V to 1.8 V, and Q_{SW} at 1.8 V increased 50% (from 15 $\mu C/cm^2$ to 23 $\mu C/cm^2$). The error bars in the graph not only reflect the variation across a 6" wafer but also include wafer-to-wafer variation as the data were collected from two 6" wafers processed using the same condition. Figure 3 illustrates the fatigue performance of the scaled PLZT thin films stressed under 5V and 3V fatigue cycles (up to 10^9 cycles). Since the thickness of the PLZT thin film is 1000 Å, the applied electric fields during fatigue process are 300kV/cm (for 3V) and 500kV/cm (for 5V). Under 5V fatigue stress, the switchable charge decreases with increasing fatigue cycles. At 5V 10^9 cycles, the switchable

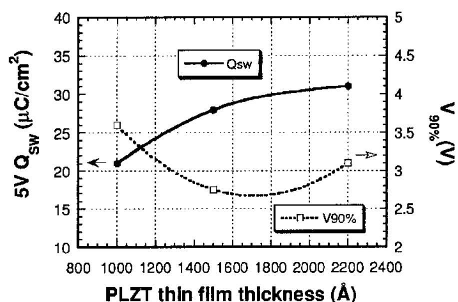

Figure 1. Switchable charge and $V_{90\%}$ as a function of PLZT thin film thickness, showing that, without process optimization, a degraded switching performance for thickness downscaled PLZT thin film capacitors is obtained. PLZT thin film capacitor structure: Pt BE/PLZT/Pt TE

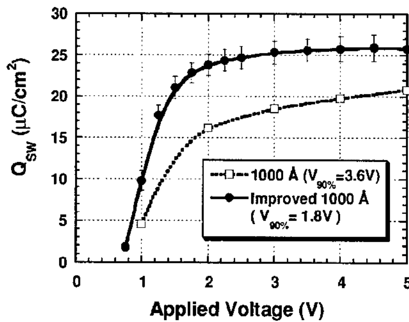

Figure 2. *Switchable charge as a function of applied voltage, showing excellent switching performance of the scaled PLZT thin films. Conventional: Pt BE/PLZT/Pt TE structure. Improved: Pt BE/PLZT/IrOx TE structure.*

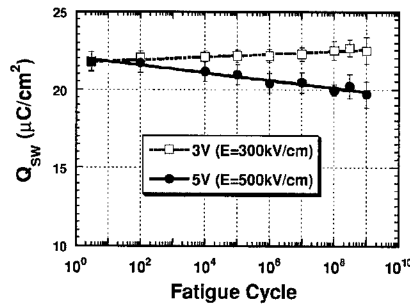

Figure 3. *Swichable charge as a function of 3V and 5V fatigue cycles, showing that the scaled PLZT thin film can stand high electrical field fatigue stress. Pt BE/PLZT/IrOx TE structure.*

charge (Q_{SW}) lost about 10% compared with its initial value. The fact that no electrical breakdown occurs during 5V (500kV/cm) fatigue process suggests that the quality of the scaled 1000 Å PLZT thin film is very high. Under 3V fatigue stress, the scaled PLZT thin films are fatigue free up to 10^9 cycles. As a matter of fact, the switchable charge even gained about 3.6% after 3V 10^9 fatigue cycles. Since the 1000 Å PLZT thin films discussed here are for 1.8V application, 3V fatigue stress is a rather severe fatigue condition. According to the voltage acceleration fatigue model [13], the scaled PLZT thin films should be fatigue free at least up to 10^{11} cycles at 1.8V.

Figure 4 shows switchable charge as a function of 2V fatigue cycles. It can be seen that, as predicted from the voltage acceleration model, the 1000 Å PLZT thin film is indeed fatigue free up to 10^{11} fatigue cycles when the film is stressed at 2V (E=200kV/cm). The improved fatigue performance is attributed to the optimization of Pb concentration [14] and crystallization temperature of PZT thin films. Figure 5 compares the 3V fatigue performance of PLZT thin films prepared with and without process optimization. Even though IrOx thin film is applied as

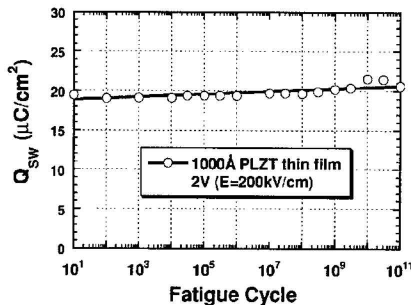

Figure 4. *2V switchable charge as a function of 2V fatigue cycles, showing that the scaled PLZT thin film is fatigue free up to 10^{11} fatigue cycles. Pt BE/PLZT/IrOx TE structure.*

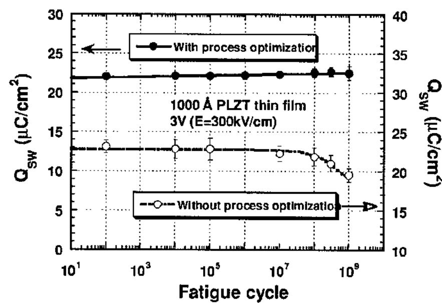

Figure 5. *3V swichable charge as a function of 3V fatigue cycles, showing the effect of process optimization on PLZT thin film capacitors with IrOx TE. Pt BE/PLZT/IrOx TE structure.*

top electrode, without PLZT thin film process optimization, the switchable charge (Q_{SW}) lost about 15% after 10^9 fatigue cycles. Whereas PLZT thin film capacitors prepared using optimized process showed no loss in Q_{SW}, indicating that a carefully optimized PLZT thin film processing is essential for improved fatigue performance.

For FRAM applications, a good switching and fatigue properties of PLZT thin films is not enough. Retention performance, which is defined as the ability to maintain a stored data state between the time of a write pulse and a subsequent read, is another critical performance metric. S.D. Traynor et al. introduced a measurement technique to quantitatively evaluate the retention performance, both same-state and opposite-state, of ferroelectric thin film capacitors, allowing the determination of the usability of the ferroelectric thin film in integrated ferroelectric memory [15]. Figure 6 shows the 1.8V retention performance of same-state charge (Q_{SS}). Q_{SS} is very stable with increasing baking time at 150°C. The extrapolated Q_{SS} post 10 years baking at 150°C is 18 μC/cm^2, which is much higher than the sensing level. Figure 7 shows the aging performance of 1.8V opposite-state charge (Q_{OS}). Though Q_{OS} decreases with increasing baking time at 150°C, the extrapolated Q_{OS} post 10 years baking at 150°C is 8.0 μC/cm^2, which is still higher than the sensing level of 6.0 μC/cm^2. This indicates that the 1000 Å PLZT thin film capacitors is ready for next generation FRAM device such as low operating voltage FRAM.

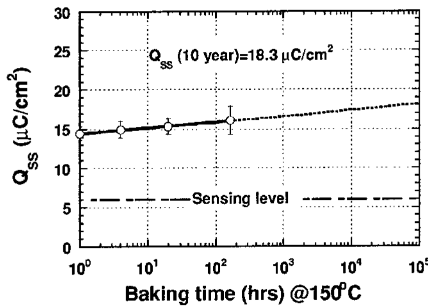

Figure 6. Same-state charge (Q_{SS}) as a function of baking time at 150°C, showing stable Q_{SS} over long time baking at high temperature. Pt BE/PLZT/IrOx TE structure.

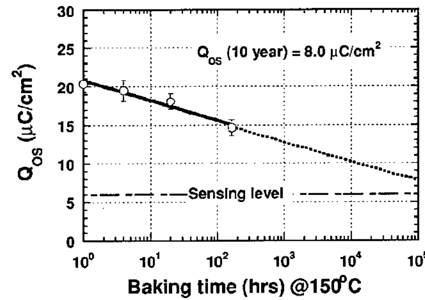

Figure 7. Opposite-state charge (Q_{OS}) as a function of baking time at 150°C, showing Q_{OS} still above sensing level after 10 years baking at 150°C. Pt BE/PLZT/IrOx TE structure.

CONCLUSIONS

Excellent ferroelectric performance including switching, endurance and data retention performance was obtained on RF magnetron sputtered PLZT thin films with thickness scaled down to 1000Å. Low voltage switching property ($V_{90\%}$ =1.8V) with decent switchable charge (1.8V Q_{SW} = 20~24 μC/cm^2) was obtained. The scaled PLZT thin films were fatigue free up to 10^{11} fatigue cycles at 200kV/cm electrical stress field. Good retention performance was obtained on the 1000Å PLZT thin films. After 10 years baking at 150°C, the opposite-state charge, a metric that reflects the imprint performance, was still higher than the sensing level of FRAM device.

ACKNOWLEDGEMENTS

The authors are grateful to ULVAC Japan Ltd for providing ZX-1000 sputtering system. The authors also greatly appreciate the contributions of Mr. Rick Bailey on electrical characterizations.

REFERENCES

1. R. D. Nasby, J. R. Schwank, M. S. Rodgers, and S. L. Miller, *Integrated Ferroelectrics*, **2**, 91(1992).
2. E. L. Colla, D. V. Taylor, A. A. Tagantsev, and N. Setter, *Applied Physics Letters*, **72**(19), 2478(1998).
3. I-Wei Chen, and Y. Wang, *Applied Physics Letters*, **75**(26), 4186(1999).
4. M. Brazier, S. Mansour, and M. McElfresh, *Applied Physics Letters*, **74**(26), 4032(1999).
5. S. A. Mansour and R. W. Vest, *Integrated Ferroelectrics*, **1**, 57(1992).
6. X. F. Du and I. -Wei Chen, *Journal of Applied Physics*, **83**(12), 7789(1998).
7. S. H. Kim, D. J. Kim, J. G. Hong, S. K. Streiffer, and A. I. Kingon, *Journal of Materials Research*, **14**(4), 1371(1999).
8. F. Chu, G. Hickert, T. D. Hadnagy, and K-K. Suu, *Integrated Ferroelectrics*, **26**, 47(1999).
9. N. Izumi, Y. Fujimort, T. Nakamura, and A. Kamisawa, *IEICE Transactions on Electronics*, **E81-c**(4), 513(1998).
10. K. Matsuura, K. Takai, T. Tamura, H. Ashida, and S. Otani, *IEICE Transactions on Electronics*, **E81-c**(4), 528(1998).
11. I. Stolichnov, A. Tagantsev, and N. Setter, *Applied Physics Letters*, **75**(12), 1790(1999).
12. J. Yin, T. Zhu, Z. G. Liu, and T. Yu, *Applied Physics Letters*, **75**(23), 3698(1999).
13. T. D. Hadnagy, S. D. Traynor, and D. I. Dalton, *Integrated Ferroelectrics*, **16**, 219(1997).
14. F.Chu and G. Fox, *12th International Symposium on Integrated Ferroelectrics (ISIF2000)*, Session D, 18C, March 12-15, 2000, Aachen, Germany
15. S. D. Traynor, T. D. Hadnagy, and L. Kammerdiner, *Integrated Ferroelectrics*, **16**, 63(1997).

Mat. Res. Soc. Symp. Proc. Vol. 655 © 2001 Materials Research Society

Nanoscale electromechanical phenomena in ferroelectric thin films

C. S. Ganpule, A. L. Roytburd, V. Nagarajan, A. Stanishevsky, J. Melngailis, E. D. Williams, and R. Ramesh
Materials Research Science and Engineering Center, University of Maryland, College Park, MD 20742

ABSTRACT

Focused ion beam milling was used to fabricate ferroelectric islands in Pb-Zr-Ti-O thin films. The islands ranged in size from 200μm×200μm to 0.3μm×0.3μm. The inverse piezoelectric effect was studied in these islands as a function of their size by tracking the surface displacement of the top electrode of the island (under an applied electric field) using an atomic force microscope (AFM). It was found that there was a substantial increase in the piezoresponse as the size of the island decreased below 100μm×100μm. This increase was attributed to the elastic deformation of the substrate.

INTRODUCTION

Ferroelectric (FE) films are increasingly being used as micro-actuator elements in micro-electromechanical systems (MEMS). In such applications it is desirable to get the maximum surface displacement in the ferroelectric film-substrate couple for a given applied electric field. Constraints induced by the substrate generally decrease the piezoresponse of films [1,2]. This is true if one considers the electrically induced strains in the film. However, it is possible to get surface displacement of the film-substrate couple, which is comparable or larger than that of a free-standing film. This is due to the elastic deformation of the substrate and its contribution to the film-substrate surface displacement.

EXPERIMENTAL DETAILS

Experimental evidence of the important role of a substrate follows from atomic force microscopy (AFM) investigation of the piezoresponse of delineated islands of a ferroelectric film as a function of its in-plane size. $Pb_{1.0}(Nb_{0.04}Zr_{0.28}Ti_{0.68})O_3$ (PNZT) thin films with a thickness of 1600Å and grain size of ~1000 Å were deposited by sol-gel processing onto platinized Si wafers with a bottom electrode of the conducting oxide, La-Sr-Co-O. The films had a symmetric electrode structure with top electrodes of Pt on La-Sr-Co-O. A strong structural orientation with the preferred c-axis along the normal to the films was observed. Test capacitor structures in the size range of 200μm -0.3μm were

fabricated by focused Ga ion beam milling [3,4]. This structure in which the ferroelectric layer surrounding it was milled out to produce an island like geometry is shown in figure 1. As a comparison, structures with similar size but with only the top electrode patterned by focused ion beam milling were produced, as illustrated in figure 2.

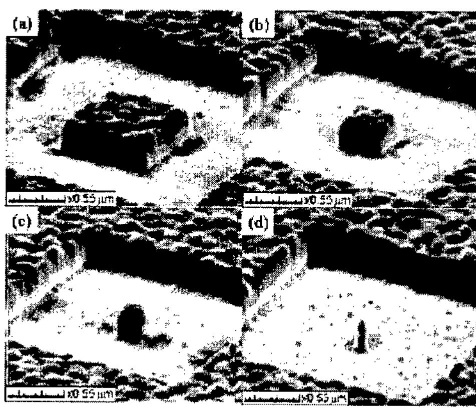

***Figure 1**. Scanning ion beam image of ferroelectric PNZT island milled by focused ion beam milling (size of islands: (a) 0.8μm x 0.8μm, (b) 0.4μm x 0.4μm, (c) 0.25μm x 0.25μm and (d) 0.07μm x 0.07μm).*

An accelerating voltage of 50kV, dose of $8x10^{17}$ ions/cm^2 and a beam size of 6-20nm (MICRION 2500) was used to delineate the structures. As milled structures showed ion-beam induced damage but a 650 °C anneal for 30 minutes recovered the properties.

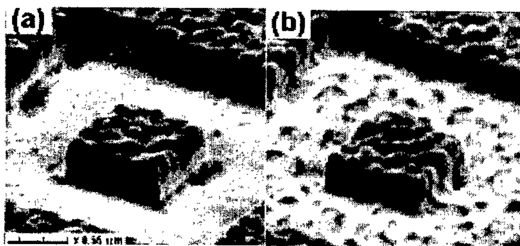

***Figure 2**. (a) Scanning ion beam image of ferroelectric PNZT island milled by focused ion beam milling (size of island: 0.8μm x 0.8μm) (b) Scanning ion beam image of a structure with only the top electrode milled by focused ion beam milling.*

The AFM technique to measure piezoresponse has been described elsewhere [4,5]. The technique is based on the detection of the piezoelectric response of a ferroelectric thin film when probed using an alternating current (ac) field. The amplitude and phase of

the film vibration give an estimate of the magnitude and sign of the piezoelectric coefficient and hence that of the local polarization. A direct current (dc) voltage is applied to the top electrode through the AFM tip to write the domain state. In our experiments a small ac field was superimposed on the dc field to read the domain states. Thus a hysteresis loop is traced out by plotting the tip vibration signal as a function of the write voltage (figure 3). It is important to note that the AFM piezoresponse technique measures the dynamic surface displacement under a constant dc bias. By normalizing this displacement with the thickness of the FE film one can arrive at the d_{33} values under a constant probing ac field.

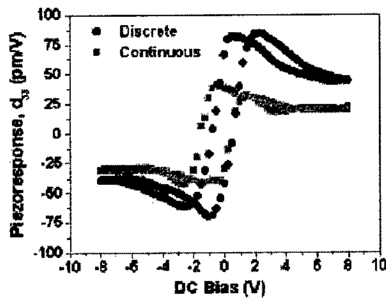

Figure 3. *Typical piezoresponse loop of a structure with island geometry (labeled 'discrete') as compared to a structure with only top electrode milled (labeled 'continuous'). Size of structures: 0.3µm x 0.3µm*

The piezoresponse of the ferroelectric structures was studied as a function of the size of the island and this is plotted in figure 4. As a comparison, the piezoresponse of structures with only the top electrode patterned (figure 2) but with the ferroelectric layer continuous was also studied as a function of the electrode size. While in this case the piezomodulus

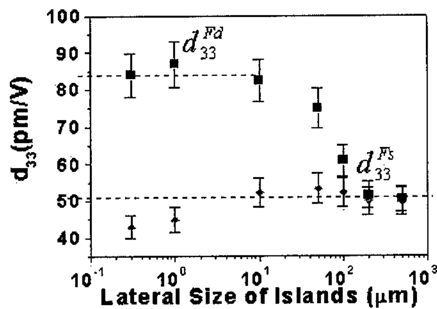

Figure 4. *Piezoresponse (d_{33}(pm/V)) as a function of the lateral size of the island (■). Also shown is the data for structures with only top electrode milled out (◆).*

showed only a small decrease as the size of the patterned top electrode decreased, the piezomodulus d_{33} of the constrained film, in which the ferroelectric has been milled down all the way till the lower Pt/LSCO interface, shows a step-like dependence on the in-plane size of FE islands.

DISCUSSION

The fact that d_{33} increases by more that 35% as the island size decreases from 200μm to ~ 100μm cannot be explained by the change of stress state in the film. The in-plane dimension of the film is much larger than its thickness (l/h > 100). Therefore, the relaxation of stress near the film edge does not change the average strain in the film. To understand this effect we have analyzed the elastic response of the substrate to the piezodeformation in the film [6]. It is possible to show that for a thin film on a thick substrate, the d_{33} as measured through the strain in the film is given by

$$d_{33}^{Fs} = d_{33} - \frac{2s_{13}^F}{s_{11}^F + s_{12}^F} d_{13} \qquad \ldots(1)$$

where $d_{13}=d_{23}$ and d_{33} are the components of piezomodulus of the tetragonal FE crystal. s_{11}^F, s_{12}^F and s_{13}^F are the components elastic compliance of the tetragonal ferroelectric film; and s_{11}^s and s_{12}^s that of the substrate layer. The d_{33} as measured through the surface displacement of the film-substrate couple is given by

$$d_{33}^{Fd} = d_{33} - \frac{2s_{13}^F}{s_{11}^F + s_{12}^F} d_{13}\left(1 - \frac{s_{12}^s}{s_{13}^F}\right) \qquad \ldots(2)$$

Thus the specific increase in the piezoresponse due to the elastic deformation of the substrate is given by

$$\Delta d = d_{33}^{Fd} - d_{33}^{Fs} = \frac{2s_{12}^s}{s_{11}^F + s_{12}^F} d_{13} \qquad \ldots(3)$$

For $s_{12}^s = -2.1\times10^{-12} m^2N^{-1}$, $s_{11}^F + s_{12}^F = 6\times10^{-12} m^2N^{-1}$ and $d_{13} = 59\times10^{-12} m/V$ [7], $\Delta d = 41.3\times10^{-12} m/V$. The deformation of the substrate becomes essential if the in-plane dimension of the film, l, becomes smaller than the substrate thickness. Then the elastic field does not reach the boundary of the substrate and the effect of external clamping of the substrate becomes unimportant. However, d_{33}^{Fd} approaches d_{33}^{Fs} for island sizes comparable to or larger than the substrate thickness.

CONCLUSIONS

Thus, we obtain the explanation for the substantial increase in the piezoresponse of a thin ferroelectric film on a thick substrate as a function of decreasing in-plane size of the film. This effect is a manifestation of the elastic substrate response to the piezodeformation of a constrained ferroelectric film. The film surface displacement under

electrical field depends on in-plane size of the film as well as on elastic properties and external clamping of a substrate while the piezostrain of the film does not depend on these parameters if the substrate is much thicker than the film. Finally, it is important to note that the electromechanical responses of the thin piezoelectric film can be significantly altered by changing the lateral dimensions of the film in contact with the substrate. Indeed, in recent studies, we have observed that 90° domain walls, which typically do not move in thin films, can actually move when the in-plane dimensions are in the sub-micron range. These results therefore have very significant implications for MEMS devices as well as sub-micron memory devices. Clearly, considerable further research is necessary.

ACKNOWLEDGEMENTS

This work is supported by NSF under grants DMR 9632521 and DMR 9903279

REFERENCES

1. K. Lefki and G. J. M. Dormans, J. Appl. Phys. **76**, 1764 (1994).
2. A. L. Roytburd, S. P. Alpay, V. Nagarajan, C. S. Ganpule, S. Aggarwal, E. D. Williams and R. Ramesh, Phys. Rev. Lett. **85**, 190 (2000).
3. J. Melngailis, J. Vac. Sci. Technol B **5**, 469 (1987).
4. C. S. Ganpule, A. Stanishevsky, Q. Su, S. Aggarwal, J. Melngailis, E. Williams, and R. Ramesh, Appl. Phys. Lett., **75**, 409 (1999).
5. J. A. Christman, R. R. Woolcott, Jr., A. I. Kingon, and R. J. Nemanich, Appl. Phys. Lett., **73** , 3851 (1998). G. Zavala, J. H. Fendler and S. Trollier-McKinstry, J. Appl. Phys. **81**, 7480 (1997).
6. A. L. Roytburd, C. S. Ganpule, A. Stanishevsky, E. D. Williams, J. Melngailis, and R. Ramesh, unpublished.
7. M. J. Haun, E. Furman, S. J. Jang and L. E. Cross, Ferroelectrics **99**, 45 (1989).

Mat. Res. Soc. Symp. Proc. Vol. 655 © 2001 Materials Research Society

Preparation of sub-100nm thickness PZT thin films with Chemical Solution Deposition method for low voltage operation

Yong Kyun Lee, June Key Lee, Chang Jung Kim, Insook Yi, Ilsub Chung

Microelectronics Lab, Material and Device Sector, Samsung Advanced Institute of Technology, P.O. Box 111, Suwon, Korea 440-600
Phone:82-31-280-9336, fax:82-31-280-9349, Email : yklee@sait.samsung.co.kr

ABSTRACT

PZT thin films with a thickness of 70 nm were successfully fabricated using a modified solution combined with $PbTiO_3$ seed layer. Throughout various approaches, we found that the microstructure of PZT thin film plays an important role in determining the electrical properties such as hysteretic properties and leakage currents, particularly when the thickness is below 100 nm. We modified the precursor system to improve the microstructure in PZT thin film. In addition, we also adopted a thin $PbTiO_3$ seed layer to enhance the initial nucleation density. Finally, we could obtain good electric properties similar to those obtained from 240 nm thick PZT film. The hysteretic properties is excellent enough to operate at a low voltage (2V) for a high density FRAM application.

INTRODUCTION

PZT is one of the well-known ferroelectric material for the non-volatile memory application due to the high remnant polarization value. A wide variety of preparation techniques have employed to produce PZT thin films. Among these methods, the CSD(chemical solution deposition) process offers several advantages, including low processing temperature, composition control, uniform homogeneity, ease of fabrication over large areas, and low cost.[1-3] Recently, 4Mbit FRAM was successfully fabricated using PZT thin film, in which about 200 nm thick PZT film was applied for 3.3V operation.[4] However, as for the higher density FRAM, it is necessary to reduce the PZT film thickness due to not only the process issue but also the operating voltage. In spite of such requirements, there were only limited efforts addressed to reduce PZT film thickness.

Generally, it is hard to fabricate PZT thin film with the thickness below 100nm. Meng et. al. varied thermal annealing route with different single-annealed-layer in thickness from the same precursor solution. They found that the degree of (111) orientation in films increases as the

thickness of single-annealed-layer decrease. They could make PZT thin film with the thickness of 40 nm, but the hysteretic properties seemed to be very leaky.[5] Soyama et. al. deposited PZT thin films with thickness of 90 nm by increasing the initial nucleation density of PZT precursor gel film using modified sol-gel solutions.[6] Similarly, Wouter et. al. demonstrated a 75 nm thick PZT film using modified CSD solution.

In this study, we deposited PZT thin films with the thickness around 100nm, by using three different methods. Firstly, PZT thin films were prepared with a conventional method by just changing the spin-coating parameter and diluting solution concentration.[7] Secondly, we utilized etch-back and wet cleaning technology to reduce PZT film thickness.[8] Finally, we modified the sol-gel solution to control the network structure. In an effort to enhance microstructural properties, we employed $PbTiO_3$ (PTO) seed layer.

EXPERIMENTAL PROCEDURES

The sol-gel solutions were prepared from lead acetate trihydrate, titaniun tetra-iso-propoxide, zirconium tetra-n-propoxide, acetic acid and n-propanol.[7] In order to suppress the formation of secondary phases, 15% excess Pb precursor was added. Compositional Zr/Ti ratio was 52/48 and PTO seed layer was used to enhance the crystallization of PZT films. PZT films were deposited onto Pt(270nm)/Ti(30nm)/SiO_2(250nm)/Si(100) substrate. For the etch-back and wet cleaning experiment, 240nm thick PZT films were utilized and detailed process is described reference 7. After depositing the top Pt electrode with a thickness of 100nm, top Pt and PZT films were consecutively etched by Tegal® 6540 dry etcher with the gas mixture of Ar-Cl_2-CF_4.[9] The size of patterned capacitors were 100 x 100 μm^2.

The physical properties of the films were characterized using X-ray diffraction and field emission scanning electron microscope (FE-SEM). Electrical properties including ferroelectric characteristics were evaluated using Radiant Technologies RT66A system and Kiethely I-V measurement system. The thickness of PZT films were measured by Nanometrics.

RESULTS AND DISCUSSION

At first, we tried to reduce the PZT film thickness either by increasing rpm of the spin coater or by using the diluted solution. As shown in the figure 1, for the thickness below 130 nm, all of the images obtained using FE-SEM give secondary phases at the surface or at the grain boundaries. The hysteresis loops of those samples are given in the figure 2. The loops were measured with 3V triangular signal. However, the hysteresis loops were not measurable with 5V signal due to the high leakage current. The obtained results indicated that the conventional approach yields a poor crystallinity and unsaturated hysteresis loop. Since we believe the microstructure plays an important role in determining the electrical properties of the PZT thin

film, we need to find an alternative approach which can improve the microstructure. Therefore, we tried a different approach, namely, etch-back and wet cleaning method to improve the microstructure even for the thin PZT. A blank etch using ICP and then followed wet cleaning yields a reduced thickness of PZT thin film. By applying a multiple procedure, we can obtain a desired thickness from the original thickness. The surface image after etch-back and cleaning is given in the figure 3. The surface is clean without showing any secondary phases. The electrical properties shown in figure 4 clearly indicated better electrical properties in terms of leakage current and Q-V response compared with those obtained from the conventional method.

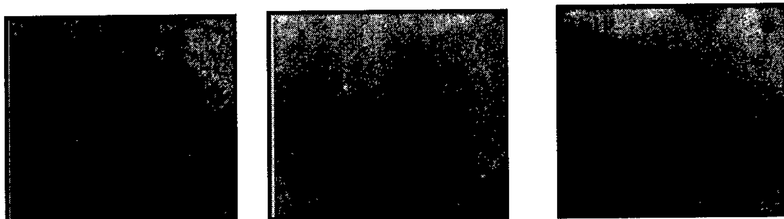

Fig. 1 FE-SEM images of PZT(52/48) films with Various thickness

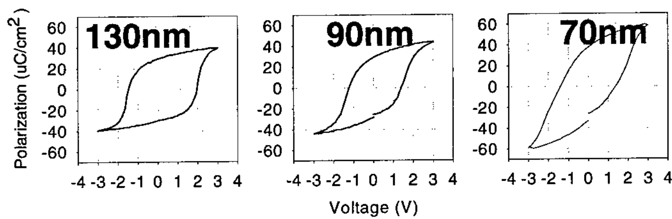

Fig. 2 Hysteresis Loops of PZT (52/48) films with various thickness

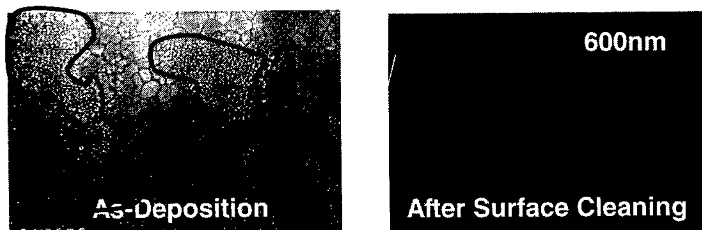

Fig. 3 The FE-SEM images of PZT Etch-back And surface cleaning process

The saturation tendency in the Q-V behavior improved but the leakage current in I-V characteristics is still high enough to modify the hysteresis loop, which is particularly serious when the thickness of the PZT film is reduced around 70 nm (refer to figure 4).

The etch-back and surface cleaning approach gives a good surface morphology but still problem incorporated with the high leakage current. That means the additional improvement in the crystallinity is necessary to suppress the leaky behavior.

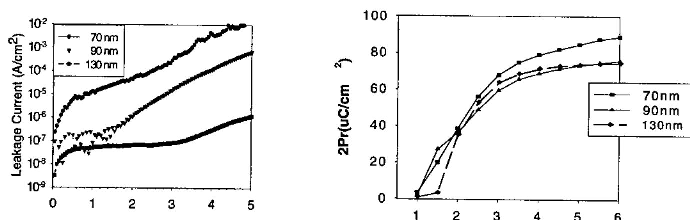

Fig. 4 Electronic properties of PZT films with etch-back and surface cleaning process

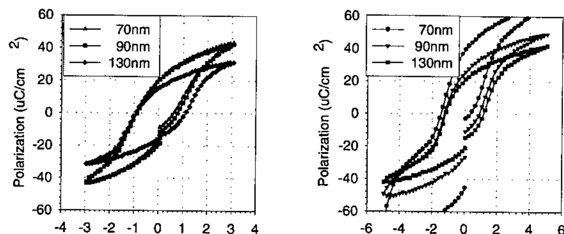

Fig. 5 Hysteresis Loops of PZT films with Etch-back and Surface cleaning process

Here remind us is to use PTO seed layer in order to control the initial nucleation stage. It is well known that the presence of a seeding layer strongly affects the crystallization temperature, microstructure, and the texture of the films. Ishikawa et al. applied PTO seed layer to provide a nucleation site for PZT crystallization [10]. They found that the introduction of the seeding layer lowers the crystallization temperature and makes it possible to obtain films composed of very fine grains. Similarly, Cattan et. al. studied the role of PTO seed layer as a function of the thickness. They insisted the gradual evolution of the lattice parameters in the nucleation stage of PTO films. They found that the PZT layers that grew on PTO buffer layers were dramatically influenced by the plane orientations at the surface of PTO.[9] When we studied the role of PTO

seed layer on the PZT thin film, we found a improved microstructure and a leakage behavior. At present, it is not clear yet why the presence of PTO seed layer yielded the better response in the hysteresis loop and Q-V curve. However, one possible explanation is a increase in Ti/Zr ratio due to the out-diffusion of Ti from PTO layer. The other explanation is attributed to the fact that the presence of PTO seed layer would modify the nucleation stage by enhancing the nucleation sites. Since the vacancy caused by volatile Pb and out-diffused Pb to Pt electrode, PZT thin film below 100nm thickness would be hard to exhibit good ferroelectric properties.

The final approach to obtain ultra thin PZT film for the thickness below 100 nm is done by modifying solution. XRD patterns given in the figure 6 indicates that (100) intensity is dramatically suppressed in PZT film made using the modified solution compared to that made using the normal solution. Such a variation in a microstructure due to the solution change is similar to that due to the presence of PTO seed layer. That means the new solution would play a similar role as the PTO seed layer did during the initial nucleation. The electrical properties such as hysteresis loop, Q-V and I-V are given in the figure 7. The hysteresis loop was able to measure even with 5V without any distortion because of the low leakage currents

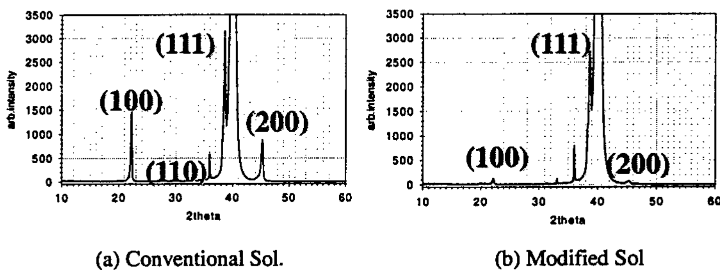

(a) Conventional Sol. (b) Modified Sol

Fig. 6 XRD patterns of PZT con.(conventional) Sol and mod.(Modified) solution PZT(52/48), PZT on Pt

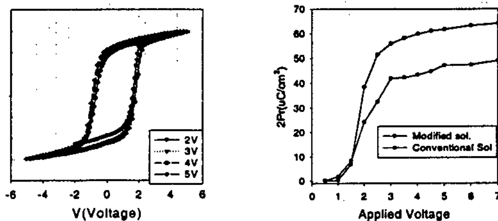

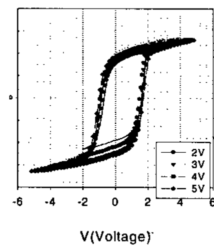

(a) PZT(mod. Sol)/PTO

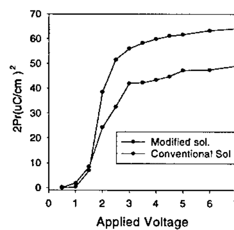

(b) Q-V curves

Fig. 7 Electronic Properties of PZT(52/48) on PTO seed layer

In addition, the multiple measurement varying applied voltage from 2 V to 5V indicates the early saturation in the polarization at 2V. The Q-V response in terms of the switching charge shows a quick response as well as the higher value of switching charge. The results indicate that we can obtain ultra thin PZT with the thickness of 70 nm by combining PTO seed layer with the modified solution.

CONCLUSION

In order to deposit sub-100nm PZT thin film, we have tried three methods. In conventional method with varying solution concentration, we could not obtain secondary phase free PZT film. By performing etch-back and wet cleaning process, secondary phases were completely removed but PZT films were not applicable because of high leakage currents. In order to improve microstructural properties, PTO seed layer and modified solution were attempted. From this approach, we could finally obtain excellent ferroelectric properties of PZT thin film with the thickness of 70nm. Hysteretic properties, and leakage currents is sufficient for low voltage FRAM operation

REFERENCE

(1) S.L. Swartz, IEEE Trans. Electron. Insul. 25 (1990) 935.

(2) I.H. Parker, A.F. Tasch, Circuits Devices Mag. 6 (1990) 17.

(3) L.A. Burill, K.G. Brooks, J. Appl. Phys. 75 (1994) 4501.

(4)D.J. Jung, et.al., IEDM Technical Digest, pp. 279-282. 1999

(5) X.J.Meng, et.al., "Dependence of texture development on thickness of single-annealed-layer in sol-gel derived PZT thin films", Thin solid Films, 368, 22-25, 2000

(6) N. Soyama, et. al., "Preparation of PZT Thin Films for Low Voltage Application by Sol-Gel Method", to be published

(7) Wanin Lee and June Key Lee, Materials Research Bulletin, Vol.30, No.10, 1185 (1995)

(8) J.K. Lee et. al., " A Novel Cleaning Method of Dry Etch Damaged Layer in PZT Thin Film Capacitor", J. Appl. Phys., 86, p63-76 , 1999

(9) Chee Won Chung, Wanin Lee, and June Key Lee, Integrated Ferroelectrics, Vol.11, 259 (1995)

(10)Kenji Ishikawa. et. al., "Effect of PbTiO3 Seeding Layer on the Growth of sol-gel derived Pb(Zr0.53Ti0.47)O3 Thin Film". Jpn. J. Appl. Phys. Vol. 37. Pp. 5128-5131, 1998

(11)E. Cattan. et al., "Structure control of Pb(Zr,Ti)O3 films using PbTiO3 buffer layers produced by magnetron sputtering" Appl. Phys. Lett. 70(13) march. 1997

Mat. Res. Soc. Symp. Proc. Vol. 655 © 2001 Materials Research Society

Characterization of Ferroelectric Property of c-axis and non-c-axis Oriented Epitaxially Grown Bismuth Layer-Structured Ferroelectric Thin Films with Different m-numbers Prepared by MOCVD

Takayuki Watanabe, Tomohiro Sakai, Atsushi Saiki[1], Keisuke Saito[2], Toyohiko Chikyo[3], and Hiroshi Funakubo
Department of Innovative and Engineered Materials, Tokyo Institute of Technology,
4259 Nagatsuta-cho, Midori-ku, Yokohama-shi, Kanagawa 226-8502, Japan
[1]Research Cooperation Section, Tokyo Institute of Technology,
2-12-1 O-okayama, Meguro-ku, Tokyo 152-8550, Japan
[2]Application Laboratory, Analytical Department, Philips Japan, Ltd.,
35-1 Sagamiono 7-chome, Sagamihara-shi, Kanagawa 228-0803, Japan
[3]National Research Institute for Metals, Tsukuba Laboratory,
1-2-1 Sengen, Tsukuba-shi, Ibaraki 305-0047, Japan

ABSTRACT

Epitaxial thin films of bismuth layer-structured ferroelectrics (BLSF) with different m-numbers, i.e., $Bi_2VO_{5.5}$ (BVO) (m=1), $SrBi_2Ta_2O_9$ (SBT) (m=2), and $Bi_4Ti_3O_{12}$ (BIT) (m=3), were grown by metalorganic chemical vapor deposition (MOCVD). (001)-oriented films were deposited on (100)$SrTiO_3$. (114)-oriented BVO, (116)-oriented SBT, and (118)-oriented BIT films were deposited on (110)$SrTiO_3$. Moreover, (102)-oriented BVO, (103)-oriented SBT, and (104)-oriented BIT films were deposited on (111)$SrTiO_3$. On (100), (110), and (111)$SrTiO_3$ substrates, c-axis of the deposited films was tilted about 0°, 45°, and 56°, respectively, against perpendicular to the surface of the substrates irrespective of m-number. This suggests the growth of crystallographic equivalent orientation. The distinctive surface morphology originated to the feature of the film orientation was observed. The dielectric constant and the leakage current of c-axis-oriented film was smaller than that of non-c-axis-oriented one, indicating smaller dielectric constant and leakage current along c-axis than a- or b-axes. A larger ferroelectric anisotropy was ascertained for SBT and BIT films. Furthermore, the evaluated spontaneous polarization along a- and c- axes of BIT from the data of the epitaxially grown BIT films well agreed with the reported one for the single crystal. This suggests the ferroelectric property was not strongly affected by the strain in the films.

INTRODUCTION

Thin films of bismuth layer-structured ferroelectrics (BLSF) have been investigated for a ferroelectric random access memory (FeRAM) application because of its good ferroelectric properties, especially high fatigue endurance. We have already reported that the epitaxially grown $SrBi_2Ta_2O_9$ (SBT) and $Bi_4Ti_3O_{12}$ (BIT) films have high fatigue endurance [1, 2]. However, BLSF thin films with different m-number have not been systematically investigated. The understanding of the common feature of BLSF is essential to find out suitable BLSF material for FeRAM applications. In this study, epitaxial $Bi_2VO_{5.5}$ (BVO) (m=1), SBT (m=2), and BIT (m=3) films with c- and non-c-axis-orientations were systematically grown and characterized to find out the common feature of crystal growth and the electrical property.

EXPERIMENTAL DETAILS

About 200-nm thick BVO, SBT, and BIT films were deposited by metalorganic chemical vapor deposition (MOCVD) at 500-880 °C using an apparatus having a vertical cold-wall type reaction chamber. Trimethyl bismuth [$Bi(CH_3)_3$] was commonly used as Bi source. Triethoxy vanadium oxide [$VO(O{\cdot}C_2H_5)_3$], strontium bis-hexaethoxy tantalate {$Sr[Ta(O{\cdot}C_2H_5)_6]_2$}, and tetra-isopropoxy titanium [$Ti(O{\cdot}i{\text -}C_3H_7)_4$] were also used as source materials for BVO, SBT, and BIT film preparation, respectively. O_2 gas was introduced into the reactor as an oxidant gas. The details are described in elsewhere [1-3]. $SrTiO_3$ (STO) single crystals with various orientations , (100), (110), and (111) orientations, were used as substrates. A 100 μmΦ Pt was used as a top electrode and the epitaxially grown $CaRuO_3$ and $SrRuO_3$ films were grown on STO substrates by MOCVD to be used as bottom electrode: $(100)_c CaRuO_3$//(100)STO, $(100)_c SrRuO_3$//(100)STO, $(110)_c SrRuO_3$//(110)STO, and $(111)_c SrRuO_3$//(111)STO [4,5]. The voltage step and the wait duration for the I-V measurement with the top electrode at positive bias were 10 mV and 20 ms, respectively.

RESULT AND DISCUSSION

Epitaxial films were grown on (100), (110), and (111)STO substrates irrespective of the m-number by adjusting the deposition condition. Figure 1 shows the example of the XRD reciprocal space mapping of BIT films deposited on STO substrates with different orientations. (00l)-, (118)-, and (104)-oriented films were epitaxially grown on (100), (110), and (111)STO substrates, respectively. Moreover, it was also ascertained that one, two and three oriented domains were observed along in-plane direction for (00l)-, (118)-, and (104)-oriented films, respectively, from the analysis of Fig. 1.

Figure 2 shows the cross-sectional TEM image of the (00l)-oriented BVO film grown on (100)STO substrate. A stack structure corresponding to $(Bi_2O_2)^{2+}$ and $(VO_{5.5})^{2-}$ layers were clearly observed parallel to [011]STO, suggesting an epitaxial growth of BVO film. Table 1 summarizes the orientation of the epitaxial films. An equivalent epitaxial relationship between the film and the substrate was obtained irrespective of m-number [1-3].

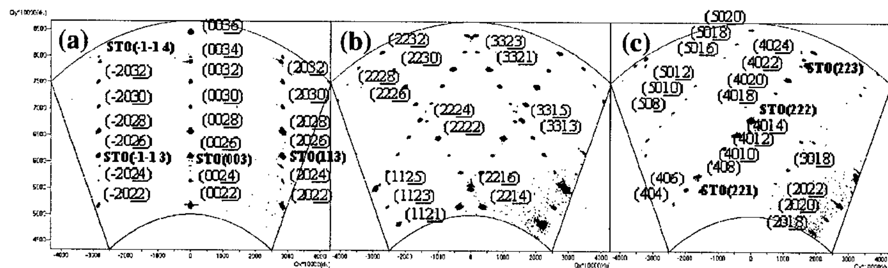

Figure 1 XRD reciprocal space mappings of (a) (00l)BIT//(100)STO, (b) (118)BIT//(110)STO, and (c) (104)BIT//(111)STO.

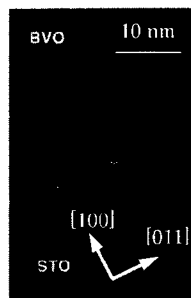

Figure 2 Cross-sectional TEM image of the (001)BVO film grown on (100)STO substrate.

Table 1 Crystal growth relationship between epitaxial BLSF films and STO substrates.

m	Substrate / Film	$(100)SrTiO_3$	$(110)SrTiO_3$	$(111)SrTiO_3$
3	$Bi_4Ti_3O_{12}$	(001)	(118)	(104)
2	$SrBi_2Ta_2O_9$	(001)	(116)	(103)
1	$Bi_2VO_{5.5}$	(001)	(114)	(102)
Tilting angle of c-axis		~ 0°	~ 45°	~ 55°
No. of in-plane domain orientation		1	2	3

Figure 3 shows the AFM images of the (001)-, (118)-, and (104)-oriented BIT films deposited on bottom oxide electrodes. In the case of the (001)-oriented BIT film, a plate like morphology was observed and the root mean square of the surface roughness (R_a) was 0.547 nm. Figure 4 shows the cross section of the same film shown in Fig. 3(a). The gap of the height of each plate-like region was about 1.6 nm corresponding to the half of c-axis lattice parameter. On the other hand, the columnar grains growing to one direction and triangular grains were observed for the (118)- and (104)-oriented films, respectively. The R_a was 3.4 nm for the (118)-oriented film and that of (104)-oriented film was 55.5 nm. The roughness of the BIT film surface increased in the following order: (001)-, (118)-, and (104)-orientation. These tendencies were also observed for BVO and SBT films with different orientations [3]. Therefore, it was concluded that the surface roughness is the character originated to the film orientation based on the fact that the flatness of the substrates were basically the same.

Figure 5 shows the relative dielectric constant (ε_r) of (a) (001)-oriented BVO, SBT, and BIT films and (b) (114)-oriented BVO, (116)-oriented SBT, and (118)-oriented BIT films, non-c-axis-oriented films as a function of a measurement frequency with amplitude of 20 mV in the range from 1 kHz to 1 MHz. Exact electrical property of (102)-oriented BVO, (103)-oriented SBT, and (104)-oriented BIT was not obtained due to the large leakage current. All ε_r were independent of the frequency. As the m-number increased, the ε_r increased irrespective of the film orientation. Moreover, non-c-axis-oriented films showed higher ε_r than c-axis-oriented BVO,

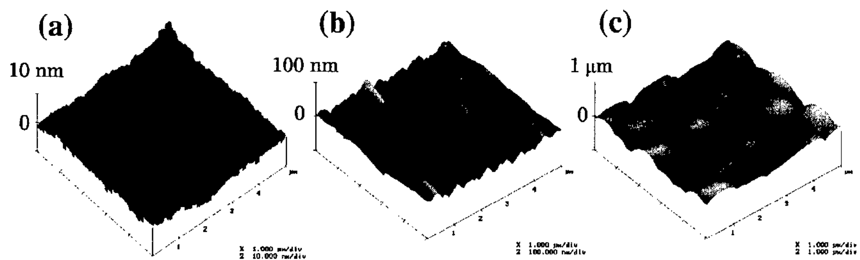

Figure 3 AFM images of the (a) (001)-, (b) (118)-, and (c) (104)-oriented BIT films.

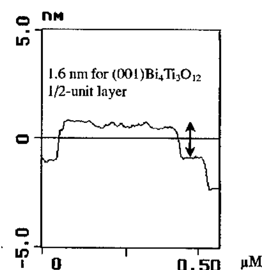

Figure 4 AFM cross section of the same film as shown in Fig. 3(a).

SBT, and BIT films. This is common feature of the BLSF materials and indicates that c-axis has smaller ε_r than a- and b- axes in good agreement with the reported data for the single crystal [6].

Figure 6 shows the leakage current density for the BVO, SBT, and BIT films with equivalent orientation. Non-c-axis-oriented films showed larger leakage current density than c-axis-oriented ones. A. Fouskova *et al.* reported that the leakage current along a-axis is 30 times larger than that along c-axis for BIT single crystal [7]. This can be explained by the high resistivity of the $(Bi_2O_2)^{2+}$ layer. On the other hand, the leakage current density also increased in the following order: SBT, BIT, and BVO. This is the reason that the polycrystalline SBT film has been most widely investigated as a practical FeRAM material. However, it is usually the case that leakage currents across perovskite thin films are generally pointed out to be limited by the electrode interface properties or by carrier trapping phenomena near the electrode, so the further investigation is essential.

Figure 7 shows the P-E hysteresis loops of (a) c-axis-oriented SBT and BIT and (b) (116)-oriented SBT and (118)-oriented BIT films measured by using triangular wave with the frequency of 5 kHz and 20 Hz for SBT and BIT, respectively. The ferroelectricity of the (001)- and (114)-oriented BVO film was confirmed by scanning nonlinear dielectric microscope, but its remanent polarization was less than 1 μC/cm^2 in good agreement with the reported value for BVO single crystal [8]. A large ferroelectric anisotropy was confirmed for SBT and BIT films as

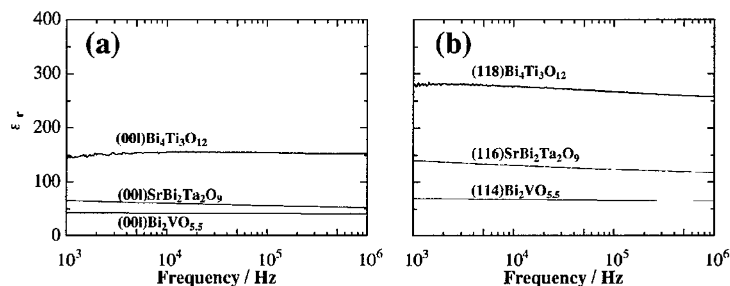

Figure 5 Relative dielectric constant (ε_r) of (a) (001)-oriented BVO, SBT, and BIT (b) (114)-oriented BVO, (116)-oriented SBT, and (118)-oriented BIT films.

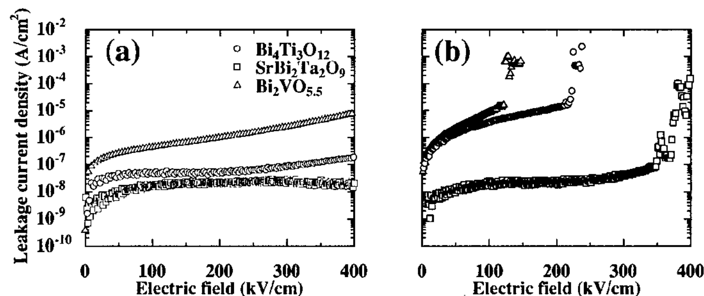

Figure 6 Leakage current density of (a) c-axis-oriented films and (b) (114)-oriented BVO, (116)-oriented SBT, and (118)-oriented BIT films.

shown in Fig. 7. Furthermore, as predicted from the crystal structure, BIT (m=3, odd) showed ferroelectricity but SBT (m=2, even) along c-axis. The estimated spontaneous polarization (P_s) values along a- and c-axes were 0 and 22 $\mu C/cm^2$ for the SBT film and 4.0 and 48.4 $\mu C/cm^2$ for the BIT film, respectively. As a result, the Ps value of BLSF film almost agreed with those of single crystal and the calculation from the crystal structure [6, 9], suggesting a small contribution of a strain remained in the film. In fact, the lattice constants of the epitaxial SBT film were found to be almost the same as reported ones for SBT powder [10]. The films, although epitaxial, are apparently not coherently strained to match the lattice spacing of the STO substrates. Therefore, these strain-free characters of BLSF film are suitable for a multi-stack structure in FeRAM devices.

CONCLUSION

c-axis- and non-c-axis-oriented BLSF films with different m-number, i.e., BVO, SBT, and BIT thin films, were epitaxially grown on STO substrates by MOCVD. Three kinds of epitaxial

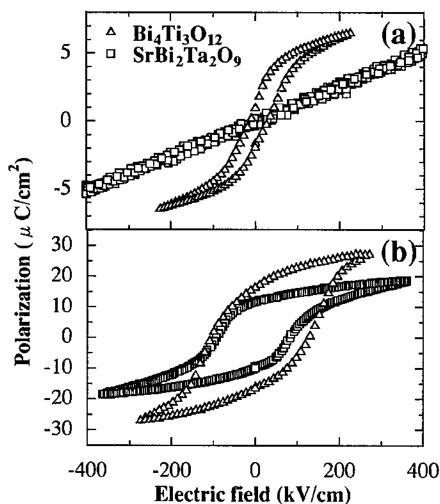

Figure 7 P-E hysteresis loops of (a) (00l)-oriented SBT and BIT (b) (116)-oriented SBT and (118)-oriented BIT films.

films with equivalent orientation were obtained for all materials. The surface morphology of the films depended not on substances but strongly on the orientation of the films. ε_r increased as the m-number increased and was smaller for c-axis-oriented-film than non-c-axis-oriented films, indicating the smaller ε_r along c-axis. Furthermore, a large ferroelectric anisotropy depending on the film orientation and m-number dependence of ferroelectricity along c-axis was ascertained. The estimated P_s values along the a- and c-axes were 22.0 and 0 $\mu C/cm^2$ for the SBT film and 48.4 and 4.0 $\mu C/cm^2$ for BIT film, respectively. These estimated P_s values were almost the same as the reported values for the calculation from the SBT powder and BIT single crystal.

REFERENCES

1. K. Ishikawa and H. Funakubo, *Appl. Phys. Lett.*, **75**, 1970 (1999).
2. T. Watanabe, K. Saito, and H. Funakubo, *J. Mater. Res.*, **16**, (2001) (in press).
3. T. Sakai, T. Watanabe, K. Matsuura, Y. Cho, and H. Funakubo, *submitted for publication.*
4. N. Okuda, K. Saito, and H. Funakubo, *Jpn. J. Appl. Phys.*, **39**, 572 (2000).
5. N. Higashi, N. Okuda, and H. Funakubo, *Jpn. J. Appl. Phys.*, **39**, 2780 (2000).
6. S. E. Cummins and L. E. Cross, J. Appl. Phys., **39**, 2268 (1968).
7. A. Fouskova and L. E. Cross, *J. Appl. Phys.*, **41**, 2834 (1970).
8. K. Shantha and K. B. R. Varma, *Mater. Res. Bull.*, **32**, 1581 (1997).
9. Y. Shimakawa, Y. Kubo, Y. Nakagawa, T. Kamiyama, H. Asano, and F. Izumi, *Appl. Phys. Lett.*, **74**, 1904 (1999).
10. K. Saito, K. Ishikawa, I. Yamaji, T. Akai, and H. Funakubo, *Integ. Ferro.*, (in press).

Mat. Res. Soc. Symp. Proc. Vol. 655 © 2001 Materials Research Society

MOCVD OF Ir AND IrO_2 THIN FILMS FOR PZT CAPACITORS

M.Shimizu*, K.Kita, H.Fujisawa and H.Niu
Department of Electronics, Faculty of Engineering, Himeji Institute of Technology, 2167 Shosha, Himeji, Hyogo 671-2201, Japan
* mshimizu@elnics.eng.himeji-tech.ac.jp

ABSTRACT

Ir films were prepared on SiO_2/Si at 275-500°C by MOCVD (Metalorganic Chemical Vapor Deposition) using a new Ir precursor, Ir(EtCp)(cod) (iridium(ethylcyclopentadienyl)(1,5-cyclooctadiene) : $Ir(C_2H_5C_5H_4)(1,5\text{-}C_8H_{12})$. Ir films prepared at 275-300°C showed highly reflecting surfaces with Rrms roughness (root-mean-square roughness) of 1.4-10nm. At 500°C, Ir and IrO_2 mixture-oriented films were grown. Ir films deposited at 300°C on patterned SiO_2/Si substrates with aspect ratios of 0.3-2.0 showed good step coverage of 70-85%. Auger analysis revealed that Ir film had no incorporation of carbon and oxygen, and that Ir films performed well as a diffusion barrier in PZT/Ir/SiO_2/Si structure.

INTRODUCTION

A variety of metal and conductive oxide materials has been reported for electrode and barrier materials of non-volatile ferroelectric random access memories (FeRAMs) and high density dynamic random access memories (DRAMs). The choice of electrode materials is one of most important key issues because electrical properties are strongly influenced by electrode materials. Among many materials, Ir and IrO_2 have been extensively investigated since the report on fatigue free PZT capacitors with Ir/IrO_2 composite electrodes in 1994 [1,2]. Good diffusion barrier properties, good electrical conductivity and high resistance to hydrogen atmosphere make them promising candidates for electrode and barrier materials [3-6].

In general, Ir and IrO_2 films have been prepared by the sputtering method due to its convenience and commercial-based production. However, for the realization of future FeRAMs and DRAMs with a three dimensional stack structure, metalorganic chemical vapor deposition (MOCVD) technique will be indispensable because of its highly conformal growth, high growth rate, relatively low deposition temperature and compatibility of LSI process.

There have been several reports on the MOCVD of Ir films. A variety of Ir precursors were used in these reports to prepare Ir films, such as IrCp(cod) (Cp : cyclopentadienyl, cod : 1,5-cyclooctadiene) [7], Ir(MeCp)(cod) (Me : CH_3) [7-9], $Ir(acac)_3$ (acac : acetyacetonate) [10-13], Ir(thd)(cod) (thd : 2,2,6,6-tetramethyl-3,5-heptanedionate) [13,14]. These precursors are solid and have a low vapor pressure. Therefore, the sublimation method [7,10-14] and liquid delivery method [8] were used.

In this study, we used a new Ir precursor, Ir(EtCp)(cod) ($Ir(C_2H_5C_5H_4)(1,5\text{-}C_8H_{12})$), to

prepare Ir and IrO_2 films. This precursor is liquid at room temperature and has a higher vapor pressure than those Ir precursors mentioned above. Crystalline properties, surface morphology, step coverage and diffusion barrier characteristics of MOCVD-Ir films are described.

EXPERIMENTS

In our experiments, a new Ir precursor, Ir(EtCp)(cod), was used [15,16]. This precursor is a yellowish liquid at room temperature. Melting point is 14°C, and vapor pressure is 0.1Torr at 105°C, which is considerably higher than that of previous solid Ir precursors. Therefore, Ir vapor was introduced into the reactor using conventional bubbling method. Figure 1 shows the schematic diagram of MOCVD equipment used for Ir and IrO_2 films. The CVD reactor was made of quartz and the substrate susceptor was heated by IR lamp. Argon and oxygen were used as a carrier gas and co-reactant gas, respectively. The substrate used was SiO_2/Si. Growth conditions are summarized in Table I.

Crystalline structure was examined by the X-ray diffraction method (XRD). Surface morphology and cross sectional view were observed using scanning electron microscopy (SEM) and scanning probe microscopy (SPM). Film composition and diffusion barrier properties were analyzed using Auger electron spectroscopy (AES).

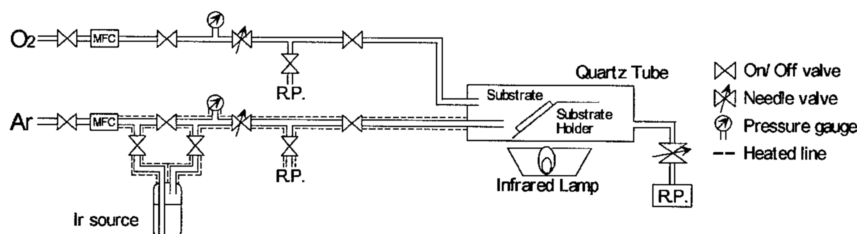

Fig.1 *Schematic diagram of MOCVD equipment for Ir and IrO_2 films.*

Table I Growth conditions of Ir films.

Substrate temperature	275-500°C
Reactor pressure	2Torr
Carrier gas flow rate (Ar)	100sccm
Reacting gas flow rate (O_2)	10, 20sccm
Precursor temperature	100°C
Substrate	SiO_2/Si

RESULTS AND DISCUSSION

Ir films were prepared on SiO_2/Si at substrate temperatures ranging from 275 to 500°C. Small amount of oxygen (10 or 20%) was introduced as a co-reactant to assist the pyrolysis of Ir precursor [7-9,11,12]. X-ray diffraction patterns of films obtained at various substrate temperatures and at an oxygen concentration of 20% are shown in Fig.2. (111)- oriented Ir films were successfully grown at substrate temperatures higher than 275°C. When the substrate temperature was 500°C, IrO_2 peak was observed. IrO_2 and Ir mixture-oriented films were also grown at oxygen concentration of 10% at 500°C.

Grain size of Ir films increased as deposition temperature increased as shown in Fig.3. Surface roughness (root mean square roughness : Rrms) increased from 10 to 35nm as the substrate temperature increased from 300 to 500°C. Ir films prepared at 275 and 300°C showed highly reflective surfaces and Rrms of 1.4-10nm. Fig.4 shows SPM image of the

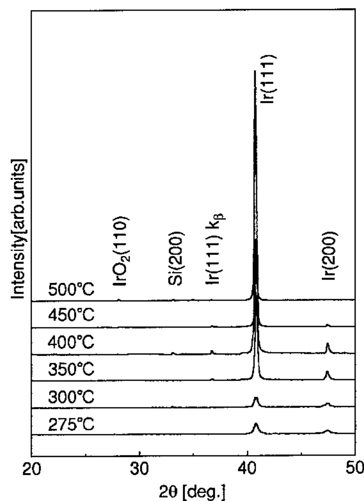

Fig.2 *X-ray diffraction patterns of Ir films prepared at various temperatures (O_2 concentration : 20%).*

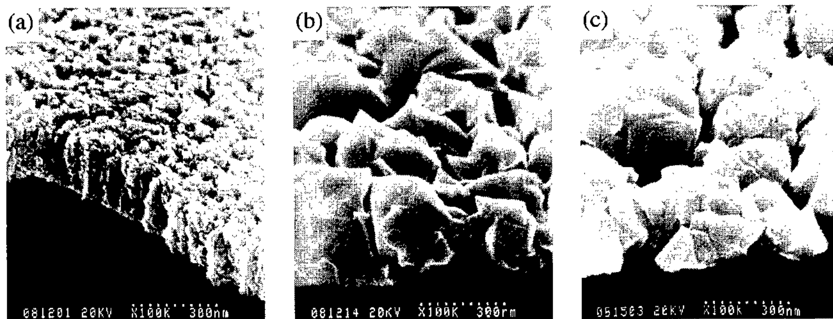

Fig.3 *SEM microphotographs of the surface of Ir films prepared at (a) 300°C, (b) 400°C and (c) 500°C, respectively (O_2 concentration : 20%).*

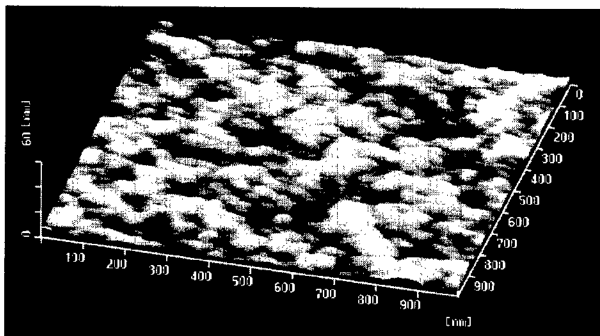

Fig.4 *SPM image of Ir film prepared at 300°C (O_2 concentration : 10%).*

surface of Ir film with Rrms of 1.4nm prepared at 300°C and at an oxygen concentration of 10%.

Growth rates of Ir films deposited at 275°C with oxygen concentrations of 10 and 20% were 0.3 and 5.0nm/min, respectively. They were considerably lower than those of Ir films prepared at 300°C with oxygen concentrations of 10 and 20%, 3.3 and 6.6nm/min, respectively.

Step coverage characteristic of Ir films on various patterned substrates with aspect ratios of 0.3-2.0 was observed by SEM. Figure 5 shows cross sectional SEM photographs of Ir films deposited on patterned substrate with an aspect ratio of 1.5 by MOCVD and sputtering. MOCVD-Ir films on various patterned substrates showed good step coverage of 70-85%, which was considerably higher compared with 20-25% of sputtered-Ir films.

In order to examine the incorporation of impurities into Ir films, Ir film prepared at 300°C was analyzed using AES. From depth profile of AES analysis, as shown in Fig.6, no signal from C and O was observed in the film. Diffusion barrier characteristics for PZT(200nm)/Ir(50,100nm)/SiO_2/Si structure were also examined using AES. Fig.7 shows the depth profiles of PZT/Ir/SiO_2/Si for different thicknesses of Ir. Both PZT and Ir were

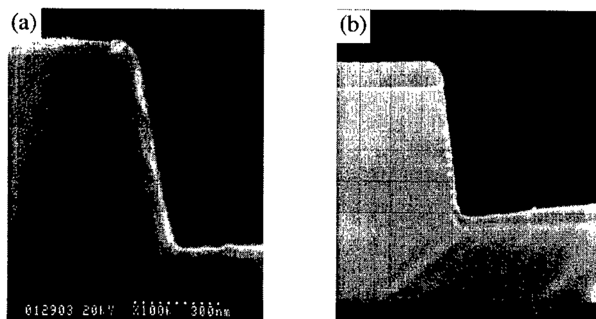

Fig.5 *SEM photographs of Ir films deposited on patterned substrate with an aspect ratio of 1.5 by (a) MOCVD and (b) sputtering.*

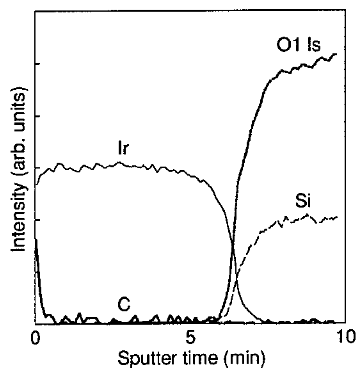

Fig.6 *AES depth profile of Ir film prepared on SiO_2/Si at 300°C.*

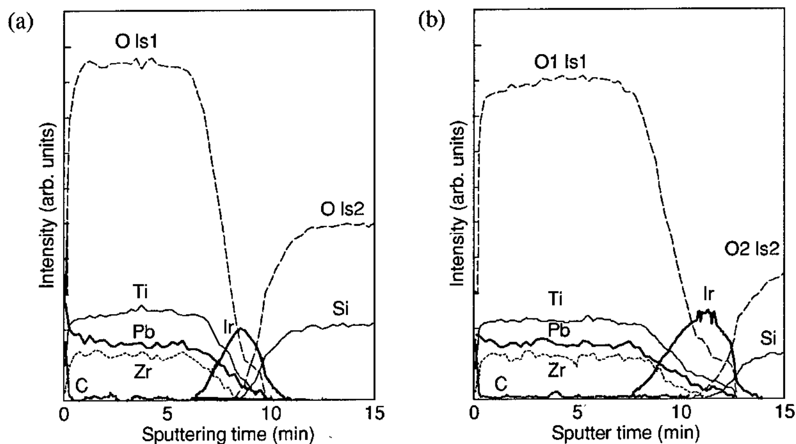

Fig.7 *AES depth profiles of PZT/Ir/SiO_2/Si multi structure with Ir thicknesses of (a) 50nm and (b) 100nm.*

prepared by MOCVD at 560 and 300°C, respectively. This Auger analysis indicates that MOCVD-Ir films act as a good diffusion barrier against elements of PZT.

CONCLUSIONS

Ir films were successfully prepared by MOCVD using Ir(EtCp)(cod) as a new Ir precursor. Surface roughness and grain size of films increased as deposition temperature increased. Ir films prepared at 275 and 300°C had metallic mirror surfaces with Rrms roughness of 1.4-10nm. Ir films prepared at 300°C showed good step coverage of 70-85% and acted as a good diffusion barrier in a PZT/Ir/SiO_2/Si structure. Preparation of single phase IrO_2 films are now under investigation.

ACKNOWLEDGEMENTS

The authors would like to thank High Purity Chemical Laboratory Co. Ltd. for providing the Ir precursor. This work was partly supported by the Grant-in-Aid for Scientific Research No.12450131, 12650348, 11750265 and 12134207 from Ministry of Education, Science, Sports and Culture, by the Japan Society for Promotion of Science (JSPS-RFTF96P00105), and by the research grant of Himeji Institute of Technology.

REFERENCES

1. T.Nakamura, Y.Nakao, A.Kamisawa and H.Takasu, *Appl.Phys.Lett.*, **65**, 1522 (1994).
2. T.Nakamura, Y.Nakao, A.Kamisawa and H.Takasu, *Jpn.J.Appl.Phys.*, **33**, 5207 (1994).
3. M.Shimizu, H.Fujisawa, S.Hyodo, S.Nakashima and H.Niu, *Mater.Res.Soc.Symp.Proc.*, **493**, 159 (1998).
4. K.K-Abdelghafar and Y.Fujisaki, *Jpn.J.Appl.Phys.*, **37**, L804 (1998).
5. T.Sakoda, K.Aoki and Y.Fukuda, *Jpn.J.Appl.Phys.*, **38**, 5162 (1999).
6. T.S.Moise, S.R.Sommerfelt, G.Xing, L.Colomb, T.Sakoda, S.R.Gilbert, A.Loke, S.Ma, R.Kavari, L.A.Wills, T.Hsu, J.Amano, S.T.Johnston, D.J.Vestyck, M.W.Russel and S.M.Bilodeau, *Int.Electron Device Meet.Tech.Dig.*, 940 (1999).
7. J.B.Hoke, E.W.Stern and H.M.Murry, *J.Mater.Chem.*, 1, 551 (1991).
8. S.K.Dey, J.Goswami, C-G.Wang and P.Majhi, *Jpn.J.Appl.Phys.*, **38**, L1052 (1999).
9 Y.-M.Sun, X.-M.Yan, N.Mettlach, J.P.Endle, P.D.Kirch, J.G.Ekerdt, S.Madhukar, R.L.Hance and J.M.White, *J.Vac.Sci.Technol.*, **A18**, 10 (2000).
10. N.V.Gelfond, F.V.Tuzikov and I.K.Igumenov, *Thin Solid Films*, **227**, 144 (1993).
11. R.Vergas, T.Goto, W.Zhang and T.Hirai, *Appl.Phys.Lett.*, **65**, 1094 81994).
12. Y.-M.Sun, J.P.Endle, K.Smith, S.Whaley, R.Mahaffy, J.G.Ekerdt, J.M.White and R.L.Hance, *Thin Solid Films*, **346**, 100 (1999).
13. T.Gerfin, W.J.Halg, F.Atamny and K.Dahmen, *Thin Solid Films*, **241**, 352 (1993).
14. C.Xu, F.Dimeo Jr., T.H.Baum and M.Russel, *Mater.Res.Soc.Symp.Proc.*, **541**, 129 (1999).
15. Japanese Patent Laid-open No.11-292888 (1999).
16. M.Shimizu, K.Kita, H.Fujisawa, N.Tomozawa and H.Niu, in *Proc. 12th IEEE Int.Symp. Applications of Ferroelectrics* (in press).

Integration and Electrodes I

Mat. Res. Soc. Symp. Proc. Vol. 655 © 2001 Materials Research Society

ELECTRODES AND BARRIERS FOR DRAM AND FERAM: PROCESSING, INTEGRATION, AND FUNDAMENTALS

K.L. SAENGER[1], P.C. ANDRICACOS[1], S.D. ATHAVALE[2], J.D. BANIECKI[2], C. CABRAL, JR.[1], G. COSTRINI[2], K.T. KWIETNIAK[1], R.B. LAIBOWITZ[1], J.J. LIAN[3], Y. LIMB[3], D.A. NEUMAYER[1], and M.L. WISE[3]
[1] IBM Research Division, T.J. Watson Research Center, Yorktown Heights, NY 10598,
[2] IBM Microelectronics, Hopewell Junction, NY 12533,
[3] Infineon, Hopewell Junction, NY 12533.

ABSTRACT

Materials requirements for electrodes and barriers in high density dynamic random access memory (DRAM) and ferroelectric random access memory (FERAM) are reviewed, and some approaches to barrier materials and device geometries are described. Electrode/barrier topics covered in more detail include Pt reactivity with Si-containing barriers and dielectric overlayers, the application of a Bragg-Brentano x-ray diffraction technique to quantitatively probe Pt and Ir electrode morphology and thickness changes during ferroelectric processing, the stability of metal oxide electrode materials in reducing ambients, electrode patterning techniques (including Pt electroplating), and electrical properties of 3-D capacitors in 256k arrays as a function of top electrode annealing treatments.

INTRODUCTION

The conditions used for the deposition and processing of high-epsilon (HE) dielectric and ferroelectric (FE) materials in high density DRAM and FERAM devices place severe demands on the electrode and barrier materials. FE/HE materials are typically deposited and/or processed in oxidizing environments in the temperature range 550 - 700°C on "oxygen stable" electrodes that can withstand these conditions without forming insulating oxides. In particular, the electrode surfaces must remain free of low-epsilon oxides to avoid reducing the effective capacitance of the FE/HE layer. In addition, low resistance electrical contacts must be maintained between the electrode and underlying devices. These requirements have led to the general integration strategy of using electrode materials of noble metals and/or conductive noble metal oxides, with oxidation-resistant diffusion barriers between the electrode and underlying (silicon) contact plug.

Electrode/Barrier Requirements

Favored oxygen-stable electrode materials include the noble metals Pt, Ir, and Ru, alloys of these noble metals, and the conducting noble metal oxides RuO_2 and IrO_2. All of these materials have relatively high work functions (4.7-5.8 eV), and do not form insulating oxides when exposed to oxygen at elevated temperatures.

The diffusion barrier material (between the electrode and underlying contact plug) must be conductive, resistant to the formation of an insulating oxide, a barrier to diffusion of oxygen and (silicon) plug material, and stable with respect to reaction with the electrode material. Fig. 1 shows two geometrical approaches for incorporating barriers into FE/HE device structures: a non-recessed barrier geometry (Fig. 1a), and a recessed barrier geometry (Fig. 1b).

Some failure modes for barrier layers are illustrated in Fig. 2 for the case of a simple stack electrode, silicon contact plug, and recessed barrier.

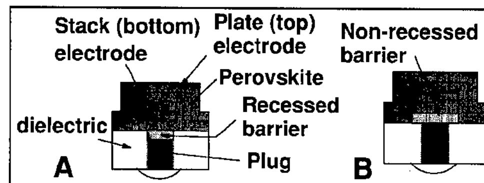

Figure 1. Two barrier geometries: (a) recessed; (b) non-recessed.

Approaches to Barrier Materials

Barrier materials are typically deposited (rather than in-situ formed). Of the deposited barrier materials used for FE/HE applications, the metal nitrides are among the most common, including TiN, TaN, TiAlN, and TaSiN [1]. TiAlN [2] and TaSiN are more oxidation-resistant than TiN or TaN. TaSiN is of particular interest because it is amorphous (and thus lacking fast diffusion paths along grain boundaries) over a wide temperature and composition range.

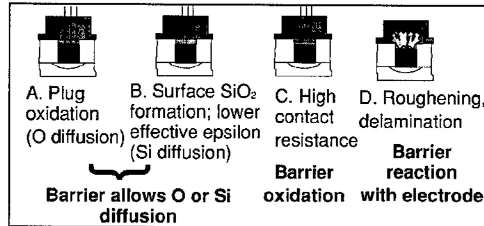

Figure 2. Barrier failure modes: (a) O diffusion; (b) Si diffusion; barrier (c) oxidation; (d) reaction.

A variety of TaSiN compositions have been investigated for use as oxidation- resistant barrier materials [3, 4, 5]. The range of optimum compositions for FE/HE barrier applications is identified in the ternary Ta-Si-N phase diagram of Fig. 3 excerpted from Ref. 5: Ta(20-25 at.%)-Si (20-45 at.%)- N(35-60 at.%). Qualitatively, the Ta content must be high enough for sufficient electrical conductivity, the SiN content must be sufficient for Si- and O-barrier function, and the N content must be sufficient to tie up the barrier's Si and prevent it from reacting with the electrode.

In-situ formed barriers have been proposed as alternatives to deposited barriers [6]. In this approach, an in-situ M-O-Si barrier layer comprising metal M from the electrode and Si from the plug is formed during the initial phases of a silicidation reaction which is stopped by pileup of oxygen incorporated from the annealing ambient. The main concern with this approach is the conductivity of the M-O-Si barrier.

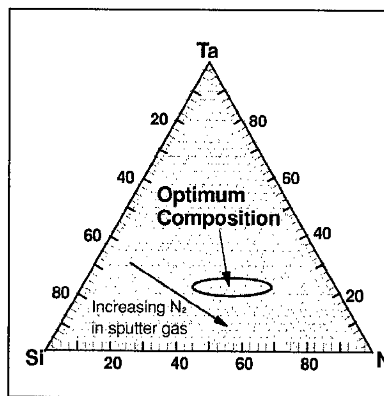

Figure 3. Ternary phase diagram showing optimum TaSiN composition

A more radical approach to the problem of integrating a suitable barrier is illustrated schematically in Fig. 4, which shows a process flow for a "bottom-electrode-last" capacitor [7]. In contrast to conventional processing, where the bottom electrode and its contact to the underlying plug must survive FE/HE deposition without the formation of low-k oxides, the bottom electrode is put on last, *after* FE/HE deposition. The key

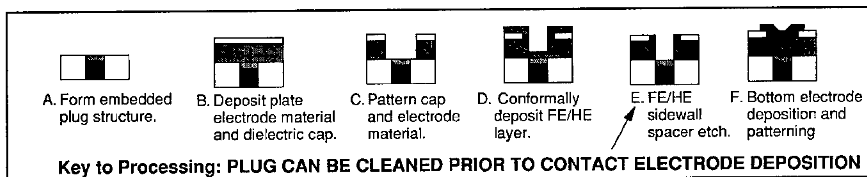

***Figure 4**. Process flow for "bottom electrode last" capacitor.*

advantage of the bottom-electrode-last process flow it that it allows the plug contact surface to be cleaned prior to bottom electrode deposition, although this comes at the cost of restricting the FE/HE layer area to the plate electrode sidewalls. Additional concerns are the requirement for a sidewall spacer etch of the FE/HE material, and the need for a sufficiently gap-filling bottom electrode deposition process.

EXPERIMENT

Deposition of Electrodes and Barrier Materials

TaSiN was deposited on room temperature substrates by reactive sputtering from a $TaSi_2$ target using a N_2/Ar working gas (36% N_2) having a total flow of 50 sccm, and a power of 1000 W. The Pt films were sputter-deposited on heated (350°C) substrates from a Pt target, using an Ar working gas and powers of 300 W (for the 10 nm films) or 1000 W (all others). The Ir films were sputter-deposited on heated (250°C) substrates from an Ir target, using an Ar working gas and a power of 1000 W. The IrO_2 was deposited on heated (250°C) substrates by reactive sputtering from a Ir target, using a O_2/Ar working gas (50% O_2) having a total flow of 50 sccm, and a power of 500 W.

Deposition of FE/HE and Passivating Dielectrics

The $PbZr_xTi_{1-x}O_3$ (PZT) films used in the thickness fringe study were prepared by chemical solution deposition (CSD) from a mixture of zirconium and titanium butoxyethoxides and lead ethylhexanoate dissolved in butoxyethanol. The $Ba_{0.65}Sr_{0.35}TiO_3$ (BSTO) films used in the capacitors fabricated for the electrical measurements were formed by metal-organic chemical vapor deposition (MOCVD) [1] at 650°C. The 80 nm-thick passivating Al_2O_3 and SiNx layers deposited on the IrO_2 films were formed by either room temperature reactive sputtering from an Al_2O_3 target in O_2/Ar, or by a 250°C plasma-enhanced chemical vapor deposition (PECVD) process using $SiH_4/NH_3/N_2$. PECVD conditions for other SiO_2 films deposited on Pt are described in the text.

Analysis and Sample Treatments

Rapid thermal anneals (RTAs) of 5 min duration were performed on sample pieces ~2 x 2 cm^2 in size in 760 Torr of N_2 or O_2 in an AG Heatpulse using a ramp rate of 35 °C/sec. Longer (15-20 min) anneals in N_2 and forming gas (5% H_2 in Ar) were performed in a quartz tube furnace.

Rutherford Backscattering Spectroscopy (RBS) for composition analysis was performed with 2.3 MeV ^{4}He ions, and the Bragg-Brentano θ–2θ x-ray diffraction scans were performed with a Philips PW1729 diffractometer using Cu Kα radiation and a 2θ range of 20-70°.

RESULTS AND DISCUSSION

Reactions of Pt Electrodes with Si-containing Dielectrics and Barriers

Pt layers on clean silicon readily react to form silicides (e.g., PtSi, Pt_2Si) during low temperature ($\gtrsim$350-400°C) annealing in inert ambients. Here we describe (i) how TaSiN layers with nominally suitable compositions for barrier use can react with Pt overlayers, and (ii) how PtSix formation can occur when Si-containing PECVD dielectric overlayers are deposited on Pt (presumably through reactions of the Pt with Si-containing radicals in the deposition plasma).

Fig. 5 shows data for a 100 nm-thick Pt film sputter-deposited on a TaSiN barrier layer having an RBS-determined Ta-Si-N composition of 22-31-47. The substrate temperature for the Pt depositions was 350°C, and the depositions were either in situ (Pt deposited on TaSiN without an intervening air exposure) or ex-situ (Pt deposited on TaSiN after a 3-day air exposure). No Pt-Si reaction peaks are seen in the as-deposited film (Fig. 5a) or in the air-exposed film (Fig. 5c) after a 650°C/5 min anneal in N_2. However, this same anneal produces strong Pt_3Si peaks in the in-situ deposited film. RBS data indicates low levels (1.5 at.%) of silicon throughout the Pt, suggesting that the Pt_3Si phase is dispersed throughout the Pt and not confined to a surface layer. Overall, these results suggest that a thin native oxide is formed at the Pt-TaSiN interface in the air-exposed samples, and that TaSiN layers not being exposed to air may require higher-nitrogen-content compositions to prevent reactions with Pt.

Platinum silicide formation may also occur during the deposition of PECVD dielectric overlayers. This is illustrated in Fig. 6, which shows the x-ray diffraction spectra of three Pt

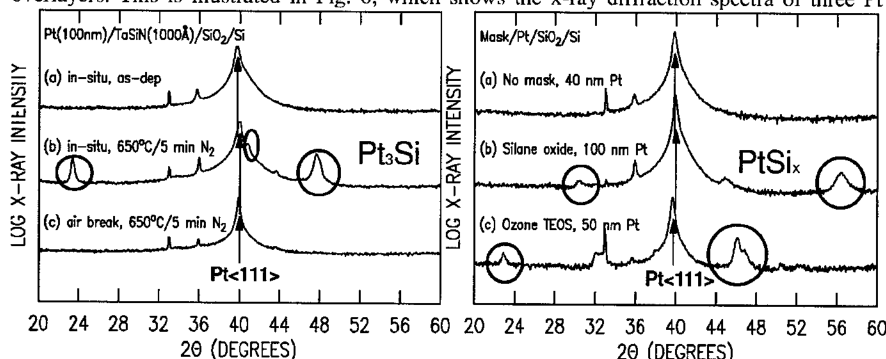

Figure 5. *X-ray diffraction spectra of Pt(100 nm) films on TaSiN: (a) Pt in-situ deposited, no anneal; (b) Pt in-situ deposited, followed by 650°C/5 min N_2; (c) Pt ex-situ deposited (after a 3-day air break), followed by 650°C/5 min N_2. Note peaks from the Pt_3Si phase in (b).*

Figure 6. *X-ray diffraction spectra of Pt films on SiO_2 (a) as-deposited Pt(40 nm), (b) Pt(100 nm) after deposition of 750 nm "silane" SiO_2; (c) Pt(50 nm) after deposition of 200 nm "ozone TEOS" SiO_2.*

films deposited on SiO_2/Si substrates. Fig. 6a shows a reference spectrum for an as-deposited 40 nm-thick Pt film with no overlayer; Fig. 6b shows the spectrum for a Pt(100 nm) film after the deposition of a 750 nm thickness of a 400°C silane oxide (from $SiH_4/N_2O/N_2$); and Fig. 6c shows the spectrum of a Pt(50 nm) film after the deposition of 200 nm of a 400°C ozone TEOS (from $TEOS/O_3/O_2$). The silicide peaks after ozone TEOS deposition were again identified as Pt_3Si. Again, the Pt_3Si phase appears to be distributed throughout the thickness of the Pt film, based on the fact that the relative intensity of the Pt_3Si peaks (relative to Pt) was not changed by a CF_4/O_2 reactive ion etch used to remove the top half of the Pt film.

These results indicate that Si can be incorporated into Pt electrodes from both overlayers and underlayers, and that this factor should be considered in any integration scheme. However, a certain amount of dielectric-Pt reaction may be desirable, since anecdotal evidence indicates that dielectric overlayers showing PtSix peaks have better adhesion to the underlying Pt.

Thickness Fringe Probe of Pt and Ir Electrodes

Here we describe the technique of Bragg-peak thickness fringe analysis and show how it can be used to probe thin (10-20 nm) Pt and Ir electrode layers on a variety of substrates [8,9]. Thickness fringe analysis is normally restricted to single crystal films since polycrystalline films typically lack the necessary structural coherence (such as might be realized with a collection of identically oriented grains whose lateral dimensions greatly exceed the film thickness). In addition, thickness fringe analysis normally requires high-resolution diffractometers to resolve fringes in the film thickness range of interest (e.g., 50 - 500 nm for silicon-on-insulator (SOI) applications [10]). However, thin Pt and Ir films deposited by physical vapor deposition are usually highly textured (with a strong 111 orientation) and, after a post-deposition grain growth anneal, can have a grain size many times the film thickness. This allows thickness fringes to be observed with Bragg-Brentano x-ray diffraction using normal resolution [8,9]. The fringe contrast (or modulation amplitude) provides a qualitative measure of film roughness, and the spacing of the thickness fringes provides a quantitative measure of film thickness. Film thickness is *approximately* equal to $\lambda/[\Delta 2\theta * \cos \theta_B]$, where λ is the x-ray wavelength (0.154 nm for Cu Kα), θ_B is the Bragg angle (equal to $2\theta/2$, where 2θ is the location of the intensity maximum in a θ-2θ scan), and $\Delta 2\theta$ is the fringe spacing in

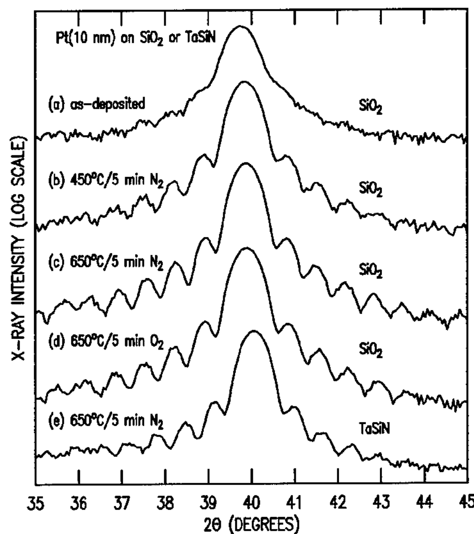

Figure 7. *The 111 reflection from Pt(10 nm)/SiO_2 films (a) as-deposited; (b) after 450°C/5 min N_2; after 650°C/5 min in N_2 (c) or O_2 (d). Same as (c), except for TaSiN substrate.*

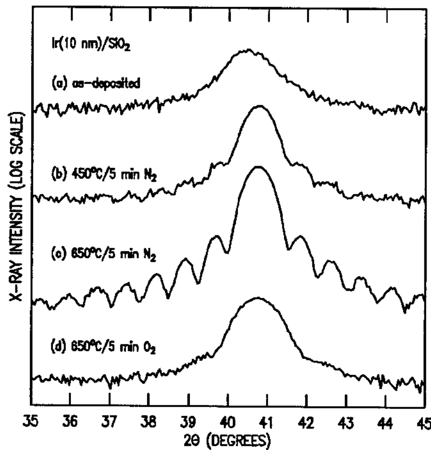

Figure 8. The 111 reflection from Ir(10 nm) films: (a) as-deposited; (b) after 450°C/5 min N_2; after 650°C/5 min in (c) N_2 or (d) O_2.

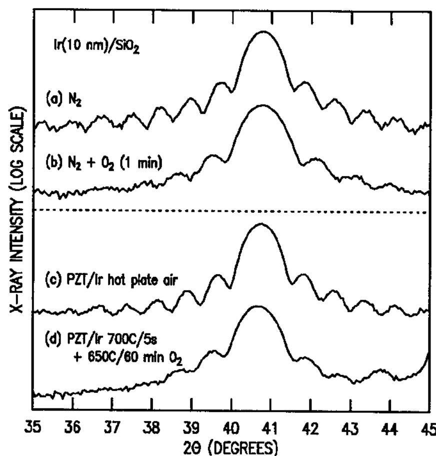

Figure 9. The 111 reflection from Ir(10 nm) films (a) before and after 650°C/1 min O_2; (b) before and after PZT crystallization (700°C/ 5 s + 650°C/60 min O_2).

2θ space [11], although more exact expressions (derived by Zolotoyabko using an extended kinematical approach [11, 8]) were employed to obtain the thickness values used here.

Figs. 7 and 8 show x-ray diffraction data for nominally 10 nm-thick sputter-deposited Pt (Fig. 7) and Ir (Fig. 8) films after a variety of annealing treatments. No fringes were observed in the as-deposited films (Figs. 7a and 8a). In Pt, fringes are clearly present after annealing in N_2 at 450°C for 5 min (Fig. 7b), and substantially stronger after annealing in N_2 at 650°C for 5 min (Fig. 7c). Oxygen annealing at 650°C for 5 min produces fringes nearly identical to those produced by the same anneal in N_2 (Fig. 7d), indicating the absence of Pt oxidation, and Pt deposited on air-exposed $TaSiN/SiO_2$ (nominal Ta-Si-N composition 20-30-50) also showed strong fringes after N_2 annealing at 650°C for 5 min.

In contrast to the results for Pt, only hints of fringes can be seen in Ir after the 450°C/5 min N_2 anneal (Fig. 8b). However, the fringes are quite strong after N_2 annealing at 650°C for 5 min (Fig. 8c). The absence of fringes in the sample annealed in O_2 at 650°C for 5 min suggests that the IrO_2 formation disrupts the ordering and grain growth of the Ir film (Fig. 8d).

Fig. 9 shows two examples of how changes in Ir fringe spacing can be used to quantitatively determine the amount of Ir consumed by oxidation during different types of processing. The films for both experiments were first given a fringe generation anneal in N_2 at 650°C. Figs. 9a - 9b show data for a bare Ir film before (Fig. 9a) and after (Fig. 9b) thermal oxidation in an atmosphere of O_2 at 650°C for 5 min, and Figs. 9c - 9d show data for an Ir film coated with a chemical solution deposited PZT(230 nm) layer, before (Fig. 9c) and after (Fig. 9d) PZT crystallization in an atmosphere of O_2 (700°C/5 s + 650°C/60 min). The bare Ir film had an initial thickness of 12.6 nm, 2.4 nm of which was consumed by oxidation, and the PZT-coated film had an initial thickness of 12.4 nm, 1.2 nm of which was consumed by oxidation. The PZT film clearly had a protective effect, since less Ir was consumed for a much longer anneal. A more

complete description of these experiments can be found in Ref. 9, and applications of this technique to the detection of Ir lattice damage induced by reactive ion etching can be found in Ref. 8.

Stability of IrO_2 in Reducing Ambients

The conductive metal oxides RuO_2, IrO_2, and PtOx can lose oxygen in reducing environments. The partial pressure of oxygen required to prevent decomposition at a given temperature can be estimated with the use of Ellingham plots [12], shown schematically in Fig. 10. Free energy values $\Delta G = \Delta H - T\Delta S$ are plotted vs. T for different metal oxides (e.g., MO_2 and $M'O_2$), along with values of $\Delta G = RT \log p_{O2}$ for selected oxygen pressures p_{O2}. The temperature point at which these two ΔG lines intersect indicates the equilibrium p_{O2} for that metal oxide at that temperature. Thermodynamic data for RuO_2 and IrO_2 can be found in Ref. 13.

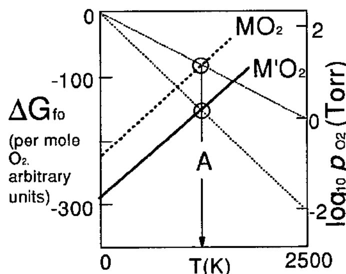

Figure 10. Schematic Ellingham plot. At temperature A, decomposition of the more stable $M'O_2$ is prevented by a p_{O2} of 10 mTorr, whereas 1 Torr is required for the less stable MO_2.

According to recent measurements [14], an oxygen partial pressure pO_2 of ~20 mTorr is required to prevent IrO_2 decomposition at 600°C. This result is in good agreement with thermodynamic predictions, which also indicate that a pO_2 of 100 mTorr would be needed at a temperature of 650°C. Most FE/HE deposition processes are situated in the stable region of the pO_2/temperature parameter space, but care may be needed to ensure sufficient oxygen during "degas" steps when the substrates are heated to temperature. RuO_2 is significantly more stable than IrO_2, but most PtOx ($0.1 < x < 1.4$) materials will lose oxygen at 650°C even in 760 Torr of O_2 [15].

While IrO_2 films will begin to decompose during annealing at very low pO_2, decomposition is not instantaneous and can be further slowed by the presence of overlayers. Here we examine the effect of nitrogen or forming gas (5% H_2 in Ar) anneals on bare and passivated IrO_2 films prepared on poly-silicon/SiO_2/Si substrates. Fig. 11a - 11c show x-ray diffraction traces of the as-deposited IrO_2 films, with and without overlayers of 80 nm of a 250°C $SiH_4/NH_3/N_2$ PECVD SiNx or a room temperature, reactively sputtered Al_2O_3. All three IrO_2 films showed identical XRD traces, suggesting that the H in the SiNx deposition process did not produce significant reduction. However, a hint of a shoulder at the Ir111 position is visible in the bare sample that received a N_2 anneal at 400°C for 5 min (Fig. 11d), and the Ir111 peak is clearly visible in the sample that received a N_2 anneal at 650°C for

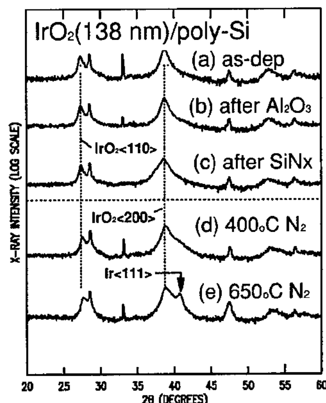

Figure 11. X-ray diffraction spectra of IrO_2 films on poly-Si: (a) as-deposited; after deposition of 80 nm Al_2O_3 (b) or SiNx (c); bare IrO_2 after N_2 anneals at 400°C for 20 min (d) or 650°C for 5 min (e).

5 min (Fig. 11e).

All three IrO_2 samples subjected to a 20 min anneal in forming at 400°C (bare, and coated with Al_2O_3 or SiNx) delaminated from the substrate and turned into a wispy Ir dust.

Electrode Patterning Issues

Ru-based electrodes (Ru and RuO_2) are relatively easy to pattern subtractively by reactive ion etching (RIE) in oxygen-based plasma [16], due to the volatility of the RuO_4 etch product. In contrast, Pt- and Ir-based electrodes lack volatile oxides or halides. Plasma-based patterning at moderate temperatures (<100°C) thus relies on physical sputtering as the etch dominant mechanism. This leads to the problem shown in Fig. 12a: Pt "ears" formed by Pt redeposition on a non-erodible thick mask. At the other extreme, Fig. 12b shows the sloped Pt sidewalls that can result from RIE with an erodible mask.

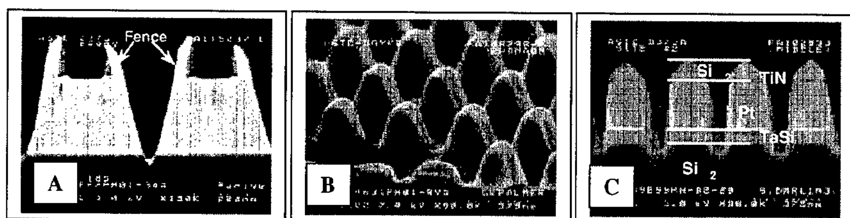

Figure 12. *Electrode geometries resulting from various Pt RIE processes: (a) redeposited Pt "ears" or "fences;" (b) sloped sidewalls; (c) vertical sidewalls.*

TiN and other metal nitrides can be acceptable mask materials for low temperature (<100°C) Cl_2-based Pt RIE if O_2 is added to the RIE gas mixture to improve Pt-to-TiN selectivity [17]. SiO_2 masks can work with hot (>>100°C) RIE processes, because Pt etch rates and Pt-to-SiO_2 selectivity greatly increases with increasing temperature. Fig. 12c shows Pt electrodes patterned in an Applied Materials hot DPS tool with a SiO_2(0.6μm)/TiN(30 nm) hard mask and >350°C chuck temperature.

Patterning approaches based on through-mask electroplating have also been proposed [18] and demonstrated [19,20]. Fig. 13 shows a schematic of the through-mask plating process. Fig. 14 shows electrodes made with this process at a stage in processing corresponding to Fig. 13d. Plating was performed on 8" wafers in a 65°C KOH solution of "Pt A salt" (Engelhard) at 6.0 mA/cm^2 (0.415A) for 140s, using a 50 nm-thick Pt plating base and a 200 nm-thick mask of

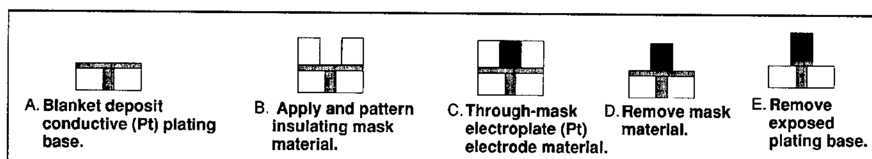

Figure 13. *A schematic illustration of a through-mask plating process.*

PECVD ozone TEOS which was removed by an HF dip after plating. The electrodes have a diameter of 0.18 μm, a height of 0.2 μm, and a pitch of 0.4 μm. Integration concerns include reactions of the dielectric mask with the underlying Pt plating base (although this can improve mask-to-seed layer adhesion), and erosion of the dielectric mask by the plating solution (which can lead to the non-vertical sidewalls seen in the plated Pt features of Fig. 14c).

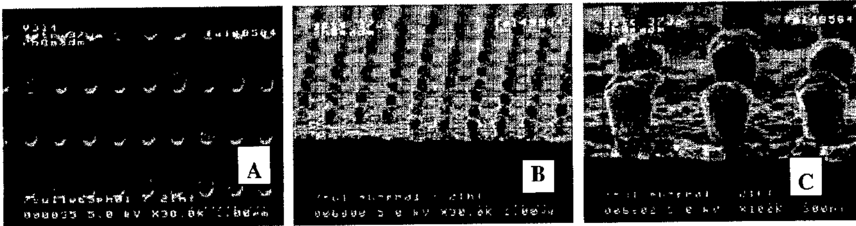

Figure 14*. Scanning electron micrographs of plated Pt electrodes on a Pt plating base: top view (a); side views (b) and (c).*

Capacitance and Plug Resistance in 256k 3-D Capacitor Arrays

Here we describe the effects of 15-20 min post- electrode anneals on the leakage, capacitance and plug resistance of capacitors in 256k 3-D arrays as a function of annealing ambient (atmospheric pressure O_2, or N_2 with 20 ppm O_2) and temperature (400-550°C) [21]. The capacitors have a trilayer recessed barrier and a bottom electrode area of ~0.4 μm^2. The geometries of the capacitors and plug arrays are shown schematically in Fig. 15.

Top electrode annealing is needed to reduce capacitor leakage current to acceptable levels. As can be seen from Fig. 16, satisfactory leakage is seen wth O_2 annealing at temperatures above 400-450°C. *Some* reduction in leakage is obtained by annealing in N_2, but the leakage reductions are not enough for N_2 to be considered a viable replacement for O_2.

Fig. 17 shows that capacitance per cell (C_{cell}) changes with annealing in O_2, but is not affected by annealing in N_2. In O_2, C_{cell} gradually increases with annealing temperature, reaching a maximum at an annealing temperature of 500°C. But anneals at temperatures above 500°C produce large drops in capacitance, a result which we attribute to the formation of a low-k series capacitance from barrier and/or plug oxidation. However, the important thing to note from Figs. 16 and 17 is that there is a "process window" for oxygen annealing in the 400-450°C range that provides both acceptable leakage and capacitance.

Fig. 18 tracks how the individual plug resistance values R_{plug} are affected by BSTO deposition and subsequent annealing. R_{plug} is about 20 kΩ prior to BSTO

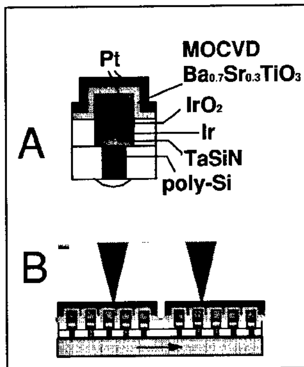

Figure 15*. Capacitor geometry (a); array schematic (b).*

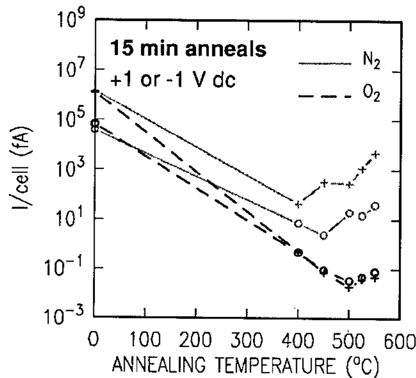

Figure 16. Cell leakage vs. anneal temperature in N_2 or O_2. Conditions: +1 V (+); -1 V (o).

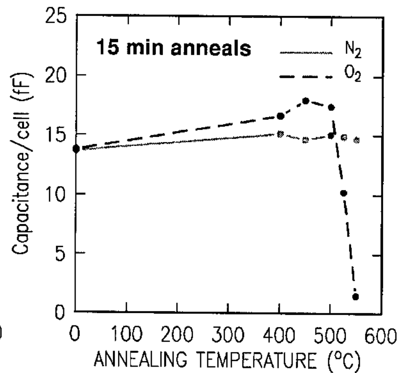

Figure 17. Cell capacitance vs. anneal temperature in N_2 or O_2.

deposition, and increases to 35-40 kΩ after BSTO and top electrode deposition. R_{plug} becomes unacceptably high (~1 MΩ) after oxygen annealing at 500°C for 15 min, but remains tolerable after anneals in O_2 or N_2 at 400-450°C for 20 min. Interestingly, the BSTO has a protective effect against plug oxidation: after a 500°C/15 min O_2 anneal, R_{plug} without BSTO is 33 MΩ vs. 1 MΩ with the BSTO in place.

CONCLUSIONS

Much progress has been made in identifying, processing, and integrating barrier and electrode materials for use with ferroelectric and high-epsilon materials, although many challenges remain. "Middle ground" oxidizing conditions reflecting a compromise between the higher oxygen exposures preferred for FE/HE deposition and processing, and the somewhat lower oxygen exposures that can be tolerated by the barrier materials, will probably be necessary for conventional ("bottom electrode first") process flows.

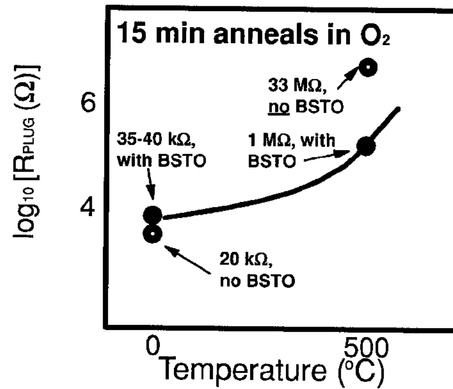

Figure 18. Resistance of ~0.2μm diameter plugs vs. annealing conditions.

ACKNOWLEDGMENTS

The following people are thanked for helpful discussions and/or for various contributions to sample preparation or analysis: P.S. Andry, R. Carruthers, T. Dimitri, C. Jahnes, C. Lin, A.J. Kellock, D.E. Kotecki, I.C. Noyan, S.M. Rossnagel, T.M. Shaw, and Y. Wang.

REFERENCES

1. D.E. Kotecki, J.D. Baniecki, H. Shen, R.B. Laibowitz, K.L. Saenger, J.J. Lian, T.M. Shaw, S.D. Athavale, C. Cabral, Jr., P.R. Duncombe, M. Gutsche, G. Kunkel, Y.-J. Park, Y.-Y. Wang, and R. Wise, IBM J. Res. Develop. **43** 367 (1999).
2. M.C. Hugon, J.M. Desvignes, B. Agius, I.C. Vickridge, D.J. Kim, and A.I. Kingon, Nucl. Instrum. Methods Phys. Res. B, **161-163** 578 (2000).
3. T. Hara, T. Kitamura, M. Tanaka, T. Kobayashi, K. Sakiyama, S. Onishi, K. Ishihara, J. Kudo, Y. Kino, and N. Yamashita, J. Electrochem. Soc. **143** L264 (1996); T. Hara, M. Tanaka, K. Sakiyama, S. Onishi, K. Ishihara, and J. Kudo, Jpn. J. Appl. Phys. **36** L893 (1997).
4. A. Grill, C. Jahnes, and C. Cabral, Jr., J. Mat. Res. **14** 1604 (1999).
5. C. Cabral, Jr., K.L. Saenger, D.E. Kotecki, and J.M.E. Harper, J. Mater. Res. **15** 194 (2000).
6. K.L. Saenger, A. Grill, T.M. Shaw, D.A. Neumayer, C. Lin, and Y.Y. Wang, Mat. Res. Soc. Symp. Proc. **541** 119 (1999).
7. K.L. Saenger, J.H. Comfort, A. Grill, and D.E. Kotecki, U.S. Patent No. 5 914 851 (22 June 1999).
8. K.L. Saenger and I.C. Noyan, J. Appl. Phys., in press for March 15, 2001 issue.
9. K.L. Saenger and D.A. Neumayer, J. Appl. Phys., in press for March 15, 2001 issue.
10. T. Ahilea, E. Zolotoyabko, J. Hartwig, M. Ohler, and E. Prieur, J. Appl. Phys. **84** 6076 (1998).
11. E. Zolotoyabko, J. Appl. Cryst. **31** 241 (1998).
12. R.A. Swalin, *Thermodynamics of Solids*, John Wiley and Sons, New York, 1972, pp. 113-116.
13. Jehn, H. Speck, W. Hehn, E. Fromm, and G. Horz, *Physics Data: Gases and Carbon in Metals (Thermodynamics, Kinetics, and Properties)* Pt. XX: Platinum Metals (2), Fach-informations-zentrum Energie (1982).
14. S.Y. Cha and H.C. Lee, Jpn. J. Appl. Phys. **38** L1128 (1999).
15. K.L. Saenger and S.M. Rossnagel, Mat. Res. Soc. Symp. Proc. **596** 57 (2000).
16. T. Yunogami and K. Nojiri, J. Vac. Sci. Technol. B, **18** 1911 (2000).
17. M.C. Chiang, F.M. Pan, H.C. Cheng, J.S. Liu, S.H. Chan, and T.C. Wei, J. Vac. Sci. Technol. A **18** 181 (2000).
18. P.C. Andricacos, J.H. Comfort, A. Grill, D.E. Kotecki, V.V. Patel, K.L. Saenger, and A.G. Schrott, U.S. Patent No. 5 789 320 (4 August 1998).
19. H. Horii, B.T. Lee, H.J. Lim, S.H. Joo, C.S. Kang, C.Y. Yoo, H.B. Park, W.D. Kim, S.I. Lee, and M.Y. Lee, 1999 Symposium on VLSI Technology (Kyoto, Japan 14-16 June 1999), Digest of Technical Papers **103** (1999).
20. C.Y. Yoo, H.B. Park, D.S. Hwang, H. Hideki, W.D. Kim, H.J. Lim, Y.W. Park, S.I. Lee, and M.Y. Lee, Mat. Res. Soc. Symp. Proc. **596** 11 (2000).
21. J.D. Baniecki et al., in preparation.

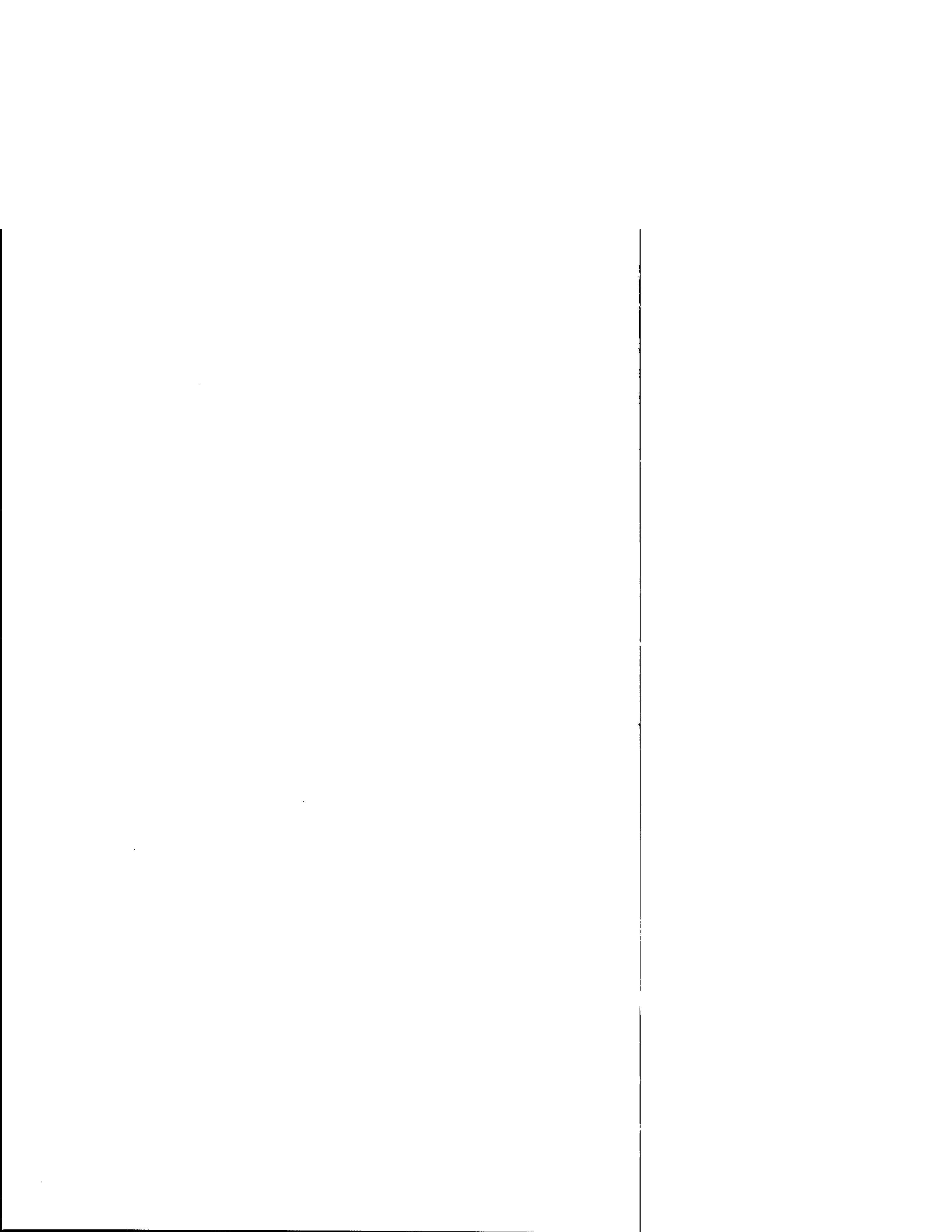

Mat. Res. Soc. Symp. Proc. Vol. 655 © 2001 Materials Research Society

OXIDATION RESISTANCE OF TaSiN DIFFUSION BARRIERS FOR STACKED CAPACITORS

* F. LETENDU (1), * M.C. HUGON (1),* B. AGIUS (1), ** I VICKRIDGE, *** F. AYGUAVIVES, *** A.I. KINGON
* LCFIO, bat 503, Université Paris Sud, 91405 Orsay cedex, France.
** GPS, Tour 23, Université Paris 6 et 7, 75251 Paris, France.
*** Dept. of Materials Science and Engineering, North Carolina State University, Raleigh, NC, USA.
(1) Present address: LPGP , bat 210, Université Paris sud, 91405 Orsay, France.

ABSTRACT

Due to its resistance to oxidation, TaSiN is a promising candidate as an electrically conductive barrier layer for integration of high permittivity oxides in advanced memory devices. In this study we report on the properties and the resistance to oxidation of TaSiN thin films deposited by reactive magnetron sputtering and processed by rapid thermal annealing (RTA) in $^{18}O_2$ at 650°C. In order to determine the composition, RBS (Rutherford Backscattering Spectroscopy) and NRA (Nuclear Reaction Analysis) techniques have been used. ^{18}O depth profile concentrations were measured after RTA using the narrow (fwhm=100eV) resonance at 151 keV in the nuclear reaction $^{18}O(p,\alpha)^{15}N$.

INTRODUCTION

The use of ferroelectric (FeRAM) and high dielectric constant (DRAM) perovskite oxides, in advanced memory devices, requires the presence of a diffusion barrier between the capacitor's bottom electrode layer and the poly-Si plug. This barrier must prevent chemical electrode/plug interactions and plug oxidation, and must remain electrically conductive after annealing in oxygen.

Al-Ta bilayers as well as a number of refractory metal nitrides have been proposed as oxygen diffusion barriers, including TiN, TaN and compositions of TaSiN and TiAlN. $Ta_xSi_yN_z$ alloys (TaSiN in the following) are amorphous, ternary mixtures of the three elements which are electrically conductive over a wide range of compositions. A systematic study of this material as an oxygen diffusion barrier has not been extensively reported and only a few papers have been published. [1, 2, 3]

In this paper, we report on the properties and the oxidation behavior of TaSiN thin films deposited by reactive magnetron sputtering of a $TaSi_2$ target, using a new analytical tool in this field:^{18}O tracer profiling. The composition of TaSiN films has been optimized in order to prevent oxidation of the underlying Si as well as to maintain a low electrical resistivity under high temperature oxidation, up to 650°C.

EXPERIMENTAL PROCEDURE

TaSiN films, with thicknesses ranging from 80 to 120 nm, were deposited at room temperature by reactive rf magnetron sputtering of a $TaSi_2$ target in an Ar-N_2 atmosphere. Thin film properties were studied as a function of rf power density (from 1.6 to 4 W/cm^2) and N_2 to Ar flow ratio for three different pressures (0.5, 1 and 3 Pa). The distance (z) between substrate and target was fixed at 7 cm. According to the kinetic theory of the gases[4], we can consider, in our particular deposition conditions, that when the gas pressure is lower than 1 Pa, the mean free path of the atoms ejected from the target is higher than z and the transport regime in the plasma can be considered as ballistic. For a gas pressure

higher than 3 Pa, only N atoms are unthermalized. The different deposition parameters are summarized in table 1.

The thermal stability of TaSiN, as an oxygen diffusion barrier, has been investigated under typical conditions for device processing: as-deposited films with different N content were subjected to rapid thermal annealing (RTA) at 650°C under 1 atm of $^{18}O_2$ (96.99 % isotopic enrichment). In this paper, annealing conditions will be presented as follow: temperature [650°C] / heating rise time [2 s] / heating time [30 s] (650°C/2s/30s).

The as-deposited and annealed samples were studied using atomic force microscopy (AFM) to characterize surface morphology, X-ray reflectometry to determine film thicknesses and 4-point probe to measure film resistivity. Rutherford backscattering spectroscopy (RBS) was used for quantitative determination of Ta content in the films. Oxygen, nitrogen and silicon content of thin films were determined respectively using the following selective nuclear reactions : $^{16}O(d,p_0)^{17}O$, $^{14}N(d,\alpha)^{12}C$, $^{14}N(d,p)^{15}N$, and $^{28}Si(d,p)^{29}Si$. For these analyses, TaSiN thin films were deposited on GaAs and/or SiO_2/Si substrates.

Study of oxygen behavior after RTA has been possible thanks to the use of the very narrow (fwhm = 100 eV) resonance in the nuclear reaction $^{18}O(p,\alpha)^{15}N$ at 151 keV. The depth profile of interest was deduced by comparison of the data with theoretical excitation curves calculated for assumed concentration profiles with the SPACES [5] simulation program.

Table 1: deposition conditions.

Power density (W/cm^2)	*Pressure (Pa)*	*Ar flow rate (sccm)*	*Flow ratio N_2 / Ar (%)*
1.6 - 4	0.5	20	5, 7.5, 10
	1	50	2
	3	100 and 50	0.5, 1, 2, 3 (Ar f. r. = 100 sccm) 2 (Ar f. r. = 50 sccm)

RESULTS

As deposited films:

Figure 1 shows AFM images (2.5*2.5 μm^2) corresponding to the surface of TaSiN films deposited respectively at 0.5 Pa and 3 Pa. It is seen that when decreasing the pressure the surface of the film becomes smoother. This result can be explained by the difference in energy of the incident atoms arriving on the film surface. Indeed, the sputtered atoms have more energy at low pressure since they are unthermalized. It is reasonable to expect that they should have a greater surface mobility allowing them to reach the nucleation sites more easily, which might induce a lower roughness.

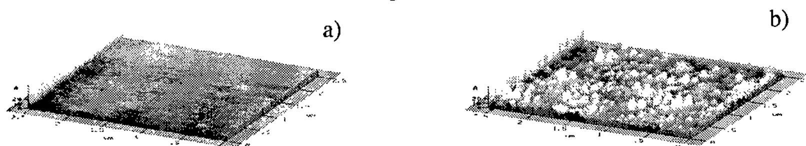

Fig 1: AFM image for films deposited at a) 1 Pa ; b) 3Pa.
These two films were made under identical conditions of flow (Ar = 50sccm ; N_2 = 1 sccm) and power density (2.65W/cm^2).

Figures 2 and 3 show the atomic density (in at./cm^3), the total density (in g/cm^3) and the resistivity of as deposited TaSiN thin films as a function of the rf power density at respectively 0.5 Pa and 3 Pa. First, we notice that whatever the deposition parameters, the ratio of Si/Ta stays close to that of the target (Si/Ta=2). However, the nitrogen content always decreases with increasing rf power density. This could be explained by a competition between nitrogen adsorption at the target surface and its sputtering rate: at low power density, the sputtering rate being low, the target surface is continuously re-covered by nitrogen so the corresponding deposited films are nitrogen rich. When power density increases, the sputtering rate increases as well and the cathode surface begins to be uncovered so the TaSiN thin films become nitrogen poor [6]. Above 3.2W/cm^2, even if the composition ratio Si/Ta remains close to 2, Ta and Si atomic contents decrease whatever is the gas pressure in the chamber. This effect could actually be attributed to a change of porosity that has been observed experimentally when TaSiN films are deposited at high power density. In addition, the regime in which we choose to deposit our films will also affect the oxygen contamination. In fact, one can see in figure 2c and 3c that the oxygen contamination is much higher in the thermalized regime (3 Pa) than in the ballistic regime (0.5 Pa). At low pressure and for a power density between 1.5 and 3.5W/cm^2, this contamination does not depend of the film thickness. This result suggests (or indicates) that oxygen is not incorporated during deposition but after taking out the samples from the reactor chamber. The fact that the contamination increases with power density could be attributed to a roughness effect. Experimental observations by AFM are currently in progress. At high pressure (3 Pa) oxygen reaches a minimum value (fig 3c) when Ta and Si contents are maximum (i.e near 2.65 W/cm^2). For a given power density we have seen that oxygen content varies linearly with thickness meaning that it is present through all the film and not only at its surface. This oxygen certainly comes from the residual vaccum which mainly consists of H_2O.

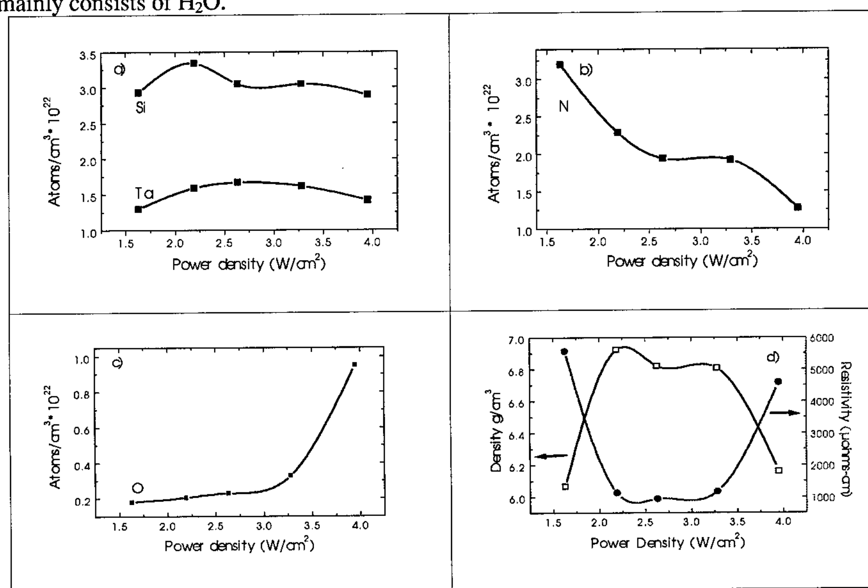

Fig 2: films deposited at 0.5 Pa with N_2/Ar=5% :a) atoms of Ta and Si / cm^3 ; b) atoms of N / cm^3 c) atoms of O / cm^3; d) evolution of resistivity and density.

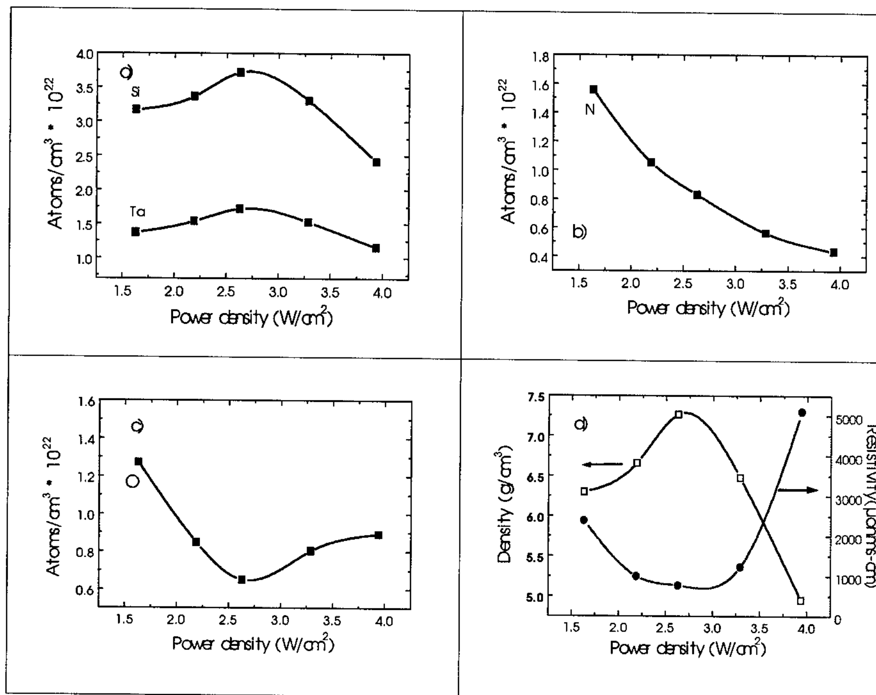

Fig 3: films deposited at 3 Pa ; N_2/Ar=0.5% :a) atoms of Ta and Si / cm^3, b) atoms of N / cm^3
c) atoms of O / cm^3, d) evolution of resistivity and density

Since the composition ratio Si/Ta is almost the same for all the films we have studied the influence of N content on the resistivity for low oxygen contamination thin films (fig 4). These films were deposited at low pressure, 0.5 and 1 Pa with power densities between 1.6 and 3.2 W/cm^2. For a nitrogen content above 35% the resistivity becomes very high. Note that films made at higher power densities (over 3.5W/cm^2) are not considered as they are porous and exhibit high resistivity: their properties are independent of nitrogen content.

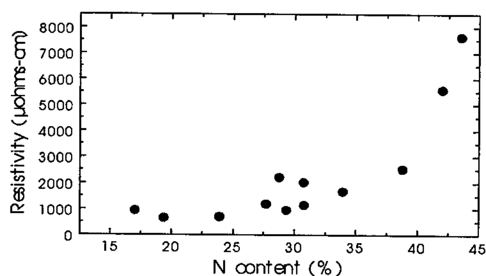

Fig 4: resistivity as a function of N content

Annealed films :

After a RTA at 650°C under $^{18}O_2$, the films remain amorphous and no Ta loss has been observed within the accuracy of RBS technique. In contrast with the RTA of TiAlN barriers, this annealing treatment does not induce any variation in N content. [6] Since TaSiN films are deposited directly on Si subtrates, we cannot extract any information about the Si behavior during annealing. Table 2 shows the number of ^{18}O atoms incorporated into the TaSiN films during RTA. For low pressure (0.5Pa), ^{18}O incorporation depends on power density. Figure 5 shows the excitation curve and the corresponding depth profile obtained by resonance nuclear reaction analysis for three different deposition conditions. Power density of 2.65 W/cm^2 and low pressure (0.5 Pa) induce a superficial oxidation of TaSiN films. However, when either decreasing the power density to 2.2 W/cm^2 or increasing the pressure to 3 Pa it turns out that the resistance against oxidation resistance is reduced. Indeed, the oxide layer created by the out-coming oxygen spread over a much larger thickness in the film which clearly indicates a lower oxidation resistance.

Table 2: properties of TaSiN films.

Pressure (Pa)	Power density (W/cm^2)	Flow ratio N_2/Ar	Composition as eposited (on GaAs)	Resistivity as deposited(μ ohms-cm)	O^{18}/cm^2 (on Si)
0.5	2.2	5%	$Ta_{21}Si_{45}N_{31}O_3$	1130	$7.5*10^{16}$
0.5	2.65	5%	$Ta_{25}Si_{46}N_{26}O_3$	939	$3.4*10^{16}$
0.5	2.2	7.5%	$Ta_{19}Si_{39.5}N_{39}O_{2.5}$	2519	$6.4*10^{16}$
0.5	2.65	7.5%	$Ta_{23}Si_{41}N_{32}O_4$	2002	$3.35*10^{16}$
3	2.65	2%	$Ta_{20}Si_{38}N_{27}O_{15}$	3321	$8*10^{16}$

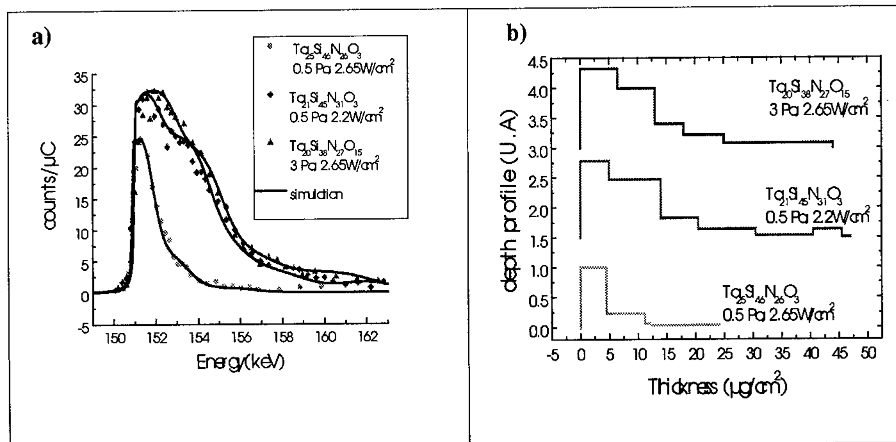

Fig 5: a) excitation curve and simulation
b) depth profile of ^{18}O.

CONCLUSION

In this paper we have shown the importance of the deposition parameters in the obtention of oxidation resistance TaSiN thin films. As-deposited films made at 0.5 and 1 Pa exhibit more desirable qualities than those made at 3 Pa in terms of surface roughness and oxygen contamination. Power density and pressure have a crucial effect on oxidation resistance. Films made at low pressure (0.5 Pa) and a power density of 2.65 W/cm^2 present high oxidation resistance. XPS measurement are forms at the surface of the barrier layer.

REFERENCES

[1] A. Grill, C. Jahnes and C. Cabral Jr., *J. Mater. Res.* **14** (4), 1604 (1999).

[2] T. Hara, M. Tanaka, K. Sakiyama, S. Onishi, K. Ishihara and J. Kudo, *Jpn. J. Appl. Phys.* **36**,,893 (1997).

[3] C. Cabral Jr., K.L. Saenger, D. E. Kotecki, J. M. E. Harper, *J.Mater. Res.* **15** (1), 194 (2000).

[4] W. D. Westwood, J. Vac. Technol. 15 (1), 1 (1978)

[5] I. Vickridge and G. Amsel, *Nucl. Instr. And Meth. In Phys. Res.* **B45**, 6 (1996).

[6] F. Ayguavives, B. Ea-Kim, P. Aubert, B. Agius and J. Bretagne, *Appl. Phys. Lett.* **73** (8), 1023 (1998).

[6] M.C. Hugon, J.M. Desvignes, B. Agius, I Vickridge, D.J. Kim and A.I. Kingon, *Nucl. Instr. And Meth. In Phys. Res.* **B 161-163**, 578 (2000).

Mat. Res. Soc. Symp. Proc. Vol. 655 © 2001 Materials Research Society

Highly Stable Ir-Ta-O Electrode for Ferroelectric Material Deposition

Fengyan Zhang, Sheng Teng Hsu, Jer-shen Maa, Yoshi Ono, Ying Hong, Weiwei Zhuang, Shigeo Ohnishi*, Wendong Zhen* and Norito Fujiwara*
Sharp Laboratories of America, Inc., 5700 NW Pacific Rim Blvd. Camas, WA 98607, USA
*Sharp Corporation, Tenri-city, Nara632-8567, Japan

ABSTRACT

Ir-Ta-O composite bottom electrode has extraordinary high temperature stability. It can maintain good conductivity and integrity even after 5min annealing at 1000 °C in oxygen ambient. The thermal stability of Ir-Ta-O on different substrates has been studied. It shows that Ir-Ta-O is also very stable on Si and SiO_2 substrates. No hillock formation and peelings of the bottom electrode were observed after high temperature and long time annealing in O_2 ambient. SEM, TEM, XRD, and AES have been used to characterize the Ir-Ta-O film and the interfaces between Ir-Ta-O bottom electrode and Si or SiO_2 substrate. The composition and conductivity changes of the electrode during oxygen ambient annealing and the interdiffusion issue will be discussed. Furthermore, Ir-Ta-O/SiO_2/Si capacitor with 30Å gate oxide was fabricated and the C-V and I-V characteristics were measured to confirm the stability of Ir-Ta-O on thin gate oxide.

INTRODUCTION

Thin films of Ir, Pt, Ru, IrO_2 and RuO_2 have been extensively studied for the application as electrode materials in FeRAM and DRAM devices[1-10]. In addition to the advantages of chemical stability and low resistivity, noble metal oxides can also improve the fatigue property of ferroelectric material such as PZT by preventing space charge formation at the electrode and ferroelectric material interface. However, some problems, such as hillock formation and film peeling caused by stresses, poor adhesion, and oxidation of the barrier layer, have limited the application of these electrodes in very high temperature in oxygen ambient, which is the required deposition and annealing condition for some ferroelectric materials such as $SrBi_2Ta_2O_9$.

It has been reported previously that grain boundary precipitation can inhibit hillock formation, improve the structural stability, and enhance the barrier property of thin films[11]. Yoon et al [12, 13] found RuO_2 stuffed Ta barrier was more resistant to oxidation and oxygen diffusion than nitrogen stuffed polycrystalline nitride. There was no increase in sheet resistance even after 800°C annealing for 30 min in air. They also found RuO_2 stuffed Pt can prevent the oxygen diffusion up to 650°C for 30 min. A Ru-Ti alloy with high Ru composition was found to have better thermal stability and better barrier properties against interdiffusion of Si and oxygen than Ru metal alone[14].

Comparing with Pt and Ru, Ir has been reported to have better barrier property against oxygen diffusion. Ta and TaN are more resistant to oxidation than Ti and TiN are. The refractory nature of both Ta and Ir, and the high formation temperature of their compounds have assumed their increased thermal stability of the Ta-Ir system [15] . It is expected that the oxygen diffusion resistance and structural stability of the Ir-Ta system

can be further improved by oxygen incorporation. The purpose of this paper is to study the effect of Ta and oxygen addition into the Ir film. The microstructure and phase changes of Ir-Ta-O thin film during oxygen ambient annealing have been characterized. The thermal stability of Ir-Ta-O on different substrates was studied. The electrical properties of Ir-Ta-O/SiO2/Si capacitor were characterized by C-V and I-V measurements.

EXPERIMENT

The Ir-Ta-O/Ta/Si structure was fabricated first. The silicon (100) p-type wafer was dipped in dilute HF solution, DI water rinsed and spin dried before loading into a sputtering chamber. The base pressure of the sputtering chamber was around $3x10^{-7}$ Torr. The sputtering chamber was equipped with two separate sputtering targets. The purity of the 4-inch diameter Ta and Ir targets are 99.95% and 99.8% respectively. Ta film was deposited by DC sputtering in pure Ar. The thickness is about 30 nm. Ir-Ta-O film was deposited by reactive sputtering Ir and Ta in Ar-O_2 mixture with flow ratio of Ar: O_2 at 1:1. The thickness is about 200nm. The chamber pressure was maintained at 10 mTorr for Ir-Ta-O film deposition. The DC power on both Ir and Ta targets was about 300 W. The deposition sequence was as follows: Ta layer was deposited on the Si substrate first, then the Ir-Ta-O film was deposited on the Ta layer. The deposition was performed at room temperature. After deposition of the films, the Ir-Ta-O/Ta/Si structure was annealed in furnace in oxygen atmospheric ambient at 800°C for 30, 60, and 90 min respectively. The microstructure and phase changes of the Ir-Ta-O film were characterized by X-ray diffraction. The morphology changes of the structure were examined by scanning electron microscopy and transmission electron microscopy. Sheet resistance changes of the films were measured by four-point probe.

Secondly, the Ir-Ta-O/Si and Ir-Ta-O/SiO_2 structures were fabricated. The deposition condition of the Ir-Ta-O film on Si and SiO_2 substrates was the same as mentioned above. The Ir-Ta-O/Si and Ir-Ta-O/SiO_2 structure were also annealed in oxygen ambient at 800°C for 10 min. . The composition and the interdiffusion between different layers were analyzed by auger electron spectroscopy depth profile. In order to study the effect of thickness increase of Ir-Ta-O film on the structure stability, an Ir-Ta-O(200nm)/SiO2 (3.0nm)/Si (500nm) stack structure was fabricated by stack etching. This structure was also annealed in O_2 ambient at 800°C for 10 min. SEM was used to study the stability of this structure.

Thirdly, the Ir-Ta-O(200nm)/SiO_2(3.0nm)/Si capacitors were formed on 150mm diameter p-type (100) Si substrates. Openings were made in 1000Å thermal oxide by photo patterning and HF wet etching, followed by gate oxidation using a O_2/N_2O recipe at 850 °C that results in a 30Å nitrided oxide. Then Ir-Ta-O was deposited on SiO_2 using the same condition as mentioned above. The Ir-Ta-O/SiO_2/Si capacitor was then fabricated by dry etching Ir-Ta-O film. The capacitor sizes are of 100 x 100 μm^2, 200 x 200 μm^2 and 400 x 400 μm^2 respectively. C-V and I-V characteristics were measured on an HP4284A before and after oxygen ambient annealing.

RESULTS AND DISCUSSION

Figure 1 is the TEM picture of the as deposited Ir-Ta-O film . In contrast to the typical large grain and columnar structure observed in e-beam evaporated and DC sputtered Ir and Pt films, this Ir-Ta-O film exhibited a finer polycrystalline granular structure.

It has confirmed that the thickness, the conductivity and phases of the Ir-Ta-O film are rather stable once most of the Ir and Ta was oxidized to IrO_2 and Ta_2O_5 [16]. Figure 2 is the XRD spectrum and sheet resistance changes of the Ir-Ta-O film after 800°C annealing for 30, 60, and 90 min annealing in oxygen ambient. No significant phase changes are observed after different duration time annealing. The sheet resistance maintained almost the same after the initial decreasing that is believed to be caused by the crystallization and grain growth of the Ir-Ta-O film [16].

AES depth profile were obtained on both Ir-Ta-O/Si and Ir-Ta-O/SiO_2/Si samples as shown on Figure 3 and Figure 4. They showed that the interfaces between Ir-Ta-O and Si , and between Ir-Ta-O and SiO_2 are very stable. No significant interdiffusion observed

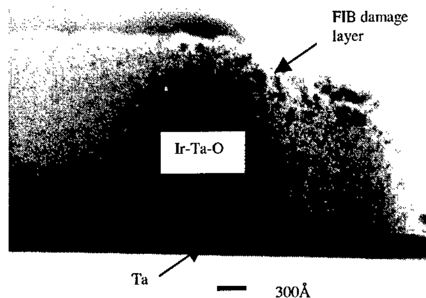

Figure 1. TEM cross-section of Ir-Ta-O/Ta/Si Structure

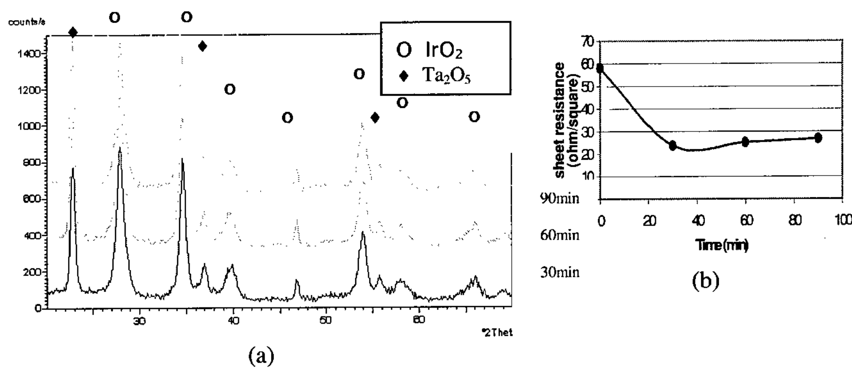

Figure 2. Long time annealing of Ir-Ta-O for 30, 60, 90 min respectively.
(a) XRD spectra; (b) sheet resistance changes

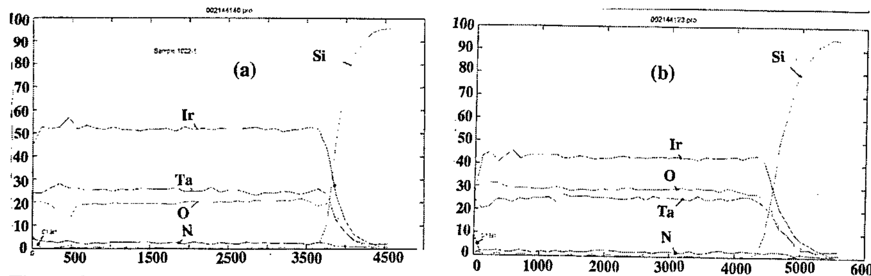

Figure 3. AES spectra of Ir-Ta-O/Si structure (a) before and (b) after oxygen annealing at 800°C for 10min

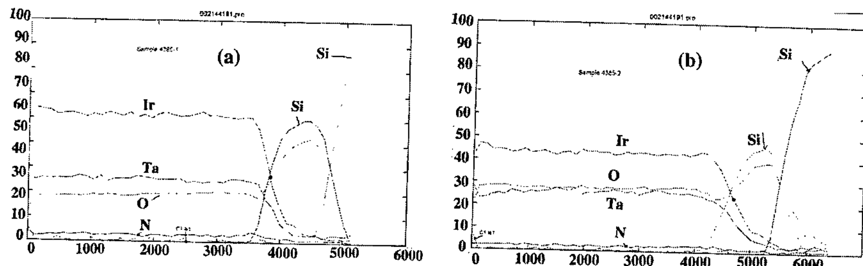

Figure 4. AES spectra of Ir-Ta-O/SiO_2/Si structure (a) as deposited, (b) after oxygen annealing at 800°C for 10min

after 800°C 10 min annealing in oxygen ambient. But this does not eliminate the possibility of thin SiO_2 layer formation at the Si surface because of the existence of oxygen at the interfaces. In order for this film to be used in some type of FeRAM and DRAM devices, in which low contact resistance is required between the bottom electrode and polysilicon substrate, an oxidation resistant barrier layer is required. It can be seen from Figure 3 (b) and Figure 4 (b) that the further oxidation of Ir-Ta-O film after annealing is uniformly across the whole film thickness, which means that oxygen can diffuse through the Ir-Ta-O film.

It has been found that the thickness of Ir-Ta-O film increased after high temperature annealing due to the oxidation of the Ir and Ta. Similar increasing of the thickness was observed for Ru enriched Ru-Ti alloy during oxygen ambient annealing[14]. But their results showed that the oxidation only occurred at the surface and that prevented further oxidation of Ru-Ti layer. In contrast, the Ir and Ta in the Ir-Ta-O film were almost totally oxidized. This was probably due to high Ta ratio in the Ir-Ta-O film.

Figure 5 is the shallow trench isolation (STI) structure after stack etching of Ir-Ta-O /SiO_2 (3.5nm) / Si (500nm). Figure5 (a) is the just etched structure and figure 5 (b) is the etched structure after 800°C 10min annealing in oxygen ambient. Although there are some thickness and volume increasing after annealing, no destructive structure failure observed. CVD ILD deposition can easily fill the silicon trench and obtain good step coverage.

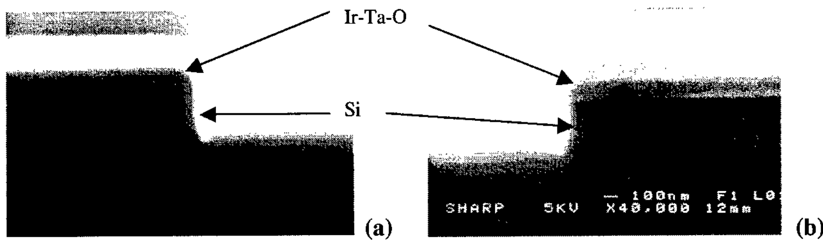

Figure 5. Structure stability of of Ir-Ta-O /SiO_2 (3.0nm) / Si (500nm) (a) as etched, (b) after 800°C annealing for 10min. in oxygen ambient

For Ir-Ta-O/SiO_2/Si capacitor, C-V characteristics measured on both the as deposited and annealed Ir-Ta-O/SiO_2/Si capacitors. The C-V characteristics of the as deposited capacitor show leakage problem as shown on figure 6 (a). This is due to the Ir and Ta metal existed in the as deposited Ir-Ta-O film. After 800°C annealing in oxygen ambient for 10 min, Ir and Ta metal were oxidized to IrO_2 and Ta_2O_5, the interface of Ir-Ta-O and SiO_2 interface was also improved. Excellent C-V characteristics were obtained as shown on figure 6 (b). The C-V characteristic can be further improved after a forming gas annealing at 450°C for 15 min due to the improvement of the SiO_2 and Si interface. Figure 6 (c) and (d) show that the leakage current through the capacitor also decreased dramatically after oxygen and forming gas annealing.

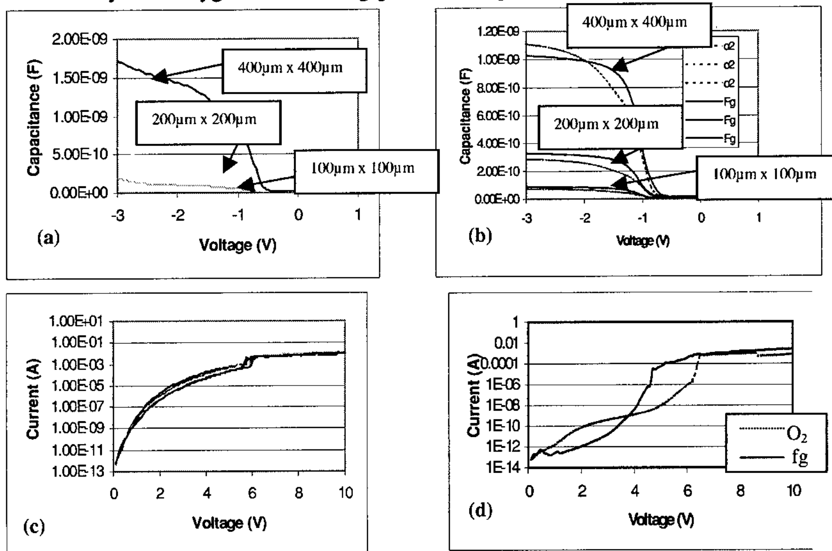

Figure 6. C-V and I-V characteristics of Ir-Ta-O/SiO_2/Si capacitor (a), (c) as deposited, (b), (d) after annealing (o2 --- O_2 annealing, fg--- Forming gas annealing)

CONCLUSION

The Ir-Ta-O film showed very high temperature stability. High conductivity was maintained and no structural failure such as large hillock formation and film peeling were observed after 800°C annealing for 90 min. The Ir and Ta in the Ir-Ta-O film were oxidized during annealing. The microstructure of the Ir-Ta-O film after high temperature oxygen ambient annealing is a polycrystalline mixture including IrO_2 and Ta_2O_5 phases. The C-V and I-V characteristics of Ir-Ta-O/SiO_2/Si capacitor show that this film is also very stable on thin gate oxide. It is a good candidate as bottom electrode for MFMOS type single transistor application, especially when the ferroelectric films need to be deposited and annealed at high temperature in oxygen ambient.

REFERENCES:

1) P.D. Hren, S. H. Rou, H. N. Al-Shareef, K.D. Gifford, O. Auciello, and A.I. Kinggon, *Integarated Ferroelectrics*, **2**, 311 (1992)

2) J.O. Olowolafe, R. E. Jones, A.C. Campbell, P.D. Maniar, R.I. Hegde, and C.J. Mogab, *Mat Res Soc. Symp. Proc.*, **243**, 355 (1992)

3) T. Nakamura, Y. Nakao, A. Kamisawa and H. Takasu, *Appl. Phys. Lett.* **65**, 1522 (1994)

4) T. Nakamura, Y. Nakao, A. Kamisawa and H. Takasu, *Jpn. J. Appl. Phys. Lett.* **33**, 5207 (1994)

5) Fengyan Zhang, Tingkai Li, Tue Nguyen, Sheng Teng Hsu, Ferroelectric Thin Films VII, *Mat Res Soc. Symp. Proc* (1998) (to be published)

6) Seung-Hyun Kim, J.G. Hong, J.C. Gunter, H. Y. Lee, S.K Streiffer, and Angus I. Kingon, *Mat Res Soc. Symp. Proc.* **493**, 131(1997)

7) G. –R. Bai, A. Wang, I-Fei Tsu, C.M. Foster, and O. Auciello, *Integarated Ferroelectrics,* **21**, 291 (1998)

8) A. Grill, R.Laibowitz, D. Beach, D. Neumayer and P.R. Duncombe, *Integarated Ferroelectrics,* **14**, 211 (1997)

9) Katsuhiro Aoki, Yukio Fukuda, Ken Numata, and Akitoshi Nishimura, *Jpn. J. Appl. Phys.* Vol. **34** , 5250 (1995)

10) J.J. Lee, C. L. Thio, and S.B. Desu, *J. Appl. Phys.* **78**(8) 5073 (1995)

11) S. Wolf, *Silicon Processing,* Lattice Press (Sunset Beach, California, 1990), Vol. **2**, p271

12) Dong-Soo Yoon, Hong Koo Baik, Sung-Man Lee, Sang-In Lee, Hyun and Hwack Joo Lee, *J. Vac. Sci. Technol.* B **16**(3), May/Jun , 1137(1998)

13) Dong-Soo Yoon, Hong Koo Baik, Sung-Man Lee, Sang-In Lee, Hyun and Hwack Joo Lee, *Appl. Phys. Lett.* V **73**, 324 (1998)

14) Ray-Hua Horng, Dong-Sing Wuu, Luh-Huei Wu, Ming-Kwei Lee, Shih-Hsiung Chan, Ching-Chich LEU, Tiao-Yuan Huang and Simon Min SZE, *Jpn. J. Appl. Phys.*, **37**, L1274 (1998)

15) D.K. Wickenden, M. J. Sisson, A. G. Todd, and M.J. Kelly, *Solid State Electronics,* **27**, 515 (1984)

16) Fengyan Zhang, Jershen Maa, Sheng Teng Hsu, Shigeo Ohnishi and Wendong Zhen, *Jpn. J. Appl. Phys.* **38**, L1447 (1999)

Mat. Res. Soc. Symp. Proc. Vol. 655 © 2001 Materials Research Society

Etching Characteristics of Noble Metal Electrode

St. Schneider, H. Kohlstedt, and R. Waser
Institut für Festkörperforschung, Forschungszentrum Jülich
Jülich, 52425, Germany

ABSTRACT

The objective of this work was to develop a process to pattern noble metal electrodes. To systematically investigate possible reactive etch process regions, characterized by volatile etch products, we used a reactive ion beam etching (RIBE) tool with a filament free ICP source. This configuration gives us exact control over the beam energy and the current density, and allows to use reactive gases. An energy dispersive quadrupole mass spectrometer is fitted to the chamber for in situ monitoring.

We study the influence of the beam energy and the beam current impinging on the wafer surface as well as it's angular dependence. Several additives to the chlorinated process chemistry are investigated and characterized in terms of their role to help to increase the etch rate, maintain a vertical profile, or to enhance process selectivity.

The main focus of the study is on Platinum. Blanket films were used to describe the influence of the material, and analysis were carried out to characterize the process in terms of etch rate, residues and selectivity.

INTRODUCTION

A reactive etch process to pattern noble metal electrodes is considered necessary for DRAM integration and desirable for FRAM application in near terms. However, few information has been released to the public literature so far [1]. A potential process has to meet the well known stringent requirements like a steep slope of the side wall, a minimal change in the feature size, no fences, and no residues on the wafer. Yield considerations from manufacturing impose totally different requirements like high mean time between clean (MTBC) to be able to cut down production costs.

Due to the lack of a chemical etch rate one either ends up with quite steep side walls, to the cost of redeposition on the mask material (fences), or with fence free structures with very poor control over the feature size and an unacceptable slope [2-5]. Furthermore sputter etching offers only a very limited selectivity to the mask as well as the substrate. Beside those disadvantages a sputter process results in a coating of the inside walls of the etch chamber leading to particle problems as well as plasma instabilities, requiring often wet cleans of the tool.

To understand the high temperature etch process of Platinum we systematically investigated different etch regimes and plasma chemistries. In order to separate the plasma physic from the surface chemistry, we choose a Reactive Ion Beam Etching (RIBE) tool, instead of a conventional plasma reactor.

The main advantage of ion beam etching tools is the precise control over the beam energy as well as the beam current density in contrast to plasma reactors, where those plasma parameters are a result of the energy input from the generators and have to be measured for each process.

EXPERIMENTAL SETUP

Our Ionfab 300^{plus} from Oxford Plasma Technology is able to handle 6" as well as 4" wafers. The beam source is designed filament free with an inductively coupled plasma (ICP) source powered with a 13.56 MHz generator. This enables us to feed reactive gases like flourine, chlorine, or bromine containing chemistries directly into the source region.

The beam extraction takes place through a set of two grids (acceleration and screen grid) which accelerate and focus the beam. A filamentless beam neutralizer (FBN) mounted on top of the discharge chamber takes care of the charge neutrality of the beam to etch insulating specimen as well. The process region extending to a beam energy up to 1000 eV and beam currents up to 300 mA is comparable to industrial plasma reactors.

The wafer is clamped to a temperature controlled electrode with Helium-backside cooling to ensure thermal coupling. In the low temperature regime (-15°C up to 80°C) a dedicated chiller controls the electrode temperature while in the high temperature regime (50° up to 300°C) a resistant heating system takes over the temperature control.

The wafer can be rotated during the process as well as tilted towards the beam. The large distance between plasma generation inside the source and the wafer surface becomes only a disadvantage if the etch process is dominated by activated neutrals which relax very rapidly.

A further advantage of ion beam etching tools is the large dimension of the process chamber, which eases the use of probes without interfering with the beam and potentially tampering with the process. To study the process mechanisms an energy dispersive quadrupole mass spectrometer (Hiden EPQ) is attached to the chamber. The mass regime of the probe extents from 0 amu up to 500 amu with a resolution below 1 amu. The energy range goes from 0 to ± 1000 eV with a resolution below 1 eV. The system configuration is shown in Figure 1.

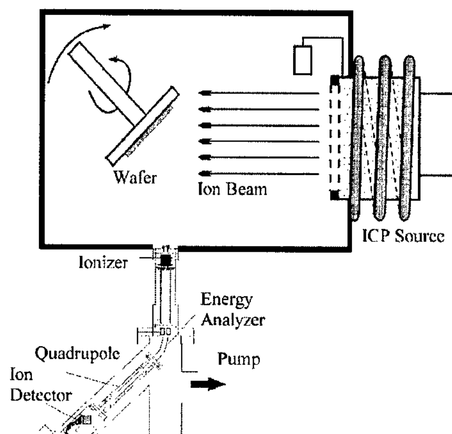

Figure 1. Reactive Ion Beam Etching tool with attached energy dispersive quadrupole mass spectrometer

EXPERIMENTAL RESULTS

Energy dependence of the etch rate

The energy dependence of the platinum etch rate was investigated to get a baseline for the sputter etch regime, as well as to confirm compatibility of the ion source process regime with conventional plasma reactors. As can be seen in Figure 2, the etch shows the expected behavior and starts at a threshold energy (about 30 eV), increases linear with increasing energy and drops off slightly to a parabolic dependence at higher energies and beam currents larger as 100 mA. For the ion density dependence of the etch rate a very similar behavior is found. The etch rate increases linear with increasing beam current in the range from 75 mA to 250 mA.

As a quite high threshold energy is required to start the etch in the sputter driven etch regime, an *in situ* plasma clean of the chamber walls (to remove the deposited material) is hardly possible.

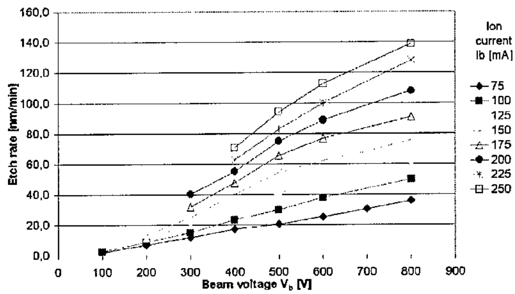

Figure 2. Ion energy dependence of the Platinum etch rate for a pure Chlorine low temperature (20°C) process.

High temperature etching

A possible solution to increase the volatility of the etch products is to increase the etch temperature in conjunction with the use of reactive gases. The vapor pressure of Platinumtetrachloride is at room temperature at about the typical lower limit of the process pressure of 1 mTorr and reaches about 700 mTorr for elevated temperature (300 °C). The aim in using reactive chemistry at higher temperatures, is not so much to increase the etch rate, but

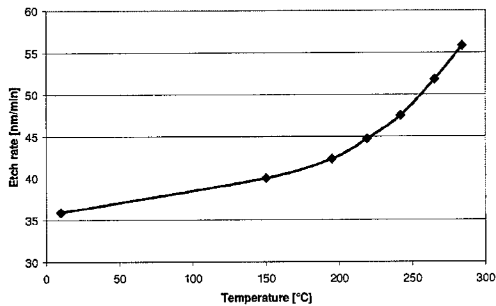

Figure 3. Temperature dependence of the Platinum etch rate for pure Chorine. The exponential dependence is a sign for the chemical nature of the etch, The etch rate starts to increase significantly at around 200-250 °C

much more to be able to control the slope and the feature size by generating volatile etch products. As they can simply be pumped away and re-deposition on the sidewalls of the mask material and the chamber walls is suppressed.

Experimental data confirm the platinum etch rate of a pure chlorine processes to start to increase significantly above 200-250 °C wafer temperature. The dependence of the etch rate with temperature follows a exponential function, which is a clear sign the etch mechanism being of chemical nature (see Figure 3). A physical etch (sputtering) would be temperature invariant.

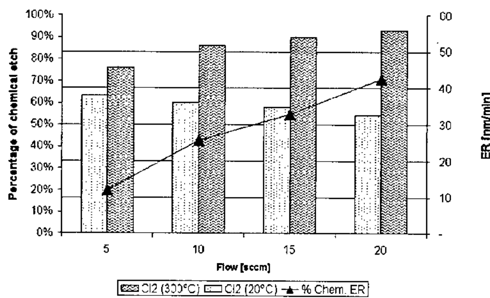

Figure 4. Platinum etch rate dependence on total flow for a Chlorine process at low (20°C) and at high (300 °C) temperature, respectively. At low temperature the etch is physical – sputtering only. The increase at high temperatures is chemically induced. The increment of the etch in ratio to the pure physical sputter rate is plotted as the percentage of the chemical etch.

The total flow is one important parameter to tailor the etch behavior. As can be seen in Figure 4, the dependence of the etch rate is opposite for low and for high temperatures with increasing flow. In the low (room temperature) region the Platinum etch rate decreases with increasing flow, while in the high temperature region (300°C), the etch rate increases with increasing flow. From the mass spectrum shown in Figure 5 we can learn, that for higher gas flows the dissociation yields more Cl^+ ions. At low temperature, the platinum etch process is a pure sputter process, thus with an increasing Cl^+ the concentration of Cl_2^+ concentration decreases and the average mass decreases, too. A decreasing mass results in turn in a drop of the sputter rate. In the high temperature region, on the other hand it is favorable to have a complete dissociation of the Chlorine in the plasma, to offer Cl^+ ions to the Platinum surface, which react to form volatile $PtCl_4$.

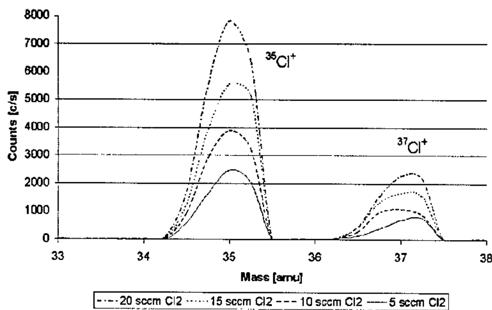

Figure 5. Mass spectrum of a Chlorine process for different gas flows.

As is true for the pure sputter etch regime at low temperatures, also the high temperature etch regime requires a threshold energy to be passed - as Platinum is not etched spontaneously- before significant etch takes place. If the beam energy on the other hand is increased too high, the remaining sputter component prevails over the chemical component. The total etch rate still increases, but the fraction of the chemical etch rate decreases, rendering this regime not useful for a successful process. This is shown in Figure 6 where the relative enhancement of the etch rate in the high temperature region in contrast to the room temperature region is plotted versus the beam energy.

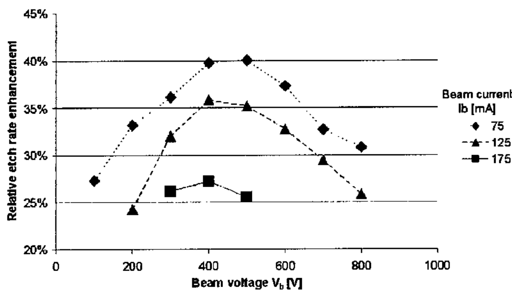

Figure 6. Chemical etch rate enhancement for Chlorine high temperature (300°C) processes in contrast to the low temperature (20 °C) region for constant process parameters.

Angular dependence of the etch rate

Ion beam etching systems are frequently used in the production of magnetic read heads for hard disc drives, as those materials hardly form volatile etch products, too. The advantage of being able to tilt the wafer is used to sputter re-deposited material away. This concept will not work, as soon as steep sidewalls together with precise control over the feature size is required. Nevertheless, it is important to know the angular dependence of the etch rate, e.g. for modeling purposes. For low bias voltage process regimes, the random movement component of the ions toward the sheath boundary may become important due to a broadening of the angular ion distribution function.

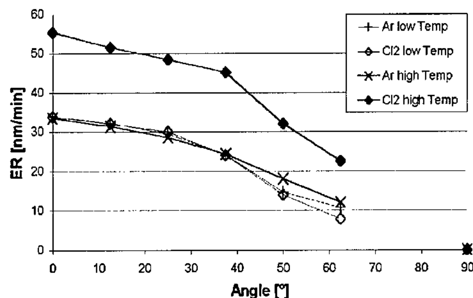

Figure 7. Angular dependence of the Platinum etch rate for Chlorine and Argon processes at low (20 °C) and high (300 °C) temperature, respectively.

The Platinum etch rate drops off somewhat sub cosine like for an increasing angle as can be seen in Figure 7. No pronounced peaks of the etch rate at higher angles are found in neither the low temperature nor the high temperature region. This does not depend on the process chemistry (Argon or Chlorine).

Plasma additives

The most common hardmask used for high temperature application would be a silicon oxide based material. To preserve the mask integrity during the etch is important to control the feature size. A pure chlorine process would be to aggressive. The addition of oxygen to the plasma chemistry helps to decrease the SiO_2 etch rate and adjust the selectivity to the mask material, as well as to the substrate.

CONCLUSION

Etching Platinum chemically at high temperatures is feasible. The exponential dependence of the Platinum etch rate with increasing temperature is a clear evidence for the chemical nature of the etch mechanism. A physical etch would be temperature independent.
In a process window of about 300-500 eV ion energy the ratio of chemical to physical etch is maximized. The dissociation ratio of Chlorine in the plasma is strongly dependent on the total gas flow and thus allows to control the chemical character of the etch.
Additives, like oxygen, allow to control the reactivity and the selectivity, especially to preserve the mask integrity in case a silicon based hard mask is used.

REFERENCES

1. S. Yokoyama, et al., *Jpn. J. Apl. Phys.* Vol 34 (1995) pp.767-770
2. K.R. Milkove, C.X. Wang, *J. Vac. Sci. Technol.*, **A 15**, 596 (1997)
3. K.R. Milkove, J.A. Coffin, C.Dzionkowski, *J. Vac. Sci. Technol.*, **A 16**, 1483 (1998)
4. H. Kim, et a., *J. Vac. Sci. Technol.*, **A 17**, 2151 (1999)
5. K. Kwon, et al., *J. of the Electrochem. Society*, **147** (5) 1807-9 (2000)

Mat. Res. Soc. Symp. Proc. Vol. 655 © 2001 Materials Research Society

Process Degradation of a Ferroelectric Capacitor

Seigen Otani and Tetsuro Tamura

F project, Fujitsu Labs. Ltd.
10-1 Morinosato-Wakamiya, Atsugi, Kanagawa 243-0197, Japan
Phone: +81-46-250-8231 Fax: +81-46-248-3473 e-mail: sotani@flab.fujitsu.co.jp

ABSTRACT

Ferroelectrics used in a memory device such as $(Pb,La)(Zr,Ti)O_3$ (PLZT) are vulnerable to reducing atmosphere and lose remanent polarization easily. In the semiconductor processes, hydrogen gas is generated both from deposition gas of interlayer dielectric and from reaction between metals and moisture in the dielectric. Improving the ferroelectrics resistance to reducing environments is required for the planarization and multi-layer interconnections in future devices. Loss of remanent polarization is related to the imprint properties of the capacitor and can be improved by controlling the deposition condition of sol-gel PLZT and annealing IrO_x electrode in oxygen.

INTRODUCTION

A ferroelectric random access memory or FeRAM is a non-volatile memory combining both ROM and RAM advantages. Its fast write and high write endurance as well as low power consumption make it superior to other types of non-volatile memories. As the structure of FeRAM is similar to that of DRAM, FeRAM can be fabricated basically using conventional semiconductor processes. In the semiconductor processes, however, the processes in a reducing atmosphere such as the deposition of inter layer dielectric(ILD) films and N_2-H_2 anneal after the capacitor processes are used. Oxygen defects in a ferroelectric capacitor are easily generated in a reducing atmosphere. As a result, it brings about the degradation of capacitor properties such as lowering of the switching charge and the degradation of the data retention property[1-6]. Therefore, in the fabrication of the FeRAM device, it becomes an important problem to prevent the degradation of the capacitor. We present here results of the degradation of the capacitor properties caused by the ILD processes.

EXPERIMENT

The schematic cross section of the 0.5μm –FeRAM unit cell (cell size:27.3 μm^2) is shown in Figure 1[7]. A capacitor is fabricated on top of the Si based dielectric which encapsulates the CMOS and protects

it during the fabrication of the ferroelectric film. In this work, we fabricated the ferroelectric capacitor stacks using Pt/IrO_2 electrode and PZT film deposited by a spin on conventional Sol-Gel method. The 1st inter layer dielectric(ILD) was deposited on the capacitor, and then the contact holes were fabricated on the top electrode and the source area of the transistor. Subsequently, the PZT capacitor was annealed in an oxygen ambient in order to recover the degradation of the capacitor characteristics by the 1st ILD. After TiN local interconnect (LI) formation, 2nd ILD deposition, Al layer was connected to both the W-plug and the LI. After the metalization, the passivation film was deposited.

The polarization-voltage hysteresis loop was measured using a Radiant Technologies RT6000S ferroeletric tester. The imprint characteristics were measured by Sawyer-Tower circuit using the method of Traynor et al [8]. The measurement voltage was applied to the bottom electrode, while the top electrode was grounded.

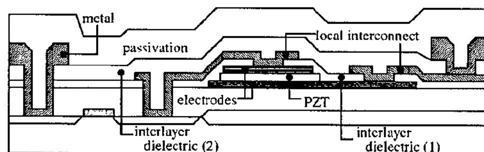

Figure 1. Schematic cross section of a 0.5μm-FeRAM unit cell.

RESULT and DISCUSSION

Process Degradation

The characteristics of a 50μm.square discrete PZT capacitor after each processing step is shown in figure 2. Figure 2(a) shows the value of the switching charge(Qsw). Qsw degradation after each process was not observed except for the fabrication of 1st ILD on a capacitor. Figure 2(b) shows the imprint characteristics after each process. Imprint was measured using capacitor test simulation technique [8]. In the conventional 2T2C FeRAM cell, the bottom electrode of PZT capacitor is connected with a Plate Line(PL) and the top electrode is connected with a pair of Bit Lines(BL or /BL). The two capacitors connected with BL and /BL are donated as BL and /BL capacitors which are in the states opposite to each

other. In the measurement two pulses, read/write or read/restore sequences are applied to a pair of discrete capacitors as CAP A and CAP B correspond to the BL and /BL capacitors. CAP A is written into the positive polarization state and CAP B is written into the negative. And then, the capacitors go through a 150℃ bake for 88h. After the bake, the subsequent pulses are applied to switch the polarization into the opposite state. After 30sec, the remanent polarization is read and the charge is denoted as Qos (opposite state).

The imprint characteristics are strongly affected by process damages, as a result, the value of Qos became zero after fabrication of the passivation film. Thus in the case of inserting the damages in the capacitor by the ILD process, even though the value of Qsw did not vary, it becomes impossible to read the FeRAM data after long term retention.

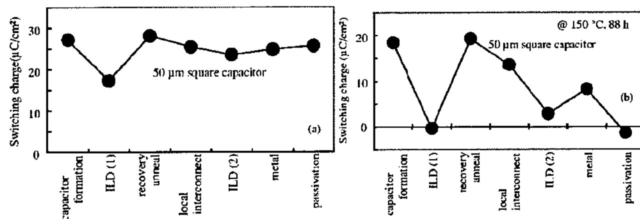

Figure 2. Process degradation of PZT capacitor.

(a)switching charge, (b) imprint characteristics

Variation of capacitor characteristics caused by ILD deposition

To investigate the effect of fabrication condition of ILD on capacitor degradation, we measured hysteresis properties of the capacitor removed the ILD after CVD deposition of various kind of ILD on the PZT capacitor. All these ILD were deposited at 400℃. The result is shown in figure 3. In the Ozone(O_3)TEOS, the change of the hysteresis loop was very small. While, in the Plasma TEOS and the SiH_4 oxide film, the capacitor were significantly degraded, that is, the voltage shift in the hysteresis loop occurred and Qsw also decreased.

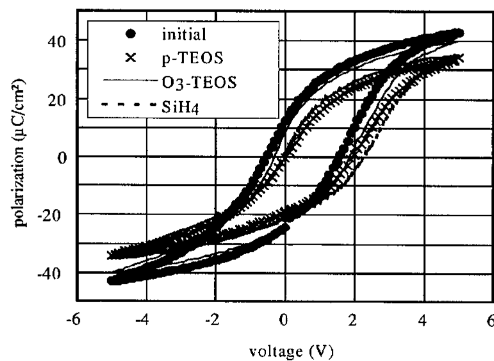

Figure 3. The effect of fabrication condition of ILD on hysteresis properties.

To investigate the differences in the hysteresis characteristics caused by various ILD processes, we analyzed the gaseous species using a residual gas analyzer caused by heating these ILD films which were directly deposited on a Si wafer (figure 4). As a result, in the Plasma TEOS and the SiH_4 oxide film, hydrogen was generated at about 400℃. On the contrary, in the O_3-TEOS, a large quantity of water was generated even at low temperatures of about 200℃, however, little hydrogen was generated in the range of measured temperature. This result clearly indicates that the properties of PZT capacitor are influenced only by hydrogen.

We compared the hydrogen distribution in the PZT film for samples before and after the ILD deposition. Typical SIMS depth profile for the plasma TEOS films on the PZT capacitors is shown in Fig.5. The amount of hydrogen increased by one order of magnitude digit, after deposition and etching of the plasma TEOS film. Furthermore, when an oxygen anneal of 600℃ for 1h was done to recover the ferroelectric properties, the amount of hydrogen returned to its initial state.

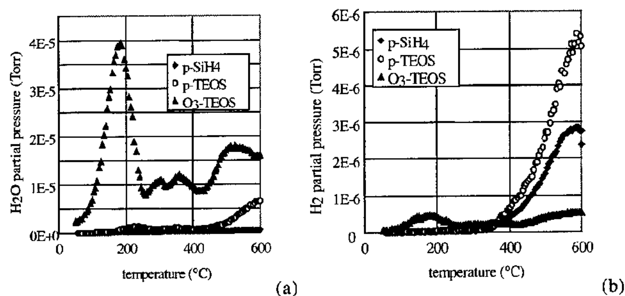

Figure 4. Removal of (a)H_2O and (b)H_2 from the ILD

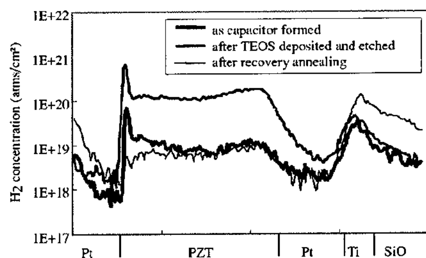

Figure 5. The variation of hydrogen concentration in the PZT before and after deposition of the Plasma TEOS Film

Hydrogen generation caused by the reaction between water in ILD film and metal interconnection

In the structure of an O_3-TEOS film on a PZT capacitor, capacitor degradation is small, because there is little hydrogen in the O_3-TEOS film. In the existence of metal interconnection under the O_3-TEOS film, however, the ferroelectric properties degrade. The switching charge after deposition of the ILD film such as an O_3-TEOS film(800nm) or a plasma TEOS film(200nm), which is fabricated on a metal interconnection / PZT capacitor, is shown in Table.1 for reference. The deposition condition of the O_3-TEOS film and the plasma TEOS film are 400℃ for 30min and 400℃ for 3min, respectively. The

switching charge of the PZT capacitor with the O_3-TEOS film is smaller than that of the capacitor with the plasma TEOS film. On the other hand, the amount of hydrogen generated from the plasma TEOS film is lager than that generated from the O_3-TEOS film, this result shows a reverse tendency for the capacitor degradation. In the case, as there exist an ILD film and a metal interconnection on a PZT capacitor, hydrogen gas don't make contact with the PZT capacitor directly. Therefore, the effect of hydrogen generated from the ILD films on the capacitor degradation may be not large.

Table 1. The variation of switching charge on deposition condition of ILD films

Deposition Condition of ILD Films	Switching Polarization (Qsw)
p-TEOS(200nm) 400℃, 3min	44μ C/cm²
O_3-TEOS(800nm) 400℃, 30min	33μ C/cm²

From the experiment mentioned above, we hypothesized that the capacitor degradation may be caused by a reaction between water generated from ILD film and metal interconnection. To verify the hypothesis, we measured the amount of degas (hydrogen) by heating from a metal on a Si oxide film. When there exists an Al on a Si oxide film, hydrogen generated from near 300℃ (Figure 6). On the other hand, in the case of only Al or only Si oxide film, there could not be observed the generation of hydrogen up to 350℃. From the results, hydrogen may be generated owing to an oxidation reaction between Al and water containing a Si oxide film. The oxidation reaction may be expressed as follows.

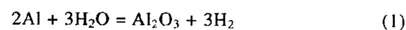

$$2Al + 3H_2O = Al_2O_3 + 3H_2 \qquad (1)$$

For the same reason, capacitor properties are strongly influenced by the deposition condition of metal interconnection. The variation of the switching charge on the sputtering condition of Al is shown in Figure 7. The switching charge decreased with increasing temperature and sputtering time. Generally, after fabrication of an ILD film on a PZT capacitor followed contact hall etching, oxygen anneal is carried out to recover the capacitor properties. In the device using TiN local interconnect (LI), however, oxygen anneal can't be carried out after fabrication of LI.

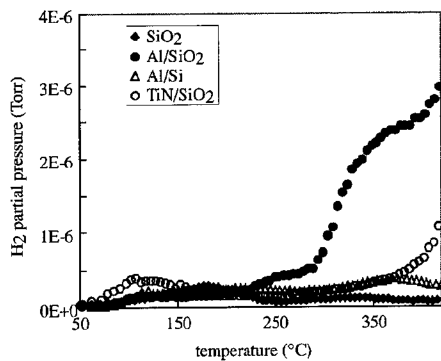

Figure 6. Degas(hydrogen) by heating from a metal on a Si Oxide film

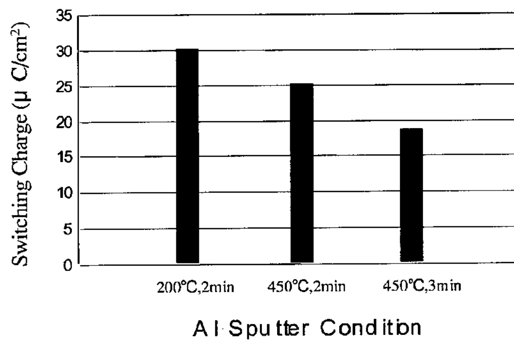

Figure 7. The Variation of switching charge on Al sputter condition

The effect of fabrication condition of a capacitor on hydrogen endurance and imprint property

Hydrogen endurance and imprint property of a capacitor strongly depend on the fabrication condition of the capacitor. Therefore, we examined the case of a sol-gel PLZT capacitor, for example. The bottom electrode is Pt(200nm)/IrO_2(50nm), which was deposited by sputtering. The PLZT solutions (Pb:La:Zr:Ti=110:3:45:55) were dropped onto the electrode and spin-coated at 3000 rpm for 15sec using a spinner. The coated films were baked to evaporate the solvent and to remove the organic materials at 350-370℃ for 10 min in air(pyrolysis treatment). The process of coating and baking was repeated 4 times, so that the thickness of PLZT film was 300nm. Furthermore, the films were annealed at 700℃ for

60 sec in an oxygen atmosphere with a heating rate of 125℃/sec in a RTA system for crystallization. Finally, after the fabrication of the top electrode(Pt/IrO_2) of 50×50 μm^2 using an ion milling etcher, 2nd anneal was done at 400-600℃ for 1hr to remove the ion damage of milling.

We investigated the effect of the temperature of pyrolysis and 2nd anneal on the hydrogen endurance and the imprint property of the PLZT capacitors (Figure 8). Hydrogen baking was carried out in N_2 + 5% H_2 7.6 Torr, at 150℃ for 2hr. As the temperature of pyrolysis and 2nd anneal is high, the hydrogen endurance and the imprint property of the PLZT capacitors show a good tendency. The grain size of PLZT increased with increase in the temperature of pyrolysis, that is, the range of the grain size is from 150nm at 350℃ to 300nm at 370℃. In the grain boundary, oxygen vacancies and lead diffusion easily generate. Therefore, when the grain size of PLZT is large, the hydrogen endurance and the imprint property of the PLZT capacitors are good due to reduction of the contribution of the grain boundary. On the other hand, the temperature of the 2nd anneal has no effect on the grain size of PLZT. The effect of higher temperature of the 2nd anneal may increase the PLZT crystallinity and improve the oxidation of IrO_2.

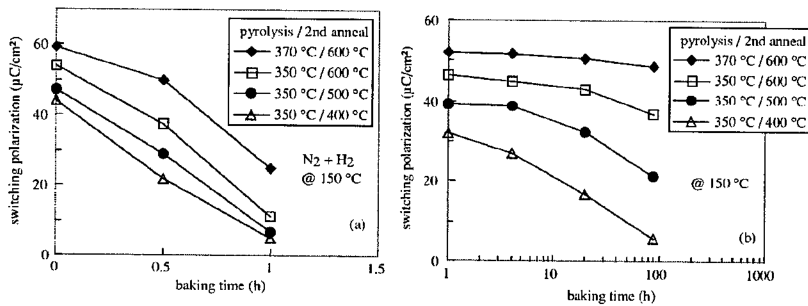

Figure 8. The effect of fabrication condition of sol-gel PLZT capacitors on the hydrogen endurance and the imprint property.

CONCLUSIONS

The degradation of the ferroelectric capacitors is caused by a hydrogen atmosphere during deposition of the ILD and hydrogen generated from an oxidation reaction between water in the ILD and metal interconnection. In future high density FeRAM devices, planerized multi layer interconnections, with an ILD containing water will be used. In that case, the issue of the degradation of the ferroelectric capacitors will become more serious. Therefore, it is necessary to improve the hydrogen endurance of the

ferroelectric capacitors. In this stage, the mechanism of hydrogen degradation is not clear, however, the properties of the capacitors are improved by increasing the grain size of the PLZT.

REFERENCES

1. C.H.P.Lupis., Chemical Thermodynamics of Materials(North-Holland, New York, p.134, 1983
2. W.L.Warren.et al., J.Appl.Phys, 77, p.6695, 1995
3. H.Miki.et al., Jpn. J.Appl.Phys, 36, p.1132, 1997
4. J.P.Han.,et al., Appl.Phys.Lett, 71, p.1267,1997
5. K.Kushida-Abdelghafar,et al., Jpn. J.Appl.Phys, 37, p.804, 1998
6. J.T.Evans.,et al., Jpn.J.Appl.Phys, 38, p.5361, 1999
7. T.Yamazaki,et al., IEDM Digest of Technical Papers, p.613, 1997
8. S.D.Traynor,et al., Integrated Ferroelectrics, 16, p.669, 1997

Mat. Res. Soc. Symp. Proc. Vol. 655 © 2001 Materials Research Society

DEGRADATION OF FERROELECTRIC $Pb(Zr,Ti)O_3$ UNDER REDUCING CONDITIONS

Yuichi SHIMAKAWA* and Yoshimi KUBO
Fundamental Research Laboratories, NEC Corporation, Tsukuba 305-8501, Japan
* *y-shimakawa@ah.jp.nec.com*

ABSTRACT

The degradation mechanism of $Pb(Zr,Ti)O_3$ (PZT) under reducing conditions was revealed. In contrast to the significant decrease in the sample weight of $SrBi_2Ta_2O_9$ due to decomposition, the weight of $Pb(Zr,Ti)O_3$ samples change little during H_2-annealing at typical process temperatures. Although no apparent changes were detected by thermogravimetric and x-ray diffraction measurements after annealing, *the PZT material did actually change*. The main mechanism of the degradation is introduction of oxygen defects into the materials. The oxygen defects produce a donor level within the band gap, and light absorption by this donor level accounts for the change in sample appearance from white to black. Different endurance behaviors of materials against reducing conditions were also found: $PbZrO_3$ decomposes through oxygen dissociation more easily than $PbTiO_3$. Oxygen atoms in $PbZrO_3$ are more weakly bonded to Zr than to Ti in $PbTiO_3$ because of a significant anti-bonding component in the hybridized orbitals.

INTRODUCTION

Ferroelectric $PbZr_{1-x}Ti_xO_3$ (PZT) and $SrBi_2Ta_2O_9$ (SBT) are leading candidate materials for use in FeRAM applications, and thin-film capacitors based on them have been intensively studied. Recently, however, serious challenges in integrating the oxide-ferroelectric capacitors into a standard LSI have emerged [1-3]. In thin-film capacitors, for example, leakage current significantly increases and ferroelectric polarization severely decreases after the device fabrication process, which usually includes an annealing step at 350-550 °C in a H_2-containing reducing atmosphere.

Although many papers have reported on the degraded properties of oxide thin-film capacitors [1-5], few studies on the mechanisms of the degradation during fabrication have been done. In our previous papers on SBT ferroelectric oxides, we demonstrated that solid-state chemistry analysis of bulk ceramic samples helps us better understand the fabrication process for FeRAM devices [6,7]. With this approach, we can see material degradation in exaggerated forms; thus, we can investigate such degradation quantitatively. In the present study, we applied a similar solid-state analysis to PZT ferroelectric compounds, and we revealed a possible degradation mechanism of PZT under a reducing atmosphere [8]. Material stability of PZT perovskites against H_2-annealing was also investigated and the results were compared with that of SBT.

EXPERIMENTAL RESULTS AND DISCUSSION

Ceramic powder samples of PZT were prepared by solid-state reaction. $Pb(Zr_{0.48}Ti_{0.52})O_3$ was synthesized from a mixture of $PbTiO_3$ (PTO) and $PbZrO_3$ (PZO). Changes in the sample during annealing were traced by measuring changes in the sample weight by a thermogravimetric (TG) analysis system. Argon gas containing 4% H_2 was used for the reducing conditions, whereas 100% O_2 was used for the oxidizing conditions. X-ray diffraction (XRD) measurements were carried out to identify the resultant phases of the materials.

Figure 1 shows the changes in the sample weight of PZT during 4% H_2 annealing at 350-500 °C after initial rapid heating (20 °C/min) up to that temperature range. The results for SBT [6] are also shown. In contrast to the significant decreases in the sample weight of SBT due to decomposition, the weight of the PZT samples changes little during the annealing at these typical process temperatures even after eight hours. The figure also shows powder XRD patterns of the annealed samples, and they are quite similar on the whole to that of the as-made sample.

Although we saw no apparent degradation after the H_2-annealing from the TG and XRD measurements, *the PZT material had actually changed* during the annealing. As the H_2-annealing temperature increases, the as-made white sample changes to black through gray. The H_2-annealed black and gray samples change to *almost* white after subsequent annealing in O_2, but the color does not reach exactly the same white as that of the initial sample. An orange-yellow tint can be seen in these close-to-white samples.

To determine the origin of the change in the sample appearance, the XRD patterns of three samples, which were as-made, H_2-annealed at 550 °C, and O_2-reannealed at 450 °C, were examined carefully. As shown in Fig. 2, the patterns of the annealed samples show very weak additional peaks. The H_2-annealed sample shows a weak diffraction peak at $2\theta = 36°$ that originated from Pb (2 0 0). Note that the observed intensity of the Pb (2 0 0) peak is less than 100 cps, while the main peak intensity of PZT is more than 30,000 cps. This three orders of magnitude difference implies that only 0.3% Pb is included in the H_2-annealed PZT sample. A small amount of PZT decomposes, and Pb metal is then produced in the reducing atmosphere. The subsequent O_2-annealed sample shows a weak diffraction peak of PbO (1 1 1) at $2\theta = 29°$. It can thus be considered that the dissociated Pb from PZT changes to PbO (masicott) in the oxidizing atmosphere. The color of the masicott PbO is orange-yellow, which is consistent with the observation that the O_2-reannealed sample had an orange-yellow tint.

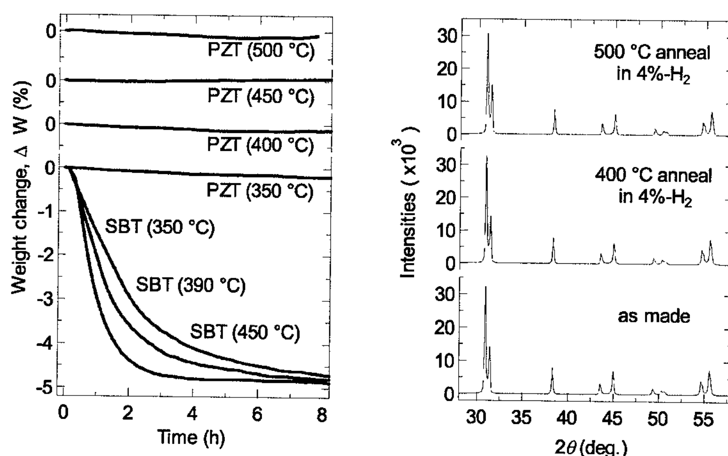

Fig. 1. Weight change (%) of PZT in 4% H_2 at 350-500 °C, and XRD patterns of the as-made and annealed samples. TG measurements for SBT are also shown.

Does the Pb metal produced in the reduced sample cause the change in the sample from white to black? We do not think so, because the amount of Pb (less than 0.3%) is too low to cause all of the change in the sample appearance. It would be more reasonable to conclude that the PZT itself is changed by the annealing in the reducing atmosphere. Systematic changes in the lattice constants of the reduced PZT samples against the H_2-annealing temperatures clearly demonstrate that the PZT itself has actually changed. As shown in Fig. 3, the lattice constant a increases while c decreases after the annealing in H_2. Lead and/or oxygen defects in PZT are possibly introduced under the reducing conditions [4,5], and they slightly modify the crystal structure. Since the reduced black sample *almost* recovered its whiteness through the subsequent annealing in oxygen, the oxygen defects must be the main mechanism that best explains the change in the sample appearance after the annealing in H_2 and O_2 atmospheres.

The change in the sample appearance brought about by the oxygen defects is well explained in terms of the change in the electronic structure. We calculated the electronic structure by the discrete variational $X\alpha$ (DV-$X\alpha$) cluster method using the program SCAT [9]. Although we calculated the electronic structure of $PbTiO_3$ (PTO) perovskite, we can discuss the essential features of the electronic structure of PZT from this calculation. Figure 4 shows a cluster model of $(Pb_{12}Ti_2O_{11})^{10+}$, which is used for the calculation on stoichiometric PTO material. The calculated energy levels near E_F and the density of states (DOS) are also shown in the figure. The valence band top mainly consists of Pb 6s states, and the conduction band bottom consists of empty Ti 3d states. The band gap between the valence band top and conduction band bottom is about 3.2 eV, and this wide gap makes the PTO and PZT materials transparent to visible light. In a polycrystalline sample, we see a white color due to diffuse reflection of light.

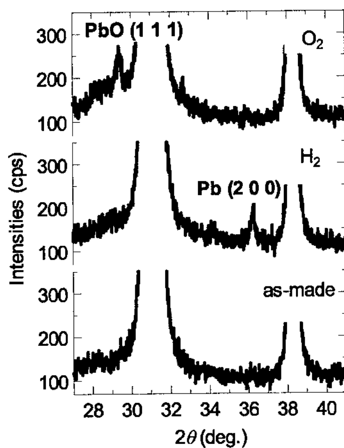

Fig. 2. XRD patterns of as-made (bottom), H_2-annealed (center), and O_2-reannealed (top) samples.

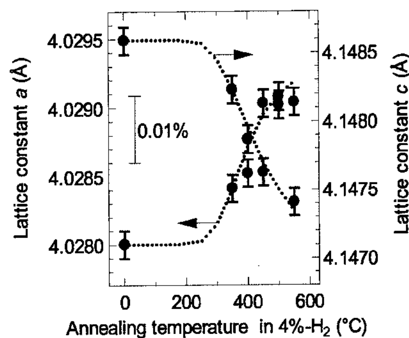

Fig. 3. Changes in lattice constants of reduced samples against H_2-annealing temperatures.

We calculated the electronic structure of PTO with the oxygen defects by using the $(Pb_{12}Ti_2O_{10})^{10+}$ cluster model, in which the center oxygen atom is removed from $(Pb_{12}Ti_2O_{11})^{10+}$. The result of this calculation is shown on the left-hand side of Fig. 4. Note that the oxygen defects in PTO produce a donor level within the band gap. The donor level lies 0.6 eV below the conduction bottom, and this narrow gap absorbs light with wavelengths in the visible light region. This absorption accounts for the change in the sample appearance from white to black.

Below, we will discuss the stability of the perovskite materials against H_2-annealing. In sharp contrast to the significant decomposition of SBT, the PZT perovskites appear able to endure the reducing conditions (Fig. 1). The significant difference in material stability between PZT and SBT thin films was reported in Ref. [2], and the result is consistent with the present one. This is because oxygen atoms in ABO_3 perovskite are strongly bonded to a B-site cation in a BO_6 octahedron. In SBT, on the other hand, oxygen atoms in the Bi_2O_2 layers are weakly bonded to Bi; thus, the oxygen dissociation from the layers triggers the decomposition. This fact is evident when we compare the Madelung potential at each ionic site in PZT and SBT as shown in Table I. In SBT, the Madelung potential at the oxygen site in the Bi_2O_2 layer is significantly low.

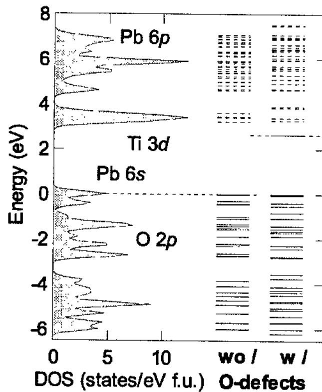

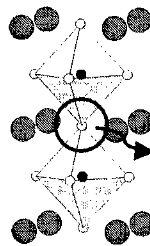

Fig. 4. Cluster models of $(Pb_{12}Ti_2O_{11})^{10+}$ (without O-defects) and $(Pb_{12}Ti_2O_{10})^{10+}$ (with O-defects), and their total DOS and energy levels.

Table I. Madelung potential (eV/valence) at each site of PZT and SBT. O^{2-} (*Oc*) denotes oxygen ions in the octahedra, and O^{2-} (Bi_2O_2) denotes oxygen ions in the Bi_2O_2 layers in SBT.

PZT

Pb^{2+}	Ti^{4+} / Zr^{4+}	O^{2-} (*Oc*)
-9.8	-11.2	+11.7

SBT

Sr^{2+}	Bi^{3+}	Ta^{5+}	O^{2-} (*Oc*-1)	O^{2-} (*Oc*-2)	O^{2-} (*Oc*-3)	O^{2-} (Bi_2O_2)
-8.1	-11.5	-10.0	+13.5	+10.6	+14.6	+6.5

We have found, however, interesting differences in the material endurance of the perovskite-structure oxides against reducing conditions. Figure 5 shows the changes in the sample weight of PTO, PZT and PZO during annealing at 450 °C in a 4% H_2-containing reducing atmosphere, and XRD patterns of PTO and PZO before and after the annealing. In contrast to the practically constant weight of the PTO and PZT samples, the weight of PZO gradually decreases, suggesting decomposition of the material. The XRD pattern of the H_2-annealed PZO sample apparently includes the diffraction peaks of Pb decomposed from the PZO. The observed decrease in the sample weight is probably caused by oxygen dissociation due to the decomposition of $PbZrO_3$ into Pb and ZrO_2. These results clearly demonstrate that PZO decomposes more easily than PTO.

It was also found that the difference between material stability of PTO and PZO is closely related to the difference in the bonding characteristics of the *B*-cation and oxygen in the BO_6 octahedron in ABO_3. The bonding characteristics were investigated in terms of the analysis of hybridized orbitals by calculating the electronic structure of $(Pb_{27}Ti_8O_{36})^{14+}$ and $(Pb_{27}Zr_8O_{36})^{14+}$ clusters. In PTO and PZO, the overlap of Ti 3*d* (Zr 4*d*) partial densities of states with the primarily O 2*p* valence band, which ranges from 0 to -7 eV, indicates considerable hybridization of the orbitals. Since the calculation was done for the same cubic cluster, except that the lattice constants and atoms (Ti and Zr) were different, the differences appearing in the results are due solely to the replacement of Ti by Zr. Cubic lattice constants obtained from averages of reported lattice constants of PTO and PZO were used to exclude the ionic size effect. Figure 6 shows the density of states of PTO and PZT, and the bond overlap population (BOP) of the Ti-O, Zr-O, and Pb-O bonds. The BOP parameter gives the number of occupied electrons of the bonding (B) and anti-bonding (AB) hybridized orbitals, and it provides information of bond strength. Note that the BOP below E_F between the Ti-O and Zr-O bonds is significantly different, while that of the Pb-O bonds is similar in both compounds. The Ti-O bonds mainly consist of hybridized bonding orbitals, whereas the Zr-O bonds include both bonding and anti-bonding orbitals. We thus conclude that oxygen atoms in PZO are weakly bonded to Zr compared to those to Ti in PTO.

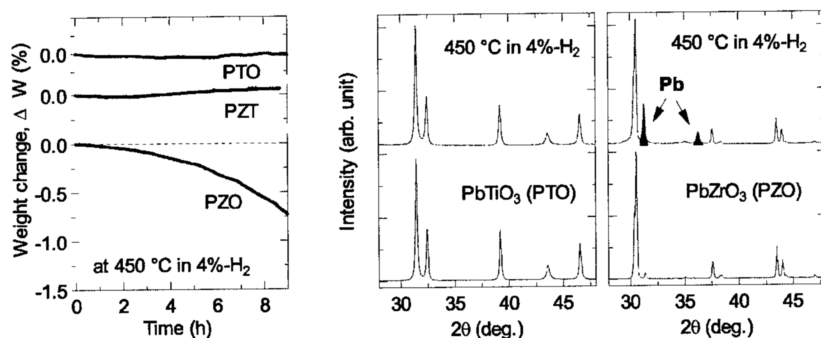

Fig. 5. Weight change (%) of PTO, PZT, and PZO in 4% H_2 at 450 °C, and XRD patterns of PTO and PZO before and after annealing.

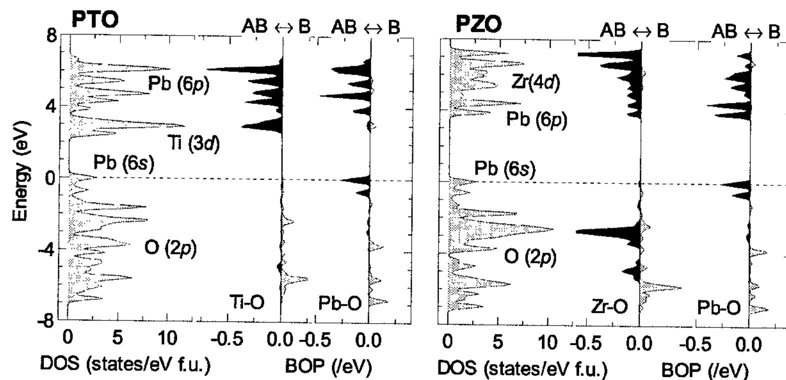

Fig. 6. Total density of states (DOS) and bond overlap population (BOP) of PTO and PZO perovskites. AB and B denote anti-bonding and bonding components, respectively, in hybridized orbitals of bonds.

CONCLUSIONS

Our solid-state chemistry analysis reveals the degradation mechanism of ferroelectric PZT oxides under reducing conditions. The reported degraded properties of thin-film capacitors are considered to be caused by such degradation of materials. It was found that the main mechanism of the degradation is introduction of oxygen defects into the materials. The oxygen defects produce the donor level within the band gap, and this level can increase the leakage current in capacitors. We also found different endurance behaviors of materials against H_2-annealing: Although PZT perovskites appear able to endure against a reducing atmosphere better than SBT, a small amount of decomposition was observed. In PZT, oxygen atoms bonded to Zr are more easily dissociated than those bonded to Ti. Regarding the use of the PZT materials in capacitor devices, a Zr-rich material would have inferior material endurance against the H_2-containing reducing conditions.

REFERENCES

[1] R. E. Jones. Jr., P. D. Maniar, R. Moazzami, P. Zurcher, J. Z. Witowski, Y. T. Lii, P. Chu, and S. J. Gillespie, Thin Solid Films **270**, 584 (1995).
[2] T. Hase, T. Noguchi, and Y. Miyasaka, Integr. Ferroelectr. **16**, 29 (1997).
[3] J-P. Han and T. P. Ma, Appl. Phys. Lett. 71, 1267 (1997).
[4] S. Takatani, K. Kushida-Abdelghafar, and H. Miki, Jpn. J. Appl. Phys. **36**, 435 (1997)
[5] W. L. Warren, D. Dimos, B. A. Tuttle, G. E. Pike, R. W. Schwartz, P. J. Clews, and D. C. McIntyre, J. Appl. Phys. **77**, 6695 (1995).
[6] Y. Shimakawa and Y. Kubo, Appl. Phys. Lett. **75**, 2839 (1999).
[7] Y. Shimakawa and Y. Kubo, *Ferroelectric Thin Films VIII* (Material Research Society, Pittsburgh, PA, 2000), p. 131.
[8] Y. Shimakawa and Y. Kubo, Appl. Phys. Lett. **77**, 2590 (1999).
[9] S. Adachi, M. Tsukada, and C. Satoko, J. Phys. Soc. Jpn. **45**, 875 (1978).

Mat. Res. Soc. Symp. Proc. Vol. 655 © 2001 Materials Research Society

Degradation of Ferroelectric Capacitors during Metal Etching and Ashing Processes

Chanro Park, O Sung Kwon, Yeo Song Seol, Jin Woong Kim and Hee Koo Yoon
Advanced Process-Etch, Memory R & D Div., Hyundai Electronics Industries
San 136-1, Ami-ri, Bubal-eup, Ichon-si, Kyongki-do, 467-701, Korea

ABSTRACT

Polarization degradation due to metal etch and/or photoresist(PR) strip processes has been investigated for Pt/$SrBi_2Ta_2O_9$(SBT)/Pt ferroelectric capacitors. Interconnect metal line consisting of TiN/Al/Ti/TiN/Ti layers has been patterned by normal photolithography and plasma etch processes. We used two different sources for metal etcher, helicon or electron cyclotron resonance(ECR) source, and stripped the PR with either microwave or helicon source stripper. Polarization degradation was evaluated by measuring switching and non-switching polarization of the ferroelectric capacitors.

Neither etch machine nor etch parameters played an important role for determining polarization of the ferroelectric capacitors. Photoresist strip process, however, significantly affected the polarization of the ferroelectric capacitors. Factors affecting polarization of the ferroelectric capacitors were presence of hydrogen and plasma density during the strip process. Hydrogen atoms and protons produced by H_2O or NH_3 plasma penetrated through the dielectric layer and caused hydrogen induced damage. Thus the hydrogen damage was dependent on strip temperature and time. Photoresist strip with high density plasma results in charging damage to ferroelectric capacitors. It is believed that charges from the plasma are trapped at domain boundaries and interfaces, leading to polarization degradation. Damage free metal etching process for the ferroelectric capacitor was applied for the fabrication of the fully working ferroelectric random access memory.

INTRODUCTION

Ferroelectric random access memory(FeRAM) has been attracted great attention as a non-volatile memory, because of its low operation power and high read/write speed[1]. However, there are challenges that should be overcome for the realization of the FeRAM. Fatigue, retention and imprint characteristics should meet the requirement for long term operation[2]. Processes that do not affect to the electrical properties of the ferroelectric capacitor should also be established.

Various plasma etching processes, such as capacitor etching, contact etching, and metal etching are required for the fabrication of the FeRAM. Plasma etching can cause damage to the ferroelectric capacitors. Plasma etching damage can lead to deterioration of the electrical properties such as reduction of remnant polarization and increase of leakage current. Plasma etching damage can be recovered by thermal annealing at high temperature. Metal etching damage, however, can not be recovered by annealing process, because annealing temperature is higher than the melting point of the interconnecting Al metal line. Thus it is necessary to etch metal line without damage to the ferroelectric capacitors. In this paper, we investigated the effect of metal etching on the polarization characteristics of the ferroelectric capacitors. We studied the effects of plasma parameters and process gases on polarization of the ferroelectric capacitors. Finally we addressed the conditions for damage-free metal etching process.

EXPERIMENTAL DETAILS

Samples were prepared by the following sequence. Bottom Pt layer with glue TiO_x was grown on thermally oxidized silicon wafer by DC magnetron sputtering. SBT ferroelectric film deposition by metalorganic decomposition method was followed by top Pt layer deposition. The ferroelectric capacitors were patterned by reactive ion plasma etching. Capacitor etching damage was recovered by thermal annealing at high temperature in oxygen atmosphere. After deposition of interlayer dielectric, and contact hole etching, the 2nd recovery annealing was conducted. Interconnecting metal deposition was followed by metal line patterning by plasma etching with PR barrier.

Metal etching was conducted with two different machines, Machine A (M/C A) and Machine B (M/C B). Normal metal etcher consists of 2 chambers, etcher and PR stripper. M/C A has ECR source etcher and microwave-downstream source PR stripper. M/C B adopts helicon source for both etcher and PR stripper. The gas chemistry of the etcher was same for M/C A and M/C B, Cl_2/BCl_3, while that of stripper was different for both machines. Strip gases for M/C A were O_2/N_2, and those of M/C B were H_2O/CF_4. The plasma density of the etcher for both machines is estimated to be same order of magnitude. While plasma density of stripper for M/C B is much higher than M/C A.

Test pattern consisting of 2.4 ×3.7 μm^2 capacitor array was measured to monitor polarization characteristics after metal etching. Polarization measurements were done by Radiant Technologies RT66A.

RESULTS AND DISCUSSION

The difference between switching and non-switching polarization, ΔP, of the capacitors after metal etching showed different magnitude depending on etching machine(Fig. 1). Etching in M/C A revealed larger ΔP than etching in M/C B. Polarization reduction after etching in M/C B could be originated from either etcher or stripper, or both. Process split was conduced to identify whether etcher or stripper is responsible for the damage to the capacitor. Split conditions are listed in Table 1. As observed in fig. 1, process 1 did not cause damage, while process 2 resulted in reduction of polarization. If damage occurred due to etcher, then process 3 would result in

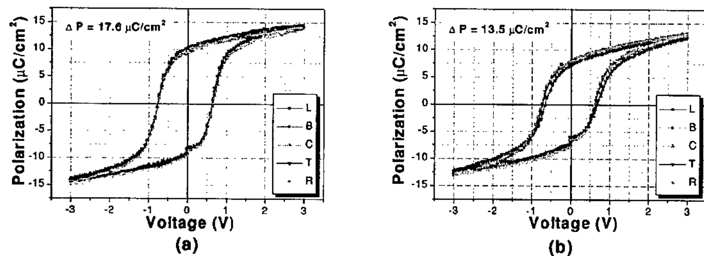

Fig. 1. Hysteresis loops of the ferroelectric capacitors after metal etching in (a) M/C A and (b) M/C B. M/C A resulted in larger ΔP than M/C B. The L, B, C, T and R in the figures represent measurement position in a wafer left, bottom, center, top and right, respectively.

reduction of polarization. On the other hand, if damage occurred due to stripper, then process 4 would result in reduction of polarization. Figure 2 reveals the hysteresis loops after metal etching with process 3 and process 4. From the figure, we can conclude that strip process in M/C B is responsible for damage to ferroelectric capacitors.

Table 1. Split conditions to find out process responsible for damage

	Etcher	Stripper	Remark
Process 1	M/C A	M/C A	No Damage
Process 2	M/C B	M/C B	Damage
Process 3	M/C B	M/C A	?
Process 4	M/C A	M/C B	?

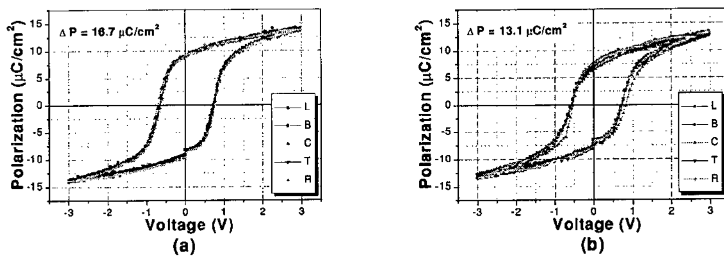

Fig. 2. Hysteresis loops after metal etching with (a) Process 3, and (d) Process 4.

As mentioned above, plasma source and strip gases of stripper of M/C B is different from those of M/C A. Strip gases in M/C B contain H_2O, a source of hydrogen. Annealing at hydrogen atmosphere is known to cause damage to ferroelectric capacitors due to hydrogen incorporation to ferroelectric layer[3]. Although the exact mechanism of damage due to hydrogen is not clear yet, incorporated hydrogen is reported to reduce oxide ferroelectric layer[4] or to combine with oxygen in ferroelectric layer inhibiting polarization reversal[5]. Aside from the gas chemistry difference, plasma density of helicon source is much higher than normal microwave-downstream source. The high plasma density could cause charging damage to ferroelectric capacitors.

First, effect of hydrogen on ferroelectric capacitors was investigated by adding NH_3 gas during strip process in M/C A. Figure 3 and 4 show the effect of NH_3 on the polarization of the ferroelectric capacitors. By increasing the chuck temperature during strip process, polarization reduction was observed for O_2/N_2 /NH_3 plasma. On the other hand, polarization reduction was not observed for O_2/N_2 plasma(not shown here). Strip time also affected to the polarization of the capacitors. As shown in fig. 4, polarization gradually decreases with increasing strip time. The decrease of polarization with temperature and time can be interpreted by diffusion of hydrogen atom or proton through dielectric oxide layer. It is reported that diffusion coefficient of hydrogen in interconnect metal line is very low, thus diffusion occurs through oxide layer[6]. Because diffusion coefficient becomes larger at higher temperature, the polarization decreases at higher temperature. Longer strip time means larger diffusion distance, resulting in polarization decrease.

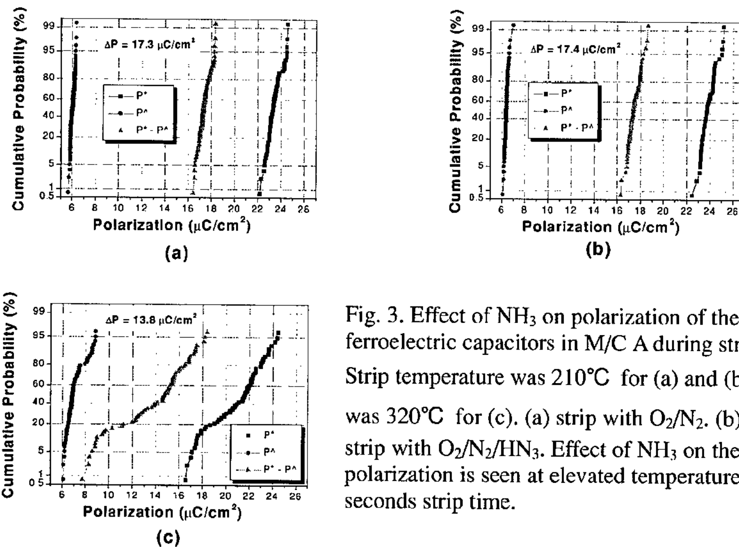

Fig. 3. Effect of NH_3 on polarization of the ferroelectric capacitors in M/C A during strip process. Strip temperature was 210°C for (a) and (b), and was 320°C for (c). (a) strip with O_2/N_2. (b) and (c) strip with $O_2/N_2/HN_3$. Effect of NH_3 on the polarization is seen at elevated temperature for 90 seconds strip time.

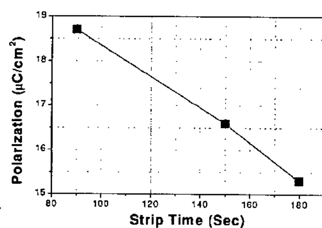

Fig. 4. Effect of strip time on polarization. Strip was done in M/C A with $NH_3/O_2/N_2$ plasma at 210°C.

It is known that hydrogen molecule dissociated into hydrogen atoms by catalytic effect of Pt top electrode[7]. The dissociated hydrogen atoms diffuse into ferroelectric layer during forming gas anneal. However, hydrogen - containing plasma does not require catalytic effect of top electrode because hydrogen atom and proton can be generated by dissociative reaction of NH_3 in the plasma. Thus, strip with hydrogen – containing plasma can be more harmful to the ferroelectric capacitor than forming gas annealing.

Above results propose that ferroelectric capacitor damage in M/C B can be ascribed to due to hydrogen. Thus we changed the strip gas chemistry of M/C B from H_2O/CF_4 to O_2/N_2. Figure 5 shows hysteresis loops after metal etching in M/C B by using (a) H_2O/CF_4 and (b) O_2/N_2 gases during strip process. As can be seen in the figure, polarization reduction also occurred for O_2/N_2 plasma, where there is no hydrogen source. This means that ferroelectric capacitor damage can be induced without hydrogen. Capacitors etched in M/C A, where no damage to ferroelectric capacitor occurred, and then exposed to Ar plasma at stripper of M/C B also resulted in polarization decrease (not shown here). These results propose that etch damage can be induced without hydrogen during strip process. Ruling out the strip gas effect, the only difference among two strippers in M/C A and M/C B is the plasma density. Thus, it is postulated that charging of the capacitors during strip process is partly responsible for the decrease of polarization.

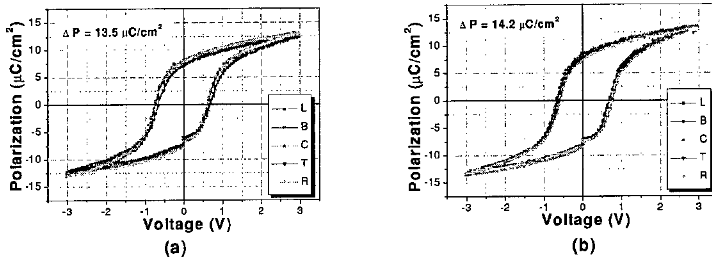

Fig. 5. Hysteresis loops after metal etching in M/C B by using (a) H_2O/CF_4 and (b) O_2/N_2 gases during strip process.

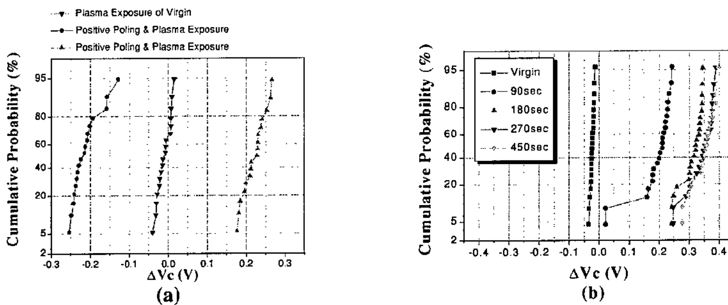

Fig. 6. (a) ΔVc before and after plasma exposure of virgin and poling treated capacitors. Poling leads to shift of ΔVc with respect to non-poling treated capacitors depending on poling direction. Plasma exposure time is 90 sec. (b) ΔVc initially increases with plasma exposure time, and then saturates at 270 sec.

Experiments were conducted to find out whether capacitors were really charged or not when exposed to plasma. Capacitors were poling treated after metal etching in M/C A. Capacitors were poling treated by applying 3V at top or bottom electrode, and then removing the applied voltage. Both the virgin and poling treated capacitors were exposed to microwave downstream O_2/N_2 plasma. Figure 6(a) shows ΔVc, the difference between positive, |+Vc|, and negative |-Vc| coercive voltages, before and after exposure to low density plasma. The virgin capacitors show very small ΔVc, while poling treated capacitors resulted in large ΔVc. The shift direction of ΔVc depends on poling directions. Positive poling treated capacitors shows negative ΔVc, and *vice versa*. Then, we investigated the effect of plasma exposure time on ΔVc of negative poling treated capacitors. ΔVc initially increases as the exposure time increases and then saturates as shown in Fig 6(b). The shifts of ΔVc depending on polarization direction and plasma exposure time strongly suggest that charges from the plasma be trapped at the capacitors. Charges from the plasma are supposed to be trapped at the polarization heads of ferroelectric domains. The trapped

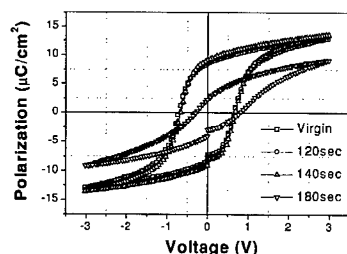

Fig. 7. Hysterisis loops as a function of exposure time to middle density plasma.

charges form space charge, and thus exert electric field. The space charge field resulted in shift of hysteresis loop. When the charge fluence from the plasma is small, the charges are trapped only at the interfaces between electrodes and ferroelectric layer. If the charge fluence exceeds critical limit, charges may be trapped at the grain boundaries and domain walls. The trapped charges can prevent domain reversal and thus decrease polarization. Figure 7 shows evidence of charging induced capacitor damage. The capacitors are exposed to middle density plasma at various time. The hysteresis loops show little change upto 140 sec., and then significant degradation is observed at 180 sec. These results propose that charging damage occur at high charge fluence. Comparing to microwave downstream source(~10^6/cm^2)[8], middle density plasma(~10^{10}/cm^2) has more than four to five orders of magnitude higher density. Thus, reduction of polarization can not be observed when the capacitors are exposed to low density plasma, such as microwave downstream source. If the plasma density is very high, the ferroelectric capacitors can be easily damaged, ash shown in Fig. 5(b).

CONCLUSIONS

In summary, metal etching damage to the ferroelectric capacitors was investigated. The damage was induced by hydrogen incorporation to the ferroelectric capacitors when the plasma contained hydrogen during strip process. Damage was also caused by charging of the ferroelectric capacitors during strip at high density plasma. Thus, it is necessary to use low density plasma without hydrogen containing gas during PR strip process for damage free metal etching of the ferroelectric capacitors.

REFERENCES

1. D. Takashima and I. Kunishima, *IEEE J. Solid-State Circuits*, **33**, 787 (1998).
2. S. Tanaka, R. Ogiwara, Y. Itoh, T. Miyakawa, Y. Takeuchi, S. Doumae, H. Takenaka, and H. Kamata, *IEEE Trans. Electron Devices*, **47**, 781 (2000).
3. K. Kushida-Abdelghafar, H. Miki, K. Torii, and Y. Fujisaki, *Appl. Phys. Lett.*, **69**, 3188 (1996).
4. J. Im, O, Auciello, A. R. Krauss, D. M. Gruen, R. P. H. Chang, S. H. Kim, and A. I. Kingon, *Appl. Phys. Lett.*, **74**, 1162 (1999).
5. S. Aggarwal, S. R. Perusse, C. W. Tipton, R. Ramesh, H. D. Drew, T. Venkatesan, D. B. Romero, V. B. Podobedov, and A. Weber, *Appl. Phys. Lett.*, **73**, 1973 (1998).
6. N. S. Saks, R. B. Klein, R. E. Stahlbush, B. J. Mrstik, and R. W. Rendell, *IEEE Trans. Nucl. Sci.*, 40, 1341 (1993).
7. Y. Shimamoto, K. Kushida-Abdelghafar, H. Miki, and Y. Fujisaki, *Appl. Phys. Lett.*, **70**, 3096 (1997).
8. J. Shi, M. Kamarehi, D. Shaner, S. Rounds, S. Fink, and D. Ferris, *Solid State Technology*, **38**, (1995).

Mat. Res. Soc. Symp. Proc. Vol. 655 © 2001 Materials Research Society

200 °C PREPARATION OF SiN_x PASSIVATION FILMS FOR PZT FERROELECTRIC CAPACITORS BY CATALYTIC CVD

Toshiharu Minamikawa,[*,**] Yasuto Yonezawa,[**] Yoshikazu Fujimori,[*,***] Takashi Nakamura,[***] Atsushi Masuda,[*] Hideki Matsumura[*]
*Japan Advanced Institute of Science and Technology, 1-1 Asahidai, Tatsunokuchi, Ishikawa 923-1292, JAPAN, minami@irii.go.jp
**Industrial Research Institute of Ishikawa, Ro-1 Tomizu-machi, Kanazawa, Ishikawa 920-0223, JAPAN
***Rohm Co., Ltd., 21 Saiin Mizosaki-cho, Ukyo-ku, Kyoto 615-8585, JAPAN

ABSTRACT

Feasibility of SiN_x passivation films at low substrate temperatures prepared by catalytic chemical vapor deposition (Cat-CVD) is studied for ferroelectric nonvolatile random access memories (FRAMs). SiN_x films were prepared at low substrate temperatures of 100 °C, 175 °C and 200 °C using Cat-CVD. Adjusting on flow rate ratio of SiH_4/NH_3, the refractive index of SiN_x film, deposited at 175 °C and 200 °C, measured by ellipsometry is controlled around 2.0. SiN_x films, with the refractive index around 2.0, deposited at only 200 °C show the following properties. 1) No oxidation during air exposure for 3 months was observed for the films. 2) Etching rate of the films in buffered HF is 20 nm/min. The dense SiN_x film, which is resistive for oxidation in air exposure and dissolution in buffered HF, is prepared at 200 °C and the film is suitable to the passivation of ferroelectric capacitors.

INTRODUCTION

Ferroelectric nonvolatile random access memories (FRAMs) are powerful devices because of their high-speed operation, low power consumption, long endurance and large-scale integration with simple structures. Devices on a scale larger than 1 Mb have been produced using lead zirconate titanate ($Pb(Zr,Ti)O_3$) [1,2]. However, it has been shown that PZT films are degraded by processes carried out at high temperatures and under reductive ambient [3], the stress of the passivation film and hydrogen penetration from such passivation film [4]. It has been reported that device-quality SiN_x films, for example, with stoichiometric composition, low hydrogen content, low chemical etching rate, low stress and conformal step-coverage, are prepared by catalytic chemical vapor deposition (Cat-CVD), often called hot-wire CVD [5,6]. However, deoxidization on the substrate surface due to active hydrogen in Cat-CVD processes may occur, since SiH_4 and NH_3 gases are decomposed by catalytic cracking reaction with a heated catalyzer. Sample temperature is also elevated, since the sample is heated by both thermal radiation from the catalyzer around 1800 °C and thermal transport by gas molecules. So far, we reported that no degradation for ferroelectric $Pb(Zr_{0.52}Ti_{0.48})O_3$ (PZT) capacitors occurs by exposure to active NH_3 gas cracked on catalyzer, when the sample temperature is lowered below 200 °C by controlling the heat flow from the catalyzer [7-9].

In this study, we carried out the preparation of SiN_x films on Si by Cat-CVD at low substrate temperatures, at which the ferroelectricity of PZT is not degraded, examined the properties of such SiN_x films and the ferroelectricity of PZT capacitors covered with SiN_x films deposited by Cat-CVD.

EXPERIMENTAL

SiN_x films were prepared using the Cat-CVD apparatus. The experimental setup is schematically illustrated in Fig. 1. We used two Cat-CVD apparatuses. One is called screw-Cat-CVD system for small sample (2 cm x 2 cm) in which the substrate was fixed on substrate holder by screw, the other was called ESC-Cat-CVD system for 4 inch wafer in which the substrate was fixed on substrate holder using electrostatic chuck (ESC) [10]. The substrate temperature is controlled in both apparatuses since the substrate has good thermal contact with thermal-controlled substrate holder. A tungsten wire was used as the catalyzer. It was placed with a distance of 4 cm from the substrate, and kept parallel to the substrate holder. The catalyzer was heated to 1800°C. The temperature of the catalyzer (T_{cat}) was estimated by an electronic infrared pyrometer placed outside a quartz window. A thermocouple was mounted on the substrate holder adjacent to the substrate to monitor the substrate temperature (T_s). Before deposition, real T_s was measured using a thermocouple mounted on substrate at ambient of 1.3 Pa NH_3, when power supply to catalyzer and temperature of substrate holder were varied [9].

Prior to deposition, the pressure in the reactor was pumped down to less than 5.0×10^{-4} Pa using a turbo molecular pump. The deposition conditions for screw-Cat-CVD system and ESC-Cat-CVD system are summarized in Table 1 and Table 2, respectively.

The ferroelectric capacitor shown in Fig. 1 was fabricated as follows. The bottom electrode consisting of Pt/IrO_2 was formed on a SiO_2/Si wafer. The PZT ($Pb(Zr_{0.52}Ti_{0.48})O_3$) film of 300 nm thickness was produced by a conventional sol-gel process. The crystallization of the PZT

Table 1. Deposition condition of SiN_x films for screw-Cat-CVD system.

Parameter	Set point(s)
SiH_4 flow rate	0.5 - 2.0 sccm
NH_3 flow rate	42 sccm
Substrate temperature T_s	100 °C, 200 °C* 170 °C 300 °C
Catalyzer temperature T_{cat}	1800 °C
Power supply to catalyzer	450 W, 600 W
Diameter of catalyzer	0.4 mm, 0.5 mm
Length of catalyzer	150 cm, 138 cm
Space of catalyzer	10 cm x 10 cm
Catalyzer - substrate gap	4 cm
Reactor pressure	1.3 Pa
Deposition time	3 - 10 min
Substrate size	2 cm x 2 cm

*Only when the substrate temperature was 200 °C, parameters of power supply, diameter and length were 600 W, 0.5 mm and 138 cm, respectively.

Table 2. Deposition conditions of SiN_x films for ESC-Cat-CVD system.

Parameter	Set point(s)
SiH_4 flow rate	1.5 - 4.0 sccm
NH_3 flow rate	200 sccm
Substrate temperature T_s	200 °C
Catalyzer temperature T_{cat}	1800 °C
Power supply to catalyzer	850 W
Diameter of catalyzer	0.5 mm
Length of catalyzer	185 cm
Space of catalyzer	16 cm x 17 cm
Catalyzer - substrate gap	4 cm
Reactor pressure	1.3 Pa
Deposition time	2 – 10 min
Substrate size	4 inch

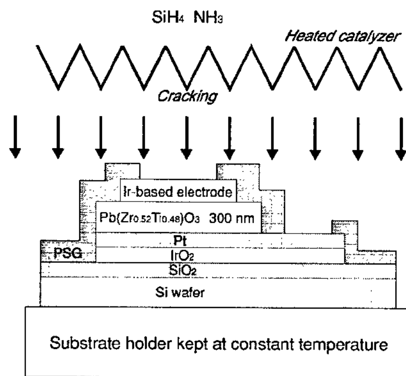

Fig. 1. Schematic illustration of ferroelectric capacitor and treatment.

films was carried out using rapid thermal annealing (RTA) at 700 °C for 1 min. The top Ir-based electrode was then deposited. After that, the capacitor was covered with SiO_2 doped with phosphorus (PSG), and contact holes were fabricated.

The polarization vs. electric field (P-E) hysteresis loop was observed using a Sawyer-Tower circuit at 1 kHz. Thickness and refractive index of SiN_x films on Si were measured by ellipsometry using light of 632.8 nm. SiN_x films on Si wafer were also observed by infrared measurement. The etching rate of the SiN_x film on Si at room temperature in buffered HF (16BHF) was examined.

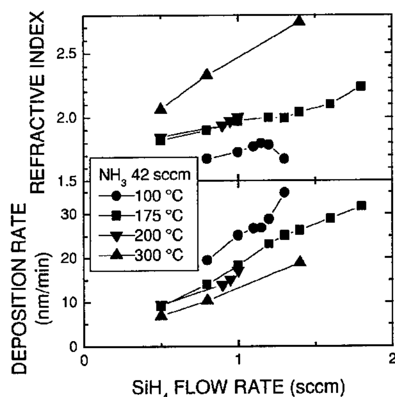

Fig.2. Deposition rate and refractive index of SiN_x films on Si wafer as a function of SiH_4 flow rate.

RESULTS AND DISCUSSION

As shown in Table 1, the preparation of SiN_x films on Si substrate was carried out at various substrate temperatures and SiH_4 flow rates using screw-Cat-CVD system. Figure 2 shows the deposition rate and the refractive index of SiN_x films, as a function of SiH_4 flow rate at substrate temperatures of 100 °C, 175 °C, 200 °C and 300 °C. The deposition rate becomes higher depending on an increase in SiH_4 flow rate. When the SiH_4 flow rate is the same, the lower the substrate temperature induces the higher the deposition rate. The refractive index except for the substrate temperature of 100 °C becomes larger depending on an increase in SiH_4 flow rate. High rate deposition of the SiN_x films with refractive index of 2.0 is carried out, when the substrate temperature is lower. We previously reported that the film deposited at 175 °C is oxidized and that deposited at 200 °C is not during air exposure for 10 days [9]. However, the refractive index of SiN_x films deposited at the substrate temperature of 100 °C is not over 2.0 for the present deposition conditions.

As shown in Table 2, the preparation of SiN_x films for the purpose of deposition on the wafer with the ferroelectric devices is carried out at substrate temperature of 200 °C using

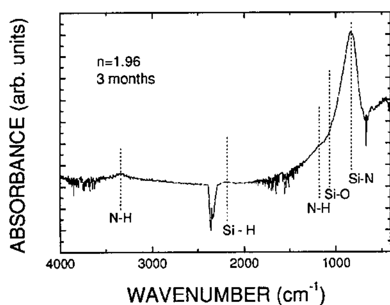

Fig. 3. FT-IR spectrum of SiN_x film on Si wafer deposited at 200 °C.

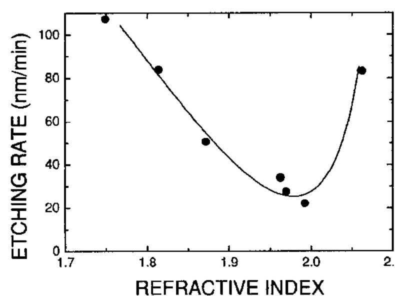

Fig. 4. Etching rate of SiN_x films in the buffered HF (16BHF) as a function of refractive index of SiN_x films.

ESC-Cat-CVD system. Figure 3 shows the FT-IR spectrum for the SiN_x film with refractive index of about 2.0 deposited at 200 °C in 3 months after the deposition. The remarkable signal around 1050-1080 cm^{-1} corresponding to the Si-O stretching mode [11] is not observed at the spectrum even after air exposure for 3 months. No oxidation during air exposure for 3 months is observed for the SiN_x film deposited at 200 ºC. The dense SiN_x film, which is resistive for oxidation in air exposure, is prepared at 200 ºC. Etching rate of SiN_x films prepared at 200 ºC in buffered HF (16BHF), is shown in Fig. 4. Etching rate shows minimum value about 20 nm/min at refractive index of SiN_x films around 2.0.

SiN_x films were also deposited at 200 °C on the wafer with the ferroelectric devices, using ESC-Cat-CVD system. Figure 5 shows the P-E hysteresis loops for the capacitors before (dotted line) and after the deposition of the SiN_x film (solid line). Property of ferroelectric capacitor covered with SiN_x film is not degraded with the each maximum applied voltage. It was found that no degradation due to deposition occurs for ferroelectric properties of the capacitor.

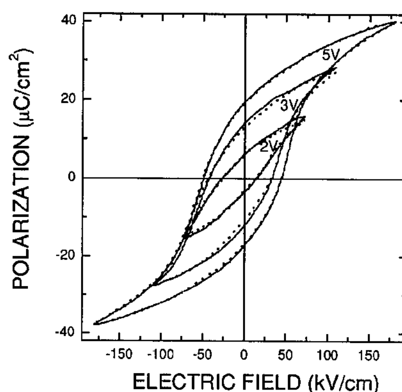

Fig. 5. P-E hysteresis loops for capacitors before (dotted line) and after the deposition of SiN_x film (solid line) as a parameter of maximum applied voltage.

The dense SiN_x films, which are resistive for oxidation in air exposure and dissolution in buffered HF, are obtained by Cat-CVD even at 200 °C, where the ferroelectric properties of PZT are not damaged.

CONCLUSIONS

We investigated the preparation of SiN_x films at low substrate temperature using Cat-CVD. Adjusting on flow rate ratio of SiH_4/NH_3, the refractive index of SiN_x film, deposited at 175 °C and 200 °C, measured by ellipsometry is controlled around 2.0. So far, the followings are found about SiN_x films, with the refractive index around 2.0, deposited at 200 °C: 1) No oxidation during air exposure for 3 months is observed for the films. 2) Etching rate of the films in buffered HF is 20 nm/min. The dense SiN_x film, which is resistive for oxidation in air exposure and dissolution in buffered HF, is prepared at 200 °C.

It is concluded that the SiN_x films prepared at 200 °C by Cat-CVD, inducing no degradation for ferroelectricity, are expected as the passivation film on ferroelectric devices.

ACKNOWLEDGEMENTS

This work is in part supported by the R&D Projects in Cooperation with Academic Institutions "Cat-CVD Fabrication Processes for Semiconductor Devices" entrusted from the New Energy and Industrial Technology Development Organization (NEDO) to the Ishikawa Sunrise Industries Creation Organization (ISICO) and carried out at Japan Advanced Institute of Science and Technology (JAIST).

REFERENCES

[1] S. Onishi, K. Hamada, K. Ishikawa, Y. Ito, S. Yokoyama, J. Kudo and K. Sakiyama: Tech. Dig. 1994 Int. Electron Devices Meeting, San Francisco, 1994, p. 843.

[2] N. Tanabe, T. Matsuki, S. Saitoh, T. Takeuchi, S. Kobayashi, T. Nakajima, Y. Maejima, Y. Hayashi, K. Amanuma, T. Hase, Y. Miyasaka and T. Kunio: Dig. Tech. Pap. 1995 Symp. VLSI Technology, Kyoto, 1995, p. 123.

[3] Y. Fujisaki, K. Kushida-Abdelghafar, Y. Shimamoto and H. Miki: J. Appl. Phys. **82,** 341 (1997).

[4] P. Boher, M. Renaud, L. Ijzendoorn and Y. Hily: Appl. Phys. Lett. **54,** 511 (1989).

[5] S. Okada and H. Matsumura: Jpn. J. Appl. Phys. **36,** 7035 (1997).

[6] S. Okada and H. Matsumura: Mater. Res. Soc. Symp. Proc. **446,** 109 (1997).

[7] T. Minamikawa, Y. Yonezawa, T. Nakamura, Y. Fujimori, A. Masuda and H. Matsumura: Jpn. J. Appl. Phys. **38,** 5358 (1999).

[8] T. Minamikawa, Y. Yonezawa, Y. Fujimori, T. Nakamura, A. Masuda and H. Matsumura: Mater. Res. Soc. Symp. Proc. **596,** 271 (2000).

[9] T. Minamikawa, Y. Yonezawa, A. Heya, Y. Fujimori, T. Nakamura, A. Masuda and H. Matsumura: Ext. Abst. 1st Int. Conf. Cat-CVD (Hot-Wire CVD) Process, Kanazawa, 2000, p. 253.

[10] M. Karasawa, A. Masuda, K. Ishibashi and H. Matsumura: Ext. Abst. 1st Int. Conf. Cat-CVD (Hot-Wire CVD) Process, Kanazawa, 2000, p. 117.

[11] D. V. Tsu, G. Lucovsky and M. J. Mantini: Phys. Rev. B **33**, 7069 (1986).

BST, Gate Materials, and DRAM: Fundamentals and Technology

Mat. Res. Soc. Symp. Proc. Vol. 655 © 2001 Materials Research Society

Investigation of Dead Layer Thickness in $SrRuO_3/Ba_{0.5}Sr_{0.5}TiO_3/Au$ Thin Film Capacitors

L. J. Sinnamon, R. M. Bowman and J. M. Gregg
Department of Pure and Applied Physics
Queen's University Belfast
Belfast BT7 1NN

ABSTRACT

Thin film capacitors with barium strontium titanate (BST) dielectric layers of 7.5 to 950 nm were fabricated by Pulsed Laser Deposition. XRD and EDX analyses confirmed a strongly oriented BST cubic perovskite phase with the desired cation stoichiometry. Room temperature frequency dispersion ($\varepsilon_{100\ kHz}/\varepsilon_{100\ Hz}$) for all capacitors was greater than 0.75. Absolute values for the dielectric constant were slightly lower than expected. This was attributed to the use of Au top electrodes since the same sample showed up to a threefold increase in dielectric constant when Pt was used in place of Au. Dielectric constant as a function of thicknesses greater than 70 nm, was fitted using the series capacitor model. The large interfacial parameter ratio d_i/ε_i of 0.40 ± 0.05 nm implied a significant dead-layer component within the capacitor structure. Modelled consideration of the dielectric behaviour for BST films, whose total thickness was below that of the dead layer, predicted anomalies in the plots of d/ε against d at the dead layer thickness. For the SRO/BST/Au system studied, no anomaly was observed. Therefore, either (i) 7.5 nm is an upper limit for the total dead layer thickness in this system, or (ii) dielectric collapse is not associated with a distinct interfacial dead layer, and is instead due to a through-film effect.

INTRODUCTION

The decrease in dielectric constant with film thickness is a well-established observation in thin film ferroelectric capacitors. This decrease can be effectively modelled by assuming the existence of very low dielectric constant 'dead layers' at the electrode-ferroelectric interfaces.[1] These interfacial dead layers act as parasitic capacitors in series with the bulk-like ferroelectric and hence the decrease in dielectric constant is said to follow the 'series capacitor model.' In this model, the effective capacitance of a thin film dielectric layer is given by:

$$\frac{1}{C_{eff}} = \frac{1}{C_b} + \frac{1}{C_i} \tag{1}$$

where subscripts *b*, and *i* refer to bulk and interface respectively. If the interfacial dead layer thickness d_i is independent of the total thickness d, then:

$$\frac{d}{\varepsilon_{eff}} = \frac{d_b}{\varepsilon_b} + \frac{d_i}{\varepsilon_i} = \frac{d}{\varepsilon_b} + d_i\left(\frac{1}{\varepsilon_i} - \frac{1}{\varepsilon_b}\right) \tag{2}$$

It is usually assumed that either $\varepsilon_b >> \varepsilon_i$[1] or $d_b >> d_i$[2] giving a linear relationship between d/ε_{eff} and d with a gradient of $1/\varepsilon_b$ and y-axis intercept of d_i/ε_i.

Despite the wide acceptance of the dead layer concept, an experimentally consistent explanation for the nature of such layers is not yet evident. Various models have been proposed: low dielectric constant space charge layers;[3] oxygen depletion zones adjacent to metals with a high oxygen affinity;[4] formation of surface states;[4] local diffusion of electrode material into the ferroelectric;[5,6] lattice-mismatch-induced ion vacancy formation;[7] chemically distinct surface phase;[8] intrinsic surface polarisation effects;[9,10] depolarisation fields due to incomplete screening by the electrodes;[11,12] intrinsic suppression of polarization at the electrode;[13] Schottky barrier, and associated depletion layer formation, as a result of band-bending at the ferroelectric-electrode interface.[14] Unfortunately none of the above is definitive nor free from contradictory evidence. Further, while direct imaging has occasionally shown distinction between bulk and interface,[15] usually high resolution transmission electron microscopy shows no evidence of interfacial layers.[14,16,17]

Some research suggests that a well-defined dead-layer may not be necessary for experimental agreement with the 'series capacitor' model. In this respect, the phenomenological thermodynamic approach used by Desu[18] to rationalise the existence of dead layers in fact introduces an interfacial energy per unit *area*, rather than per unit volume, such that the dead layer is not afforded a finite thickness. Despite this, the model had been successfully employed to predict the decrease in dielectric constant with thickness.[19] Basceri *et al.*[20] point out that although the concept of a dead layer is usually invoked to explain the observed thickness behaviour of the dielectric constant, other mechanisms could also fulfil the thermodynamic requirement. For example a long-range co-operative mechanism acting throughout the film could cause the dielectric constant to change with thickness. This is particularly pertinent given the recently observed soft-mode hardening in $SrTiO_3$ films.[21]

So, while the series capacitor model has been successfully used to fit many experimental systems it does not, in itself, conclusively demonstrate the presence of dead layers. In fact there is very little published data on the physical nature or formation of dead layers. The additional problem of the incompatibility of many published works due to differences in deposition methods and electrode materials makes it difficult to establish the behaviour of the dielectric constant over an extensive thickness range. In this paper we report the results of a comprehensive study of the effect of thickness on dielectric constant in low loss $MgO/SrRuO_3/Ba_{0.5}Sr_{0.5}TiO_3/Au$ thin film capacitors. We show that this system generates a particularly strong parasitic capacitor component, and yet find no evidence for a distinct dead layer down to a total dielectric thickness of 7.5 nm.

METHOD

Thin film capacitors were fabricated by Pulsed Laser Deposition (PLD) on commercial single crystal {100} MgO substrates. An energy density of ~1.5 Jcm^{-2} on the target surface was supplied from a KrF excimer laser with $\lambda = 248$ nm (Lambda Physik COMP*ex* 205*i*). Growth conditions were typically a substrate temperature of 800 ºC and chamber pressure of 0.15 mbars O_2 for both the $SrRuO_3$ (SRO) electrode and (Ba,Sr)TiO_3 (BST) dielectric. All films were annealed at 650 ºC in 1 bar O_2 for 15 to 60 minutes depending on the thickness of the BST. The BST film thickness was obtained by interpolation from measurements made using an Alpha-Step 200 profilometer (Tencor Instruments) for films over 400 nm thick, and from Keissig fringes apparent on X-rays of films under 50 nm (interference between X-rays scattered from the top and

bottom surfaces of the film). Thermal evaporation of Au top electrodes (radius = 0.75 mm) through a hard mask enabled dielectric measurements to be performed using an HP 4263B precision LCR meter. An Oxford Instruments cryostat and Lakeshore temperature controller facilitated dielectric measurements from 100 to 400 K.

RESULTS AND DISCUSSION

Crystallographic characterisation (Figure 1) shows successful growth of SRO and BST perovskite phases, with strong out-of-plane (θ-2θ X-ray diffraction) and in-plane (plan-view electron diffraction inset) orientation. The out-of-plane lattice constants of BST and SRO were measured as 3.966 ± 0.004 Å and 3.93 ± 0.01 Å respectively which compare well with bulk values. Energy Dispersive X-ray analysis (Jeol 733 Superprobe) showed the (Ba+Sr):Ti ratio in the BST to be close to unity (1 ± 0.03). A slight imbalance in the Sr:Ba ratio was noted (1.14 ± 0.05), giving an overall film composition of $Ba_{0.47}Sr_{0.53}TiO_3$. The effect on the dielectric constant of such a small stoichiometric change in the 'A' cation ratio is negligible.[22]

Dispersion in dielectric constant with frequency (Figure 2) and dielectric loss values (Figure 3 (a)) were monitored, and found comparable to literature.[17,23] Dielectric constant as a function of BST film thickness is shown in Figure 3 (a), taken at 400 K so that inherent thickness effects could be distinguished from Curie anomaly suppression (for bulk $Ba_{0.5}Sr_{0.5}TiO_3$ T_c = 248 K[24]). Very thin capacitors showed a flat temperature dependence of dielectric constant and tan δ (except for the occasional result with enhanced ionic conduction above 350 K. For these capacitors lower temperature values were used). The absolute magnitude of the dielectric constants are somewhat lower than reported for other BST thin film systems.[25,26] This suppression appears to be caused by the BST/Au interface, since measurements made on the *same* BST sample using both Au and Pt top electrodes revealed up to a threefold increase in the dielectric constant associated with Pt compared with that measured using Au top electrodes. For our capacitor structures, with d > 70 nm, values extracted from Figure 3 (b) using the series capacitor model were $\varepsilon_b = 1000 \pm 200$ and $d_i/\varepsilon_i = 0.40 \pm 0.05$ nm. The solid line is the fit generated from these values showing that the system follows the model and thus acts as if dead layers are present. The value of the d_i/ε_i ratio controls the decrease in ε with thickness as shown

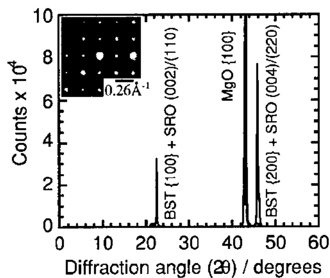

Figure 1. Typical θ - 2θ X-ray diffraction trace of SRO/BST(220 nm) structure with in-plane TEM diffraction pattern of BST (inset).

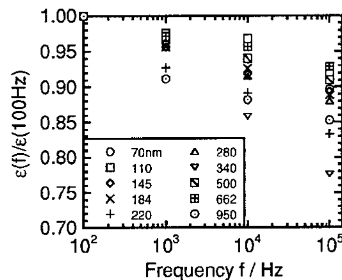

Figure 2. Frequency dispersion of dielectric constant for capacitors of 70 – 950 nm.

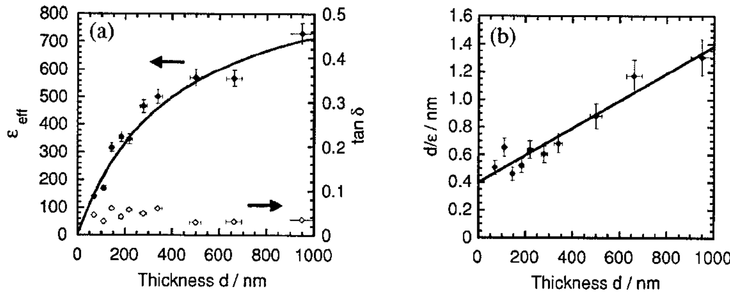

Figure 3. (a): Dielectric constant and tan δ as a function of BST thickness from 70 – 950 nm measured at 400 K. The solid line shows the fit generated using the model parameters extracted from 3 (b). (b): d/ε as a function of BST thickness d from 70 – 950 nm. The solid line is the linear fit to the data (R^2 = 0.93).

by Figure 4. This d_i/ε_i ratio is relatively large (compare with 0.05 nm for Pt/BST/Pt,[27] 0.13 nm for Pt/PZT/Al and 0.08 nm for Ag/PZT/Ag,[28] 0.12 nm for Pd/BST/Au/Ti,[29] and 0.887 nm for Al/BST/Al[30]), and the effect of the parasitic capacitor component is therefore apparent even in relatively thick films. However, the fact that d_i and ε_i are inseparable in the conventional series capacitor model, means that neither the dead layer thickness nor the dielectric constant is well defined.

It was hypothesised that if a physically distinct dead layer exists, then when the total thickness of the dielectric is less than the thickness of the dead layer, some deviation from the conventional series capacitor model would be expected. The model defines the dead layer as having a constant ε_i, thus when $d > d_i$, ε_{eff} is given by the combination of the layers as prescribed by equation (2), but when $d \leq d_i$, ε_{eff} becomes constant (ε_i). This case is shown schematically as (i) in Figure 5. This scenario which produces a step function in dielectric constant through the film is physically unlikely so we have considered a more continuous fall-off function (parabolic reduction in ε_i within the dead layer). In this case when $d \leq d_i$, ε_{eff} is given by:

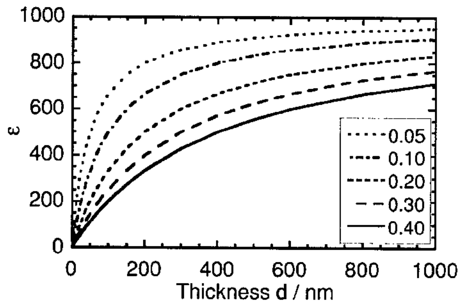

Figure 4. Effect of d_i/ε_i value on decrease of ε with thickness.

$$\varepsilon_{eff} = -\frac{\varepsilon_b d}{d_i\left[\left(\frac{d}{d_i}\right)-2\right]} \qquad (3)$$

As can be seen in Figure 5, in both of these cases a sharp anomaly is exhibited in the *d/ε against log(d)* function at $d = d_i$. The case of the dead layer being attributed no finite thickness is added to Figure 5 (iii) to demonstrate that the anomalies generated in (i) and (ii) do not occur, and hence that an observed anomaly could be confidently interpreted as yielding a value for d_i.

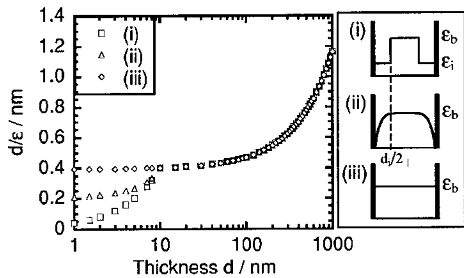

Figure 5. Simulations of d/ε behaviour using the series capacitor model for the cases when (i) ε_i is constant, (ii) ε_i decreases parabolically, (iii) there is no distinct dead layer. For (i) and (ii), the total thickness of the dead layer, d_i was set at 10 nm.

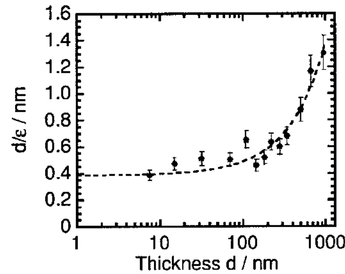

Figure 6. d/ε as a function of BST thickness down to 7.5 nm. The function expected for a dead layer of zero thickness is shown by the dashed line using the parameters from Figure 3 (b).

Capacitors with BST thicknesses less than 70nm were grown to investigate the presence of an anomaly and hence demonstrate the dead-layer thickness in the SRO/BST/Au system. Although the tan δ values increased to 0.6 at 10 kHz for the 7.5 nm film, the frequency dispersion was unchanged. As can be seen in Figure 6, the experimentally determined *d/ε* against *log(d)* plot of all results from 7.5 – 950 nm shows that the dielectric behaviour for films below 70 nm obeys the series capacitor model with the same parameters as those extracted from the series above 70 nm. The expected curve for the case of no dead layer is shown by the dashed line which must have a y-axis intercept of (0.40 ± 0.05) nm, according to the previous analysis. As can be seen no anomaly in the experimental results is observed for BST thicknesses down to 7.5 nm.

CONCLUSIONS

The result of Figure 6 shows no evidence for the presence of dead layers down to a thickness of 7.5 nm, despite the expectation that the SRO/BST/Au system should possess a substantial parasitic component. Therefore either:

(i) dielectric collapse in thin film ferroelectrics is not associated with a distinct interfacial dead layer, and is instead due to a through-film effect, or

(ii) 7.5 nm represents an upper limit on the total dead layer thickness for the SRO/BST/Au system, with an associated maximum average ε_i of ~19.

Further work is under way using much smaller electrode areas and much thinner BST films to experimentally verify or otherwise the existence of dead layers with finite thickness.

ACKNOWLEDGEMENTS

The authors gratefully acknowledge financial support from DFHETE, the EPSRC, NICAM and The Royal Society, as well as the collaboration of AVX / Kyocera and technical assistance from Stephen McFarland, Paddy Gaffikin and Mike Higgins.

REFERENCES

[1] K. Amanuma, T. Mori, T. Hase, T. Sakuma, A. Ochi, Y. Miyasaka, Jpn. J. Appl. Phys. **32,** 4150 (1993).
[2] H. Li, W. Si, A. D. West, X. X. Xi, Appl. Phys. Lett. **73,** 464 (1998).
[3] V. G. Bhide, R. T. Gonhalekar, S. N. Shringi, J. Appl. Phys. **36,** 3825 (1965).
[4] G. Teowee, C. D. Baertlein, E. A. Kneer, J. M. Boulton, D. R. Uhlmann, Integrated Ferroelectrics, **7** 149 (1995).
[5] I. Stolichnov, A. Tagantsev, N. Setter, J. S. Cross, M. Tsukada, Appl. Phys. Lett. **75,** 1790 (1999).
[6] D. Choi, B. Kim, S. Son, S. Oh, K. Park, J. Appl. Phys. **86,** 3347 (1999).
[7] M. Izuha, K. Abe, N. Fukushima, Jpn. J. Appl. Phys. **36,** 5866 (1997).
[8] V. Craciun, R. K. Singh, Appl. Phys. Lett. **76,** 1932 (2000).
[9] C. Zhou, D. M. Newns, J. Appl. Phys. **82,** 3081 (1997).
[10] K. Natori, D. Otani, N. Sano, Appl. Phys. Lett. **73,** 632 (1998).
[11] P. Wurfel, I. P. Batra, Phys. Rev. B **8,** 5126 (1973).
[12] Y. G. Wang, W. L. Zhong, P. L. Zhang, Phys. Rev. B **51,** 5311 (1995).
[13] O. G. Vendik, S. P. Zubko, L. T. Ter-Martirosayn, Appl. Phys. Lett. **73,** 37 (1998).
[14] C. S. Hwang, B. T. Lee, C. S. Kang, K. H. Lee, H. Cho, H. Hideki, W. D. Kim, S. I. Lee, M. Y. Lee, , J. Appl. Phys. **85,** 287 (1999)
[15] S. Paek, J. Won, K. Lee, J. Choi, C. Park, Jpn. J. Appl. Phys. **35,** 5757 (1996).
[16] Y. Sakashita, H. Segawa, K. Tominaga, M. Okada, J. Appl. Phys. **73,** 7857 (1993).
[17] W. Jo, D. C. Kim, H. M. Lee, K. Y. Kim, J. Korean Phys. Soc. **34,** 61 (1999).
[18] S. B. Desu, Mat. Res. Soc. Symp. Proc. **541,** 457 (1999).
[19] K. Abe, S. Komatsu, Jpn. J. Appl. Phys. Pt 2 **32,** L1157 (1993).
[20] C. Basceri, S. K. Streiffer, A. I. Kingon, R. Waser, J. Appl. Phys. **82,** 2497 (1997).
[21] A. A. Sirenko, C. Bernhard, A. Golnik, A. M. Clark, J. Hao, W. Si, X. X. Xi, Nature, **404,** 373 (2000).
[22] T. Nakamura, Y. Yamanaka, A. Morimoto, T. Shimizu, Jpn. J. Appl. Phys. **34,** 5150 (1995).
[23] B. Nagaraj, T. Sawhney, S. Perusse, S. Aggarwal, R. Ramesh, V. S. Kaushik, S. Zafar, R. E. Jones, J. H. Lee, V. Balu, J. Lee, Appl. Phys. Lett. **74,** 3194 (1999).
[24] *Landolt-Börnstein Numerical Data and Functional Relationships in Science and Technology*, New Series Group III: Crystal and Solid State Physics, Vol. 16(a), edited by K. H. Hellwege (Springer-Verlag, 1981).
[25] W. Lee, I. Park, G. Jang, H. Kim, Jpn. J. Appl. Phys. **34,** 196 (1995).
[26] M. Izuha, K. Abe, M. Koike, S. Takeno, N. Fukushima, Appl. Phys. Lett. **70,** 1405 (1997).
[27] W. Lee, H. Kim, S. Yoon, J. Appl. Phys. **80,** 5891 (1996).
[28] J. J. Lee, S. B. Desu, Ferroelectric Letters, **20,** 27 (1995).
[29] S. Yamamichi, H. Yabuta, T. Sakuma, Y. Miyasaka, Appl. Phys. Lett. **64,** 1644 (1994).
[30] N. Ichnose, T. Ogiwara, Jpn. J. Appl. Phys. **34,** 5198 (1995).

Mat. Res. Soc. Symp. Proc. Vol. 655 © 2001 Materials Research Society

PREPARATION AND CHARACTERIZATION OF MFM AND MFIS STRUCTURES USING $Sr_2(Ta_{1-x}, Nb_x)_2O_7$ THIN FILM BY PULSED LASER DEPOSITION

Masanori Okuyama, Toshiyuki Nakaiso and Minoru Noda
Area of Materials and Device Physics, Department of Physical Science, Graduate School of Engineering Science, Osaka University, 1-3 Machikaneyama-Cho, Toyonaka, Osaka 560-8531, Japan

ABSTRACT

$Sr_2(Ta_{1-x}, Nb_x)_2O_7$(STN) ferroelectric thin films have been prepared on SiO_2/Si(100) substrates by the pulsed laser deposition (PLD) method. Preferential (110) and (151)-oriented STN thin films are deposited at a low temperature of 600°C in N_2O ambient gas at 0.08 Torr. A counterclockwise C-V hysteresis was observed in the metal-ferroelectric-insulator-semiconductor (MFIS) structure using $Sr_2(Ta_{0.7}, Nb_{0.3})_2O_7$ on SiO_2/Si deposited at 600°C. Memory window in the C-V curve spreads symmetrically towards both positive and negative directions when applied voltage increases and the window does not change in sweep rates ranging from 0.1 to $4.0x10^3$ V/s. The C-V curve of the MFIS structure does not degrade after 10^{10} cycles of polarization reversal. The gate retention time is about $3.0x10^3$ sec when the voltages and time of write pulse are $\pm$15V and 1.0 sec, respectively, and hold bias was -0.5 V.

INTRODUCTION

In recent years, ferroelectric nonvolatile memory devices have attracted much attention from the viewpoints of high-speed and large-scale signal processing. There are generally two kinds of nonvolatile memories using ferroelectric thin films. One is memory using a ferroelectric capacitor with large polarization-voltage (P-V) hysteresis, and the other is the metal-ferroelectric-(insulator-)semiconductor (MF(I)S)-FET type of memory which has a ferroelectric thin film gate.[1),2)] Among memory devices, the FET type is excellent as the memory state is read out nondestructively and is suited for large-scale integration because it obeys the scaling rule. In this device, however, high-temperature fabrication of ferroelectric films often degrades the performance of a device by interdiffusion of component materials of the ferroelectric film to the Si substrate and also degrades characteristics of other devices fabricated in the same chip. Especially, using the SBT and PZT films in ferroelectric memory devices, Bi and Pb component atoms easily diffuse into the substrate. Thus, we have attempted to prepare ferroelectric thin films at low temperatures by pulsed laser deposition (PLD)[3)]. The voltage applied to a ferroelectric film, on the other hand, decreases when the ferroelectric film has a high dielectric constant. By considering these situations, $Sr_2(Ta_{1-x}, Nb_x)_2O_7$ (STN)[4)] was selected as the ferroelectric material. STN has adequate spontaneous polarization although too large spontaneous polarization in conventional ferroelectric materials such as PZT and $PbTiO_3$ is not good for MFIS structure. Moreover, STN has a low dielectric constant, low coercive force and good thermal stability compared to bismuth-layer-structured ferroelectrics which are becoming key materials in nonvolatile memory devices.[5)-7)] Spontaneous polarization of STN occurs along the c-axis. Moreover, it is noted that the STN is not easily deoxidized and degraded little by hydrogen because it is a

bismuth- and lead-free material,[8),9)] and its remanent polarization, coercive force and dielectric constant are controlled by adjusting its composition ratio.[4),8)] STN films have been prepared so far by sol-gel method[8)-13)], and the deposition temperature was still high. In our previous study,[14)] STN thin films are prepared by pulsed laser deposition (PLD) and their dielectric properties are characterized. In this study, we report on the electrical properties of MFIS diodes using STN ferroelectric thin film prepared by PLD method.

2. EXPERIMENTAL DETAILS

The laser used for the PLD was an ArF excimer laser with a wavelength of 193 nm. The laser beam was focused by a quartz lens onto an $Sr_2(Ta_{1-x}, Nb_x)_2O_7$ ceramic target rotating in a vacuum chamber. The target was an $Sr_2(Ta_{1-x}, Nb_x)_2O_7$ (x=0.2-0.4) ceramic disk and the substrates used were SiO_2/Si(100) wafers fabricated by dry thermal oxidation and Pt/Ti/SiO_2/Si(100). The composition ratio (x) was mainly set to around 0.3 in this experiment because stable ferroelectricity is observed at room temperature,[14)] and the composition ratio of 0.3 is estimated to be suitable considering Curie temperature of STN(x=0.3), about 550°C.[4)] The substrate temperature (T_s) during the deposition was varied from 500 to 600°C using a ceramic heater and a chromel-alumel thermocouple in a substrate holder. The ambient gas during the deposition was N_2O, and the pressure was 0.08 Torr. The details of the deposition conditions are listed in Table I. Finally, Al (250 μmϕ, 100 nm thickness) top electrodes and AuSb bottom electrodes were formed.

Crystalline structures of deposited films were analyzed by X-ray diffraction (XRD)(RINT 2000) and Raman spectroscopy. Surface morphologies and cross-sectional views were observed by scanning electron microscopy (SEM) and atomic force microscopy (AFM). The P-E hysteresises were measured at 1 kHz using a Sawyer-Tower circuit, and the current density-electric field (J-E) characteristics were measured using a precise current amplifier (Model 617 Keithley). For MFIS structures, the capacitance-voltage (C-V) characteristics, the fatigue and memory retention properties were measured using C-V plotters (HP4280A, Hewlett Packard and Model 410, Princeton Applied Research).

RESULTS AND DISCUSSIONS

Figure 1 shows XRD patterns of STN (x=0.2, 0.3 and 0.4) films on Pt/Ti/SiO_2/Si(100) wafers in N_2O atmosphere at 600°C. The films were deposited at an N_2O pressure of 0.08 Torr under ArF laser irradiation with a repetition frequency of 5 Hz. (110) and (151) peaks of STN were obtained for every composition ratio. Figure 2 shows P-E hysteresis loops of STN films measured by a Sawyer-Tower circuit at 1 kHz. The STN films were prepared at a substrate temperature of 600°C in N_2O ambient gas at 0.08 Torr. Ferroelectric hysteresises were confirmed for the films at compositions of x=0.2 and 0.3. For x=0.3, the

Table I. Detail of deposition condition.

Target	$Sr_2(Ta_{1-x}, Nb_x)_2O_7$ ceramic disk x=0.2 - 0.4
Substrate	Pt(111)/Ti/SiO_2/Si SiO_2/Si(100)
Substrate temperature	500 - 600 °C
Gas	N_2O
Gas pressure	0.08 Torr
Laser	ArF excimer
Repetition frequency	5 Hz
Beam size	0.03 cm²
Strength	3.0 J/cm² shot
Deposition time	45 min
Target-substrate distance	15 mm

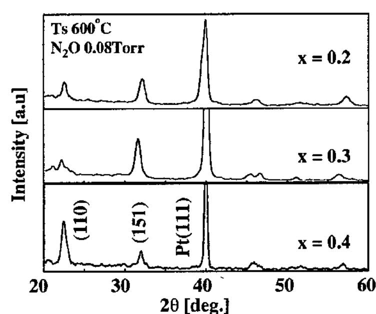

Fig. 1. XRD patterns of STN(x=0.2, 0.3 and 0.4) films deposited on $Pt/Ti/SiO_2/Si$ substrates in N_2O atmosphere at 600°C.

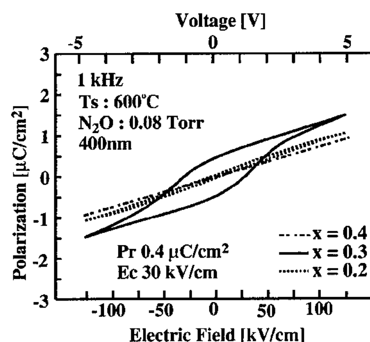

Fig. 2. P-E hysteresis loops of STN films with x = 0.2, 0.3 and 0.4.

remanent polarization (P_r) was 0.4 $\mu C/cm^2$ and the coercive field (E_c) was 30 kV/cm. The dielectric constant at room temperature was about 55 at 1 MHz, and this value is much lower than those of SBT and PZT. Figure 3 shows J-E characteristics of as-deposited and post-annealed STN films. Leakage current in the post-annealed film is found to be lower than that in as-deposited film. The currents seem to consist mainly of Schottky conduction at low electric field and Fowler-Nordlheim contribution at high electric field, respectively.

Figure 4 shows XRD patterns of STN (x=0.3) films on $SiO_2/Si(100)$ wafers. The films were deposited at 600°C in an N_2O pressure of 0.08 Torr under ArF laser irradiation with a repetition frequency of 5 Hz. (110), (151), (172) and (153) peaks of STN are observed in the as-deposited film, however, its crystallization is a little poor compared to that of STN film on $Pt/Ti/SiO_2/Si(100)$ substrate. Sharp peaks of

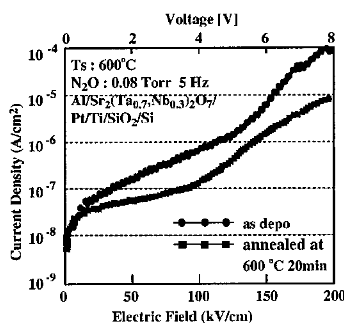

Fig. 3. J-E characteristics of as-deposited and post-annealed STN (x=0.3) films.

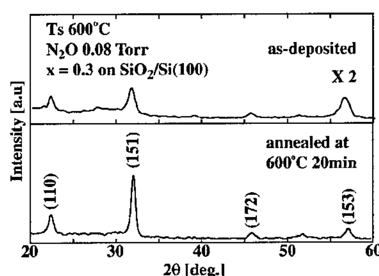

Fig. 4. XRD patterns of as-deposited and post-annealed STN(x=0.3) films on $SiO_2/Si(100)$ substrates.

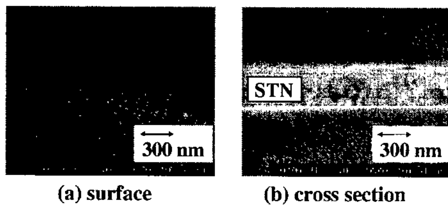

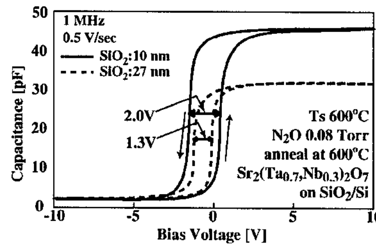

Figs. 5. (a) Surface morphology and (b) cross-sectional view of STN film obtained by SEM.

Fig. 6. C-V characteristics of MFIS structure.

STN, on the other hand, are observed in the film post-annealed in O_2 at 600°C for 20 min and the crystalline was improved. Figures 5(a) and (b) show surface morphology and cross sectional structure of the STN film grown at 600°C in N_2O, respectively. A flat surface morphology is observed, and the average of surface roughness (R_a) is 1.10 nm. The grain sizes of STN thin films are as large as 30 to 50 nm and a dense structure is observed.

Figure 6 shows the C-V characteristics (measurement frequency: 1 MHz) of the Al/STN(x=0.3)(400 nm)/SiO_2(10, 27 nm)/n-Si(100) (MFIS) structures at a sweep voltage ranging from -10 V to +10 V. Counterclockwise C-V hysteresises were observed in the MFIS structures, and their memory windows were about 1.3 V for SiO_2 thickness of 27 nm and 2.0 V for the thickness of 10 nm, respectively. These memory windows are smaller than the value estimated from $2E_c$ of P-E hysteresis. However, it is well known that ferroelectricity of the films on amorphous SiO_2 film is a little worse than that on Pt/Ti/SiO_2/Si, so this phenomenon does not show disagreement with the P-E hystetesis. Slope of the C-V curve near

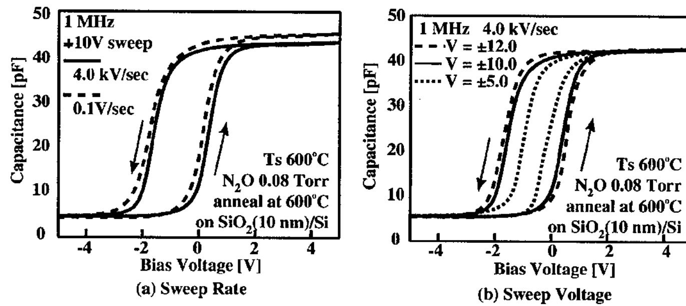

Figs. 7. Fast C-V characteristics of MFIS structure, (a) dependence on sweep rate and (b) sweep voltage.

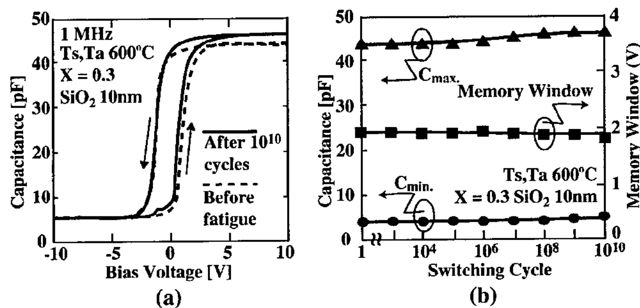

Figs. 8. Fatigue properties of MFIS structure, (a) C-V curves and (b) minimum and maximum of capacitance, C_{min} and C_{max}, and memory window.

depletion region is steep and show a low interface state density. Figure 7(a) shows the C-V characteristics of MFIS structure using 10 nm SiO_2 buffer layer as a parameter of sweep rate. Its memory window changes little at sweep rates ranging from 0.1 to 4.0×10^3 V/s when sweep voltage amplitude was ± 10 V, so that it is plausible that this memory window is caused by ferroelectricity of the STN film, but little by ion drift. Figure 7(b) shows the C-V characteristics of MFIS structure as a function of sweep voltage. Its memory window spreads symmetrically toward both positive and negative directions when applied voltage width is increased to ± 10 V, and almost saturates beyond ± 10 V. Figures 8(a) and (b) show fatigue properties of the memory window and minimum and maximum capacitance (C_{min} and C_{max}) values in MFIS structure at sweep voltage width of ± 10 V and sweep rate of 0.5 V/s. It is found from the figures that little fatigue degradations of memory window, C_{min} and C_{max} and C-V curve are observed. Moreover, it is considered from the slope of the C-V curve shown in Fig. 8(a) that interface state or trap density does not rather change or decrease slightly in the voltage-increasing and decreasing traces by switching pulses. The reason of these phenomena is not clear at present stage, however, we think for one reason that these phenomena are related to strain of M-F and/or F-I interfaces that relaxed by fatigue pulses, and their surface morphology.

Figure 9 shows memory retention characteristics of MFIS structures at write pulse time of 1.0 s and hold voltage of –0.5 V as a function of write voltage. The retention time becomes longer when write voltage is increased, because the ferroelectric film is polarized enough. It saturates at about 3000 s at write voltage of ± 10 V. This result corresponds well to saturation behavior of memory window shown in Fig. 7(b). One of the reasons for these short retention time is the leakage current of STN ferroelectric layer, thus, we think the retention time becomes longer when the leakage current is more suppressed.

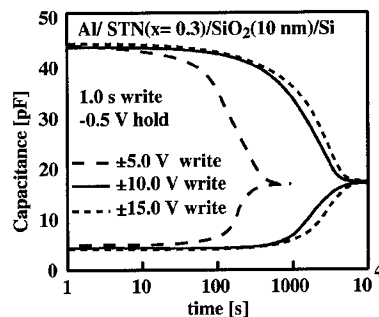

Fig. 9. Memory retention characteristics of MFIS structure as a function of write voltage.

CONCLUSIONS

$Sr_2(Ta_{1-x}, Nb_x)_2O_7$ thin films are prepared by pulsed laser deposition on $Pt/Ti/SiO_2/Si$ and $SiO_2/Si(100)$ substrates. These films have preferential (110) and (151)-orientation, when deposited in N_2O ambient gas at 600°C. P-E hysteresis loops are observed for $Sr_2(Ta_{1-x}, Nb_x)_2O_7$ thin films on $Pt/Ti/SiO_2/Si$ substrates when the composition ratio is 0.2 and 0.3. For $Sr_2(Ta_{0.7}, Nb_{0.3})_2O_7$ thin films, the remanent polarization is 0.4 $\mu C/cm^2$, the coercive force is 30 kV/cm and the dielectric constant is about 55. Counterclockwise C-V hysteresis is observed in the MFIS structure and its memory window is about 2.0 V, and little change is observed in the C-V curve when the sweep rate was ranged from 0.1 to 4.0×10^3 V/s. The memory retention time is about 3000 s. Finally we believe that STN ferroelectric thin films are sufficiently applicable for MFIS-FET memory devices.

ACKNOWLEDGMENTS

This work was partially supported by the Research for the Future Program supported by the Japan Society of the Promotion of Science and Rohm Co.,Ltd and semiconductor technology academic research center.

REFERENCES

1) Y. Higuma, Y. Matsui, M. Okuyama, T. Nakagawa and Y. Hamakawa: Jpn. J. Appl. Phys. Suppl. **17-1** (1978) 209.
2) T. Hirai, T. Goto, K. Teramoto, T. Nishi and Y. Tarui: Jpn.J.Appl.Phys. **33** (1994) 5219.
3) H. Sugiyama, T. Nakaiso, Y. Adachi, M. Noda and M. Okuyama: Jpn.J.Appl.Phys. **39** (2000) 2131.
4) S. Nakamatsu, M. Kimura and T. Kawamura: J.Phys.Soc.Jpn. **38** (1975) 819.
5) E. Tokumitsu, G. Fujii and H. Ishiwara: Appl.Phys.Lett. **75** (1999) 575.
6) S. B. Xiong and S. Sakai: Appl.Phys.Lett. **75** (1999) 1613.
7) T. Kijima and H. Matsunaga: Jpn.J.Appl.Phys. **38** (1999) 2281.
8) Y. Fujimori, N. Izumi, T. Nakamura and A. Kamisawa: Jpn.J.Appl.Phys. **37** (1998) 5207.
9) Y. Fujimori, T, Nakamura and A. Kamisawa: Jpn.J.Appl.Phys. **38** (1999) 2285.
10) C. H. Son, H. D. Nam, S. W. Jang and H. Y. Lee: J.Kor.Phys.Soc. **32** (1998) 1434.
11) M. Shoyama, A. Tsuzuki, K. Kato and N. Murayama: Appl.Phys.Lett. **75** (1999) 561.
12) A. V. Prasadarao, U. Selvaraj and S. Komarneni: J.Mater.Res. **10** (1995) 704.
13) K. Okuwada, S. Nakamura and H. Nozawa: J.Mater.Res. **14** (1999) 855.
14) T. Nakaiso, H. Sugiyama, M. Noda and M. Okuyama: Jpn.J.Appl.Phys. to be published.

Mat. Res. Soc. Symp. Proc. Vol. 655 © 2001 Materials Research Society

New Pt/(Bi,La)$_4$Ti$_3$O$_{12}$/Si$_3$N$_4$/Si MFIS Structure for FET-Type Ferroelectric Memories by the Sol-Gel Method

Takeshi Kijima, Yoshihisa Fujisaki and Hiroshi Ishiwara
Frontier Collaborative Research Center
Tokyo Institute of Technology
4259 Nagatsuta, Midori-ku, Yokohama 226-8503, Japan

ABSTRACT

The well c-axis-oriented $Bi_{3.25}La_{0.75}Ti_3O_{12}$ films with good crystallinity and good surface morphology were obtained at temperatures higher than 600℃. It was also found in a Pt / 100nm-$Bi_{3.25}La_{0.75}Ti_3O_{12}$ / 3nm-Si_3N_4 / Si (metal / ferroelectric / insulator / semiconductor) structure that C-V characteristics showed a hysteresis loop with a memory window of about 1V and both the high and low capacitance values kept at zero bias voltage did not change for more than 3 hours.

INTRODUCTION

Since first experimental demonstration of MFS-FET (metal / ferroelectric / semiconductor field effect transistor) by Moll and Tarui [1], MFS-FET has been expected as a nonvolatile ferroelectric memory device with nondestructive readout operation. In the MFS structure, the ferroelectric thin films must be directly deposited on Si substrate. However, the interface reactions between ferroelectric materials and the Si substrate make it difficult to obtain a good ferroelectric / Si interface [2][3][4]. Thus, an MFIS structure (metal / ferroelectric / insulator / semiconductor) has extensively been investigated recently in order to avoid such an interface reaction.

In the MFIS structure, it is desirable from a viewpoint of the data retention characteristics to choose a ferroelectric film with a small remanent polarization and to use it in the saturated polarization condition [5]. For this application, (Bi,La)$_4$Ti$_3$O$_{12}$ is an important candidate, because it is known to be fatigue-free [6] and its remanent polarization Pr and coercive field Ec are as small as 4 μ C/ cm^2 and 4kV/cm along the c-axis. However, the Pr and Ec values are as large as 50 μ C/cm^2 and 50kV/cm along the a-axis. Thus, it is important in the use of this material to control the crystallite orientation in the film.

This paper demonstrates the MFIS diode characteristics using the n- and p-type Si substrates to make the ferroelectric gate structured FETs of p- and n-channel. In order to form the MFIS structure, thin Si_3N_4 layers were first formed on Si substrates using atomic nitrogen radicals.[7]

The method we used was the direct nitrification of a Si substrate by which we have obtained good MIS (Metal / Insulator / Semiconductor) characteristics even after the high temperature post annealings .

Then, $(Bi,La)_4Ti_3O_{12}$ films were deposited on the Si_3N_4 / Si structures using the spin-coating method of sol-gel solutions and the optimum conditions to obtain well c-axis-oriented $(Bi,La)_4Ti_3O_{12}$ films were investigated. In the optimization procedure, the La content was fixed at 0.75, but such parameters as the Bi content in the sol-gel solution, temperatures of pre-annealing and crystallization annealing, crystallization ambient, and so on were changed.

EXPERIMENTAL

First, Si_3N_4 thin layers were formed on either n-type or p-type Si(100) single crystal substrates using atomic nitrogen radicals. The native oxide of the substrates was removed before the film formation and the substrates were exposed to atomic nitrogen radicals at 800℃for 60 min. Then, the samples were annealed at 850℃ in O_2 atmosphere for 20 min to improve the interface property. A typical thickness of the Si_3N_4 layer was about 3 nm. Then, $Bi_{3.25}La_{0.75}Ti_3O_{12}$ (BLT) films were formed by the sol-gel method on the Si_3N_4 layer. In order to form a BLT film, the sol-gel solution was spin-coated on the Si_3N_4 / Si structure. Then, it was pre-annealed in air either at 400℃ or at 500℃ for 10 min on a hot plate and annealed either in O_2 or in air at temperatures ranging from 600℃ to 800℃ for 20min using an RTA (rapid thermal annealing) furnace. The crystalline structure and the surface morphology of the films were characterized by X-ray diffraction (XRD) analysis and scanning electron microscopy (SEM). For the electrical measurements of $Pt/Si_3N_4/Si$ (MIS) and $Pt/BLT/Si_3N_4/Si$ (MFIS) structures, Pt top electrodes were deposited by vacuum evaporation method at room temperature. The capacitance-voltage (C-V) characteristic and the retention time measurements were carried out at 1MHz with an LCR meter (4275A, Yokogawa Hewlett-Packard).

RESULTS AND DISCUSSION

First, formation of BLT films was attempted using stoichiometric BLT sol-gel solution. However, no X-ray diffraction (XRD) peak was observed in the deposited film even after the film was annealed at 800℃ in O_2 ambient. Then, in order to enhance the crystallization of the BLT films on Si_3N_4/Si, 2.5 to 7.5% excess-Bi solutions were used as well as the crystallization ambient was changed from O_2 to air.

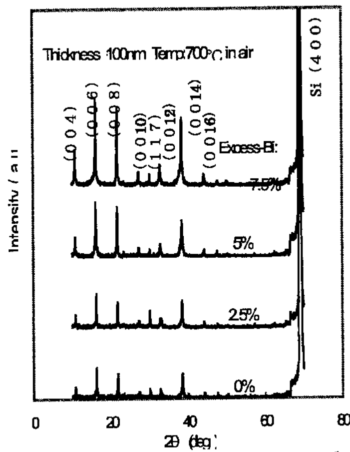

Figure 1. XRD patterns for 100nm-thick $Bi_{3.25}La_{0.75}Ti_3O_{12}$ films annealed at 700℃.

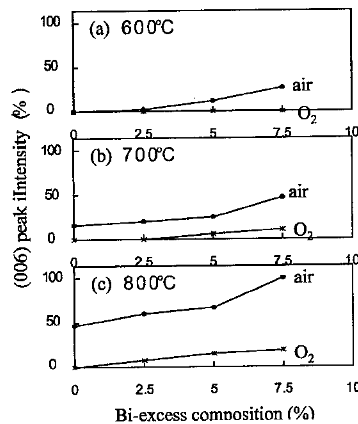

Figure 2. Relationships between the excess-Bi composition and XRD (006) peak intensity at 600, 700 and 800℃.

In this experiment, the film thickness was fixed at 100nm using a single spin-coating process and the pre-annealing temperature was kept at 400℃. Figure 1 shows typical XRD patterns for four BLT films with different Bi compositions which were crystallized at 700℃ in air ambient. In this figure, most reflection peaks originate from the c-plane of the BLT films, but small (117) peaks still remain in the patterns at the 2 θ value of 30°, which means that further optimization is necessary to obtain perfectly c-axis oriented BLT films. It is interesting to note that the film with the stoichiometric Bi composition is crystallized at 700℃ by changing the annealing ambient from O_2 to air.

Figure 2 shows variation of the (006) peak intensity plotted as functions of the excess-Bi composition, the crystallization temperature, and the crystallization ambient. It can be seen from the figure that the peak intensity becomes stronger in air ambient, at the higher annealing temperature, and at the larger Bi composition. It can also be seen that the crystallization characteristics at 800℃ in O_2 ambient are almost the same as those at 600℃ in air. We conclude from these results that BLT films are crystallized in air more easily than in O_2 ambient regardless of the annealing temperature and that the difference is more pronounced at higher temperatures.

Next, the film thickness dependence was investigated. In this experiment, all samples were formed by single spin-coating of sol-gel solutions. The pre-annealing temperature was fixed

at 400℃ and the crystallization annealing was conducted in air. Variation of the (006) peak intensity is shown in Fig.3, which is plotted as functions of the film thickness, the annealing temperature, and the excess-Bi composition. As can be seen from the figure, the peak intensity is almost proportional to the film thickness when the annealing temperature is 600℃, or when the excess-Bi composition is smaller than or equal to 2.5% at the annealing temperatures of 700 and 800℃. On the other hand, when the excess-Bi is more than 5%, there exist optimum thicknesses at which the (006) peak intensity becomes maximum. The values are 75 and 50 nm for annealing temperatures of 700 and 800℃, respectively. It was also found that the surface morphology of the BLT films degraded when the film thickness exceeded the optimum value.

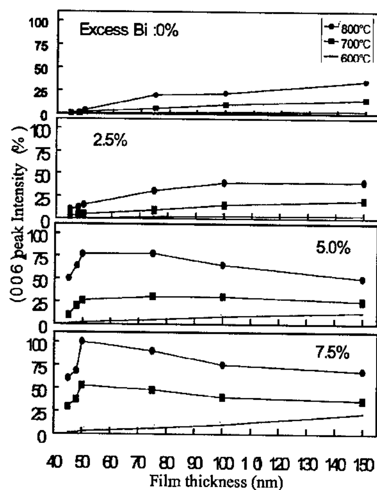

Figure 3. Relationships between film thickness and XRD (006) peak intensity.

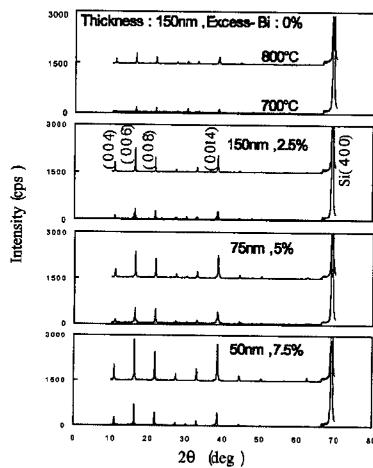

Figure 4. XRD patterns for the $Bi_{3.25}La_{0.75}Ti_3O_{12}$ films annealed at 700℃ and 800℃.

XRD patterns for the films with the optimum film thicknesses are summarized in Fig.4 in which the films were crystallized either at 700℃ or at 800℃. As can be seen from the figure, all films have strong prepared orientation along the c-axis and the films with 5% and 7.5%

excess-Bi compositions are almost a single phase when they are annealed at 800℃. Figure 5 shows SEM micrographs of the cross section and the surface for a typical BLT film, which was annealed at 800℃ in air. As can be seen from the figures, the interface between the BLT film and Si substrate is very sharp and the surface morphology of the film is good. We conclude from these result that almost perfectly c-axis-oriented BLT films can be obtained by carefully choosing such parameters as excess-Bi composition, film thickness, and pre-annealing and crystallization temperatures.

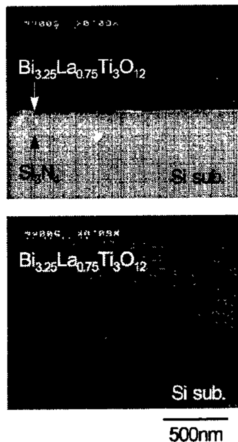

Figure 5. Cross section and plane view SEM micrographs for a $Bi_{3.25}La_{0.75}Ti_3O_{12}$ film.

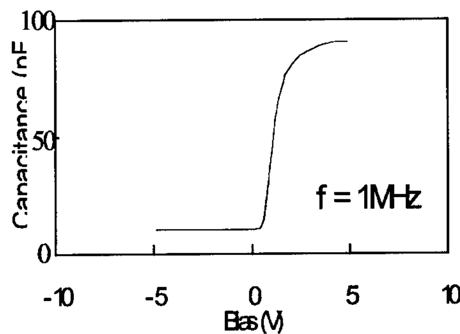

Figure 6. Capacitance-voltage characteristics of a Pt / Si_3N_4 / n-type Si MIS structure.

It is known that the c-axis oriented $Bi_4Ti_3O_{12}$ (BIT) can be easily obtained because of the strong anisotropic property of the crystalline growth speed. BLT is believed to have the similar anisotropic property, because a part of Bi atoms of BIT were replaced with La. Hence, c-axis oriented BLT film can be also easily obtained. Furthermore, Si_3N_4 buffer layer is amorphous, which also enhances the c-axis oriented film growth. Besides these factors, by optimizing growth conditions, such as excess-Bi composition, film thickness, and pre-annealing and crystallization temperatures, we succeeded in the growth of c-axis oriented BLT films on Si_3N_4 / Si substrates.

Prior to C-V measurements of MFIS diodes, C-V characteristics of Pt / Si_3N_4 / Si MIS diodes were measured at a frequency of 1MHz. A typical result for a 3nm-thick Si_3N_4 layer is shown in Fig.6. As can be seen from the figure, no hysteresis loop appears in the C-V characteristic and the transition from accumulation to inversion states is very sharp, which means that the interface properties between the Si_3N_4 layer and the Si substrate are excellent.

Next, electrical properties of the MFIS diodes were characterized. In order to obtain a

wide memory window in the C-V characteristics of MFIS diodes, it is necessary to use a thick ferroelectric film, because the memory window width is equal to the coercive voltage of the ferroelectric film under the saturated polarization condition. As discussed in the previous section, however, the optimum film thicknesses for the higher annealing temperatures are as thin as 75 and 50nm for the excess-Bi solutions of 5% and 7.5%, respectively. Thus, in order to obtain a thick c-axis-oriented film with good crystallinity, the whole spin-coating and crystallization processes were repeated twice.

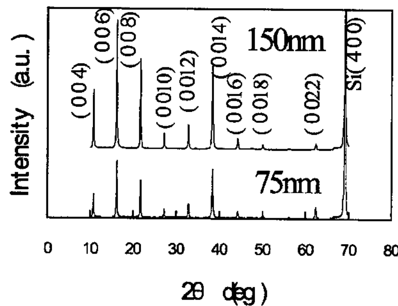

Figure 7. XRD patterns for 75-nm-thick and 150-nm-thick $Bi_{3.25}La_{0.75}Ti_3O_{12}$ on p-type Si substrates.

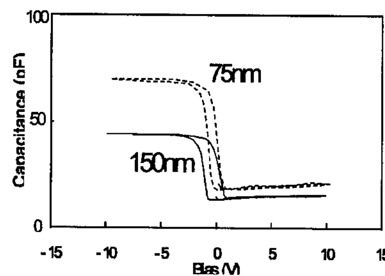

Figure 8. Capacitance-voltage characteristics of Pt / BLT / Si_3N_4 / p-type Si diodes with different BLT film thicknesses.

Figure 7 shows XRD patterns for 150nm-thick and 75nm-thick BLT films. In this figure, the 75-nm-thick film was prepared by spin-coating 5% excess-Bi solution on a p-type Si wafer covered with 3-nm-thick Si_3N_4 layer, by pre-annealing at 400℃, and by annealing at 700℃ in air, while the 150-nm-thick film was done by repeating the above process twice. As can be seen from the figure, each reflection peak is twice higher in the 150-nm-thick film, which means that the crystalline quality of the thicker film is as good as that of the thinner film. C-V characteristics for these samples are shown in Fig.8, in which the DC bias voltage ranging from −10V to +10V was applied. It can be seen from the figure that both C-V characteristics have hysteresis loops with the clockwise direction and the capacitance changes are rather sharp. It can also be seen that the accumulation capacitance is about twice larger in the 75-nm-thick film, while that the memory window width is twice wider in the 150-nm-thick film, as expected from the difference of the film thickness. The memory window width in the 150-nm-thick film is about 2V.

Next, in order to ascertain the effectiveness of the c-axis-oriented film, C-V characteristics for c-axis-oriented and randomly oriented films were compared. The BLT films were formed by spin-coating 10% excess-Bi solution on n-type Si wafers covered with 3-nm-thick Si_3N_4 layers. The spin-coating and crystallization processes were repeated twice and 100-nm-thick films were formed. The crystallization annealing conditions were the same (at

800℃ in air) for the both samples, but only the pre-annealing temperature was different. That is, the pre-annealing was conducted at 400℃ for the c-axis-oriented film, while it was done at 500℃ for the randomly oriented film. XRD patterns for these samples are shown in Fig.9. As can be seen from the figure, the c-axis orientation is almost perfect in the sample of Fig.11(a), while a strong (117) peak appears in the XRD pattern in Fig.11(b). This result is well explained by our previous work, which shows that the crystallization starts at 500℃ for MOCVD-grown $Bi_4Ti_3O_{12}$ films.[8]

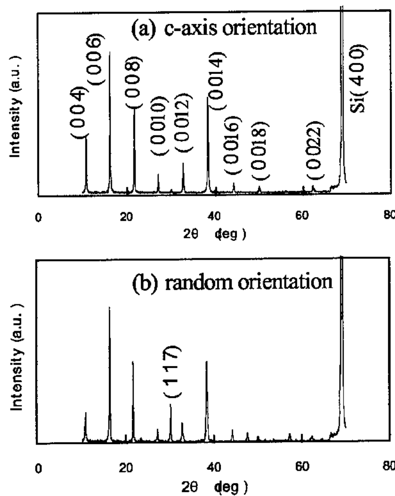

Figure 9. XRD patterns for 100nm-thick $Bi_{3.25}La_{0.75}Ti_3O_{12}$ films crystallized on n-type Si substrates at 800℃. (a) c-axis-oriented film (b) randomly oriented film

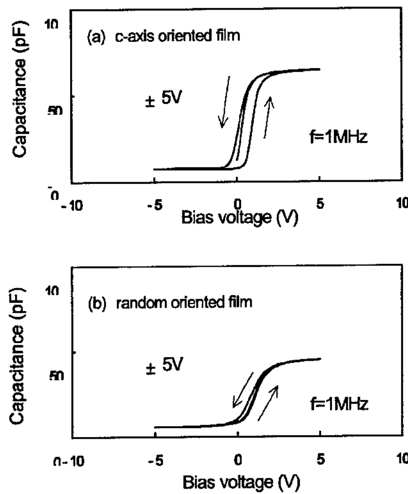

Figure 10. Capacitance-voltage characteristics of Pt / BLT / Si_3N_4 / n-type Si diodes. (a) c-axis-oriented film (b) randomly oriented film

C-V characteristics for the Pt / BLT (100nm) / Si_3N_4 (3nm) / Si structures are shown in Fig.10. The memory window width in the c-axis-oriented film is about 1.2V for a voltage sweep of ±5V. On the other hand, the width in the film which contains (117) crystallites is very narrow for the same voltage sweep amplitude. When the BLT film has random orientation, only a small minor loop can be used because the remanent polarization of the film is very large. On the other hand, a larger memory window can be obtained with a c-axis oriented BLT film, because

almost saturated polarization can be used in the c-axis-oriented film with a small remanent polarization.

In addition, it is found that the accumulation capacitance of the MFIS structure with the BLT film containing (117) crystallites is smaller than that of the c-axis oriented BLT film. This result seems to be contradictory to the generally known fact that a (117) oriented BLT film has a higher dielectric constant than a c-axis oriented BLT film. However, this result can also be explained by the fact that only a minor loop in the P-E characteristics is used in the sample shown in Fig.10(b), since an equivalent dielectric constant along a minor loop is much smaller than that along a saturated loop. We conclude from these results that a c-axis oriented BLT film is very suitable for the MFIS-FET applications.

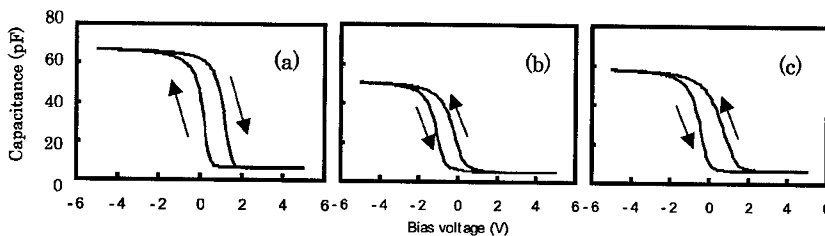

Figure 11. *Capacitance-voltage characteristics of (a) radical, (b) thermal and (c) plasma Si_3N_4 films.*

Finally, we have compared various kinds of Si_3N_4 films for the buffer layer in the MFIS structure. One of (b) the SiN was made by thermal nitrification at 950℃ for 10 sec using NH_3 as a process gas. The other one was made by the nitridation by (c) NH_3 plasma at 400℃. Thickness of these films were about 3nm. The C-V hystelesis curves wereshown in Fig. 11. It was clear that the hystelesis loops of these two curves originated from the charge trappings taking the direction of the loop appearance into account. This is because that these two Si_3N_4 films use the hydrogen termination to make Si dangling bonds electrically inactive, the dissociation of hydrogen terminators during the high temperature oxidation process creates large amount of carrier traps in MFIS diodes. To the contrary, (a) the radical nitrified Si_3N_4 film was essentially damage free and hydrogen free, nothing would take place during the oxidation process at high temperatures. Therefore, it was proved that high performance ferroelectric films with low residual mobile carriers could be synthesized under the oxidation conditions at high temperatures on the newly developed radical nitrified Si_3N_4 buffer layer.

the retention property of MFIS structure with newly radical Si_3N_4 was examined at room temperature. After the write bias voltage of +5V or −5V was applied to the sample, the time dependence of the capacitance was measured at zero bias voltage. The result is shown in Fig.12, which shows that the capacitance change is negligible for 3 hours. As can be seen from the inset of the figure, the measurement at zero bias voltage is not necessarily advantageous from a

viewpoint of the retention time, because the C-V characteristics are shifted to the positive voltage direction and the point B in the figure is located in the depletion state, where the depolarization field becomes larger because of existence of the depletion layer capacitance. We conclude from these results that the c-axis-oriented BLT film is also excellent from a view point of the retention characteristic.

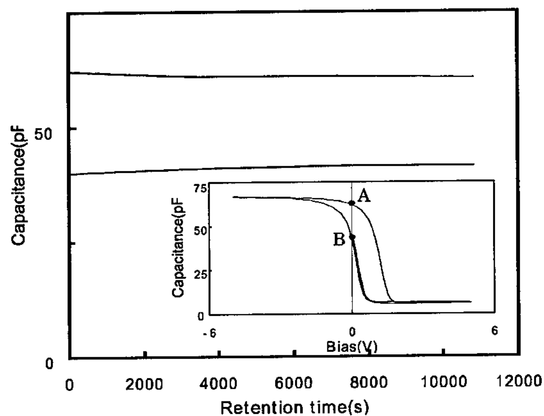

Figure 12. Variation of the zero bias capacitance of a Pt / 100nm-$Bi_{3.25}La_{0.75}Ti_3O_{12}$ / 3nm-Si_3N_4 / p-type Si MFIS diode with time at room temperature.

CONCLUSION

Almost perfectly c-axis-oriented $Bi_{3.25}La_{0.75}Ti_3O_{12}$ films were formed by spin-coating of sol-gel solutions on Si_3N_4 layers which had been formed on Si substrates using atomic nitrogen radicals. The $Bi_{3.25}La_{0.75}Ti_3O_{12}$ film was not crystallized even at 800℃ when a stoichiometric solution was used and it was annealed in O_2 ambient. Thus, 2.5 to 7.5% excess-Bi solutions were used and almost perfectly c-axis-oriented films were obtained at temperatures higher than 600℃ after optimization of such parameters as preannealing temperature, crystallization temperature, crystallization ambient, and so on. The Pt / 100nm-$Bi_{3.25}La_{0.75}Ti_3O_{12}$ / 3nm-Si_3N_4 / Si MFIS (metal / ferroelectric / insulator / semiconductor) diodes showed hysteretic characteristics in the C-V (capacitance vs. voltage) plot with a typical memory window of about 1.2V and the retention time estimated from the zero bias capacitance was longer than 3hours.

ACKNOELEDGMENT

This work was performed under the auspices of the R&D Projects in Cooperation with Academic Institutions (Next-Generation Ferroelectric Memory) supported by NEDO (New Energy and Industrial Technology Development Organization in Japan) and managed by FED (R&D Association for Future Electron Devices).

REFERENCES

1. J. L. Moll and Y. Tarui: IEEE Trans. Elect. dev. ED-10(1963)338
2. S. Y. Wu: Ferroelectrics 11 (1976) 379.
3. Y. Matsui, M. Okuyama, M. Noda and Y. Hamakawa: Appl. Phys. A 28 (1982) 161.
4. D. R. Lampe, D. A. Adams, M. Austin, M. Polinsky, J. Dzimianski, S. Sinhaloy, H. Buhay, P. Brabant and Y. M. Liu: Ferroelectrics 133 (1992) 61.
5. S. M. Yoon, E. Tokumitsu and H. Ishiwara: Jpn. J. Appl. Phys., 39 (2000)2119.
6. B. H. Park, B. S. Kang, S. D. Bu, T. W. Noh, J. Lee and W. Jo, Nature 401(1999)682.
7. Y. Fujisaki and H. Ishiwara: submitted to Jpn. J. Appl. Phys.
8. T. Kijima and H. Matsunaga, Jpn. J. Appl. Phys., 38(1999)2281.

Mat. Res. Soc. Symp. Proc. Vol. 655 © 2001 Materials Research Society

Ferroelectric Properties of La-doped $Bi_4Ti_3O_{12}$ Thin Films deposited directly on Si by pulse-injection MOCVD

Joon Hyeong Kim, Jin Yong Kim*, and Hyeong Joon Kim
School of Materials Science and Engineering, Seoul National University, Seoul 151-742, Korea.
*Inter-university Semiconductor Research Center, Seoul National Univ., Seoul 151-742, Korea.

ABSTRACT

$(Bi,La)_4Ti_3O_{12}$ (BLT) thin films were prepared on Si(100) substrates by the pulse injection metalorganic chemical vapor deposition (MOCVD) process, in which Ti and La precursors were injected with periodic pauses while Bi precursor was supplied continuously. In case of the pulse injection method, the film composition was relatively uniform and the Bi content at the interface was increased. The BLT films, which were deposited by the pulse injection MOCVD, showed better crystallinity and thinner interfacial amorphous layer than the continuous BLT films. The continuous BLT films, although measured at 1 MHz, showed similar C-V characteristics to those measured at low frequency region, and their flatband voltages also shifted severely to the negative voltage direction. On the other hand, the pulse BLT films exhibited clockwise ferroelectric hysteresis in the C-V curves. The memory window and the leakage current density were about 2V and 1.46×10^{-7} A/cm^2 at 9V (180 kV/cm), respectively.

INTRODUCTION

Ferroelectric thin films such as Bi-based layered perovskite ($SrBi_2Ta_2O_9$, $Bi_4Ti_3O_{12}$, and etc.) and $Pb(Zr,Ti)O_3$ thin films have been extensively investigated for nonvolatile ferroelectric random access memory (FeRAM) devices.[1-3] Comparing with FeRAM using the MFM (metal/ferroelectric/metal) capacitor, a MFS-FET-type (metal/ferroelectric/semiconductor field effect transistor) memory is more advantageous due to its nondestructive readout (NDRO) operation and simple structure.[4] Recently, the $(Bi,La)_4Ti_3O_{12}$ (BLT) thin film deposited on $Pt/Ti/SiO_2/Si$ was reported to have the high P_r value and good fatigue endurance.[5] However, there has been no report about the BLT films deposited directly on Si substrate. Moreover, no satisfactory results have been reported as a gate material for MFS-FET when other ferroelectric thin films were deposited on Si substrate without any buffer layers. In a MFS capacitor with a poor interface between ferroelectric film and semiconductor, as a bias voltage polarity is changed across the gate, the charge (electron or hole) trapping from the semiconductor to the trap sites in the interface of the film and de-trapping can be occurred. So, the hysteresis by charge trapping, not by ferroelectric polarization switching, or reduced memory window screened by charge trapping can be shown in C-V curve.[2] Therefore, it is very important to obtain a good interface between ferroelectric layer and Si substrate in order to get the wide memory window by ferroelectric polarization switching. Several research groups have adopted the buffer layers, such as CeO_2, MgO, and Y_2O_3, in order to improve the interface by preventing the film constituents and Si substrate from inter-diffusion reaction.[6-8] However, in metal/ferroelectric/insulator/semicondutor (MFIS) structure, there is a drawback: when the voltage across the gate is applied, the ratio of the electric field applied to a ferroelectric film and a buffer layer is inversely proportional to that of their dielectric constants. Although CeO_2, MgO, and Y_2O_3 have relative high dielectric constants of 10 to 20 ranges, the sufficient electric field

can not be applied to the Bi-based ferroelectric film with dielectric constants of 100 to 150. Therefore, it is necessary to use a buffer layer with higher dielectric or to deposit it directly on Si substrate without any buffer layer. In this work, we investigated the structural and electrical properties of BLT thin films deposited directly on Si substrate by MOCVD and the effect of the pulse injection of precursors (precursors are injected with periodic pauses of a constant period.) on the film properties.

EXPERIMENTAL DETAILS

BLT thin films were deposited on p-type Si (100) substrates by low-pressure metal-organic chemical vapor deposition (MOCVD). The tripenylbismuth [$Bi(C_6H_5)_3$], titanium isopropoxide [$Ti(OC_3H_7)_4$] and tris(2,2,6,6-tetramethyl-3,5-heptanedionato) lanthanum (III) [$La(TMHD)_3$] were used as Bi, Ti and La precursors, respectively. TMHD stands for tetramethylheptanedionato ($C_{11}H_{19}O_2$). The typical deposition conditions are summarized in Table I. BLT thin films were prepared by two different methods.[9] One is a continuous deposition method, where BLT thin films were deposited without any interruption of precursor input (we call them the continuous BLT thin films).The other is a pulse injection deposition, where the vapors of Ti and La precursors were injected with periodic pauses of a constant time interval while the vapor of Bi precursor was supplied continuously in order to supplement deficient-Bi contents in the film, as shown in Fig. 1 (the pulse BLT thin films). Input and pause periods (t_{pause}) of Ti and La precursors were 60 s and 120 or 240 s, respectively.

The microstructure was characterized by scanning electron microscopy (SEM) and transmission electron microscopy (TEM). The film composition was analyzed by energy dispersive spectroscopy (EDS) and auger electron spectroscopy (AES). Also, crystallinity and crystallographic phases were identified by x-ray diffraction (XRD) method. The Pt top electrodes were deposited at room temperature by dc-magnetron sputtering using a shadow mask and their area was 1×10^{-3} cm^2. The fabricated metal-ferroelectric-semiconductor (MFS) capacitors were post-annealed at 800℃ in oxygen atmosphere. The capacitance-voltage (C-V) characteristics were measured under superposing 30 mV small ac signal by a HP 4280A 1 MHz C-V meter.

In C-V measurements, the gate voltage (V_{gs}) applied to the metal electrode was swept from the accumulation to inversion mode of Si (from $-V_{gs}$ to V_{gs}: forward scan) and then swept back (backward scan) with a gate voltage sweep rate of 0.2 V/sec.

Table I. Deposition condition of the BLT film.

Deposition pressure		5 Torr
Deposition temperature		600℃
O_2 flow		400 sccm
Dilute Ar flow		90 sccm
$Ti(OC_3H_7)_4$	Temperature	33℃
	Pressure	100 Torr
	Carrier Ar flow	60 sccm
$Bi(C_6H_5)_3$	Temperature	125℃
	Carrier Ar flow	100 sccm
$La(TMHD)_3$	Temperature	190℃
	Carrier Ar flow	100 sccm

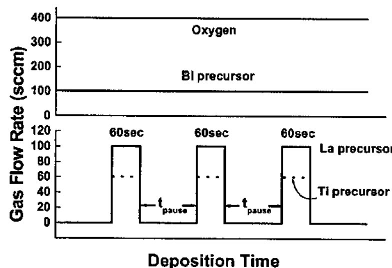

Figure 1. The schematic gas flow of the precursors by pulse injection method with periodical repetition of input and pause.

RESULTS AND DISCUSSIONS

Microstructural Properties

Figure 2 shows the x-ray diffraction patterns of the as-deposited BLT films on (100) Si substrates by the continuous method and pulse-injection method, as well as the films post-annealed at 800°C under 100 % oxygen atmosphere for 30 min after top platinum electrode fabrication. As shown in Fig. 2 (a), the as-deposited continuous BLT films (t_{pause}= 0 sec) showed the mixture of Bi-deficient pyroclore ($(Bi,La)_2Ti_2O_7$) phase with perovskite phase. In case of the pulse BLT films, it was found that the diffraction peaks of perovskite phases increased, even though the weak pyroclore peaks appeared. With increasing the pause time period of the pulse-injection method, not only was pyroclore phase reduced but the film crystallinity also improved. The differences in crystallographic structures of the films may result from the film compositions. There was no remarkable change of the diffraction patterns after post-annealing except that the perovskite peaks intensities increased, as shown in Fig. 2 (b). The XRD patterns after annealing revealed that a good crystalline perovskite film with no preferred orientation was obtained when the pause time was as long as 240 sec.

Surface micrographs of the films of Fig. 2 are shown in Fig. 3, where it is seen that the microstructure is significantly modified with the pause time and annealing. As the pause time increased, the crystallites became bigger and the faceted rectangular shapes were developed on the film surface. It is considered as a result obtained from longer deposition time, the enhanced surface migration during the pause time, and the increased Bi content enough to make the films stoichiometric. After annealed at 800°C under O_2 atmosphere, the films showed rounded crystallite shapes and agglomerated grains, which implies that solid-state reactions, such as diffusion, phase transformation, recrystallization, and grain growth, occurred during the annealing.

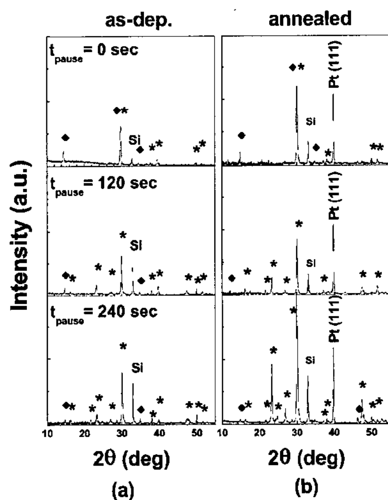

Figure 2. XRD patterns of the BLT films deposited at 600℃ with various t_{puase}; (a) as-deposited films and (b) the annealed films. (★ and ◆ stand for the perovskite phase and pyrochlore phase, respectively.)

Figure 4 (a) shows the AES depth profiles of the as-deposited continuous and the pulse BLT films. Lanthanum in the continuous BLT film was piled up at the film/substrate interface and decreased in the bulk region of the film, while bismuth was very deficient at the film/substrate interface. In case of the continuous method, few Bi atoms were incorporated in the film at the initial growth stage, which resulted from a low sticking coefficient [10] and high volatility [11] of Bi_2O_3 on Si surface. On the other hand, the composition of pulse BLT film was relatively uniform as compared to that of the continuous BLT film, although the exact quantitative analysis was not possible from these data. These results indicate that the participation of Bi atoms in the film formation reaction was enhanced during the pause time of the other precursors inputs in the pulse-injection method.

The TEM cross-section image of the continuous BLT film [Fig. 5 (a)] clearly shows that there was an amorphous interfacial layer, of which thickness was about 22.5 nm. From the EDS analyses, the atomic concentrations of Bi, Ti and La in this layer were found to be 8 %, 69 % and 23 %, while those in the film bulk region were 29 %, 56 %, and 15 %, respectively. This result is consistent with the AES depth profiles in Fig. 4 (a). On the other hand, the pulse BLT films showed no interfacial layer although the 2.5 nm SiO_2 was formed unintentionally between the film and Si surface, as shown in Fig. 5 (b).

The profiles of the film component after post-annealing are shown in Fig. 4 (b). As compared to Fig. 4 (a), La concentration became more uniform, while Bi was slightly accumulated near the film surface region. In the continuous BLT films, Bi content increased and La content was reduced at the interface after annealing. This is considered to be due to the recrystallization of BLT crystallites adjacent to the interface, which is confirmed with the reduced thickness of the amorphous interfacial layer, as shown in Fig. 6. (a). On the other hand, the thicker interfacial layer of the pulsed BLT film [Fig. 6 (b)] may result from oxidation of Si substrate, which is consistent with slow slopes of oxygen and silicon profiles of Fig. 4 (b).

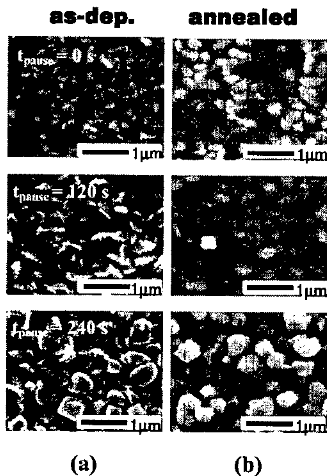

Figure 3. SEM micrographs of the BLT films with various t_{pause}; (a) as-deposited films and (b) the annealed films

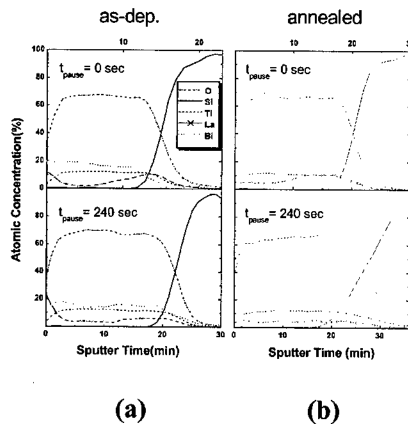

Figure 4. AES depth profiles of the continuous and pulse BLT films; (a) as-deposited films and (b) annealed films.

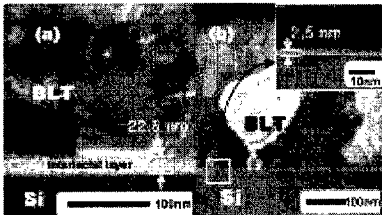

Figure 5. Cross-section TEM images of the (a) continuous and (b) pulse BLT films. (Dark Field Image)

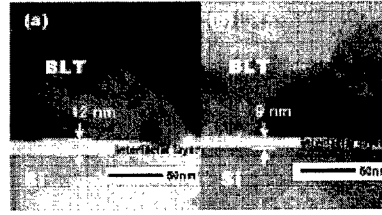

Figure 6. Cross-section TEM images of the (a) continuous and (b) pulse BLT films after annealed.

Ferroelectric Properties

The capacitance-voltage (C-V) characteristics of the MFS capacitors are plotted in Fig. 7 to examine their switching behavior. The C-V curves of a Pt/continuous BLT/Si capacitor measured at 1 MHz had similar characteristics to those measured at low frequency, as shown in Fig. 7 (a). This may be due to the formation of an inversion layer beyond the gate. The inversion layer affects electrons (minority carriers) response time and the minority carriers follow even the high frequencies ($f > 1$ kHz).[12-13] With an amount of positive fixed oxide charges located near the interface, the silicon surface can be strongly inverted for zero gate bias.

The theoretical flatband voltage calculated by the work function difference between Pt electrode and Si substrate (doping level of $10^{15}/cm^3$) is 0.43V. However, the flatband voltage of the continuous BLT film shifted severely toward negative voltage with a value of about −2.8 V, as shown in Fig. 7 (a). On the other hand, the flatband voltage of the pulse BLT thin film was 0.1V, as shown in Fig. 7 (b). These results imply that the positive fixed oxide charges existed at the interface in both films and the continuous BLT film had more fixed oxide charges than the pulse BLT film. The large amount of fixed oxide charges in the continuous BLT film are considered to originate from the interfacial amorphous layer and defective crystallites that crystallized during annealing.

As shown in Fig. 7 (b), the C-V curve of a Pt/pulse BLT/Si capacitor clearly shows the regions of accumulation, depletion, and inversion, and the clockwise hysteresis loops were clearly observed. The memory window increased up to 2V as the sweep voltages increased from 3 to 9V, indicating that ferroelectric dipole switching operated well. At 3V and 5V sweep, the memory window increased symmetrically as a function of gate bias voltages. In low voltage sweeps, the ferroelectric polarization switching behavior occurred without any charge injection. In a high voltage sweeps from 7 to 9V, however, the C-V curve shifted toward more negative voltage in backward scan than toward positive voltage in forward scan. This asymmetric memory window can be explained by interface trapped charges. To explain the asymmetric increase of memory window, we establish two assumptions: First, charges in semiconductor surface can trap and detrap with the gate bias polarity due to the shallow trap sites at the interface. Second, the ferroelectric polarization is not fully saturated at the sweep voltage region.

When a negative gate bias is applied to the metal electrode in forward scan, the charges (accumulated holes in the semiconductor side) are injected into traps at the ferroelectric/semiconductor (F/S) interface. The ferroelectric shift of the C-V curve in forward scan is suppressed since the ferroelectric polarization is partially compensated with interface trapped charges.

On the other hand, when applying a positive bias to the metal electrode, the trapped holes are emitted to Si substrate. So, the threshold voltage decreases by *ferroelectric polarization alone*,

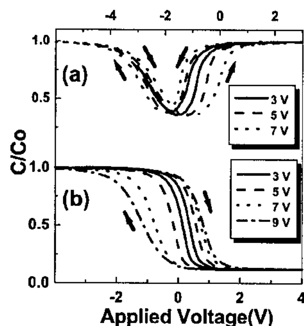

Figure 7. C-V characteristics of Pt/(a) continuous and (b) pulse BLT/p-Si structure measured at 1 MHz.

and the C-V curve shifts toward more negative voltage than in forward scan. Additional current-voltage (I-V) measurement at room temperature gave the leakage current density of 1.46×10^{-7} A/cm^2 at 9 V (180 kV/cm).

CONCLUSIONS

BLT films were successfully prepared directly on Si(100) substrates by the pulse injection MOCVD process, in which Ti and La precursors were injected with periodic pauses while Bi precursor was supplied continuously. The pulse injection method was very effective to supplement the deficient Bi content at initial growth stage. The pulse BLT films showed better crystallinity and interface between the film and Si substrate than the continuous BLT films. The pulse BLT films showed better ferroelectric properties. Memory windows of a Pt/pulse BLT/Si capacitor increased up to 2 V as a function of the gate sweep voltages while the continuous BLT film showed a similar behavior to the low frequency C-V characteristics due to high defect density at the interface.

REFERENCES

1. Jin-Ping Han and T. P. Ma, Appl. Phys. Lett. **72**, 1185 (1998).
2. S. Y. Wu, IEEE Trans. Electron Devices **21**, 499 (1974); T. Kijima and H. Matsunaga, Jpn. J. Appl. Phys. **38**, 2281 (1999).
3. C. H. Peng and S. B. Desu, J. Am. Ceram. Soc. **77**, 1799 (1994).
4. B. M. Melnick, J. Gregory, and C. A. Paz-de Araujo, Integr. Ferroelectr. **11**, 145 (1995).
5. B. H.Park, B. S. Kang, S. D. Bu, T. W. Noh, J. Lee, and W. Jo, Nature **401**, 682 (1999).
6. Y. T. Kim and D. S. Shin, Appl. Phys. Lett. **71**, 3507 (1997).
7. N. A. Basit and H. K. Kim, Appl. Phys. Lett. **73**, 3941 (1998).
8. H. N. Lee, M. H. Lim, Y. T. Kim, T. S. Kalkur, and S. H. Choh, Jpn. J. Appl. Phys. **37**, 1107 (1998).
9. S. K. Lee, Ph. D Dissertation : Seoul National University, Seoul, Korea (2000).
10. S. Migita, Y. Kasai, H. Ota, and S. Sakai, Appl. Phys. Lett. **71**, 3712 (1997).
11. C. D. Theis, J. Yeh, and D. G. Schlom, Appl. Phys. Lett. **72**, 2817 (1998).
12. E. H. Nicollian and J. R. Brews, *MOS (Metal Oxide Semiconductor) Physics and Tecnology* (Wiley, New York, 1982), p. 150.
13. W. C. Yi, J. S. Choe, C. R. Moon, and S. I. Kwun, Appl. Phys. Lett. **73**, 903 (1998).

Mat. Res. Soc. Symp. Proc. Vol. 655 © 2001 Materials Research Society

THE PROPERTIES OF MFMOS AND MFOS CAPACITORS WITH HIGH k GATE OXIDES FOR ONE TRANSISTOR MEMORY APPLICATIONS

TINGKAI LI, SHENG TENG HSU, HONG YING, AND BRUCE ULRICH
Sharp Laboratories of America, Inc, 5700 NW Pacific Rim Blvd. Camas, WA 98607

ABSTRACT

MFMOS and MFOS (M: Metal, F: Ferroelectrics, O: Oxide, S: Silicon) capacitors with high k gate oxides, such as ZrO_2, HfO_2 thin films, have been fabricated for one transistor memory applications. Experimental results showed that ZrO_2 and HfO_2 have no serious reaction or diffusion into silicon substrate. Due to their high dielectric constant, the operation voltages of MFMOS capacitors are reduced. . The MFMOS capacitor exhibits 2V memory window. For lead germanium oxide (PGO) on ZrO_2 and PGO on HfO_2 MFOS memory cells the memory windows are 1.8 V and 1.6 V, respectively, which are large enough for one-transistor memory applications. The basic mechanism for one-transistor memory applications was also discussed.

INTRODUCTION

Ferroelectric-gate controlled devices, such as metal-ferroelectric-silicon (MSF) FET, were studied as early as 1950s[1-4]. There are several groups of investigators actively research on ferroelectric-gate controlled memory transistors in recent years[5-9]. The typical device structures are Metal–Ferroelectric–Insulator–Silicon (MFIS) FET, Metal–Ferroelectric–Metal–Silicon (MFMS) FET, and Metal–Ferroelectric– Metal–Oxide–Silicon (MFMOS) FET. These devices have very small memory cell size and non-destructive read out (NDRO). Therefore, fatigue is not a major issue for these devices. However, there is no reliable memory device fabricated yet. This is because the difficulty in selecting appropriate ferroelectric and dielectric materials in addition to the complicated integration processes for one transistor memory device fabrication.

The basic operation principal for MFMOSFET and MFOSFET memory transistors are depicted in Fig. 1 and Fig. 2. When the ferroelectric material is poled towards the gate electrode, positive charges are induced at the channel. The threshold voltage of the transistor is very large. The transistor is programmed to the "off" state ("0" state). Similarly negative charges are induced at the channel when the ferroelectric material is poled toward the channel. The threshold voltage of the transistor is low and the device is programmed to the "on" state ("1" state). During read operation, the sense amplifier detects the state of the MFMOSFET. If there is a current, it is "1"; if there is no current, it is "0". This is the basic operation mechanism of MFMOS and MFOS one-transistor memory devices. The operation voltage and the memory window are important properties of a memory transistor.

The operation voltage of MFMOS and MFOS is V_{OP}, where $V_{OP} = V_O + \underline{V}_F$ and V_O and V_F are the voltages across oxide and ferroelectric capacitor, respectively. In order to reduce operation voltage, V_O should be as small as possible. Since $V_O = Q_o/\underline{C}_o$, where Q_O and C_O are the electrical charge and capacitance of the oxide capacitor, decreasing the thickness or increasing the dielectric constant of gate insulator thin films reduces V_O.

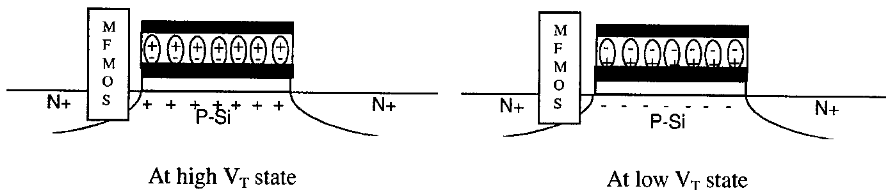

At high V_T state At low V_T state

Figure 1. The operation mechanism for MFMOSFET devices

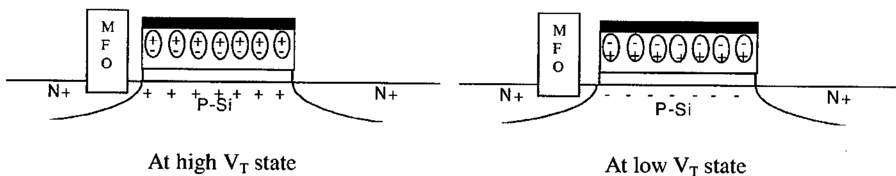

At high V_T state At low V_T state

Figure 2. The operation mechanism for MFOSFET devices

For memory window, the general drain current versus gate voltage plot for a memory transistor is depicted in Fig. 3. At "0" state the device is non-conductive while at "1" state the device is conductive. The essential condition for n-channel memory transistor is that the threshold voltage of the device at "0" state should be larger than the operating voltage and the threshold voltage for the transistor at "1" state should be larger than 0.0V, as shown in Fig. 3a. If the threshold voltage at "1" state is negative, the leakage current of the device is too large as is shown in Fig. 3b.

The memory window is equal to $2Pr/C_{FE}$, where, Pr and C_{FE} are the remnant polarization and capacitance of ferroelectric capacitor, respectively. The remnant polarization value larger than 0.2 $\mu C/cm^2$ of a ferroelectric thin film is enough for the ferroelectric-gate FET's applications. It is virtually impossible to maintain positive threshold voltage at "1" state if the Pr is too high. The maximum induces charge of SiO_2 thin film is about 3.5 $\mu C/cm^2$ for an electric field of 10 MV/cm. The film may breaks down at the higher electrical field. Therefore, we have to select a

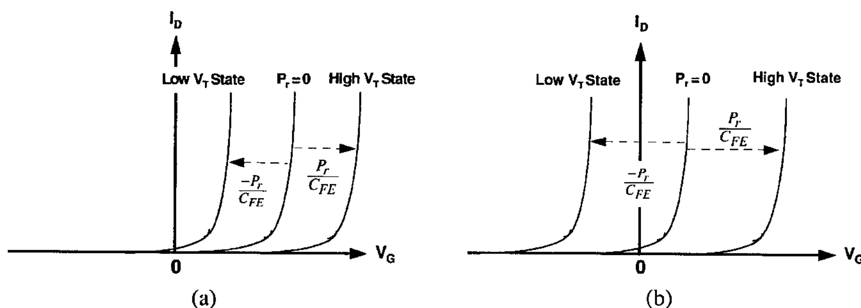

(a) (b)

Fig. 3 The memory window and threshold voltages for MFMOSFET devices

ferroelectric material with low dielectric constant. Memory retention is a critical issue for memory transistor. The experimental results show that ferroelectric thin film with a saturated and square hysteresis loop and a larger coercive field have excellent retention properties. In order make a reliable one-transistor memory device, the ferroelectric thin film should have a saturated and square hysteresis loop, low polarization value, low dielectric constant, and an appropriate coercive field. For these reasons, ferroelectric $Pb_3Ge_5O_{11}$ (PGO) with lower polarization (Pr) values and dielectric constant have been selected for one-transistor memory applications[10-11]. On the other hand, high gate oxide capacitance results in low programming voltage, and large memory windows. Therefore, PGO and high k gate oxides have been selected for one-transistor memory applications.

The experimental methods

P type Si wafers were used as the substrates of MFMOS and MFOS memory transistor fabrication. The Si wafers were cleaned, then remove surface oxide by HF dips etching. After that, 3.5 – 15 nm thick ZrO_2 or HfO_2 thin films were sputtered on the Si substrates. The Si wafers with ZrO_2 or HfO_2 were annealed at 500 – 550°C with pure oxygen for fully oxidation. Then barrier layer Ti (20 nm thick) was deposited on the oxide layer by sputtering, following by the deposition of bottom electrodes using electron beam evaporation. An oxide MOCVD reactor was used to grow c-axis oriented PGO thin films. For MFOS memory cell, PGO thin films were directly deposited on ZrO_2 or HfO_2. Finally, the top electrodes were formed.

The phases of the films were identified using x-ray diffraction. The compositions of the PGO films were analyzed using ultra high resolution X-ray photoelectron Spectrometer (XPS). The capacitence of the PGO MFM and MFMOS capacitors were measured using Keithley 182 CV analyzer. The ferroelectric properties of the PGO MFM capacitors were measured by a standardized RT66A tester.

The experimental results

Experimental analysis showed that ZrO_2 and HfO_2 have no serious reaction or diffusion into silicon substrate. Only very thin SiO_2 or silicide films were found in the interface between ZrO_2, HfO_2 and silicon substrate[12]. Therefore, ZrO_2 and HfO_2 can be used as gate oxides for PGO

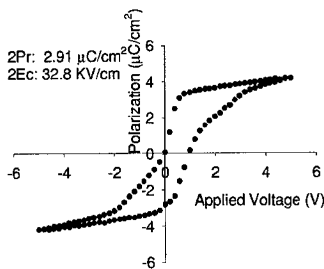

Fig. 4 Hysteresis loop of PGO MFM capacitor with 10 nm ZrO_2 thin film

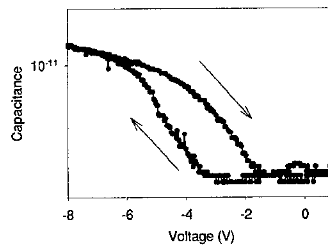

Fig. 5 Memory window of PGO MFMOS with 10 nm ZrO_2 thin film

MFMOS and MFOS one-transistor memory applications. Fig. 4 showed the hysteresis loop of PGO MFM capacitor. A square and saturated hysteresis loop with 2 Pr value of 2.91 μC/cm2 and 2 Ec value of 32.8 kV/cm were obtained. The CV measurement also showed that the dielectric constant of PGO thin films was about 40. Compared with other ferroelectric materials such as $SrBi_2Ta_2O_9$ with dielectric constant of 300 and $Pb(Zr_{0.5}Ti_{0.5})O_3$ with dielectric constant of 800, PGO thin film has very small dielectric constant, which is good for one-transistor memory applications. Figure 5 presents a typical a typical C-V curve of PGO MFMOS with thickness 10 nm ZrO_2. The memory window is about 2V at a programming voltage of 8V. The presence of an interfacial layer of SiO_2 may resulted the higher the operation voltage. Reducing the thickness of PGO and ZrO_2 can reduce the programming voltage. These data show that PGO thin films with high k gate oxide are promising for one-transistor memory applications.

Due to their simple structure and processes, PGO MFOS memory cell with high k gate oxides was also investigated. Figure 6 and 7 are the X-ray patterns of PGO thin films deposited

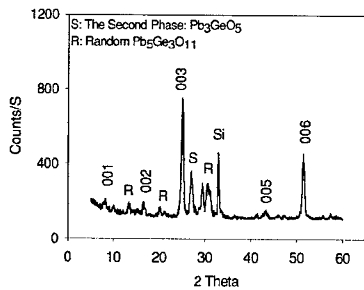

Fig. 6 X-ray pattern of PGO thin films deposited on ZrO_2

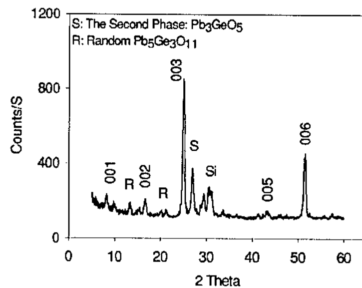

Fig.7 X-ray pattern of PGO thin films deposited on HfO_2

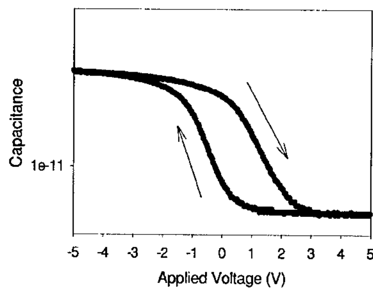

Fig. 8 Memory window of PGO on ZrO_2 MFOS Capacitor .

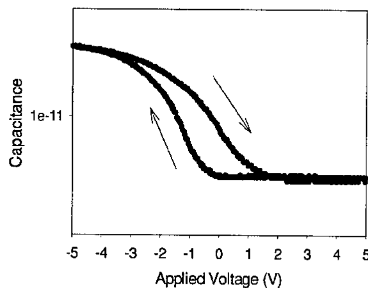

Fig. 9 Memory window of PGO on HfO_2 MFOS capacitor

on ZrO_2 and HfO_2 respectively. The experimental results showed that ZrO_2 and HfO_2 have no serious reactions with PGO thin films, and high c-axis oriented PGO thin films can be formed on ZrO_2 and HfO_2. Figures 8 and 9 are the operation voltages and memory windows of PGO on ZrO_2 MFOS and PGO on HfO_2 MFOS capacitors, respectively. The operation voltages of PGO on ZrO_2 MFOS and that of PGO on HfO_2 MFOS capacitors are about 6 V. The memory windows of PGO on ZrO_2 MFOS and that of PGO on HfO_2 MFOS capacitors are 1.8 V and 1.6 V, respectively, which are large enough for one-transistor memory applications.

CONCLUTIONS

The PGO on high dielectric constant insulator MFMOS and MFOS capacitors have been fabricated. ZrO_2 and HfO_2 can reduced the operation voltages of PGO MFMOSFET and MFOSFET memory cell. The memory windows of the memory transistor is larger than 1.5V.

REFERENCES

1. Looney, D.H., Semiconductive translating device, US Patent 2791758 (1957).
2. Brown, W.L., Semiconductive device, US Patent 2791759 (1957).
3. Ross, I.M., Semiconductive translating device, US Patent 2791760 (1957).
4. Morton, J.A., Electrical switching and storage, US Patent 2791761 (1957).
5. Kijima, T., and Matsunaga, H. Jpn. J. Appl. Phys. 38, 2281 (1999).
6. Imada, S., Shouriki, S., Tokumitsu, E., and Ishiwara, H. Jpn. J. Appl. Phys. 37, 6497 (1998).
7. FuJimori, Y., Izumi, N., Nakamura, T., and Kamisawa, A., Jpn. J. Appl. Phys. 38, 2285 (1999).
8. Tingkai Li, Fengyan Zhang and Sheng Teng Hsu, Appl. Phys. Lett. 74 (2) 296 (1999).
9. Tingkai Li, Sheng Teng Hsu, J. J. Lee, Yufei Gao and Mark Engelhard, Mat. Res. Soc. Symp. Proc. Vol. 596, 443 (2000).
10. Tingkai Li, Fengyan Zhang, Yoshi Ono and Sheng Teng Hsu, Integrated Ferroelectrics, 26, 1-4, 777 (1999).
11. Tingkai Li, Fengyan Zhang and Sheng Teng Hsu, Mat. Res. Soc. Symp. Proc. Vol. 541, 579 (1999).
12. Laegu Kang, Byoung-Hun Lee, Wen-Jie Qi, Yong-Joo Jeon, Renee Nieh, Sundar Gopalan, Katsunori Onishi and Jack C. Lee, Mat. Res. Soc. Symp. Proc. Vol. 592, 81(2000).

Mat. Res. Soc. Symp. Proc. Vol. 655 © 2001 Materials Research Society

Improvement of Retention Property of $YMnO_3/Y_2O_3/Si$ MFIS Capacitor

Norifumi Fujimura Daisuke Ito, Kousuke Kakuno and Taichiro Ito
Dept. of Applied Materials Science, Graduate school of Engineering, Osaka Prefecture University, 1-1 Gakuen-cho, Sakai, Osaka 599-8531, Japan fujim@ams.osakafu-u.ac.jp

ABSTRACT

We have been proposing $YMnO_3$ with low remanent polarization and permittivity as a ferroelectric gate transistor, and reported that c-oriented $YMnO_3$ films were obtained on (111)Si with (111) oriented Y_2O_3 buffer layer. The ferroelectricity was confirmed by pulsed C-V measurement. However, the retention property was not satisfied because of its poor crystallinity. To improve the crystallinity of $YMnO_3$ films, deposition conditions of Pulsed Laser Deposition (PLD) were optimized. The laser power, oxygen pressure and introducing Ozone gas are effective for maintaining the stoichiometry during the deposition. Improvement of the crystallinity of the $YMnO_3$ film makes the retention property better. We also demonstrate the use of epitaxially grown Y_2O_3 buffer layer to improve the crystallinity of the $YMnO_3$ films.

INTRODUCTION

Ferroelectric nonvolatile random access memory (FeRAM) has attracted much attention due to its nonvolatile operation and high access speed [1]. We proposed the use of $YMnO_3$ thin films for the ferroelectric gate transistor [2-5]. Because $YMnO_3$ has a relatively low permittivity and remanent polarization and does not include volatile elements such as Pb and Bi, it should have several advantages over $Pb(Zr_{1-x}Ti_x)O_3$ and $SrBi_2Ta_2O_9$. Highly (0001)-oriented $YMnO_3$ films were obtained on (111)MgO, (0001)ZnO/(0001)sapphire, (111)Pt/(0001)sapphire and (111)Si substrates using a (111) oriented Y_2O_3 buffer layer, which is an element composed of $YMnO_3$. The Y_2O_3 has larger dielectric constant compared to SiO_2, and higher chemical stability than the other insulator materials [6]. Although we succeeded in obtaining an Y_2O_3/Si capacitor with excellent dielectric properties [7], the dielectric properties of $YMnO_3$ on the top of the Y_2O_3 layer still needed to be improved. The retention time of the polarization was about 60 s. To improve the retention property, although the energy band alignment should be carefully designed and quite low leakage current should be achieved, square P-E hysteresis is also required. As only [0001] is the polarization axis in the case of $YMnO_3$, orientation distribution of [0001] is responsible for the retention property. Therefore, we have concentrated to obtain the $YMnO_3$ films with excellent crystallinity.

In this paper, the initial stage of $YMnO_3$ growth on a single crystal substrate is carefully studied to optimize the deposition conditions. The results are applied to obtain the good films on Y_2O_3/Si substrate. The effect of the crystallinity of the epitaxially grown Y_2O_3 layer on the crystallinity of $YMnO_3$ films is also discussed.

EXPERIMENTS

To optimize the deposition conditions of the $YMnO_3$ thin film, (111) MgO was used because the composition of the film were able to be evaluated without the effect of other elements such as Si, Pt and Y from Y_2O_3 buffer layer during energy-dispersive X-ray spectroscopy (EDX) measurement. A pulsed laser deposition (PLD) method was used for $YMnO_3$ deposition. Sintered

ceramic pellets of stoichiometric $YMnO_3$ were used as targets for PLD. To measure the P-E characteristics, (111)Pt/(0001)sapphire substrate was used. A sputtering system was used for depositing the Pt layer. To study the effect of PLD conditions on the crystallinity of YMnO3 films, the substrate temperature and the oxygen gas pressure were varied from 700 to 850 °C, and 1×10^{-6} to 10^{-3} torr respectively. In some cases, Ozone was introduced in the O_2 gas. The laser power density was varied from 1.9 to 2.8 J/cm^2. The thickness of the $YMnO_3$ thin films was varied from 10 to 200 nm. After optimizing the deposition condition of the $YMnO_3$ film, the film was deposited on the (111) oriented Y_2O_3/Si substrate. The Y_2O_3 film was a (111) oriented film (not epitaxial one) and there is a SiO_2 layer underneath, because the deposition was performed by a sputtering method. However, the existence of 10 nm thick-SiO_2 layer was very important to maintain an excellent interfacial dielectric property. Dielectric measurements were conducted with a platinum top electrode sputtered through a shadow mask with the area of 900 μm^2 The capacitance-voltage (C-V) characteristic was measured using an LCR meter (HP4284A) by applying a small ac amplitude and frequency signal of 10 mV and 100 kHz respectively. The polarization-electric field (P-E) measurement was performed using a Sawyer-Tower circuit. Current-Voltage (I-V) property was also measured.

Eventually, deposition of epitaxial Y_2O_3 was attempted by using PLD system to obtain an epitaxial $YMnO_3$ film with excellent crystallinity.

RESULTS AND DISCUSSION

Figure 1 displays the ionic arrangement of $YMnO_3$ with a hexagonal crystal structure ($C_{6v}{}^3$). Because the polarization axis exists just along the <0001>, the crystallinity (orientation distribution of c-axis) is very important for getting a square P-E hysteresis, which is one of the keys for improving the retention property. A typical P-E hysteresis loop obtained from a Pt/200 nm-thick $YMnO_3$/Pt/sapphire capacitor deposited by the previous condition is shown in Fig. 2. The deposition conditions are exactly the same as those used in Ref. 5. The remanent polarization P_r and coercive field E_c of are 0.15 $\mu C/cm^2$ and 30 kV/cm respectively. The paraelectric component of the dielectric capacitance, C_p, in the P-E characteristic of the film is 1.55 $\mu F/cm$. To improve the retention properties of the film, this C_p should be eliminated.

As the RHEED pattern of the film at the thickness of 10 nm shows a diffused streak pattern, we attempted to study the initial stage of $YMnO_3$ growth.

A change in the film composition (Y/Mn ratio) with increasing the thickness is shown in Fig. 3. Obvious composition change is observed. Although compositional deviation from the stoichiometry is not observed at the film thickness of over 50 nm, an yttrium-rich layer should be formed at the initial stage of

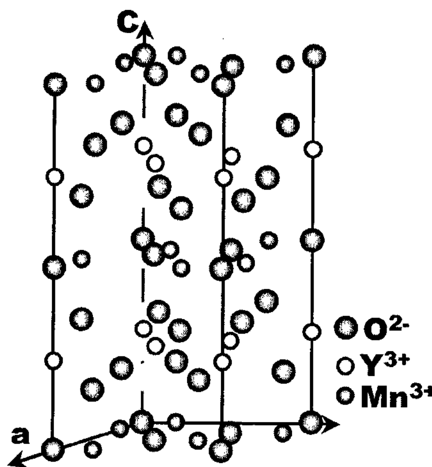

Figure 1 Ionic arrangement of $YMnO_3$

film growth. To optimize the film composition at the fixed thickness of 10 nm, the dependence of the laser power density and gas pressure are evaluated (Figs. 4 and 5). A laser power density of more than 2.4 J/cm^2 or the oxygen pressure of more than 1×10^{-3} Torr makes the $YMnO_3$ stoichiometry even at the thickness of 10 nm. It is also recognized that the use of ozone (4% in O_2) improves the stoichiometry of the films. Although using high laser power density and gas pressure are effective for obtaining stoichiometric film, the number of droplets that are thermally produced increases with increasing the laser power density and the gas pressure

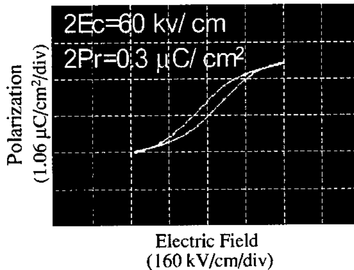

Figure 2 P-E hysteresis of the film Deposited using previous conditions

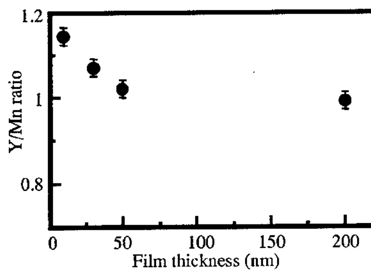

Figure 3 Change in composition against the film thickness

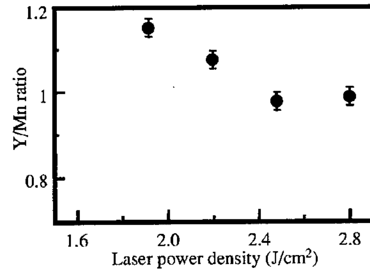

Figure 4 Change in composition against the laser power density

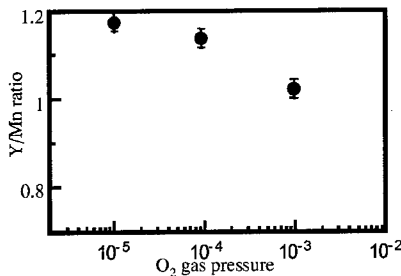

Figure 5 Change in composition against the O_2 pressure

during deposition. Therefore, gas (4 % ozone in O_2) pressure of 1×10^{-4} torr and the laser power density of 2.4 J/cm^2 were selected as the optimal deposition conditions. Other conditions are; the substrate temperature of 800 °C and reputation of the laser pulse of 1 Hz. By using above optimized deposition conditions, FWHM of the XRD rocking curve that indicates orientation distribution along [0001] improved from 2° to 1.2°. The RHEED pattern of the film is also improved.

Ferroelectric properties of the film on (111)Pt/(0001)sapphire substrates deposited optimized conditions are evaluated. The P-E hysteresis loop with a remanent polarization of 0.71 μC/cm^2

and a coercive electric field Ec of 40 kV/cm is observed shown in Fig. 6. These values are improved compared to those from un-optimized $YMnO_3$ films containing an yttrium-rich initial layer (Fig. 1). The paraelectric component of the dielectric capacitance, C_p calculated from Fig. 6 is 7.82 μF/cm^2, which is quite large compared to that calculated from the P-E hysteresis shown in Fig. 2.

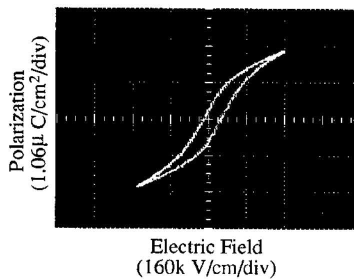

Figure 6 P-E behavior of the sample deposited using optimized conditions

The C-V behaviors are measured using the $YMnO_3$ film deposited on (111) oriented Y_2O_3/Si substrate. The C-V curve clearly displays memory window and it does not change by varying the sweep rate. Figure 7 shows change in the memory window against the sweep bias voltage. It saturates at around 2.0 V, which is identical to the 2 E_c of P-E hysteresis (coercive field calculated using Fig. 6). The retention properties of the $YMnO_3$ film deposited using un-optimized condition (solid line) and optimized condition (doted line) are shown in Fig. 8. Obvious improvement of retention property is observed.

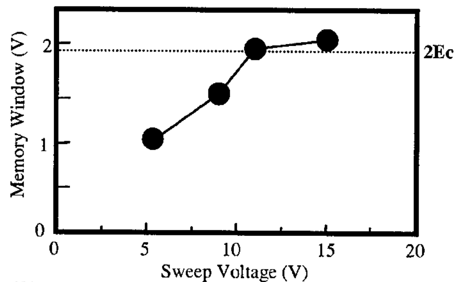

Figure 7 Change in memory window against the sweep bias voltage

Although we have succeeded in fabricating highly oriented $YMnO_3$ without non-stoicheometric initial layer, which shows improved ferroelectric and its retention properties, further improvement of the retention property is required. Therefore, we attempted to obtain epitaxial $YMnO_3/Y_2O_3$/Si structure without SiO_2 layer at the Y_2O_3/Si interface.

So far, Y_2O_3 was deposited by sputtering system with the O_2 gas pressure of 1×10^{-3} torr, which yields the SiO_2 layer at the interface. Therefore, PLD was used for the deposition of epitaxial Y_2O_3 film. Figure 9 shows the TED pattern of the epitaxially grown Y_2O_3/Si. The deposition was performed under the oxygen (4 % ozone) pressure of 1×10^{-8} torr. Although quite

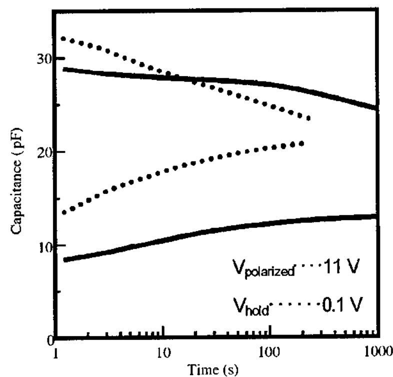

Figure 8 Retention properties of the samples using un-optimized (doted line) and optimized (solid line) deposition conditions

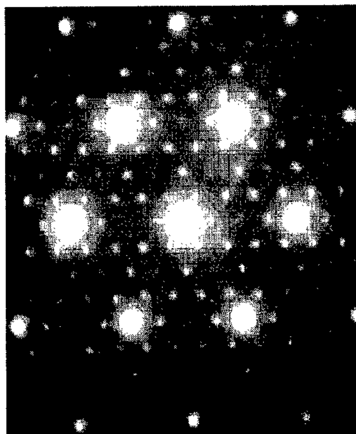

Figure 9 Transmission Electron Diffraction pattern from the Epitaxially grown Y_2O_3/Si

excellent Y_2O_3 film is obtained, the C-V measurement was not able to be done due to its high leakage current. This high leakage current is resulted in the oxygen deficiency caused by the low oxygen pressure (1×10^{-8} torr) during Y_2O_3 deposition. By surviving with the oxygen pressure during deposition and oxygen and/or hydrogen annealing, C-V property was improved (Fig. 10). The dielectric permittivity calculated with the capacitance at the accumulation region, 16.5 indicates that there is no SiO_2 layer at the Y_2O_3/Si interface.

Although epitaxially grown $YMnO_3$ films were successfully obtained and it shows good C-V property, the retention properties were not able to be measured because the film broke down above 7 V (before polarization saturation). The poor voltage resistivity should come from change in the surface morphology of the Y O layer by the deposition of YMnO film.

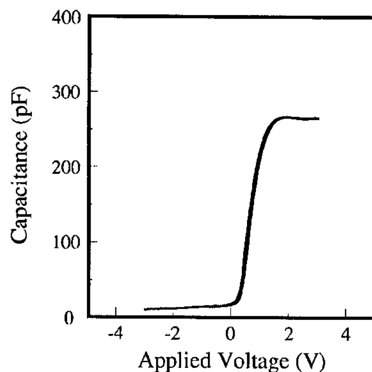

Figure 10 C-V property of Epitaxial Y_2O_3/Si

CONCLUSIONS

We attempted to improve the P-E characteristic by optimizing the initial stage of the film growth. It was confirmed that an yttrium-rich layer was formed at the initial stage of film growth, which caused orientation distribution. Eventually, stoichiometric $YMnO_3$ films without an initial layer were obtained by optimizing the laser power density and the oxygen pressure. Adding ozone to the oxygen gas was effective for decreasing the deposition gas pressure while maintaining the high crystallinity. The P-E characteristic of $YMnO_3$ thin film on Pt/Sapphire was greatly improved. We also demonstrated that the possibility of $YMnO_3/Y_2O_3$/Si epitaxial structure for the ferroelectric gate transistor.

ACKNOWLEDGMENTS

Support from a Grant-in-Aid for Scientific Research (B), No. 10555220, priority area (B) No. 12134206, from the Ministry of Education, Science, Sports and Culture of Japan, is gratefully acknowledged.

REFERENCES

1) J. F. Scott and C. A Paz de Araujo: Science **246** (1989) 1400.
2) N. Fujimura, S. Azuma, N. Aoki, T, Yoshimura and T. Ito: J. Appl. Phys. **80** (1996) 7084.
3) T. Yoshimura, N. Fujimura, N. Aoki, K. Hokayama, S. Tsukui, K. Kawabata and T. Ito: Jpn. J. Appl. Phys. **36** (1997) 5921.
4) T. Yoshimura, N. Fujimura and T. Ito: Appl. Phys. Lett. **73** (1998) 414.
5) T. Yoshimura, N. Fujimura, D. Ito and T. Ito: J. Appl. Phys. **87** (2000) 3444.
6) H. Fukumoto, T. Imura and Y. Osaka: Appl. Phys. Lett. **55** (1989) 360.
7) D. Ito, T. Yoshimura, N. Fujimura, and T. Ito: Appl. Surf. Sci. **159-160** (2000) 138.
8) S. L. Miller, R. D. Nasby, J. R. Schwank, M. S. Rodgers, and P. V. Dressendorfer: J. Appl. Phys. **68** (1990) 6463.

Integration and Electrodes II

Mat. Res. Soc. Symp. Proc. Vol. 655 © 2001 Materials Research Society

SUPPRESSION OF OXIDATION OF AN EPITAXIAL (100)ZrN FILM ON Si DURING THE DEPOSITION OF Ir FILM

SADAYOSHI HORII*, SUSUMU HORITA
Japan Advanced Inst. of Science and Technology, School of Material Science, Ishikawa, JAPAN
*Delegated from Kokusai Electric Co.,Ltd, Toyama, JAPAN

ABSTRACT

The epitaxial (100)ZrN film on the (100)Si substrate is oxidized during Ir film sputtering deposition on (100)ZrN/(100)Si structure. Although the oxidation could be suppressed somewhat by increasing the deposition rate of the Ir film, it was not enough. In order to suppress the oxidation completely, 10 pieces of 10 × 10 mm^2 Zr metallic plates were circularly placed on the non-erosion area of the Ir disc target. Using this target, the oxidation of the ZrN film was suppressed perfectly. Also, by adjusting of the diameter of the placed Zr circle, the contamination caused by Zr to the Ir film is avoided.

INTRODUCTION

For an integrated FeRAM(Ferroelectric Random Access Memory) higher than 4 Mbit, a stacked capacitor cell structure is required as a modification of a lateral transistor capacitor. In this case, a direct electrical contact must be formed from the source or drain of the transistor to the bottom of the capacitor via a conducting barrier layer which prevents reaction between the ferroelectric film and the Si. On the other hand, a single crystalline thin film is more attractive than a polycrystalline one because it exhibits greater stability, uniformity of material properties, and higher performance of the device. So, we have been researching the epitaxial growth of $PbZr_{1-x}Ti_xO_3$ (PZT) films on Si substrates[1-5] with the epitaxial buffer layers of $\{(ZrO_2)_{1-x}(Y_2O_3)_x\}$ (YSZ)[6-8].

In order to obtain an epitaxial ferroelectric thin film for a stacked capacitor cell structure, an epitaxial bottom electrode and barrier layer must be prepared directly on the Si substrate. Transition metal nitrides with NaCl structure have high electrical conductivity, low Shottky barrier[9], and thermal and chemical stabilities. Among them, ZrN has a lattice constant of 0.457 nm and can be grown epitaxially on (100)Si[10,11]. So, we used a ZrN film as a barrier layer for the PZT capacitor on Si. In order to improve the fatigue performance of the PZT film, an Ir film was inserted between the ZrN and the PZT film. By sputtering method, we obtained an epitaxial (100)Ir/epitaxial (100)ZrN double metallic film on (100)Si and then an epitaxial (001)PZT film on the Ir/ZrN film[12]. However, the ZrN film was found to be completely oxidized during the Ir film deposition because of a small amount of residual oxygen including its related compound gases, e.g. H_2O and CO, in the sputtering chamber. So, in order to suppress the oxidation of the ZrN film during the Ir film deposition, we proposed a new sputtering target in which small Zr metallic plates were circularly placed on the non-erosion area of the Ir disc target since Zr has a strong gettering effect with oxygen[13]. In this paper, chemical composition analysis of Ir/ZrN/Si

structure showed the complete suppression of the ZrN oxidation and no Zr contamination in the deposited Ir film.

EXPERIMENTAL

The deposition conditions for the ZrN, Ir and PZT films are shown in Table I. The epitaxial ZrN films were deposited on n-type (100)Si substrate by RF reactive sputtering with Ar + N_2 gas and a metallic Zr target. The sputtering was carried out under a vacuum of less than 6×10^{-6} Pa using a diffusion pump. Just before loading the Si substrate into the deposition chamber, the surface oxide layer was removed by 1% HF solution. Prior to the deposition, the Zr metallic target was cleaned by pre-sputtering for 15 min with Ar gas to remove the surface contaminated layer. We used two kinds of the sputtering targets for the Ir film deposition. One was a conventional Ir metallic disk target and the other is a composite disk target in which 10 pieces of 10 × 10 mm^2 Zr plates are circularly placed on the Ir target as shown Fig. 1. Since a small amount of the sputtered Zr particles from the composite target act as getter to residual oxygen, oxidation of the ZrN film can be suppressed. In order to control the oxidation and the impurity of Zr in the Ir film, the diameter of the placed Zr circle was changed from 58 to 78 mm. PZT films were deposited on the Ir/ZrN/Si structures by RF reactive sputtering with Ar + O_2 gas. In order to keep the Pb content of the film stoichiometric, 16 pieces of 10-mm-diameter PbO pellets were circularly placed on a 4-inch-diameter $Pb_{1.1}(Zr_{0.52}Ti_{0.48})O_3$ disc target. The Si substrate attached to a tantalum electrode was heated by flowing electric current. The sample temperature was checked by an infrared pyrometer and a thermocouple. The crystallographic properties of the films were investigated by X-ray diffraction (XRD). The chemical composition was analyzed by X-ray photoelectron spectroscopy (XPS). The resisitivity of ZrN film and Ir/ZrN layer were measured by four points prove method.

RESULTS AND DISCUSSION

Figure 2 shows $N_2/(Ar+N_2)$ flow ratio dependence of resistivity of the ZrN film and FWHM of ZrN(200). From this figure, it can be seen that the FWHM of ZrN(200) decreases with decreasing

Table I. Sputtering deposition conditions.

Film	ZrN	Ir	PZT
Target	Zr Metal (4 inch-ϕ)	Ir Metal(4 inch-ϕ) or composite Ir +Zr	$Pb_{1.1}Zr_{0.52}Ti_{0.48}O_3$ (4 inch-ϕ) +PbO Pellets(10 mm-ϕ)×16
Substrate Temperature	850°C	500 - 600°C	600 - 650°C
Deposition Pressure	0.5 Pa	0.5 - 4 Pa	0.5 Pa
Sputtering Gas	Ar + N_2 (Ar/N_2=19/1~5/5)	Ar or N_2(4%H_2)	Ar + O_2 (Ar/O_2=9/1)
RF Power Density	0.32 W/cm^2	0.038 - 1.52 W/cm^2	0.64 W/cm^2
Thickness	50 nm	20 - 200 nm	200 - 300 nm

$N_2/(Ar+N_2)$ flow ratio and the ZrN films have the low resistivity of 11 to 16 μΩcm. At lower N_2 flow ratio, nitridation of Zr atom is take place on the Si substrate rather than on the Zr target. Also, compared with Zr nitride (ZrN) molecule, Zr atom migrates more easily to the suitable lattice site of the Si substrate or the deposited ZrN film. Therefore, it can be expected that the ZrN film at the lower N_2 ratio has better crystalline quality.

Figure 3 shows the XRD patterns of the ZrN/Si structures before(broken line) and after(solid line) the Ir film deposition. The Ir films for (a) and (b) were deposited at the deposition rates of 0.5 and 25 nm/min respectively, using the Ir target. Also, the Ir film for (c) was deposited at 25 nm/min using the Ir + Zr target with Zr circle of 78 mm. From Fig. 3 (a), we can observe a strong Ir(200) and a weak Ir(111) peaks so that this Ir film has (100) orientation. However, the ZrN(200) peak disappears and the other peak appears at $2\theta=34.6^{\circ}$ which is from ZrO_2 phase based on the XPS depth profiles of Ir/ZrN/Si structures as shown late in Fig. 4. This means that the ZrN film was oxidized with residual oxygen in the chamber during the Ir film deposition. This seems unusual because the base pressure for the Ir film deposition was less than 7×10^{-6} Pa and the sputtering gas was high purity of 99.9999%. Furthermore, we can even obtain a good metallic ZrN film without oxidation using the same chamber and same gas as the Ir film deposition. This oxidation of the ZrN film is probably due to the fact that Ir is a strong catalysis that chemically activates the residual oxygen.

In order to suppress the oxidation of the ZrN film, we tried to increase the deposition rate of the Ir film. From Fig. 3 (b), by increasing the deposition rate the peak intensity of ZrN(200) is decreased by about 1/3 after the Ir film deposition. This result suggests that the thicker Ir film acts as a diffusion barrier to excited oxygen. Although increasing the deposition rate has some effect suppressing the oxidation of the ZrN film, it is not sufficient. Then, in order to perfectly prevent the

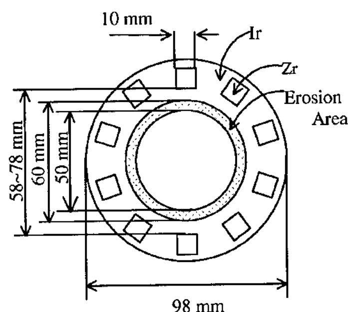

Fig. 1 Schematic drawing of the new composite sputtering target. 10 pieces of 10×10 mm^2 Zr plate are circularly placed on Ir target. The diameter of the placed Zr circle is changed from 58 to 78 mm.

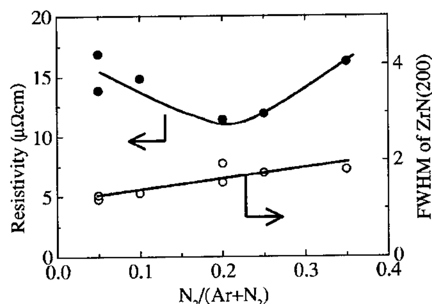

Fig. 2 $N_2/(Ar+N_2)$ flow ratio dependences of ZrN film resistivity and FWHM of ZrN(200).

ZrN film from oxidation, we used a new composite Ir + Zr target and the XRD pattern of the samples shown in Fig. 3 (c). As you can see from this figure, the peak intensity of ZrN(200) is not changed even after the Ir film deposition. This means that the oxidation of the ZrN film was perfectly suppressed due to the strong gettering effect of the sputtered Zr particles during the Ir film deposition.

Figure 4 shows the XPS depth profiles of Ir/ZrN/Si structure, where (a) and (b) are the same samples as Figs. 3 (a) and (c), resplectively. From Fig. 4 (a) , it is found that the Zr nitride film contains a large amount of oxygen and its chemical composition to $ZrN_{1-x}O_x$ was changed. On the contrary, in Fig. 4 (b), oxygen signal is hardly observed in the ZrN film, which means that no oxygen diffused from the sputtering atmosphere to the ZrN to the ZrN film through the ZrN film. These results are consistent with Fig. 3 (a) and (b).

Figure 5 shows the XPS Zr3d spectra of the Ir films deposited with the Ir + Zr target, where the diameter of placed Zr circle of (a), (b), (c), (d) and (e) are 78, 73, 68, 63, and 58 mm, respectively. From Figs. 5 (a) and (b), the Zr3d signals are not

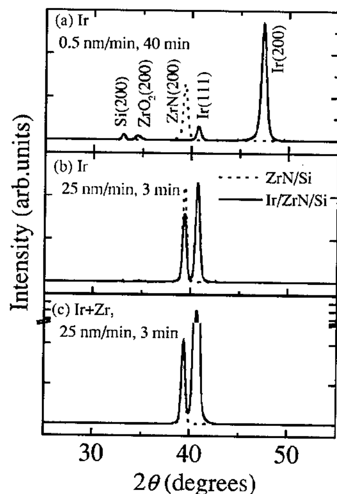

Fig 3. XRD patterns of the ZrN/Si structures before and after the Ir film deposition. The Ir films were deposited at the deposition rate of (a) 2.5 and (b) 25 nm/min using a Ir target. The Ir film for (c) was deposited at 25 nm/min using a Ir + Zr target with Zr circle diameter of 78 mm.

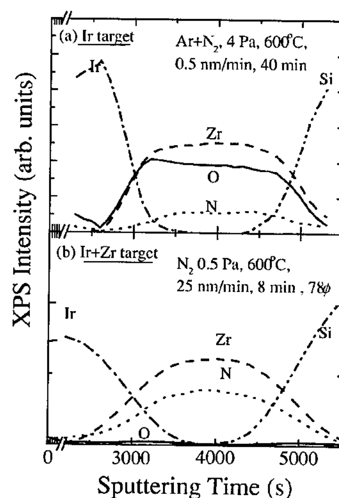

Fig 4. XPS depth profiles of Ir/ZrN/Si substrate structures. The samples of (a) and (b) are the same ones as Figs. 3 (a) and (c), respectively.

observed and the impurity of Zr in the Ir film is estimated to be less than 0.5 at. %. However, in Figs. 5 (d) and (e), Zr signals clearly appear. From these results, we can say that the Zr contamination is reduced less than 0.5 at % by setting the circle diameter more than 73mm.

Figure 6 shows the peak intensity ratio of ZrN(200) before and after each process and the resistivities of ZrN and Ir/ZrN layers of each deposition process of PZT/Ir/ZrN/Si structure. The Ir film was deposited to 200 nm thick using the Ir + Zr target with diameter of 78 mm. The measurement of the Ir/ZrN film after the PZT film deposition was performed after etching the PZT film by diluted HF solution. The ideal resistivity is calculated, assuming the Ir and ZrN films form a parallel resistance. In this calculation, we used the measurement value 12.4 μΩcm of the Ir film deposited on an insulator of a YSZ film as a resistivity of Ir. This Ir film was deposited with the same condition as the Ir film on the ZrN/Si substrate. From this figure, it is found that the peak intensity of ZrN(200) dose not change before and after each film deposition of Ir and PZT. It is also found that the resistivity of the Ir/ZrN layer after the Ir film deposition is equal to the ideal value and that the resistivity after the PZT film deposition is also equal to the value before the PZT film deposition. From this result, it is concluded that the Ir film acts as a diffusion barrier to oxygen during the PZT film deposition.

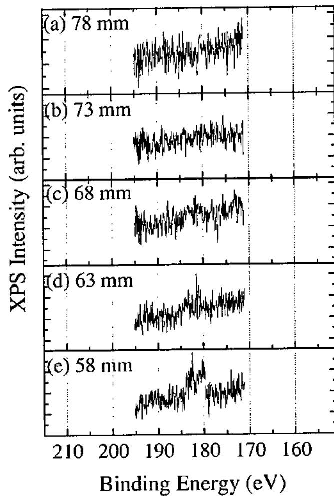

Fig. 5 XPS spectra of Zr3d in the Ir films. The samples were deposited using a Ir + Zr target with circle diameter of (a) 78, (b) 73, (c)68, (d) 63 and (e) 58 mm, respectively.

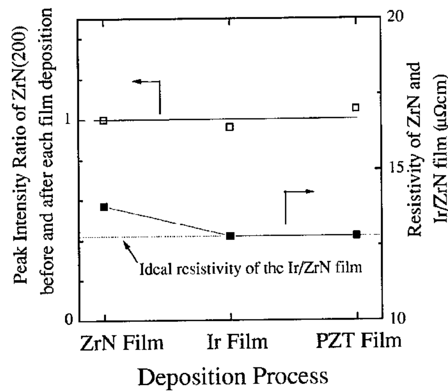

Fig. 6 The peak intensity ratio of ZrN(200) before and after each process and resistivities of ZrN and Ir/ZrN films of each deposition process of the PZT/Ir/ZrN/Si structure. The ideal value is calculated, assuming the Ir and ZrN films formed a parallel resistance.

CONCLUSION

We has investigated the crystalline, chemical composition, and electrical properties of the Ir/ZrN layered electrode on the (100)Si substrate. We found that the crystalline quality of the epitaxial (100)ZrN film was improved by decreasing the N_2 flow ratio and the resistivity of the ZrN film was low, between 11 to 16 μΩcm. Next, it was found that the oxidation of the ZrN film due to residual oxygen during the Ir film deposition can be suppressed somewhat by increasing the deposition rate. Further, by using a composite Ir + Zr target, we can completely suppress the oxidation, due to the gettering effect of Zr to the residual oxygen. Also, for the samples deposited with the composite target, the XPS depth profiles and spectra showed a low oxygen content in the ZrN film and low Zr content in the Ir film. Finally, the resistivity of Ir/ZrN film was about 13 μΩcm and the XRD peak of ZrN(200) did not change even after the PZT film deposition. So, it can be concluded that using the composite target is useful to obtain the low resistivity of the Ir/ZrN layered electrode on Si.

ACKNOWLEDGMENT

This work was partly supported by the Sasagawa Scientific Research Grant from the Japan Science Society and the Grant-in-Aid for Scientific Research(c) from Japan Society for the Promotion of Science.

REFERENCES

1. S. Horita, T. Kawada and Y. Abe, Jpn. J. Appl. Phys. **35**, L1357(1996).
2. S. Horita, T. Naruse, M. Watanabe, A. Masuda, T. Kawada and Y. Abe, Appl. Surf. Sci **117/118**, 429(1997).
3. S. Horita, S. Horii and S. Umemoto, Jpn. J. Appl. Phys. **37**, 5141 (1998).
4. S. Horita and S. Horii, Mar. Res. Soc. Symp. Proc. **541**, 351 (1998).
5. S. Horii, S. Yokoyama, H. Nakajima and S. Horita, Jpn. J. Appl. Phys. **38**, 5378 (1999).
6. S. Horita, T. Tajima, M.Murakawa, T.Fujiyama and T. Hata, Thin Solid Films **229**, 17 (1993).
7. S. Horita, Y. Nakao and T. Fujiyama, Jpn. J. Appl. Phys. **34**, 1942 (1995).
8. S. Horita, Y. Abe and T. Kawada, Thin Solid Films **281/282**, 28 (1996).
9. M. Wittmer, J. Vac. Sci. Technol, **A3**. 1797(1985).
10. B. N. Oshcherin, V. A. Tkachenko and D. M. Pantov, Phys. Chem. Mech. Surf. **2**, 1451(1984).
11. M. B. Lee, M. Kawasaki, M. Yoshimoto, M. Kumagai and H. Koinuma, Jpn. J. Appl. Phys. **33**, 6308 (1994).
12. S. Horii, S. Yokoyama and S. Horita, Mar. Res. Soc. Symp. Proc. **596**, 85 (2000).
13. S. Horii and S. Horita, 12th IEEE ISAF 2000 Proc. to be published.

Mat. Res. Soc. Symp. Proc. Vol. 655 © 2001 Materials Research Society

Property Improvement of PLZT Capacitor Using $CaRuO_3$ Top Electrode

HIROSHI FUNAKUBO, NORIYUKI HIGASHI, AND NORIKAZU OKUDA

Department of Innovative and Engineered Materials,
Interdisciplinary Graduate school of Science and Engineering,
Tokyo Institute of Technology
G1-405, 4259, Nagatsuta-cho, Midori-ku Yokohama, 226-8502, Japan

ABSTRACT

$SrRuO_3$ and $CaRuO_3$ films prepared by MOCVD were compared not only in term of their own properties but for their characteristics as the top electrodes of (Pb, La)(Zr, Ti)O_3[PLZT] capacitor, especially for H_2 degradation. Resistivity of $CaRuO_3$ and $SrRuO_3$ films increased after heat treatment in H_2-containing atmosphere, but was recovered by a heat treatment at 600 °C under O_2 atmosphere. When $SrRuO_3$ and $CaRuO_3$ films deposited at 600 °C were used as top electrodes, the remanent polarization(Pr) value of $SrRuO_3$/PLZT/Pt and $CaRuO_3$/PLZT/Pt capacitors were almost the same as the values for capacitors with a Pt top electrode. After a heat treatment in a 3 % H_2 atmosphere at 200 °C, followed by one in O_2 atmosphere at 450 °C, Pr value was perfectly recovered for both of $SrRuO_3$ and $CaRuO_3$ films. The leakage current become the smallest when using 50 nm-thick $CaRuO_3$ film as a top electrode. Moreover, no degradation was observed for fatigue test up to 10^{10} cycles when MOCVD-$CaRuO_3$ films were used as top electrodes. These data show that MOCVD-$CaRuO_3$ film with thin thickness is a useful top electrode for PLZT capacitor.

INTRODUCTION

Pb(Zr,Ti)O_3[PZT] film has been widely investigated for an application to nonvolatile ferroelectric random access memory (NVFeRAM). Strongly dependence of ferroelectric property of PZT film on the electrode material is widely known. Especially, oxide electrodes are known to improve the H_2 and fatigue degradations. Among them, $SrRuO_3$ and $CaRuO_3$ are one of the most promising materials because it has the same perovskite structure as PZT and high conductivity. For high density NVFeRAM, high step coverage is essential for not only PZT but also electrode. Therefore, MOCVD preparation of $SrRuO_3$ and $CaRuO_3$ films is the most important preparation technique because of its high step coverage.

One big problem with a $SrRuO_3$ electrode material is the large current leakage relative to Pt electrode. J.Cross et al.[1] reported the formation of $SrPbO_3$ at the grain boundary of PZT film by the diffusion of Sr element from $SrRuO_3$ to PZT and increased the leakage of PZT film. On the contrary, Yamamoto et al.[2] reported that the resistivity of $CaPbO_3$ is more than three order higher than that of $SrPbO_3$. Therefore, $CaRuO_3$ top electrode is expect to lowering the leakage character of PZT capacitor because of the low conductivity of $CaRuO_3$ even if this compound formed at the grain boundaries.

We have succeed for the first time in preparing $SrRuO_3$ and $CaRuO_3$ film by MOCVD[3-7]. In the previous study, we investigated the composition effect of $SrRuO_3$ top electrode on the ferroelectric property of $SrRuO_3$/(Pb, La)(Zr, Ti)O_3[PLZT] /Pt capacitor[7]. In the present study, we compared MOCVD-$SrRuO_3$ and $CaRuO_3$ not only in term of their own properties but for the characteristics as the top electrodes of PLZT capacitor, especially for H_2 degradation.

EXPERIMENTAL PROCEDURE

$SrRuO_3$ and $CaRuO_3$ films were prepared at 600 °C by MOCVD[3-7]. We have already ascertained that there is no degradation of property of PLZT film under $SrRuO_3$ and $CaRuO_3$ deposition condition by MOCVD at 600 °C[7]. 200 nm-thick PLZT film prepared on (111)Pt/Ti/SiO_2/Si substrate by sol-gel method was used as a substrate to check the character of a top electrode. 50 nm and 100 nm-thick $SrRuO_3$ and $CaRuO_3$ films were deposited on it through a 100 μmϕ metal mask and without metal mask. 100 nm-thick and a 100 μmϕ Pt top

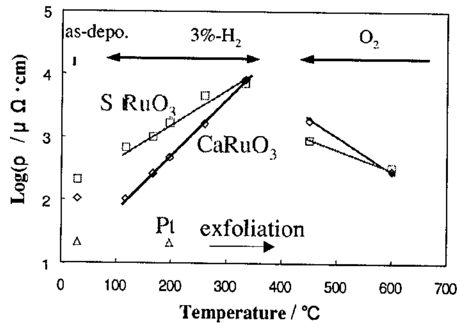

Fig. 1 Room temperature conductivity of $CaRuO_3$ and $SrRuO_3$ films together with that of the Pt film as a function of the heat treatment temperature under various atmosphere.

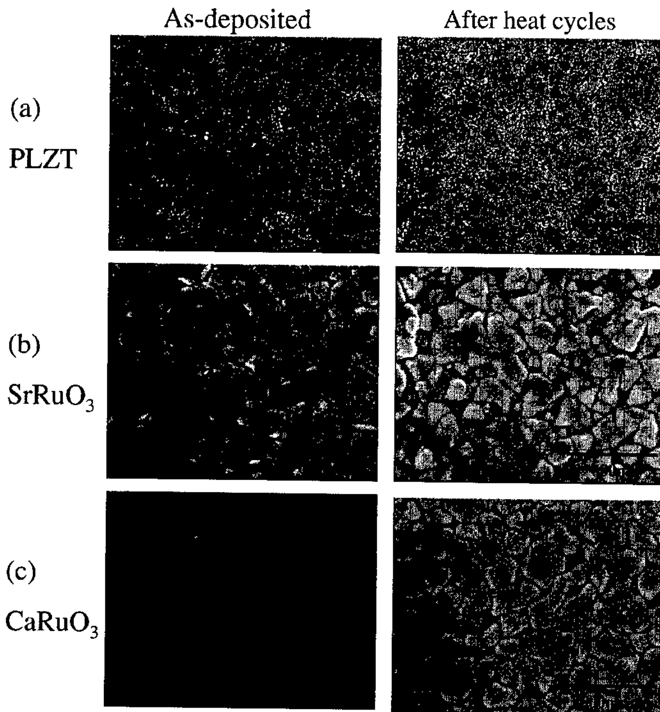

Fig. 2 SEM micrographs of before and after the heat treatment as shown in Fig. 1 (a): PLZT, (b): $SrRuO_3$ and (c): $CaRuO_3$.

electrode was also prepared by evaporation method as a reference. On the other hand, $LaAlO_3$ was also used as a substrate to check the electrical conductivity of $SrRuO_3$, $CaRuO_3$ and Pt themselves. Resistivity was measured by using standard four-point probe techniques at room temperature for films deposited on (100)$LaAlO_3$ substrates without metal mask.

These films were heat treated at 3 % H_2 + 97 % Ar atmosphere at various temperatures for 30 min, followed by heating in O_2 at 450 °C for 30 min.

RESULTS AND DISCUSSION

Degradation of $SrRuO_3$ films by H_2 heat treatment and Its Recovery

Figure 1 shows the temperature dependence of the room temperature conductivity of the $SrRuO_3$ and $CaRuO_3$ films together with that of the Pt film. The Pt film peeled off above 250 °C heat treatment in 3 % H_2 atmosphere. As deposited $CaRuO_3$ film had lower resistivity than $SrRuO_3$. However, the resistivity of both films increased with increasing the treatment temperature in the 3 % H_2 atmosphere. However, it decreased under the heat treatment of O_2 atmosphere at 450 °C for 30 min and was perfectly equal to the original value at 600 °C for 30 min as shown in Fig.1. This result shows that the resistively of these films increased when heat treated under H_2 atmosphere, but recovered by O_2 heat treatment. This character is suitable for the top electrode.

Figure 2 shows the SEM micrograhs of $SrRuO_3$ and $CaRuO_3$ films together with PLZT films before and after the heat treatment as shown in Fig. 1. No obvious changes were induced by this treatment. Likewise, no changes were observed in composition or crystal structure by X-ray fluorescence (XRF) and diffraction (XRD) analysis, respectively.

Degradation of $CaRuO_3$/PLZT/Pt and $SrRuO_3$/PLZT/Pt capacitors by H_2 heat treatment and its recovery

Figure 3 shows the change of the P-E hysteresis loops of $SrRuO_3$/PLZT/Pt and $CaRuO_3$/PLZT/Pt capacitors with the various heat treatment. 50 and 100 nm-thick $SrRuO_3$ and $CaRuO_3$ films were deposited by changing the deposition time. P-E hysteresis loops of the as-deposited film was basically the same irrespective of top electrode substance and thickness. After heat treated at 200 °C in 3 % H_2 atmosphere, hysteresis loops become small and shifted along axis of electric field. This change can be considered to be originated to the decrease of the resistivity of the top electrode as shown in Fig.1 and/or the ferroelectricity change of PLZT itself. However, after heat treated at 450 °C in O_2 atmosphere for 30 min, P-E hysteresis was almost recovered. After 30 min more, it was perfectly recovered as same as that of as-deposited one.

Figure 4 shows the leakage character of the same films as shown in Fig. 3. Leakage character was almost unchanged by the heat treatment regardless of the atmosphere conditions. Leakage current of $CaRuO_3$ top electrode was smaller than that of $SrRuO_3$, especially for thin films. J.Cross also reported that the leakage of $SrRuO_3$/PLZT/Pt capacitors decreased with the decrease of thickness of the $SrRuO_3$ top electrode[1]. They reported the decrease of the amount of $SrPbO_3$ at grain boundary of PLZT films. Therefore, it is possible that a similar mechanism is present with $SrRuO_3$.

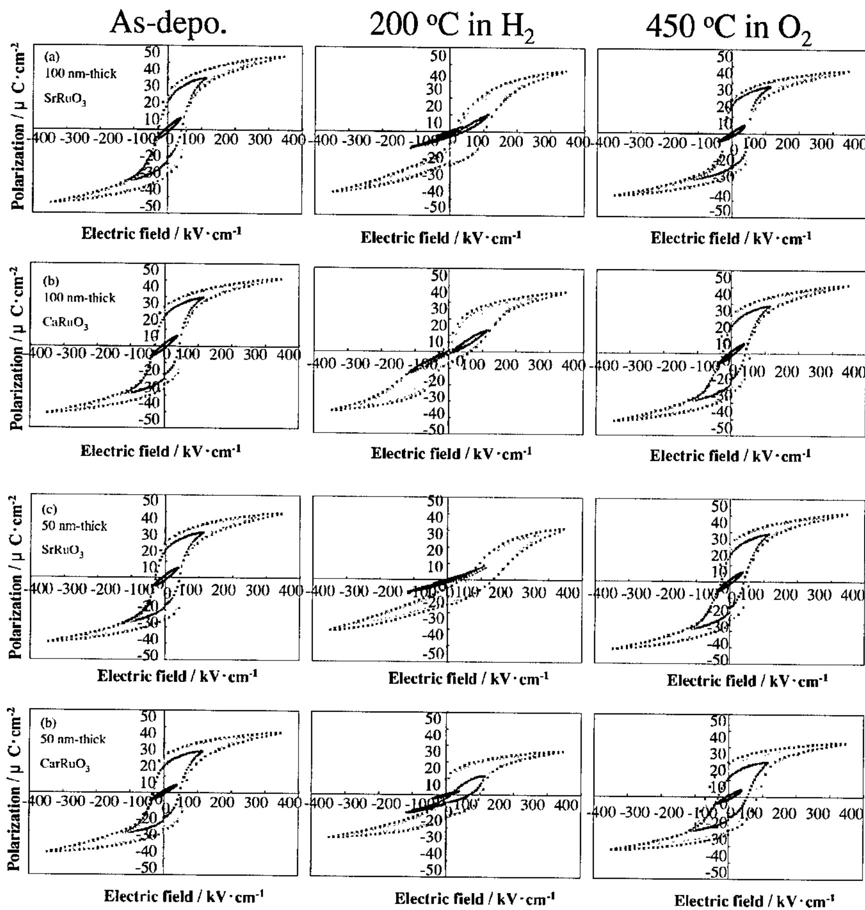

Fig. 3 Room temperature P-E hsyteresis change with the heat treatment condition.
(a) 100 nm-thick $SrRuO_3$ top electrode, (a) 100 nm-thick $CaRuO_3$ top electrode, (a) 50 nm-thick SrRuO top electrode, (a) 50 nm-thick CaRuO top electrode.

Figure 5(a) and (b), respectively show the fatigue endurance of 50 nm $CaRuO_3$/PLZT/Pt and 50 nm $SrRuO_3$/PLZT/Pt capacitors before and after the heat treatment using 6V amplitude show in Fig. 3. Obvious fatigue was not observed when $CaRuO_3$ and $SrRuO_3$ top electrodes were used. Fig. 5(c) shows the data using Pt top electrode. Degradation was observed even at 10^3 cycles before the heat treatment. This results shows that MOCVD-$CaRuO_3$ and $SrRuO_3$ films are useful for the PLZT capacitor with their high recovery character by heat treatment under O_2 atmosphere. Moreover, $CaRuO_3$ film with small thickness has the most superior, lower leakage character.

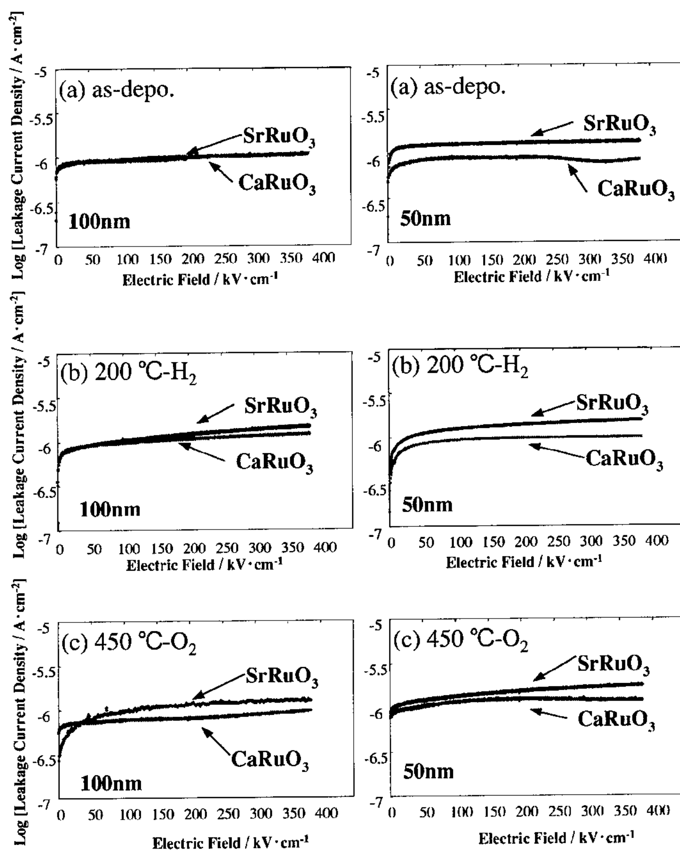

Fig. 4 Leakage character of (a) as-deposited, (b) after 3% H_2 atmosphere at 200 °C, and (c) O_2 atmosphere at 450 °C.

CONCLUSION

MOCVD-$SrRuO_3$ and $CaRuO_3$ films were compared not only in term of their own properties but for their characteristics as the top electrodes of PLZT capacitor for H_2 degradation. Resistivity of both of $SrRuO_3$ and $CaRuO_3$ films increased after heat treatment in H_2-containing atmosphere but was recovered by a heat treatment at 600 °C under O_2 atmosphere. Pr value of $SrRuO_3$/PLZT/Pt and $CaRuO_3$/PLZT/Pt capacitors was almost the same as the values for Pt/PLZT/Pt capacitor. After a treatment in a 3 % H_2 atmosphere at 200 °C, followed by one in O_2 atmosphere at 450 °C, Pr value was almost recovered for both of $SrRuO_3$ and $CaRuO_3$ films. The leakage current becomes the smallest when using 50 nm-thick $CaRuO_3$ film as a top electrode. Moreover, no degradation was observed for fatigue test up to 10^{10}

cycles. These data show that MOCVD-$CaRuO_3$ film with small thickness is a useful top electrode for PLZT ferroelectric capacitor.

ACKNOWLEDGEMENT

The authors would like to thank Dr. S.Otani of Fujitsu ltd., for providing the substrates.

REFERENCES

1) J.Cross, M.Fujiki, M.Tsukada, K.Matsuura, S.Otani, M.Tomotani, Y.Kataoka and Y.Goto, *Integ.Ferro.*, **25**, 263-271 (1999).
2) A.Yamamoto, N.R.Khasanova, F.Izumi, X.J.Wu, T.Kamiyama, S.Torii and S.Tajima, Chem.Mater., 11, 747-753 (1999).
3) N.Okuda, N.Higashi, K.Ishikawa, N.Nukaga and H.Funakubo, Mater. Res. Soc. Proc., 596, 79-84(2000).
4) N.Okuda and H.Funakubo, Jpn. J. Appl Phys., 39, 572-576 (2000).
5) N.Okuda, T.Matsuzaki, K.Shinozaki, N.Mizutani and H.Funakubo, Trans. Mater. Res. Soc. Jpn., 24, 51-54 (1999).
6) N.Higahi, N.Okuda and H.Funakubo, Jpn.J.Appl.Phys., 39, 2780-2783 (2000)
7) N.Okuda, N.Higashi, T.Watanabe and H.Funakubo, Integ.Ferro., in press.

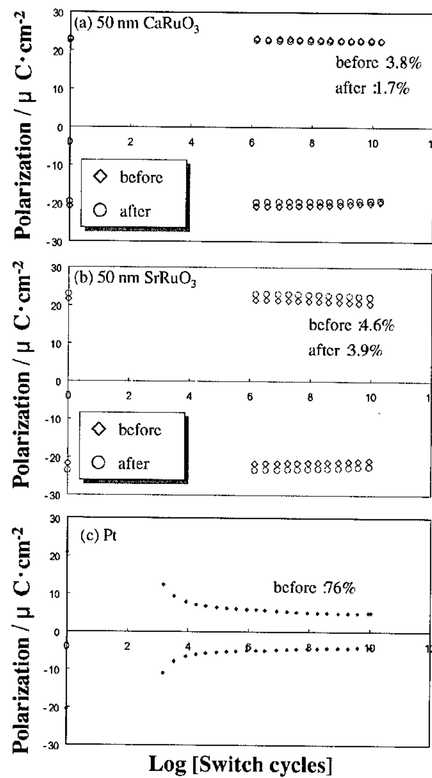

Fig. 5 Fatigue property of (a) 50 nm-$CaRuO_3$/PLZT/Pt, (b) 50 nm-$SrRuO_3$/PLZT/Pt, and (c) Pt/PLZT/Pt capacitors before and after the heat treatment as shown in Fig. 3.

Mat. Res. Soc. Symp. Proc. Vol. 655 © 2001 Materials Research Society

Characterization of Conductive RuO_2 Thin Film as Bottom electrodes for Ferroelectric Thin Films.

S. Bhaskar, P. S. Dobal, S. B. Majumder and R. S. Katiyar
Department of Physics, University of Puerto Rico, Rio Piedras campus, San Juan, PR 00931.

ABSTRACT

Ruthenium Oxide (RuO_2) thin films were prepared on silicon substrates by solution chemistry technique. X-ray Diffraction (XRD), Atomic Force Microscopy (AFM), micro-Raman, X-ray photoelectron spectroscopy (XPS), and four probe Van-der-paw technique were used for the film characterization. X-ray analysis shows a rutile structure in these films. The films annealed at 700°C showed lowest resistivity of 29 x 10^{-5} ohm-cm. The presence of E_g, A_{1g}, and B_{2g} modes is consistent with the Raman spectrum of rutile phase. These modes as well as additional unidentified band at about 477 cm^{-1} were investigated by temperature dependent Raman studies. Based on the result, band at 477 cm^{-1} that disappears above 370 K is attributed to hydrated RuO_2 present in the films. XPS analysis show stoichiometric rutile RuO_2 present in the films. Small concentrations of $RuCl_3$, RuO_3 and hydrated RuO_2 were also detected. $Pb_{0.9}La_{0.15}TiO_3$ (PLT15) thin films were deposited on RuO_2/Si substrates and characterized for its ferroelectric properties to demonstrate that solution deposition technique offers an alternative approach for preparing high quality RuO_2 bottom electrodes.

INTRODUCTION

Oxide electrodes, such as ruthenium oxide (RuO_2), lanthanum strontium cobalt oxide (LSCO), strontium ruthenate ($SrRuO_3$), and yttrium barium copper oxide (YBCO) are attractive candidates to be used as bottom electrodes for ferroelectric memory devices [1]. Among these, RuO_2 with tetragonal rutile structure exhibits various interesting properties such as lower bulk resistivity (~40 μΩm), good thermal stability, and diffusion barrier capability [2]. These properties make RuO_2 a good candidate material for bottom electrodes in high dielectric constant and ferroelectric thin film capacitors.

Deposition techniques like rf-sputtering [3], pulsed laser deposition [4] and chemical vapor deposition [5] have been widely used to synthesize RuO_2 thin films. Few reports are available on growth of RuO_2 thin films by solution chemistry technique and on surface characterization by XPS and micro Raman spectroscopy.

In this paper we report the synthesis of RuO_2 thin films on silicon substrates using the solution chemistry technique. The surface and structural characterization of these films were done by XPS, XRD, and micro-Raman spectroscopy. Of central interest is the evaluation of the quality of RuO_2 thin films in terms of their structure, composition, stoichiometry, and electrical conductivity for oxide bottom electrodes in ferroelectric thin films.

EXPERIMENTAL

$RuCl_3.x.H_2O$ was used as a precursor material was dissolved in absolute alcohol and diluted to 0.05M/L for coating. The precursor solution was spun coated on the silicon substrates

at 3000 rpm for 20s. The films were annealed in the temperature range 300°C – 700°C for 10 mins followed by quenching to room temperature. The films were about 700 nm thick. The details of the film preparation are described elsewhere [6]. Phase analysis was performed using X-ray diffractometer (Siemens D5000) with CuKα radiation (1.5405Å). The crystallite sizes in the films were calculated from the XRD data using Scherrer's equation [7]. The surface morphology of the films was imaged in non-contact mode using an AFM (Nanoscope IIIa Multimode AFM from Digital Instruments). Chemical composition and peak energy shifts in the samples were analyzed using X-ray photoelectron spectrometer (XPS) (Physical Electronics, PHI5600 ESCA system) using Al Kα radiation. Raman measurements were performed using a Jobin-Yvon T64000 spectrophotometer consisting of a double premonochromator coupled to a third monochromator/spectrograph with 1800 grooves/mm grating. The 514.5 nm radiation of an Ar^+ laser was focused in a less than 2 micron diameter circle area by using a Raman microprobe with an 80X objective. The scattered light, dispersed by the spectrophotometer was detected by a CCD detection system. Room temperature electrical resistivity of the RuO_2 films was measured using the conventional four probe Van der Paw method.

RESULTS AND DISCUSSIONS

XRD, AFM and electrical characterization

Figure 1 shows the X-ray diffractogram of RuO_2 films annealed in the temperature range 400°C to 700°C. Films were polycrystalline in nature and all the peaks in the figure were identified with RuO_2 phase. The films remained amorphous at 300°C and crystallized into rutile structure at 400°C. As the firing temperature was increased, sharpness of the XRD peaks and an increase in the average crystallite size was observed. The crystallite sizes in these films calculated from X-ray data are given in Table I. The lattice parameters calculated from the diffraction pattern of the RuO_2 film annealed at 700°C ('a'=0.4501 nm; 'c' = 0.3089 nm) agree with the JCPDS (40-1290) diffraction file and previously published data [8]. Thus, it can be

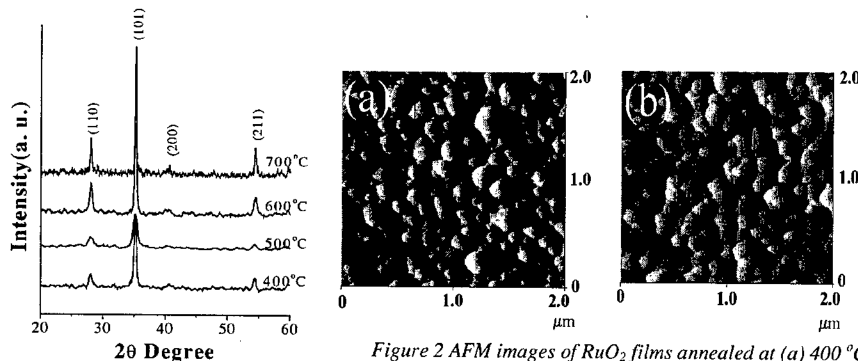

Figure 1 X-ray diffractogram of RuO_2 films annealed in the temperature range 400°C to 700°C

Figure 2 AFM images of RuO_2 films annealed at (a) 400 °C and (b) 700°C

concluded that the solution deposited films on Si substrates crystallize in the stoichiometric RuO_2 phase.

Figure 2 shows the AFM images of RuO_2 films annealed at (a) 400°C and (b) 700°C. Films fired at 400°C have non-uniform grain distribution with an average surface roughness value of 30 nm. Also particulate like features are observed in the films. Films annealed at 700°C have dense microstructure, increased grain growth and a more uniform grain distribution in the RuO_2 films. The average surface roughness for these films was lower with a value of 20 nm.

Table I. The crystallite size and room temperature resistivity of the RuO_2 films annealed at different temperatures

Annealing Temperature (°C)	Crystallite Size (nm)	Resistivity (μΩ-m)
400°C	47	4.86
600°C	90	3.57
700°C	96	2.92

The room temperature resistivity values for the films annealed at different temperatures as measured by the four probe method are summarized in Table I. The least value of resistivity was 29 x 10^{-5}ohm-cm for the film annealed at 700°C. This value of resistivity is comparable to the best reported values achieved by other techniques [2-4]. The marginal decrease of film resistivity with increased annealing temperature could be due to improved crystallinity.

Micro-Raman Analysis

Room temperature Raman spectra of the RuO_2 films annealed at 700 °C is shown in Figure 3. The three major Raman bands, namely E_g, A_{1g}, and B_{2g} modes of RuO_2 are located at about 523, 646 and 710 cm^{-1} respectively [9]. We also observed an additional band at about 477 cm^{-1} in the Raman spectra indicated by as question mark in the figure. The B_{1g} phonon mode was not observed due to its very weak intensity. There is inconsistency in the assignment of B_{1g} mode frequency of RuO_2 in the literature [10,11]. We have estimated the B_{1g} phonon frequency using the rigid ion model proposed by Katiyar [12] that satisfactorily reproduces the normal mode frequencies in MgF_2 and other rutile compounds.

Following Katiyar [12] the zero wavevector Raman frequencies may be expressed as

$$K(\omega^2_{B2g} - \omega^2_{A1g}) = C_1(A_3 - B_3) + C_2Z^2 \qquad (1)$$

$$K\omega^2_{B1g} = C_3(A_3 - B_3) + C_4Z^2 \qquad (2)$$

$$K\omega^2_{Eg} = C_5(A_2 - B_2) + C_6(A_3 - B_3) + C_7Z^2 \qquad (3)$$

where $K = e^2/2\upsilon$ (here 'e' is the electronic charge, υ the unit cell volume), A_i and B_i are dimensionless potential constants defined in ref.12. Z is the effective charge parameter and C_i 's are structural related constants. In the rigid ion model with short range central axially symmetric forces and long range Coulomb forces, the constants C_i are uniquely determined at any given temperature using lattice constants a_o and c_0 for RuO_2. By using our experimental value of ω_{B2g} = 715, ω_{A1g} = 646 and considering the metallic like nature of RuO_2, peak frequency of ω_{B1g} was

estimated to be 70 cm^{-1} with an error of about 20%. Our calculated B_{1g} phonon frequency was

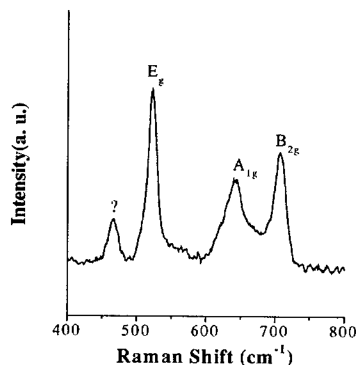

Figure 3 Room temperature Raman spectra of the RuO_2 films annealed at 700 °C

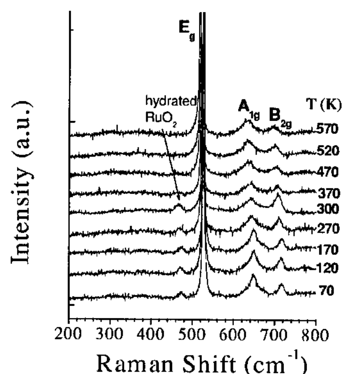

Figure 4 Temperature dependent (70 – 570K) Raman spectra of RuO_2 films

found closer to 97 cm^{-1} by Huang et al [11] as compared to the relatively high phonon frequency of 165 cm^{-1} observed as a very weak Raman feature by Rosenblum et al [10].

The peak frequency of A_{2g} (ω_2) silent mode is related to the frequencies of $B_{1g}(\omega_1)$, $A_{1g}(\omega_3)$, and $B_{2g}(\omega_4)$ modes by [13]

$$\omega^2_2 = \omega^2_4 + \omega^2_1 - \omega^2_3 \quad \text{........................(4)}$$

Substituting ω_1 = 715, and ω_3 = 646, we obtain the frequency of A_{2g} (ω_2) silent mode at 314 and 321 cm^{-1} for the calculated (ω_1 = 70) and experimental [11] (ω_1 = 97) values respectively. This rules out the possible origin of the unknown 477 cm^{-1} mode in our spectra, from disorder induced silent A_{2g} mode.

Figure 4 shows the temperature dependent Raman spectra of RuO_2 film recorded in the temperature range 70-570K. As we note from the figure, the unassigned band at 477 cm^{-1} appears in the spectrum at all temperatures below 300K and disappears completely above the temperature of 350K. It is generally known that RuO_2 behaves as hygroscopic oxide. Despite the lack of any vibrational spectroscopic data for direct comparison, there are ultra violet spectroscopic (UVS) [14] and XPS [15] studies of the system that support the formation of hydrated RuO_2 Therefore, we assign the band at 477 cm^{-1} due to hydrated RuO_2 in the film.

XPS Analysis

XPS provides a valuable complementary technique for assigning oxidation states and stoichiometry of the oxides. Figure 5 shows the binding energies of various peaks in the XPS spectra of RuO_2 films annealed at 700°C. Peaks in the spectra were identified with. Carbon C 1s (285.5 eV),.Ru doublet peaks of Ru $3d_{3/2}$ (285 eV) and Ru $3d_{5/2}$ (281 eV) and Ru 3p states. In addition, small concentrations of chlorine and silicon are also detected. A slow scan XPS was

performed on Oxygen (O 1s) and Ru doublet (Ru $3d_{5/2}$) peak in the binding energy range 527-533 eV and 278 - 292 eV, respectively and from the peakfit analysis, Ru is identified in the chemical state of RuO_2, $RuCl_3$, and RuO_3 [16].

The intended chemical state of ruthenium is rutile tetragonal RuO_2. But the presence of $RuCl_3$ and RuO_3 can be related to the film preparation technique, which uses $RuCl_3.x.H_2O$ precursor material for the high temperature deposition process in oxygen ambient. The relatively rapid cooling process that the film undergoes after deposition enhances the formation of RuO_3 species on the surface [16]. At annealing temperatures of 700°C and above, Si diffusion to RuO_2 films is a common problem [14]. However, these contaminants do not have a dominant effect on the resistivity of the films at annealing temperatures 700°C and below.

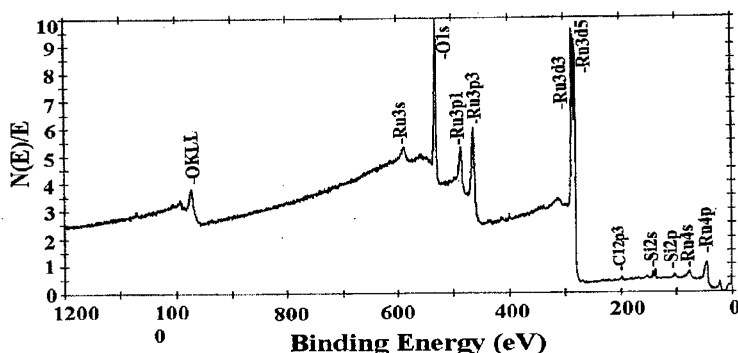

Figure 5 XPS spectra of RuO_2 films annealed at 700°C

Ferroelectric Properties of $Pb_{0.9}La_{0.15}TiO_3$ thin films .

Figure 6 (a) and (b) show the dielectric and ferroelectric measurement results of $Pb_{0.9}La_{0.15}TiO_3$ (PLT15) thin films on RuO_2/Si bottom electrode synthesized by solution chemistry technique. Films exhibit a dielectric constant and loss of 470 and 0.048 (at 100 kHz) respectively. P-E loops show low polarization values and DC leakage characteristics. Detailed investigation on the structural and electrical properties of PLT15 films on these electrodes will be published elsewhere [17]. Good crystallinity, fine grain sizes, and smooth surface morphology of RuO_2 films serve them as bottom electrodes for ferroelectric thin films.

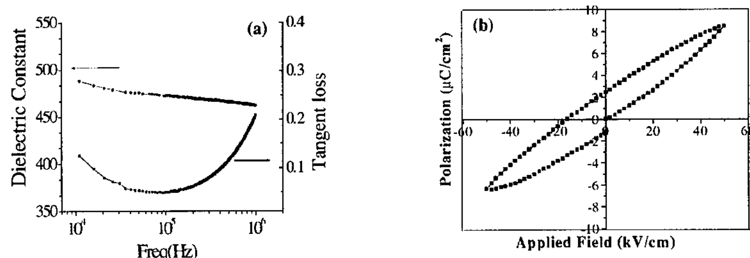

Figure 6 (a) Dielectric and (b) P-E loop of PLT15 thin films on RuO_2/Si bottom electrode

CONCLUSIONS

The oxide electrodes on Si substrates were successfully characterized in terms of their structure, composition, stoichiometry, and conductivity. RuO_2 films prepared by solution chemistry technique crystallize into polycrystalline RuO_2 phase at a temperature as low as 400°C. Lattice parameter calculations from XRD data indicate the stoichiometric RuO_2 phase. Minimum room temperature resistivity of RuO_2 films was observed for films annealed at 700°C (29×10^{-5} ohm-cm). Micro-Raman analysis confirms the rutile tetragonal phase of RuO_2 in our films and the observation of an unassigned Raman band at 477 cm^{-1} was investigated in detail. Using XPS data, and temperature dependent Raman studies, this Raman mode was assigned to hydrated RuO_2. XPS analysis confirms the presence of Ru in the intended chemical state of RuO_2. Also the small concentrations of $RuCl_3$ and RuO_3 detected in our films is due to film preparation technique using $RuCl_3.x.H_2O$ as precursor material.

ACKNOWLEDGEMENTS

This work is supported in parts by DAAG55-98-1-0012 and NASA NCC5-518 grants. The X-ray diffraction facilities developed by Dr. A. Martinez were utilized in this work.

REFERENCES

1. G. Teowee, J. M. Boulton, S. Hassan, K. McCarthy, F. McCarthy, T. J. Bukowski, T. P. Alexander, and D. R. Uhlmann, *Int. Ferroelectrics* **18**, 287 (1997).
2. L. Krusin-Elbaum, M. Wittmer, and D. S. Yee, *Appl. Phys. Lett.* **50**, 1879 (1987).
3. E. Kolawa, F. C. T. So, W. Flick, X.-A Zhao, E. T-S Pan, and M. A. Nicolet, *Thin Solid Films* **173**, 217 (1989).
4. Q. X. Jia, S. G. Song, S. R. Foltyn, and X. D. Wu, *J. Mater. Res.* **10**, 2401 (1995).
5. M. L. Green, M. E. Cross, L. E. Papa, K. J. Schnoes, and D. Brasen, *J. Electrochem. Soc.* **132**, 2677 (1985).
6. S. Bhaskar, S. B. Majumder, P. S. Dobal, R. S. Katiyar, A. L. Morales Cruz, and E. R. Fachini, *Proceedings of Materials Research Society Symposium* vol **606**, 69 (2000).
7. D. Cullity, *Elements of X-ray diffraction* (Addition-Wesley publishing Co., Inc USA 1967) p261.
8. J. Malek, A. Watanabe, and T. Mitsuhashi, *Thermochim. Acta*, **282/283**, 131 (1996).
9. S. Y. Mar, C. S. Chen, Y. S. Huang, and K. K. Tiong, *Appl. Surf. Sci.* **90**, 497 (1995).
10. S. S. Rosenblum, W. H. Weber, and B. L. Chamberland, *Phys. Rev.* **B 56**, 529 (1997).
11. Y. S. Huang and Fred H. Pollak, *Solid State Commun.* **42**, 921 (1982).
12. R. S. Katiyar, *J. Phys. C* **16**, 1087 (1970); *ibid* **3**, 1693 (1970).
13. P. S. Porto, P. A. Fleury, and T. C. Damen, *Phys. Rev.* **154**, 522 (1967).
14. R. Kotz, *Appl. Surf. Sci.* **47**, 109 (1991).
15. H. J. Lewerenz, S. Stucki, and R. Kotz, *Surf. Sci.* **126**, 463 (1983).
16. K. S. Kim and N. Winograd, *J. of Catal.* **35**, 66 (1974).
17. S. Bhaskar, S. B. Majumder, P. S. Dobal, R. S. Katiyar and S. B. Krupanidhi, *J. Appl. Phys.* (submitted).

Ferroelectric Non-Volatile Memories—Technology and Fundamentals II

Mat. Res. Soc. Symp. Proc. Vol. 655 © 2001 Materials Research Society

Properties of Au/$Pb(Zr_{0.52}Ti_{0.48})O_3$/ $Bi_4Ti_3O_{12}$/p-Si Ferroelectric Memory Diodes

Jun Yu[1] Hua Wang[1,2] Xiaomin Dong[1] Wenli Zhou[1] Yunbo Wang[1] Lili Zhu[1]

1 Department of Electronic Science & Technology, Huazhong University of Science & Technology, Wuhan, 430074, China

2 Department of Electron & Information, Guilin institute of Electronic Technology, Guilin, 541004, China

Abstract

A ferroelectric memory diodes that consists of Au/$Pb(Zr_{0.52}Ti_{0.48})O_3/Bi_4Ti_3O_{12}$/p-Si multilayer configuration was fabricated by pulsed laser deposition (PLD) technique. The ferroelectric properties and the electrical characteristics of the ferroelectric film system were investigated. The polarization-voltage curve of $Pb(Zr_{0.52}Ti_{0.48})O_3/Bi_4Ti_3O_{12}$ thin films system had an asymmetry hysteresis loop with P_r=20μC/cm^2 and E_c=48 kV/cm, and the decay in remnant polarization was only 10% after 10^9 switching cycles. The C-V curve and the I-V curve showed memory effects derived from the ferroelectric polarization of PZT/BIT films. The current density was 6.7×10^{-8}A/cm^2 at a voltage of +4V, and the conductivity behavior is discussed. The results suggested that the growth of the BIT ferroelectric layer is helpful to good ferroelectric properties, fatigue and capacitance retention characteristics.

Key words: Ferroelctric diodes, $Pb(Zr_{0.52}Ti_{0.48})O_3$, $Bi_4Ti_3O_{12}$, buffer layer, pulsed laser deposition

In recent years, ferroelectric memories have attracted much attention due to the promise of high speed, high density, low operation-voltage, radiation hardness and low power consumption [1, 2]. $Pb(Zr,Ti)O_3$ (PZT) has been widely studied for ferroelectric random-access memories (FRAMs), metal-ferroelectric-semiconductor field-effect transistors (MFS-FETs) and ferroelectric memory diode (FMD)[2-4] due to its higher permitivity(ε_r), higher remanent polarization(*Pr*) and lower coercive field (*Ec*). FMD is a kind of ferroelectric memory with a metal-ferroelectric-semiconductor (MFS) structure like an MFS-FETs, but it allows a lower voltage operation than an MFS-FETs and provides nonvolatile memory without a data storage capacitor or floating gate. However, the synthesis of PZT thin films on a Si substrate, which is important for practical applications, is rather difficult and the serious interaction and interdiffusion between PZT ferroelectric films and Si substrate lead to low retention and large leakage current, which are the fundamental properties of ferroelectric memory. To obtain a good interface and highly oriented ferroelectric films on silicon substrate, CeO_2, SiO_2 and CaF_2 have been widely introduced as buffer layers between the ferroelectric films and the Si substrate [4-6]. But these buffer layers are not ferroelectric materials themselves and their permitivity(ε_r) are much lower than PZT's, which will increase the operation voltage and impair the ferroelectric properties of ferroelectric memory. To solve the interface problem, we introduced $Bi_4Ti_3O_{12}$ (BIT) as the buffer layer between PZT and Si substrate. The BIT is a kind of ferroelectric material itself with a permitivity(ε_r) of 200 and its lattice parameters are a=0.541nm, b=0.545nm, c=3.28nm, the lattice parameters of c-axis oriented BIT match the lattice parameters of Si(100) very well.

In this paper, the preparation of the ferroelectric memory diodes that consisted of

Au/PZT/BIT/p-Si multilayer configuration using PLD technique is described. In order to characterize their memory effect, polarization-voltage (P-V) hysteresis loop, capacitance-voltage (C-V) characteristics, current-voltage (I-V) characteristics of the ferroelectric memory diode were measured respectively. The results were performed and discussed.

In our experiments, a quasi molecule laser generator (EMG201MSC type made by Lamda Physik) with a wave length of 308nm was used. The pulse duration was 28ns, and the maximal output of single pulse energy was 300mJ. During the film deposition, the laser beam was focused by a quartz lens to obtain an energy density of $3J/cm^2$ at an incidence angel of 45°, the pulse frequency was 8Hz and the target-substrate distance was 40mm. There were four target holders mounted on a disk, which could be rotated to bring the desired target in line of the laser beam for laser ablation and could obtain multilayer thin films systems. Two of these holders were loaded with single-phase pellets of $Pb(Zr_{0.52}Ti_{0.48})O_3$ and $Bi_4Ti_3O_{12}$ with a diameter of 25mm and a thickness of 5mm. An oxygen jet directed at the substrate was used to enhance the incorporation of oxygen into the films during the film deposition.

(100) oriented p-type silicon wafers with a resistivity of 6-9 Ω·cm were cleaned by a standard process. The vacuum chamber was evacuated to below 10^{-5}Torr before deposition. The substrate temperature was controlled using a chromel-alumel thermocouple contacted with the center of the heater block. The films were deposited at the substrate temperature of 530℃ for PZT and 650 ℃ for BIT. The deposited ambient was oxygen with pressure of 100mTorr. The thickness of PZT layer was 300nm, meanwhile the BIT layer was 100nm thick, which were estimated by using Rudolph research/Auto III ellipse polarimeter. The front electrode, with a thickness of 50nm and a diameter of 0.4mm, was patterned by a shadow-mask-process.

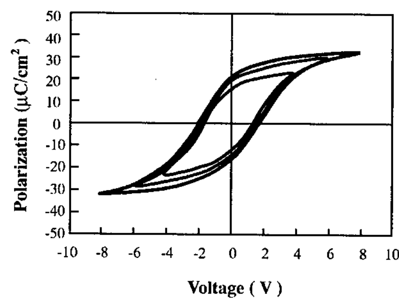

Fig.1 Hysteresis loops of PZT/BIT thin films system with various applied voltages

The hysteresis loops were measured with conventional Sawyer-Tower circuit to test the ferroelectricity of the thin films. Figure 1 shows the polarization-voltage (P-V) hysteresis loops of the PZT/BIT thin films system deposited on a high-doped p-Si wafer at various applied voltages. It can be seen that the PZT/BIT thin films system had a well-saturated hysteresis loops, a larger remnant polarization (P_r) of $20\mu C/cm^2$ and a lower coercive field of 48 kV/cm at a voltage of 8V, and the hysteresis loops get saturation with increasing the applied voltage. As for the asymmetry in the P-V hysteresis loop, this can be understood by considering the difference of stress at the interface of M/F and F/S as well as the effect of the dissymmetry built-in electric field at the different applied bias voltage.

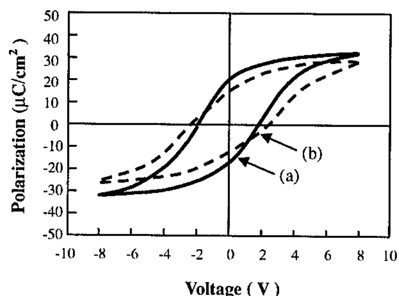

Fig.2 Hysteresis loops (a) before (b) after 10^9 switching cycles.

The decay in remnant polarization (P_r) of the PZT/BIT thin films system as function of switching cycles was also studied. This was conducted by applying 10kHz bipolar pulses of 8V amplitude. Figure 2 shows the hysteresis loops before and after 10^9 switching cycles. As shown in Fig.2, the remnant polarization of the PZT/BIT thin films system had decreased from 20 $\mu C/cm^2$ to 18 $\mu C/cm^2$ after 10^9 switching cycles, the decay in P_r was only about 10% of the initial value. Meanwhile the coercive field had increased from 48 kV/cm to 53 kV/cm, the increase in E_c was around 12% of the initial value.

Figure 3 is a typical 100kHz capacitance-voltage (C-V) curve of Au/PZT/BIT/p-Si ferroelectric diodes at bias voltages between -4.5V and +4.5V. The diameter of the electrode was 0.4mm. It can be seen that the pattern of the C-V curve was similar to that of a normal MOS structure. It clearly showed the regions of accumulation, depletion and inversion. It is important that the C-V curves went clockwise, which means that ferroelectric hysteresis of the PZT/BIT thin films had controlled the Si surface potential and showed a memory effect due to polarization [7].

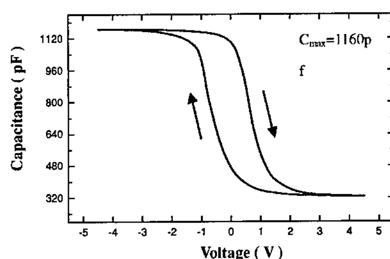

Fig.3 Capacitance versus bias voltage characteristics of Au/PZT/BIT/p-Si heterostructure between -4.5 and 4.5 bias voltage at a bias frequency of 100kHz.

Data retention is an important property for use in nonvolatile memories. Capacitance retention is the embodiment of the ability of the switching charge retention, which is related to the reliability of the ferroelectric memories.

Curves (a) and (b) of Fig.4 show the retention characteristics (capacitance as a function of retention time) of the ferroelectric diode at room temperature for up to 10 hours after withdrawing the applied bias. The measurement frequency of the small ac signals was 1MHz, and the applied bias voltages were +5V in curve (a) and –5V in curve (b). In Fig.4, curve (a) illustrate that the capacitance increases rapidly in a short time (region of inversion) after withdrawing the applied bias of +5V, then followed a gentle variety. The capacitance increase was only 12% in 10 hours. Curve (b) of Fig.4 shows that the capacitance decreases sharply at the initial short period (region of depletion) after removing the applied bias of –5V, then varied slowly in a long time. The capacitance dropped from 1150pF to 1091pF in 10 hours. The variety of capacitance was about 5% of the initial value, which indicated that the ferroelectric diode is possessed of good capacitance retention properties.

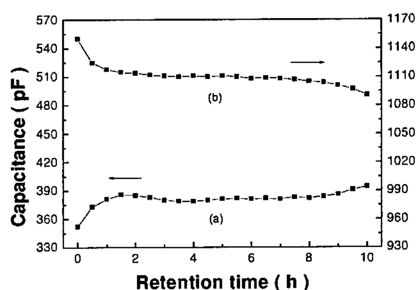

Fig.4 C-t curve of Au/PZT/BIT/p-Si (a) after withdrawing the bias voltage of +5V, (b) after withdrawing the bias voltage of -5V

The Current-Voltage (I-V) characteristics of the diodes were measured by using ZC43 high resistance meter. Figure 5 (a) and (b) illustrate the current density dependence of the voltage at positive and negative bias voltage respectively. As shown in Fig.4, the current density was only

$-5.3\times10^{-10}A/cm^2$ at a bias voltage of -4V, it is smaller about two order of magnitude than that at a bias voltage of +4V, the latter is $6.7\times10^{-8}A/cm^2$. This could be well explained using the p-p heterostructure effect between ferroelectric layer and p-Si substrate. The hysteresis loops of I-V curves of the Au/PZT/BIT/p-Si ferroelectric diodes had been observed (shown in Fig.6), which conducted by applying bias voltage varied first from 0V to +4V, then from +4V to -4V, and finally from -4V to 0V at a step of 0.2V. This is different from the I-V curve of traditional diodes. Distinctly, the hysteresis loop of I-V curve originated from the remnant polarization of ferroelectric layer [8].

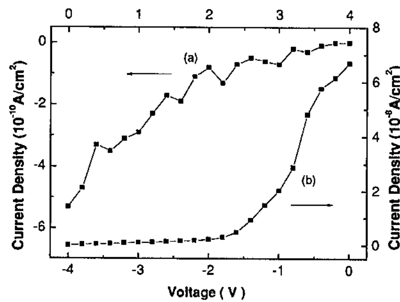

Fig.5 Current density dependence of voltage (a) at negative voltages (b) at positive voltages

In order to investigate the leakage mechanisms, the positive I-V curve of the Au/PZT/BIT/p-Si system, which obtained by applying bias voltage varied from 0V to +3V, then from +3V to 0V at a step of 0.08V, was transformed into a more obvious plot and illustrated in Fig.7. The ratio of logarithm of current with voltage is about 1.0 below 1 V, while it is around 2.0 in the voltage range of 2.2~3.0 V. The results suggest that in different voltage regions different conduction mechanism dominate. The current linearly depends on voltage at a relatively low voltage, i.e. the conduction in this region displays an ohmic behavior. The current transportation in ferroelectric thin films at the high voltage region is normally ascribed to the space-charge limited current [9]. As a result, out of the proposed models, ohmic current and space charge limited current give the best explanation of our experimental I-V curve.

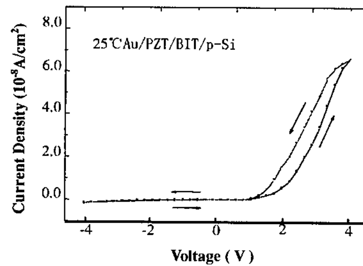

Fig.6 Current density versus bias voltage characteristics of Au/PZT/BIT/p-Si diode

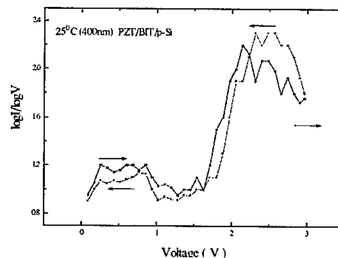

Fig.7 I-V curve analysis in positive direction of PZT/BIT/p-Si

In conclusion, we have shown the ferroelectric properties and the electrical characteristics of the Au/PZT/BIT/p-Si ferroelectric memory diodes fabricated by pulsed laser deposition (PLD) technique. The clockwise hysteresis loop in C-V curve indicated that the ferroelectric hysteresis of the PZT/BIT thin films had controlled the Si surface potential and showed a memory effect due to polarization. The dominant conduction mechanism is different in different voltage regions: ohmic current in lower voltage region and space charge limited current in higher voltage region. The results suggested that the growth of the BIT ferroelectric layer is helpful to good ferroelectric properties, fatigue and capacitance retention characteristics.

This work was supported by the National Natural Science Foundation of China under contract No.69771024.

References

[1] J. F. Scott and C. A. Araujo. Ferroelectric Memories. Science, 1989: 246: 1400-1405.

[2] S. Sinharoy, H. Buhay, D. R. Lampe, et al. Integration of ferroelectric thin films into nonvolatile memories. J. Vac. Sci. Tech. 1992: A10 (4): 1554-1561.

[3] Y. Watanabe, M. Tanamura, Y. Matsumots. Memory retention and switching speed of ferroelectric field-effect in $(Pb,La)(Ti,Zr)O_3$ / La_2CuO_4:Sr heterostructure. Jpn. J. Appl. Phys. 1996: 35(2B): 1564-1568.

[4] H. Tadahiko, T. Kazuhiro, N. Takeharu. Formation of metal / ferroelectric / insulator / semiconductor structure with a CeO_2 buffer layer. Jpn. J. Appl. Phys., 1994: 33(P,1.9B): 5219-5222.

[5] Jun Yu, Zhao Jianhong, Wenli Zhou, et al. Formation and characteristics of $Pb(Zr,Ti)O_3$ field-effect transistor with a SiO_2 buffer layer. Appl. Phys. Lett. 1997: 70(4): 490-492.

[6] H. Buhay, S. Sinharoy, W. H. Kasner. Pulsed Laser Deposition and ferroelectric Characterization of Bismuth Titanate Films. Appl. Phys. Lett. 1991: 58(14): 1470-1472.

[7] Y. S. Wu. A new ferroelectric memory device, metal-ferroelectric-semiconductor transistor. IEEE Trans. electron. Dev., 1974: ED-21: 499-504.

[8] P. W. M. Blom, R. M. Wolf, J. F. M. Cillessen, et al. Ferroelectric Schottky Diode. Phys. Rev. Lett. 1994: 73(15): 2107-2110.

[9] J. F. Scott, C. A. Araujo, B. M. Melick, et al. Quantitative measurement of space charge effect in lead-zirconate-titanate memories. J. Appl. Phys. 1991: 70(1): 382-386.

Mat. Res. Soc. Symp. Proc. Vol. 655 © 2001 Materials Research Society

Direct Comparison of Structural and Electrical Properties of Epitaxial (001)-, (116)-, and (103)-Oriented $SrBi_2Ta_2O_9$ Thin Films on $SrTiO_3$ and Silicon Substrates

H. N. Lee, A. Pignolet, S. Senz, C. Harnagea, and D. Hesse
Max-Planck-Institut für Mikrostrukturphysik, Weinberg 2, D-06120 Halle/Saale, Germany

ABSTRACT

Anisotropies of the properties of the bismuth-layered perovskite $SrBi_2Ta_2O_9$ (SBT) have been investigated using epitaxial thin films grown by pulsed laser deposition both on conducting Nb-doped $SrTiO_3$ (STO) single crystal substrates and on Si(100) substrates. It has been found that the three-dimensional epitaxy relationship SBT(001)||STO(001); SBT[1$\bar{1}$0]||STO[100] can be applied to all SBT thin films on STO substrates of (001), (011), and (111) orientations. An about 1.7 times larger remanent polarization was obtained in (103)-oriented SBT films than in that of (116) orientation, while the (001)-oriented SBT films revealed no ferroelectricity along their *c*-axis. Non-*c*-axis-oriented SBT films with a well-defined (116) orientation were also grown on silicon substrates for the first time. They were deposited on Si(100) covered with a conducting $SrRuO_3$(110) bottom electrode on a YSZ(100) buffer layer.

INTRODUCTION

Getting epitaxial $SrBi_2Ta_2O_9$ (SBT) films (a = 0.5531 nm, b = 0.5534 nm, and c = 2.4984 nm [1]) is an important issue for applications in high-density ferroelectric random access memories (FRAMs). Epitaxial films are needed to overcome the problems related to the lack of uniformity in polycrystalline films [2]. The latter arise, because in high-density memories the lateral sizes of the individual structures approach both the sizes of the grains in polycrystalline films and the size of the ferroelectric domains. One solution to circumvent these non-uniformity problems is to use epitaxial thin films. As the vector of the spontaneous polarization ($\mathbf{P}_s$) in SBT is directed perpendicularly to the *c* axis, specifically along its *a* axis, the growth of non-*c*-axis-oriented SBT films is of particular significance for applications to planar-capacitor-type FRAMs. The epitaxial growth of SBT films both with *c*-axis and non-*c*-axis orientations was investigated on single crystal substrates such as $SrTiO_3$ (STO), $LaSrAlO_4$, etc. [3-5]. Particularly, the epitaxial orientation relationship of either SBT or $SrBi_2Nb_2O_9$ (SBN) films grown on (011)- and (111)-oriented STO substrates has been debated, for instance whether the (001) plane of SBT or SBN films is exactly parallel to the (001) plane of STO substrates in the non-*c*-axis-oriented SBT/SBN films with (116) and (103) orientations on STO(011) and STO(111) substrates [3-5], or whether a small deviation occurs. In this work, we report the epitaxial orientation relationship investigated by means of x-ray diffraction ϕ scans as well as a comparison between the structural and electrical properties of *c*-axis and non-*c*-axis-oriented SBT films grown on STO and on Si(100) substrates. For the application of epitaxial films in high-density ferroelectric nonvolatile memories, non-*c*-axis-oriented SBT films *on silicon* will be needed.

EXPERIMENTAL

The deposition conditions used for the film growth along with the various characterization methods are described in detail elsewhere [5,6]. Briefly, the 250 nm thick SBT films were grown both on single crystalline Nb-doped STO with (001), (011), and (111) orientations and on yttria-stabilized ZrO_2-buffered (YSZ-buffered) Si(100) substrates covered with conducting $SrRuO_3$ (SRO) bottom electrodes. All the films were grown by pulsed laser deposition using a KrF excimer laser (λ = 248 nm). Pt top electrodes with an area of 1.1×10^{-3} cm^2 were deposited by rf-sputtering at room temperature through a stainless steel shadow mask. After top electrode deposition, the samples were annealed at 750 °C for 30 min. in an oxygen ambient to stabilize the contact between SBT and Pt. To characterize the structural and electrical properties, x-ray diffraction (XRD), cross-sectional transmission electron microscopy (TEM), scanning force microscopy (SFM), and a TF2000 thin film analyzer (AixACCT) were used.

EPITAXIAL (001)-, (116)-, AND (103)-ORIENTED SBT FILMS ON STO SUBSTRATES

Figure 1 shows XRD ϕ scans of the (001)-, (116)-, and (103)-oriented SBT films on (001)-, (011)-, and (111)-oriented STO substrates, respectively. Details on θ-2θ and pole figure scans were published elsewhere [5]. In order to record the patterns, the reflections of SBT(113) and SBT(00<u>10</u>) were used at ψ = 65°, 46.5°, and 55.8°, respectively. In the case of (001)-oriented SBT films on (001)-oriented STO substrates, the SBT(001) plane is exactly parallel to the STO (001) plane satisfying the epitaxy relationship SBT(001)||STO(001); SBT[1 $\bar{1}$ 0]||STO[100]. For non-*c*-axis-oriented epitaxial films, the (001) planes of (116)- and (103)-oriented SBT films are *not* exactly parallel to the STO(001) planes of (011)- and (111)-oriented STO (in which case we would have ψ = 45° and 54.7°, resp.), as shown in Figs. 1(b) and 1(c). These angle deviations of 1.5° and 1.1° correspond to the tilt angle between the SBT(001) plane and the underlying STO(001) plane for (116)- and (103)-oriented SBT films on (011)- and (111)-oriented STO, respectively. Therefore, since the (116), respectively (103) planes are *exactly* parallel to the STO(011), respectively STO(111) planes, small angular deviations up to ~2° from the three-dimensional unique epitaxy relationship SBT(001)||STO(001); SBT[1 $\bar{1}$ 0]||STO[100] have to be taken into consideration, if the latter is applied to all SBT films on STO substrates of (001), (011), and (111) orientations.

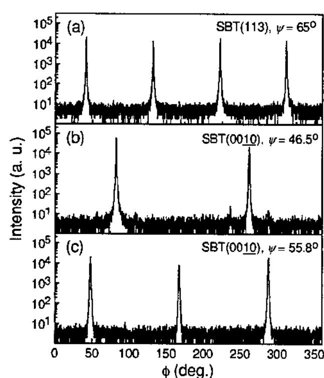

Figure 1. XRD ϕ scans of the SBT films on (a) (001)-, (b) (011)-, and (c) (111)-oriented STO substrates. ψ = 0° corresponds to the substrate surface, perpendicular to the plane defined by the incident and reflected x-ray beams.

Due to the tilt of the *c* axis of SBT films with respect to the substrate surface, the directions of the vector $\mathbf{P}_s$ of the spontaneous polarization in (001)-, (116)-, and (103)-oriented SBT films are 90°, ~59°, and ~34° away from

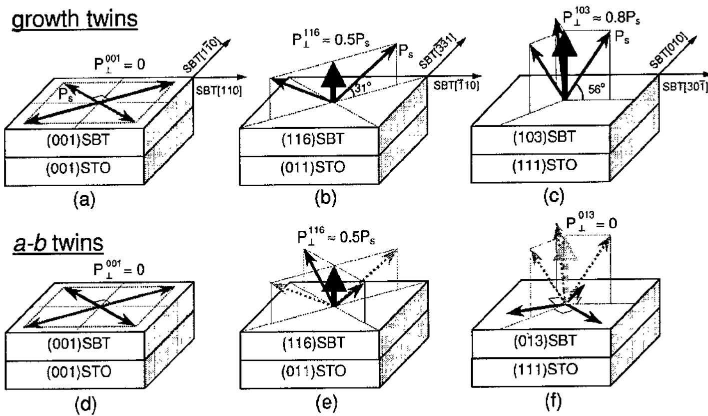

Figure 2. Schematic drawing of polarization components of the growth twins of (a) (001)-, (b) (116)-, (c) (103)-oriented SBT thin films, and the *a-b* twins of (d) (001)-, (e) (116)-, and (f) (013)-oriented films on (001)-, (011)-, and (111)-oriented STO substrates, respectively. The vertical components of the spontaneous polarization ($P_\perp$) with respect to the substrate surface are represented as thick solid arrows.

the substrate normal, respectively. Therefore, the polarization of SBT films can be estimated by comparing the recorded ferroelectric hysteresis loops using SBT films having different orientations, assuming full switching. The components of $\mathbf{P}_s$ perpendicular to the substrate surface are proportional to the values of $P_\perp^{001} = |P_s| \cdot \cos 90° = 0$, $P_\perp^{116} = |P_s| \cdot \cos 59° = 0.5|P_s|$, and $P_\perp^{103} = |P_s| \cdot \cos 34° = 0.8|P_s|$. Accordingly, the *c*-axis-oriented SBT film reveals a zero normal polarization and the (103)-oriented SBT film has an about 1.7 times larger normal polarization value than the (116)-oriented film as schematically shown in Figs. 2(a)–2(c).

Figure 3 (left) shows the ferroelectric *P–E* hysteresis loops of (001)-, (116)-, and (103)-oriented SBT films. In the case of (001) orientation, the film reveals no ferroelectricity in the direction normal to the film [Fig. 3 left(a)]. Moreover, an about 1.7 times higher remanent

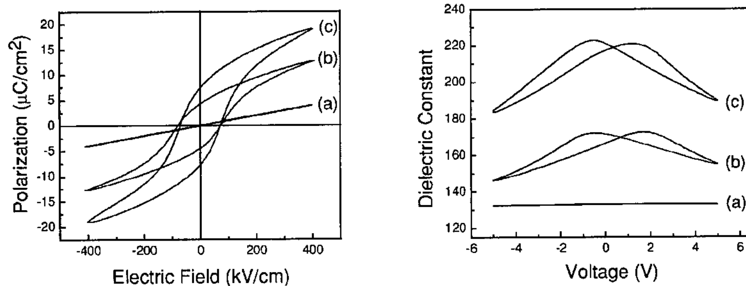

Figure 3. *P–E* (left) and *C–V* (right) hysteresis loops of (a) (001)-, (b) (116)-, and (c) (103)-oriented SBT films. The remanent polarization values of (116)- and (103)-oriented films are 4.3 and 7.4 μC/cm², respectively, exhibiting a ratio of their remanent polarization (P_r^{103}/P_r^{116}) of ~1.7.

polarization was recorded for the (103)-oriented SBT film than for the (116)-oriented SBT film [Figs. 3 left(b) and (c)]. The ratio of polarization values, $P_r^{103}/P_r^{116} \approx 1.7$, agrees well with the calculated value even though the absolute polarization values are lower than expected, *cf.* Refs. 3 and 4. Please note that the direct comparison is valid, and the experimental ratio is so nicely consistent with the computed one, because our samples were deposited on substrates having different orientations during the same run, in exactly *the same conditions.*

Dielectric constants of all SBT films on (001)-, (011)-, and (111)-oriented STO substrates were calculated by recording *C–V* curves as shown in Fig. 3 (right). Like the *P–E* curves, no hysteresis loop was observed in the case of the *c*-axis-oriented SBT film [Fig. 3 right(a)]. Non-*c*-axis-oriented SBT films [Figs. 3 right(b) and (c)] exhibited ferroelectric hysteresis loops showing a higher dielectric constant than the *c*-axis-oriented SBT film. The calculated dielectric constants of (001)-, (116)-, and (103)-oriented SBT films measured at 5 V in a direction normal to the film were about 133, 155, and 189, respectively.

Twinning of *a* and *b* axes in SBT has not yet been reported. The difference of lattice parameters between *a* and *b* is too small (~0.3 pm) to evidence it by XRD analyses. However, exactly because of this very small difference, and due to the fact that no large displacements are required to "switch" the two axes, some twinning must exist. Moreover, since the polarization is directed along the *a* axis, it is most probably influenced by an applied electric field. We have tried to find an evidence of the *a-b* twins by piezoresponse-SFM using SBT films grown on STO(111) substrates. The reason to use the SBT film on the STO(111) is that for (001)-oriented SBT films, both *a* and *b* axes are lying parallel to the substrate surface [Figs. 2(a) and 2(d)], and for (116)-oriented SBT, the *a* and *b* axes both are lying 31° away from the substrate surface, thus having a component along the normal direction, but for symmetry reason being not distinguishable [Figs. 2(b) and 2(e)]. In the case of (103)-oriented SBT, the *a* axis ($\mathbf{P}_s$ vector direction) is lying 56° away from the substrate surface and the *b* axis is lying parallel to the substrate surface. But, if we consider that *a-b* twinning is present, (013)SBT has its *a* axis lying parallel to the substrate surface and its *b* axis 56° away from the substrate surface. In this case, the film has no component of the polarization normal to the film and cannot reveal ferroelectricity along the substrate normal [Fig. 2(f)]. These two types of behavior were qualitatively confirmed by local in-plane and out-of-plane hysteresis loops recorded by piezoresponse-SFM using two different SBT grains of a (103)-oriented SBT film as shown in Fig. 4. In Fig. 4(a), a *higher* piezoresponse along the out-of-plane direction was recorded than along the in-plane direction. On the other hand, in Fig. 4(b), a *lower* piezoresponse along the out-of-plane direction was recorded than

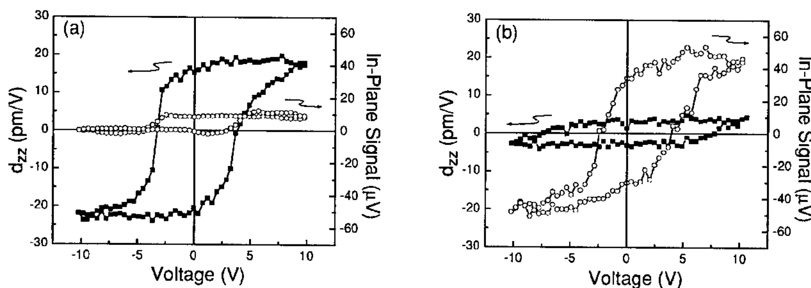

Figure 4. Local piezoresponse hysteresis loops of (a) (103)- and (b) (013)-oriented SBT grains exhibiting evidence of the presence of the *a-b* twinning of SBT films.

along the in-plane direction. Therefore, we can infer that the former piezoresponse was recorded from a (103)-oriented SBT grain and the latter one was recorded from a (013)-oriented SBT grain revealing an *a-b* twinning of SBT films.

NON-*c*-AXIS-ORIENTED SBT FILMS ON Si(100) SUBSTRATES

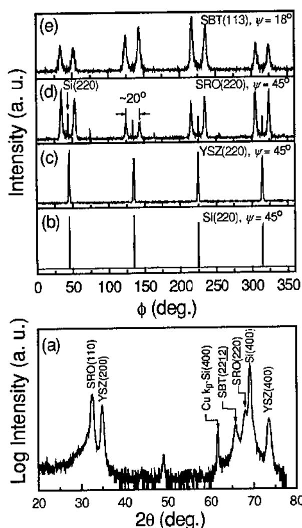

Figure 5. X-ray diffraction (a) θ-2θ scan and (b)–(e) ϕ scans of a SBT/SRO/YSZ/Si(100).

As discussed in the introduction, non-*c*-axis-oriented SBT films will be of practical importance *only* if they are grown on a technologically relevant substrate, such as silicon. We succeeded to grow (116)-oriented SBT films on a Si-based substrate, using a (110)-oriented $SrRuO_3$ (SRO) electrode. Figure 5(a) shows an XRD θ-2θ scan of a SBT(116)/SRO(110)/YSZ(100)/Si(100) heterostructure. The ϕ scans in Figs. 5(b)–5(e) demonstrate the perfect in-plane orientations of SBT, SRO, and YSZ on Si(100). The SRO layer [Fig. 5(d)] and the SBT film [Fig. 5(e)] display a characteristic peak splitting of $\Delta\phi \approx 20°$. An equivalent azimuthal angle of ~20° between neighboring SBT grains was observed in the surface morphology of the (116)-oriented SBT films by SFM (Fig. 6). The reason for the presence of this azimuthal angle, as well as for the observed peak splitting in the ϕ scans, is a specific "*diagonal rectangle-on-cube*" epitaxy relationship of SRO (110) on YSZ(100) minimizing the lattice mismatch as schematically shown in Fig. 7. (The lattice mismatch along the diagonal direction is –6.3%, which is comparable to the mismatch of 8.1% along the SRO<110> or YSZ<100> directions.) Since there are four positionings to arrange the respective diagonals, four different azimuthal orientations of the (110)-oriented SRO grains, or four variants, result exhibiting characteristic angles of 19.5°. Due to the two-fold positioning of SBT variants on each azimuthal SRO variant,

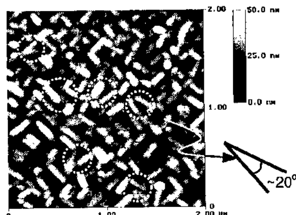

Figure 6. SFM topography image of a (116)-oriented SBT thin film on SRO(110)/YSZ(100)/Si(100).

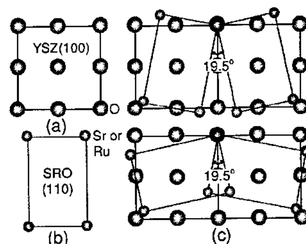

Figure 7. Schematic of the *diagonal rectangle-on-cube* epitaxy of SRO(110) on YSZ(100): (a) YSZ(100), (b) SRO(110), and (c) four variants of SRO on YSZ.

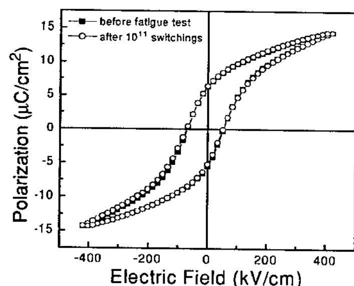

Figure 8. *P–E* hysteresis loops of a Pt/SBT(116)/SRO(110) capacitor.

the SBT film has *eight* azimuthal variants, which again exhibit characteristic angles of ~20°. The following orientation relationship has been deduced from the XRD investigations: SBT(116)||SRO(110)|| YSZ(100)||Si(100); SBT[110]||SRO[100], and SRO[111]||YSZ<110>||Si<110> including four azimuthal SRO orientations and eight corresponding azimuthal SBT orientations. Both the SRO and SBT grains corresponding to the different azimuthal variants can be visualized by cross-section TEM images (not shown here). The grains are ~50 nm in lateral size, and the azimuthal SBT domain pattern replicates the one in the SRO layer. The SBT/SRO interface has a characteristic roof-like morphology while the other interfaces are plane and sharp [6].

P–E hysteresis loops of a (116)-oriented SBT film are shown in Fig. 8. The loops were recorded before a fatigue test, and after 10^{11} switching cycles using 1 MHz fatigue pulse at 5 V, respectively. The remanent polarization ($2P_r$) and the coercive field ($2E_c$) were about 12 μC/cm^2 and 120 kV/cm, respectively, for a maximum electric field of 420 kV/cm. The film revealed excellent fatigue endurance even after 10^{11} switching cycles.

CONCLUSIONS

Anisotropies in the ferroelectric properties of *c*-axis- and non-*c*-axis-oriented SBT films were investigated. The (103)-oriented SBT films exhibited an about 1.7 times larger out-of-plane polarization component than the (116)-oriented SBT films, while the (001)-oriented SBT films exhibited no component of the polarization along their *c*-axis direction. An evidence of *a-b* twinning in (103)-oriented SBT films was found by local SFM piezoresponse analysis. Moreover, (116)-oriented SBT films have been successfully grown on SRO(110)/YSZ(100)/ Si(100) substrates. A specific diagonal-type rectangle-on-cube epitaxy of SRO on YSZ enables the growth of non-*c*-axis-oriented SBT films on Si substrates.

REFERENCES

1. A. D. Rae, J. G Thompson, and R. L. Withers, Acta Cryst., **B48**, 418 (1992).
2. A. Gruverman, Appl. Phys. Lett., **75**, 1452 (1999).
3. T. Suzuki, Y. Nishi, M. Fujimoto, K. Ishikawa, and H. Funakubo, Jpn. J. Appl. Phys., **38**, L1265 (1999); K. Ishikawa and H. Funakubo, Appl. Phys. Lett., **75**, 1970 (1999).
4. J. Lettieri, M. A. Zurbuchen, Y. Jia, D. G Schlom, S. K. Streiffer, and M. E. Hawley, Appl. Phys. Lett., **76**, 2937 (2000); *ibid*, **77**, 3090 (2000).
5. H. N. Lee, A. Visinoiu, S. Senz, C. Harnagea, A. Pignolet, D. Hesse, and U. Gösele, J. Appl. Phys., **88**, 6658 (2000).
6. H. N. Lee, S. Senz, A. Visinoiu, A. Pignolet, D. Hesse, and U. Gösele, Applied Physics A, **71**, 101 (2000); H. N. Lee, S. Senz, C. Harnagea, A. Pignolet, D. Hesse, and U. Gösele, Appl. Phys. Lett., **77**, 3260 (2000).

Mat. Res. Soc. Symp. Proc. Vol. 655 © 2001 Materials Research Society

MOCVD kinetics of precursors for ferroeletric SBT film

A. Baeri, G.G. Condorelli, I.L. Fragalà
Dipartimento di Scienze Chimiche, Università di Catania, - 95125 Catania, Italy

ABSTRACT

The metal organic chemical vapour deposition kinetics of $Sr(hfa)_2(tet)$ (H-hfa =1,1,1,5,5,5-hexafluoroacetylacetone and tet= tetraglyme) and $Bi(C_6H_5)_3$ single precursors have been studied upon varying operational deposition parameters, namely temperature and precursor partial pressure. These precursors are of interest for the MOCVD of SBT ferroeletric thin films. Depending upon experimental conditions, deposition processes occur either in the reaction rate limited regime or in the mass transport regime. Kinetics controlled by reaction rates ($T_{deposition}$< 673 K) gives insights on the process mechanisms. The activation energies of the Sr and Bi deposition processes have been determined from the Arrhenius plots.

$SrBi_2Ta_2O_9$ films were grown on industrial $Pt/Ti/SiO_2/Si$ substrates and perovskite phase films were obtained after annealing in O_2 environment at 1073K.

INTRODUCTION

SBT ferroeletric films have been extensively investigated for Fe-RAM application due to their endurance resistance[1]. SBT films have been prepared by several techniques such as sol-gel[2], metalorganic deposition (MOD) [3], pulsed laser ablation[4] and metalorganic chemical vapor deposition (MOCVD)[5]. This last technique is best suited for semiconductor industry because of the superior step coverage compared to other deposition techniques. The phenomenological aspects of MOCVD fabrication of SBT film using various Bi and Sr sources as well as their electrical properties have been reported in many papers. However, if careful control of the properties of films grown for industrial application is to be achieved, it is important to understand factors affecting film growth. In this context, the kinetics and deposition mechanisms of single precursors play a critical role as far as industrial scaling-up is concerned. Little has been reported on the kinetics of the deposition of SBT precursors. Some kinetic investigations have been reported during multicomponent SBT deposition using the $Bi(CH_3)_3$-$Sr(Ta(O\,C_2H_5)$ system [6] and the $Sr(tmhd)_2$-$Bi(C_6H_5)_3$-$Ta(OC_2H_5)_5$ (Htmhd=2,2',6,6'-tetramethylheptan-3,5-dione) system [7]

This paper reports on deposition kinetics of single component films using $Sr(hfa)_2(tet)$ (H-hfa =1,1,1,5,5,5-hexafluoroacetylacetone and tet= tetraglyme) or $Bi(C_6H_5)_3$ precursors. Kinetic results obtained from single component deposition have been applied to SBT fabrication using $Sr(hfa)_2(tet)$, $Bi(C_6H_5)_3$ and $Ta(OC_2H_5)_5$ precursors in O_2.

EXPERIMENTAL

Experiments were performed in reduced-pressure, horizontal cold wall reactors for single and multi component depositions. Single component MOCVD system consists of a gas-handling facility, a stainless steel evaporator, a reactor tube and a vacuum system. The quartz reactor inner diameter was 2.4 cm and the total length was 40 cm. Temperatures of the evaporator, connecting lines and reaction zones were controlled by EUROTHERMS Controls

within ±2 K. Connecting lines (stainless steal) were always held at slightly higher temperatures than the sublimator to prevent condensation. Flow rates were controlled (within ±2 sccm) using MKS flow controllers.

SBT depositions were performed in a multi-component, horizontal, MOCVD reactor made of a 80cm-lenght quartz tube (id=8 cm). The reactor consists in contiguous sections for precursor sublimation, gas mixing and film deposition. Each section was independently heated within ±2K using computer-controlled hardware.

Typical dynamic MOCVD conditions adopted pre-purified Ar (99.999%) as carrier gas (100 sccm) and O_2 (O_2 99.999%) as reaction gas (500 sccm). Films were deposited on $Pt/TiO_2/SiO_2/Si$ substrates placed on a susceptor heated in the 573 K – 773 K temperature range and at a total pressure of 6 Torr. Sublimation temperatures were in the 373-423K and 403-443K ranges for $Sr(hfa)_2tet$ and $Bi(C_6H_5)_3$ sources, respectively.

In all experiments the total quantity of the sublimed precursor was determined by weight loss measurements.

Grazing angle x-ray diffraction (XRD) spectra were obtained with a Bruker AXS D5005 X-ray Diffractomer equipped with a copper anode and an attachment for thin film measurements. Measurements were performed with a detector scan from $20° < 2\theta < 70°$. The angle between the X-ray source and the sample surface was fixed at 0.5°.

Surface morphologies and film compositions were analysed by scanning electron microscopy (SEM), performed with LEO 1400 Microscope, equipped with EDX microanalysis. Growth rates were estimated by EDX and SEM cross sections.

RESULTS AND DISCUSSION

Kinetics of the precursors

The nature of films deposited using either $Sr(hfa)_2(tet)$ or $Bi(C_6H_5)_3$ precursors in the 573°C-773K temperature range has been investigated using XRD. In the investigated temperature range, depositions performed from $Sr(hfa)_2(tet)$ –O_2 and $Bi(C_6H_5)_3$ –O_2 systems lead to the formation of SrF_2 and Bi_2O_3, respectively.

Experiments were made to define operating conditions in which film growth takes place under either reaction rate or mass transport rate limited regimes.[8]

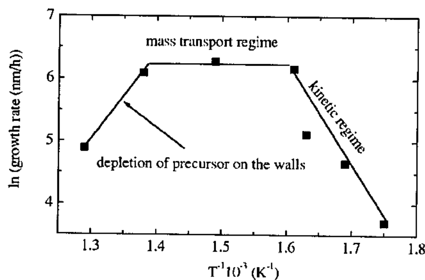

Fig. 1 SrF_2 growth rate as function of temperature

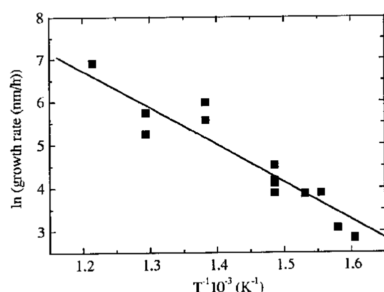

Fig. 2 Bi_2O_3 growth rate in function of temperature

Figure 1 shows SrF_2 growth rate as function of temperature. Below 673K the growth rate is reaction rate limited since the ln of the deposition rate depends linearly on the reciprocal of the temperature. The apparent activation energy is 130± 8 kJ/mol. In the 723- 623 K the deposition rate is constant (mass transport rate limited regime). Beyond 743K a remarkable fall-off is observed due to precursor depletion.

Figure 2 shows Bi_2O_3 growth rate as function of deposition temperature. In this case, the ln of the growth rate *vs* 1/T depends linearly in the entire temperature range as expected for reaction rate limited processes. The apparent activation energy (E_{Bi}) of film formation is markedly lower (70 ± 5 kJ/mol) than that obtained for Sr.

The effects of Sr(hfa)$_2$(tet) partial pressure (P_{Sr}) upon the growth rate of SrF_2 was investigated at different temperatures. Under reaction rate limited regime (T<400°C) the growth rate does not depend upon P_{Sr} in the investigated range (0.1-2 mTorr). The value of the growth rate was 43± 2 nm/h. The reaction is of zero order with respect to Sr(hfa)$_2$(tet). This behaviour indicates that the rate limiting step involves a surface reaction where the active sites become saturated under high Sr(hfa)$_2$(tet) partial pressure.

Experiments carried out at T=673K (mass transport rate limited regime) show (figure 3) that the deposition rate depends linearly on Sr(hfa)$_2$(tet) partial pressure in the investigated range (0.1-2 mTorr). Therefore, under these conditions the growth rate can be expressed as:

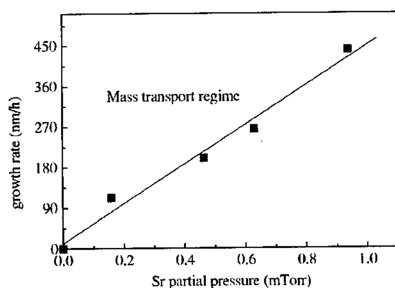

Fig. 3 Sr(hfa)$_2$(tet) growth rate as function of Sr(hfa)$_2$(tet) partial pressure

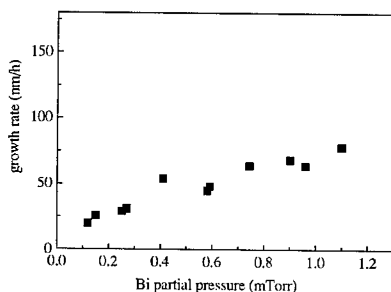

Fig. 4 Bi_2O_3 growth rate as function of $Bi(C_6H_5)_3$ partial pressure

$$G_{Sr} = h \cdot P_{Sr} \tag{1}$$

where the constant h obtained from figure 3 (h=432 nm*h^{-1} mTorr^{-1}) is a mass transferr coefficient [8]. Since under mass transport limited regime growth rate is independent upon temperature, Eq. 1 represents growth rate in the 673K<T<743K temperature range.

The dependence of Bi_2O_3 growth rate at 673K upon $Bi(C_6H_5)_3$ partial pressure (P_{Bi}) is reported in figure 4. The growth rate of Bi precursor increases with P_{Bi}, but rate dependence is not linear. Curve slope becomes smaller upon increasing P_{Bi}, thus showing the shape of a Langmuir adsorption isotherm [9].

The study of the dependence of the Bi_2O_3 growth upon both temperature and P_{Bi} suggest that in the investigated temperature range the reaction rate determining step involves a surface reaction. Therefore, at constant temperature the growth rate depends on the fraction of the surface (θ) occupied by the adsorbed precursors [9]. Since θ can be related to P_{Bi} by the adsorption isotherm, growth rate of Bi_2O_3 can be expressed as:

$$G_{Bi} = k \cdot \theta = k \cdot \frac{K_{ad} p_{Bi}}{1 + K_{ad} p_{Bi}} \tag{2}$$

where k is the kinetic constant of precursor surface reaction and K_{ad} is the equilibrium constant of precursor adsorption.

For low values of P_{Bi} , the term $K_{ad} P_{Bi}$ can be neglected with respect to unity ($K_{ad} P_{Bi}$ << 1) and eq. 2 become:

$$G_{Bi} = k \cdot K_{ad} p_{Bi} = k' p_{Bi} \tag{3}$$

Temperature dependence can be included in the rate equation, by re-writing k' as Aexp($-E_{Bi}/RT$) (with A=3.4 10^7 nm*h^{-1} from figure 2).

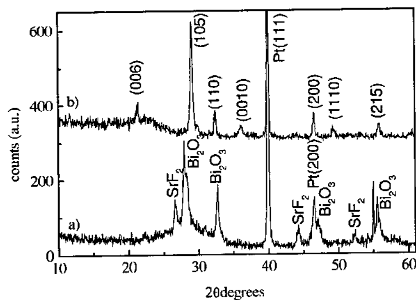

XRD patterns of a) as-deposited film of b) film annealed at 1073K under O_2

SBT deposition

The obtained equation has been used to deposit the Sr-Bi-Ta O(F) matrix with the correct Sr/Bi metal ratio 1 / 2.2 .

In order to obtain high growth rates, depositions were performed at 723K since higher temperatures determine a fall off of the SrF_2 growth rate and lower temperatures lead to lower rates. From Eq. 1 and 3, a G_{Bi} / G_{Sr} ratio of 2.2 can be obtained at P_{Sr} / P_{Bi} ratio=0.3

Operating conditions are reported in table 1.

Figure 5 shows the XRD patterns of as-deposited and annealed film. As deposited films consist of Bi_2O_3 and the SrF_2 phases, while no Ta-containing crystalline phases can be detected from the XRD spectrum.

In order to obtain perovskite phase (figure 5), films were annealed for one hour under O_2 at 1073K.

Table 1. Sublimation conditions adopted for SBT deposition

Precursors	Sublimation temperature (K)	Carrier gas (Ar) (sccm)	Partial pressure (mTorr)
$Sr(hfa)_2(tet)$	373	100	0.2
$Bi(C_6H_5)_3$	393	100	0.6
$Ta(OCH_2CH_3)_5$	413	100	1.6

CONCLUSIONS

The deposition kinetics of $Sr(hfa)_2(tet)$ and $Bi(C_6H_5)_3$ have shown that the $Sr(hfa)_2(tet)$ deposition process occurs under reaction rate limited regime below 673K, whilst above this temperature growth rate was mass transport rate limited.

In the 573-773 K temperature range $Bi(C_6H_5)_3$ deposition occurs under reaction rate limited regime. For both precursors, reaction mechanisms involve surface reactions. Simple kinetic equations were obtained assuming that precursor adsorption takes place according to Langmuir isotherm.

The single component kinetic equations have been applied to multicomponent deposition in order to obtain SBT film of correct composition.

Studies on the kinetics of the deposition processes of single component films revealed of interest for both the understanding of reaction mechanisms determining film formation as well as for the optimization of the synthetic route of more complex multicomponent phases.

REFERENCES

1. C.A. Arauyo, J.D. Cuchiaro, L.D. Mcmillan, M.C. Scott and J.F. Scott, Nature **374**, 627 (1995)
2. T.J.Boyle, C.D.Bucheit, M.A.Rodriguez, H.N.Al-Shareef, B.A.Hernandez, B.Scott, and J.W.Ziller, J. Mater. Res., **11,** 9 (1996)
3. S.B.Desu and T.K.Li, Mater.Sci.Eng. **B32**, 562 (1995)
4. S.B.Desu and D.P.Vijay, Mater.Sci.Eng. **B32**, 75 (1995)
5. T.LI, Y.Zhu, S.B. Desu, C.H. Peng, M.Nagata Appl.Phys.Lett. **68,** 5 (1996)
6. H.Funakubo, N. Nukaga, K.Ishikawa, H.Kokubun, H.Machida, K.shinozaki, N.Mizutani, Ferroelectrics 232 (1999)
7. Y. Zhu, S.B. Desu, T. Li, S.Ramanathan, M.Nagata, J. Mater. Res., **12** 3 (1997)
8. M. L. Hitchman, K. F. Jensen, Chemical Vapor Deposition (Eds, M. L Hitchman, K. F. Jensen), Academic Press, London, (1993), p. 6.
9. G. C. Bond, Catalysis by Metals Academic Press, London, (1962), p.126.

Mat. Res. Soc. Symp. Proc. Vol. 655 © 2001 Materials Research Society

PREPARATION AND CHARACTERIZATION OF Ba AND Nb SUBSTITUTED $SrBi_2Ta_2O_9$ COMPOUNDS

Rasmi R. Das, P. S. Dobal, A. Dixit, W. Perez, M.S. Tomar*, R. E. Melgarejo* and Ram S. Katiyar
Department of Physics, University of Puerto Rico, San Juan PR 00931-3343
* Department of Physics, University of Puerto Rico, Mayaguez PR 00681

ABSTRACT

Bi-layered ferroelectric compounds are considered most promising for non-volatile memory applications due to their high fatigue endurance. We have prepared $SrBi_2Ta_2O_9$ powders with Ba (A sites) and Nb (B sites) substitutions using a novel solution based route. The powders were pressed and sintered at 1050°C to obtain high quality targets. Thin films were prepared using these ceramic targets on $Pt/TiO_2/SiO_2/Si$ substrates using pulsed laser deposition (PLD) technique. The effects of growth conditions on phase formation as well as structural and electrical properties in films are studied. Initial results on films show good hysteretic characteristics. Though phase formation begins at much lower temperature, these films crystallize in a complete layered perovskite phase when prepared at 700°C. Optical phonon modes in these materials exhibit systematic variations with changing compositions. The changes in the Raman spectra are explained in terms of Ba and Nb substitutions at A and B sites, respectively. The temperature dependence of Raman spectra exhibits the substitution induced changes in the transition temperatures of these materials.

INTRODUCTION

Due to recent advances in thin film growth technology, the interest in investigating ferroelectric materials has increased manyfold because of their potential applications in memory devices, sensors and actuators, IR detectors, transducers, microwave devices and others [1-3]. Lead zirconate titanate (PZT) is one of the most promising materials for integrated ferroelectric devices, especially for memory applications [4]. Because of imprint and fatal fatigue failure of these ferroelectrics, a new series of compounds so called Bi-layered perovskites, in particular $SrBi_2Ta_2O_9$ (SBT), were proposed by Scott et al [3]. The low leakage current, low operating voltage, fast switching speed and negligible fatigue up to 10^{12} electric cycles are the advantages of layered perovskite for memory applications [5]. The lattice structure of these family of compounds is described by a general formula $(A_{m-1}B_mO_{3m+1})^{2-}(Bi_2O_2)^{2+}$, where A is mono, di, trivalent cation and B is quatro or pentavalent cation and 'm' is the number of perovskite unitcells sandwiched between two bismuth oxide slabs [6]. In case of SBT, m=2, which shows displacive transition from the symmetry I4/mmm to $A2_1am$. In this transition, the Sr ion at the A-site of the pseudoperovskite layer moves towards O-Ta-O octahedral chain, which is the origin of ferroelectricity [7,8].

In this work, we reported the preparation of A and B-site substituted SBT thin films by PLD technique. The effect of replacement of A-site Sr with different Ba concentrations and B-

site Ta by Nb on structural and electrical properties of SBT compounds are studied using x-ray diffraction (XRD), micro-Raman spectroscopy, dielectric and hysteresis measurements.

EXPERIMENTAL DETAILS

Mixed powders of composition $Sr_xBa_{1-x}Bi_2Ta_{2-y}Nb_yO_9$ with y = 0, x = 0.2, 0.5, 0.7, 0.8, 1 and x = 1, y = 2 were synthesized by sol-gel route. The processed powders are pressed to pellets of 2.5 cm diameter each and sintered at 1050 °C for 3h to get densified targets for laser ablation. Thin films of above compounds were grown on $Pt/TiO_2/SiO_2/Si$ substrates using PLD technique. An KrF (λ=248nm) excimer laser with energy density of about 2.5 J/cm^2 and pulse repetition rate of 5 Hz was focused to a rotated ceramic target at 45° angle to the target normal. During deposition the substrate temperature was varied between 500 - 750°C with oxygen pressure at 100 mTorr. Phase formation and crystallographic orientation of the processed powders, as grown and annealed films were identified using X-ray diffractometer (Siemens D 5000) with Cu Kα radiation. Raman spectra were recorded using a "Instruments SA" T6400 spectrograph consisting of a double monochromator coupled to the third stage with 1800 grooves/mm grating in backscattering geometry. The 514.532 nm radiation from a "Coherent" Innova 99 Ar^+ laser was focused over less than 2 μm diameter circular spot using a Raman micro probe with 80X objective. A heater from "Leitz Waltzer" was employed for recording the Raman spectra at higher temperatures. The thickness of the films were measured by filmetrics F 20. All films were top electroded by Au of thickness 200 nm and diameter 500 μm using DC magnetron sputtering. The frequency dispersion of dielectric constant and dissipation factor were examined in the frequency range 1 kHz to 1 MHz with an oscillating voltage 100 mV using HP 4294A impedance analyzer. Hysteresis loops of field dependent polarization were measured at virtual ground mode using Radiant tester RT 6000HVS.

DISCUSSIONS

Thin films of various compositions by changing Ba concentration in SBT compound is shown in Fig 1. All films were deposited at substrate temperature 750°C with ablation pressure of 100 mTorr. A systematic shift of the most intense peak (115) was observed at 29° towards lower diffraction angle with increasing Ba concentration. This confirmed that Ba is replacing Sr that results increase in lattice parameter. Increase of lattice parameter with Ba concentration might be attributed to higher ionic radii of Ba. Splitting of (115) diffraction peak established that the films were crystallized in orthorhombic structure. There was no evidence of pyrochlor phase in the films grown at 750°C.

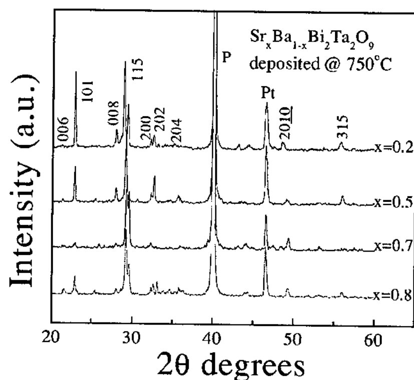

Fig 1. X-ray diffractograms of $Sr_xBa_{1-x}Bi_2Ta_2O_9$ films.

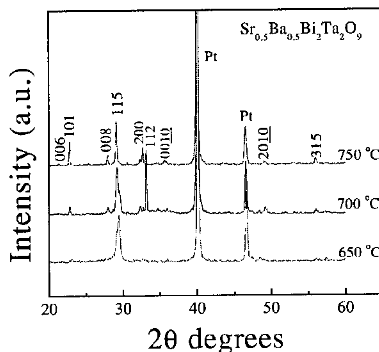

Fig 2: Diffraction Patterns of $Sr_{0.5}Ba_{0.5}Bi_2Ta_2O_9$ films.

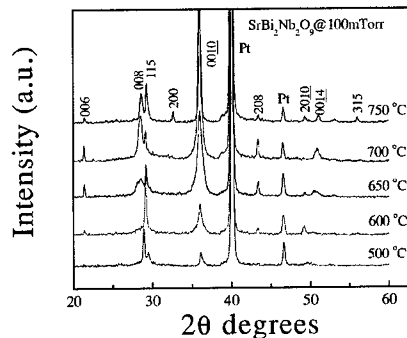

***Fig 3** : X-ray diffraction patterns of SBN film.*

Fig 2 shows the x-ray diffraction patterns of the films ablated from $Sr_{0.5}Ba_{0.5}Bi_2Ta_2O_9$ target at 100 mTorr oxygen pressure and at various substrate temperatures. It was noticed that increasing substrate temperature leads to preferential c-axis orientation, confirmed with the presence of (008) diffraction line. The film deposited at 650°C has broad (115) peak which could be due to smaller grain size. There is a systematic shift of most intense peak (115) towards lower diffraction angle with increasing substrate temperature. This is attributed to thermal stress between the film and the substrate during the growth process. A minor amount of florite phases were observed in the films grown at substrate temperature above 700°C.

$SrBi_2Nb_2O_9$ (SBN) films were prepared at different substrate temperatures from 500-750 °C at ablation pressure of 100 mTorr. θ-2θ scans of the as grown SBN films are given in Fig 3. The c-axis orientation of the films is more pronounced at higher substrate temperatures, which was confirmed by the increasing intensity of (006), (008) and (00<u>10</u>) reflections.

In Fig.4, the room temperature Raman spectra of $Sr_xBa_{1-x}Bi_2Ta_2O_9$ (SBBT) films, grown at 750°C substrate temperature, are shown for x = 0.2, 0.5, 0.7 and 0.8 compositions. The peak frequencies of Raman modes from these films were found similar to those observed in corresponding ceramic compositions. Increasing Ba content in these materials decreases the peak frequencies of A_{1g} mode at 58 cm^{-1} and E_g mode at 163 cm^{-1} originating from Bi(z) and Ta(x-y) vibrations, respectively [9]. The frequency of 830 cm^{-1} mode that originates from the symmetric stretching of TaO_6 octahedra does not involve Ba or Sr atoms. However, the frequency of

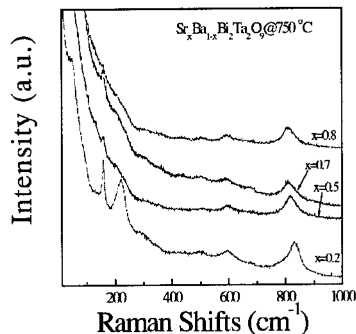

***Fig 4.** Room temperature Raman spectra of SBBT films deposited at 750 °C.*

this mode increases with increasing Ba composition. Such behavior could be associated with the mass and ionic radii differences of Ba and Sr atoms that influence the environment and hence the force constant.

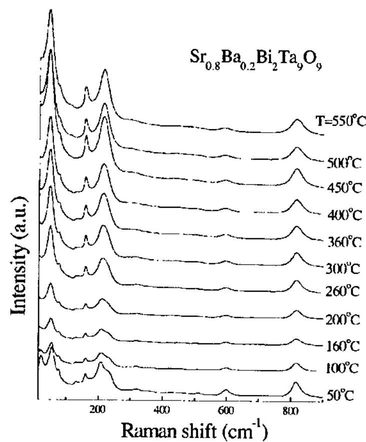

Fig 5. Temperature dependent Raman spectra of SBBT sample at x = 0.8.

Temperature variation of Raman spectra from $Sr_xBa_{1-x}Bi_2Ta_2O_9$ (SBBT) compositions was studied. As shown in Fig. 5, the 28 cm^{-1} mode, which exhibits very strong dependence on A site composition, disappears about 200 °C. The overall mode intensity does not show drastic variation at orthorhombic to tetragonal phase transition. However, the 58 cm^{-1} mode softening stops in the tetragonal phase. This behavior can be seen in Fig. 5 where the mode frequency remains constant above orthorhombic to tetragonal phase transition at about 300°C from x = 0.8 composition sample.

Micro-Raman spectroscopy was also utilized to study the B-site substitution in layered compounds. Room temperature Raman spectra of as-grown SBN films are shown in Fig 6. Increasing substrate temperature results in better crystallization of ablated material that can be seen through relatively intense and sharper features in the Raman spectra of 750°C prepared film. Annealing the as-grown films at temperatures equal to their growth temperature did not reveal any significant improvement in the crystallization. The films prepared at 700°C (Fig. 6) and annealed at the same temperature (Fig. 7) show identical features in the Raman spectra. However, improved crystallinity was observed when these films were annealed at higher temperatures.

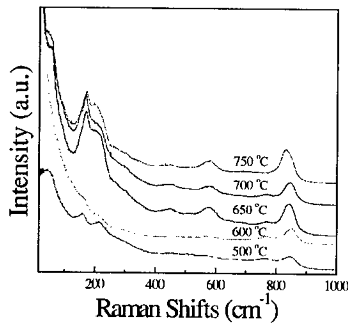

Fig 6. Micro-Raman spectra of as grown SBN films at various substrate temperatures.

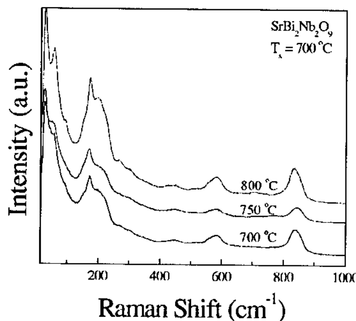

Fig 7. Room temperature Raman spectra of SBN films annealed at different temperatures.

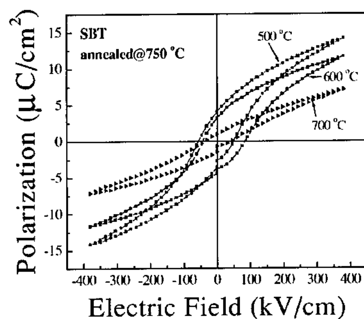

Fig 8: Hystresis loops of SBT films annealed at 750 °C.

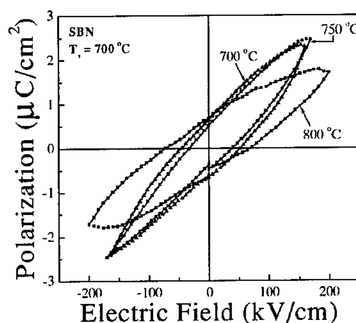

Fig 9: P-E hystereis loops of SBN films deposited at 700 °C.

Figure 8 shows the typical hysteresis loops for SBT films grown at 500, 600, 700°C and annealed at 750°C for 1h in oxygen ambient. The films deposited at 500 °C show relatively better ferroelectric properties such as maximum polarization (P_m = 14.2 μC/cm^2), remanent polarization (P_r = 4.3 μC/cm^2) and the coercive field (E_c ~ 50 kV/cm. The films deposited at 700 °C show weak ferroelectric properties (P_m = 7.3μC/cm^2), (P_r = 1μC/cm^2) and the coercive field (E_c ~ 50 kV/cm). The film deposited at 600°C showed E_c = 85 kV/cm. These observations suggest that polarization value decreases with increasing substrate temperature. This is attributed to increase of preferential c-axis orientation with increasing growth temperature.

Effect of annealing on ferroelectric properties of SBN films was examined. Fig 9 shows the P-E hysteresis loops of SBN films deposited at 700°C and annealed at different temperatures. The films show maximum polarization $2P_m$ (~ 4.6, 5 and 3.6 μC/cm^2), remanent polarization $2P_r$ (~ 1.25, 1 and 1.5 μC/cm^2) and coercive field E_c (51, 37 and 67 kV/cm) at annealing temperatures 700, 750 and 800°C, respectively. This small value of polarization is expected due to highly c-axis oriented films as explained in x-ray diffraction results of the films.

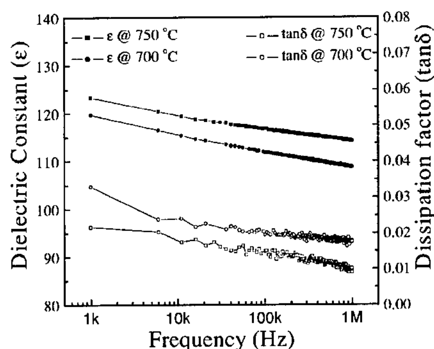

Fig 10: Dielectric dispersion characteristic curves of SBN films deposited at 700 °C, annealed at 700 and 750 °C.

Frequency dependent dielectric constant and dissipation factor of SBN films deposited at 700 °C and post annealed at 700 and 750°C are plotted in Fig 10. The film annealed at 750°C has dielectric constant about 115 and loss factor 0.009 at 100 kHz,

whereas the film annealed at 700°C has dielectric constant about 110 with loss tangent 0.018. Relatively high value of dielectric constant with low loss factor in 750°C annealed film is attributed to larger grain size of the films.

CONCLUSION

Ba and Nb substituted $SrBi_2Ta_2O_9$ ceramics were processed using a novel solution based route. Thin films were deposited from these ceramic targets on $Pt/TiO_2/SiO_2/Si$ substrates using PLD technique. The effects of growth conditions on crystallization as well as structural and electrical properties in films were investigated. Initial results of films show good hysteretic characteristics. Though phase formation begins at much lower temperature, these films crystallize in a complete layered perovskite phase when prepared at 700°C, established via micro-Raman studies. Increase of SBT lattice parameter with Ba concentration confirmed the substitution at A-site. A systematic variation of optical phonon modes at 58 cm^{-1} (A_{1g}), 163 cm^{-1} (E_g) and 830 cm^{-1} with the change in compositions is attributed to the mass and ionic radii of cations. Substitution induced changes in transition temperatures of these materials show that, transition temperature is inversely proportionate to ionic radii of cations. Effect of doping in SBT is reducing ferroelectric and dielectric properties of these materials. Detailed correlation of structural and electrical properties are under active investigation.

ACKNOWLEDGEMENT

This work is supported in parts by DAAG55-98-1-0012, NASA-NCC5-518, NSF-DMR 9801759 grants.

REFERENCES

1. J.F. Scott and C.A. Paz de Araujo, *Science* **246**, 1400, (1989).
2. J.F. Scott, *Ferroelectrics Review*, **1**, 1, (1998).
3. R. Watton, *Integ. Ferroelec.*, **4**, 175, (1994).
4. C. K. Kowk, D. P. Vijaya, S.B. Desu, N. R. Parikh and E.A. Hilll, *Integ. Ferroelec.*, **3**, 121, (1993).
5. S. Bhattacharyya, S.S.N. Bharadwaja, and S.B. Krupanidhi, *Appl. Phys. Lett.*,**75**, 2656 (1999).
6. E.C. Subbarao, *J. Phys. Chem. Solids*, **23**, 665, (1962).
7. Y. Shimakawa, Y. Kubo, Y. Nakagawa, S. Goto, T. Kamiyama, H. Asano and F. Izumi, *Phys. Rev.*, **B 61**, 6559, (2000).
8. Y. Shimakawa and Y. Kubo, Y. Nakagawa, T. Kamiyama, H.Asano and F. Izumi., *Appl. Phys. Lett.*, **74**, 1904, (1999).
9. R.E. Melgarejo, M.S. Tomar, P.S. Dobal and R.S. Katiyar, *J. Mater. Res.*, **15**, 1661, (2000).

Mat. Res. Soc. Symp. Proc. Vol. 655 © 2001 Materials Research Society

Role of the Electrode Morphology, Thickness and Orientation in the Ferroelectric Performance of Epitaxial $Pb(Zr,Ti)O_3$ Thin Films

Cesar Guerrero, Florencio Sánchez, José Roldán, Frank Güell[1], María V. García-Cuenca, Cesar Ferrater and Manuel Varela
Universitat de Barcelona, Departament de Física Aplicada i Òptica,
Av. Diagonal 647, E-08028 Barcelona, SPAIN
[1]Universitat Rovira i Virgili, Lab. Física Aplicada i Cristal·lografia,
E-43005 Tarragona, SPAIN

ABSTRACT

A comparison of pulsed laser deposited $PbZr_{0.53}Ti_{0.47}O_3$ (PZT) thin film capacitors with $SrRuO_3$ (SRO) and $LaNiO_3$ (LNO) electrodes on (001) yttria-stabilized zirconia (YSZ) and lattice matched (001) $LaAlO_3$ substrates is presented. Both electrode materials allow for the formation of ferroelectric capacitors with large remnant polarization (20-30 $\mu C/cm^2$) and negligible fatigue, although slight differences arise regarding the promotion of either the rhombohedral or tetragonal phases of PZT. Far more crucial seems to be the tendency of $SrRuO_3$ to develop a rougher surface at either small (<30 nm) or large thickness (>100 nm), and on YSZ substrates. In those cases a highly defective and possibly low dielectric interface forms between the electrode and the ferroelectric layer, resulting in greatly degraded ferroelectric performance. $LaNiO_3$ is free from these limitations except for the cracks forming at very large thickness (>300 nm), and therefore appears as a more versatile electrode material.

INTRODUCTION

Ferroelectric thin films are of great interest for a wide range of applications such as pyroelectric and piezoelectric sensors, microwave devices, microactuators, and most remarkably, non-volatile random-access memories (NVRAMs) [1]. One of the most popular ferroelectric materials is $PbZr_xTi_{1-x}O_3$ (PZT) in the vicinity of the morphotropic phase boundary ($x \approx 0.53$), where the bulk ceramics show a maximum in the remnant polarization to coercive field ratio [2]. Early efforts on the fabrication of PZT capacitors with platinum electrodes ultimately showed that fatigue degradation -i.e. loss of remnant polarization with cumulative switching- is practically impossible to overcome. The origins and mechanisms of fatigue are still controversial, thought it seems related to accumulation of oxygen vacancies at the electrode/ferroelectric interface, as was first suggested by the discovery that epitaxial capacitors with superconducting $YBa_2Cu_3O_7$ electrodes do not show significant fatigue [3]. It is commonly acknowledged now that oxide electrodes are indispensable to obtain fatigue-free $PbZr_xTi_{1-x}O_3$ capacitors. Simple oxides like RuO_2 and IrO_2 are desirable from the point of view of device fabrication, but they are not particularly well suited for the fabrication of pure perovskite PZT. Therefore, growing attention has been paid to a few conductive oxides of the perovskite family, chiefly $La_{0.5}Sr_{0.5}CoO_3$ [4] and to a lesser extent $SrRuO_3$ [5] and $LaNiO_3$ [6]. All these materials show electrical resistivities of a few hundred $\mu\Omega \cdot cm$ and have been used to fabricate fatigue-free PZT thin film capacitors. However, clear criteria for the choice of the electrode material have not given yet. In this work, we report on the comparison of the microstructure and ferroelectric properties of PZT capacitors with $SrRuO_3$ and $LaNiO_3$ electrodes on $LaAlO_3$ (001) and YSZ (001) substrates.

EXPERIMENTAL DETAILS

The thin film heterostructures were deposited by pulsed laser deposition with a 248 nm KrF excimer laser at a 10 Hz repetition rate and a 1.8 J/cm^2 fluence. High-density ceramic targets with nominal compositions $SrRuO_3$, $LaNiO_3$, and $Pb_{1.1}Zr_{0.53}Ti_{0.47}O_3$ were used to fabricate SRO/PZT/SRO and LNO/PZT/LNO capacitors. The optimum deposition parameters for each material were determined previously [6-8], and are detailed in Table I. The top electrodes were deposited at relatively low temperature and high oxygen pressure in order to minimize damage to the underlying ferroelectric film. Arrays of 0.7×0.7 mm^2 parallel plate capacitors were defined by depositing the top electrodes through a laser-patterned alumina foil mask, placed almost in contact with the substrate. The crystalline structure of the films was studied with a four-circle X-ray diffractometer with CuKα radiation whereas their morphology was observed by scanning electron microscopy (SEM) and atomic force microscopy (AFM). Transmission electron microscopy (TEM) analysis of selected samples was also performed. Polarization-electric field hysteresis loops were measured with a Sawyer-Tower circuit; measurements of polarization fatigue in the PZT layer were conducted by means of the pulse-switching technique.

Table I. Deposition parameters and layer thicknesses of the PZT capacitors in this study.

	Temperature (°C)	O_2 pressure (mbar)	Thickness (nm)
Bottom Electrode	725 (SRO) 650 (LNO)	0.1	20-400
PZT	600	0.34	200-300
Top Electrode	600	0.2	200

RESULTS AND DISCUSSION

XRD profiles of representative samples are shown in Figure 1. The samples grown on $LaAlO_3$ perovskite substrates show the usual cube-on-cube epitaxy. Narrow phi scan peaks (not shown here, FWHM ~1.0°) and (002) rocking curves (0.3-0.6° for the PZT layers) are indicative of high crystalline quality. Due to the non-cubic nature of both $SrRuO_3$ (orthorhombic) and $LaNiO_3$ (rhombohedral), and the formation of domain patterns, the corresponding rocking curves usually have the anomalous shapes shown in the insets of Figure 1a. In both cases the PZT rocking curves are gaussian-like single peaks, in appearance not influenced by the domain patterns of the underlying electrodes.The 2θ positions of the

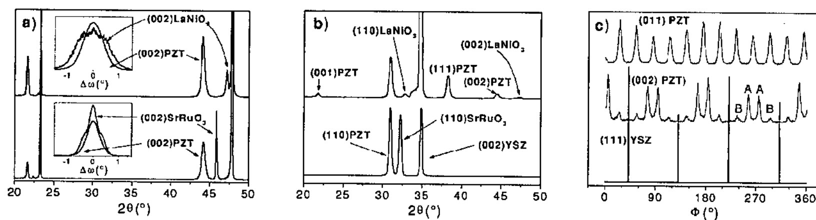

Figure 1. XRD profiles of the PZT capacitors. **a)** 2θ scans of the samples on $LaAlO_3$ and (inset) (002) rocking curves. **b)** 2θ scans of the samples on YSZ. **c)**: Φ-scans of the samples on YSZ; top: (011)-family of reflections of the (111) oriented PZT crystallites on LNO/YSZ; center: (002)-type reflections of the (110) oriented crystallites on either SRO/YSZ or LNO/YSZ; bottom: (111)-type reflections of the YSZ substrate

PZT (002) reflections (44.0° on LNO, 44.4° on SRO), combined with measurements of out-of plane (103) and (301) reflections, as well as reciprocal lattice mapping of the (303) and (002) areas lead to the conclusion that the PZT grown on SRO is rhombohedral with a=4.07 Å, while on LNO it is tetragonal (a=4.05 Å, c=4.09 Å), fully oriented with the *c* axis parallel to the growth direction. The phase stability near the morphotropic phase boundary is greatly affected by biaxial stress [9]. Therefore, differences in thermal and mismatch related stress should be responsible for the differences in the phase formation in the PZT layer. The presence of a domain pattern in the bottom electrode may also play a role by disrupting of the crystalline order and thus modifying the stress field. It is worth noting that the phase stability can be tuned by modifying the deposition parameters, e.g. tetragonal PZT can be obtained on $SrRuO_3$ when deposited at higher substrate temperatures (750°C), although in that case the samples do suffer from extensive lead deficiency.

The samples deposited onto YSZ substrates show different crystalline orientation depending on the electrode material (Fig. 1b). The SRO/PZT/SRO heterostructures are (110) oriented, which is geometrically favorable because the lattice parameter of YSZ (cubic, a=5.14 Å) is approximately √2 times larger than the pseudo-cubic lattice parameter of SRO (a≈3.93 Å). Two different families of crystallites appear according to their in-plane arrangement, namely those with the [-110] direction of the films aligned with either [110] or [120] of the substrate (A-type and B-type peaks, respectively, in the Φ-scan of Figure 1c). In spite of the similar lattice parameter (a_{LNO}≈3.83 Å), the LNO/PZT/LNO heterostructures are preferentially (111) oriented. There are also (110) oriented crystallites, but they must be minority as the peak height ratio is (I_{110}/I_{111} ~7) for bulk PZT [PDF 33-784]. Both (110) and (111) families of crystallites are epitaxially grown on the substrate, as can be deduced by the Φ-scans of Figure 1c.

The morphology and microstructure of the PZT films are heavily dependent on those of the bottom electrode, which, in turn, are influenced by the nature of the electrode material itself, as well as by the deposition conditions, substrate, and thickness. SEM images of representative samples grown on $LaAlO_3$ and YSZ with different electrode thickness are shown in Figures 2 and 3. For both electrodes, an electrode thickness around 60 nm is adequate to achieve a flat surface (Fig. 2d and 3d) with roughness below 1 nm (measured by AFM) and optimum electrode resistivity (~150 μΩ·cm) [6,8]. Deviation from the optimum thickness derives in undesirable effects, which are much more pronounced in the case of $SrRuO_3$. The $SrRuO_3$ films thinner than ~30 nm are non-continuous but composed of square grains (size 120 nm) forming a tile-like pattern (Fig. 3e), similar to that reported by Satyalakshmi et al. [10]. This is the cause of very poor electrical conductivity and, most importantly, this non-continuous morphology propagates upwards to the ferroelectric film (Fig. 3b), resulting in short-circuited capacitors. Very thick SRO electrodes (>100 nm) are also inadequate as small hillocks (10-20 nm high, 300 nm in diameter) develop. The resulting surface roughness (3-6 nm measured by AFM), is high enough to originate a very poor electrode- ferroelectric interface (as shown in the bright-field TEM image in Figure 4a), because of the particular deposition conditions: high oxygen pressure (resulting in low adatom mobility because of the gas-phase collisions in the ablation plume) and high deposition ratio (1 nm/sec). Both conditions are required to minimize lead reevaporation and achieve correct stoichiometry in the films because the target ($Pb_{1.1}Zr_{0.53}Ti_{0.47}O_3$), is only slightly lead enriched. The $LaNiO_3$ films show a far wider useful thickness range, as films in the 20-300 nm range show flat surface (rms roughness of a few Å) and low electrical resistivity (~150 μΩ·cm). Figure 4b shows the clean interface formed between PZT and a 200 nm $LaNiO_3$ bottom electrode. Thicker films, however, may develop cracks (Fig. 3e), which disturbs the growth of the PZT film (Fig. 3b) and increases the electrode resistivity [6].

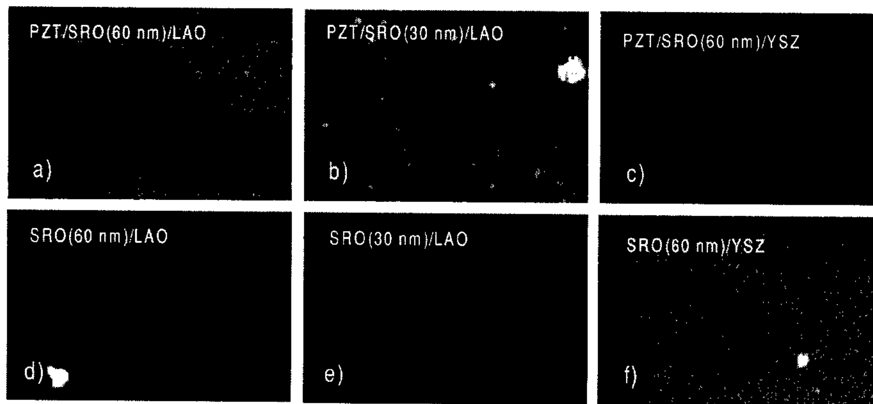

Figure 2. SEM micrographs of various PZT samples with $SrRuO_3$ electrodes

SEM images of representative samples grown on YSZ with a bottom electrode thickness of 60 nm are shown in Figures 2c, 2f, 3c and 3f. The SRO films are composed of rounded grains with a typical size of 90 nm, the same as the overgrowing PZT film. LNO forms a much smoother surface without a distinct granular structure. The PZT grown on this surface forms small grains averaging under 60 nm. Again, the roughness of the surface of the electrode plays a determinant role as the PZT films on SRO, in spite of their epitaxial growth and larger grain size, do not show measurable ferroelectricity, while the small-grained polycrystalline films on flat LNO present the well shaped hysteresis loops shown in Figure 5a.

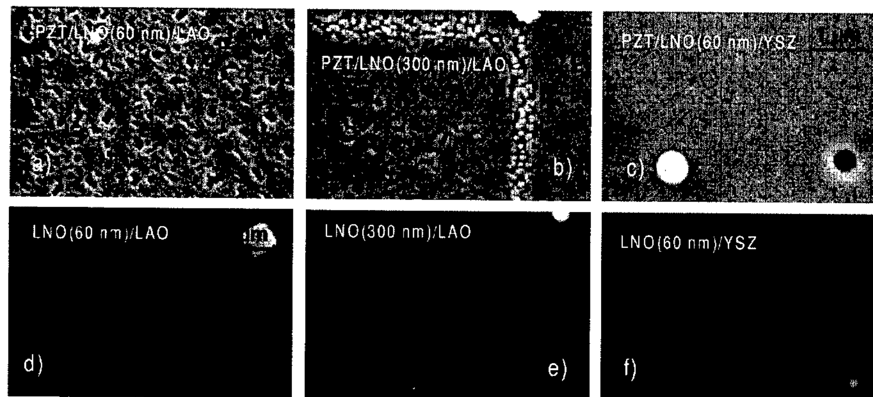

Figure 3. SEM micrographs of various PZT samples with $LaNiO_3$ electrodes

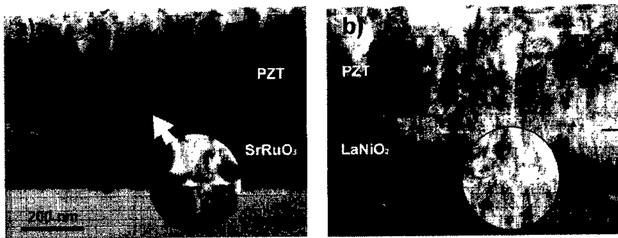

Figure 4. a) Bright-field TEM micrograph of a PZT sample on $LaAlO_3$ with 250 nm $SrRuO_3$ bottom electrode. **b)** Image of a PZT sample on $LaAlO_3$ with 200 nm $LaNiO_3$ electrode. Each inset shows a closer view of the ferroelectric-electrode interface.

The remnant polarization, ~20 $\mu C/cm^2$ is somewhat lower than in the epitaxial LNO/PZT/LNO capacitor on $LaAlO_3$ (30 $\mu C/cm^2$), the latter having a better alignment of the polar axis with the applied field. The voids between PZT grains that can be observed on Fig. 2a (and also on Fig 3a) do not seem to be detrimental to the performance of the capacitor, because these voids do not propagate downwards to the bottom electrode (Fig 4b). The SRO/PZT/SRO(60 nm)/$LaAlO_3$ capacitors have remarkably lower coercive field and slightly lower remnant polarization (25 $\mu C/cm^2$, Fig 5b) than their LNO counterpart. This is typical of rhombohedral versus tetragonal PZT. The sample in Fig 4a, grown on rougher SRO, has much lower remnant polarization (6.5 $\mu C/cm^2$), also shown in Fig. 5b. In all the samples the dependence of the coercive field with the frequency of the 20 V_{p-p} triangular measuring signal is of the kind $f = f_0 e^{-\gamma/E_c}$(Fig 6a), first reported by Wieder [11] for $BaTiO_3$ single cristals. The activation field γ has low values of 250-300 kV/cm irrespective of the electrode type, indicative of very fast switching behavior. Fatigue tests were also performed by means of the pulse switching technique [12], where double bipolar square pulses are applied to the capacitor, and the transient currents flowing through a series resistor are recorded, so that polarizations can be calculated by integration of these currents. Square ±10 V, 40 kHz pulses were used to fatigue the capacitors. All the samples were virtually fatigue-free at least up to 10^{10} switching cycles (Fig 6b). No clear dependence of the fatigue behavior on the electrode type and condition was observed.

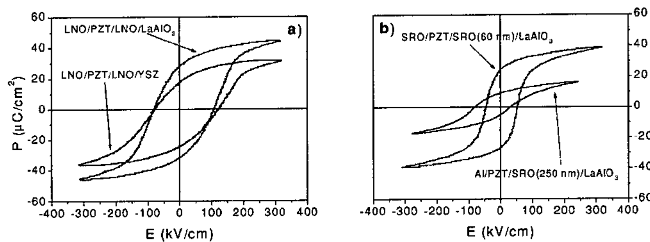

Figure 5. P-E Hysteresis loops of representative PZT capacitors.

CONCLUSIONS

PZT thin film capacitors with $SrRuO_3$ (SRO) and $LaNiO_3$ (LNO) electrodes were studied. Flat bottom electrodes allowing good electrical performance of the capacitor are readily obtained with $LaNiO_3$ on YSZ and $LaAlO_3$ substrates in a wide thickness range (20-300 nm). $SrRuO_3$ is more prone to develop

surface roughness, but when the thickness is kept around an optimum value of ~60 nm, it allows to prepare high-quality rhombohedral PZT in the vicinity of the morphotropic phase boundary with very low coercive field (40 kV/cm at 10 Hz). Both electrode materials effectively suppress ferroelectric fatigue.

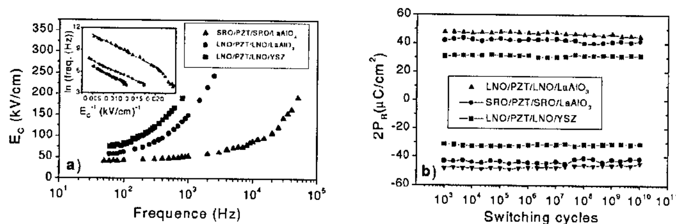

Figure 6. a) Frequence dependence of the coercive field. The activation field γ is the slope of the ln(frequence) versus E_C^{-1} plot. **b)** Switching endurance of the PZT capacitors.

ACKNOWLEDGEMENTS

Financial support by the CICYT of the Spanish Government (Project MAT99-0984) is acknowledged. This work has been supported by the Comissionat per a Universitats i Recerca of the Departament de Presidència de la Generalitat de Catalunya.

REFERENCES

1. J.F. Scott, C.A. Paz de Araujo, Science 246 (1989) 1400.
2. B. Jaffe, W.R. Cook, Jr., H. Jaffe, Piezoelectric Ceramics, Academic Press, New York, 1971.
3. R. Ramesh, W.K. Chan, H. Gilchrist, B. Wilkens, T. Sands, J.M. Tarascon, V.G. Keramidas, J.T. Evans, F.D. Gealy, D.K. Fork, Mat. Res. Soc. Symp. Proc. 243 (1992) 477.
4. O. Auciello, R. Dat, R. Ramesh, Ferroelectric Thin Films: Synthesis and Basic Properties, in: C.A. Paz de Araujo, J.F. Scott, G.W. Taylor (Eds.), Gordon and Breach, Amsterdam, 1996, pp. 525-565.
5. C.B. Eom, R.B. Van Dover, J.M. Phillips, D.J. Werder, J.H. Marshall, C.H. Chen, R.J. Cava, R.M. Fleming, D.K. Fork, Appl. Phys. Lett. 63 (1993) 2570.
6. F. Sánchez, C. Ferrater, C. Guerrero, M.V. García-Cuenca, M. Varela, Appl. Phys. A 71 (2000) 59.
7. C. Guerrero, C. Ferrater, J. Roldán, V. Trtík, F. Benítez, F. Sánchez, M. Varela, Appl. Surf. Sci. 154-155 (2000) 500-507.
8. J. Roldán, F. Sánchez , V. Trtík , C. Guerrero, F. Benítez, C. Ferrater, M. Varela Appl. Surf. Sci. 154-155 (2000) 159.
9. S. Oh, H. M. Jang, Appl. Phys. Lett. 72, (1998) 1457.
10. K.M. Satyalakshmi, N.D. Zakharov, D. Hesse, G. Koren, Mat. Res. Soc. Symp. Proc. 541 (1999) 167.
11. H.H. Wieder J. Appl. Phys. 28 (1957) 367.
12. P.K. Larsen, R. Cuppens, G.J.M. Dormans, Pulse Switching Characterization of Ferroelectric Thin Films. In:Auciello O., Waser R., editors. Science and Technology of Electroceramic Thin Films. Dordrecht: Kluwer Academic Publishers, 1995, p201.

BST for DRAM and Gate Dielectrics

Mat. Res. Soc. Symp. Proc. Vol. 655 © 2001 Materials Research Society

THE EFFECT OF FORMING GAS ANNEALING ON Pt/(Ba,Sr)TiO_3/Pt THIN FILM CAPACITORS FOR FUTURE DRAM APPLICATIONS: ELECTRICAL PROPERTIES AND DEGRADATION MECHANISMS

J. D. Baniecki*#, C. Parks*, R.B. Laibowitz***, T. M. Shaw***, J. Lian**
*IBM Microelectronics, Semiconductor R&D Center, 1580 Route 52, Hopewell Junction, NY 12533
**Infineon Technologies, 1580 Route 52, Hopewell Junction, NY 12533
***IBM Research Div, Yorktown Heights, NY 10598
#Present address: Fujitsu Laboratories, Atsugi, Japan

ABSTRACT

We have used electrical characterization and secondary ion mass spectroscopy (SIMS) to investigate the influence of hydrogen or deuterium (H/D) on the degradation of the electrical properties of Pt/$Ba_{0.7}Sr_{0.3}TiO_3$/Pt thin film capacitors after forming gas exposure. Deuterium SIMS depth profiling shows that high deuterium concentrations can be incorporated into Pt/BSTO/Pt capacitors after forming gas annealing. The increase in H/D concentration in the film is accompanied by an increase in the leakage and dielectric relaxation current density. Voltage offsets in the capacitance-applied voltage (C-V_A) characteristics after forming gas exposure at lower temperatures (20 °C) and a suppression in the capacitance density near zero applied D.C. bias after forming gas exposure at higher temperatures, suggests that one effect of forming gas exposure to Pt/BSTO/Pt thin film capacitors is to introduce positive space charge into the BSTO film. Using an equivalent model for a ferroelectric thin film capacitor, which incorporates lower permittivity interfacial layers and a nonlinear electric field-electric displacement relationship for the film interior, the effects of a uniform distribution of positive space charge on the theoretical C-V_A and current density applied voltage (J-V_A) characteristics are investigated. It is shown the model can account for many of the observed changes that occur in the experimental C-V_A and J-V_A characteristics after forming gas exposure.

INTRODUCTION

Integration of a high dielectric constant material into a standard CMOS process flow subjects the capacitor to various ambients during processing that may degrade the electrical properties of the capacitor. One important consideration is the effect of forming gas, which is commonly used to control SiO_2/Si interface states, on the capacitance density and leakage currents of Pt/BSTO/Pt thin film capacitors. Many groups have studied the influence of forming gas exposure on the electrical properties of high dielectric constant thin film capacitors [1-11]. Most studies [4-8,11] have shown that annealing unpassivated Pt/BSTO/Pt thin film capacitors in forming gas results in a decrease in capacitance density and large increases in both leakage and dielectric relaxation currents rendering the capacitors unsuitable for DRAM applications. While it is fairly well established that catalytic metal electrodes, such as Pt, enhance the degradation in electric properties observed after forming gas annealing [1-3], the mechanism responsible for lower capacitance density and higher leakage currents after forming gas exposure is less understood. This study uses deuterium SIMS depth profiling and electrical characterization to investigate the mechanisms responsible for the reduction in capacitance density and increase in leakage current density that are often observed after exposing Pt/BSTO/Pt thin film capacitors to forming gas.

EXPERIMENT

Polycrystalline $Ba_{0.7}Sr_{0.3}TiO_3$ thin films were prepared by metal-organic chemical vapor deposition (MOCVD) [12]. The MOCVD BSTO thin films were deposited on Si/SiO_2 substrates

with sputter deposited Pt base electrodes. Top Pt electrodes were formed by either sputtering a blanket metal layer and patterning by photolithography or by electron-beam evaporation through a shadow mask. After the top electrode deposition samples were annealed in 1 atm O_2 at 550C for 15 minutes. The samples were then placed in flowing forming gas (95% Ar 5% H_2 or D_2) at room temperature or 400 °C for 20 minutes. Electrical measurements were used to characterize the complex capacitance, C-V_A, relaxation currents, and leakage current of the films. The impedance and C-V_A characteristics of the capacitors were measured using an HP4194A impedance gain phase analyzer. C-V_A curves were recorded with an A.C. oscillation level of 50 mV and frequency of 100 kHz. Current measurements were made using an HP4140B pico ammeter. A voltage step technique, which consisted of stepping the voltage in equally spaced voltage increments up to the maximum value, was used to measure the steady state leakage currents. At low voltages or temperatures longer hold times (typically 100-1000 sec) were necessary to reveal the leakage current while at higher voltages and temperatures shorter hold times (typically 2-10 sec) were applied to minimize resistance degradation behavior which was observed at longer voltage stress times. Deuterium SIMS depth profiling was used to determine the approximate deuterium/hydrogen concentration in the films. SIMS depth profiling was carried out on a Cameca 5F using a 14.4 keV Cs^+ primary beam and negative secondaries. Deuterated forming gas was used to increase the signal to background ratio. Hydrogen and deuterium forming gas exposure produced similar degradation in electrical properties. Information on the approximate deuterium concentration in the BSTO thin films was provided by a SIMS calibration standard made by implanting a known quantity of deuterium in the film.

RESULTS and DISCUSSION

Current-Time and Current-Applied Field Characteristics

Figure 1 shows the charging characteristics for a 30 nm BSTO thin film capacitor with Pt electrodes that has been exposed to forming gas at 400 °C for 20 minutes over the applied voltage range of 0 to 3 volts. The voltage step was 0.2 volts. The time dependence of the charging characteristics is similar to that observed for BSTO thin film capacitors without forming gas exposure [12]. At lower applied voltages a transient (polarization) current which follows a power law dependence, $J = J_o t^{-n}$ with $n \approx 1$, is observed and at sufficiently long times a steady state

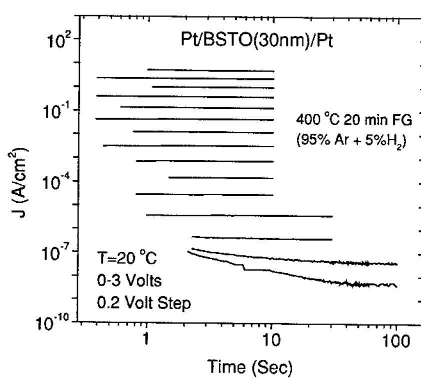

Fig. 1 Charging currents for a 30 nm MOCVD BSTO capacitor with Pt electrodes annealed at 400 C for 20 minutes in forming gas.

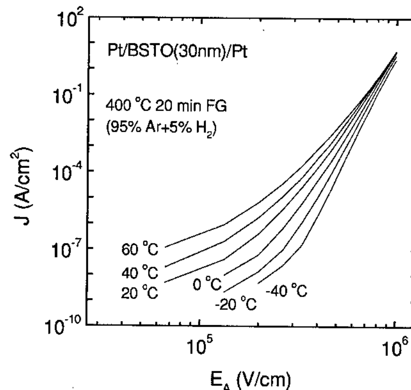

Fig. 2 Steady state current density - applied field characteristic for the same 30 nm MOCVD BSTO capacitor as shown in Fig. 1.

leakage current is approached. If the capacitor is shorted through the ammeter, a discharging current equal in magnitude but opposite in sign to the polarization current, flows from the capacitor [7]. At higher applied fields the charging currrents quickly approach a steady state value and no or very little initial transient current is observed. In addition to a power law polarization/depolarization current with power law exponent $n \approx 1$, in some cases the leakage current was observed to steadily decrease over several decades of time following a power law dependence with power law exponent n << 1. Unlike the polarization/depolarization currents this transient current was not recovered if the capacitor was shorted through the ammeter. In samples without forming gas exposure, this behavior has been attributed to charge trapping were the distribution and density of traps depends on film microstructure, texture, electrode deposition technique, and post electrode annealing treatments [13]. For the sample shown in Fig. 1, a strong time dependent leakage current at higher fields is not observed over the applied temperature (-40 to +60 °C) and time measurement (1-100 sec) interval.

Fig. 2 shows the charging current density versus applied field for the same 30 nm as shown in Fig. 1. For a given voltage the leakage current density was determined by waiting for times sufficiently long so that the charging current density approaches a steady value. As shown in Fig 2., the temperature dependence of the $J - E_A$ characteristic dramatically changes over the applied field range. At low applied fields a pronounced temperature dependence is observed, while at higher applied fields the current density becomes much less temperature dependent. The $J - E_A$ characteristic shown in Fig. 2 differs markedly from those reported for Pt/BSTO/Pt capacitors with out forming gas exposure [14-15] were the high field regime typicaly exhibits a stronger temperature dependence than that shown in Fig 2. The high field regime in Pt/BSTO/Pt capacitors with out forming gas has been reasonably fit to thermionic emission [14-15] or thermionic field emission models [16-17] where electron emission occurs by thermionic emission over an interfacial Schottky barrier or by electron tunneling at energies near the conduction band edge, respectively. In the following, we show that the data in Fig 2. can be successfully interpreted in terms of electron tunneling through the interfacial Schottky barrier.

Space Charge Accumulation in Pt/BSTO/Pt Thin Film Capacitors

Tunneling can dominate the charge transport process in Pt/BSTO/Pt thin film capacitors annealed in forming gas due to strong band bending in the film. As discussed below, the strong band bending results from high space charge concentrations introduced into the films during

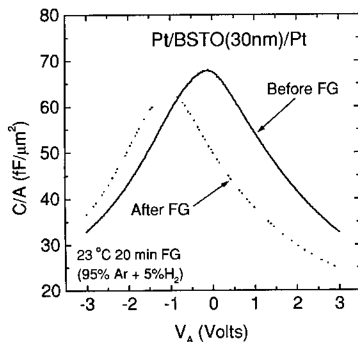

Fig. 3 C-V characteristics of a Pt/BSTO/Pt thin film capacitor prior to and after room temperature forming gas exposure

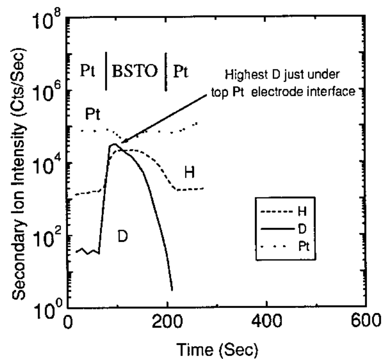

Fig. 4 SIMS depth profiles of deuterium and hydrogen for a Pt/BSTO/Pt thin film capacitor exposed for 20 minutes to forming gas at room temperature.

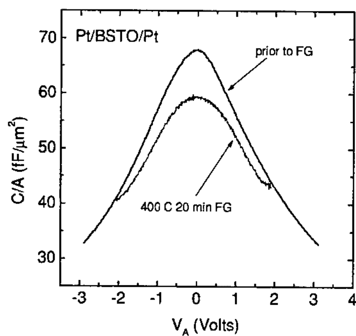

Fig. 5 C-V charcteristics of a Pt/BSTO/Pt thin film capacitor prior to and after a 400 C 20 minute forming gas exposure.

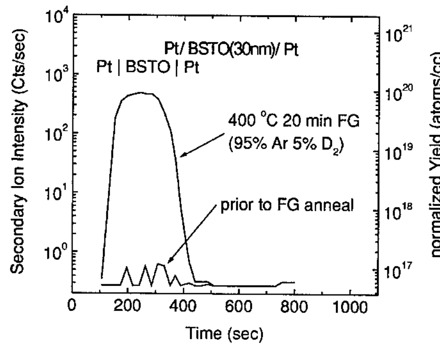

Fig.6 Deuterium SIMS depth profiles before and after a 400 C 20 minute forming gas (95% Ar + 5%D2) exposure. The approximate concentration (normalized yield) is also given.

forming gas exposure. Evidence that space charge is introduced into BSTO thin film capacitors during forming gas exposure can be obtained by comparing the C-V_A characteristics prior to and after forming gas exposure. Fig. 3 shows the C-V_A characteristic after a 20 minute room temperature (23 °C) forming gas exposure for a 30 nm MOCVD BSTO thin film capacitor with Pt electrodes. In addition to a suppression in peak capacitance, a large voltage offset (-1V) is observed in the C-V_A characteristic. The negative voltage shift is consistent with a non-uniform distribution of positive charge in the film peaked near the top Pt/BSTO interface or a negative charge distribution peaked near the BSTO/Pt bottom interface. In order to determine if the charge present in the film is due to the presence of hydrogen (H), either by incorporation of H into the film or by hydrogen induced reduction, deuterium SIMS depth profiling was used to determine the approximate distribution of D/H in the film. Fig. 4 shows the SIMS depth profiles for D and H for a 30 nm BSTO capacitor with Pt electrodes after a 20 minute room temperature deuterium forming gas (95% Ar 5% D_2) exposure. As shown in Fig. 4, a non-uniform distribution of D exists in the film which is peaked near the top Pt/BSTO interface. In addition to the non-uniform D distribution, a more homogeneous distribution of H is also observed. This H is present in the as deposited BSTO films and may be incorporated during film growth from the metal-organic precursors used in the MOCVD process. The deuterium SIMS depth profile is consistent with the shifts in the C-V_A characteristics if the deuterium is positively charged or if deuterium induced reduction (creation of positively charged oxygen vacancy defects) of the top Pt/BSTO interface has occurred.

In contrast to the room temperature forming gas exposures, annealing Pt/BSTO/Pt thin film capacitors at 400 °C in forming gas results in little voltage offset but a suppression in capacitance density at lower applied fields. Fig. 5 shows the C-V_A characteristics for a 30 nm MOCVD BSTO thin film capacitor after annealing at 400 °C for 20 minutes in forming gas. As shown in Fig. 5, the C-V_A characteristic exhibits a small voltage offset but a marked suppression in peak capacitance density near zero applied D.C. bias. As shown in Fig. 6, deuterium SIMS depth profiling indicates that a more homogeneous distribution of D is incorporated into the film for this annealing condition. After a 400 °C forming gas exposure, the approximate D concentration (normalized yield) near the film center is 9×10^{19} atoms/cm^3 indicating that high concentrations of deuterium can be incorporated into Pt/BSTO/Pt thin film capacitors after forming gas exposure. As will be shown below, the suppression in capacitance density near zero applied D.C. bias can be interpreted in terms of a uniform distribution of space charge being incorporated into the film during the 400 °C forming gas exposure.

The preceding observations suggest that positive space charge is introduced into Pt/BSTO/Pt thin film capacitors after forming gas exposure. In the case of deuterium incorporation, with forming gas as the source of deuterium, a possible reaction is

$$D_2 \rightarrow 2D \quad (1)$$

$$D + O_O \rightarrow (OD)_O^{\bullet} + e- \quad (2)$$

Reaction (1) results from the catalytic activity of Pt which enables the incorporation of H/D in BSTO films at temperatures as low as room temperature. In reaction (2) atomic D which has diffused to the Pt/BSTO interface forms an OD ion with charge compensation by a conduction band electron. In PZT films, the formation of OH bonds in the film after hydrogen forming gas exposure has been verified by Raman spectroscopy [10].

Several studies have indicated that in perovskite titanates the defect levels associated with hydroxide ions [5,18,19-20] and oxygen vacancies [21-22] are shallow. Gilbert et al [5] has simulated the possible locations for incorporation of proton (deuteron) interstitials in the perovskite lattice according to reaction (2) along with the position of the electron trapping levels in the band gap associated with each location. According to Gilbert et al, for incorporation in the Ti-O plane the trapping level is 0.08 eV below the conduction band edge, E_c, while in the Ba-O plane the trapping level is E_c -0.04 eV. The position of the trapping levels in the bandgap associated with oxygen vacancies, and in particular the second ionization level, has been somewhat controversial. Most studies place the first ionization level of the oxygen vacancy at a very shallow level (E_c -0.05 eV Hagemann et al [22]). However, the energy of the second ionization level has been considered to be both deep and shallow. In the study of Hagemann et al., a value of 0.2 eV for the second ionization level was determined. The trapping levels associated with the OH/OD and oxygen vacancy defects are sufficiently shallow that they are expected to be almost completely ionized, except in the case of nearly degenerately doped thin films, resulting in a positive space charge distribution in the film after forming gas exposure.

Influence of Space Charge on the C-V and J-V Characteristics

The preceding considerations suggest that positive space charge is introduced into the film during forming gas exposure. The SIMS data in Fig. 6, and the fact that no applied field offsets are observed in the C-V_A characteristics (Fig. 5), suggest that a more homogeneous distribution of space charge is introduced into the film during a 400 °C anneal in forming gas. In the following, the effects of a uniform distribution of space charge on the C-V_A and J-V_A characteristics of Pt/BSTO/Pt thin film capacitors that have been exposed to forming gas is determined by calculating the potential distribution in the film for various uniform space charge concentrations.

We use a common model [13,23-24] to describe a ferroelectric thin film capacitor. The thin film capacitor is comprised of an interior region, of width $d-2x_o$, and two surface layers, of width x_o, at the top and bottom electrode interfaces. The film interior has dielectric properties similar to bulk ferroelectric material and the surface layers are layers of lower permittivity material that are taken to be temperature and field independent. Such layers are often postulated to describe the thickness dependence of the thin film permittivity even after film stress and Ti nonstoichiometry have been taken into account [13,24] and may arise, for example, from a dead layer effect as described by Zhou and Newns [23]. The relationship between electric field, E_B, and displacement, D_B, of the film bulk, of width $d-2x_o$, is described using a third order power series expansion in electric displacement [25-26]

$$E_B = \alpha_1^B(T)D_B + \alpha_{11}^B D_B^{\ 3}, \quad (3)$$

where, in the absence of space charge, α_1^B is the inverse of the zero field film bulk dielectric permittivity. Taking the appropriate root of Equation (9) gives D_B as a function of E_B in the film bulk

$$D_B(x) = \frac{\zeta(E_B(x))}{2^{1/3}3^{2/3}\sqrt{\alpha_{11}^B}} - \frac{(\frac{2}{3})^{1/3}\alpha_1^B}{\sqrt{\alpha_{11}^B}\zeta(E_B(x))} \quad (4)$$

where $\zeta(E_B(x)) = \left(9\sqrt{\alpha_{11}^B}E_B(x) + \sqrt{3}\sqrt{4(\alpha_1^B)^3 + 27\alpha_{11}^B E_B(x)^2}\right)^{1/3}$. The relationship between electric displacement, D_I, and field, E_I, in the interfacial layers is

$$D_I(x) = \varepsilon_I E_I(x) \quad (5)$$

To determine the electric potential in the Pt/BSTO/Pt capacitor, Gauss' equation, $\nabla \bullet D(x) = qN_d$, is solved in the dielectric film subject to the appropriate boundary conditions. In the present model, N_d represents the net positive space charge due to the (nearly) completely ionized shallow donor levels introduced into the film during forming gas exposure as well as any contribution resulting from deep trapping levels that may be present in the film. In addition, the space charge due to injected free charge carriers, n_f, has been neglected. In the limit that the injected free charge carriers dominate the space charge in the film, space charge limited conduction (SCLC) may be observed [27]. For a uniform volume charge distribution, the electric displacement vector is continuous across the interfacial layer – film bulk interfaces and the displacement vector through out the film is given by

$$D(x) = D(0) + qN_d x \quad (6)$$

Substituting equations (4) and (5) into (6) and solving for $E(x)$ yields the electric field in each region of the film. In the top and bottom interfacial layers

$$E_I(x) = E_S(0) + \frac{qN_d x}{\varepsilon_I} \quad (7)$$

where $E_S(0)$ is the field at the top electrode/film interface, i.e. at $x = 0$. In the film bulk

$$E_B(x) = (\varepsilon_I E_s(0) + qN_d x)(\alpha_1^B + \alpha_{11}^B(\varepsilon_I E_s(0) + qN_d x)^2) \quad (8)$$

Substituting equations (7) and (8) into the definition of the electric potential, $\Phi(x) = -\int E dx$, and applying the boundary condition of continuity of the electric potential across each interfacial layer – film bulk interface gives

$$\Phi(x) = \begin{cases} \varphi(x) & 0 \le x \le x_o \\ \varphi(x_o) + (\psi(x) - \psi(x_o)) & x_o \le x \le d - x_o \\ \varphi(x_o) + (\psi(d - x_o) - \psi(x_o)) + (\varphi(x) - \varphi(d - x_o)) & d - x_o \le x \le d \end{cases} \quad (9)$$

where

$$\varphi(x) = \Phi(0) - E_S(0)x - \frac{qN_d x^2}{2\varepsilon_I} \quad (10)$$

and $\psi(x) = -\int E_B(x)dx$. The surface field $E_S(0)$ is determined by applying Kirkoff's voltage law

$$\Phi(d) = \Phi(0) - E_A d \tag{11}$$

where d is the film thickness. Once the surface field is found, by numerically solving Equation (11), Equation (9) gives the electric potential through out the film.

Once the electric field distribution in the film is calculated, the small signal capacitance per unit area at a given applied field can then be determined. For the present model, the reciprocal small signal capacitance per unit area at a given applied field measured by the impedance analyzer is

$$\frac{1}{C_{measured}(E_A)} = \frac{2x_o}{\varepsilon_I} + \frac{1}{C_B(E_A)} \tag{12}$$

where [28]

$$\frac{1}{C_B(E_A)} = \int_{x_o}^{d-x_o} \frac{dx}{\varepsilon_B(E_B(x,E_A))} \tag{13}$$

and the small signal dielectric permittivity of the film bulk is given by $\varepsilon_B = dD_B/dE_A$. Subsituting Equation (8) into Equation (4) and using the numerically determined dependence of $E_S(0)$ on E_A, yeilds an expression that gives D_B as a function of x, N_d, α_1^B, α_{11}^B, E_A, ε_I, and x_o. Differentiation of this expression with respect to E_A gives the spatially dependent small signal permittivity of the film bulk. Fig. 7 shows an example of the theoretical C-V_A characteristics at a of 20 °C for a 30 nm MOCVD BSTO thin film capacitor with uniform donor concentrations over the range of 10^{18} to $8\text{x}10^{19}$ atoms/cm^3. For the calculations the model parameter set $\alpha_1^B = 2.05 \text{ x}10^{10}$ cm/F, $\alpha_{11}^B = 7.0 \text{ x}10^{19}$ cm^5/C^{2}F, $\varepsilon_I = 60\varepsilon_o$, and $x_o = 15$ Å was used which, as will be shown below, is similar to parameter sets that provide a good fit to the experimental data. The similarity between the changes which occur in the C-V_A characteristics before and after forming gas annealing in Fig. 5, with those which occur for increasing uniform positive space charge concentrations given in Fig. 7 is evident, suggesting that one effect of the

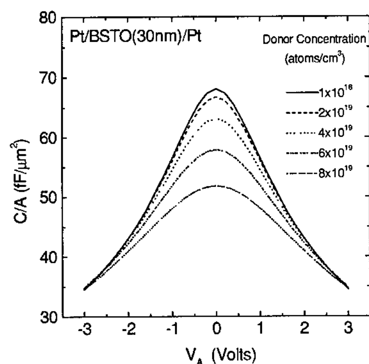

Fig.7 Theoretical C-V characteristics calculated for uniform donor concentrations over the range of 10^{18} to $8\text{x}10^{19}$ atoms/cm^3.

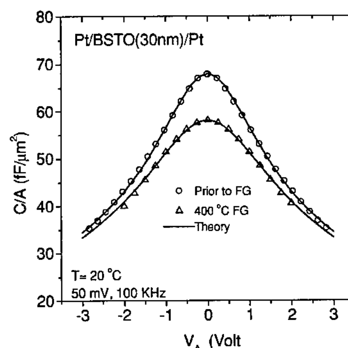

Fig.8 Theoretical and experimental C-V characteristics calculated for a Pt/BSTO/Pt thin film capacitor prior to and after 400 C forming gas exposure.

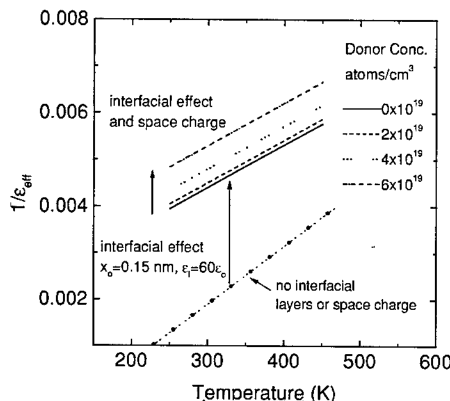

Fig.9 Theoretical reciprocal effective film relative permittivity at zero D.C. bias versus temperature for a 30 nm BSTO film.

forming gas exposure is to introduce positive space charge into the film. Fig. 8 shows a fit of the theory to the experimental $C\text{-}V_A$ characteristics prior to and after 400 °C forming gas exposure. A fit of the model to the data for the sample prior to forming gas exposure yielded α_1^B = 2.05 x10^{10} cm/F, α_{11}^B =7.0 x10^{19} cm^5/C^{2}F, $\varepsilon_I = 60\varepsilon_o$, x_o = 15 Å, and $N_d = 10^{18}$ atoms/cm^3. For the sample prior to forming gas exposure, a value of $N_d = 10^{18}$ atoms/cm^3 was used since it is close to the space charge concentrations reported by Copel et al [29] in MOCVD BSTO films deposited under similar conditions to those used in this study. Calculations using different space charge concentrations revealed that space charge concentrations less than approximately 10^{19} atoms/cm^3 exhibited a small influence on the $C\text{-}V_A$ characteristics, while above approximately 10^{19} atoms/cm^3 a more pronounced influence was observed. As a result, the choice of $N_d = 10^{18}$ atoms/cm^3 was not critical and other space charge concentrations could give equally good fits to the data provided N_d was less than approximately 10^{19} atoms/cm^3. A fit of the model to the data for the sample after 400 °C forming gas exposure yielded α_1^B = 2.07 x10^{10} cm/F, α_{11}^B = 8.2 x10^{19} cm^5/C^{2}F, $\varepsilon_I = 60\varepsilon_o$, x_o = 15 Å, and N_d = 5.4x10^{19} atoms/cm^3. While a slight modification of the fitting parameters is observed, the decrease in capacitance density near zero applied bias can almost be completely understood interms of the increased space charge density in the film. The decrease in small signal permittivity near zero applied bias in the presence of a uniform distribution of space charge has been discussed in terms of a shift in the Curie-Weiss constant due to the space charge as well as high internal electric fields near the electrode interfaces [30]. The influence of low permittivity interfacial layers and space charge, in the context of the present model, on the temperature dependence of the effective film relative permittivity ($\varepsilon_{eff} = C_{measured} d / \varepsilon_o$) at zero D.C. bias as calculated by equations (12-13) is shown in Figure (9). For the calculation, it is assumed that the first order coefficient can be expressed as $\alpha_1^B = (T - \theta) / \varepsilon_o C'$, where θ is an effective Curie-Weiss temperature that is dependent on film stress and stoichiometry (but thickness independent) and C' an effective Curie-Weiss constant. A 30 nm BSTO film with no low permittivity interfacial layers and no space charge in the dielectric is shown by the dotted line. For bulk film properties the parameter set θ = 148 K, C' = 8x10^4 K, and α_{11}^B = 8.2 x10^{19} cm^5/C^{2}F was used in the calculations. These values are similar to those reported for MOCVD BSTO films of similar thickness and stoichiometry [13,24,26]. Adding interfacial layers, with permittivity and thickness of $\varepsilon_I = 60\varepsilon_o$ and x_o = 15 Å, respectively, at the top and bottom Pt/BSTO interfaces causes a vertical shift in the Curie-Weiss plot as well as a thickness dependent modification of the slope [13-24]. Space charge causes an additional shift in the Curie-Weiss plot that, for the given parameter set, is most pronounced for space charge concentrations above 10^{19} atoms/cm^3.

In calculating the $J - E_A$ characteristics, image force lowering of the barrier must be taken into account. For thin film capacitors, a potential of the form [31]

$$\Phi_{image}(x) = \frac{q^2}{4\pi\varepsilon_o K}\left(\frac{1}{2x} + \sum_{n=1}^{\infty}\left(\frac{nd}{(nd)^2 - x^2} - \frac{1}{nd}\right)\right) \quad (14)$$

is added to $\Phi(x)$ to give the total potential in the film, $\Phi_{total}(x) = \Phi(x) + \Phi_{image}(x)$. In Equation (19) K is an appropriate high frequency relative dielectric constant and ε_o is the permittivity of free space. Fig. 10 gives an example of the potential distribution (in eV) in a 300 Å BSTO thin film capacitor at zero applied bias for donor concentrations over the range of 10^{18} – $8\text{x}10^{19}$ atoms/cm^3. The parameters used in the calculation are $\alpha_1^B = 2.05\ \text{x}10^{10}$ cm/F, $\alpha_{11}^B = 7.0\ \text{x}10^{19}$ cm^5/C^{2}F, $\varepsilon_I = 60\varepsilon_o$, $x_o = 15$ Å, and $\Phi(0) = 1.28$ eV. These values are similar to values reported in the literature for the first and third order LGD coefficients [24,26], thickness and permittivity of the so-called 'dead layer' [13,23], and effective barrier for thermionic emission [14-15], respectively. A high frequency relative dielectric constant of $K = 4.8$ was used based on values reported in the literature for the optical dielectric constant of BSTO thin films [32]. For the given parameters, significant band bending is observed for donor concentrations in the range of 10^{19}- $8\text{x}10^{19}$ atoms/cm^3. As shown by the data in Fig. 4, these space charge concentrations are precisely in the range of the D/H concentrations expected in Pt/BSTO/Pt thin film capacitors after forming gas exposure. This indicates that if the hydrogen present in the film after forming gas exposure is ionized significant band bending can occur which greatly impacts charge transport as described below.

The total current density is the sum of a current component due to the emission of carriers over the barrier [33]

$$J_{th-diff}(E_A, T) = -A^{**}T^2 \exp(-W_B(E_A)/kT) \quad (15)$$

and a component due to the tunnel emission of carriers [34]

$$J_{TFE} = -\frac{A^* T}{k}\int_{W\,min}^{W\,max} \Gamma_K(W)\ln[1 + \exp[-W/kT]]dW \quad (16)$$

In equations (15) and (16) A^{**} is the effective Richardson constant [33], A^* the effective Richardson constant for thermionic emission[34], k boltzmann's constant, T the temperature, and

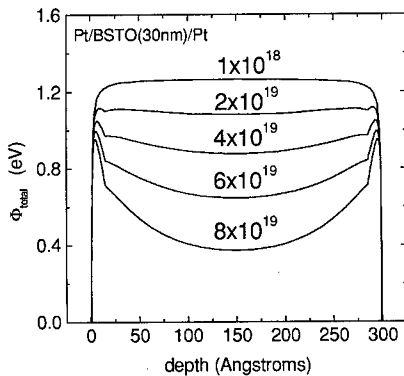

Fig.10 Theoretical potential profiles for a 30 nm BSTO capacitor calculated for uniform donor concentrations over the range of 10^{18} to $8\text{x}10^{19}$ atoms/cm^3.

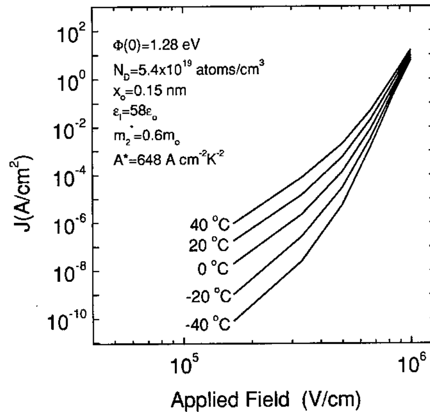

Fig.11 Theoretical J-E characteristics for a 30 nm BSTO capacitor calculated for a uniform donor concentration of $5.4\text{x}10^{19}$atoms/cm^3.

$\Gamma_k(W)$ the Kemble transmission probablilty. $\Gamma_k(W)$ is given by [34]

$$\Gamma_K(W) = \left[1 + \exp(+Q(W))\right]^{-1} \tag{17}$$

where

$$Q(W) = \frac{4\pi}{h}\int_{x_1}^{x_2} \sqrt{2m_2^*(q\Phi_{total}(x) - W)}dx \tag{18}$$

In Equation (18) h is Plank's constant, m^*_2 is the tunneling effective mass, and x_1 and x_2 are the classical turning points.

Fig. 11 shows an example of the theoretical J-E_A characteristics over the temperature range of -40 to 40 °C for a 30 nm MOCVD BSTO thin film capacitor with uniform a uniform positive space charge concentration of $5.4\text{x}10^{19}$ atoms/cm^3. For the calculations the model parameter set: α_1^B = 2.07 x10^{10} cm/F, α_{11}^B = 8.2 x10^{19} cm^5/C^{2}F, $\varepsilon_I = 58\varepsilon_o$, x_o = 15 Å, A^*= 648 Acm^{-2}K^{-2}, and m_2^*= 0.6m_o was used. For the calculations shown in Figure (10), over the entire applied field range the charge transport process is dominated by thermionic field emission. The similarity between the temperature and field dependence of the theoretical current density curves given in Fig. 10 and the experimental data in Fig 2, as well as the correct order of magnitude for the current density for a reasonable parameter set for BSTO films, suggests that the increase in leakage current density after forming gas annealing results from electron tunneling through the interfacial Schottky barrier. The enhanced tunneling currents result from an increase in band bending in the thin film due to the positive space charge incorporated into the film during forming gas exposure. A further discussion of fitting the theory to the experimental J-E_A curves and of the fitting parameters is given elsewhere [35].

CONCLUSION

We have shown using deuterium SIMS depth profiling that high H/D concentrations can be incorporated into Pt/BSTO/Pt capacitors after forming gas annealing. The increase in H/D concentration in the film is accompanied by an increase in the leakage and dielectric relaxation current density. Voltage offsets in the capacitance-applied voltage (C-V_A) characteristics at lower temperatures (23 °C) and a suppression in the capacitance density near zero applied D.C. bias at higher temperatures, suggests that one effect of forming gas exposure is to introduce positive space charge into the BSTO film. Using an equivalent model for a ferroelectric thin film capacitor, which incorporates lower permittivity interfacial layers and a nonlinear electric field-electric displacement relationship for the film interior, the effects of a uniform distribution of positive space charge on the theoretical C-V_A and current density applied voltage (J-E_A) characteristics was investigated. It was shown the model can account for many of the observed changes that occur in the experimental C-V_A and J-E_A characteristics after forming gas exposure.

ACKNOWLEDGMENTS
The authors would like to thank members in the Infineon/IBM DRAM development alliance for many fruitful discussions.

REFERENCES

[1] K. Kushida-Abdelghafar, H. Miki, K. Torii, and Y. Fujisaki, Appl. Phys. Lett. 69, 3188 (1996)
[2] Y. Fujisaki, K. Kushida-Abdelghafar, Y. Shimamoto, and H. Miki, J. Appl. Phys. 82, 341 (1997)
[3] J.P. Han and T.P. Ma, Integrated Ferroelectrics 17, 471 (1997)

[4] J.D. Baniecki R. B. Laibowitz, T. M. Shaw, K. L. Saenger, P. R. Duncombe, C. Cabral D.E. Kotecki H. Shen, J. Lian, and Q.Y. Ma, J. European Ceramic Society Vol. 19, Issue 6-7, 1457 (1999)
[5] S.R. Gilbert, S.P. Tang, Y. Okuno, L. Colombo, P. Chen, S.R. Summerfelt, and T.S. Moise, Presented at the Materials Research Society Meeting, Boston, MA, Fall (1999)
[6] J. H. Ahn, P.C. McIntyre, L. W. Mirkarimi, S.R. Gilbert, J. Amano, and M. Schulberg, Appl. Phys. Lett. 77, 1378 (2000)
[7] J. D. Baniecki, C. Parks, R.B. Laibowitz, T. M. Shaw, J. Lian, and G. Costrini, Mat. Res. Soc. Symp. Proc. Vol. 596, 25 (2000)
[8] R. Liedtke, M. Grossmann, and R.Waser, Appl. Phys. Lett. 77, 2045 (2000)
[9] J. Im, O. Auciello, A.R. Krauss, D.M. Gruen, R.P.H. Chang, S.H. Kim, and A.I. Kingon, Appl. Phys. Lett. 74, 1162 (1999)
[10]S. Aggarwal, S.R. Perusse, H.D. Drew, T. Venkatesan, R. Ramesh, D.B. Romero, V.B. Podobedov, and A. Weber, Appl. Phys. Lett., Vol. 73, 1973 (1998)
[11] O.K. Tan, W. Zhu, M.S. Tse, and X. Yao, Matls. Sci. and Eng. B58, 221 (1999)
[12] D.E. Kotecki, J.D. Baniecki, H. Shen, R.B. Laibowitz, K.L. Saenger, J.J. Lian, T.M. Shaw, S.D. Athavale, C. Cabral, Jr., P.R. Duncombe, M. Gutsche, G. Kunkel, Y.J. Park, Y. Wang, and R. Wise, IBM J. Res. Develop. 43, 367 (1999)
[13] T.M. Shaw, J.D. Baniecki, R.B. Laibowitz, E. Liniger, Z. Suo, M Huang, D.E. Kotecki, and H. Shen, Program Summary and Extended Abstracts of the 9th US-Japan Seminar on Dielectric and Piezoelectric Ceramics, 179 (1999)
[14] G.W. Dietz, M. Schumacher, R. Waser, S.K. Streiffer, C. Basceri, and A. I. Kingon, J. Appl. Phys. 82, 2359 (1997)
[15] C.S. Hwang, B. T. Lee, C. S. Kang, J. W. Kim, K. H. Lee, H. J. Cho, H. Horii, W. D. Kim, S. I. Lee, Y. B. Roh, and M. Y. Lee, J. Appl. Phys. 83, 3703 (1998)
[16] G.W. Dietz and R. Waser, Thin Solid Films, Vol. 299, 53 (1997)
[17] J. C. Shin, J. Park, C.S. Hwang, H. J. Kim, J. Appl. Phys. 86, 506 (1999)
[18] T. Norby, Solid State Ionics 40/41, 857 (1990)
[19] R. Waser, Ber. Bunsenges. Phys. Chem. 90, 1223 (1986)
[20] R. Waser, J. Am. Ceram. Soc. 71, 58 (1988)
[21] H. Yamada and G.R. Miller, J. Solid State Chem. 6, 169 (1973)
[22] H.J. Hagemann and D. Hennings, J. Am. Ceram. Soc., Vol. 64, No. 10, 590 (1980)
[23] C. Zhou and D.M. Newns, J. Appl. Phys. 82, 3081 (1997)
[24] S.K. Streiffer, C. Basceri, C.B. Parker, S.E. Lash, A.I. Kingon, J. Appl. Phys., Vol.86, 4565 (1999)
[25] M.E. Lines and A. M. Glass, "Principles and Applications of Ferroelectrics and Related Materials", Clarendon Press, Oxford, 71 (1977)
[26] C. Basceri, S.K. Streiffer, and A. I. Kingon, J. Appl. Phys. 82, 2497 (1997)
[27] K.C. Kao and W. Hwang, Electrical Transport in Solids, Pergamon Press, New York, (1981)
[28] D. Kahng and S.H. Wemple, J. Appl. Phys. 36, 2925 (1965)
[29] M. Copel, P.R. Duncombe, D.A. Neumayer, T.M. Shaw, and R.M. Tromp, Appl. Phys. Lett. 70, 3227 (1997)
[30] A.M. Bratkovsky and A.P. Levanyuk, Phys. Rev. B, Vol. 61, 15042 (2000)
[31] J.G. Simmons, J. Appl. Phys. 35, 2472 (1964)
[32] S. Zafar, R.E. Jones, B. Jiang, B. White, V. Kaushik, and S. Gillespie, Appl. Phys. Lett. 73, 3533 (1998)
[33] S.M. Sze, "Physics of Semiconductor Devices", John Wiley and Sons, 246-311 (1981)
[34] E.L. Murphy and R.H. Good, Phys. Rev. 102, 1464 (1956)
[35] J.D. Baniecki, R.B. Laibowitz, T.M. Shaw, J. Lian, W. Xu, and Q.Y. Ma, submitted to J. Appl. Phys. (2000)

Mat. Res. Soc. Symp. Proc. Vol. 655 © 2001 Materials Research Society

IMPROVED DEPOSITION PROCESS OF CVD-(Ba,Sr)TiO_3 ON Ru

M. Tarutani, T. Sato, M. Yamamuka, T. Kawahara, T. Horikawa, T. Takenaga, Y. Yoneda, T. Kuroiwa, S. Matsuno and T. Shibano
Advanced Technology R&D Center, Mitsubishi Electric Corp., Hyogo, JAPAN

ABSTRACT

(Ba,Sr)TiO_3 [BST] films were deposited by the flash vaporization CVD method with a unique liquid delivery system. An inductively coupled plasma mass spectrometry [ICP-MS] analysis revealed the decline of (Ba+Sr)/Ti molar ratio of the initial BST-layer on Ru. By readjusting the flow ratio of liquid sources and using a two-step deposition method, we obtained 30-nm-thick BST films with uniform composition profile, exhibiting good electrical properties. The leakage property, however, was severely deteriorated in BST films less than 24 nm thick. A SEM observation showed the presence of micro-roughness or micro-hillocks in these films, which were confirmed to be caused by Ru oxidation. Therefore, an annealing process of the Ru electrode was added for its planarization, and the CVD process was also improved. As a result, we obtained smooth and finely crystallized ~ 20-nm-thick BST films with good electrical properties of equivalent SiO_2 thickness (t_{eq}) ~ 0.45 nm and leakage current < 1×10^{-7} A/cm^2. We also measured properties of BST films deposited on the 3-D Ru electrode. The results are briefly discussed.

INTRODUCTION

Metal/insulator/metal [MIM] (Ba,Sr)TiO_3 [BST] capacitor has attracted much attention for applications in future high-density memories [1-4]. Ruthenium is promising as the electrode material, because of its feasibility in micromachining via dry etching. The minimum feature size of the future memories is approaching less than 0.15 μm. To meet with such severe design rules, the thickness of BST needs to be limited to less than ~ 30 nm. As the film thickness decreases, it becomes more difficult to minimize leakage current, because the electrical properties of such thin BST films depend particularly on BST/Ru interface characteristics like roughness. In addition, as shown in the following, there is some peculiar property in the initial stage of BST-CVD growth on Ru that influences the BST films severely. Therefore it is necessary to improve the film formation process of CVD-BST films specially optimized for thin BST on Ru, to achieve an MIM-BST capacitor suitable for future high-density memories.

In the present paper, we report an improved formation process of CVD-BST on Ru including the control of source flow-ratio, the planarization by Ru annealing and the optimization of CVD process, which enables thin BST films of high-permittivity with low leakage. We also report on properties of BST films deposited on the 3-D Ru electrode.

EXPERIMENTAL

BST films were deposited by MOCVD method, employing a heated flash-vaporizer and a unique liquid delivery system with a mixture of source liquids and N_2 carrier gas [4, 5]. $Ba(DPM)_2$, $Sr(DPM)_2$ and $Ti(i\text{-}PrO)_2(DPM)_2$ were used as the liquid metal organic sources. THF was used as their solvent. O_2 was used as a reactant gas for BST-deposition. Deposition

temperature was 480°C and chamber pressure was 665 Pa. For electrical measurement, BST films were crystallized by a two-step deposition process [4, 6]. The Ru electrode was deposited by sputtering method at 350°C in Ar.

We employed TEM, SEM, inductively coupled plasma mass spectrometry [ICP-MS], XPS, XRD and STEM-EDX to investigate the nature of the BST films and Ru.

RESULTS

Modification of Source Flow Ratio

Figure 1 shows total (Ba+Sr)/Ti molar ratio of the BST films deposited on Ru for 2, 4 and 10 minutes at the same source flow rates, measured by ICP-MS. The sectional (Ba+Sr)/Ti-values are also inserted in Fig. 1. It is clear that the (Ba+Sr)/Ti molar ratio of the initial BST-layer on Ru was low compared to that of the upper layer. To clarify the reason for compositional decline, we investigated the deposition process in detail. We found that when all reaction gases faced the Ru surface, a sudden rise of temperature was detected by a thermocouple in a substrate stage. This phenomenon is special in the case of a bare Ru substrate and is not observed for SiO_2 or BST-coated Ru substrates. The (Ba+Sr)/Ti molar ratio of CVD-BST films generally depends on the growth temperature from 420 to 500°C [7]. Hence the deviation is considered to be due to the temperature rise caused by exothermic reaction between the reactant gases and Ru.

We investigated the optimum deposition condition, by changing the flow ratio of liquid sources, to minimize the compositional deviation [8]. Figure 2 shows the relationship between electrical properties of ~ 30-nm-thick BST films and the source flow ratio ([Ba]+[Sr])/[Ti], for the 1st BST deposition. By increasing the flow ratio, equivalent SiO_2 thickness (t_{eq}) of BST films decreased from 0.8 nm to 0.5 nm, still with low leakage current.

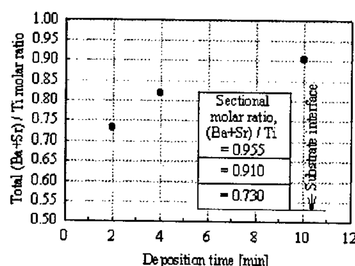

***Figure 1**. (Ba+Sr)/Ti molar ratio of CVD-BST films grown on Ru with the same source flow rates.*

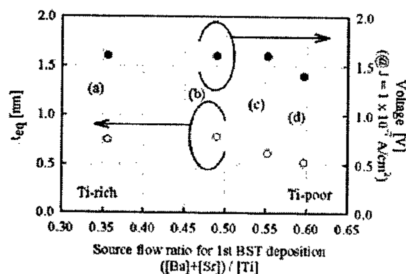

***Figure 2**. Electrical properties of CVD-BST films on Ru, (a) without and (b)-(d) with modification of the source flow ratio for the 1st BST deposition. The thickness of the BST films is ~ 30 nm.*

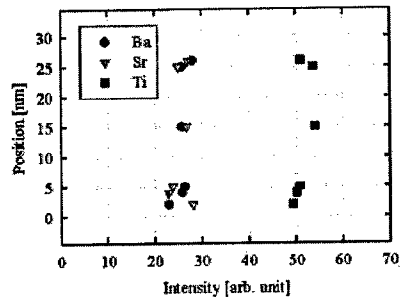

(a) (b)

***Figure 3**. (a) Cross-sectional TEM image and (b) compositional profile via STEM-EDX. BST film consists of columnar crystalline grains, and its composition is uniform across the film.*

Figures 3(a) and 3(b) show a cross-sectional TEM image of a Ru/BST/Ru structure and the composition profile measured by STEM-EDX method. This sample was deposited using source flow ratios of 0.60 and 0.36 for the 1st and 2nd BST layers, respectively. We observed that the BST films consisted of finely crystallized grains with a composition of uniform profile. We concluded that the modification in source flow ratio is effective to obtain BST films with a uniform composition profile on Ru.

Ru Planarization Process

The leakage property, however, was severely deteriorated in BST films less than 24 nm thick. The most common reason for increase of leakage current is roughness at interfaces [9]. We investigated how the BST/Ru interface altered under CVD conditions.

Figure 4 shows SEM images of the Ru surface followed by (a) O_2 anneal; (b) O_2+THF anneal after treatment (a); (c) N_2 anneal; and (d) O_2+THF anneal after treatment (c). Each treatment was done at 480°C, 665 Pa for 5 min. The treatment (a) was employed for a pre-deposition step in the conventional process to stabilize substrate temperature and chamber pressure. The treatment (b) represents CVD process, though without source gases. The as-deposited Ru surface had nanometer-scale roughness with a curved face reflecting the Ru grain. After Ru exposure to O_2, small hillocks formed on the surface as shown in Fig. 4(a). The hillocks were confirmed as Ru-oxide by XPS and XRD. These hillocks disappeared after treatment (b), indicating Ru-oxide was reduced under THF atmosphere. However, traces of the hillocks still remained as shown in Fig. 4(b), and Ru surface was rough as compared to the as-deposited surface. Such hillocks were not observed on Ru annealed in a N_2 atmosphere as shown in Fig. 4(c), and Ru surface after treatment (d) was as smooth as the as-deposited surface. Therefore, the pre-deposition process should be done in a N_2 atmosphere to minimize the roughening of the Ru surface.

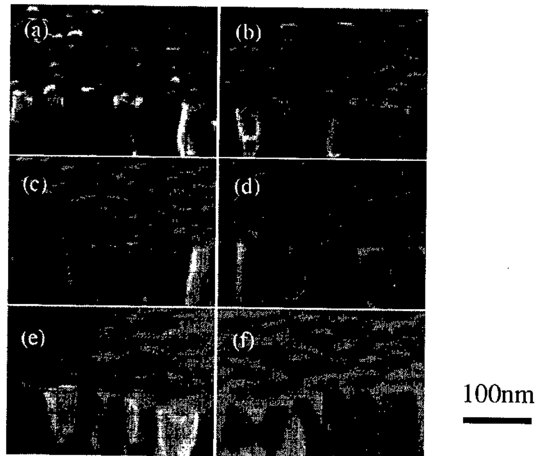

Figure 4. *SEM images of Ru surface followed by (a) O_2 anneal; (b) O_2+THF anneal after treatment (a); (c) N_2 anneal; (d) O_2+THF anneal after treatment (c); (e) 700°C vacuum anneal; and (f) treatment (e)&(d).*

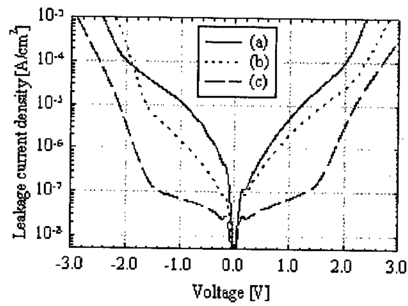

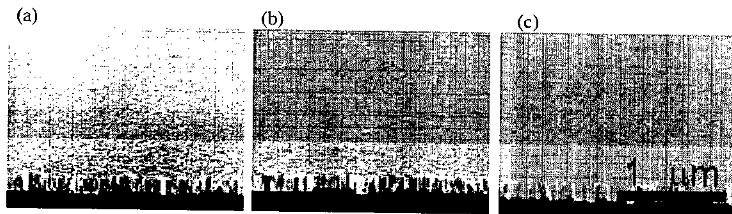

Figure 5. *Leakage properties and SEM images of 22-nm-BST/Ru prepared with (a) an O_2 pre-anneal step, (b) Ru vacuum anneal and O_2 pre-anneal steps, and (c) Ru vacuum anneal and N_2 pre-anneal steps.*

In addition, another anneal process for Ru was tested. Figure 4(e) is an SEM image of Ru after 700°C annealing in a vacuum for 1 min, showing that the Ru surface becomes smoother still. Figure 4(f) is an SEM image of the Ru surface after 700°C annealing and treatment (d), showing that the Ru surface is very smooth without hillocks.

Figure 5 shows the leakage property and SEM images of 22-nm-BST/Ru prepared with (a) O_2 pre-anneal step, (b) Ru vacuum anneal and O_2 pre-anneal steps, and (c) Ru vacuum anneal and N_2 pre-anneal steps, respectively. We observed that the BST film prepared by the (c) process had both the smoothest morphology and also the lowest leakage. Finally, by using the improved deposition process of CVD-BST on Ru, we obtained smooth and finely crystallized ~ 20-nm-thick BST films with good electrical properties of t_{eq} ~ 0.45 nm and leakage current < 1 x 10^{-7} A/cm^2.

Properties of CVD-BST on 3-D Ru Electrode

We applied the improved deposition process of BST to 3-D Ru electrodes. Figure 6 shows a cross-sectional SEM image of a 3-D Ru/BST/Ru capacitor. The storage node of Ru/TiN/Ti was fabricated using 0.35-μm scale technology. Ru micromachining was done by O_2/Cl_2 plasma etching with a SiO_2 patterned hard mask. It is important to know whether enough capacitance is obtained at the side face of the electrodes, because it is the dominant part of the electrodes used in real capacitor structures. Therefore the top face was left capped by the SiO_2-mask to enable us to measure side-face capacitance. A 25-nm-thick BST film was deposited on the patterned electrodes using the improved CVD process. Finally, Ru was deposited thereon by sputtering, followed by cell plate etching.

Figure 7 shows the leakage current property of the integrated Ru/BST/Ru capacitors. The average value of t_{eq} for the BST films was estimated to be ~ 0.8 nm. The leakage current was less than 1 x 10^{-7} A/cm^2 at 1 V. Though the properties are slightly degraded as compared to those of a flat capacitor, these experiments demonstrate that a Ru/BST/Ru capacitor is very promising for future memory applications.

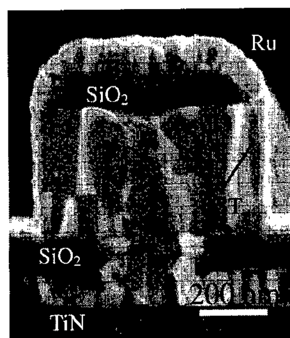

Figure 6. Cross-sectional SEM image of the 3-D Ru/BST/Ru capacitor.

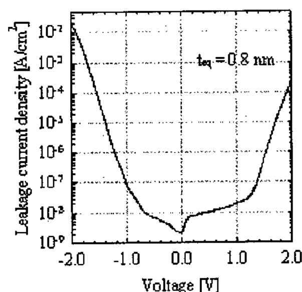

Figure 7. Leakage current-voltage characteristics of the 3-D Ru/BST/Ru capacitor.

CONCLUSIONS

Improved formation process of CVD-BST on Ru was investigated. We conclude that Ru annealing and usage of N_2 as a pre-deposition step gas prevent Ru surface from oxidizing and roughening, and thus suppress leakage current. By controlling the source flow ratio for the 1st BST deposition, it is possible to obtain BST films with a composition of uniform profile and therefore to improve the electrical properties of BST films. It is possible to obtain smooth and finely crystallized ~ 20-nm-thick BST films with good electrical properties of t_{eq} ~ 0.45 nm and leakage current $< 2 \times 10^{-7}$ A/cm^2. We showed that properties of t_{eq} ~ 0.8 nm and leakage current $< 1 \times 10^{-7}$ A/cm^2 are obtained for the 3-D Ru/BST/Ru capacitor.

REFERENCES

1. A. Yuuki, M. Yamamuka, T. Makita, T. Horikawa, T. Shibano, N. Hirano, H. Maeda, N. Mikami, K. Ono, H. Ogata and H. Abe, Tech. Dig. IEDM *1995*, pp.115-118.
2. S. Yamamichi, P-Y. Leisaicherre, H. Yamaguchi, K. Takemura, S. Sone, H. Yabuta, K. Sato, T. Tamura, K. Nakajima, S. Ohnishi, K. Tokashiki, Y. Hayashi, Y. Kato, Y. Miyasaka, M. Yoshida, and H. Ono, Tech. Dig. IEDM *1995*, pp.119-122.
3. K. Ono, T. Horikawa, T. Shibano, N. Mikami, T. Kuroiwa, T. Kawahara, S. Matsuno, F. Uchikawa, S. Satoh and H. Abe, Tech. Dig. IEDM *1998*, pp.803-806.
4. T. Horikawa, M. Tarutani, T. Kawahara, M. Yamamuka, N. Hirano, T. Sato, S. Matsuno, T. Shibano, F. Uchikawa, K. Ono and T. Oomori, *Mat. Res. Soc. Symp. Proc.*, **541**, 3-10 (1999).
5. T. Kawahara, M. Yamamuka, T. Makita, K. Tsutahara, A. Yuuki, K. Ono and Y. Matsui, *Jpn. J. Appl. Phys.*, **33**, 5897-5902 (1994).
6. T. Kawahara, M. Yamamuka, A. Yuuki and K. Ono, *Jpn. J. Appl. Phys.*, **34**, 5077-5082 (1995).
7. M. Yamamuka, T. Kawahara, A. Yuuki and K. Ono, *Jpn. J. Appl. Phys.*, **35**, 2530-2535 (1996).
8. T. Kawahara, M. Yamamuka, J. Tanimura, M. Tarutani, T. Kuroiwa, T. Horikawa and K. Ono, *Jpn. J. Appl. Phys.*, **36**, 5874-5878 (1997).
9. T. Kawahara, M. Yamamuka, A. Yuuki and K. Ono, *Jpn. J. Appl. Phys.*, **35**, 4880-4885 (1996).

Mat. Res. Soc. Symp. Proc. Vol. 655 © 2001 Materials Research Society

Manufacturability Study for Etching High-Density BST/Pt Capacitors

Jay Hwang
Applied Materials Inc., 974 E. Arques Ave., M/S 81330
Sunnyvale, CA 94086, U.S.A.

ABSTRACT

Profile control, process repeatability and productivity concerns in etching Pt electrodes are reviewed specifically for application in fabricating high-density BST/Pt capacitors. The approach of using a high temperature cathode in a high-density reactive plasma chamber has produced a repeatable >85° Pt profile, stable etch rate and low particle results over a 500-wafer marathon test. A "corrosion-like" BST defect can be prevented by adding a post etch treatment to remove any corrosive residue from the wafer surface. A feasible manufacturing solution for etching BST/Pt capacitors for future high-density DRAM application is demonstrated.

INTRODUCTION

A 4x increase in DRAM storage density in every 3~4 years has been a trend for the past 20 years [1]. As a result, the DRAM design rule is shrinking, and new changes in memory cell structure and capacitor material are being proposed to accommodate for the increasing memory density [2,3]. One of the new changes in capacitor material is to use a high-κ dielectric like BST (Barium Strontium Titanate) and a noble metal electrode like Pt (Platinum). BST has a dielectric constant in two orders of magnitude higher than the current silicon oxide in use. Pt electrode is chosen for its merits of low leakage current and good thermal stability compatible with BST deposition condition in a high temperature, high oxygen ambient environment. Because of the noble character of the material, Pt etching poses some technical challenges in the areas of profile control (pattern fidelity), process repeatability and productivity. This paper outlines how to overcome these challenges and to develop a manufacturing solution for etching Pt electrodes to form high-density BST/Pt capacitors.

PATTERN FIDELITY IN ETCH

Many papers [4-6] have discussed the difficulty of etching Pt electrodes such as the tapering of the etched profile or a fence-like residue, see Figure 1, which may be formed on the side wall of the etched profile. These issues present a problem in transferring patterns to form high-density capacitors. The difficulty is mainly due to a re-deposition of the low volatile by-products generated from the physically dominated etching processes. This problem can be addressed by applying highly reactive gas plasma and etching the wafer at an elevated temperature [7-9]. The high-temperature etch increases the volatility of the by-products while a reactive gas plasma assists in chemical etching rather than physical sputtering, therefore avoiding the re-deposition of byproducts. Figure 2 shows a result of vertical Pt profile on 0.13 μm space obtained from a high-temperature etch process in an Applied Materials DPS™ etch chamber. The etched profile is

>85°, and there is no fence-like residue. A schematic of DPS™ etch chamber is shown in Figure 3.

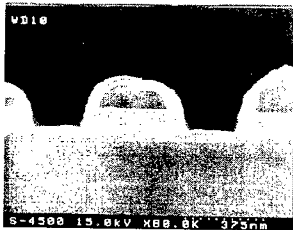

Figure 1. Fence-like residue formed on the side wall of the etched profile.

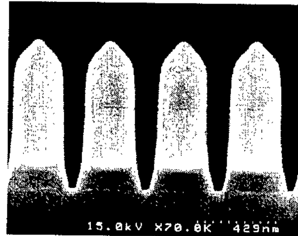

Figure 2. >85° Pt profile on 0.13 μm space.

The DPS™ etch chamber is equipped with a high temperature cathode. The plasma source outside the dielectric dome, operating at 2 MHz RF frequency, induces a high density, uniform ion flux to the wafer, and is de-coupled from a second RF source power which is capacitively biased to the wafer cathode to control ion energy. The biased cathode is operated at 13.56 MHz RF frequency. An electrostatic chuck is attached on top of the cathode, which can be heated up to 400°C for high temperature wafer processing. The dielectric dome and chamber wall is temperature controlled to promote by-product adhesion. The process chamber itself is swappable for easy wet cleaning that shortens the wet clean recovery time for better productivity.

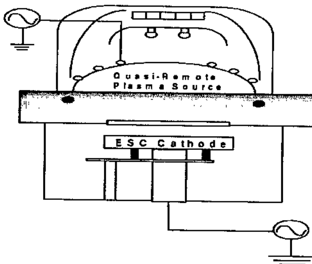

Figure 3. DPS™ etch chamber schematic.

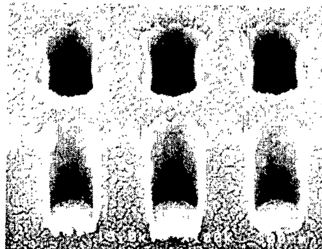

Figure 4. Forming Pt "cup" electrodes.

The high temperature DPS™ etch chamber also can be used to etch Pt for forming a "cup" or concave shape of electrodes as shown in Figure 4. The etching sequence for forming the "cup" shape electrodes is: first, etch a sacrificial layer on top of the Pt layer, followed with etching Pt layer to form separate Pt "cups", and then remove the remaining sacrificial material from inside the Pt "cups". Figure 4 shows the final result of Pt "cup" electrodes that was formed by the above sequence.

PROCESS REPEATABILITY AND PRODUCTIVITY TEST IN MARATHON

It was noticed that chamber deposits from Pt etch by-products could be electrically conductive [7]. If electrically conductive, the conductive deposits would affect RF-power coupling into plasma chamber and cause etch rate to drop as shown in Figure 5. This problem

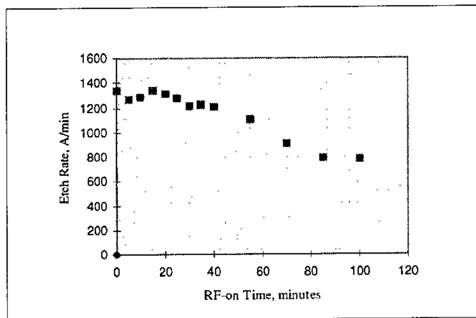

Figure 5. Etch rate dropping due to conductive by-products deposition inside the chamber.

could be resolved by modifying hardware to minimize the interference of conductive deposits to RF transmission [7]. It also could be addressed by studying the etch-parameter effect to develop an etch process that does not generate conductive by-products [10]. It was found that high temperature etching Pt with reactive gas plasma would generally make the by-products non-conductive and so produce no effect on etch rate stability.

Another concern in production is particles generated by the flaking of by-products, which could result in a premature need for wet clean. Some marathons have been conducted to check particle performance as well as process repeatability in high temperature DPS™ chamber etching Pt. Figures 6 to 8 were results from a marathon run etching 500 Pt-wafers. Figure 6 shows the particle count was <20 adders per wafer, Figure 7 shows Pt etch rate was stable within ±5 % wafer-to-wafer, and Figure 8 exhibits Pt profile on 0.2 μm features all of which were >85° throughout the marathon. These results demonstrate the feasibility of high temperature etching of Pt electrodes as a manufacturing process.

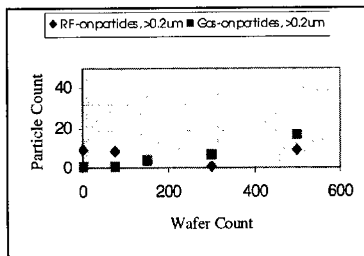

Figure 6. 500-wafer marathon in DPS™
- low particles, <20 adders per wafer

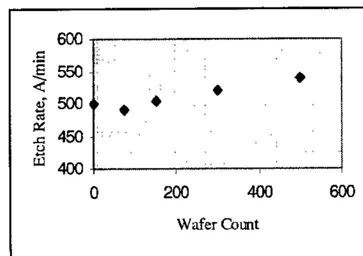

Figure 7. 500-wafer marathon in DPS™
- stable Pt etch rate, ±5 % wafer to wafer

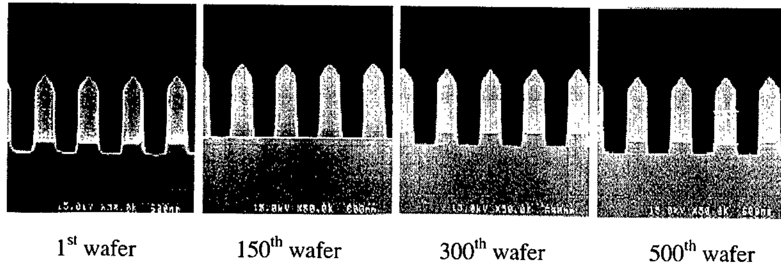

Figure 8. 500-wafer marathon in DPS™ - repeatable Pt profile result, all >85°.

POST-ETCH BST DEFECT PREVENTION

In stack capacitor fabrication, a Pt electrode is typically etched first to form a storage node, BST then deposited on it, followed with a second Pt layer deposition on the BST film. The second Pt layer would be plasma-etched to form a second electrode for BST capacitors. A "corrosion-like" type of defect would show up on the etched BST surface after etching the second electrode (see Figure 9) if a corrosive gas has been used in the etching process. The "corrosion-like" defect can be prevented by applying an additional post etch treatment to remove the corrosive residue from the wafer surface.

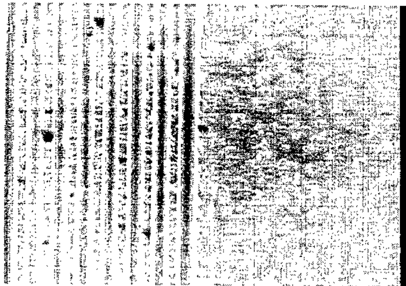

Figure 9. "Corrosion-like" BST defect resulted from using a corrosive gas.

Capacitance density as high as 80 $fF/\mu m^2$ and leakage current as low as $1x10^{-8}$ A/cm^2 have been observed on Pt/BST/Pt planar capacitors which had top Pt electrodes etched in DPS™ chamber [11]. The results were measured after the etched wafer had gone through a post etch treatment for the removal of corrosive residue and a 550 °C oxygen annealing.

SUMMARY

BST/Pt capacitors have been studied for use in high-density DRAM application. High pattern fidelity in etching Pt electrodes has been demonstrated using high temperature DPS™ chamber. Pt etch by-products are electrically non-conductive under high temperature chemical etching condition. Low particles, stable etch rate and good profile repeatability from a 500-wafer marathon result showed high temperature etching Pt electrodes could be a production-worthy process in fabrication of high-density BST capacitors. Additional treatment after etching BST may be needed to prevent a "corrosion-like" defect.

ACKNOWLEDGMENTS

Many people at Applied Materials have made tremendous efforts to help produce the results shown in this paper. Their contributions are deeply appreciated. They are (in alphabetical order): K. Chiang, C. Dornfest, P. Exline, J. Helmsen, J. Jin, Q. Liang, S. Mak, E. Mok, J.C. Moran, A. Nickles, S. Park, A. Siauw, S. Singh, H. Thai, K. Vellore, D. Wang, L. Wang, Y. Ye, C. Ying, A. Zhao.

REFERENCES

1. The National Technology Roadmap for Semiconductors, SIA, (1997)
2. D.E. Kotecki, Semiconductor International, November (1996) p109-116
3. A. Nitayama, Y. Kohyama, and K. Hieda, IEDM, 13.1.1 (1998) p355-358
4. W.J. Yoo, J.H. Hahm, H.W. Kim, C.O. Jung, Y.B. Koh, and M.Y. Lee, Jpn. J. Appl. Phys., Vol 35 (1996) p2501-2504
5. T. Shibano and T. Oomori, J. Vac. Sci. Tech. B 15(5), September (1997) p1747-1751
6. C.W. Chung and H.G. Song, J. Electrochem. Soc., Vol 144, No 11 (1997) pL294-296
7. J. Hwang, S. Mak, C. Ying, K. Chiang, and J. Jin, Proc. Semicon Korea Tech. Symp. 99, February (1999) p167-168
8. J. Hwang, S. Mak, C. Ying, K. Chiang, and J. Jin, 11th ISIF Abstracts, March (1999) p190C
9. S.D. Athavale, D.E. Kotecki, H. Shen, J. Hwang, C. Ying, D.J. Lee, and S. Mak, AVS 46th Int'l Symp. Abstracts, October (1999)
10. C. Ying, J. Jin, and J. Hwang, 199th ECS Meeting Abstracts, May (2000)
11. A. Nickles, X. Jin, S. Kher, L. Luo, C. Dornfest, J. Zhao, J. Hwang, J. Jin, and K. Chiang, 1st Int'l Conf. Adv. Mat'l & Proc. Microelec. Abstracts, March (1999)

Fundamental Properties of Ferroelectric Thin Films I

Mat. Res. Soc. Symp. Proc. Vol. 655 © 2001 Materials Research Society

Imaging Mechanism and Quantification of Scanning Probe Microscopies on Ferroelectric Surfaces

Sergei V. Kalinin and Dawn A. Bonnell
Dept. Mat. Sci. Eng., University of Pennsylvania, 3231 Walnut St,
Philadelphia, PA 19104

ABSTRACT

In the last few years a wide spectrum of non-contact, intermittent contact and contact scanning probe microscopies have been applied to imaging ferroelectric surfaces. The imaging mechanism in non-contact SPM is ultimately related to the total charge distribution on the ferroelectric surface, including both polarization and screening charges. Contact voltage modulation (piezoresponse) force microscopy (PFM) is sensitive to both local polarization via electromechanical coupling and surface charge via capacitive interactions. In the present research we analyze the electrostatic and electromechanical contrast in PFM using analytical solutions for the electrostatic sphere-dielectric plane problem and for the piezoelectric indentation problem. The contribution of electrostatic forces to the image is estimated. Variable-temperature PRI imaging of domain structures in $BaTiO_3$ is performed and the temperature dependence of the piezoresponse is compared with the Ginzburg - Devonshire theory.

INTRODUCTION

In the recent years, scanning probe microscopy (SPM) based techniques have been successfully employed in the characterization of ferroelectric surfaces on the micron and submicron level [1]. The primary SPM techniques used are variants of non-contact electrostatic SPM such as Electrostatic Force Microscopy (EFM), Scanning Surface Potential Microscopy (SSPM) and contact techniques such as Piezoresponse Force Microscopy (PFM). Both SSPM and PFM are based on voltage modulation, i.e. during imaging the piezoelectric actuator driving the cantilever is disengaged and an ac bias is applied directly to a conductive tip. In PFM the tip is brought into contact with the surface and the piezoelectric response of the surface is detected as the first harmonic component of the bias-induced tip deflection. In SSPM the tip is held at a fixed distance above the surface (typically 10-100 nm) and the first harmonic of the electrostatic force between the tip and the surface is nullified by adjusting the constant bias on the tip. A detailed analysis of EFM and SSPM imaging on ferroelectric surfaces is given by Kalinin and Bonnell [2]. Contrast formation mechanism in PFM is less understood [3-6]. Luo *et al* [7] found that the temperature dependence of piezoresponse contrast is similar to that of the spontaneous polarization. This behavior was attributed to a dominance of electrostatic interactions due to the presence of unscreened polarization bound charge as proposed by Hong *et al* [8], since electromechanical response based on the piezoelectric coefficient, d_{33}, would diverge in the vicinity of the Curie temperature. This hypothesis is also reinforced by the observations of the response on nonpiezoelectric surfaces [9] and the existence of a nulling potential that allows implementation of nanopotentiometry techniques [10]. In contrast, the existence of lateral PFM signal [11], the absence of relaxation behavior in PFM contrast as opposed to SSPM contrast [12,13] and numerous observations using both EFM/SSPM and PFM [14,15] clearly point to significant electromechanical contribution to PFM contrast. In order to resolve the apparent

inconsistency between the temperature dependence of PFM contrast and the electromechanical description, we analyze possible origins and relative magnitudes of electrostatic vs. electromechanical contributions to PFM signal.

RESULTS AND DISCUSSION

Tip-surface potential.

To quantify the electrostatic interaction between a tip of radius R and a dielectric surface with dielectric constant - κ, we calculate the tip-surface capacitance $C_d(z,\kappa)$, where z is the tip-surface separation. The solution for the conductive tip-dielectric plane problem can be found in bispherical coordinates. For a conductive tip and surface ($\kappa = \infty$) the tip-surface capacitance is

$$C_c = 4\pi\varepsilon_0 R \sinh\beta_0 \sum_{n=1} (\sinh n\beta_0)^{-1}, \tag{1}$$

where $\cosh\beta_0 = (R+z)/R$, compared to

$$C_d = 4\pi\varepsilon_0 R \sinh\beta_0 \sum_{n=1} \left(\frac{\kappa-1}{\kappa+1}\right)^{n-1} (\sinh n\beta_0)^{-1} \tag{2}$$

for the conductive tip-dielectric surface model [16]. While in the limit of small tip surface separation C_c diverges logarithmically, C_d converges to the universal "dielectric" limit

$$C_d(\kappa)_{z=0} = 4\pi\varepsilon_0 R \frac{\kappa-1}{\kappa+1} \ln\left(\frac{\kappa+1}{2}\right) \tag{3}$$

The distance dependences of tip surface capacitance and surface potential on the surface directly below the tip are shown on Fig. 1. Values are calculated for he tip radius R = 50 nm. We assume that the separation between the tip and the surface in the contact regime is ~0.1 nm corresponding to the limiting physical separation.

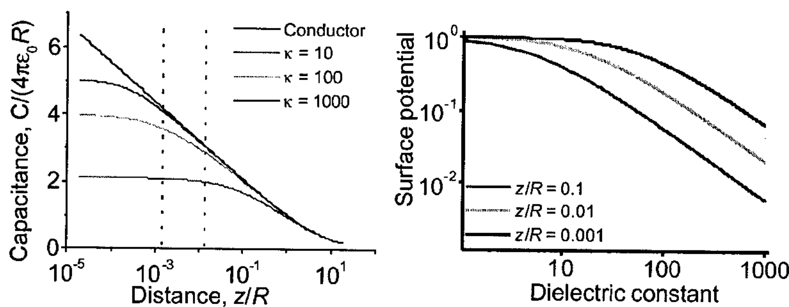

Figure 1. (a) Tip-dielectric surface capacitance compared to the metallic limit. Dotted lines delineate the region of characteristic tip-surface separations (0.1-1nm) in contact mode. (b) Surface potential below the tip for different tip-surface separations as a function of the dielectric constant of the surface.

For relatively large tip-surface separations $C_d(z,\kappa) \approx C_c(z)$, which is the usual assumption in non-contact SPM imaging. The most prominent feature of this solution is that while for low-k dielectric materials tip surface capacitance achieves the dielectric limit in contact and hence

surface potential is equal to the tip potential, this is not the case for high-k dielectrics such as ferroelectric materials. This implies that tip-surface capacitance, capacitive force and electric field are significantly smaller than in the dielectric limit. The surface potential below the tip is smaller than the tip potential and is inversely proportional to dielectric constant (Fig. 1b). This is equivalent to the presence of an effective dielectric gap between the tip and the surface that attenuates the potential. It should be noted that the presence of a "dead" layer on a ferroelectric surface [17] or a layer of native oxide on the tip augments this effect.

Electrostatic model

From Eq. (1) the capacitive contribution to electrostatic tip-surface force for z = 0.1 nm, R = 50 nm can be estimated as $F_c = 2.7 \cdot 10^{-8}(V_{tip} - V_s)^2$ N/V^2, where V_{tip} and V_s are tip and surface potentials respectively. The fact that polarization charge is almost completely screened in air allows the exclusion of the Coulombic contribution from the polarization bound charge. Moreover, even under the assumption that the tip penetrates the screening layer in the contact area, the interaction between the two will not result in tip deflection. For an effective Young modulus of material E^* = 100GPa this force is equivalent to the indentation depths of $h_c = 2.69 \cdot 10^{-11}(V_{tip} - V_s)^2$ m/V^2. Under typical operating conditions of PFM the total force acting on the tip is $F = F_0 + F_{el}$, where $F_0 = k\ d$ is indentation force exerted by the cantilever of spring constant k at setpoint deflection d and F_{el} is the electrostatic force. Electrostatic force is modulated in time as $F_{el} = F_{1\omega}\cos(\omega t)$. In the small modulation approximation, $F_{1\omega} \ll F_0$, the first harmonic of cantilever response for Hertzian indentation [18] is:

$$h_{1\omega} = \frac{1}{3}\left(\frac{3}{4E^*}\right)^{2/3} R^{-1/3} F_0^{-1/3} F_{1\omega} \qquad (4)$$

For typical imaging parameters F_0 = 100 nN, E^* = 10^{11} Pa and potential difference between the domains ΔV = 150 mV as determined from the EFM and SSPM data [2], the PFM contrast between the domains of opposite polarities is ? $h_{1\omega} = 3.02 \cdot 10^{-12}$ m/V .

Electromechanical model.

The electromechanical model of PFM contrast is remarkably similar to the well known piezoelectric indentation problem. In the classical limit [19], the coupled electromechanical problem is solved for mixed value boundary conditions; $V_s = V_{tip}$ in the contact area and the normal component of the electric field E_z= 0 elsewhere. Deformation of a piezoelectric surface occurs even when the tip is not in contact due to the non-uniform electric field. In the future discussion we distinguish two limits for the electromechanical model:

1. Strong (classical) indentation: $V = V_{\text{tip}}$ in the contact area, $E_z = 0$ elsewhere
2. Weak (field induced) indentation: contact area is negligible, $E_z \neq 0$

Strong indentation. A complete description of strong indentation limit is given by Suresh and Giannakopoulos [20], who extended the Herzian contact mechanics for piezoelectric materials. The relationship between the load, F, indentor potential, V, and indentation depths, h, is determined as

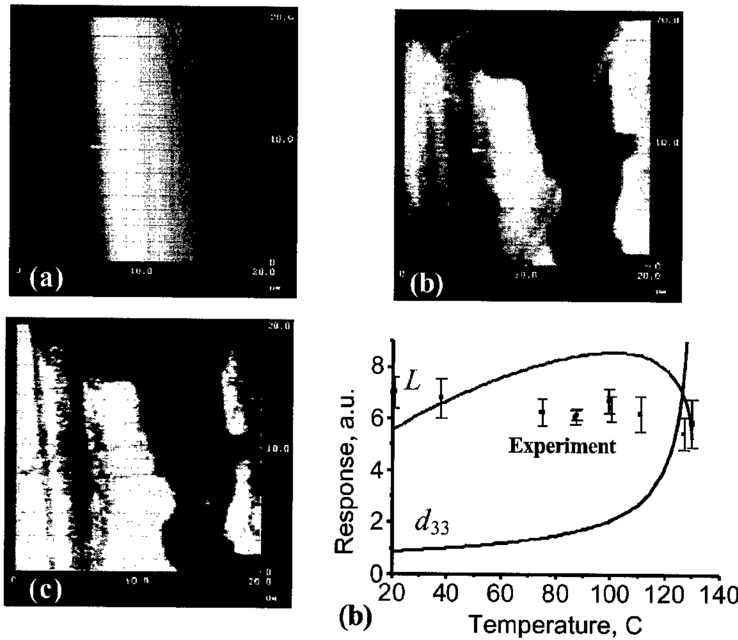

Figure 2. Surface topography (a), surface potential (b) and piezoresponse images (c) from a-c domain region on $BaTiO_3$ (100) surface and temperature dependence of PFM contrast in the weak indentation limit vs. d_{33} and experimental data (d).

$$h = \frac{a^2}{R} + \frac{2\beta}{3\alpha}V, \quad F = \alpha\frac{a^3}{R} - \beta a V \qquad \text{(5a,b)}$$

where α and β are constants dependent on material properties, a is contact are and R is tip radius of curvature. In the electromechanical model one can assume that for a relatively small indentation force and in the subresonant frequency region tip displacement is equal to surface displacement. Therefore, for small modulation amplitudes, the PFM contrast is $h_{1\omega} \approx h'(F, V_{dc})V_{ac}$, where the functional form of $h(F, V_{dc})$ is given by Eq. (5a,b). For $V_{dc} = 0$ the asymptotic analysis of Eqs. (5a,b) for c^+ orientation yields $k_0 = 4/3\ \beta/\alpha$, while for $V_{dc} \to +\infty$, $V_{dc} \to -\infty$ respective limits are $k_{+\infty} = 5/3\ \beta/\alpha$, $k_{-\infty} = 2/3\ \beta/\alpha$. These limits are independent of tip radius and contact force. The width of the transition region from $k_{-\infty}$ to $k_{+\infty}$ can be estimated from the second derivative of $h(F,V)$ at $V = 0$ as $V_0 = (9\alpha^{1/3}F^{2/3})/(2\beta R^{1/3})$. The values of PFM contrast in the strong indentation limit are relatively high and are comparable to the corresponding d_{33} values (Table I).

However, applicability of the strong indentation limit to the description of PFM contrast is limited. A shown above, in the rigid dielectric approximation $V_s << V_{tip}$ and hence the basic assumption of the strong indentation model in the contact area is not fulfilled. From the comparison of piezoelectric and capacitive charges in the contact area, the crossover between the

strong and weak indentation limit is expected at contact radius $a = \kappa_d^{-1} 1.13 \cdot 10^{-6}$ m, where κ_d is the dielectric constant of surface layer (κ_d ~ 1-80). This condition is clearly not fulfilled during PFM operation and the description of the contrast is thus done in the weak indentation limit.

Weak indentation. In the weak indentation limit, the contribution of the contact area to the total electromechanical response of the surface is neglected. Potential distribution in the tip surface junction is calculated by the rigid electrostatic model as shown above. Electromechanical response of the surface is calculated using Green's function for point force/charge as obtained by Karapetian *et al.* [21]

$$h(r) = f\frac{A}{r} + q\frac{L(s_{ij}, e_{ij}, \varepsilon_{xx}, \varepsilon_{zz})}{r}, \qquad (6)$$

where f is the point force, q is the point charge, A and L are constants dependent on material properties and r is the distance from indentation point. The surface response is:

$$h(\mathbf{r}) = L\int \frac{\sigma(\mathbf{r}_0)}{|\mathbf{r} - \mathbf{r}_0|} dS, \text{ where } \sigma(\mathbf{r}_0) = \varepsilon_0 \frac{dE_z(\mathbf{r}_0)}{dz} \qquad (7)$$

Noteworthy is that the materials properties define the PFM contrast through the coefficient L, while geometric properties of tip-surface system are described by the (materials independent) integral in Eq. (7). In the point charge approximation, PFM contrast for $BaTiO_3$ can be estimated as $h \approx 1.1 \cdot 10^{-11}$ m/V. Characteristic piezoresponse constants for different materials for strong and weak indentation limits are compared in Table I.

Table I. Piezoresponse constants for different materials.

Composition	Bulk d_{33}, m/V	Strong indentation k_0, m/V	**Weak indentation L, m^2/C**
$BaTiO_3$	$1.91 \cdot 10^{-10}$	$3.40 \cdot 10^{-10}$	**$1.76 \cdot 10^{-3}$**
PZT4	$2.91 \cdot 10^{-10}$	$4.96 \cdot 10^{-10}$	**$2.51 \cdot 10^{-3}$**
PZT5a	$3.73 \cdot 10^{-10}$	$6.04 \cdot 10^{-10}$	**$2.77 \cdot 10^{-3}$**

As can be seen from the estimates, the response is higher for electromechanical model, however, electrostatics can provide significant contribution to the contrast. For more realistic flattened tips the electromechanical contribution increases and the electrostatic contribution decreases due to larger contact stiffness. Electromechanical contrast is expected to be relatively insensitive to indentation force during PFM experiment. Finally, resolution is limited by tip radius of curvature rather than contact area.

Temperature dynamics of PFM contrast. To establish the validity of the weak indentation model, we calculated the temperature dependence of PFM contrast. Temperature dependence of electroelastic constants for $BaTiO_3$ was calculated by Ginzburg-Devonshire theory [22]. Note that no divergence is observed in $L(T)$ (Fig. 2). The physical origin of this behavior is that not only the piezoelectric constant, but also the dielectric constant increase with temperature.

CONCLUSIONS

An analytical model for electrostatic and electromechanical contrast in PFM have been developed. The characteristic features of the electrostatic contribution are:

1. Response decreases with indentation force due to higher contact stiffness
2. Contrast is expected to exhibit relaxation behavior similar to non-contact SPM

Within the electromechanical model, weak indentation is shown to describe the PFM contrast mechanism. Electromechanical contribution is estimated to be larger than electrostatic contribution approximately by a factor of 3. This implies that both electrostatic and electromechanical mechanisms are expected to contribute to the PFM contrast.

ACKNOWLEDGEMENTS

NSF Grant DMR 00-79909, Dr. A.E. Giannakopoulos and Prof. Subra Suresh (MIT), Prof. M. Cohen, Prof. V. Vitek (UPenn)

REFERENCES

1. A. Gruverman, O. Auciello, and H. Tokumoto, *Annu. Rev. Mat. Sci.* **28**, 101 (1998).
2. S.V. Kalinin and D.A. Bonnell, *Phys. Rev.* **B**, in press.
3. C. Durkan, M.E. Welland, D.P. Chu, and P. Migliorato, *Phys. Rev.* **B 60**, 16198 (1999).
4. K. Lee, H. Shin, W.K. Moon, J.U. Jeon, and Y.E. Pak, *Jpn. J. Appl. Phys.* **38**, L264 (1999).
5. C.S. Ganpule, V. Nagarjan, H. Li, A.S. Ogale, D.E. Steinhauer, S. Aggarwal, E. Williams, R. Ramesh, and P. DeWolf, *Appl. Phys. Lett.* **77**, 292 (2000).
6. A. Gruverman, *Appl. Phys. Lett.* **75**, 1452 (1999).
7. E.Z. Luo, Z. Xie, J.B. Xu, I.H. Wilson, and L.H. Zhao, *Phys. Rev.* **B 61**, 203 (2000).
8. J.W. Hong, K.H. Noh, S.I. Park, S.I. Kwun, and Z.G. Kim, *Rev. Sci. Instrum.* **70**, 1735 (1999).
9. J.W. Hong, K.H. Noh, S.I. Park, S.I. Kwun, and Z.G. Kim, *Phys. Rev.* **B. 58**, 5078 (1998).
10. T. Trenkler, P. De Wolf, W. Vandervorst, L. Hellemans, *J. Vac. Sci. Technol.* **B 16**, 367 (1998).
11. L.M. Eng, H.-J. Guntherodt, G.A. Schneider, U. Kopke, J. Munoz Saldana, *Appl. Phys. Lett.* **74**, 233 (1999).
12. V. Likodimos, X.K. Orlik, L. Pardi, M. Labardi, and M. Allegrini, *J. Appl. Phys.* **87**, 443 (2000).
13. S.V. Kalinin and Dawn A. Bonnell, *Appl. Phys. Lett.*, in press
14. A.Y. Borisevich, S.V. Kalinin, D.A. Bonnell, and P.K. Davies, *J. Mat. Res*, in press
15. T. Tybell, C.H. Ahn, J.M. Triscone, *Appl. Phys. Lett.* **75**, 856 (1999).
16. W.R. Smythe, *Static and Dynamic Electricity* (McGraw-Hill, New York, 1968)
17. T. M. Shaw, S. Trolier-McKinstry, and P. C. McIntyre, *Annu. Rev. Mater. Sci.* **30**, 263 (2000).
18. S. Timoshenko and J.N. Goodier, *Theory of Elasticity* (McGraw Hill, New York, 1951)
19. V.Z. Parton, B.A. Kudryavtsev, *Electromagnetoelasticity* (Gordon and Breach, 1988).
20. A.E. Giannakopoulos, S. Suresh, *Acta mater.* 47, 2153 (1999).
21. E. Karapetian, I. Sevostianov, and M. Kachanov, *Phil. Mag.* **B 80**, 331 (2000).
22. A.F. Devonshire, *Phil. Mag.* **40**, 1040 (1949).

Mat. Res. Soc. Symp. Proc. Vol. 655 © 2001 Materials Research Society

Nanometer Scale Domain Measurement of Ferroelectric Thin Films Using Scanning Nonlinear Dielectric Microscopy

Hiroyuki Odagawa, Kaori Matsuura and Yasuo Cho
Research Institute of Electrical Communication, Tohoku University,
Sendai, 980-8577, Japan

ABSTRACT

A very high-resolution scanning nonlinear dielectric microscope with nanometer resolution was developed for the observation of ferroelectric polarization. We demonstrate that the resolution of the microscope is of a sub-nanometer order by measurement of domains in PZT and SBT thin films. The experimental result shows that nano-sized 180° c-c ferroelectric domain with the width of 1.5 nm for PZT thin film are observed. The result also shows that the resolution of the microscope is less than 0.5 nm for the PZT thin film.

INTRODUCTION

Recently, we have proposed and developed a new purely electrical technique for imaging the state of ferroelectric polarization and local crystal anisotropy of dielectric materials, which involves the measurement of point-to-point variation of the nonlinear dielectric constant of a specimen, and is termed "scanning nonlinear dielectric microscopy" (SNDM) [1-5]. This is the first successful purely electrical method for observing the ferroelectric polarization distribution without the influence of the shielding effect by free charge. To date, its resolution has been improved down to one nanometer. Moreover, SNDM can evaluate both linear and nonlinear dielectric constants quantitatively [6], and also can evaluate the local crystal isotropy, for example, crystal polarity of ZnO thin film deposited on $LiNbO_3$ substrate without the influence of the substrate polarity [7].

In this paper, at first we briefly describe the theory for detecting polarization and the technique for the nonlinear dielectric response. Next, we report the results of the imaging of the ferroelectric domains in PZT and SBT thin films using SNDM with nanometer resolution. Especially in a measurement of PZT thin film, it was confirmed that the resolution was sub-nanometer order. We also describe the theoretical resolution of SNDM.

NONLINEAR DIELECTRIC IMAGING

First, we briefly describe the theory for detecting polarization. Precise descriptions of the principle of the microscope have been reported elsewhere (see refs.3,4). Figure 1 shows the system setup of the SNDM using the LC lumped constant resonator probe [4]. In the figure, $C_s(t)$ denotes the capacitance of the specimen under the center conductor (the needle or the cantilever) of the probe. Cs(t) is a function of time because of the nonlinear dielectric response under an applied alternating electric field $E_{p3}(=E_p\cos\omega_p t,\ f_p=5\text{kHz})$. The ratio of the alternating variation of capacitance $\Delta C_s(t)$ to the static value of capacitance C_{s0} without time dependence is given as [3]

$$\frac{\Delta C_S(t)}{C_{S0}} = \frac{\varepsilon_{333}}{\varepsilon_{33}} E_p \cos\omega_p t + \frac{\varepsilon_{3333}}{4\varepsilon_{33}} E_p^2 \cos 2\omega_p t \qquad (1)$$

where ε_{33} is a linear dielectric constant and ε_{333} and ε_{3333} are nonlinear dielectric constants. The even rank tensor, including the linear dielectric constant ε_{33}, does not change with rotation of the polarization. On the other hand, the lowest order of the nonlinear dielectric constant ε_{333} is a third-rank tensor, similar to the piezoelectric constant, so that there is no ε_{333} in a material with a center of symmetry, and the sign of ε_{333} changes in accordance with the inversion of the spontaneous polarization.

This LC resonator is connected to the oscillator tuned to the resonance frequency of the resonator. The above mentioned electrical parts (i.e. needle or cantilever, ring, inductance and oscillator) are assembled into a small probe for the SNDM. The oscillating frequency of the probe (or oscillator) (around 1.3 GHz) is modulated by the change of capacitance $\Delta C_s(t)$ due to the nonlinear dielectric response under the applied electric field. As a result, the probe (oscillator) produces a frequency modulated (FM) signal. By detecting this FM signal using the FM demodulator and lock-in amplifier, we obtain a voltage signal proportional to the capacitance variation. Each signal corresponding to ε_{333} and ε_{3333} was obtained by setting the reference signal of the lock-in amplifier at the frequency ω_p of the applied electric field and at the doubled frequency $2\omega_p$, respectively. Thus we can detect the nonlinear dielectric constant just under the needle and can obtain the fine resolution determined by the diameter of the pointed end of the needle and the linear dielectric constant of specimens.

This SNDM probe is very sensitive to resolve a very small capacitance variation with the magnitude of 10^{-22} F. For this study, the needle of the lumped constant resonator probe was fabricated using a metal-coated conductive cantilever. The radius of curvature of the chip was around 25 nm.

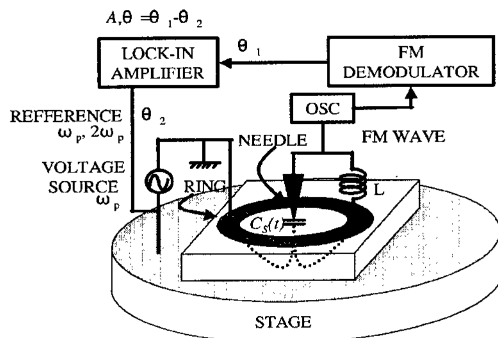

Figure 1. *Schematic diagram of SNDM.*

MEASUREMENT RESULTS

Figure 2 shows the SNDM (a) and AFM (b) images of a PZT thin film deposited on a $SrTiO_3$ substrate using metal organic chemical vapor deposition. These images are taken from the same location of the sample simultaneously. As shown in figure 2(a), it is clearly seen that each grain in the film is composed of several domains. From X-ray diffraction analysis, we have confirmed that this PZT film belongs to the tetragonal phase and the diffraction peaks, corresponding to both the c-axis and a-axis, were observed. An a-domain does not provide the SNDM signal because the crystal symmetry exists along the surface normal direction of the a-domain. Therefore dark region in figure 2(a) (no signal region) is the a-domain and the bright region in figure 2(a) (positive signal region) is the c-domain. Thus, the images show that we succeeded in observing 90° a-c domain distribution in a single grain of the film.

In contrast to the figure 2, figure 3 shows the measurement results of a PZT thin film made by sol-gel method on Pt(111) / Si substrate. In this case, the polarization direction tilts with 45° from the surface normal, because this film belongs to the tetragonal system and the crystal orientation perpendicular to the surface is [111] direction. In this figure, the 45° tilted c surface ((001) surface) at the end of the grain shown by a black region in the image is clearly observed. That is, SNDM detected the inclined c-domain which is along the 45° rotated direction from the surface normal.

Figure 4 also shows the SNDM (a) and AFM (b) images taken from a same location of SBT thin film. From the images, we found that, by using SNDM, we could easily observe the several types of domains even in SBT thin film, whose domains were relatively difficult to be observed by other methods such as piezoelectric response imaging technique by using SFM.

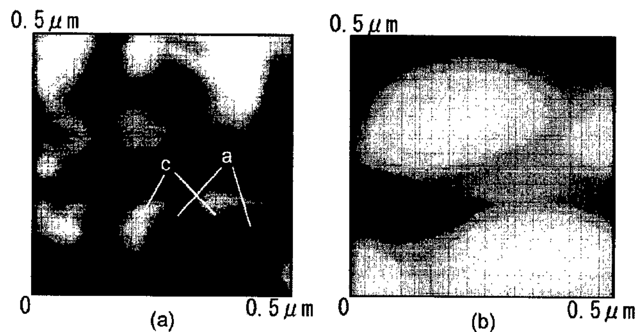

Figure 2. *Images of a PZT film on $SrTiO_3$ substrate made by MOCVD.*
(a) Domain patterns, (b) surface morphology.

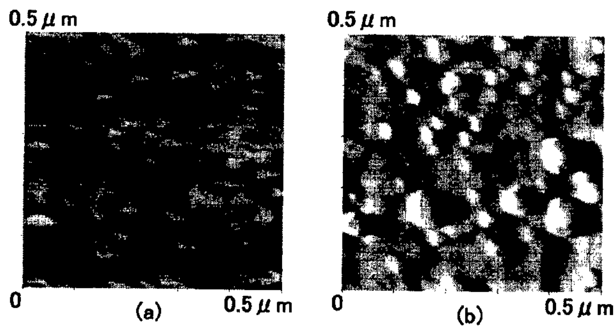

Figure 3. *Images of a PZT film on Pt / Si substrate made by sol-gel method.*
(a) Domain patterns, (b) surface morphology.

These images were taken from a relatively large area. Therefore, we also tried to observe very small domains in a PZT film fabricated on $SrTiO_3$ substrate. The results are shown in figure 5.In order to clarify the direction of the polarization, the phase image was measure. The bright area and dark area correspond to the negative polarization and the positive polarization, respectively. It shows that we can successfully observe a nano-scale 180° c-c domain structure. Figure 5(b) shows a cross sectional image taken along line A-A' in figure 5(a). As shown in figure 5(b), we measured a c-c domain with a width of 1.5 nm. Moreover we find that the resolution of the microscope is better than 0.5 nm.

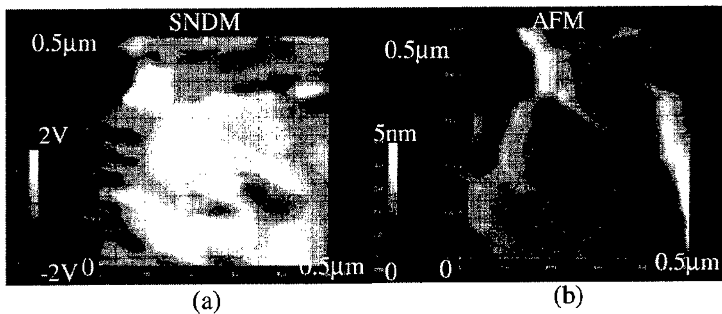

***Figure 4.** Images of a SBT film. (a) Domain patterns, (b) surface morphology.*

To clarify the reason why such high resolution can be easily obtained, even if a relatively thick needle is used for the probe, we show the calculated results of the one-dimensional image of 180° c-c domain boundary lying at y=0 (We chose y direction as the scanning direction)[8][9]. Figure 6 shows the calculated results where Y_0 is the tip position normalized with respect to the tip radius a.

The resolution of the SNDM image is heavily dependent on the dielectric constant of the specimen. For example, for the case of $\varepsilon_{33}/\varepsilon_0=1000$ and =10 nm (a needle tip with a radius of 10 nm is easily obtainable.) an atomic scale image will be able to be taken by SNDM.

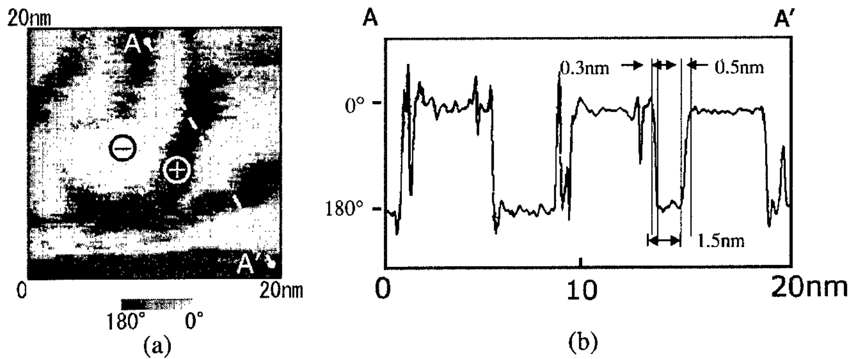

***Figure 5.** Images of a PZT film on $SrTiO_3$ substrate made by MOCVD.*

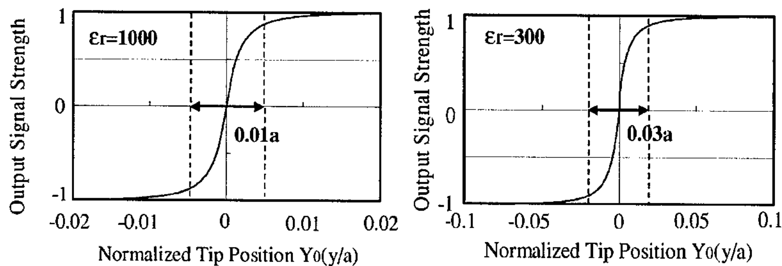

Figure 6. *Theoretical images of the 180 ° c-c domain boundary.*

CONCLUSION

We demonstrate that the resolution of the microscope is of a sub-nanometer order by measurement of domains in PZT and SBT thin films. The experimental result shows that nano-sized 180° c-c ferroelectric domain with the width of 1.5 nm for PZT thin film are observed. The result also shows that the resolution of the microscope is less than 0.5 nm for the PZT thin film. Thus the SNDM system is very useful for understanding domain structures and domain dynamics of ferroelectric thin films.

REFERENCES

1. Y. Cho, A. Kirihara, and T. Saeki, Denshi Joho Tsushin Gakkai Ronbunshi, **J78-C-1,** 593 (1995) [in Japanese].
2. Y. Cho, A. Kirihara and T. Saeki , Electronics and Communication in Japan, Part 2, (Scripta Technica, Inc) **79,** 68 (1996).
3. Y. Cho, A. Kirihara and T. Saeki, Rev. Sci. Instrum., **67**, 2297 (1996) .
4. Y. Cho, S. Atsumi and K. Nakamura, Jpn. J. Appl. Phys., **36**, 3152 (1997).
5. Y. Cho, S. Kazuta and K. Matsuura, Appl. Phys. Lett., **72**, 2833 (1999).
6. Y.Cho, S.Kazuta, K.Ohara and H.Odagawa, Jpn. J. Appl. Phys., **39**, 3086 (2000).
7. S.Kazuta, Y.Cho, H.Odagawa and M.Kadota, Jpn. J. Appl. Phys., **39**, 3121 (2000).
8. Y. Cho, Ferroelectrics [in press].
9. H. Odagawa and Y. Cho, Jpn. J. Appl. Phys. **39**, 5719 (2000).

Mat. Res. Soc. Symp. Proc. Vol. 655 © 2001 Materials Research Society

Lattice Vibrational Properties of $SrBi_2Ta_2O_9$

Ran Liu[1] and Pengdi Han[2]
[1]DigitalDNA Laboratories, Motorola,
Mesa, AZ 85202, USA
[2]University of Illinois at Urbana-Champaign, Department of Materials Science,
Urbana, IL 60801, USA

ABSTRACT

$SrBi_2Ta_2O_9$ is one of the layered perovskite ferroelectrics with excellent fatigue resistance and thus has gained great interest of semiconductor industries recently in non-volatile ferroelectric random access memory (FERAM) applications. The understanding of the lattice vibrational properties of this material can provide crucial information on its structure and dielectric behavior. In this work, we carried out Raman spectroscopy study of thin film, powder and single crystal $SrBi_2Ta_2O_9$. At temperatures above the Curie temperature, all 12 Raman modes expected from the tetragonal (I4/mmm) structure have been observed and assigned to the 4 A_{1g}, 6 E_g and 2 B_{1g} modes based the polarized Raman spectra from the single crystal samples. At lower temperature, the Raman spectra have revealed all 22 A_1 modes, but only 3 out of the 20 A_2 modes and 5 out of the 42 B_1/B_2 modes were observed in the ferroelectric phase ($A2_1am$). The soft mode was found to be of A_1 symmetry and appearing only when light polarization lay in the ab-plane.

INTRODUCTION

Bismuth layered perovskite ferroelectrics, $Bi_2A_{m-1}B_mO_{3m+3}$ (A = Na^{1+}, K^{1+}, Ba^{2+}, Ca^{2+}, Sr^{2+}, Bi^{3+},... and B = Fe^{3+}, Ti^{4+}, Nb^{5+}, Ta^{5+}, W^{6+},...), discovered by Aurivillius 47 years ago [1], have recently gained great interest for their potential application to non-volatile ferroelectric random access memories. $SrBi_2Ta_2O_9$, in particular, has been reported to have excellent fatigue resistance [2]. Detailed investigation of the lattice vibrational properties is required for understanding the structural properties associated with the ferroelectric phase transition and the polarization state and providing a knowledge base for characterization of these materials. In this work, we study the lattice vibrational properties of $SrBi_2Ta_2O_9$ using Raman spectroscopy and explore the potential application of this technique to characterization of this material.

The high temperature paraelectric phase of $SrBi_2Ta_2O_9$ has a tetragonal structure with space group $I\,4/mmm$ (a = 3.895 Å, c = 25.06 Å) [1] (see Figure 1). At temperatures below the Curie temperature (~340°C), small displacive perturbations of the parent tetragonal structure lead to an orthorhombic structure with space group $A\,2_1am$ [3, 4] (a = 5.5306, b = 5.5344, c = 24.9839 Å). Since the orthorhombic distortion is very small, we will first assign the experimental Raman lines using the undistorted parent structure $I4/mmm$ for simplicity. The pseudo-tetragonal unit cell contains one molecular formula, $SrBi_2Ta_2O_9$, and gives rise to 42 lattice vibrational modes (see Table I) and 39 optical modes. The optical modes at zero wavevector are

$$\Gamma^{T}_{opt} = 4A_{1g} + 2B_{1g} + 6E_g + 6A_{2u} + B_{2u} + 7E_u\,,$$

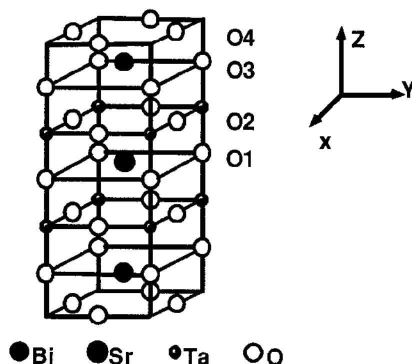

Figure 1*. Unit cell of the tetragonal $SrBi_2Ta_2O_9$ structure (I4/mmm).*

Table I. Phonon modes in the tetragonal structure.

Atom	Symmetry	Phonon Modes
Sr	D_{4h}	$A_{2u}+E_u$
Ta	C_{4v}	$A_{1g}+E_g+A_{2u}+E_u$
Bi	C_{4v}	$A_{1g}+E_g+A_{2u}+E_u$
O1	D_{4h}	$A_{2u}+E_u$
O2	C_{2v}	$A_{1g}+B_{1g}+2E_g+A_{2u}+B_{2u}+2E_u$
O3	C_{4v}	$A_{1g}+E_g+A_{2u}+E_u$
O4	D_{2d}	$B_{1g}+E_g+A_{2u}+E_u$

of which 18 are Raman active. As the E_g modes are degenerate, we expect a total of 12 Raman peaks. For the low temperature orthorhombic phase, the lattice distortion destroys the central symmetry and roughly doubles the tetragonal unit cell in such a way that the tetragonal cell diagonals in the basal plane become approximately the lattice constants a and b of the orthorhombic cell. Similar factor group analysis leads to 81 optical modes at the Brillouin-zone center:

$$\Gamma^{0}_{opt} = 21A_1 + 20A_2 + 19B_1 + 21B_2 .$$

EXPERIMENTAL

Thin film samples of $SrBi_2Ta_2O_9$ were prepared from a metal-organic solution consisting metal 2-ethylhexanoates in either xylenes or n-butyl acetate. The solution was spin coated on oxidized Si wafers with a bottom electrode consisting of DC magnetron-sputtered TiO_2 and Pt. The single crystal samples were grown from a melt consisting of Bi_2O_3, V_2O_5, TiO_2, $SrCO_3$ and B_2O_3 using a Bi_2O_3 self-flux method. $BaCO_3$. Crystals of size as large as 2 x 2 x 1.5 mm were obtained. Measurements of the temperature dependence of dielectric constant indicated that the Curie temperature is around 270°C, significantly lower than the reported value (335°C) [5] from the sintered polycrystalline samples prepared by solid state reaction. This difference is probably caused by a difference in composition. The Raman measurements were performed using a Dilor XY800 monochromator equipped with a LN_2

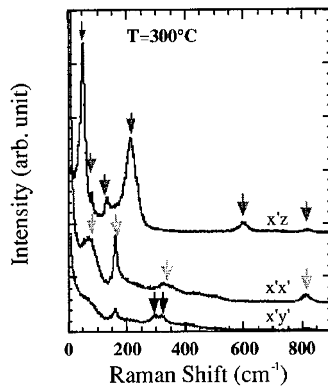

***Figure 2**. Polarized Raman spectra from a single crystal sample at 300°C, where x', y', z denote the incident or scattered polarization direction.*

cooled CCD. The laser beam of the 458 nm Ar-ion laser line was focused down to a spot of about 30 μm in diameter onto the sample surface using a 30x objective lens. A hot stage was used to heat samples from room temperature up to 300°C.

RESULTS AND DISCUSSION

Figure 2 shows polarized spectra of a single crystal $SrBi_2Ta_2O_9$ sample in the frequency range of 10 to 1000 cm^{-1}, where x, y, z are along the a, b ,c crystal axes and x'and y' are along the diagonal of the basal plane of the tetragonal structure (see Fig. 1). All 4 A_{1g} modes of the tetragonal phase appear at 75, 160, 330, and 813 cm^{-1} in the $z(x',x')z$ scattering configuration, the 2 B_{1g} modes at 295 and 320 cm^{-1} in the $z(x',y')z$ scattering configuration, and the 6 E_g modes at 51, 80, 130, 213, 600, and 810 cm^{-1} in the $y'(x',z)y$ scattering configuration. The assignments of the 12 Raman modes in the tetragonal phase are listed in Table II.

The lowest-energy E_g peak should correspond to the rigid layer mode involving a relative motion of the two Bi-O planes. This mode, as expected, appears at almost the same frequency (within ~3 cm^{-1}) for all the Bi-based layered ferroelectrics $Bi_2A_{m-1}B_mO_{3m+3}$ with different A and B metal atoms [6]. The analog of this mode can also be found in Bi-based layered high-T_c superconductors at a similar frequency [7]. The other E_g mode involving the in-plane motion of the Bi and O atoms in the BiO planes can be assigned to the 80 cm^{-1} peak. The difference between this mode and the first one is that the two atoms in the same plane vibrate out-of-phase instead of in-phase. The lowest A_{1g} mode at 75 cm^{-1}, on the other hand, should be attributed to the z-axis vibration of the heaviest Bi atoms. The E_g peak at 130 cm^{-1} and the A_{1g} peak at 161 cm^{-1} could be assigned to the in-plane and out-of-plane vibrations of Ta, respectively. The higher frequency peaks involve dominantly the lighter oxygen vibrations. The E_g peak at 213 cm^{-1} and the B_{1g} peak at 295 cm^{-1} are very likely the in-plane and the out-of-plane vibrations of the O4 atoms in the BiO planes, respectively. In the latter mode, the nearest neighboring O4 atoms of

the same planes move out-of-phase. The B_{1g} peak at 320 cm^{-1} and the A_{1g} peak at 330 cm^{-1}might correspond to the out-of-phase and in-phase z-axis vibration of the O2 atoms in the TaO planes, respectively. The in-plane vibration mode of the O4 atoms gives rise to the E_g peak at 810 cm^{-1}. Finally, we assign the E_g peak at 600 cm^{-1}, and the A_{1g} peak at 813 cm^{-1} to the in-plane and out-of-plane vibration modes of the apical oxygen atom (O3) of the TiO_6 octahedron.

Table II. Raman mode assignment for the tetragonal structure.

Frequency (cm^{-1})	Symmetry	Assignment
51	E_g	Bi-O x(y)-axis in-phase vibration
75	A_{1g}	Bi z-axis vibration
80	E_g	Bi-O x(y)-axis out-of--phase vibration
130	E_g	Ta x(y)-axis vibration
161	A_{1g}	Ta z-axis vibration
213	E_g	O4 x(y)-axis vibration
295	B_{1g}	O4 z-axis vibration
320	B_{1g}	O2 z-axis out-of-phase vibration
330	A_{1g}	O2 z-axis in-phase vibration
600	E_g	O3 x(y)-axis vibration
810	E_g	O2 x(y)-axis vibration
813	A_{1g}	O3 z-axis vibration

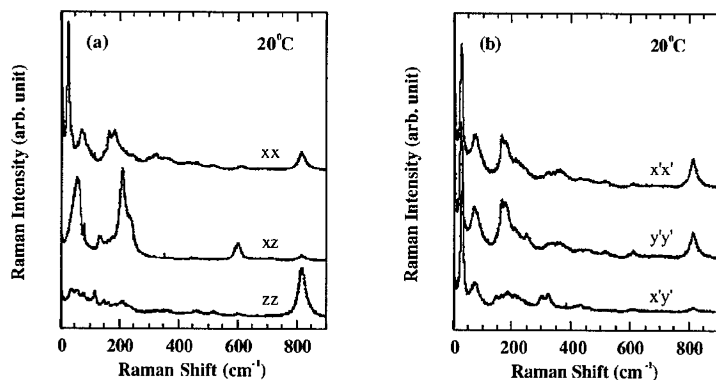

***Figure 3**. Polarized Raman spectra of a single crystal $SrBi_2Ta_2O_9$ in the orthorhombic phase (T=20 °C). The x' and y' are along the diagonals of the tetragonal unit cell.*

Figures 3a and 3b display the polarized Raman spectra from the single crystal sample in the ferroelectric orthorhombic phase. More Raman lines have emerged due to the orthorhombic distortion that leads to a doubled unit cell. The spectra taken with the parallel polarization geometry (*xx, yy, x'x'*,

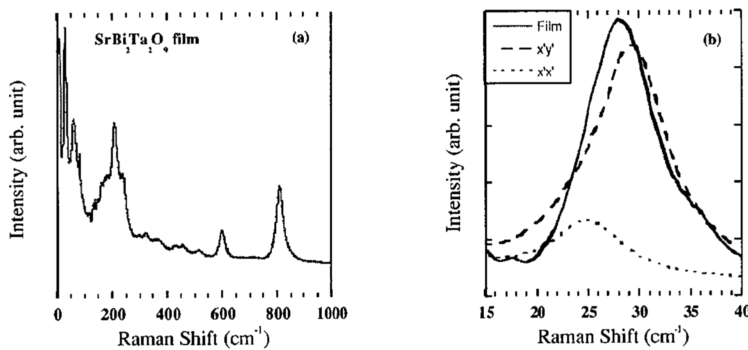

Figure 4. *Raman spectrum from a $SrBi_2Ta_2O_9$ film at room temperature (a) and the comparison of low frequency spectra from a single crystal and a film (b).*

zz) show all 21 A_1 modes at 25, 38, 60, 72, 82, 117, 144, 160, 182, 210, 230, 244, 293, 320, 365, 430, 460, 520, 603, 687, and 815 cm^{-1}. The *xz* spectrum, however, only reveals 10 of the 19 expected B_1 modes, only 4 more (at 173, 457, 516, and 716 cm^{-1}) than the correlated E_g modes in the tetragonal phase. Similarly, only 8 of the expected 20 A_2 modes have been resolved at 29, 73, 145, 190, 300, 325, 430, and 460 cm^{-1} in the *x'y'* spectrum that corresponds to the B_{1g} geometry in the tetragonal case. Figure 4(a) shows the Raman spectrum of a $SrBi_2Ta_2O_9$ film. Comparing with the polarized spectra of the single crystal, the film seems to be randomly oriented.

The most striking effect of the ferroelectric phase transition on the phonon spectra is the emergence of two strong low frequency peaks at 25 and 29 cm^{-1}, which very likely are responsible for the phase transition. Kojima and co-workers have observed a soft phonon mode in single crystal $Bi_4Ti_3O_{12}$, $CaBi_4Ti_4O_{15}$, and $SrBi_4Ti_4O_{15}$ [6]. A soft mode has also been reported by Liu and co-workers in polycrystalline $SrBi_2Nb_2O_9$ [8]. In all cases, the soft modes appear in a frequency range from 20 to 30 cm^{-1} in the ferroelectric phase. However, since both groups did not report any polarized Raman study, only one peak was seen between 20 and 30 cm^{-1} and its symmetry has not been analyzed. It is clear in Fig. 4(b) that the two peaks appearing in the *x'x'* (A_1 or A_{1g} in the tetragonal phase) and *x'y'* (A_2 or B_{1g} in the tetragonal phase) spectra of the single crystal show up as only one broader peak for the polycrystalline film. To identify the soft mode, Raman spectra were taken for the two symmetries at different temperatures between room temperature and 300°C (see Fig. 5). One can see that the frequency and the intensity of the A_1 line decreases toward zero when the sample is heated up to the transition temperature. On the contrary, the A_2 peak only softens slightly and remains at fixed frequency at the phase transition although its intensity diminishes. Therefore, the A_1 Raman line at 25 cm^{-1} is the *true* soft mode.

Figure 6 displays the squares of the lowest A_1 and A_2 peak frequencies. Again one can see that the A_2 mode only shows normal softening upon heating and remains at finite frequency near the phase transition. The temperature dependence of the squared frequency for the A_1 peak is approximately proportional to $T_0 - T$, where $T_0 = 338°C$. This strongly indicates that this mode is an underdamped soft mode and the ferroelectric phase transition is displacive. Similar phonon softening behavior has been

also observed in the film sample. However, since it was hard to separate the two lowest frequency peaks in the polycrystalline sample, the temperature dependence of the soft mode could not be determined accurately.

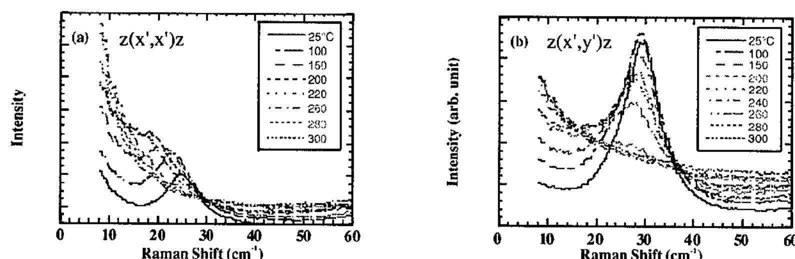

Figure 5. *Temperature dependence of the lowest frequency A_1 (a) and A_2 (b) Raman peaks.*

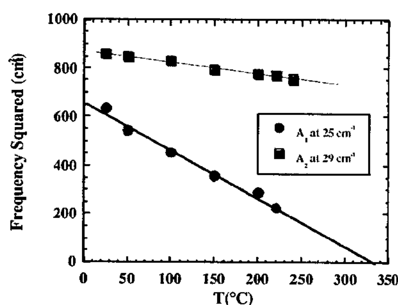

Figure 6. *Temperature dependence of frequency squared for the lowest A_1 and A_2 modes.*

CONCLUSIONS:

Raman measurements were carried out on single crystal and thin film $SrBi_2Ta_2O_9$. Polarized Raman spectra of the tetragonal phase revealed all the expected modes that can be reasonably assigned based on their symmetries and frequencies. All A_1 modes have been observed in the orthorhombic phase, but only few are seen for the less symmetric modes. The two lowest modes have been distinguished using their different symmetries. The soft mode has been found to have the A_1 symmetry.

REFERENCES

1. B. Aurivillius, *Ark. Kemi*, **1**, 449 (1949).
2. R.E. Jones, P. Zurcher, P. Chu, D.J. Talor, S. Zarfar, B. Jing, and S.J. Gillespie, *Integrated Ferroelectrics*, **15**, 199 (1997).
3. R.E. Newnham, R.W. Wolfe, R.S. Horsey, F.A. Diaz-Colon, and M.I. Kay, *Met. Res. Bull.*, **8**, 1183 (1973).
4. A.D. Rae, J.G. Thompson, and R.L. Withers, *Acta Cryst.*, **48**, 418 (1992).
5. E.C. Subbarao, *J. Phys. Chem. Solids*, **23**, 665 (1962).
6. S. Kojima, R. Imaizumi, S. Hamazaki, and M. Takashige, *Jpn. J. Appl. Phys.*, **33**, 5559 (1994).
7. Ran Liu, M.V. Klein, P.D. Han, and D.A. Payne, *Phys. Rev.* B, **45**, 7392 (1992).
8. J. Liu, G. Zou, H. Yang, and Q. Cui, *Solid State Commun.*, **90**, 365 (1994).

Mat. Res. Soc. Symp. Proc. Vol. 655 © 2001 Materials Research Society

Transient Behavior of the Polarization in Ferroelectric Thin Film Capacitors

Oliver Lohse[1], Michael Grossmann[1], Dierk Bolten[1], Ulrich Boettger[1], and Rainer Waser[2]
[1]IWE II, RWTH University of Technology, 52056 Aachen, Germany
[2]FZJ Research Center Juelich, 52425 Juelich, Germany

ABSTRACT

The understanding of the polarization switching process of ferroelectric capacitors is highly relevant for the development and optimization of FeRAM devices. We report on the characterization of $Pb(Zr,Ti)O_3$ thin films which have been studied by means of dedicated rectangle pulse measurements. Decreasing the voltage level of the excitation pulses decelerates the polarization switching significantly to the range of milliseconds and reduces the switchable polarization. In this work the influence of niobium (Nb) doping on the switching properties of PZT thin films prepared by CSD are investigated to reach the aspired conditions of low voltage operation, read and write access pulses in the range of nanoseconds. For the implementation of the transient behavior of ferroelectric capacitors in circuit design and simulation tools it is necessary to develop a model which precisely describes the polarization hysteresis, the pulse switching behavior as well as the small signal capacitance. The fundamental considerations for this model are presented, based on an ideal ferroelectric capacitor, taking into account the Curie-von Schweidler behavior. The latter is observed in non-ferroelectric high-K materials as well as in ferroelectric thin films.

INTRODUCTION

Thin films of perovskite materials such as lead zirconate titanate (PZT) [1] and layered perovskites such as strontium bismuth tantalate (SBT) [2] are being intensively studied for their application in high density ferroelectric random access memories (FeRAM) integrated circuits [3]. In addition to processing issues of integrating these materials in semiconductor technology, the ferroelectric properties and their reliability are of major interest. In comparison to non-ferroelectric barium strontium titanate (BST), where the dielectric relaxation has been extensively explored [4], relaxation in ferroelectric materials has not yet received the attention it deserves. In this work the voltage step characterization is exploited to elucidate the origin of relaxation in ferroelectric materials for the fast read and write access of the memory cell.

The intrinsic switching time of the reversal in ferroelectric thin films is assumed to be below nanoseconds [5,6]. These times are only obtained when voltages much higher then the coercitive voltage are instantaneously applied. For low voltage levels, the switching process can be very slow. This is of great interest for the application in fast access memories, since it can in principle limit the access time of the memory cell, especially, in the desired low voltage operation range. To remind the reader of the empirical equations found by W. Merz [7] which can describe the current response during a polarization reversal in ferroelectric single crystals, typical switching data measured by Pulvari and Kuebler [8] at triglycine-fluoberyllate (TGFB) are shown in Figure 1 (right). The data are characterized by the exponential equations as shown in the figure. They describe that with increasing excitation field the switching time t_s, defined as the instant of the maximum current, due to the polarization reversal, is decreased and the value of the maximum current i_{max} is increased. The activation field α in both equations is the same value. Later it will

be more useful to define the switching time t_s as the instant at which the polarization reversal is finished. This does not affect the activation field α.

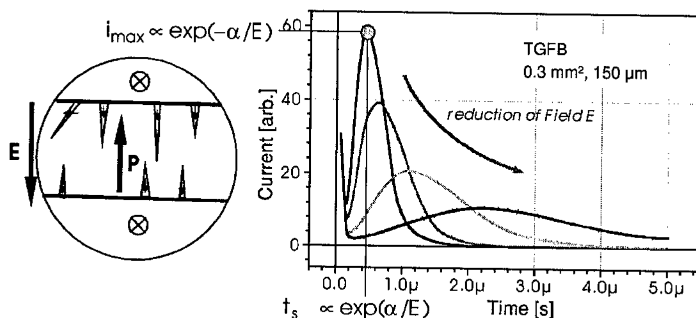

Figure 1. *Left: Schematic of domain structure during polarization reversal in ferroelectric single crystal. Right: Evoked current response with varying electrical excitation field [8]. The current maximum due to the polarization switching obeys shown the equations found by W. Merz [7].*

From the work of Merz [7] it is known that the polarization switching in ferroelectric single crystals takes place by creating nuclei of needle and wedge shape of oppositely directed domains as sketched in Figure 1 (left) and sidewise movement of the domain walls until the polarization is reversed.

It is referred to as the intrinsic ferroelectric switching, which is dependent on the rate of nucleation of opposite domain nuclei, the shape of the domains, the friction of the domain walls, the velocity of the domain walls and their dependence on the electrical field, etc.. In the following the electrical data obtained from ferroelectric thin films is examined and compared to the polarization switching data found for ferroelectric single crystals.

MODELING

The intrinsic ferroelectric polarization reversal can be modeled by the application of the Kolmogorov-Avrami (K-A) model [9,10] extended to the case of applied field dependent sidewise velocity of the domain walls. Such a method has been successfully developed by the group of Ishibashi [11-13]. They have included the field dependence of the polarization switching and modeled the *D-E* hysteresis loops depending on the excitation frequency of triangle as well of sinusoidal signals and found good agreement to experimental data of tri-glycine sulfate (TGS) single crystals. The K-A is a statistical model which describes the phase transition kinetics in infinite media and was originally developed to model the crystallization process of metals. In ferroelectrics it can describe the time dependent fractional area $c(t)$ of the switched polarization and reads in a simple form as

$$c(t) = 1 - \exp[-(t/t_0)^n] \qquad (1)$$

with t_0 being mainly determined by the nucleation rate, the wall mobility, and the applied field and n mainly by the dimensionality of the domains. Additional work on this field has been performed by the group of Shur [14].

To illustrate the effect of the intrinsic ferroelectric switching on the *P-V* hysteresis loops and on the current response to an applied voltage step the Equation (1) has been implemented into an SPICE model [15,16]. The result is shown in Figure 2. The domain wall velocity has been taken into account by using the empirical equation found by Miller and Savage [17]

$$v = v_\infty \exp(-\alpha/E) \qquad (2)$$

with v_∞ and α being constants and E being the applied electrical field.

The simulation is performed for a time independent $n = 2$ which means that no new nuclei occur and there are cylinders which grow sidewise with time.

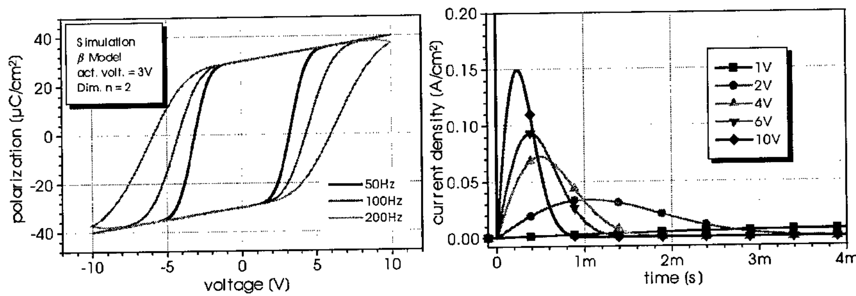

Figure 2. *P-V Hysteresis loop (left) and current response (right) on applied voltage step using K-A model implemented in SPICE.*

The output of the simulation shows the link between the Merz behavior of the transient currents and the frequency dependence of the hysteresis loop.

SAMPLE PREPARATION

The polarization switching behavior has been investigated at two different PZT thin film capacitor samples, with Zr:Ti ratio of 30:70, one sample undoped and one doped with 1% niobium (Nb). All other process parameters are kept equal. It is assumed that niobium, which is a soft dopant, counteracts the p-type conductivity arising due to lead vacancies in PZT, and increases the electrical resistivity of bulk PZT ceramics [18]. This has been confirmed by leakage current measurements carried out at both samples (see Table I)

Table I. Leakage currents at 1.4V

Nb content	Current density
0 %	$1.6 \cdot 10^{-7}$ A/cm^2
1 %	$1.3 \cdot 10^{-9}$ A/cm^2

The samples were prepared by a modified Budd and Payne [19] chemical solution deposition (CSD) method. The thickness amounts to approx. 140nm. By introducing 1% niobium the hysteresis properties are not significantly changed, and the remanent polarization reaches very good values (Figure 3).

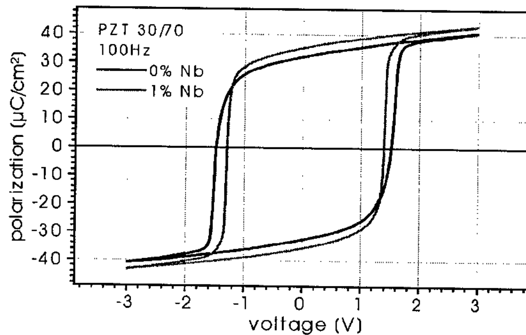

Figure 3. *P-V Hysteresis loop of undoped and Nb doped PZT 30/70.*

EXPERIMENT

A typical procedure to determine the switching behavior of ferroelectric thin films is to record the charge response of a ferroelectric capacitor on a, so called, PUND signal. (A good illustration is given in reference [20]). By means of this procedure the switchable polarization is determined as a function of the voltage and the pulse width. The method is close to the application of FRAM devices but has the drawback that the variation of the parameters also affects the prehistory of the samples. Therefore, in this work the Voltage Step Technique is used, as illustrated in Figure 4. The excitation signal consists of two hysteresis cycles to full saturation, than a waiting period of one second, to allow relaxation processes to subside, and than a voltage step to switch the polarization. The response is measured by means of a shunt resistance or a sense capacitor for short times and virtual ground for the time range of microseconds and longer. In each case, either the current response is measured and the charge is determined by integration, or the charge response is measured and the current is determined by numerical differentiation. With voltage levels of the excitation step in the range of the coercive voltage it is possible to slow down the polarization reversal and to separate it from the dielectric charging. By this, it can be guaranteed that the voltage step is fully applied during the polarization reversal, which is crucial for an evaluation of the switching currents according to Merz (see also Ref [21]).

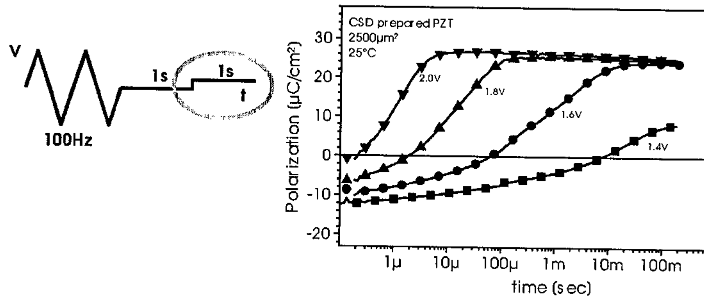

Figure 4. *Left: Excitation pattern for voltage step measurement. Right: Polarization response of CSD prepared PZT thin film.*

The determination of the absolute value of the polarization is not trivial. It is assumed that the absolute values of the positive and negative polarization in the saturation of a hysteresis loop are equal, i.e., the saturation points of a hysteresis loops are symmetrical. Hence, during the two hysteresis cycles the absolute course of the polarization is known. However, measuring the charge response of a ferroelectric thin film with a sense capacitor or an integration capacitor in virtual ground circuit (coulombmeter) has always the error introduced by the discharging of the sense capacitor. The more the discharging is reduced the slower is the measuring system concerning the response on the change of charge of the ferroelectric capacitor. Hence, it is not possible to measure the change of the charge in the period from the hysteresis loops to the voltage step (here one second) and afterwards to measure a fast charge response in the range below microseconds. Every coulombmeter is inherently either exact or fast.

Fortunately, the course of the polarization after driving the voltage to zero after the hysteresis loops is well known [22]. It exhibits a linear decrease over a logarithmic time scale as shown in Figure 5. It can be described by the equation $P = A + B \cdot \log(t)$. To determine the polarization at the instant of the voltage step the relaxation data is extrapolated.

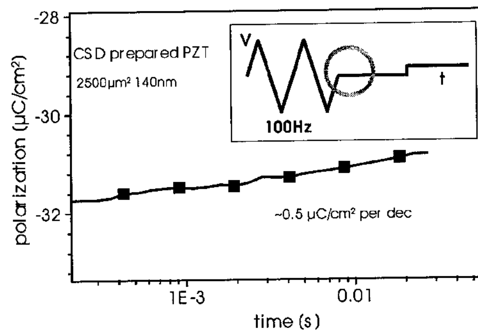

Figure 5. *Decrease of the polarization after the hysteresis loops.*

RESULTS AND DISCUSSION

The evolution of the current after applying a voltage step in undoped PZT thin film capacitors differs significantly from the evolution in ferroelectric single crystals. The current response in single crystals exhibits a 'switching hump', i.e. an increase of the current, during the polarization reversal (see Figure 1 right). Whereas in undoped PZT (Figure 6 left) the current monotonously decreases. The current response shows a Curie-von Schweidler behavior with a change of slope at the moment of the polarization reversal (Figure 6 left). So, the dominant mechanism contributing to the current is completely different. In single crystals the current is determined by the domain reversal and for thin films it is related to the dielectric loss (see also Ref. [23]).

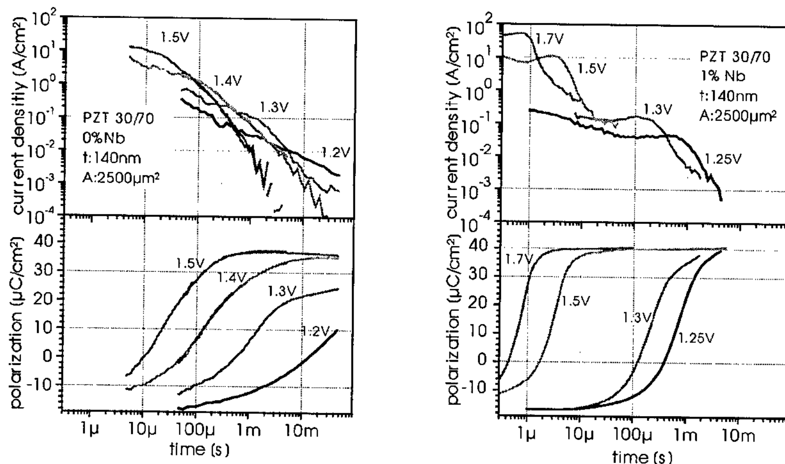

Figure 6. *Current response (upper) and evolution of polarization (lower) after applying a voltage step with varying level. Left: undoped PZT, right:1% niobium doped.*

Since it is assumed that the dielectric losses in thin films are responsible for the deceleration of the polarization, the reversal of the PZT thin film capacitor is compared to behavior in niobium doped PZT. Small signal (*C-V*) measurements revealed that the dielectric losses indeed could be reduced by niobium doping, which is shown in Figure 7. It can be observed that the dielectric capacitance in the saturation state, i.e., at a bias voltage of 3V, is not significantly affected by doping, whereas the dielectric loss is distinctly decreased.

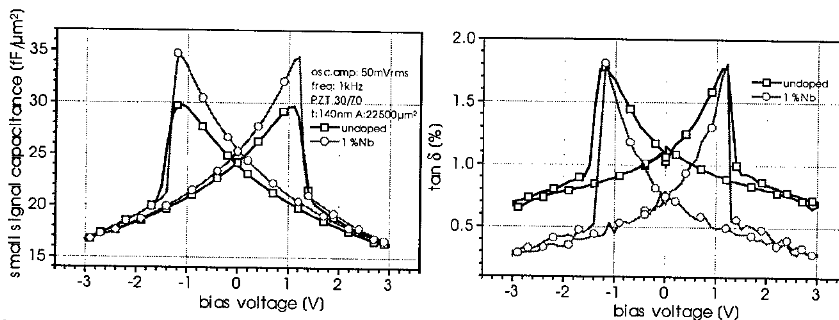

Figure 7. *Small signal capacitance (left) and loss factor tan δ (right) of undoped und Nb doped PZT vs. slowly cycled bias voltage sweep (C-V measurement).*

In Figure 6 the comparison of the course of the current and the polarization is shown of undoped and 1 % Nb doped PZT. The current response of the Nb-doped sample exhibits the switching hump which is well known from ferroelectric single crystals. So by niobium doping it is possible to reduce the Curie-von Schweidler type dielectric loss behavior and to observe the intrinsic ferroelectric switching.

For better comparison of the data, in Figure 8 the current response of Nb-doped PZT is plotted in a linear-linear diagram. It shows the same behavior in the current response as found for single crystals (Figure 1) and as simulated by implementing the K-A model (Figure 2). In principle it is possible to describe the switching time of the Nb-doped sample by means of the Merz-equations (Figure 1), however, one has to keep in mind that an important condition for the application of these equations is that the voltage has to be constant during the polarization reversal. Here, due to the sample dimensions, the voltage drop over the inevitable series resistance (50Ω internal resistance plus 50Ω of shunt resistance) reaches more than 100 mV in the case that a voltage level of 1.6V is applied. So for more precise measurements with higher voltage levels the sample pad size has to be reduced. Nevertheless, the measurements show that indeed the intrinsic ferroelectric polarization is observed. It is assumed that by reducing the capacitor electrode area the switching time can be decreased to the range of nanoseconds by adapting the voltage.

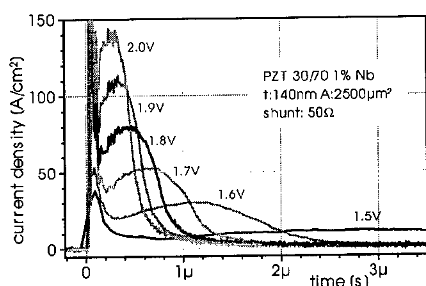

Figure 8. *Current response of Nb-doped PZT thin film plotted in linear-linear diagram.*

To estimate the switching time of these films at higher voltage levels the data are evaluated using the Merz-equations and plotted in a reciprocal-logarithmic plot in Figure 9 (right). Here, the switching time is defined as the instant at which the polarization reversal is completed, since the current response of undoped PZT shows no current maximum. For further details of the definition of the switching time the reader is referred to Ref [24] (pp.199).

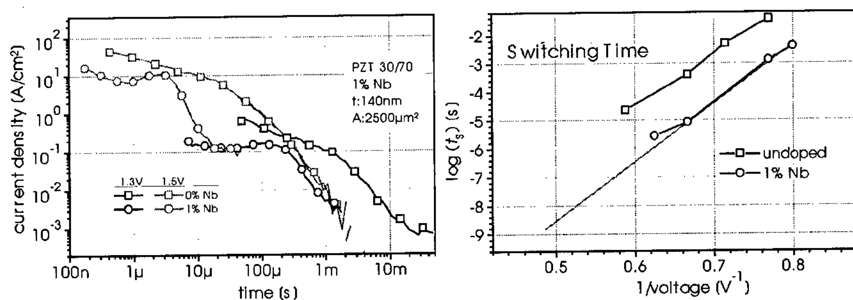

Figure 9. *Left: Comparison of current response of undoped and Nb-doped PZT.*

With increasing voltage levels the switching time is decreased and gives in good approximation a straight line in the reciprocal-log plot. It is shown that due to the niobium

doping the switching time is decreased by almost two decades. The extrapolation of the switching data of the Nb-doped samples reveals that a switching time in the nanosecond range can be expected for applied voltage levels of about 2 V. So, for the ferroelectric storage capacitor in the FeRAM device niobium doping is highly beneficial.

It is assumed that the ferroelectric polarization reversal is determined by two mechanisms, the intrinsic ferroelectric polarization reversal which arises from the nucleation of opposite domains and the field dependent movement of the domain walls and the losses of dielectric polarization processes which lead to a deceleration of the polarization reversal. In principle this can be modeled by assuming that the ferroelectric material is screened by polarization mechanisms at the film-electrode or grain-grain interface in polycrystalline thin films. These mechanisms lead to the Curie-von Schweidler behavior in ferroelectric thin films in the time domain [25-27] and the linear dispersion over a broad frequency range in the frequency domain [23].

CONCLUSIONS

The ferroelectric polarization reversal in ferroelectric thin films can be slowed down to the range of milliseconds by applying voltage step levels in the order of the coercive voltage. The comparison of the current response of undoped PZT to the polarization switching current of ferroelectric single crystals shows that they differ significantly. The transient current of undoped PZT thin film capacitors cannot be explained by the classical theory of nucleation and growth of opposite domains. Rather the current response obeys the Curie-von Schweidler law which is applicable to all kinds of electroceramic thin films, ferroelectric as well as non-ferroelectric. For 1% niobium doped PZT the dielectric losses are significantly reduced and the switching time is drastically improved by about two decades in time. The Curie-von Schweidler currents are likewise reduced significantly. This leads to the assumption that the ferroelectric polarization reversal is determined by two mechanisms, the intrinsic ferroelectric polarization reversal which arises from the nucleation of opposite domains and the field dependent movement of the domain walls and the losses of dielectric polarization processes which leads to screening of the intrinsic ferroelectric polarization switching. The physical origin of these processes has not yet been fully elucidated but some models have been proposed [28] which can describe this behavior in non-crystalline materials.

For the application of the ferroelectric capacitor under investigation as a storage device in an FeRAM this implies that it is possible to switch the polarization with a voltage pulse of approx. 2 V with a pulsewidth of a few nanoseconds in the case the dielectric loss mechanisms can be reduced. An important issue in this context is the scalability of the material, i.e., the possibility to reduce the film thickness without losing the aspired high polarization values. A reduced thickness leads to an increased field and presumably to a further reduction of the switching time or the applied voltage level, respectively.

ACKNOWLEDGEMENTS

The authors would like to acknowledge Prof. G. Arlt and R. Meyer from University of Aachen, W. Hartner, R. Bruchhaus, N. Nagel from Infineon Tech. for fruitful discussions and T. Schneller and R. Gerhardt for the support of the sample preparation. This work was supported by the German Ministry of Education and Research BMBF (contract no. 03N60075).

REFERENCES

1. S. S. Eaton, D. B. Butler, M. Parris, D. Wilson, and H. McNeillie, *IEEE ISSCC. Dig. of Tech. Pap.* 130 (1988).
2. C. A. Paz de Araujo, J. D. Cuchiaro, L. D. McMillan, M. C. Scott, and J. F. Scott, *Nature* **374**, 627 (1995).
3. J. F. Scott and C. A. Paz de Araujo, *Science* **246**, 1400 (1989).
4. J. D. Baniecki, R. B. Laibowitz, T. M. Shaw, P. R. Duncombe, D. A. Neumayer, D. E. Kotecki, H. Shen, and Q. Y. Ma, *Appl. Phys. Lett.* **72**, 498 (1998).
5. P. K. Larsen, G. L. M. Kampschoer, M. J. E. Ulenaers, G. A. C. M. Spierings, and R. Cuppens, *Appl. Phys. Lett.* **59**, 611 (1991).
6. P. K. Larsen, R. Cuppens, and G. J. M. Dormans, *Science and Technology of Electroceramic Thin Films*, **284,** *Applied Sciences*, edited by O. Auciello and R. Waser (Kluwer Academic, Netherlands, 1995), pp. 201–221.
7. W. J. Merz, *Phys. Rev.* **95**, 690 (1954).
8. C. F. Pulvari and W. Kuebler, *J. Appl. Phys.* **29**, 1742 (1958).
9. A. N. Kolmogorov, *Izv. Acad. Nauk USSR, Ser. Math.* **6**, 355 (1937).
10. M. Avrami, *J. Chem. Phys.* **7**, 1103 (1939), *J. Chem. Phys.* **8**, 212 (1940), *J. Chem. Phys.* **9**, 17 (1941).
11. H. Orihara, S. Hashimoto, and Y. Ishibashi, *J. Phys. Soc. Jpn* **63**, 1031 (1994).
12. S. Hashimoto, H. Orihara, and Y. Ishibashi, *J. Phys. Soc. Jpn* **63**, 1601 (1994).
13. Y. Ishibashi and H. Orihara, Int. Ferroelectrics 9, 57 (1995).
14. V. Shur, E. Rumyantsev, and S. Makarov, *J. Appl. Phys.* **84**, 445 (1998).
15. SPICE3 Version 3f4, *Dep. Elec. Eng. Comp. Sci., Berkeley, Univ. California.*
16. XSPICE, *Comp. Sci. Inf. Tech. Lab., Georgia Inst. Tech., Atlanta, Georgia.*
17. R.C. Miller and A. Savage, *Phys. Rev.* **115**, p.1176 (1959).
18. Y. Xu, *Ferroelectric Materials and Their Applications*, North Holland, p.130 (1990).
19. K. Budd, S. Dey, and D. Payne, *Br. Ceram. Proc.* **36**, p.107 (1985).
20. S.D. Traynor, T.D. Hadnagy, and L. Kammerdiner, *Int. Ferroelectrics* **16**, pp63 (1997).
21. O. Lohse, S. Tiedke, M. Grossmann, and R. Waser, *Int. Ferroelectrics* **22**, pp.123 (1998).
22. Y. Shimada, M. Azuma, K. Nakao, S. Chaya, N. Moriwaki, and T. Otsuki, *Jpn. J. Appl. Phys.* **36**, pp.5912 (1997).
23. O. Lohse, M. Grossmann, U. Boettger, D. Bolten, and R. Waser, *J. Appl. Phys*, **89**, accepted for publication (2001).
24. E. Fatuzzo and W. J. Merz, Ferroelectricity, *Selected Topics in Solid State Physics* (North-Holland, Amsterdam, 1967).
25. X. Chen, A. I. Kingon, L. Mantese, O. Auciello, and K. Y. Hsieh, *Int. Ferroelectrics* **3**, 355 (1993).
26. A. K. Tagantsev, A. L. Kholkin, E. L. Brooks, and N. Setter, *Int. Ferroelectrics* **10**, 189 (1995).
27. M. Schumacher, S. Manetta, and R. Waser, *J. de Physique IV* **8**, 117 (1998).
28. N. F. Mott and E. A. Davis, *Electronic Processes in Non-Cystalline Materials, Monographs on Physics* (Clarendon Press, Oxford, 1971).

Mat. Res. Soc. Symp. Proc. Vol. 655 © 2001 Materials Research Society

Self-polarization mechanism in textured pyroelectric $Pb(Ti_{1-x}Zr_x)O_3$ films

G. Suchaneck[1], G. Gerlach[1], Yu. Poplavko[2], A. I. Kosarev[3], A. N. Andronov[4]
[1]Dresden University of Technology, Institute for Solid State Electronics, Mommsenstr. 13, 01062 Dresden, Germany
[2]National Technical University of Ukraine, Peremogi Av. 37, 252056 Kyiv, Ukraine
[3]A. F. Joffe Physico-Technical Institute, ul. Polytekhnicheskaya 26, 194021 St. Petersburg, Russia;
[4]St. Petersburg State Technical University, ul. Polytechnicheskaya 29, 194251 St. Petersburg, Russia

ABSTRACT

Self-polarization of $Pb(Ti_{1-x}Zr_x)O_3$ (PZT) thin films is explained on the basis of the formation of a TiO_{2-x}-enriched interlayer close to the bottom electrode. Electrons provided by oxygen vacancies generate a n-type interface layer in the PZT at the electrode. A graded ferroelectric layer is then formed by electron injection from the bottom electrode and electron trapping on Ti^{4+} ions. A "built-in" difference in free energy forms which acts to pole the ferroelectric. Band bending was observed by contact potential difference measurements at a distance of 70 to 90 nm from the bottom electrode.

INTRODUCTION

Pyroelectric active films show a self-polarization effect, i. e., the presence of a significant amount of polarization after material synthesis without any poling treatment. Self-polarization occurs due to the presence of an internal electric field which is at least as large as the coercive field at the Curie temperature. As a consequence the film will be poled whenever it is cooled down below the paraelectric-ferroelectric transition temperature. Although already discovered in the 1960´s, the self-polarization mechanism is still an object of controversy. Self-polarization was observed in thin films prepared by different deposition techniques on different substrates [1]. Strong self-polarization occurs in sputtered PZT films with a zirconium ratio $Zr/Zr+Ti < 0.4$ [2]. These films exhibit a (111) oriented texture with a "Christmas-tree"-like domain structure [3]. The (111) orientation is not the one with largest remanent polarization, but rather the orientation which does not allow the polar vector to lie in the plane of the film. In this case, most of the ferroelectric domains have an angle of ~55° to the surface normal. Thus, 58% of polarization can be achieved normal to the substrate. Self-poling effects have also been observed in ferroelectric materials cooled below the Curie temperature in the presence of a temperature or strain gradient [4-6].

Different mechanisms of self-polarization based on stress induced and space charge induced polarization were considered [1]. Stress induced self-polarization does not exceed 10 to 15% of the polarization value achieved by poling [1], while space charge induced polarization in Ti-rich compositions reaches up to 100% of this value [2]. The presence of space charge layers is easily identified by a large enough shift of the ferroelectric hysteresis curve P(E) on the E-axis. This effect has been known in natural colemanite crystals for more than 40 years and in ferroelectric ceramics modified with acceptors for more than 20 years [7]. In this later case, the internal electric field is attributed to defect dipoles consisting of acceptor ions on the Ti sites associated with oxygen vacancies [8]. A defect chemistry based hypothesis of self-polarization including also mobile electrons was proposed in [9]. During cooling from high deposition temperature, oxygen vacancies are created under reducing conditions and are preferentially trapped near the bottom electrode. Cooling in an oxidizing

atmosphere will reduce the oxygen vacancy concentration and that of the vacancy-related complexes such as oxygen vacancies associated with lead vacancies which are formed due to the inherent PbO loss during PZT processing. In result, no internal bias field builds up. The electrical field present during cooling in reducing ambient aligns dipolar defect complexes which polarize the ferroelectric below the Curie temperature. Later the same group [10] claimed that the ability to align the defect dipoles occurs only in the ferroelectric, noncubic phase of the material, i.e. at temperatures below the Curie temperature, and defect-dipole alignment does not occur in the nonferroelectric ceramics.

Dipolar defect complexes including Pb atoms are not a good candidate for frozen dipoles causing thin film polarization by a defect chemistry mechanism. ESR shows that under illumination Pb ions are aligned even at room temperature [10]. Because of the Pb lattice site is surrounded by eight equivalent TiO_6 octahedra, the strong [111] directionality of the dipole driving force is difficult to explain. Once formed, excess Pb near the bottom platinum electrode is easily lost by Pb diffusion through the Pt layer [11]. On the other hand, PbO excess favors the formation of a (001/100) texture [12]. As far as self-polarization was obtained mostly in $PbTiO_3$ or Ti-rich PZT thin films [1], the presence of Zr containing defect complexes is not necessary.

In this work, evidence for a self-polarization mechanism based on the formation of Ti^{3+} ions in a TiO_{2-x}-rich interface layer is discussed.

EXPERIMENTAL

PZT thin films of about 1 μm thickness were deposited by RF-sputtering (13.56 MHz) on Si/SiO_2/adhesion layer/(111)Pt substrates. The zirconium ratio Zr/Zr+Ti in the ceramic target was chosen < 0.3 to obtain a strong effect of self-polarization. Film microstructure characterization was performed by AFM, electron microscopy, XRD and stress analysis by Raman piezo-spectroscopy and wafer curvature technique. Composition analysis included XPS, SIMS and glow discharge optical emission spectroscopy (GD-OES). Electrical characterization was accomplished after a top NiCr electrode deposition by DC-sputtering and consists of measurements of impedance characteristics and pyroelectric coefficients. Details of film deposition and characterization were published elsewhere [3].

Samples for work function profiling were prepared by reactive ion etching (RIE) using a CHF_3/Ar gas mixture in an Oxford Plasma Technology Plasmafab 80^+ reactor. For work function estimation, the contact potential difference (CPD) method was used. A modified Anderson method [13] was realized in an electron gun setup generating a beam with a diameter of 1.5 to 2 mm. The anode is driven by a potential U_A of 100 to 150 V while the electron energy is varied by the potential difference between the cathode and the sample. The advantage of the chosen setup with electron slow down in the retarding field between sample and anode is that the electron energy has no influence on electron current and beam focalization because in the gun all potentials are constant with respect to the cathode. Any change in the work function of the surface produces a shift of the retarding curve by an amount equal to the CPD. If the potential difference between the cathode and the sample U_{cath} corresponds to the work function difference, the current in the sample circuit saturates due to the collection of all electrons emitted by the cathode. Thus, by retarding curve measurements of different samples, the work function difference may be estimated. For calibration, a graphite sample was used which was heated to 1000 °C in vacuum before each measurement. For the graphite work function values of 4.4 to 4.8 eV are given in literature. We used a value of Φ = 4.4 eV determined by the CPD method at room temperature [14].

RESULTS AND DISCUSSION

The XPS determined composition was sensitive to ion bombardment of the sample surface [1]. The sample surface was depleted of Pb during argon bombardment. Therefore, composition profiling was performed by GD-OES. An example of a composition profile of a self-polarized PZT with (111) texture and a PbO_2 rich surface layer deposited on a thin TiO_2 seed layer is shown in figure 1.

A (111) textured platinum bottom electrode is not a sufficient condition for the deposition of (111) textured PZT films. All kinds of orientations can be obtained on Pt(111) [15]. In the case of $PbTiO_3$ deposition, a (100) texture is obtained on (111)Pt with no unintentional titanium present on the surface [16,17]. Therefore, a seeding layer of TiO_x is recommended to enhance (111) PZT nucleation [17]. One idea of TiO_2 seeding orientation effect is that titanium rich PZT lowers the perovskite transformation temperature [18]. The nucleation temperature of PZT on Pt is about 520°C compared to less than 350°C for $PbTiO_3$ [19]. On the other hand, a bare Pt(111) bottom electrode cannot provide a [111]-oriented perovskite structure as well as a bare titanium seed layer which needs partial oxidation. Titania is more effective in nucleating a (111) texture because on a (111) textured platinum electrode the electrical driving force is screened by the metals conductivity. Therefore, initially the substrate is covered on its surface by a skeleton of the perovskite structure consisting of TiO_6 octahedra matched with one of their eight faces to the (111) platinum substrate.

Actually, little is know about the structure of the TiO_x seed layer. Some initial investigations of a 1 nm thick TiO_x seed layer by Auger electron spectroscopy (AES), X-ray photoelectron spectroscopy (XPS) and X-ray photoelectron diffraction (XPD) were reported in [17]. XPS confirmed a chemical composition of TiO_2, AES complete surface coverage. Although Ti 2p XPD showed best coincidence of azimutally averaged scans with a rutile (110) structure, this gives only evidence of a rutile-like short range order and is not in contradiction to our assumption. The loss of seeding effectiveness with a larger TiO_x layer thickness is explained in our model by recrystallization of the seed layer into a rutile structure when bulk energies become dominating over surface ones.

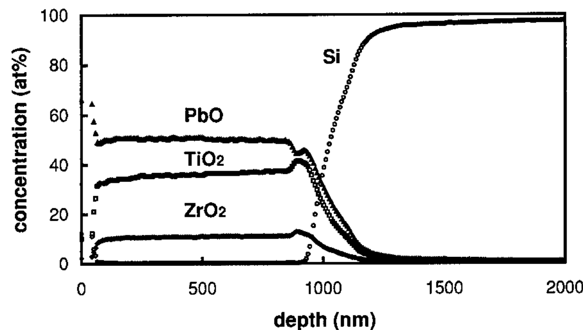

***Figure 1**. GD-OES-Profile of (111) PZT thin film deposited on TiO_x seed layer*

Thus, the Pt(111) electrode provides a peculiar texture of the TiO_x seed layer. This seed layer works as a nucleation plane of (111) PZT transforming structure information by an electrical driving force.

Figure 2 presents the secondary electron image of a sample prepared for work function profiling. The bright region at the left side corresponds to an etching process up to the platinum electrode with some residues on the surface. The dark regions at the left edge are

visible CF_x polymer films formed during reactive ion etching. The middle part with a film thickness gradient from 70 to 95 nm is located at the edge of the transition layer (cp. figure 1) and the right part has a PZT film thickness of about 130 nm. In order to preserve surface structure, the sample was cleaned only by heating up to 200°C during vacuum pumping. AES shows carbon contamination of the surface and the middle part is characterized by an enhanced Ti peak. Due to surface contamination and etch residues the work function of the left part, $\Phi = 3.6$ eV was lower than the values reported for platinum in literature (5.17 to 5.5 eV) [20,21]. On the other hand the higher resistivity of PZT film reduces the slope of the retarding curves and work function values are overestimated. For instance, strong surface charging is obtained in the right part of the sample and the estimated work function value, $\Phi = 6.60 \pm 0.22$ eV, is unusually high. Therefore, only the work function difference is determined for the middle part with the thickness gradient. The results shown on figure 3a give evidence for band bending at least up to the edge of the transition layer with a thickness of about 100 nm. This is in contradiction to C-V measurements on parallel samples with a space charge layer thickness of 8 to 15 nm [22]. Figure 3b illustrates an energy band diagram based on the one proposed by us in [22] and built assuming that the overestimation of work function due to higher resistivity and the decrease of work function due to surface contamination by etch residues are nearly of the same magnitude.

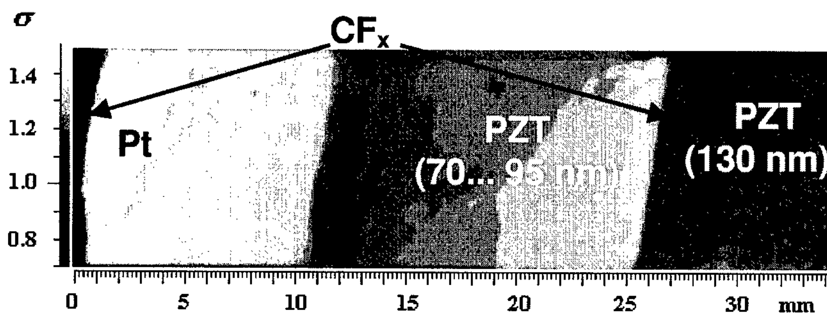

***Figure 2**. Secondary electron coefficient two-dimensional map of RIE prepared sample*

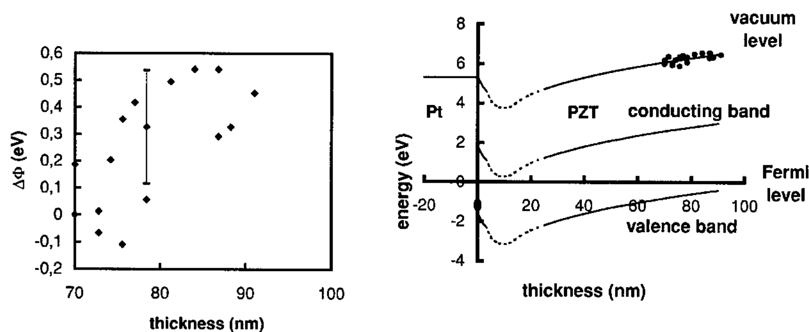

***Figure 3**. Work function profile, a - work function difference, b - energy band diagram*

In a previous work [22], we have determined refractive index and polarization profiles formed due to the presence of a non-ferroelectric interface layer. We attribute the formation of the non-ferroelectric interface layer to electron trapping at Ti^{4+} sites. The additional electron occupies anti-bonding states and thereby weakens ferroelectricity [23]. This non-ferroelectric

interface layer is also well known for PZT deposited on non-noble titanium substrates where a change of PZT stoichiometry near the electrode due to oxygen diffusion into the Ti substrate is observed [24]. A similar non-ferroelectric interface layer increasing in thickness with time is formed during electric field cycling due to vacancy migration to the region close to the electrodes [25,26]. This loss of switchable polarization by repeated polarization reversals is called ferroelectric fatigue. The fatigue resistance is improved and the leakage current is reduced if the oxygen deficient layer near the electrode is suppressed [27]. For a band bending at the Pt/PZT interface in order of $\Delta\varphi$=1 eV [22] an electric field of about 1 MV/cm is generated in a space charge layer of a thickness of d = 10 nm. This band bending leads to a significant lowering of the electron barrier induced by image forces (Schottky effect):

$$\Delta\Phi = \sqrt{\frac{e^3 \cdot \Delta\varphi}{4\pi\varepsilon\varepsilon_0 \cdot d}} = 0.14\text{eV}$$

where $\varepsilon = 7.3$ is the dielectric constant in the optical frequency region. The injected electrons occupy the lowest possible states in the band gap forming thus Ti^{3+} near E_C-0.7 eV [20]. As well known for $BaTiO_3$ [28], electrons are easily distributed within a n-type layer by polaronic conduction due to electron hopping between Ti^{4+} and Ti^{3+} ions. The Ti^{3+} containing defect in the oxygen deficient interface layer could be the postulated in [29] intrinsic neutral Ti^{3+}-V_O^{2+}-Ti^{3+} complex.

The formation of Ti^{3+} defects caused by a transition from p to n stoichiometry with AC-switching was also considered as the origin of ferroelectric fatigue [30]. Ti^{3+} with its more negatively charge than the host ion Ti^{4+} is move toward a positive charged oxygen vacancy, thus shorting the dipole and freezing in its position. Due to this fatigue-induced distortion in the oxygen octahedron, such a defect causes a local inhibition of the nucleation for the opposite domains. In this sense, the self-polarized films investigated in this work should be considered as degraded ferroelectrics.

The gradient of polarization normal to the substrate plane formed by the occupancy of electrons in Ti 3d anti-bonding states is related to a gradient of the free energy in phenomenological thermodynamic theories as discussed for graded ferroelectric devices in [31]. This "built-in" difference in free energy acts to pole the ferroelectric similar to the application of the electric field to an ungraded ferroelectric. Calculations of the thickness profile of polarization from the solution of the Euler-Lagrange equation by minimization of the free energy with given polarization boundary conditions are in progress now.

CONCLUSIONS

Deposition of PZT on platinized silicon wafers coated with a thin TiO_{2-x} seeding layer results in the formation of a polarization profile without additional poling due to the formation of a graded ferroelectric interface layer. Contact potential difference measurements demonstrate that the graded ferroelectric layer is at least as thick as the TiO_{2-x}-rich transition layer and that the thickness of the n-type layer formed due to bottom electrode-PZT interaction should be less than 70 nm.

ACKNOWLEDGMENTS

This work was supported by the German Research Council (Deutsche Forschungsgemeinschaft) as part of the Collaborative Research Center SFB422.

REFERENCES

1. G. Suchaneck, R. Koehler, P. Padmini, T. Sandner, J. Frey and G. Gerlach, *Surface Coatings and Technol.*, **116-119**, 1238-1243 (1999).
2. M. Schreiter, R. Bruchhaus, D. Pitzer and W. Wersing, *Proc. 11th IEEE Int. Symp. on Application of Ferroelectrics*, (Montreux, 1998) pp.181-185.
3. R. Köhler, G. Suchaneck, P. Padmini, T. Sandner, G. Gerlach and G. Hoffmann, *Ferroelectrics*, **225**, 57-66 (1999).
4. M. Tasson, H. Legal, J.C. Peuzin and F.C. Lissalde, *phys.stat.sol.(a)*, **31**, 729-737 (1975).
5. V.L. Gurevich, *Fizika Tverdogo Tela*, **23**, 2357-2363 (1981).
6. H.J. Sajosch and T. Narz, *Phys.Rev.*, **B41**, 3829-3831 (1990).
7. M.E. Lines and A.M. Glass, *Principles and applications of ferroelectrics and related materials*, (Clarendon Press, 1977).
8. G. Arlt and H. Neumann, *Ferroelectrics*, **87**, 109-120 (1988).
9. G. E. Pike, W. L. Warren, D. Dimos, B. A. Tuttle, R. Ramesh, J. Lee, V. G. Keramidas, and J. T. Evans, *Appl. Phys. Lett.*, **66**, 484-486 (1995).
10. W. L. Warren, G. E. Pike, K. Vanheusden, D. Dimos, B. A. Tuttle and J. Robertson, *J. Appl. Phys.*, **79**, 9250-9257 (1996).
11. T. Maeder, L. Sagalowicz and P. Muralt, *Jpn. J. Appl. Phys.*, **37**, 2007-2012 (1998).
12. S. Hiboux and P. Muralt, *Ferroelectrics*,**224**, 315-322 (1999).
13. P. Anderson, *Phys. Rev.*, **47**, 958-964 (1935).
14. R. Holm and E. Holm, *Electric Contact Handbook*, (Springer-Verlag, Berlin-Göttingen-Heidelberg, 1958).
15. K.G. Brooks, I.M. Reaney, R.D. Klissurska, Y. Huang, L. Bursil and N. Setter, *J. Mat. Res.* **9**, 2540-2553 (1994).
16. T. Tani, Z. Xu and D.A. Payne, *Mat. Res. Symp. Proc.* **310**, 269-274 (1993).
17. P. Muralt, T. Maeder, L. Sagalowicz, S. Scalese, D. Naumovic, R.G. Agostino, N. Xanthopoulos, H.J. Mathieu, L. Patthey and E.L. Bullock, *J. Appl. Phys.* **83**, 3835-3841 (1998).
18. C.K. Kwok and S.B. Desu, *J. Mater. Res.* **8**, 339-344 (1993).
19. K. Aoki, Y. Fukuda, K. Numata and A. Nishimura, *Jpn. J. Appl. Phys.* **24**, 192-195 (1995).
20. J.F. Scott, K. Watanabe, A.J. Hartmann and R.C. Lamb, *Ferroelectrics*, **225**, 83 (1999).
21. *CRC Handbook of Chemistry and Physics*, ed. R.C. Weast (CRC Press, Boca Raton, 1984), Vol. 65.
22. G. Suchaneck, R. Koehler, T. Sandner, G. Gerlach, A. Deineka, L. Jastrabik, A. I. Kosarev and A.N. Andronov, *Intergrated Ferroelectrics*, **32**, 169-177 (2001).
23. K. Miura and M. Tanaka, *Jpn. J. Appl. Phys.*, **35**, 2719-2725 (1996).
24. J.M. Bell and P.C. Knight, *Integrated Ferroelectrics*, **4**, 325-332 (1994).
25. J.J. Lee, C.L. Thio and S.B. Desu, *J. Appl. Phys.*, **78**, 5073-5078 (1995).
26. I.K. Yoo, S.B. Desu and J. Xing, *Mat. Res. Symp. Proc.* **310**, 165-177 (1993).
27. C.W. Law, K.Y. Tong, J.H. Li and K. Li, *Solid-State Electronics*, **44**, 1569-1571 (2000).
28. S. Jida and T. Miki, *J. Appl. Phys.*, **80**, 5234-5239 (1996).
29. K.A. Müller, W. Berlinger and R.S. Rubins, *Phys. Rev.* **186**, 361-371 (1969).
30. R.D. Klissurska, K.G. Brooks and N. Setter, *Ferroelectrics*, **225**, 171-178 (1999).
31. J.V. Mantese, N.W. Schubring, A.L. Michell and A.B. Catalan, *Appl. Phys. Lett.* **67**, 721-723 (1995).

Mat. Res. Soc. Symp. Proc. Vol. 655 © 2001 Materials Research Society

STRAIN-INDUCED ELEVATION OF THE SPONTANEOUS POLARIZATION IN $BaTiO_3$ THIN FILMS

W. Tian*, J. H. Haeni**, D. G. Schlom**, and X. Q. Pan*

*Department of Materials Science & Engineering, The University of Michigan, Ann Arbor, MI
**Department of Materials Science & Engineering, Penn State University, University Park, PA

ABSTRACT

A manmade ferroelectric-paraelectric heterostructure, a $BaTiO_3$ / $SrTiO_3$ superlattice, was studied to explore the effect of strain on ferroelectricity. An atomically abrupt $BaTiO_3$ / $SrTiO_3$ superlattice was grown on a (001) $SrTiO_3$ substrate by reactive molecular beam epitaxy. Both $BaTiO_3$ and $SrTiO_3$ layers were grown with their individual thicknesses less than the critical thickness for the formation of interfacial misfit dislocations, leaving the entire superlattice fully coherent with the substrate. This resulted in a uniformly and highly strained $BaTiO_3$ layer to study the effect of strain on ferroelectricity. Quantitative high-resolution transmission electron microscopy was employed to examine the atomic positions of cations and anions in the strained $BaTiO_3$ layers. It was found that the relative static displacement of cations (Ti^{4+}, Ba^{2+}) to anions (O^{2-}) is larger than that of bulk $BaTiO_3$. Our observation thus illustrates the strain-induced elevation of spontaneous polarization in $BaTiO_3$ thin films.

INTRODUCTION

As miniaturization of modern semiconductor devices continues, the size of oxide components will be reduced to the nanometer scale. At this scale, the behavior of functional oxides is strongly size- and strain-dependent and interface-controlled. Specifically, integration of ferroelectric thin films with lattice-mismatched and thermal expansion mismatched materials will introduce significant strains in the ferroelectric thin films, which in turn affects the physical properties and device performance. The strain effect thus refers to the relationship between strain acting on the material and its properties, such as the paraelectric-ferroelectric phase transition temperature (T_C), spontaneous polarization (P_s), and dielectric permittivity. Many attempts have been made to measure the effect of strain on ferroelectricity, most of them involving poly- and single-crystalline thin films [1-5]. Generally, biaxial tensile strain was found to depress the paraelectric-ferroelectric phase transition temperature, spontaneous polarization, and remanent polarization (P_r), while biaxial compressive strain had opposite effects. Theoretical work has been dedicated to calculating the strain effect [6-10]. However, the agreement between experimental results and theoretical calculations has only recently become quantitative [11,12], because of difficulties in determining the state of strain due to the polycrystalline nature of the films, residual stress, and inhomogeneity induced by defects in the lattice and film/substrate interfaces.

The artificial heterostructures (superlattices) incorporating ferro- and para-electric components with relatively large mutual lattice mismatch, on the other hand, offer many opportunities to probe ferroelectric strain effects with the added advantage that the strain tensor has a simple form. As several prior studies have demonstrated [5,13,14], if the superlattice is

grown with individual thicknesses of each component less than the critical thickness for the formation of interfacial misfit dislocations, the in-plane lattice parameters of the entire superlattice should be the constant, leaving a uniform strain with biaxial character in the epilayers. Our studies capitalize upon this advantage of the superlattice thin films.

At room temperature, $BaTiO_3$ is tetragonal (and ferroelectric) with bulk lattice parameters $a = 3.992$ Å and $c = 4.036$ Å, while $SrTiO_3$ is cubic (and paraelectric) with bulk lattice parameter $a = 3.905$ Å [15]. If we assume that the lattice constants of the thin films are fully constrained by the thick (1 mm) underlying (001) $SrTiO_3$ substrate, the combination of $BaTiO_3$ and $SrTiO_3$ layers would result in a large in-plane strain of ~2.2% at the interface. The resulting stress imposed on the $BaTiO_3$ is $\sim 10^9$ Pa, which can result in a resolvable variation in ferroelectricity.

EXPERIMENTAL

The $BaTiO_3$ / $SrTiO_3$ superlattice was grown on an (001) $SrTiO_3$ substrate by reactive molecular beam epitaxy (MBE). The MBE setup was described in detail elsewhere [16]. In this work, a superlattice with nominal individual layer thickness of five monolayers (denoted by $(BaTiO_3)_5$ / $(SrTiO_3)_5$) was grown. Molecular beams of strontium, titanium, and barium were generated using conventional effusion cells and supplied to the substrate in a sequential manner. Ozone (O_3) was used as an oxidation medium. The growth temperature was 650 °C. A cross-section transmission electron microscopy (TEM) specimen was prepared following the standard procedure which was ended with ion milling to electron transparency. High-resolution transmission electron microscopy (HRTEM) studies were performed within a 4000EX microscope equipped with Gatan Image Filter (GIF). The microscope was operated at 400 kV, giving the best point-to-point resolution of 1.7 Å. TEM images were processed using Gatan's DigitalMicrograph software. HRTEM image simulations were performed using the EMS software package [17].

The as-grown film exhibited significant leakage current and high dielectric loss. This was attributed to the high concentration of oxygen vacancies in the as-grown film because it was grown under high vacuum. To reduce the concentration of oxygen vacancies, annealing in 1 atm flowing pure oxygen was performed at 1000 °C for 13 hours. The annealed film displayed greatly improved electrical properties. [18] As we shall show below, interdiffusion is small under this annealing condition, and the superlattice structure shows quite good stability.

RESULTS AND DISCUSSION

Nano-scale control of the superlattice structure is key to investigating the intrinsic strain effect in this work. To demonstrate this, conventional TEM and HRTEM characterizations were employed to examine the microstructure and the atomic structure of the $BaTiO_3$ / $SrTiO_3$ superlattice.

Figure 1(a) shows a low-magnification cross-sectional TEM image of the film. The corresponding selected area electron diffraction (SAED) pattern is shown in Fig. 1(b), recorded with the electron beam incident along the [100]-zone axis of the $SrTiO_3$ substrate. The layers with high and low intensities in the image correspond to $SrTiO_3$ and $BaTiO_3$ layers, respectively. Excellent regularity of the superlattice is seen. In the enlarged SAED pattern [Fig. 1(c)], sharp satellite diffraction spots along the growth direction reveal the high degree of sharpness of the interfaces.

Figure 2(a) and (b) show the HRTEM images of the two samples of the same $BaTiO_3$ / $SrTiO_3$ superlattice before and after annealing, respectively. It is seen from the images that the $BaTiO_3$ / $SrTiO_3$ superlattice structure remains unchanged during annealing. This result indicates that the interdiffusion of Ba and Sr (both *A*-sites in the perovskite unit cell) is quite slow. The demonstrated stability of the superlattice structure at the relatively high temperature allows us to incorporate oxygen into the thin film by annealing without producing a solid solution of the two constituents, making the investigation of the intrinsic physical properties of such a customized oxide heterostructure possible. The low interdiffusivity between *A*-sites is most likely due to the absence of grain boundaries in the thin films. In both films, atomically abrupt interfaces were observed, and no misfit dislocations were found in any studied portion of the TEM specimen. The overall coherence of the film with the $SrTiO_3$ substrate indicates the in-plane lattice constants of the entire superlattice are the same as that of $SrTiO_3$, i.e., the $BaTiO_3$ layers are highly compressed in the *a-b* plane so as to match the lattice constant of $SrTiO_3$. Based on the crystallographic data of bulk $SrTiO_3$ and $BaTiO_3$, the in-plane (*a-b* plane) biaxial strain and the corresponding Poisson expansion along the *c*-axis of $BaTiO_3$ can be calculated. The in-plane compressive stress is 5.03 GPa by inserting $\varepsilon_{11} = 0.022$ (biaxial compressive strain in the *a-b* plane), $\nu = 0.361$, and $E = 146.2$ GPa into the formula $\sigma_0 = [E/(1-\nu)]\varepsilon_{11}$. In the

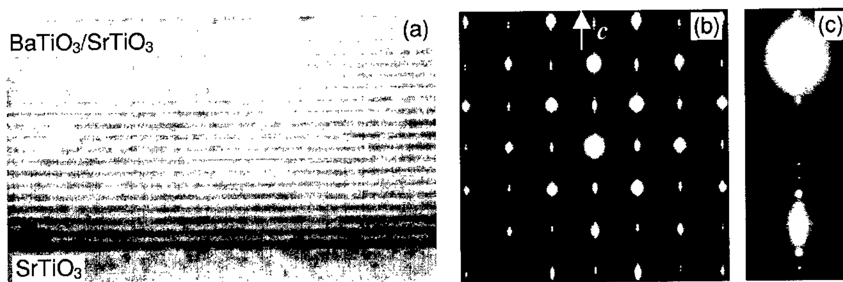

Fig. 1. (a) Low-magnification cross-sectional TEM image of a $BaTiO_3$ / $SrTiO_3$ superlattice. The layers with high and low intensities correspond to $SrTiO_3$ and $BaTiO_3$ layers, respectively. (b) The selected area electron diffraction pattern of the same film along the [100]-zone axis of $SrTiO_3$. The enlarged pattern (c) showing the superlattice reflections along the growth direction.

presence of the compressive stress in *a-b* plane, the corresponding Poisson expansion along the *c*-axis is $\varepsilon_{33} = -[2\nu/(1-\nu)]\varepsilon_{11} = 0.024$. The *c/a* ratio of the strained $BaTiO_3$ is accordingly calculated to be 1.045. To investigate the strain effect upon the crystallographic properties of $BaTiO_3$, the experimental *c/a* ratio was measured in the HRTEM image. The lattice length was measured from the positions of the intensity maxima at each barium atom column in the digitized HRTEM image. The distortion of the digital image is essentially less than 0.8%. The measured *c/a* ratio is ~1.05 which is in good agreement with the elastic calculation.

The increase of the *c/a* ratio in $BaTiO_3$ is regarded as an indication of the elevation of ferroelectricity [19], however, this phenomenon is more accurately described as the increase of the relative displacement of cations (Ti^{4+}, Ba^{2+}) to anions (O^{2-}). Cation displacement is the underlying physical mechanism by which the net dipole moment in a unit cell changes. To explore this issue, quantitative HRTEM was employed to examine the atomic positions of

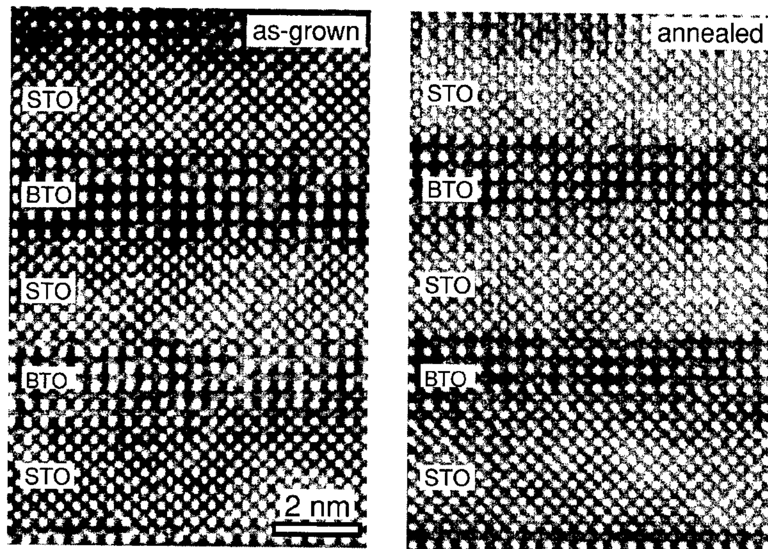

Figure 2. HRTEM images of a $BaTiO_3 / SrTiO_3$ superlattice. (a) The as-grown film (T_{sub} = 650 °C) and (b) after annealing at 1000 °C for 13 hours in flowing oxygen. It is seen that the superlattice structure is stable to relatively high temperature.

cations and anions in strained $BaTiO_3$. Figure 3(a) shows an experimental HRTEM image involving four unit cells of $BaTiO_3$, while Fig. 3(b) is the corresponding Fourier-filtered image. Fig. 3(c) is the computer simulated image using the atomic structure of bulk $BaTiO_3$ (unstrained state), which are Ba (0, 0, 0); Ti (1/2, 1/2, 1/2 +0.0135); O_I (1/2, 1/2, –0.025), O_{II} (1/2, 0, 1/2 – 0.015). It is apparent that the simulated image does not fit the experimental image well, suggesting that the atomic positions of the strained $BaTiO_3$ differ quantitatively from those of the bulk form. To clarify this possibility, the atomic positions of cations and anions of the bulk $BaTiO_3$ were modified while retaining the space group symmetry of the structure. A series of image simulations as functions of specimen thickness and objective lens focus value was subsequently performed to find the best fitting condition. Figure 4(d) shows the simulated image of the modified $BaTiO_3$ which best fits the experimental image, the modified atomic structure used in this simulation being Ba(0, 0, 0); Ti(1/2, 1/2, 1/2 +0.0135); O_I (1/2, 1/2, –0.128), O_{II} (1/2, 0, 1/2 –0.025). For displacive ferroelectrics, the polarization originating from the relative ionic displacement (ionic dipole) can be calculated by summing the ionic shifts per unit cell, e.g. $P = (1/V)\sum Z_n d_n$, where P is the polarization, V is the volume of the unit cell, Z_n is the effective charge of n-th ion, and d_n is the atomic displacement vector of the n-th ion. The ionic polarization of unstrained and strained $BaTiO_3$ is accordingly calculated to be 16.5 $\mu C/cm^2$ and 43.0 $\mu C/cm^2$, respectively. We note that the polarization measured in bulk $BaTiO_3$ along the c-axis is in fact 26 $\mu C/cm^2$ [20], indicating the ionic shifts only contribute a part of the

polarization. Nonetheless, our quantitative HRTEM studies provide evidence of a strain-induced elevation of spontaneous polarization in the strained $BaTiO_3$ thin films.

Modified Landau-Devonshire thermodynamic theories have been developed to calculate the effect of stress on the phase transition temperature and the spontaneous polarization. Using the formula relating the polarization and the internal stresses, developed by Rossetti *et al.* [7], we determined that the polarization under the compressive stress of 5.03 GPa is 47 $\mu C/cm^2$. Thus, the experimental results obtained by our HRTEM investigation are in good agreement with the theorctical calculation.

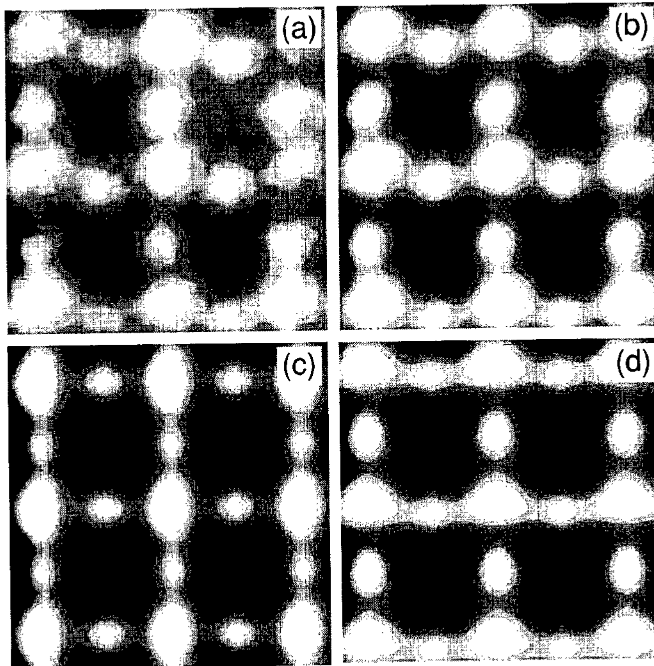

Figure 3. HRTEM images of $BaTiO_3$ involving four unit cells. (a) Experimental image, (b) the corresponding Fourier-filtered image, (c) the computer simulated image using the atomic structure of bulk $BaTiO_3$, and (d) the computer simulated image using the refined atomic structure which best fits the experimental one.

CONCLUSIONS

Using quantitative HRTEM, we were able to resolve the strain-induced elevation of spontaneous polarization in a strained $BaTiO_3$ thin film contained within in a $BaTiO_3$ / $SrTiO_3$ superlattice. In such nano-scale customized heterostructures, the strains involved are uniform

and have a simple form, enabling a quantitative comparison with theoretical calculations. Moreover, the ability to maintain such highly-strained ferroelectrics on a macroscopic scale along with the demonstrated elevated polarization enables us to tailor useful ferroelectric properties from the microscopic to the macroscopic scale.

ACKNOWLEDGMENTS

The authors gratefully acknowledge the financial support by NSF through the FRG grant DMR 9973801 for the work performed at the University of Michigan and the Department of Energy through grant DE-FG02-97ER45638 for the work performed at Penn State.

REFERENCES

1. I. N. Zakharchenko, E. S. Nikitin, V. M. Mukhortov, Y. I. Golovko, M. G. Radchenko, and V. P. Dudkevich, Phys. Stat. Sol. (a) **114**, 559 (1989).
2. K. Kushida and H. Takeuchi, Ferroelectrics **108**, 3 (1990).
3. S. B. Desu, Phys. Stat. Sol. (a) **141**, 119 (1994).
4. H. Tabata, H. Tanaka, and T. Kawai, Appl. Phys. Lett. **65,** 1970 (1994).
5. T. Kumazawa, Y. Kumagai, H. Miura, and M. Kitano, Appl. Phys. Lett. **72**, 608 (1998).
6. M. J. Haun, E. Furman, S. J. Jang, H. A. McKinstry, and L. E. Cross, J. Appl. Phys. **62**, 3331 (1987).
7. G. A. Rossetti Jr., L. E. Cross, and K. Kushida, Appl. Phys. Lett. **59**, 2524 (1991).
8. S. B. Desu, Z. J. Chen, V. P. Dudkevich, P. V. Dudkevich, I. N. Zakharchenko, and G. L. Kushlyan, in *Epitaxial Oxide Thin Films II*, edited by J. S. Speck, D. K. Fork, R. M. Wolf, and T. Shiosaki (Mater. Res. Soc. Proc. **401**, Pittsburgh, PA, 1996) pp. 195-201.
9. S. B. Desu, Z. J. Chen, V. P. Dudkevich, P. V. Dudkevich, I. N. Zakharchenko, and G. L. Kushlyan, in *Ferroelectric Thin Films V*, edited by S. B. Desu, R. Ramesh, B. A. Tuttle, R. E. Jones, and I. K. Yoo (Mater. Res. Soc. Proc. **433**, Pittsburgh, PA, 1996) pp. 345-350.
10. N. A. Pertsev, A. G. Zembilgotov, and A. K. Tagantsev, Phys. Rev. Lett. **80**, 1988 (1998).
11. N. A. Pertsev, A. G. Zembilgotov, S. Hoffmann, R. Waser, and A. K. Tagantsev, J. Appl. Phys. **85**, 1698 (1999).
12. S. K. Streiffer, C. Basceri, C. B. Parker, S. E. Lash, and A. I. Kingon, J. Appl. Phys. **86**, 4565 (1999).
13. E. D. Specht, H. M. Christen, D. P. Norton, and L. A. Boatner, Phys. Rev. Lett. **80**, 4317 (1998).
14. T. M. Shaw, A. Gupta, M. Y. Chern, P. E. Baston, R. B. Laibowitz, and B. A. Scott, J. Mater. Res. **10,** 2566 (1994).
15. Landolt-Bornstein: *Numerical Data and Functional Relationship in Science and Technology*, New Series, Group III, Vol. 3, edited by K. H. Hellwege and A. M. Hellwege (Springer, Berlin, 1969).
16. C. D. Theis and D. G. Schlom, J. Cryst. Growth **174**, 473 (1997).
17. P. A. Stadelmann, Ultramicroscopy **21**, 131 (1987).
18. W. Tian, X. Q. Pan, J. H. Hanei and D. G. Schlom, submitted to Appl. Phys. Lett.
19. Z. Y. Wang, T. Yasuda, S. Hatatani, and S. Oda, Jpn. J. Appl. Phys. **38**, 6817 (1999).
20. F. Jona and G. Shirane, *Ferroelectric Crystals* (Macmillan, New York, 1962).

Domains in Ferroelectric Thin Films

Mat. Res. Soc. Symp. Proc. Vol. 655 © 2001 Materials Research Society

Nanoscale Properties of $SrBi_2Ta_2O_9$ Thin Films

A. Gruverman[1], C. Isobe* and M. Tanaka*
Sony Corporation, Yokohama Research Center, Hodogaya-ku, Yokohama 240-0005, Japan
*Sony Corporation, Core Technology Development Center, Atsugi 243-0014, Japan

ABSTRACT

Piezoresponse scanning force microscopy (PFM) was applied to study the nanoscale mechanism of retention loss in $SrBi_2Ta_2O_9$ (SBT) thin films. Experiments were conducted by performing local polarization reversal within an individual grain with subsequent imaging of a resulting domain structure at different time intervals. The retention behavior of the films was studied as a function of switching conditions and electrode material. SFM was also used for nanoscale mapping of leakage current sites and investigation of electrical conduction mechanism at these sites. For the first time, the development of dielectric breakdown in SBT films was directly observed at nanoscale.

INTRODUCTION

The ability of ferroelectric films to maintain their polarization in the absence of external voltage provides the unique nonvolatility of ferroelectric memories [1]. However, commercial application of ferroelectric films is hindered by the degradation effects which limit the lifetime and reliability of ferroelectric-based devices. Numerous efforts have been undertaken to better understand the physical mechanism of the retention failure which manifests itself in the spontaneous reversal of polarization leading to a progressive loss of stored data. It has been proposed that retention failure in thin ferroelectric films is largely determined by the depolarizing fields resulting from incomplete compensation of the polarization charges at the film-electrode interface [2,3]. However, so far most of the studies of this effect focused on controlling macroscopic integral parameters of ferroelectric capacitors and could not provide information on the exact nature of polarization decay. In this respect, application of high resolution techniques such as scanning force microscopy (SFM) in conjunction with conventional electrical measurements may provide an opportunity to achieve a unique insight into the real physical processes which occur in ferroelectric thin films. Recently, it was shown that SFM operating in the piezoresponse mode, or piezoresponse scanning force microscopy (PFM), is a well-suited technique both for nanoscale imaging and control of ferroelectric domains and for investigation of the basic mechanism of degradation processes in ferroelectric thin films by direct observation of their domain structures [4-12]. The aim of this paper is to investigate the nanoscale retention behavior of ferroelectric $SrBi_2Ta_2O_9$ (SBT) thin films. One of the advantages of these films compared to films of the PZT family is their fatigue-free behavior [13]. However, their retention properties, which are closely related to the performance of memory devices, have been less studied [14-16]. In this article, we report on PFM studies of the mechanism of polarization retention loss in SBT films via the direct observation of their domain structures. Another issue which will be addressed here is nanoscale electrical characterization of SBT films and direct mapping leakage current sites by SFM.

EXPERIMENT

The principle of domain observation in PFM was described in detail elsewhere [4]. In brief, it is based on the detection of the local electromechanical vibration of the ferroelectric sample caused by an external ac voltage applied through the conductive tip. The voltage with a frequency ω, causes a film vibration with the same frequency due to the converse piezoelectric effect. The modulated deflection signal from the cantilever is detected using the lock-in

---

[1] Present address: North Carolina State University, Department of Materials Science and Engineering, Raleigh, NC 27695; E-mail: Alexei_Gruverman@ncsu.edu

technique. The phase of the vibration signal depends on the sign of the piezoelectric coefficient and polarization direction. This means that regions with opposite orientation of polarization should appear as regions of different contrast in the piezoresponse image.

In this study, a commercial force microscope Autoprobe CP (Park Scientific Instruments) was used. The external dc or ac voltage was applied to a standard gold coated Si_3N_4 cantilever with a spring constant of 0.1 N/m and a resonant frequency of 34 kHz. The probing tip with an apex curvature radius of about 20 nm was in mechanical contact with the film surface during the measurements (repulsive force regime). The domains were imaged by scanning the film surface while applying the 3.5 V, 10 kHz ac voltage to the tip. A topographic image of the film surface was taken simultaneously with the domain image. At the scan rate of 1 Hz, it took about 4 min to acquire one pair of images. However in some cases, this time could be reduced to 2 min or 1 min by obtaining only part of the image containing the area of interest. The time required for image acquisition determined the time resolution for retention measurements. For retention studies, local polarization reversal was induced by applying a voltage pulse of a certain polarity through the probing tip positioned at the center of a single-domain region. Subsequently, the evolution of the domain structure was monitored by acquiring piezoresponse images of the poled area at different time intervals [5]. The retention behavior was determined by measuring the time dependence of the fraction of the area retaining the switched polarization with taking into account the magnitude of the piezoresponse signal within the written domain. For this purpose, the recorded domain patterns were analyzed using the ULTIMAGE 2.5.1 image processing program [17]. This approach allowed us to obtain quantitative information on the dynamics of polarization decay at nanoscale.

Nanoscale mapping of local current and measurements of local I/V characteristics have been performed by means of SFM with a lock-in amplifier in the SFM set-up being substituted by an I/V converter. The leakage current images were obtained by scanning the sample with the tip connected to the converter while applying a constant dc bias to the bottom electrode. This approach allows direct studies of the conduction and breakdown mechanisms in ferroelectric films and establishing correlation between the film morphology and the I/V map.

The SBT samples used in this study were 140-nm-thick CVD grown films which were deposited at 400 ºC to 450 ºC followed by post annealing for 1 h at 700 ºC in an oxygen atmosphere. Two types of the bottom electrodes were used in retention measurements, namely Ir(120 nm) and Pt(180 nm) electrodes sputtered on silicon wafers with TiO_2(25nm)/SiO_2(300nm) layers. I/V measurements were conducted using SBT/Ir films. Auger electron spectroscopy of the SBT films on the Ir electrode showed the presence of a 25nm-thick IrO_2 layer at the SBT/Ir interface after annealing. Details of the film preparation have been presented elsewhere [18]. The ferroelectric testing of the samples gave the following values of remnant polarization P_r and coercive voltage V_c for an applied voltage of 5 V: P_r = 8.2 μC/cm^2 and V_c = 0.68 V for the SBT/Pt film; P_r = 6.6 μC/cm^2 and V_c = 0.85 V for the SBT/IrO_2 film.

RESULTS AND DISCUSSION

Retention behavior of SBT films

Figures 1(a) and (b) show simultaneously acquired topographic and piezoresponse images of the SBT/Pt sample. The topographic image reveals the crystallite structure with clearly resolved morphological features. By monitoring the phase of the piezoresponse signal it was determined that the dark regions in Fig. 1(b) represent domains with the polarization vector oriented toward the bottom electrode (hereafter designated "positive" domains), while the bright regions correspond to domains oriented upward ("negative" domains). According to earlier SFM data, the gray tone in the piezoresponse can be attributed to the crystallographic orientation of the grains deviating from the (100) direction [19, 20]. Note that the secondary non-ferroelectric phases of SBT which usually exhibit very different morphology could also

cause a gray tone in the piezoresponse image (for example, the small inclusions in the central part in Fig. 1(a) exhibit a gray tone in Fig. 1(b)).

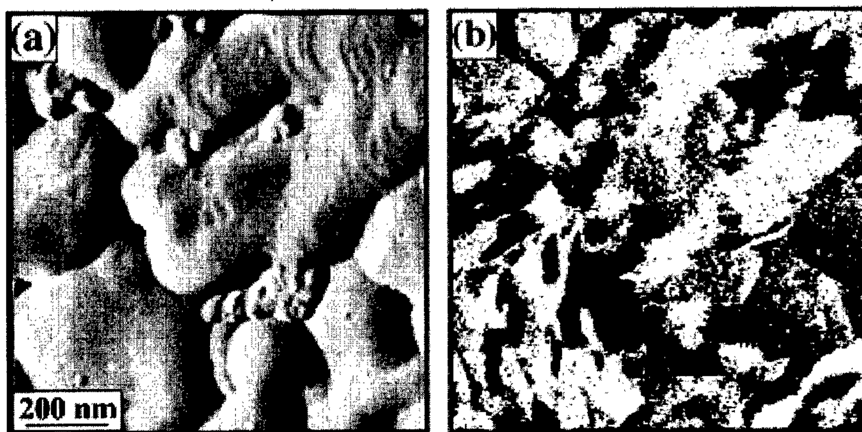

Figure 1. *Simultaneously obtained (a) topographic and (b) piezoresponse images of the* $SrBi_2Ta_2O_9$ *film on the Pt electrode. White and black regions in the piezoresponse image correspond to negative and positive domains, respectively.*

For retention measurements, single grains about 200-400 nm in size which exhibit a sharp as-grown domain contrast, were chosen. A topographic image of the SBT/Pt sample in Fig. 2(a) shows two grains, mostly in a positive polarization state (oriented downward) which was deduced from the piezoresponse image in Fig. 2(b). Application of a switching (poling) voltage pulse of -6 V, 5 s to the left grain resulted in the formation of a negative domain about 180 nm in size seen as a bright spot in the center of the grain (Fig. 2(c)). Figures 2(d), 2(e) and 2(f) illustrate the process of retention loss in the SBT/Pt film appearing as a gradual decrease in the size of the written domain due to spontaneous backswitching. As no significant change in the magnitude of the piezoresponse signal within the domain was detected, it can be stated that the backswitching process proceeds mainly through the sidewise motion of domain walls. It should be noted that the thickness of the domain walls of the shrinking domain ranges from 19 nm to 36 nm, which is larger than the value from 8 nm to 14 nm measured for the boundaries of stable domains (Fig. 1(b)). [The latter figures reflect only the thickness of the "visible" domain wall, which is determined by the experimental conditions, not the real physical thickness of the 180º domain wall which could be as thin as several unit cells]. This effect, which reflects the basic mechanism of polarization decay, is caused by the disparity between the time resolution of the imaging method and the velocity of the moving domain wall. From a quantitative analysis of the domain images it can be inferred that during the backswitching process the wall speed changes.

Figure 3 shows the time dependence of the normalized retained polarization $P(t)$ with respect to the initial polarization P_0 for different poling times. The retained polarization $P(t)$ shows a log-time dependence: $P(t) = P_0 - m\log(t/t_0)$, where m can be interpreted as a decay rate [21]. The log-time dependence suggests a broad distribution of relaxation times in SBT films even at the nanoscale level. Note that the shape of the shrinking domain becomes irregular due to the spatial variation in the wall velocity.

The above results, obtained using SBT/Pt films, concerned domains in a negative polarization state, i.e. oriented toward the film surface. However, the exaggerated asymmetry of

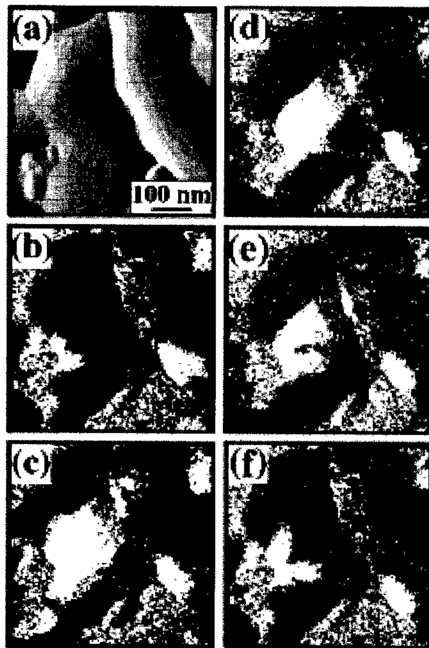

Figure 2. *Retention loss observed in the SBT/Pt film: (a) topographic image; (b) as-grown domain structure; (c) domain structure about 1 min after dc poling (-6 V; 5 s); (d-f) domain structures acquired at different time intervals after the removal of the dc bias: (d) 5 min after poling; (e) 20 min after poling; (f) 40 min after poling.*

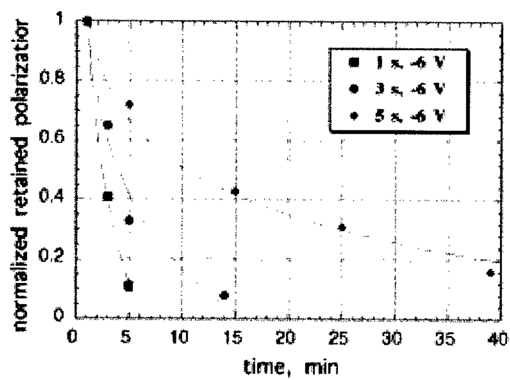

Figure 3. *Dynamics of retention loss in the SBT/Pt film for different poling times. The poling voltage is -6 V.*

boundary conditions in the tip/film/electrode heterostructure should lead to a significant difference in the stability of domains of opposite polarities due to the presence of a strong internal bias. To verify this assumption we carried out retention measurements of positive domains, i.e. oriented toward the bottom electrode, using the same experimental approach: an as-grown negative domain, detected on the film surface was switched by applying a positive voltage pulse, after which the evolution of the written positive domain was examined by acquiring piezoresponse images at different times. Indeed, it was found that positive domains exhibited quite different retention behavior compared to negative domains, namely, they were found to be fairly stable and did not show any significant dependence on switching parameters up to 96 hours of retention. This behavior is illustrated in Fig. 4(a). While the negative domain produced by a (-6 V; 1 s) voltage pulse disappeared in 6 minutes, the positive domain written by a (6 V; 1 s) voltage pulse showed almost no decay 48 hours after poling.

On the other hand, it has been found that in SBT films deposited on IrO_2 electrode domains of both polarities exhibit very good retention as illustrated in Fig. 4(b). Both negative and positive domains written by (8 V; 1 s) switching pulses showed almost no sign of relaxation to the original state for 96 h, in striking contrast to the retention behavior of the SBT films on Pt electrode. It should be noted that the threshold switching voltage in the SBT/IrO_2 sample was higher than in the SBT/Pt film and that reliable switching of the same scale in the SBT/IrO_2 sample was achieved at a higher switching amplitude.

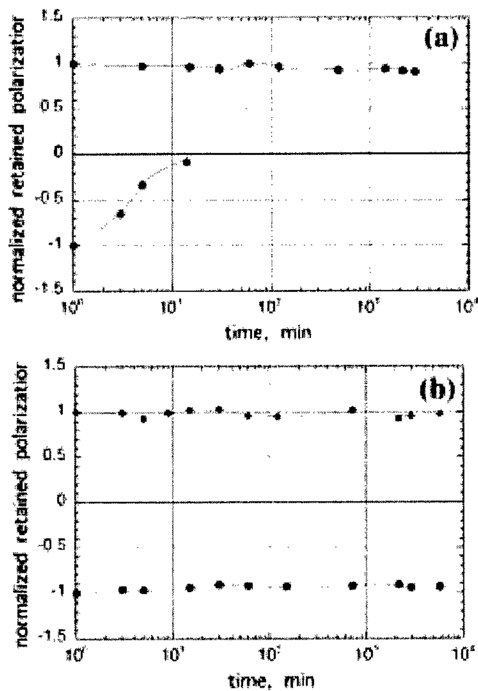

Figure 4. Retained polarization as a function of time for positive and negative domains in the (a) SBT/Pt and (b) SBT/IrO_2 film.

Retention loss in ferroelectric capacitors is generally attributed to the presence of the internal electric field due to two basic effects: incomplete screening of the depolarizing field and

formation of a depletion layer at the film/electrode interface [2, 3]. The incomplete compensation of the polarization charges by the electrode charges [3] leads to the existence of a residual depolarizing field, E_{rd}, which is compensated via redistribution of electronic charges in the interior of the film and subsequent formation of the space (screening) charge trapped near the film/electrode interface. The residual depolarizing field is polarization dependent and quickly changes its sign upon polarization reversal. At the same time, the field produced by the space charge, the screening field E_s, retains its sign long after switching, since its decay rate is determined not by the RC time constant of the electric circuit but rather by the Maxwell relaxation time, which is a function of the bulk conductivity of the film.

However, the observed difference between the retention properties of SBT/Pt and SBT/IrO_2 films suggests a strong effect of the film/electrode interface on their retention behavior. A built-in internal bias could arise at the film/electrode interface due to the difference between the work functions of the metal electrode and a semiconductor ferroelectric film. The built-in bias is not polarization-dependent and is always pointing in one direction. Formation of the built-in bias in the SBT/Pt sample can be understood from analysis of the band structure of the SBT/Pt interface [22, 23]. It has been showed that in SBT films, which behave like a p-type semiconductor, an inversion n-type layer exists near the SBT/Pt interface. Electrons entrapped at positively charged oxygen vacancies produce an internal bias in the depletion layer, which was estimated to be about 2 nm thick. From that analysis it could be inferred that the internal bias E_{bi} should point to the electrode.

In stable conditions, for as-grown domains of both polarities the residual depolarizing field is fully compensated by the screening field of the space charge. After an external bias is applied to the film to produce the opposite domain, the screening field which stabilized the original domain, tends to switch the new domain back. However, as shown above, in SBT/Pt films only negative domains follow this pattern while positive domains exhibit strong retention. The reason for this different retention behavior of opposite domains can be attributed to the presence of the built-in electric bias E_{bi} in the depletion layer. This field, which is oriented downward, generates nuclei of positive domains near the film/electrode interface triggering the backswitching process. Forward growth of these nuclei towards the film surface is driven by the screening field E_s which extends through the film thickness. As a result, the decay of the written negative domain is observed. In contrast, when a positive domain is written by the external voltage, its polarization points in the same direction as E_{bi} and, hence, the nucleation of negative domains at the interface is hampered and backswitching of the positive domain does not occur. The sidewise wall motion mechanism of polarization decay can be explained by the higher nucleation probability at the existing domain wall as such nuclei have lower energy [24]. The nuclei grow through the film forming steps on the existing domain wall. It is likely that nucleation occurs at the facets of these growing steps which leads to the apparent broadening of the moving domain wall.

The suggested model implies that the depletion layer plays an important role in the retention behavior of SBT films by triggering the backswitching process. Hence, the retention behavior would be significantly improved in the absence of the built-in electric bias at the interface. This situation could be realized by using metal oxide electrodes, such as IrO_2 which forms a more ohmic contact with SBT than Pt [23]. The oxide electrode provides a source of oxygen ions which should result in the reduced built-in field at the interface and enhanced retention. The excellent retention behavior observed in the SBT/IrO_2 films supports this model and the role of the depletion layers.

Nanoscale I/V measurements and leakage current mapping

Nanoscale measurements of the local current-voltage (I/V) characteristics and mapping of leakage current can be performed by means of SFM if a lock-in amplifier in the SFM set-up is substituted by an I/V converter [26, 27]. By positioning the tip at a selected point on the film surface and by sweeping a dc voltage, the I/V characteristics in this particular point can be

directly measured. A leakage current map can be obtained simultaneously with the topographic image by scanning the sample with the tip held under a constant dc bias. Upon an increase in the bias from scan to scan the formation of the sites of high leakage as a result of induced local

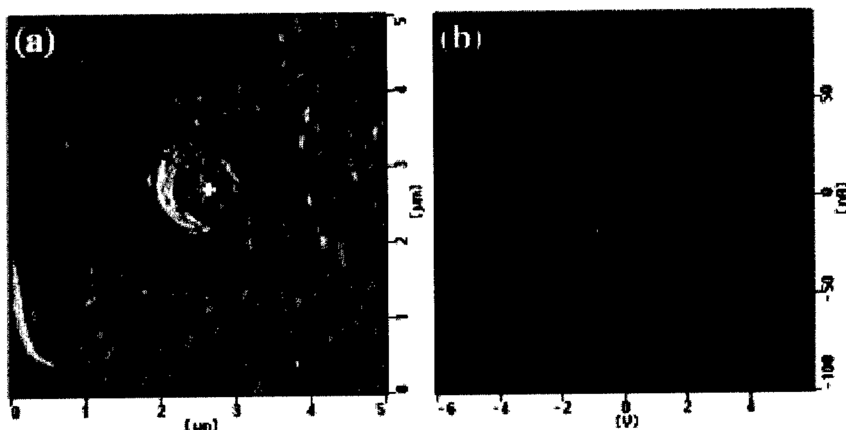

Figure 5. (a) Topographic image of the Ir/SBT/Ir capacitor. The scanning area is 5x5 μm^2; (b) I/V curve measured at the same capacitor.

dielectric breakdown can be observed. This approach allows direct studies of the conduction and breakdown mechanisms of ferroelectric films and establishing correlation between the film morphology and the I/V map. These measurements were carried out using SBT/IrO_2 films with different Sr/Bi ratio: 0.90/2.00 and 0.84/2.31; The sensitivity of our system was about 5 pA.

Figure 5(a) shows a topographic image of an Ir/SBT/Ir capacitor: the top Ir electrode of about 1 μm in diameter was sputtered on the 5x5 μm^2 plate of SBT deposited on the Ir bottom electrode. A current flow through the capacitor was measured by positioning the tip at the top electrode and by sweeping a dc voltage. The current-voltage characteristics of the capacitor for the dc voltage ranging from -6 V to 6 V are shown in Fig. 5(b). It can be seen that the I/V curve is almost symmetric for positive and negative bias and the voltage dependence of the current is quadratic above 2 V suggesting the space-charge-limited conduction mechanism [23].

Nanoscale mapping of leakage current sites revealed qualitatively different microscopic conduction mechanisms in the SBT films with different Sr/Bi ratio. Figure 6 shows the topographic and current images of the SBT (0.84/2.31) film. In the current image obtained under the –8.5 V bias, brighter regions can be seen on the gray background. Location of these regions, which represent areas with a higher level of the leakage current (of about 30 pA), coincides with location of the grain boundaries in the topographic image. This observation suggests that in the SBT (0.84/2.31) films breakdown occurs mainly along the grain boundaries. On the other hand, current images taken from the SBT(0.90/2.00) film show that breakdown in this film also begins along the boundaries of some particular grains. However, upon an increase in the dc bias the breakdown process proceeds via an increase in the leakage current through the grains themselves. This mechanism of breakdown is illustrated in Fig. 7. The leakage current measured at the -9 V bias was about 7 nA, i.e. 3 orders of magnitude higher than in the SBT (0.84/2.31) films. The reason for such a different behavior is not clear. This effect could be due to the defect structure of the grains or due to the variations in the bottom electrode properties. Further I/V measurements as well as local structure analysis are necessary to clarify why these particular grains serve as the breakdown sites.

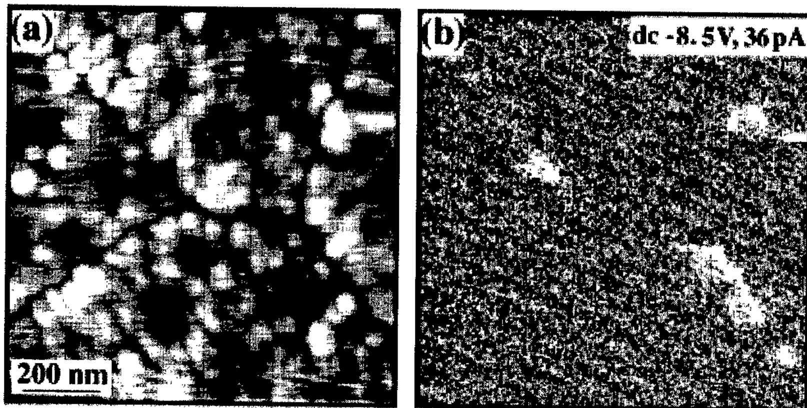

Figure 6. Topographic (a) and current (b) images of the SBT (0.84/2.31) film at the dc bias of –8.5 V. Bright regions in the current image correspond to the higher values of leakage current. The scanning area is 2x2 μm^2.

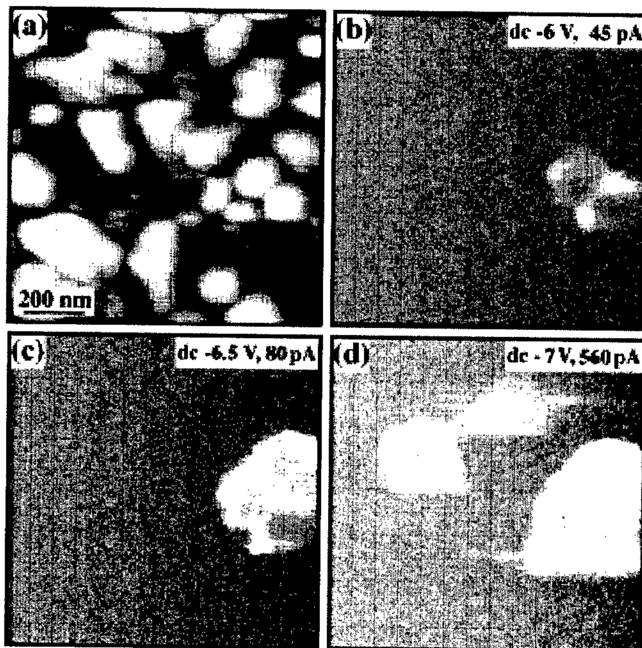

Figure 7. Topographic (a) and current (b-d) images of the SBT (0.90/2.00) film obtained at the successively increasing dc bias (b) -6 V; (c) -6.5 V; (d) -7 V. Bright regions in the current image correspond to the higher values of leakage current.

CONCLUSIONS

In this study, the nanoscale mechanism of retention loss in SBT films has been studied by means of piezoresponse force microscopy (PFM). It has been found that the retention behavior of SBT films on Pt electrodes is polarization-dependent: positive domains with the polarization vector pointing to the bottom electrode exhibit excellent stability in contrast to negative domains which show poor retention. This effect is attributed to the presence of the polarization-independent built-in bias at the SBT/Pt interface which triggers the backswitching process by nucleating positive domains. Once started, this process is further governed by the polarization-dependent space charge field which screens the original polarization state. The backswitching of negative domains, which proceeds via the sidewise motion of domain walls, shows a log-time dependence suggesting a broad distribution of relaxation times at the nanoscale level. This model is supported by the observed stability of both the positive and negative domains in the SBT films with IrO_2 electrodes due to the inhibited nucleation at the ohmic SBT/IrO_2 interface.

It has been shown that measurements of the I/V characteristics of the ferroelectric thin films and capacitors can be performed at the nanoscale level by means of SFM. Currents as low as 5 pA could be reliably detected by SFM operating in the contact mode and using a conductive probe. Nanoscale measurements of the local I/V characteristics and mapping of leakage current allows direct studies of the conduction and breakdown mechanisms of ferroelectric films and establishing correlation between the film morphology and the I/V map.

REFERENCES

1. J. F. Scott and C.A. Paz de Araujo, Science **246,** 1400 (1989).
2. I. P. Batra and B. D. Silverman, Sol. St. Commun. **11**, 291 (1972).
3. R. R. Mehta, B. D. Silverman and J. T. Jacobs, J. Appl. Phys. **44**, 3379 (1973).
4. A. Gruverman, O. Auciello, and H. Tokumoto, Integrated Ferroelectrics, **19**, 49 (1998).
5. A. Gruverman, H. Tokumoto, S. A. Prakash, S. Aggarwal, B. Yang, M. Wuttig, R. Ramesh, O. Auciello, and V. Venkatesan, Appl. Phys. Lett. **71**, 3492 (1997).
6. T. Hidaka, T. Maruyama, I. Sakai, M. Saitoh, L. A. Wills, R. Hiskes, S. A. Dicarolis and J. Amano, Integrated Ferroelectrics **17**, 319 (1997).
7. I. K. Yoo, B. M. Kim, and S.J. Park, Mat. Res. Soc. Symp. Proc. Vol 493, 299 (1998).
8. C. S. Ganpule, A. Stanishevsky, Q. Su, S. Aggarwal, J. Melngailis, E. Williams, and R. Ramesh, Appl. Phys. Lett. **75**, 409 (1999).
9. J. W. Hong, W. Jo, D. C. Kim, S. M. Cho, H. J. Nam, H. M. Lee, and J. U. Bu, Appl. Phys. Lett. **75**, 3183 (1999).
10. W. Jo, D. C. Kim, and J. W. Hong, Appl. Phys. Lett. **76**, 390 (2000).
11. S. Hong, E. L. Colla, E. Kim, D. V. Taylor, A. K. Tagantsev, P. Muralt, K. No and N. Setter, J. Appl. Phys. **86**, 607 (1999).
12. M. Alexe, C. Harnagea, D. Hesse, and U. Gösele, Appl. Phys. Lett. **75**, 1793 (1999).
13. C. A. Araujo, J. Cuchiaro, L. D. Macmillan, M. C. Scott, J. F. Scott, Nature **374,** 627 (1995).
14. K. Amanuma, and T. Kunio, Jap. J. Appl. Phys. **35**, Part 1, 5229 (1996).
15. Y. Shimada, K. Nakao, A. Inoue, M. Azuma, Y. Uemoto, E. Fujii, and T. Otsuki, Appl. Phys. Lett. **71**, 2538 (1997).
16. M. Grossmann, O. Lohse, D. Bolten, U. Boettger, R. Waser, W. Hartner, M. Kastner, and G. Schindler, Appl. Phys. Lett. **76**, 363 (2000).
17. A. Gruverman, Appl. Phys. Lett. **75**, 1452 (1999).
18. C. Isobe, T. Ami, K. Hironaka, K. Watanabe, M. Sugiyama, N. Nagel, K. Katori, Y. Ikeda, C. D. Gutleben, H. Yamoto and H. Yagi, Integrated Ferroelectrics, **14**, 95 (1997).
19. A. Gruverman, K. Hironaka, Y. Ikeda, K.M. Satyalakshmi, A. Pignolet, M. Alexe, N.D. Zakharov and D. Hesse, Integrated Ferroelectrics **27**, 159 (1999).
20. A. Gruverman, and Y. Ikeda, Jpn. J. Appl. Phys. **37**, Part 2, L939 (1998).
21. J. M. Benedetto, R. A. Moore, and F. B. McLean, J. Appl. Phys. **75**, 460 (1994).
22. J. F. Scott, Integrated Ferroelectrics **9**, 1 (1995).
23. J. F. Scott, Annu. Rev. Mater. Sci. **28**, 79 (1998).
24. R. C. Miller and G. Weinreich, Phys. Rev. **117,** 1460 (1960).
25. J. M. Benedetto, R. A. Moore, and F. B. McLean, J. Appl. Phys. **75**, 460 (1994).
26. Z. Xie, E. Z. Luo, J. B. Xu, I. H. Wilson, H. B.Peng, L. H. Zhao, and B. R. Zhao, Appl. Phys. Lett. **76**, 1923 (2000).
27. C. Yoshida, A. Yoshida, and H. Tamura, Appl. Phys. Lett. **75**, 1449 (1999).

Mat. Res. Soc. Symp. Proc. Vol. 655 © 2001 Materials Research Society

Cellular Domain Architecture of Stress-free Epitaxial Ferroelectric Films

S. P. Alpay [1], A. L. Roytburd, V. Nagarajan, L. A. Bendersky [2], and R. Ramesh
Department of Department of Materials and Nuclear Engineering, University of Maryland, College Park, MD 20742, U.S.A.
[1]Department of Metallurgy and Materials Engineering and Institute of Materials Science, University of Connecticut, Storrs, CT 06269, U.S.A.
[2]Materials Science and Engineering Laboratory, National Institute of Standards and Technology, Gaithersburg, MD 20899, U.S.A.

ABSTRACT

Epitaxial ferroelectric films undergoing a cubic-tetragonal phase transformation relax internal stresses due to the structural phase transformation and the difference in the thermal expansion coefficients of the film and the substrate by forming polydomain structures. The most commonly observed polydomain structure is the *c/a/c/a* polytwin that relieves the internal stresses only partially. Relatively thicker films may completely reduce internal stresses if all three variants of the ferroelectric phase are brought together such that the film has the same in-plane size as the substrate. In this article, we provide experimental evidence on the formation of the 3-domain structure based on transmission electron microscopy in 450 nm thick (001) $PbZr_{0.2}Ti_{0.8}O_3$ films on (001) $SrTiO_3$ grown by pulsed laser deposition. X-ray diffraction studies show that the film is fully relaxed. Experimental data is analyzed in terms of a domain stability map.

INTRODUCTION

Polydomain formation in epitaxial ferroelectric films undergoing a cubic-tetragonal phase transformation is a mechanism that relaxes internal stresses that are a result of the lattice misfit due to the structural phase transformation and the difference in the thermal expansion coefficients of the film and the substrate. The polydomain structure consists of the three possible orientational domains of the tetragonal phase separated from each other by elastically compatible 90° domain walls. Figure 1a shows all possible orientational variants of the ferroelectric phase and possible polydomain structures due to a cubic-tetragonal transformation. Ferroelectric films are deposited at temperatures above the transition temperature and the internal stresses are usually completely relaxed by misfit dislocations at this temperature [1,2]. Thus, just before the structural phase transformation at T_C the films are usually stress-free and tensile internal stresses develop below T_C due to the phase transformation. Therefore, most common microstructure observed in epitaxial films $PbTiO_3$ [2] and tetragonal $Pb(Zr,Ti)O_3$ solid solutions [4] is the *c/a/c/a* polydomain consisting of alternating platelets of *c*-domains with the tetragonal axis perpendicular to the film-substrate interface and *a*-domains with the *c*-axis of the tetragonal film along [100] or [010] directions, called a_1- and a_2-domains, respectively (Figure 1b). The *c/a/c/a* polytwin structure relaxes the internal stresses only partially by reducing the biaxial stress state to a uniaxial one. The internal stresses due to lattice misfit can be completely reduced if all of the three variants of the tetragonal phase are arranged such that the film has the same in-plane size as the substrate [5,6]. In this article, we present experimental results that confirm the existence of 3-domain structures in epitaxial ferroelectric films and we show that the internal stresses in these ferroelectric films are indeed completely relaxed.

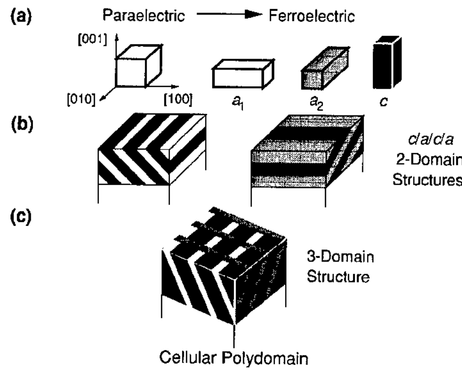

Figure 1. (a) Cubic paraelectric phase and the three ferroelectric tetragonal variants, (b) the simple 2-domain c/a/c/a polydomain structures, and (c) the cellular 3-domain architecture.

THEORY

If a ferroelectric film is grown epitaxially on a thick cubic substrate such that $(001)_{film}$ is parallel to $(001)_{substrate}$, the misfit due to the difference in lattice parameters of the film and the substrate may be described by the following misfit strain tensors for a_1-, a_2-, and c-domains, respectively, as:

$$\hat{\varepsilon}_1^M = \begin{pmatrix} \varepsilon_T' & 0 & 0 \\ 0 & \bar{\varepsilon}_M & 0 \\ 0 & 0 & \bar{\varepsilon}_M \end{pmatrix} \quad \hat{\varepsilon}_2^M = \begin{pmatrix} \bar{\varepsilon}_M & 0 & 0 \\ 0 & \varepsilon_T' & 0 \\ 0 & 0 & \bar{\varepsilon}_M \end{pmatrix} \quad \hat{\varepsilon}_3^M = \begin{pmatrix} \bar{\varepsilon}_M & 0 & 0 \\ 0 & \bar{\varepsilon}_M & 0 \\ 0 & 0 & \varepsilon_T' \end{pmatrix}, \qquad (1)$$

where $\varepsilon_T' = \bar{\varepsilon}_M + \varepsilon_T$, $\bar{\varepsilon}_M = (a - \bar{a}_S)/\bar{a}_S$ is the effective misfit strain, $\varepsilon_T = (c-a)/a$ is the tetragonality of the ferroelectric lattice, a and c are the unconstrained lattice parameters of the film, and $\bar{a}_S$ is the effective substrate lattice parameter taking into account the relaxation by misfit dislocations at the deposition temperature T_G [1,2]. For a homogenous mixture of domains, the condition for complete relaxation of the average stress is $<\varepsilon_{xx}>=<\varepsilon_{yy}>=0$, where $<\varepsilon_{xx}>$ and $<\varepsilon_{yy}>$ are the average strains along [100] and [010] directions, i.e.:

$$\alpha_1 \hat{\varepsilon}_1^M + \alpha_2 \hat{\varepsilon}_2^M + \alpha_3 \hat{\varepsilon}_3^M = \begin{pmatrix} 0 & 0 & 0 \\ 0 & 0 & 0 \\ 0 & 0 & (\alpha_1 + \alpha_2)\bar{\varepsilon}_M + \alpha_3 \varepsilon_T' \end{pmatrix}. \qquad (2)$$

Here, α_1, α_2, and α_3 are the volume fractions of a_1-, a_2-, and c-domains, respectively ($\alpha_1+\alpha_2+\alpha_3=1$). Full relaxation is attained is attained for $\alpha_1=\alpha_2$, and:

$$\alpha_3 = 2\bar{\varepsilon}_M / \varepsilon_T + 1, \qquad (3)$$

if $-(\varepsilon_T/2) < \bar{\varepsilon}_M < 0$. The resultant domain structure is due to (*i*) relaxation by misfit dislocations at T_G and (*ii*) relaxation by polydomain formation below the transformation temperature T_C. These

two different mechanisms are taken into account through the dislocation density dependence of the misfit strain, i.e., $\bar{\varepsilon}_M$, and the tetragonality, ε_T.

The architecture of the 3-domain structures is dictated by the energy of the interdomain interfaces, the energy of the junctions where the three domains come together, and by the microstresses at the film-substrate interface [7]. These factors increase the total energy of the system although the elastic energy of macrostresses is effectively reduced to zero. Their interplay results in a critical thickness below which the 3-domain state is not stable [5]. A complete theoretical treatment of the 3-domain structures will be presented in a future article.

EXPERIMENTAL RESULTS AND DISCUSSION

Experimentally, 450 nm thick (001) $PbZr_{0.2}Ti_{0.8}O_3$ (PZT) films on (001) $SrTiO_3$ (STO) substrates were deposited at 650°C and 100 mTorr oxygen partial pressure by pulsed laser deposition (PLD). X-ray diffraction (XRD) experiments for all samples were done on a four-circle Siemens D5000 diffractometer with monochromatic Cu K_α radiation. Crystallographic characterization was accomplished with standard θ-2θ scans, θ–rocking curves, and ϕ-scans. Epitaxial growth in the samples was established from ϕ-scans and the presence of only 00*l* type reflections in the θ-2θ diffraction pattern. A Phillips 430 transmission electron microscope (TEM) operated at 300 keV was employed to obtain plan-view microstructures. The samples were prepared by dimpling and ion milling from the substrate side.

The θ-2θ diffraction pattern in the 40-50° range is shown in Figure 2a. The lattice parameters calculated from the 200 and 002 θ-2θ diffractions of PZT give a=0.3930 nm and c=0.4130 nm, very close to the lattice parameters of the target and the bulk lattice parameters [8], indicating that the epitaxial stresses are completely relieved. The fraction of c-domains is approximately 0.80, established form the relative integrated intensities of the 200 and 002 PZT θ–rocking curves following the methodology of Hsu and Raj and Kang *et al.* [9].

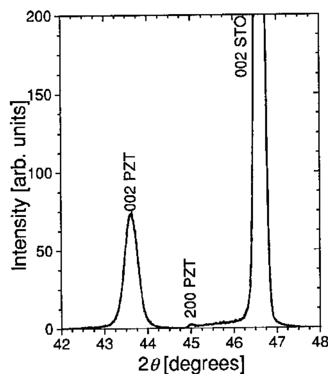

***Figure 2.** XRD pattern of the sample in the 40-50° range.*

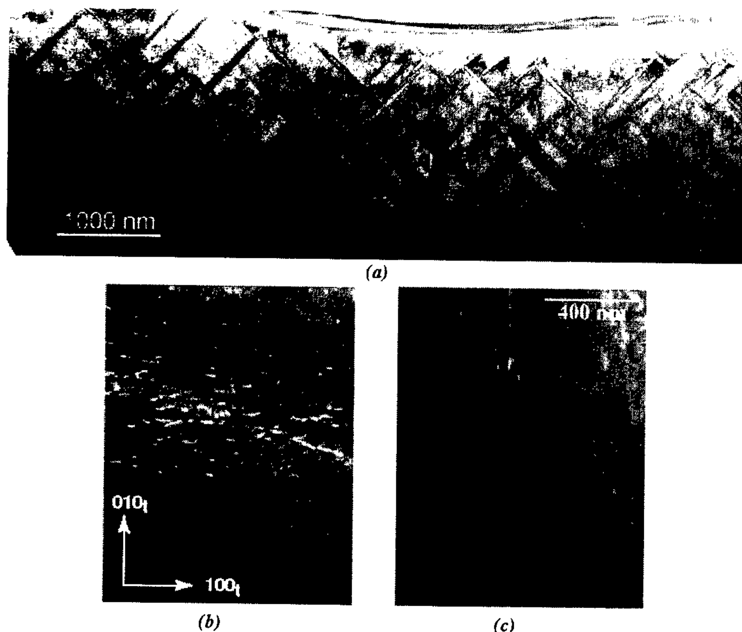

Figure 3. *(a) Bright field micrograph taken from a plane-view TEM sample showing the cellular arrangement of all the three domains and (b) and (c)dark field image staken with(100) and (010) reflections.*

The plane view TEM micrograph in Figure 3a displays the microstructure that consists of all the three possible domains of the tetragonal ferroelectric phase. The film is divided into cells of c-domains in the (001) plane bound by a_1- and a_2-domains along the [100] and [010] directions, respectively. The c-domain fraction is consistent with XRD results and the fractions of a_1-and a_2 domains are equal as predicted theoretically. Furthermore, high-resolution TEM reveals the presence a pseudo-orthogonal network of misfit dislocations with Burgers vectors **b**=[100] and **b**=[010] (see Fig. 3b and c). Spacing between dislocations is ~40 nm, corresponding to a linear density of 0.0025 nm^{-1}. Since the tetragonality for PZT is approximately 5.2 % [8] and the observed c-domain fraction is ~0.80, $\bar{\varepsilon}_M = (a-\bar{a}_S)/\bar{a}_S$ should be equal to ~0.5 %. Therefore, $\bar{a}_S$ should be 0.3954 nm at room temperature (compared to the bulk lattice parameter of STO which is 0.3905 nm [8]), corresponding to a 73 % relaxation by misfit dislocations when extrapolated to the deposition temperature (thermal expansion coefficient of STO=$11\text{x}10^{-6}$ °C^{-1}). The theoretical linear dislocation density is approximately 0.0030 nm^{-1}, in good agreement with experimental observation.

The results can be elegantly combined on a domain stability map as shown in Figure 4 using the effective misfit strain concept [1,2] and the temperature dependencies of the lattice parameters of the film and the substrate. The domain stability map is constructed by comparing the total elastic energies of all possible single domain and polydomain structures following the formalism of our previous article [10]. Full theoretical derivation leading to the domain stability

map and its analysis will be given elsewhere. It can be shown that a_1- and a_2-single domains are not stable for any given pair of $\bar{\varepsilon}_M$ and ε_T. Furthermore, the $c/a/c/a$ polytwins are also unstable because for any pair of $\bar{\varepsilon}_M$ and ε_T, their energy is always larger than either the single domain c, the $a_1/a_2/a_1/a_2$ polydomain, or the 3-domain structure. The lower and upper limits of the c-domain fraction α_3 [see Eq. (3)] for the 3-domain structure define the phase stability boundaries between $a_1/a_2/a_1/a_2$ and the 3-domain state and the 3-domain state and the single domain c, respectively (α_3=0, i.e., ε_T=-2ε_M and α_3=1, i.e., ε_M=0). Within the stability area of the 3-domain structure, α_3 gradually changes from 0 to 1 as the misfit approaches 0. To compare theoretical analysis with experimental results, the effective misfit strain and tetragonality pairs for the PZT film on STO substrate are evaluated at different temperatures and their respective positions on

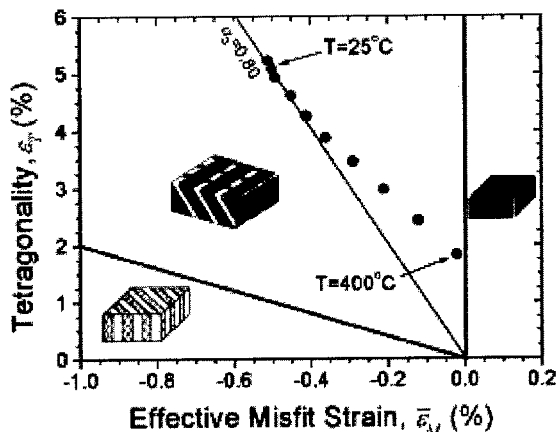

Figure 4. Domain stability map for 450 nm thick (001) PZT films on (001) STO substrates. Filled circles represent the expected position of the theoretical effective misfit strain and tetragonality pairs at different temperatures form 25°C to 400°C. On the thin line in the 3-domain region (equi-fraction line), the c-domain fraction is constant and is equal to 0.80.

the domain stability map are marked (see Figure 4, full circles). On the thin line given by $\varepsilon_T = -10 \cdot \bar{\varepsilon}_M$, α_3 is constant and is equal to 0.80 [see Eq. (3)]. This line passes through the point [$\bar{\varepsilon}_M$ (25°C), ε_T (25°C)], indicating that the c-domain fraction is ~0.80 at room temperature. α_3 increases with increasing temperature since the slopes of the equi-fraction lines approach the vertical axis given by $\bar{\varepsilon}_M$=0.

The domain structure shown in Figure 3a may play an important role in the switching characteristics of ferroelectric films. We have shown experimentally that the switching in (001) PZT films on (001) $LaAlO_3$ substrates proceeds faster in thicker films (~400 nm) compared to thinner films of thickness $h \leq 100$ nm under pulsed testing conditions [11]. The microstructure of the films observed via TEM changed from a single-domain state (h<60 nm) to a polydomain structure ($h \geq$ 60 nm) with gradual decline in the c-domain fraction coupled with increase in the density of 90° domain walls. The polydomain formation was accompanied by relaxation of

internal stresses. Although it is difficult to single out the formation of polydomain structure as the only reason for faster switching in these films with increasing h, together with atomic force microscopy studies that show heterogeneous nucleation of reversed domains at 90° domain walls in 400 nm PZT films on STO substrates [12], it is reasonable to hypothesize that they have a distinct contribution to the process of polarization reversal.

CONCLUSION

We have shown that in epitaxial tetragonal ferroelectric films, the internal stresses may be completely relaxed with the formation of a polydomain structure that consists of all the three variants of the ferroelectric tetragonal phase. TEM observations prove the existence of such structures and x-ray diffraction studies show that the internal stresses are indeed relieved by the creation of the three-domain architectures. A domain stability map is constructed that takes into account the possibility of the formation of the 3-domain structures. Theoretically predicted domain fraction is in excellent agreement with experimental results. The specifics regarding the dislocation structure, full TEM and XRD analysis, and theory can be found in [13].

ACKNOWLEDGEMENT

The authors gratefully acknowledge the support by NSF under Grant No. DMR-9903279.

REFERENCES

1. J. S. Speck and W. Pompe, *J. Appl. Phys.*, **76,** 466 (1994).
2. S. P. Alpay, V. Nagarajan, L. A. Bendersky, M. D. Vaudin, S. Aggarwal, R. Ramesh, and A. L. Roytburd, *J. Appl. Phys.*, **85,** 3271 (1999).
3. B. S. Kwak, A. Erbil, J. D. Budai, M. F. Chrisholm, L. A. Boatner, and B. J. Wilkens, *Phys. Rev. B*, **49,** 14865 (1994).
4. C. M. Foster, G. R. Bai, R. Csencsits, J. Vetrone, R. Jammy, L. A. Wills, E. Carr, and J. Amano, *J. Appl. Phys.*, **81,** 2349 (1997).
5. A. L. Roitburd, Phys. Stat. Sol. (a), **37,** 329 (1976); A. L. Roytburd and Y. Yu, *Ferroelectrics*, **144,** 137 (1993).
6. S. P. Alpay and A. L. Roytburd, *MRS Proc.*, **474**, 407 (1997).
7. A. L. Roytburd, *J. Appl. Phys.*, **83,** 228; 239 (1998).
8. W.-Y. Hsu and R. Raj, *Appl. Phys. Lett.*, **67,** 792 (1995);Y. M. Kang, J. K. Ku, and S. Baik, *J. Appl. Phys.*, **78,** 2601 (1995).
9. *Landolt-Börnstein, Numerical Data and Functional Relationships in Science and Technology*; *Vol. 16*, edited by K.-H. Hellwege and A. M. Hellwege (Springer Verlag, Berlin, 1981).
10. S. P. Alpay and A. L. Roytburd, *J. Appl. Phys.*, **83,** 4714 (1998).
11. V. Nagarajan, I. G. Jenkins, S. P. Alpay, H. Li, S. Aggarwal, L. Salamanca-Riba, A. L. Roytburd, and R. Ramesh, *J. Appl. Phys.*, **86,** 595 (1999).
12. C. S. Ganpule, V. Nagarajan, H. Li, A. S. Ogale, D. E. Steinhauer, S. Aggarwal, E. Williams, R. Ramesh, and P. De Wolf, *Appl. Phys. Lett.*, **77**, 292 (2000).
13. A.L. Roytburd, S.P. Alpay, L.A. Bendersky, V. Nagarajan, and R. Ramesh, *J. Appl. Phys.*, in press.

Mat. Res. Soc. Symp. Proc. Vol. 655 © 2001 Materials Research Society

Near field optical second harmonic imaging of the polydomain structure of epitaxial $PbZr_xTi_{1-x}O_3$ thin films

H.Y. Liang, I.I. Smolyaninov, C.H. Lee, and C.C. Davis
Electrical and Computer Engineering Department, University of Maryland, College Park, MD 20742, USA
V. Nagarajan and R. Ramesh
Department of Materials and Nuclear Engineering, University of Maryland, College Park, MD 20742, USA

ABSTRACT

Near field optical second harmonic microscopy has been applied to imaging of the c/a/c/a polydomain structure of epitaxial $PbZr_xTi_{1-x}O_3$ thin films in the $0<x<0.4$ range. An uncoated adiabatically tapered fiber tip was employed in our microscope which, according to our previous research [5] could yeild a resolution of up to 80 nm. Experimentally measured near-field second harmonic images have been compared with the results of theoretical calculations. Good agreement between theory and experiment has been demonstrated. Thus, novel optical technique for nanometer scale ferroelectric domain imaging has been developed.

INTRODUCTION

Ferroelectric thin films attract much current attention for applications in nonvolatile random access memories [1] because of the ability of these materials to sustain spontaneous polarization below the Curie temperature. The ultimate performance of thin film memory devices depends on the spatial-temporal properties of individual ferroelectric domains. A better understanding of these properties requires experiments performed with nanometer spatial and sub-nanosecond temporal resolution. Near-field optical microscopy may be the technique of choice for such purposes. Optical second harmonic generation is widely used to characterize the average structure and crystal orientation of ferroelectric films [2]. Near-field second harmonic microscopy is the logical extension of these far-field teniques. The main advantages of near-field second harmonic microscopy in comparison with other scanning probe techniques, such as the recently developed piezoresponse atomic force microscopy [3], are the possibility of fast time-resolved measurements, and substantially smaller perturbation of the sample under investigation.

EXPRIMENTAL SETUP

Our experimental setup is shown in Fig.1. Weakly focused light (illuminated spot diameter on the order of 50μm) from a Ti:sapphire laser system consisting of an oscillator and a regenerative amplifier operating at 810 nm (repetition rate up to 250 kHz, 100-fs pulse duration, and up to 10 μJ pulse energy) was directed at an angle of incidence around 50° onto the sample surface. Excitation power at the sample surface was kept well below the ablation threshold. The local SHG was collected using an uncoated adiabatically tapered fiber tip, which is pulled at the end of a single mode fiber by the standard heating and pulling procedure. Tip curvature was measured using a scanning electron microscope. A fiber tip with an end diameter of about 50nm was scanned over the sample surface with a constant tip-surface distance of a few nanometers using shear force feedback control. As a result,

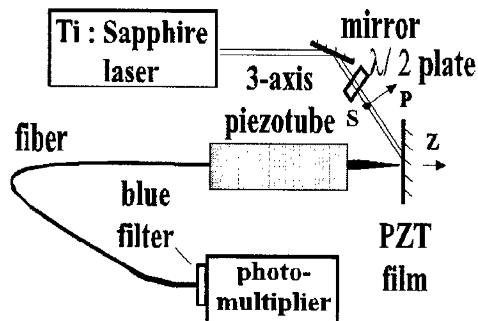

Figure 1. Schematic view of our near-field SH microscopy setup. P- and S- polarization directions of the fundamental light are indicated.

surface topography images were obtained while simultaneously recording the SH near-field images.

EXPRIMENTAL RESULTS AND DISCUSSION

1. Near-field image of a/c/a/c structures

Optical second harmonic generation (SHG) is a sensitive technique for characterization and investigation of the symmetry properties of different samples [4]. It is known to be affected by crystal structure, magnetic and ferroelectric order, mechanical strain, etc. Very recently we have introduced an apertureless near-field optical technique for second harmonic imaging using a bare tapered optical fiber tip externally illuminated with femtosecond laser pulses [5]. We have presented initial evidences of high spatial resolution of this technique (of the order of 80 nm), and indicated its sensitivity to local crystal symmetry. In this paper, we apply our technique to the imaging of polydomain c/a/c/a structures (consisting of alternating c-domains with the tetragonal axis perpendicular to the film-substrate interface, and a-domains with the c axis of the tetragonal film along either [100] or [010] directions of the substrate) that are commonly observed in thin epitaxial $PbZr_xTi_{1-x}O_3$ films in the $0<x<0.4$ range, and in many other ferroelectric films such as $BaTiO_3$, $PbTiO_3$, $KNbO_3$, etc[6].

A typical set of images of a 0.5 μm thick pulsed laser deposited epitaxial $PbZr_xTi_{1-x}O_3$ film grown on a centrosymmetric $La_{0.5}Sr_{0.5}CoO_3$ (LSCO) substrate obtained under excitation with P-polarized fundamental light is presented in Fig.2. The SH image in Fig.2(b) obtained under illumination with P-polarized fundamental light clearly shows fine grid-like structure of SHG from the film surface consistent with the known arrangement of c- and a-domains in the film that is visible in the high vertical resolution AFM image of the film in Fig.2(c) [6]. Spatial distribution of fundamental light was also measured and did not show any similar variations on this scale.

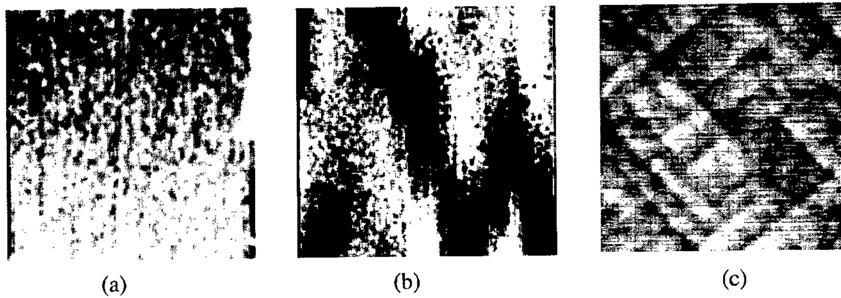

Figure 2. (a) topographical and (b) SH near-field optical image of a $PbZr_xTi_{1-x}O_3$ film. Images were 1.5 μm by 1.5 μm. Average number of SH photons collected through the tip was of the order of 200 photons per second. (c) 1.5 μm by 1.5 μm AFM image of the same film. "Grid" structure corresponds to the boundaries of a-domains.

2. Rotation symmetry of near field SHG from single crystal $BaTiO_3$

In order to understand the main contrast mechanisms in the SH images, we performed a study of the polarization properties of the near- and far-field SH signal using a poled single crystal of $BaTiO_3$ as a sample ($BaTiO_3$ and $Pb(Zr_xTi_{1-x})O_3$ have similar perovskite structure and belong to the same tetragonal symmetry class). Phase-matched SHG is prohibited in the bulk of $BaTiO_3$ because of its strong dispersion [7]. As a result, the measured SH signal originates at the surface, which makes the experimental situation look very similar to the case of a thin film. Near-field SH signal dependencies on the polarization of the fundamental light for three different poling directions of $BaTiO_3$ crystal are shown in Fig.3. The SH signal exhibits 4-fold symmetry with respect to polarization angle rotation in the case (a) of poling direction located in the incidence plane of the fundamental light parallel to the crystal surface. The symmetry becomes 2-fold in the case (b) when the optical axis is perpendicular to the incidence plane. In case (c) (when the poling direction is perpendicular to the crystal surface) SH signal is much weaker than in cases (a) and (b). Big differences between these dependencies indicate that the near-field SHG may be used to recover local poling direction

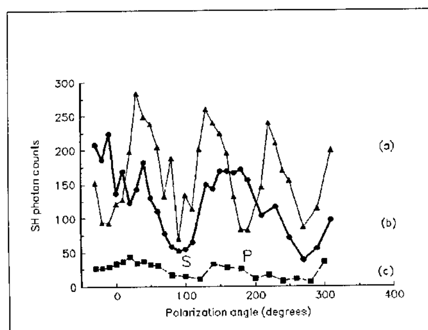

Figure 3. Near-field SH signal dependencies on the polarization of fundamental light for three different poling directions of $BaTiO_3$ crystal (shown in Fig.4) with respect to the incoming fundamental light. P- and S- polarization directions of the fundamental light are indicated.

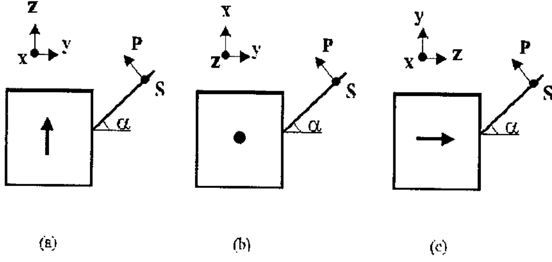

Figure 4. Orientation of the $BaTiO_3$ crystal with respect to the illuminating fundamental light for curves (a), (b), and (c) in Fig.3.

in thin ferroelectric films. In order to do this, we must achieve some theoretical understanding of the reasons for such a difference.

Surprisingly, most of the features of the near-field SHG may be understood from a very simple theoretical model described below. Let us consider fundamental light illuminating the tip of the microscope located near the $BaTiO_3$ crystal surface. Three different cases of the poling vector orientation are shown in Fig.4(a,b,c), where α is the incidence angle, and the z-axis is chosen to coincide with the poling direction of the crystal. All three cases may be considered in a similar way, so we will concentrate on case (b) and only present the final results for the cases (a) and (c). Let us consider the fundamental optical field distribution in the tip-sample region at distances much smaller then the wavelength λ of the fundamental light. In this region the quasi-electrostatic approximation may be used. The tip shape may be approximated as an ellipsoid with a very high aspect ratio. For P-polarized excitation light and y-component (the component perpendicular to the sample surface) of the optical field the exact analytic solution of the Laplace equation gives $E_{tip}(\omega)=\varepsilon E_{y0}(\omega)$ where ε is the dielectric constant of the tip, E_{y0} is the incoming field and E_{tip} is the y-component of the field just below the tip apex. As a result, for the incidence angles α around $\pi/2$ the local SHG under the tip is enhanced by a factor of n^8 (since $I(2\omega)_{tip}=E^2_{tip}(2\omega)=E^4_{tip}(\omega)=n^8E^4_{y0}(\omega)$), where n is the tip refractive index. Assuming n=1.6 the enhancement factor equals about 40. It may be even higher (of the order of $(2\varepsilon)^4$) in the vicinity of a sample surface with a high dielectric constant, such as a metal or a ferroelectric, due to the image potential. In our discussion to follow, we will not consider any particular value of the field enhancement factor. Instead, we denote the fundamental field enhancement factor by γ. The fundamental optical field components under the tip apex at a polarization angle ϕ can be written as:

$$E_x = E\cos\phi\cos\alpha, \qquad E_y = (\gamma/\varepsilon_b)E\cos\phi\sin\alpha, \qquad E_z = E\sin\phi, \qquad (1)$$

where ε_b is the dielectric constant of $BaTiO_3$, ϕ=0 and ϕ=90° correspond to P-polarized and S-polarized excitation light respectively. Taking into account the non-zero components of the second harmonic susceptibility tensor for $BaTiO_3$: $\chi^{(2)}_{yyz} = \chi^{(2)}_{xxz} = \chi^{(2)}_{yzy} = \chi^{(2)}_{xzx} = 17.7\times10^{-12}$ m/V, $\chi^{(2)}_{zyy} = \chi^{(2)}_{zxx} = -18.8\times10^{-12}$ m/V, and $\chi^{(2)}_{zzz} = -7.1\times10^{-12}$ m/V (where z is the poling direction) [8], the second harmonic field components at the tip apex may be written as:

$$D^{(2)}_x = \chi^{(2)}_{xzx}E^2\sin^2\phi\cos\alpha, \qquad D^{(2)}_y = (\gamma/\varepsilon_b)\chi^{(2)}_{xzx}E^2\sin^2\phi\sin\alpha, \qquad (2)$$

$$D^{(2)}_z = (\gamma^2/\varepsilon_b^2)\chi^{(2)}_{zxx}E^2\cos^2\phi\sin^2\alpha + \chi^{(2)}_{zxx}E^2\cos^2\phi\cos^2\alpha + \chi^{(2)}_{zzz}E^2\sin^2\phi$$

If we assume that the microscope tip collects only dipole radiation, the second harmonic optical signal will be proportional to

$$I^{(2)} = D^{(2)}{}_z{}^2 + D^{(2)}{}_x{}^2 \qquad (3)$$

(SH dipoles that oscillate along the y-direction do not radiate towards the tip). Similar calculations of the field at the tip apex are easy to perform for cases (a) and (c). Let us point out that within our model the angular dependencies of the field E for the points in space around the tip apex should be approximately the same as in (1). Only the enhancement factor γ is different for these points (its value changes from a maximum just under the tip apex to γ=1 far from the apex). So, in the final result one must replace the factors γ^4 and γ^2 by the average values $<\gamma^4>$ and $<\gamma^2>$ taken over all the area around the tip apex where the SH signal is collected.

The final results of our calculations are presented in Fig.5. The best agreement with experimentally measured symmetry properties of the near-field SH polarization curves was achieved in the γ = 5 -7 range for the field enhancement factor. This is reasonably close to the expected value of $\gamma = 2\varepsilon_{tip}$. A much smaller value of the SH signal in case (c) is a consequence of the fact that $I^{(2)}$ contains terms proportional to $<\gamma^4>$ in the cases (a) and (b), but in case (c) the SH signal $I^{(2)}$ is proportional to $<\gamma^2>$:

$$I^{(2)} = D^{(2)}{}_x{}^2 + D^{(2)}{}_y{}^2 = (<\gamma^2>/\varepsilon_b{}^2)\chi^{(2)}{}_{xzx}{}^2E^4(\sin^2 2\phi \sin^2\alpha + \cos^4\phi \sin^2 2\alpha) \qquad (4)$$

The transition from near-field mode to far-field mode of the microscope operation (which corresponds to an increase in the tip-sample separation from a few nanometers to a distance of a few wavelengths of light) can be described mathematically within our model as a transition from γ = 5 - 7 to γ=1 (no field enhancement by the tip). Results of numerical calculations for such a transition performed using (3) are also in good qualitative agreement with our experiment results. Both theoretical and experimental data have the same symmetry of the SH polarization dependencies in the near-field and far-field zones. This indicates that our simple model provides an adequate description of the essential physics involved in near-field observation of SHG from ferroelectric samples.

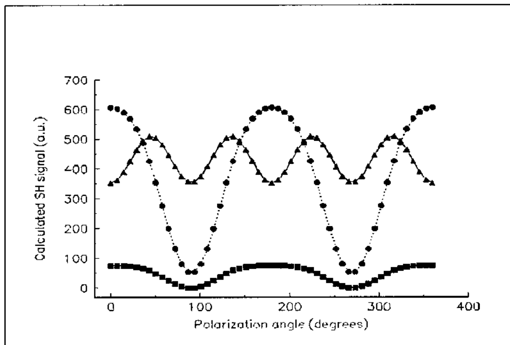

Figure 5. Theoretical near-field SH signal dependencies on the polarization angle of fundamental light obtained in the geometry (a), (b) and (c) from Fig.4 for the field enhancement factor γ = 7 and α = 45°.

Based on the developed understanding of the SHG contrast due to differences in ferroelectric poling directions, we have calculated spatial distribution of local SHG from a typical $PbZr_xTi_{1-x}O_3$ film area showing c/a/c/a polydomain structure assuming 100nm spatial resolution of the microscope. The results of such calculations are presented in Fig.6 for the case of P-polarized excitation light. As it is evident from Fig.3, SHG from c-domains forms a low background of the image. Much brighter SHG from 30-50 nm wide a-domains forms a grid-like structure that corresponds to the real geometry of domains (with some corrugations due to 100 nm spatial resolution of the microscope). Thus, the grid-like features observed in Fig.2(b) may be identified as a-domains of the $PbZr_xTi_{1-x}O_3$ film.

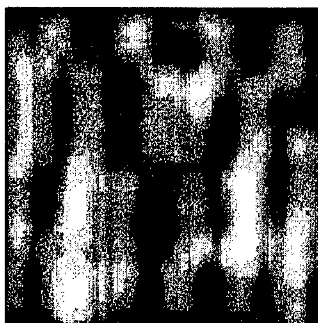

Figure 6. Calculated 1.5 μm by 1.5 μm image of SHG from a typical c/a/c/a polydomain film structure obtained assuming 100 nm spatial resolution of the microscope and experimentally measured (Fig.3) SH contrast between different poling directions.

Reference

1. O. Auciello, J. F. Scott, and R. Ramesh, *Physics Today*, **N7**, 22-27 (1998)
2. L. D. Rotter, D. L. Kaiser, and M. D. Vaudin, *Appl. Phys. Lett.* **68**, 310 (1996)
3. A. Gruverman, H. Tokumoto, A. S. Prakash, S. Aggarwal, B. Yang, M. Wutttig, R. Ramesh, O. Auciello, and T. Venkatesan *Appl. Phys. Lett.* **71**, 3492 (1997)
4. Y.R. Shen, *The Principles of Nonlinear Optics*. (Wiley, New York, 1984)
5. I. I. Smolyaninov, H. Y. Liang, C. H. Lee, C. C. Davis, S. Aggarwal, and R. Ramesh, *Optics Letters* **25**, 835-837 (2000); I.I. Smolyaninov, H.Y. Liang, C.H. Lee, and C.C. Davis, *J. of Appl. Phys.* **89**, 206-211 (2001).
6. S. P. Alpay, V. Nagarajan, L. A. Bendersky, M. D. Vaudin, S. Aggarwal, R. Ramesh, and A. L. Roytburd, *J.Appl.Phys.* **85**, 3271-3277. (1999)
7. I. I. Smolyaninov, C. H. Lee, and C. C. Davis, *Phys.Rev.Lett.* **83**, 2429-2432. (1999)
8. F. Zernike, and J. E. Midwinter, *Applied Nonlinear Optics* (Wiley, New York, 1973)

Processing, Properties, and Characterization

Mat. Res. Soc. Symp. Proc. Vol. 655 © 2001 Materials Research Society

ORIENTATION SELECTION IN SOL-GEL DERIVED PZT THIN FILMS

G. J. NORGA and LAURA FÈ
IMEC vzw, Kapeldreef 75, B 3001 Leuven, Belgium

ABSTRACT

Motivated by the growing impact of PZT film orientation on ferroelectric film properties as film thickness is scaled down, we present basic studies on orientation selection in sol-gel derived PZT films, using pre-annealed Pt/Ti electrode layers as a model electrode system. FTIR was used to study, on a real temperature scale, chemical reactions in the films during the initial thermal steps prior to crystallization. We found that the chemical structure of the pyrolyzed film has a much larger impact on orientation selection than has previously been realized. In addition to pyrolysis conditions, the ambient used for the crystallization step was found to play a crucial role in orientation selection. As film thickness decreases, excessive oxygen incorporation in the films is seen to result in the loss of the preferential (111) texture when crystallization is performed in air. By performing crystallizations in N_2, 40 nm thick PZT films with a strongly preferential (111) orientation could be obtained.

INTRODUCTION

Chemical solution deposition (CSD) is an established technique to prepare high quality $Pb(Zr_{1-x},Ti_x)O_3$ (PZT) ferroelectric thin films for integration with silicon integrated circuitry. The large effect of orientation on P_r, poling behavior, and hysteresis loop abruptness has emphasized the need for methods to tightly control film orientation [1]. Due to the continued reduction of the operating voltage of silicon ICs, the reduction in the switching voltage of the films has become especially urgent in light of their application in nonvolatile memories based on destructive readout of a ferroelectric capacitor [2-4]. In our previous investigations on sol-gel derived PZT films, we uncovered the loss of preferential (111) orientation as the principal cause for hysteresis loop slanting and P_r reduction, observed in sub-100 nm PZT films on Pt electrodes [5]. This demonstrates the growing impact of film orientation on ferroelectric film properties as film thickness is scaled down.

A good model system for basic studies on orientation selection in PZT is self-textured (111) Pt. Polycrystalline Pt films with a sharp (111) fiber texture are readily obtained in a reproducible way by sputtering on SiO_2/Si substrates using a thin (~10 nm) Ti layer to promote adhesion. In the literature on orientation selection in PZT, there is general agreement that the two dominant PZT orientations commonly observed on (111) Pt, PZT (100) and PZT (111), can be traced to the minimal PZT surface and minimal PZT/Pt interface energy configurations of the PZT nucleus on a (111) textured Pt electrode surface, respectively [6]. Moreover, it has been proposed that the (111) orientation of the PZT nucleus on a Pt (111) surface is energetically favored over the (100) PZT orientation in case a thin crystalline TiO_2 seeding layer is present [7].

For sol-gel derived PZT films on (111) textured Pt electrodes, a great variety of factors have been shown to affect the relative amounts of (111) and (100) oriented material in the films after crystallization. Examples of such factors are precursor type and homogeneity [8-11], the Pb excess [12], type and heat treatment of the bottom electrode [13-15], as well as the temperatures

and heating rates applied for pyrolysis and crystallization [16]. A variety of models exist to explain these dependencies [6, 15-18]. For instance, Brooks *et al.* have speculated that variations in the valence of Pb are responsible for the observed variation in the PZT(111)/PZT(100) intensity ratio as a funtion of pyrolysis temperature [15]. Huang *et al.* [17] propose that oxidation reactions of the precursor are responsible for the reduction of Pb and the subsequent formation of Pt_3Pb intermetallic, thought to serve as template for PZT (111) growth. Schwartz *et al.* [18] have shown that variations in the crystallization temperature, as a result of variations in precursor chemistry, can drastically alter the nucleation mechanism and hence the properties of sol-gel prepared PZT films.

These observations convincingly demonstrate that the amorphous PZT gel to crystalline perovskite transformation mechanism is influenced significantly by chemical factors, as could be expected for a truly chemical preparation method such as sol-gel. However, the absence from the cited work of chemical structure studies, performed directly on the film during thermal processing, limits their applicability beyond the specific precursor chemistry employed. In this paper, we will firstly demonstrate that fundamental chemical information obtained from FTIR can greatly clarify the relationship between the thermal process sequence and the resulting orientation. Building on the insights gained from the FTIR studies, we present a comparison between the orientation selection behavior for films with standard thickness (200 nm) with reduced thickness (200 – 40 nm) films.

EXPERIMENTAL

Precursor solutions of three different Zr/Ti ratios (40/60, 30/70, 20/80) were prepared according to the procedure developed by Nouwen *et al.* [19]. This method has the peculiarity of using butoxyethanol, a less harmful and less reactive solvent compared with the more commonly used methoxyethanol. Pb acetate, and Zr and Ti propoxide were used as metal starting compounds. Precursor solutions were deposited by spin coating wafers at 3000 rpm for 30 s onto annealed Pt/Ti bottom electrodes. These bottom electrodes were prepared by deposition, using RF sputtering, of 10 nm Ti followed by 100 nm Pt on thermally oxidized (100) Si wafers. The reactive Pt/Ti stack was subsequently stabilized by rapid thermal annealing (RTA) at 700°C for 5 minutes in O_2. The result of this heat treatment is the presence of a small amount of TiO_2 on top of Pt (111), making PZT (111) the energetically preferred orientation [20].

To study chemical evolution after deposition, the films were fired on a hot plate at a temperature varying between 50 and 600C for two minutes and analyzed with absorption-reflection infrared spectroscopy (AR-FTIR). This technique, which allows the identification of organic species left in the film, takes advantage of the fact that the PZT is deposited on a highly reflective surface like platinum. The AR-FTIR apparatus consists of an infrared spectrometer and a specular variable angle reflectance attachment [21]. To optimize the signal intensity an incident angle of 50 degrees was used.

To investigate the effect of processing parameters on chemical evolution with temperature, PZT films, with thickness varying from 40 to 200 nm, were fabricated using different heating schedules and analyzed by AR-FTIR prior to crystallization. Different thicknesses were obtained by employing different dilution ratios of the precursor in the butoxyethanol solvent. Both the pyrolysis temperature, the number of pyrolysis steps, and their duration was varied. Crystallization was performed at 600C, 30 min on hotplate in air, unless specified differently. A

measure for the degree of preferential orientation of the films was obtained by comparing the θ–2θ XRD peak intensities.

RESULTS AND DISCUSSION

Absorption-reflection FTIR spectra of sol-gel PZT films on Pt electrodes

Figure 1 summarizes the chemical and structural information obtainable from FTIR measurements on sol-gel derived PZT films. Shown are the spectra recorded for a 30/70 PZT film prepared using butoxyethanol as the solvent, as a function of temperature [22]. In the as spun film, a broad band is observed between 700 and 450 cm^{-1}, which relates to vibrations of the metal-oxygen bond. As the temperature is increased, this band gradually sharpens and at 600C, when the film is fully crystallized, only a sharp peak at 690 cm^{-1}, attributed to MO_6 octahedra vibration [11], is present. The band between 1566 and 1414 cm^{-1}, due to acetate groups, starts to decrease as the temperature increases and disappears completely between 300 and 350C. In the same temperature range (300-350C), a band between 1500 and 1300 cm^{-1}, attributed to carbonates, appears. The presence of this band up to 550C indicates the persistence of carbonates until just below the temperature where the crystallization starts.

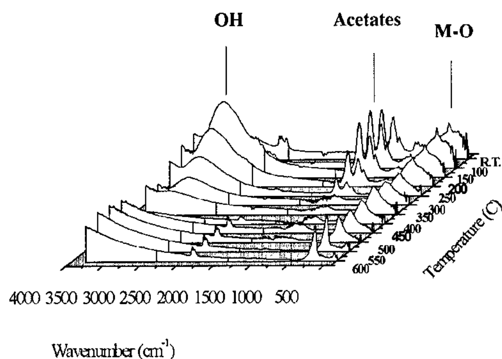

Figure 1: AR-FTIR spectra as function of temperature for a 30/70 PZT film. The evolution of the OH band (3380 cm^{-1}), which increases up to 200ºC and decreases to disappear at 400ºC, gives insight in hydrolysis and condensation. Acetate bands (1600-1400 cm^{-1}) change into carbonate, which are present up to 550ºC. The sharpening of the MO_6 band (700-450 cm^{-1}) allows to monitor PZT crystallization.

The broad OH band (~3380 cm^{-1}), a salient feature of the AR-FTIR spectra, is of particular importance because it allows to monitor the presence of metal hydroxide, a necessary intermediate between the metal alkoxide and metal oxide bonding states. The intensity of the OH band increases up to 200C when the hydrolysis reaction (1) causes the number of hydroxyl groups to peak:

$$M\text{-}OR + H_2O \rightarrow M\text{-}OH + R\text{-}OH \quad (1)$$

Above 200C, the intensity of this band starts to decrease as a result of condensation reactions (2), (3), to disappear entirely when the condensation process is complete:

$$M\text{-}OH + M\text{-}OH \rightarrow M\text{-}O\text{-}M + H_2O \quad (2)$$

$$M\text{-}OR + M\text{-}OH \rightarrow M\text{-}O\text{-}M + ROH \quad (3)$$

Interestingly, the kinetics of the condensation process, as reflected in the temperature dependence of the intensity of the OH band, were found to depend strongly on the details of the pyrolysis treatment. Figure 2 compares the AR-FTIR spectra for PZT 30/70 films subjected to two distinct pyrolysis treatments: 200C (2 min) followed by 350C (2 min); or 350C (2 min) only. In the case where a prior "drying" step at 200C is applied, the OH band vanishes almost completely when subjected to a subsequent pyrolysis step at 350C, indicating the full condensation of OH bonds to yield M-O-M (reaction (2)). Meanwhile, if the sample is brought directly to 350C without prior drying step, a sizeable amount of OH bonds is left in the film at 350C. We propose that due to the omission of the drying step, not all of the OR bonds have a chance to hydrolyze before the condensation reactions start. As a result, condensation in the film subjected to a single 350C step does *not only* involve the reaction of two OH groups to produce one water molecule (2) but also the reaction of OH with OR to produce alcohol (3). Presumably, the slower kinetics of the latter reaction (3) compared to reaction (2) explains the persistence of residual OH groups in the film pyrolyzed at 350C.

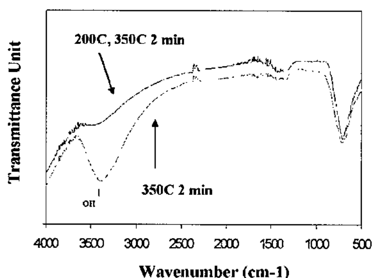

Figure 2: AR-FTIR spectra of two 30/70 PZT films pyrolyzed at 350C, 2 min. In one case a drying step at 200C for 2 min was applied prior to the pyrolysis step at 350C. The difference in the intensity of the OH band should be noticed.

Effect of residual organics on orientation selection in PZT

A first example of how the AR-FTIR technique can provide insights in the role of chemical factors in orientation development, is shown in Figures 3 and 4. Figure 3 compares the AR-FTIR spectra of two identical 30/70 PZT films, subjected to two different pyrolysis treatments. Film 1 received a 10 s pyrolysis treatment at 350C, whereas for film 2 the 350C steps was performed for 2 min. As can be seen from the AR-FTIR spectra, film 2 is acetate-free while film 1 contains still

acetates due to the shorter pyrolysis time. This difference in chemical structure turns out to have a large influence on orientation development after crystallization. XRD patterns of the films crystallized at 600C for 30 min on hot plate, shown in Figure 4, demonstrate that while film 1 is strongly (111) oriented, film 2 has a mixed (111)/(100) texture.

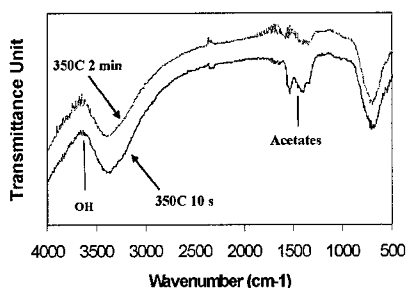

Figure 3: AR-FTIR spectra of 30/70 PZT films pyrolyzed for different times at 350C. The one that was pyrolyzed for 10 seconds still contains large amounts of acetates while in the film that was subjected to a 2 min pyrolysis step, acetates have already transformed into carbonates.

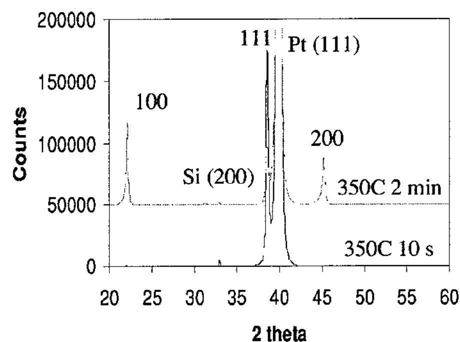

Figure 4: XRD patterns of the same two films of Figure 3 after crystallization at 600C for 30 min on a hot plate. The film pyrolyzed for 10 seconds shows a much higher degree of (111) orientation than the one subjected to a 2 min pyrolysis step.

Z. Huang *et al.* [17] have proposed that burning off of organic molecules originating from the precursor can locally reduce the oxygen partial pressure in the film, resulting in the reduction of PbO to metallic lead at the Pt/PZT interface. They also demonstrate the (transient) formation of a Pt_3Pb inter-metallic, which serves as a template for (111) growth of the PZT. Table 1 gives an overview of the interfacial compounds proposed by other authors to promote nucleation of (111) textured PZT grains in CSD-derived PZT films on Pt.

(111)	(100)	Ref.
Pt_3Ti	Self-textured, F-face	6
$Pt_{5-7}Pb$	PbO	16
Pt_3Pb	-	17
O-deficient pyrochlore	O-excess pyrochlore (Pb^{4+}/Pb^{2+})	15

Table 1: Interfacial phases proposed by other authors to explain the texture selection of sol-gel derived PZT on Pt (111) electrode layers.

We note that all the transient phases, believed to induce (111) growth, are stabilized in a reducing ambient. Hence, the strong (111) texture in the film pyrolyzed for a shorter time period can be linked to the presence of oxidizable carbon in the form of acetate molecules, as observed by FTIR. The burn-off of acetate to CO_2 and H_2O during the crystallization step is likely to have lowered the oxygen partial pressure at the PZT/Pt interface to the point where it caused the formation of one of the transient compounds, shown in Table 1. In conclusion, these results demonstrate that texture development is not solely dependent on the pyrolysis *temperature* as shown earlier by Brooks *et al.* [15], but on the *duration* of the pyrolysis treatment as well.

Effect of residual OH groups

Figure 5 shows the effect of the difference in OH band intensity which was discussed above, on film texture. Again, a large difference in film texture is seen, even though the pyrolysis temperature is the same in both cases. The larger OH bond density in the pyrolyzed film, caused by the omission of the drying step at 200C, obviously results in a lesser degree of orientation of the crystallized film.

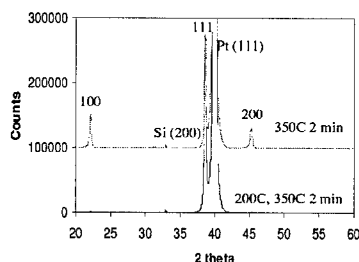

Figure 5: XRD patterns after crystallization at 600C on HP for 30 min for two 30/70 PZT films, pyrolyzed at 350C for 2 min. The PZT peaks are indicated. In one case, a drying step at 200C for 2 min was applied prior to pyrolysis. The film that experienced the 200C drying step prior to pyrolysis features a much larger PZT (111) / PZT (100) XRD peak intensity ratio.

A proof that these observations are more generally valid is given in Figure 6, which shows the effect of a prior drying step at 200C on the (111) PZT peak intensity after crystallization, for films pyrolyzed at 350C, 400C and 450C. For pyrolysis at 400C and 450C, the decrease in the (111) PZT intensity as the drying step at 200C is omitted, is still observed, even though the effect is less pronounced than for pyrolysis at 350C.

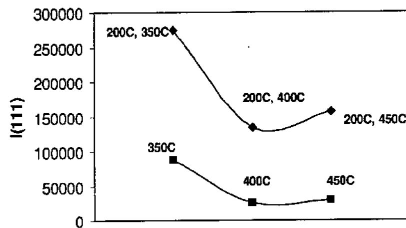

Figure 6: Effect of pyrolysis temperature and drying step at 200C on the intensity of the PZT (111) peak for 200 nm thick 30/70 PZT films. Both the drying and pyrolysis steps were performed for 2 min. All the films were crystallized at 600C on hot plate for 30 minutes.

In Figures 7 and 8, some thermodynamical arguments are presented which could explain why the presence of OH bonds in the film as it transforms from amorphous to crystalline, can result in a mixed oriented film. The details of this model are presented in a forthcoming paper [23]. The presence of OH bonds in the amorphous metal oxide imparts an excess Gibbs free energy to the film. When OH bonds are removed through condensation reaction (2), internal free volume is eliminated by densification, resulting in a reduction of the excess Gibbs free energy term.

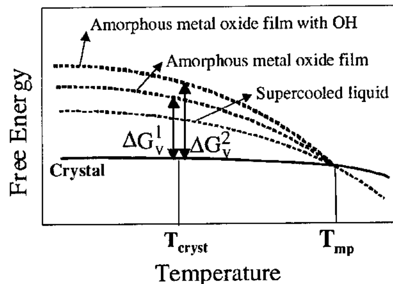

Figure 7: Schematic diagram of the Gibbs free energy G as a function of temperature, for the crystalline perovskite phase, the ideal supercooled liquid, and a sol-gel derived amorphous film with and without OH bonds present (adapted from Ref. 18). $|\Delta G^1_v|$, the driving force for crystallization of a metal oxide film in which all OH bonds have been removed by condensation, is smaller than $|\Delta G^2_v|$, the driving force in case a large amount of OH bonds are still present in the film. (T_{mp} and T_{cryst} are the melting and crystallization temperatures, respectively.)

The excess Gibbs free energy of the OH containing film also increases the thermodynamical driving force for transformation from the the amorphous metal oxide to the crystalline perovskite (Figure 7). As illustrated in Figure 8, this increase in the thermodynamical driving force lowers the barrier for heterogeneous nucleation, allowing the nucleation of (100) oriented PZT to happen along with the energetically favored (111) PZT.

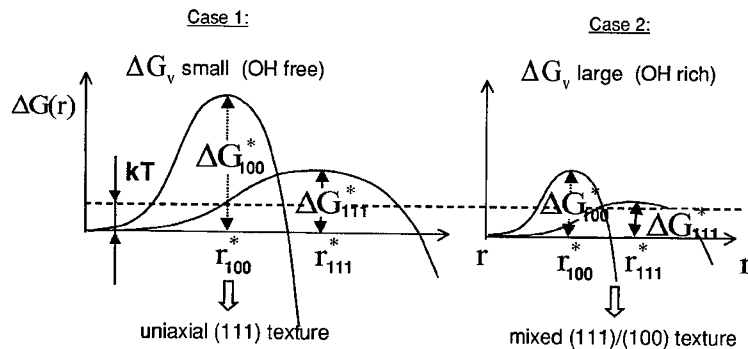

Figure 8: Free energy of a growing perovskite nucleus at the PZT/Pt interface, as a function of nucleus radius. For films containing OH, the driving force is increased, resulting in a reduction of the barrier height for nucleation of both (111) and (100) oriented PZT grains.

Orientation selection in thin (< 100 nm) films

Films with thicknesses down to 40 nm were prepared to assess the effect of film thickness on orientation selection mechanisms. While for 200nm thick films, orientation is significantly affected by pyrolysis treatment, electrode characteristics, Pb excess, and heating rate during crystallization (Figure 9), the influence of these factors vanishes as the film thickness is scaled down below 100 nm. This effect is illustrated in Figure 10, which shows, as a function of film thickness, the influence of two different pyrolysis treatments on the (111)/(100) orientation ratio. We identified the oxygen partial pressure in the crystallization ambient as the single, dominant factor affecting orientation in sub-100 nm films. As shown in Figure 11, the orientation of films crystallized in air shifts to fully (100) as their thickness is reduced below 100 nm. Meanwhile, if the crystallization is carried out in N_2, the orientation of the films becomes fully (111), regardless of film thickness. This effect is further illustrated in Figure 12, which demonstrates that the effect of crystallization in N_2 is to "switch" the film orientation from purely (100) for a 40 nm thick film crystallized films in air to purely (111) for a 40 nm thick film crystallized in O_2. We propose that for sub-100 nm films, the greater transparency of the film to O_2 from the crystallization ambient leads to an increased oxygen partial pressure at the PZT/Pt interface, resulting in the suppression of the (111) PZT growth mode. The suppression of the (111) PZT orientation as film thickness is reduced is thus consistent with PZT (111) templating on one of the interfacial compounds listed in Table 1, which can be formed at the Pt/PZT interface under non-oxidizing conditions.

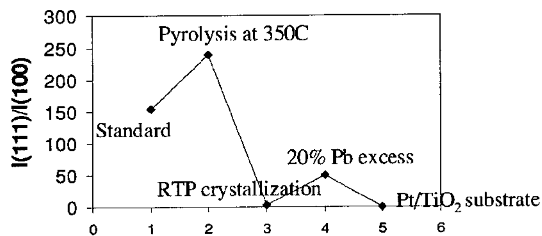

Figure 9: Effect of different factors on the I(111)/I(100) peak intensity ratio in 20/80 PZT films with a thickness of 200 nm. Pyrolysis was carried out at 200C, 2 min followed by 400C, 2min, unless indicated differently.

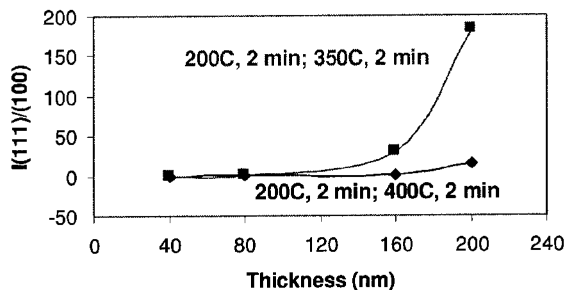

Figure 10: Effect of film thickness on the I(111)/I(100) orientation ratio for films subjected to two different pyrolysis treatments (350C, 2 min; and 200C, 2 min followed by 350C, 2 min).

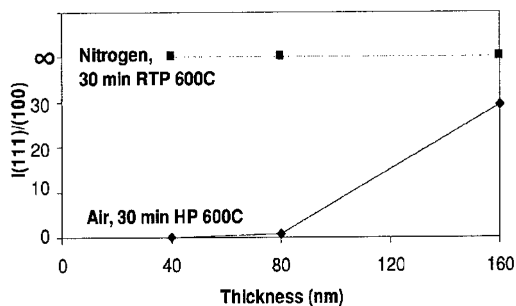

Figure 11: Effect of film thickness on the I(111)/I(100) orientation ratio for films subjected to two different crystallization treatments.

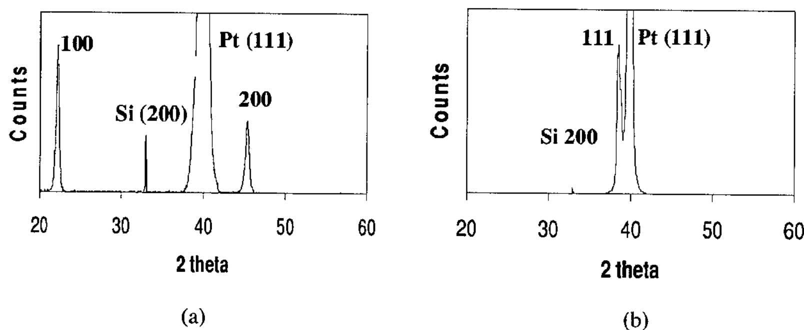

Figure 12: XRD spectra for 40 nm thick films, crystallized (a) in air (hot plate, 30 min, 600C), and in N_2 (RTP, 30 min, 600C).

CONCLUSIONS

Chemical processes occurring in the precursor during the thermal steps preceding crystallization may have a larger effect on orientation selection than has previously been realized. Monitoring the chemical reactions in the films during pyrolysis by AR-FTIR has allowed us to identify two distinct cases where chemical structure has a clear impact on orientation. Firstly, the presence of residual organics in the film was shown to favor (111) textured growth. The likely mechanism is templating on an interfacial compound formed under reducing conditions at the PZT/Pt interface. Secondly, films with a large density of OH bonds prior to crystallization consistently turn out poorly oriented. By performing a drying step at 200C prior to the pyrolysis step, the (111)/(100) ratio of the films is increased as the films are OH free upon crystallization. We suggest that OH groups, present at the moment when the film starts to crystallize, impart an excess Gibbs free energy to the film, resulting in a greater thermodynamical driving force for crystallization from the amorphous metal oxide to the perovskite. This increased thermodynamical driving is believed to be responsible for the activation of (100) growth mode along with the energetically preferred (111) orientation.
As film thickness is reduced, orientation selection becomes controlled by the oxygen partial pressure during the crystallization treatment. In the sub-100 nm thickness regime, this effect is dominant over other factors such as pyrolysis conditions, heating rate during crystallization, electrode properties, and Pb excess. By performing crystallizations in N_2, 40 nm thick PZT films with a strongly preferential (111) orientation could be obtained.

ACKNOWLEDGEMENTS

The authors wish to thank Dr. D. Wouters for fruitful discussions and support for the work. G. J. N. is a postdoctoral fellow of the Fund for Scientific Research- Flanders (Belgium).

REFERENCES

[1] S. Hirano, T. Yogo, K. Kikuta, Y. Araki, M. SaitohS. Ogasahara, J. Am. Ceram. Soc. **75**, 2785 (1992).
[2] K. R. Udayakumar, P. J. Schuele, J. Chen, S. B. Krupanidhi, L. E. Cross, J. Appl. Phys. **77**, 3981 (1995).
[3] L. E. Sanchez, Y.-W. Shu, I. K. Naik, Appl. Phys. Lett. **56**, 2399-401 (1990).
[4] K. Amanuma, T. Mori, T. Hase, T. Sakuma, A. Ochi, Y. Miyasaka, Jpn. J. Appl. Phys **32**, 4150 (1993).
[5] D.J. Wouters, G. Norga, H. E. Maes, Mat. Res. Soc. Symp. Proc. **541**, 381 (1999).
[6] T. Tani, Z. Xu, D.A. Payne, Mater. Res. Symp. Proc. **310**, 295 (1993).
[7] P. Muralt, T. Maeder, L. Sagalowicz, S Hiboux, S. Scalese, D. Naumovic, R. G. Agostino, N. Xanthopoulos, H. Mathieu, L Patthey, E.L. Bullock, J. Appl. Phys. **83**, 3835 (1998).
[8] C.D.E. Lakeman, D.A. Payne, J. Am. Ceram. Soc. 72, 3091 (1992)
[9] M. Kosec, B. Malic, Journal-de-Physique-IV-(Proceedings) **8**, 17 (1998).
[10] B. Malic, M. Kosec, K. Smolej, S. Stavber, J. Euro. Cer. Soc. **19**, 1345 (1999).
[11] P.R. Coffman, C.K. Barlingay, A Gupta, S.K. Dey, J. Sol-gel Science and Technology **6**, 83 (1996)
[12] G. J. Norga, J. Maes, E. Coppye, L. Fè, D. J. Wouters, O. Van der Biest, J. Mater. Res. **15**, 2309 (2000).
[13] G.A.C.M Spierings, J.B.A. Van Zon, P.K. Larsen, M. Klee, Integr. Ferroelectr. **3**, 283 (1993).
[14] G.J. Willems, D. J. Wouters and H.E. Maes, Integr. Ferroelectr. **15**, 19 (1997).
[15] K. G. Brooks, I. M. Reaney, R. Klissurska, Y. Huang, L. Bursill, N. Setter, J. Mater. Res. **9**, 2540 (1994).
[16] S. Chen, I. Chen, J. Am. Ceram. Soc. 77, 2332 (1994)
[17] Z. Huang, Q. Zhang, R. W. Whatmore, J. Appl. Phys. **86** (3), 1662 (1999).
[18] R.W. Schwartz, J.A. Voigt, B.A. Tuttle, D.A. Payne, T.L. Reichert, R.S. DaSalla, J. Mater. Res. **12**, 444 (1997)
[19] R. Nouwen, J. Mullens, D. Franco, J. Yperman, L.C Van Poucke, Vibrational Spectroscopy, **10**, 291 (1996).
[20] D. J. Wouters, G. J. Willems, H. E. Maes, Integr. Ferroelectr., **15**, 79 (1997).
[21] B. Elvers, H. Hofmann. "Ullmann' s Encyclopedia of industrial chemistry" **B5** VCH Weinheim, 455 (1994).
[22] L. Fè, G. J. Norga, D.J Wouters, R. Nouwen, L.C Van Poucke, J. Sol-gel Science and Technology, **19**, 149 (2000).
[23] L. Fè, G. J. Norga, D.J Wouters, H. E. Maes, G. Maes, Submitted to J. Mater. Res.

Mat. Res. Soc. Symp. Proc. Vol. 655 © 2001 Materials Research Society

SURFACE REACTION MECHANISMS IN THE CHEMICAL VAPOR DEPOSITION OF (Ba,Sr)TiO_3 FILMS

M. Yamamuka, T. Kawahara, M. Tarutani, T. Horikawa, T. Oomori, and T. Shibano
Advanced Technology R&D Center, Mitsubishi Electric Corporation
8-1-1 Tsukaguchi-Honmachi, Amagasaki, Hyogo 661-8661, Japan

ABSTRACT

Surface reaction mechanisms in the chemical vapor deposition of (Ba,Sr)TiO_3 [BST] films were studied by investigating the effects of O_2 gas and source supply ratios on the characteristics of atomic incorporation rates. The atomic incorporation rates of Ba, Sr, and Ti increased with increasing incident flux of each source material, and then the values of the atomic incorporation rates became saturated. The saturated values increased monotonously with increasing O_2 gas flow rate, in a range where atomic incorporation reactions might be controlled by the kinetics on the film surface (kinetically limited). Accordingly, O_2 gas may effect the behavior of film precursors on BST film growth surfaces. From this, we assumed a CVD model, where the precursors are transported onto the film surface and adsorbed on adsorptive sites, and where the O_2 gas has an effect on the formation of the adsorptive sites. With this model, atomic incorporation rates and overall sticking coefficients for the CVD of BST films were numerically simulated, and were in good agreement with experimental results for several O_2 flow rates and source supply ratios.

INTRODUCTION

Three-dimensional (3D) stacked cells with high-dielectric-constant (Ba,Sr)TiO_3 [BST] film have been proposed for Gbit-scale memories and beyond. Capacitors with such stacked cells require the BST film prepared by a chemical vapor deposition (CVD) method to have conformal step coverage. For this purpose, various apparatuses and processes for preparing BST thin films by liquid-source CVD have been developed to fabricate stacked capacitors in Gbit-scale integration [1-2]. The source materials have usually been bis (dipivaloylmethanato) barium [$Ba(DPM)_2$], bis (dipivaloylmethanato) strontium [$Sr(DPM)_2$], and titanium bis (isopropoxyl) bis (dipivaloylmethanato) [$Ti(i\text{-}PrO)_2(DPM)_2$] dissolved into organic solvent tetrahydrofuran (THF:C_4H_8O). There is a report of conformal trench coverage values of >70% with a trench having an aspect ratio of 3.3 for CVD-BST films [3].

In order to improve the step coverage, it is important to understand the chemistry of precursors on the film surfaces. Accordingly, we measured the atomic densities contained in CVD-BST films using an X-ray fluorescence (XRF) method, and investigated characteristics of the atomic incorporation rates of Ba, Sr, and Ti at several source gas supply ratios at different substrate temperatures. Moreover, we discussed a CVD model for BST film under the assumption of the Langmuir isotherm adsorbing mechanism. In the model, adsorptive sites were assumed to be formed on the BST growth film surface. This assumption made it possible for film precursors to be adsorbed on the sites with their own sticking coefficients. Here, the sticking coefficients of the Ba and Sr precursors were considered to be affected by the species of precursors adsorbed thereon. Numerical simulations were performed on the assumed model, and calculated atomic incorporation rates showed a good agreement with the experimental results [4].

To further understand the surface reaction mechanisms in the CVD process, we studied the effects of O_2 gas and source supply ratios on the behavior of precursors on the film surface. As reported in our previous paper [5], BST film characteristics including the step coverage are

strongly dependent on the O_2 gas rates and source supply ratios in the CVD atmosphere. Therefore, we investigated the characteristics of atomic incorporation rates for BST films prepared for several O_2 gas flow rates and source supply ratios. Then, we assumed a CVD model, where the effects of O_2 gas were introduced into our previous model. Numerical simulations were performed on the assumed model, and atomic incorporation rates were calculated in the CVD for several O_2 flow rates and source gas supply ratios. Moreover, overall sticking coefficient β_{ov} in the CVD of BST was estimated from the step coverage of the BST film deposited on the trench substrate. The obtained results were discussed by comparing them with calculated results using the atomic incorporation rates.

EXPERIMENT

Figure 1 shows a schematic diagram of the liquid source CVD apparatus used for the experiment. The source materials were $Ba(DPM)_2$, $Sr(DPM)_2$, and $Ti(i\text{-}PrO)_2(DPM)_2$ dissolved in THF. A mixture of these solutions was fed into a vaporizer, and then the vaporized gas and carrier N_2 gas were mixed with oxidizer gas in a mixer. The resulting mixture was then introduced onto a heated substrate through a gas nozzle, and following this, the BST thin film was deposited onto a Si substrate. The film deposition conditions were as follows: an oxidizer gas flow rate of 1.0 slm, a substrate temperature T_s of 480 ℃, a reactor pressure P of 5 Torr, and a carrier N_2 flow rate of 0.2 slm. Here, the oxidizing gas consisted of O_2 gas diluted with N_2 gas, where the ratio of O_2 was in the range of 0.1 - 1.0. The flow rates of the supplied Ba, Sr, and Ti sources and their ratios γ = $[Ba(DPM)_2+Sr(DPM)_2]/[Ti(i\text{-}PrO)_2(DPM)_2]$ are summarized in Table I. The atomic densities of Ba, Sr, and Ti in the BST film were measured using an XRF method to investigate the atomic incorporation rates.

RESULTS AND DISCUSSION

Characteristics of atomic incorporation rates

Figures 2(a), 2(b), and 2(c) show atomic incorporation rates of Ba, Sr, and Ti as a function of the O_2 flow rate for several γ of 0.10-0.85. Here, the value of the O_2 flow rate corresponds to the rate of O_2 in the oxidizer gas (O_2+N_2) flow rate. In Figs. 2(a)-2(c), the atomic incorporation rates of Ba, Sr, and Ti (I_{Ba}, I_{Sr}, I_{Ti}) increase monotonously with increasing O_2 flow rate from 0.1 to 1.0 slm, implying that O_2 gas might activate film deposition reactions. Moreover, the increasing rates of I_{Ba}, I_{Sr}, and I_{Ti} differ with γ. Therefore, we replotted the experimental results of I_{Ba}, I_{Sr}, and I_{Ti} as a function of the incident flux of each source material F_i (i=Ba,Sr,Ti) onto the substrate for O_2 flow rates of 0.1, 0.5, and 1.0 slm, as shown in Figs. 3(a), 3(b), and 3(c), respectively.

In these figures, the symbols represent the experimental results of I_i. The flux F_i was estimated using the gas pressure values, the gas flow rates, and the residence time of the gases in the reactor. In Figs. 3(a) and 3(b), I_{Ba} and I_{Sr} increase monotonously with increasing incident flux in the range of F_{Ba} or F_{Sr} from 0.3×10^{17} to 0.7×10^{17} $cm^{-2}\cdot s^{-1}$ for O_2 flow rates of 0.1, 0.5, and 1.0 slm, where atomic incorporation reactions might be controlled by mass transport [6]. On the other hand, in the range of F_{Ba} or F_{Sr} from 0.7×10^{17} to 1.5×10^{17} $cm^{-2}\cdot s^{-1}$, such reactions might be controlled by the kinetics on the film surface [6], because the I_{Ba} or I_{Sr} values became saturated. The saturated values increase monotonously with increasing O_2 flow rate from 0.1 to 1.0 slm. Therefore, these experimental results suggest that O_2 gas activates the behavior of film precursors on the film surface in the CVD of BST. Similar characteristics were observed in the experimental results of I_{Ti} shown in Fig. 3(c). The experimental results of I_{Ti} were saturated in the range of F_{Ti} from 2.0×10^{17} to 5.0×10^{17} $cm^{-2}\cdot s^{-1}$, and decreased with

decreasing O_2 flow rate from 1.0 to 0.1 slm. Here, the decreasing rate of I_{Ti} tended to increase with increasing γ-values. This suggests that the activating effects of O_2 gas may increase with increasing densities of Ba or Sr precursors on the film surface.

A CVD model for BST films

In the above section, it was found that O_2 gas might strongly effect the surface reactions in the CVD of BST. Therefore, we extended the CVD model by introducing effects of O_2 gas on the behavior of film precursors on the surface. A schematic diagram of the model is shown in Fig. 4. In the extended model, precursors adsorbed on the film surface decompose, and oxygen is adsorbed thereon. Then, the decomposed products with adsorbed oxygen are assumed to behave as adsorptive sites on the film surface. The effects of O_2 gas on Ba or Sr precursors might differ from those on Ti precursors in experimental results. It has been reported that the bonds of Ba-O or Sr-O are most easily broken in the molecules of $Ba(DPM)_2$ or $Sr(DPM)_2$ [7]. Therefore, we assumed that Ba-O or Sr-O bonds come to be broken in adsorbed Ba or Sr precursors, and that the oxygen decomposed from the O_2 gas comes to be adsorbed thereon. Then, adsorptive sites are formed as shown in Fig. 4. On the other hand, it has also reported that the bonds of Ti-O do not decompose easily in the molecules of $Ti(i\text{-}PrO)_2(DPM)_2$ [8]. Then, as shown in Fig. 4, we assumed that adsorptive sites from Ti precursors could be formed without O_2 gas.

From the assumptions of the above CVD model, I_{Ba}, I_{Sr}, and I_{Ti} were formulated. In the range of F_i (i=Ba,Sr,Ti) where incorporation reactions might be controlled by mass transport, atomic incorporation rates are assumed to be mainly determined by the values of F_i. Then, I_i can be expressed as,

$$I_i = \beta_i F_i = (1-\theta_{Ti})\ \beta_{i1} + \theta_{Ti}\beta_{i2}, \quad \text{(i=Ba,Sr)} \qquad (1)$$

$$I_{Ti} = \beta_{Ti} F_{Ti}, \qquad (2)$$

where θ_{Ti} is the coverage of the Ti precursors adsorbed on the film surface. In addition, β_{i1} and β_{i2}, (i=Ba,Sr) are the sticking coefficients on the adsorptive sites consisting of the Ti precursors and those consisting of all other precursors except the Ti precursors, respectively. Values of β_{i1}, β_{i2},, and β_{Ti} are summarized in Table II; they were estimated from a part of the experimental results in Figs. 3(a)-3(c). On the other hand, in the range of F_i controlled by the kinetics on the film surface, the atomic incorporation rates may be limited by the surface density of the adsorptive sites. Therefore, I_i (i=Ba,Sr,Ti) can be expressed as,

$$I_{Ba} = A_{Ba}\,\rho\,\{(1-\theta_{Ti})\,\alpha(O_2) + \theta_{Ti}\,\beta_{Ba2}/\beta_{Ba1}\}, \qquad (3)$$

$$I_{Sr} = A_{Sr}\,\rho\,\{(1-\theta_{Ti})\,\alpha(O_2) + \theta_{Ti}\,\beta_{Sr2}/\beta_{Sr1}\}, \qquad (4)$$

$$I_{Ti} = A_{Ti}\,\rho\,\{(1-\theta_{Ti})\,\alpha(O_2) + \theta_{Ti}\}, \qquad (5)$$

where ρ denotes the surface density of the adsorptive sites. The factor $\alpha(O_2)$ in Eqs. (3)-(5) indicates the coverage of the oxygen atoms on the film surface. Here, $\alpha(O_2)$ is a function of the O_2 gas flow rate. Values of the sticking coefficients are shown in Table II; I_{Ba}, I_{Sr}, and I_{Ti} were numerically simulated using Eqs. (1)-(5). Numerical results of I_{Ba}, I_{Sr}, and I_{Ti} are shown by the solid lines in Figs. 3(a), 3(b), and 3(c), respectively. As shown in these figures, the numerical results of I_{Ba}, I_{Sr}, and I_{Ti} are in good agreement with the experimental results.

Overall sticking coefficients

Figures 5(a), 5(b), and 5(c) show cross-sectional SEM micrographs of the BST film step coverage at O_2 flow rates of 0.1, 0.5, and 1.0 slm, respectively. The source supply ratio γ is 0.5. The step consisted of a 1 μm-thick SiO_2 layer formed on the Si substrate, and the ratio of the trench depth to the width D/W =2.5. The step coverage of d_{min}/d_{max} in Figs. 5(a), 5(b), and 5(c) are about 80, 60, and 40%, respectively, where d_{min} and d_{max} are the film thicknesses on

sidewalls near the bottom and on the top surface. This implies that the sidewall coverage tends to be reduced as the O_2 flow rate increases. Moreover, values of d_{min}/d_{max} obtained for the trenches of D/W =0.5-2.5 are shown in Fig. 6. In this figure, the solid lines represent calculated coverage obtained using a trench-deposition-method [5]. By comparing the calculated values with the experimental results for d_{min}/d_{max}, we estimated overall sticking coefficient β_{ov} values as 0.0001, 0.002, and 0.005, respectively. This suggests that β_{ov} increases drastically with increasing O_2 flow rate. Figure 7 shows β_{ov} values at several γ-values. The figure also shows β_{ov} values obtained from the calculated values of I_{Ba}, I_{Sr}, and I_{Ti} in Figs. 3(a)-3(c) by the solid lines. As shown in this figure, both of the experimental and simulated β_{ov} values increase with increasing γ, and the increasing rate of β_{ov} increases with increasing O_2 flow rate from 0.1 to 1.0 slm. Accordingly, these results imply that the model shown in Fig. 4 which includes effects of O_2 appropriately explains the surface reaction mechanisms in the CVD of BST.

CONCLUSIONS

Surface reaction mechanisms in the CVD of BST films were studied by investigating the effects of O_2 gas and source supply ratios on the characteristics of atomic incorporation rates. The atomic incorporation rates of Ba, Sr, and Ti increased with increasing incident flux of each source material, and then their values became saturated. The saturated values increased monotonously with increasing O_2 gas flow rate, in a range where atomic incorporation reactions might be controlled by the kinetics on the film surface. Accordingly, these experimental results suggest that O_2 gas may effect the behavior of film precursors on the film growth surface in the CVD of BST. From this, we assumed a CVD model, where the film precursors adsorbed on the film surface decompose, and where the oxygen is adsorbed thereon. We further assumed that the decomposed products with adsorbed oxygen come to behave as the adsorptive sites on the film surfaces, and that these sites come to adsorb the successive film precursors. Then, the atomic incorporation rates and overall sticking coefficients for the CVD of BST films were numerically simulated on the assumed model, and were in good agreement with experimental results at several O_2 flow rates and source supply ratios.

REFERENCES

1. A.Yuuki, M.Yamamuka, T.Makita, T.Horikawa, T.Shibano, N.Hirano, H.Maeda, K.Ono, and H.Abe: *Dig. Int. Electron Device Meet.* (IEEE, New York, 1995) p. 115.
2. T.Horikawa, M.Tarutani, T.Kawahara, M.Yamamuka, T.Satoh, S.Matsuno, F.Uchikawa, and K.Ono: *Material Research Society Symposium Proceedings, 1998* (Material Research Society, Pittsburgh, Pennsylvania, 1998) Vol. 355, p. 114.
3. T.Kawahara, M.Yamamuka, A.Yuuki, and K.Ono: Jpn. J. Appl. Phys. 34 (1995) 5077.
4. M.Yamamuka, T.Kawahara, M.Tarutani, T.Horikawa, T.Oomori, and K.Ono: J. Appl. Phys. 86 (1999) 1082.
5. M.Yamamuka, T.Kawahara, T.Horikawa, and K.Ono: Jpn. J. Appl. Phys. 36 (1996) 2559
6. K.Eguchi and M.Kiyotoshi: Integrated Ferroelectrics. 14 (1997) 39.
7. Hyun-Kyu Ryu *et al.*: J. Electrochem. Soc. 147 (2000) 1132.
8. Hyun-Kyu Ryu *et al.*: J. Electrochem. Soc. 146 (1999) 1121.

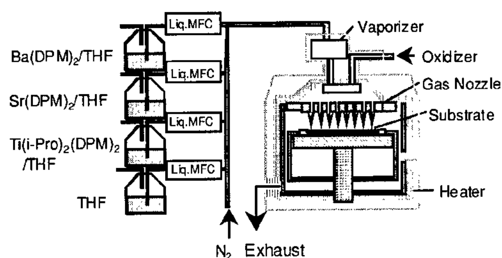

Fig. 1 Schematic diagram of a CVD-BST apparatus.

Table I. Supply source flow rate

Liquid source flow rate	
$Ba(DPM)_2$	2.7 - 8.0 μ mol/min
$Sr(DPM)_2$	2.7 - 8.0 μ mol/min
$Ti(i\text{-}Pro)_2(DPM)_2$	19.0 - 31.0 μ mol/min
Source concentrations	
$\gamma = \{Ba(DPM)_2 + Sr(DPM)_2\} / \{Ti(i\text{-}Pro)_2(DPM)_2\}$	0.10 - 0.85

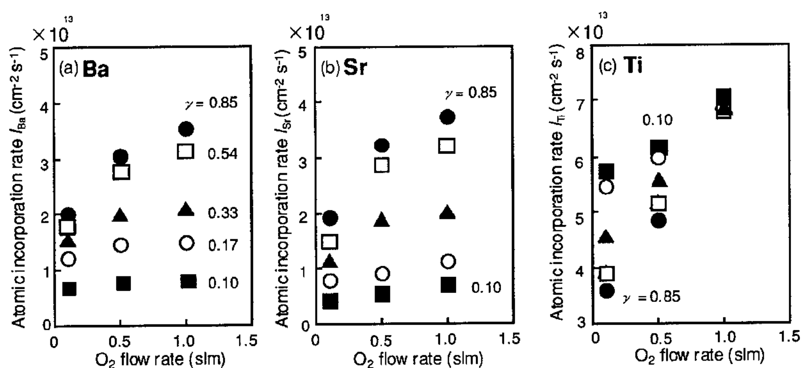

Fig. 2 Atomic incorporation rates of (a) Ba, (b) Sr, and (c) Ti as a function of supply O_2 flow rate for different source concentrations γ from 0.10 to 0.85. Here, the atomic incorporation rates were obtained using an XRF method.

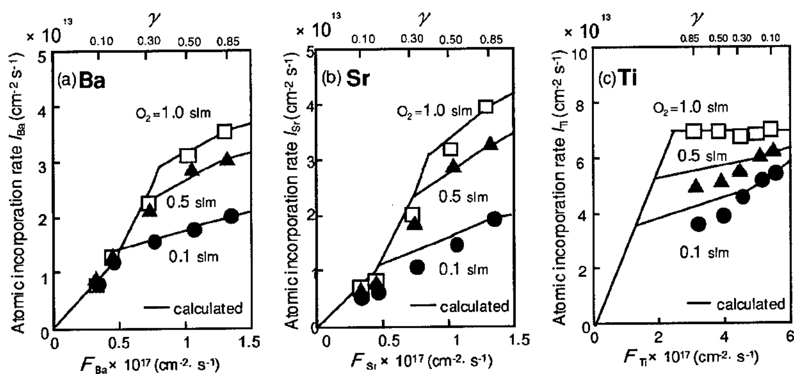

Fig. 3 Atomic incorporation rates of (a) Ba, (b) Sr, and (c) Ti as a function of each source material flux incident onto a substratet for different supply O_2 flow rates. Here, the symbols represent the experiments and solid lines indicate calculated results.

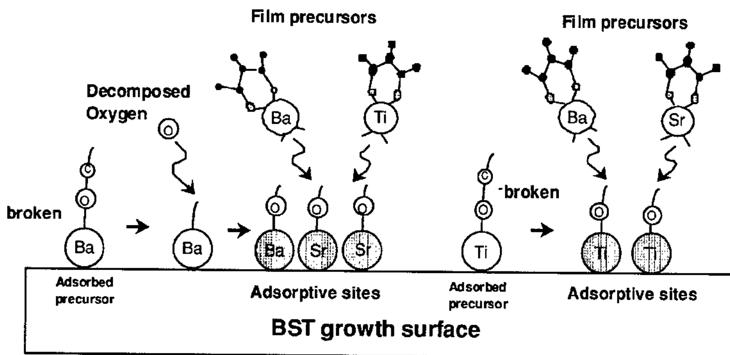

Fig. 4 Schematic diagram of a CVD model for BST film introducing contributions of O_2 gas into the formation of adsorptive sites on the film surface.

Table II Sticking coefficients of film precursors

species i	β_{i1}	β_{i2}
Ba	9.4×10^{-4}	1.3×10^{-4}
Sr	1.0×10^{-3}	8.9×10^{-5}
Ti	1.6×10^{-4}	1.6×10^{-4}

$$\beta_{Ba}=(1-\theta_{Ti})\beta_{Ba1}+\theta_{Ti}\beta_{Ba2}$$
$$\beta_{Sr}=(1-\theta_{Ti})\beta_{Sr1}+\theta_{Ti}\beta_{Sr2}$$
$$\beta_{Ti}=\beta_{Ti1}=\beta_{Ti2}$$

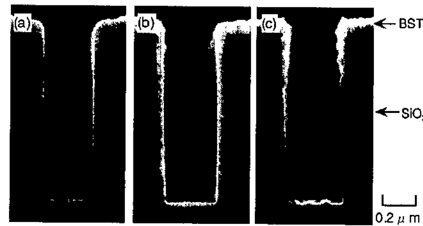

Fig. 5 Cross-sectional SEM of the BST film step coverage for D/W =2.5 obtained in the cases of (a) O_2 0.1slm, (b) O_2 0.5slm, and (c) O_2 1.0slm.

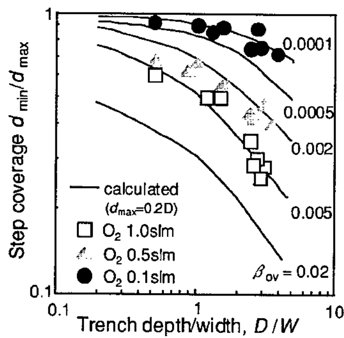

Fig. 6 Plots of d_{min}/d_{max} versus W/D in cases of O_2 gas flow rates of 0.1, 0.5, and 1.0 slm. Here, the solid lines represent calculated results obtained by Monte Carlo simulation for several sticking coefficients.

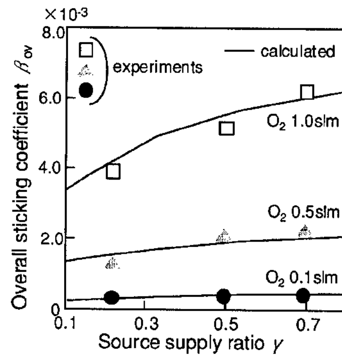

Fig. 7 Overall sticking coefficients for BST film deposition, numerically and experimentally obtained as a function of the source supply ratio; the experiments were performed by a trench-deposition-method.

Mat. Res. Soc. Symp. Proc. Vol. 655 © 2001 Materials Research Society

Growth of $(Ba,Sr)TiO_3$ Thin Films in a Multi-wafer MOCVD Reactor

P. Ehrhart[1], F. Fitsilis[1], S. Regnery [1,2], C. L. Jia[1], H.Z. Jin[1], R. Waser[1], F. Schienle[2], M. Schumacher[2], and H. Juergensen[2]
[1)]IFF-Forschungszentrum Jülich, D-52425 Jülich, Germany
[2)]Aixtron AG, D-52072 Aachen, Kackertstr.15-17, Germany

ABSTRACT

We report on the performance of a planetary multi-wafer MOCVD reactor which handles 5 six inch wafers simultaneously. The reactor is combined with a liquid delivery system which mixes the liquid precursors from three different sources: 0.35 molar solutions of $Ba(thd)_2$ and $Sr(thd)_2$ and a 0.4 molar solution of $Ti(O\text{-}i\text{-}Pr)_2(thd)_2$. The microstructure and the film stress were investigated by X-ray diffraction and the composition of the films was determined by X-ray fluorescence analysis. As a direct consequence of the reactor design we obtain a high uniformity of the films over 6 inch wafers, as well as high efficiencies for the precursor incorporation. Film growth is discussed within a wide parameter field and the finally achieved electrical properties, e.g., permittivity, loss tangent, leakage current, are discussed in relation to the microstructural properties.

INTRODUCTION

$(Ba_xSr_{1-x})TiO_3$, (BST), is one of the prime candidates as a high-k-dielectric in integrated high-density capacitors for future multi-GBit DRAM memory cells[1] as well as for dielectric tuneable devices and remarkable progress has been achieved in the metal-organic chemical vapor deposition (MOCVD) of thin BST films[2-5]. Most of the experimental reactors used for the development of mass production tools presently have a single wafer showerhead design[3-5] and we report as a comparison on the performance of a planetary multi-wafer reactor offering extremely high throughput due to possible batch mode processing which results in low cost of ownership. We report on the properties of BST films which were deposited on $Pt/TiO_2/SiO_2/Si$ wafers. The composition and microstructure of the films were routinely investigated by X-ray diffraction (XRD) and X-ray fluorescence (XRF) analysis using different calibration standards prepared by chemical solution deposition. Additional substrates without Ti adhesion layer were used for the XRF analysis since the penetration depth of the X-ray beam is too large to distinguish the Ti of the BST from the Ti of the adhesion layer. The electrical properties were investigated after sputter-deposition and structuring of Pt top electrodes.

BST properties depend critically on the stoichiometry, the microstructure, as well as on the films thickness. For the present discussion we select films of a composition around $(Ba_{0.7}Sr_{0.3})TiO_3$. Through process variations we grew a broad field of BST thin films with different stoichiometry, i.e. different ratios of the Group-II/Ti content. We first discuss the thickness dependence of the film properties and concentrate then on films with a thickness of 30nm, which is close to envisaged application for DRAMS. We selected films which are slightly Ti rich to discuss the influence of the growth temperature (565°C to 655°C) on the microstructure and the electrical properties; the influence of the sample stoichiometry is discussed additionally for films deposited at 625 and 565°C.

FILM DEPOSITION

An AIXTRON 2600G3 Planetary Reactor® was used, which can handle five 6-inch wafers simultaneously. The gas inlet is in the center of the reactor providing a pure horizontal gas flow, which makes this reactor a radial flow system. A liquid precursor delivery system, ATMI-300B[6], mixes the liquid precursors of three different sources: 0.35 molar solutions of $Ba(thd)_2$ and $Sr(thd)_2$ and a 0.4 molar solution of $Ti(O\text{-}iPr)_2(thd)_2$. The liquid mixture is delivered by a micro-pump to the vaporizer on top of the reactor. The process conditions are summarized in Table 1. All temperatures referred in this paper are susceptor temperatures. The actual wafer surface temperatures are measured to be at least 25°C lower.

The efficiency of the precursor use, defined as the ratio of the quantity deposited on all 5 wafers and the amount of the individual precursor elements contained in the consumed liquid, is an important parameter for the costs of ownership. The observed values of 45% for Ti and 35-40% for Ba and Sr are extraordinarily high as compared to the values reported for conventional showerhead reactors[3]. As these efficiencies were similar for the range of temperatures investigated we may conclude that all depositions were achieved within the mass-transport limited reaction range. Finally, due to the gas-foil rotation principle we obtained a good homogeneity of stoichiometry and film thickness over 6" wafers[7]. These results are supported by recent ellipsometric measurements which yield as an example a thickness of 32,4 ± 0,4 nm and a stoichiometry variation of 53,8 ± 0,3 at% Ti . Similarly small differences were observed between the five simultaneously processed wafers (mean thickness 32,3 ± 0,2 nm).

Table 1: Typical deposition conditions

Susceptor temperature	565 – 655°C
Reactor pressure	2 mbar
O_2 flow rate	50-500 sccm
N_2O flow rate	50-500 sccm
Liquid source feeding rate	0.08ml/s
Vaporization temperature	225 – 245°C

sccm: standard cm^3 per minute

MICROSTRUCTURAL PROPERTIES

Fig.1a shows the XRD patterns of slightly Ti-rich films deposited at different temperatures on Pt-substrates with a strong (111)-texture. We observe a very strong (100)-texture for depositions above 595°C and a transition to more polycrystalline and finally poorly crystalline growth at lower temperatures. With increasing Ti-content we observe an additional trend of a decrease of the (100)-texture as shown in Fig. 1b for a deposition temperature of 595°C. The (100)-oriented films observed at high deposition temperatures show a width of the rocking curves of only 2-3 degrees; as this width is similar to that of the underlying Pt[7], we observe locally a nearly epitaxial growth. This perfectly columnar growth is further documented by the details of the line profiles as shown in Fig. 2: thickness fringes are clearly visible in high resolution scans. The wavelength of the oscillations, $\Delta\theta$, yields immediately the film thickness, $d = \lambda / (2 \cdot \Delta\theta \cdot \cos\theta)$; λ is the wavelength of the Cu-Kα radiation used.

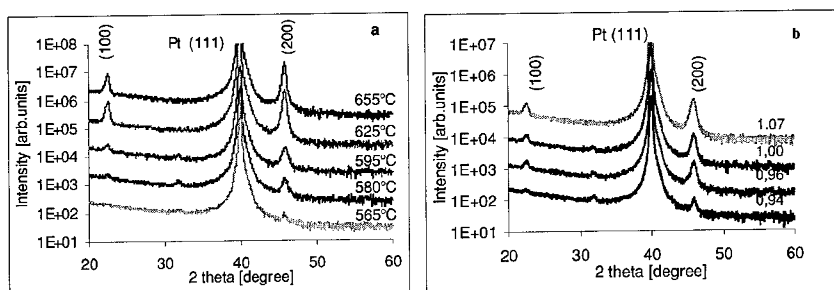

Fig.1: a) XRD-diagrams for films deposited at different temperatures. All films are slightly Ti rich, (GrII/Ti = 0.95-0.97). b) films of different stoichiometry deposited at 595°C.

The thickness obtained for the thin samples shown in Fig. 2 is in very good agreement with the XRF estimation obtained using the ideal density of BST of 5.758 g/cm³. These results indicate perfectly mono-crystalline (100)-oriented grains and sharp interfaces. This conclusion is supported by HRTEM, Fig. 3, which directly demonstrates this (100)-orientation of the BST on (111)-Pt and the clean and sharp interfaces. Lowering the deposition temperature to 625°C yields a damping of the oscillations which indicates less perfect alignment and at 595°C the oscillations are no longer visible. For depositions at $T \geq 625°C$, the dominant (100)-growth is stable over a rather wide range of stoichiometries (Gr-II/Ti = 0.92 to 1.03), and only if the films are far off stoichiometric there is a polycrystalline growth.

The absolute value of the lattice parameter, as measured normal to the film plane, is, however, smaller than the expected bulk value. This difference results from a tensile stress of the film, which is thermally induced during cooling down of the film due to the different thermal expansion coefficients of BST and of the Si-substrate. Detailed strain measurements[8] yield a tetragonal distortion of the film which can be quantified by the distortion $\varepsilon = \Delta d/d$ with values between -0.6 and -1.1% or by the c/a-ratio = $(d+\Delta d)/d$ with values between 0.994 and 0.989. From this distortion, the film stress, σ, can be estimated and stresses between 500 and 900MPa were observed. Within these variations the expected dependence from the deposition temperature cannot be verified, as there are additional variations due to different film and/or substrate perfection, which cannot be separated. The c/a-ratio is always smaller than 1, thus opposite to the ferroelectric phase, which is characterized by a larger c-axis. The substrate induced opposite lattice distortion yields therefore a plausible argument for the suppression of the phase transition in these films.

There is indication for a steady increase of the (100)-texture with increasing Group-II content for films grown at lower temperatures as demonstrated at the example of Fig. 1b. In addition, small changes of the peak-profile as well as of the average lattice parameter, are observed in spite of larger errors, due to the weaker and broader peaks. Fig. 4 summarizes the lattice parameters for films which had a dominant (200)-reflection; there is no change observed for the Ti-rich samples and a steady increase with a rising GrII-content as regards the Gr-II rich samples. Similar observations had been reported for $SrTiO_3$ films[9] and attributed to the incorporation of the excess Gr-II elements in the form of Ruddlesden Popper phases. In addition, we observe a change of the

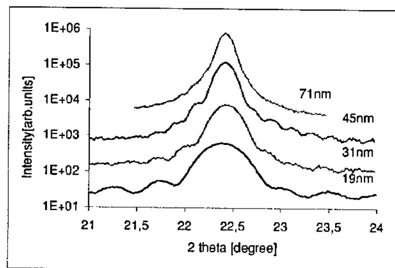

Fig. 2: Thickness oscillations close to the (100)-reflection of samples grown at 655°C.

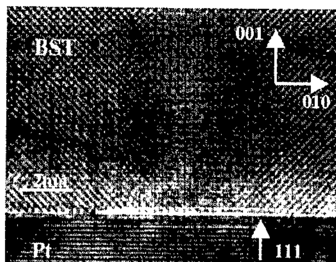

Fig. 3: HRTEM micrograph showing the Pt-BST interface for a sample deposited at 655°C.

peak profile along with the variation of the average lattice parameter, there is a broadening and a tail to the low angle side which indicates an inhomogeneous incorporation of the excess group-II elements. Remarkable is the fact, that these structures seem not very stable, as there is a rearrangement to a more homogeneous structure during annealing in oxygen at a temperature of 550°C which is necessary after deposition of the Pt-top-electrodes.

For the Ti-rich samples there is no indication for a change of the lattice parameter and also no change of the line profile. Such a behavior is compatible with the formation of stable precipitates of amorphous TiOx at the grain boundaries as it has been observed at very high Ti content[10], and there is no indication for the incorporation of larger amounts of surplus Ti in the interior of the grains.

ELECTRICAL PROPERTIES

For the electrical characterisation Pt top electrodes were deposited by magnetron sputtering. Electrode sizes of a diameter between 0.1 to 1.13 mm were obtained by a lift-off process. An additional post-annealing was performed ex-situ. The standard characterisation included the dielectric permittivity, ε_r, measured at a frequency of 1 kHz and the dissipation loss, $\tan\delta$. More

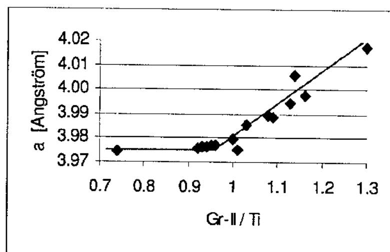

Fig. 4: Dependence of the average lattice parameter, a, on the stoichiometry.

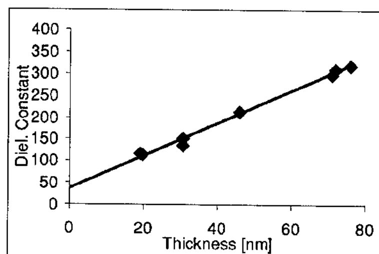

Fig. 5: Thickness dependence of the dielectric constant.

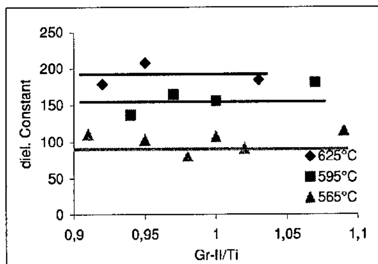

Fig. 6: Permittivity, ε_r, as a function of stoichiometry and deposition temperature.

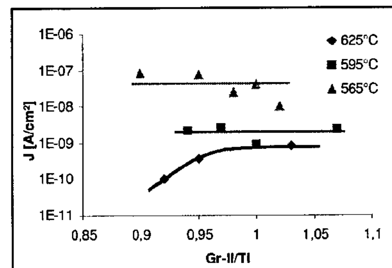

Fig.7: Leakage current, J, as a function of stoichiometry and deposition temperature.

detailed investigations include the leakage current, the frequency dependence of the relative permittivity and the relaxation characteristics as well as the response to DRAM pulses. All measurements were performed at room temperature.

Fig. 5 shows the permittivity for the crystallographic perfect samples shown in Fig. 2. The scatter of the data points may be caused by the somewhat different stoichiometry of the samples (Gr-II/Ti ≈0.93 corresponding to 51.8%Ti). We observe the expected increase with thickness, which has been discussed in terms of dead/or interface layer[1]. Applying this model we obtain an interface capacitance of 120 fF/µm² and a bulk permittivity of $\varepsilon = 670$. Compared to published results[11] the bulk value seems in good agreement to samples of similar stoichiometry, however the interface capacitance is lower by a factor of two. The reason for this difference needs further investigation.

Fig. 6 and 7 summarize the dependence of the dielectric permittivity, ε_r, and of the leakage current, J, of films with a thickness of ≈30nm on the deposition temperature and on the film stoichiometry. In spite of the change in the lattice parameter (Fig. 4), which indicates a different incorporation of the surplus elements and the change in crystallinity and/or texture, Fig. 1b, no obvious change close to the ideal stoichiometric ratio of Gr-II/Ti = 1 is observed. More obvious is, however, a dependence on the deposition temperature, i.e., a decrease of ε_r with decreasing temperature. In particular, we obtain a typical value of $\varepsilon_r \approx 208$ for Ti-rich films (GrII/Ti ≈ 0.97) grown at 625°C, which corresponds to a specific capacitance of C/A = 59.1 fF/µm². For a film at 565°C this value is reduced to $\varepsilon_r \approx 110$ or 30.2 fF/µm². Similar to earlier results[7] we observe an almost constant dispersion of the permittivity over the whole frequency range from 1 Hz to 1 MHz. The leakage current at 1 V bias (Fig.7) shows similar dependencies on stoichiometry and crystallinity as permittivity, i.e. an improvement with deposition temperature and only minor dependence on stoichiometry. The dissipation factor, tanδ, has values between 0,002-0,004 and shows no systematic variation within the investigated range of deposition parameters. DRAM pulse measurements[8] on all samples showed less than 5% loss of charge in the first second after pulse load up to a field of 300 kV/cm. No strong dependence on stoichiometry was observed again.

CONCLUSION

$(Ba_{0.7}Sr_{0.3})TiO_3$ films of 30nm thickness were grown at different deposition temperatures and with different stoichiometry within a planetary reactor and structure property relations could be investigated within a broad range of parameters.
For deposition temperatures over 600°C we obtain a perfect (100)-fiber structure on Pt-(111), which is revealed by thickness fringes in the XRD scans and very clean and sharp interfaces in HRTEM. The incorporation of the excess Gr-II elements yields an increase of the lattice parameter within rather unstable structures which rearrange during post-annealing at 550°C. Ti excess has no influence on the XRD pattern.
Electrical data show an improvement with increasing deposition temperature and only minor changes with stoichiometry although there are major changes in the microstructure. The electrical data for the strongly textured films seem well suited for DRAM application, e.g., $C/A \approx 60fF/\mu m^2$ and $J=3{,}7\cdot10^{-10}$ A/cm² at 1 V. At the lowest deposition temperature of 565°C polycrystalline growth is observed. Nevertheless, electrical data, such as $C/A \approx 30fF/\mu m^2$, are still in a range suitable for DRAM application.

Acknowledgements
The authors greatly acknowledge the help of W. Krumpen in the course of the XRF analysis.

References

1. A.I. Kingon, S.K. Streiffer, C. Basceri, S.R. Summerfelt, *MRS Bulletin* **21**, 7, 46 (1996)
2. B.W. Wessels, *Annu. Rev. Mater. Sci.* **25**, 525 (1995) and references therein.
3. C.S. Kang, H.-J. Cho, C.S. Hwang, B.T. Lee, K.-H. Lee, H Horii, W. D. Kim, S.I. Lee, and M.Y. Lee, *Jpn J. Appl. Phys.* **36**, 6946 (1997).
4. H. Shen, D.E. Kotecki, R.J. Murphy, M. Zaitz, R.B. Laibowitz, T.M Shaw, K.L. Saenger, J. Banecki, G. Beitel, V. Klueppel, H. Cerva, , *MRS Symp. Proceed.* **493**, 33 (1998).
5. T. Horikawa, M. Tarutani, T. Kawahara, M. Yamamuka, N. Hirano, T. Sato, S. Matsuno, T. Shibano, F. Uchikawa, K. Ono, T. Oomori, *MRS Symp. Proceed.* **541**, 3 (1999).
6. P.C. VanBuskirk, S. Bilodeau, J. F. Roeder, P. S. Kirlin, *Jpn. J. Appl. Phys.* **35**, 2520 (1996).
7. P. Ehrhart, F. Fitsilis, S. Regnery, R. Waser, F. Schienle, M. Schumacher, M. Dauelsberg, P. Strzyzewski, and H. Juergensen, accepted for publication in *Integrated Ferroelectrics*.
8. F. Fitsilis, S. Regnery, P. Ehrhart, R. Waser, F. Schienle, M. Schumacher, M. Dauelsberg, P. Strzyzewski, and H. Juergensen, accepted for publication in *J. European Cer. Soc.*
9. M. Yoshida, H. Yabuta, S. Sone, H. Yamaguchi, K. Arita, and Y. Kato, *Electrochemical Society Proceedings* **97-25,** 1109 (1977).
10. S. Stemmer, S.K. Streiffer, N.D. Browning, and A.I. Kingon, *Appl. Phys. Letters* **74,** 2432 (1999).
11. S.K. Streiffer, C. Basceri, C.B. Parker, S.E. Lash, and A.I. Kingon, *J. Appl. Phys.* **86,** 4565 (1999).

Fundamental Properties of Ferroelectric Thin Films II

Mat. Res. Soc. Symp. Proc. Vol. 655 © 2001 Materials Research Society

Piezoresponse Measurements for $Pb(Zr,Ti)O_3$ Island Structure Using Scanning Probe Microscopy

H.Fujisawa, K.Morimoto, M.Shimizu, H.Niu, K.Honda[1] and S.Ohtani[1]
Department of Electronics, Faculty of Engineering, Himeji Institute of Technology, Shosha 2167, Himeji, Hyogo 671-2201, JAPAN
[1]Fujitsu Laboratory Ltd, 10-1 Wakamiya Morinosato, Atsugi, Kanagawa 243-0197, JAPAN

ABSTRACT

Piezoresponse measurements using scanning probe microscopy (SPM) were performed for island structures at the initial growth stage of $Pb(Zr,Ti)O_3$ (PZT) (Zr/Ti=0/100, 24/76 and 74/26) thin films prepared by metalorganic chemical vapor deposition(MOCVD). Deposition times were varied from 5s to 7min to control the size of PZT islands. When deposition times were shorter than 3min, (111)-oriented triangular-shaped PZT islands were observed before forming a continuous film. The width and height of PZT islands deposited at 3min were 160 and 70nm for Zr/Ti = 0/100, 100 and 30nm for Zr/Ti = 24/76, and 80 and 20nm for Zr/Ti = 74/26, respectively. The size of islands decreased with increasing the Zr composition. Hysteresis loops due to polarization switching were observed in the phase difference and displacement of piezoresponse measured using scanning probe microscopy (SPM). This result proves that nano-size PZT islands have weak ferroelectricity. The minimum width and height of PZT islands which showed ferroelectricity were 70 and 30nm for Zr/Ti=24/76.

INTRODUCTION

Recently, many efforts have been made toward the realization of megabit scaled non-volatile ferroelectric random access memories (NV-FeRAMs) using 1 transistor and 1 capacitor (1T1C) cell structure. To go beyond megabit NV-FeRAMs, will require the reduction in the capacitor size and thickness of ferroelectric thin films below $1\mu m^2$ and 100nm, respectively. In such small ferroelectric capacitors, size effects will have large influences on electrical properties of ferroelectric thin films.

There have been a variety of reports on the size effects of thin films. For example, the calculated value of remanent polarization was reported for $SrBi_2Ta_2O_9$ films with decreasing grain size and film thickness [1]. We have also reported on the thickness dependence of electrical properties of epitaxial $Pb(Zr,Ti)O_3$ (PZT) thin films grown on $SrRuO_3/SrTiO_3(100)$ [2-4]. In these studies, it was found that PZT thin films with thickness of 40nm showed D-E hysteresis loops with high remanent polarization ($Pr\sim40\mu C/cm^2$) [2-4]. However, the area ($>\phi50\mu m$) of capacitors was much larger than that expected in high-integrated NV-FeRAMs. Therefore, it is still unknown whether capacitors show good ferroelectricity or not when the capacitor area is

reduced below 1μm^2.

At the initial stage of metalorganic chemical vapor deposition (MOCVD) growth of $PbTiO_3$ (PTO) and PZT thin films, island structures are observed before a continuous film is formed [5, 6]. These island structures are isolated from each other and can be considered as sub-micron ferroelectric capacitors except for the absence of top electrodes. Therefore, using these island structures, ferroelectric properties of sub-micron capacitors can be easily investigated without complicated manufacturing processes. Our recent interests have been focused on whether the island structure showed ferroelectricity or not [7, 8]. From transmission electron microscopy (TEM) observations, it was found that PTO islands had twin structure (90° domain) derived from tetragonal structure and that they could have ferroelectricity from the viewpoint of crystalline structure [7]. In addition, it was also shown that PZT island structures had ferroelectricity by piezoresponse measurements using scanning probe microscopy (SPM) [8].

In this study, we reported on details of piezoresponse measurements using SPM for PZT island structures with different compositions at the initial stage of MOCVD growth.

EXPERIMENTAL PROCEDURE

$Pb(Zr,Ti)O_3$ (PZT) (Zr/Ti=0/100, 24/76 and 74/26) island structures were grown on $Pt(111)/SiO_2/Si$ substrates at 580°C by MOCVD. Triethyl n-pentoxy lead ($(C_2H_5)_3PbOCH_2C(CH_3)_3$), tetra-tertiary-butoxy zirconium ($Zr(O\text{-}t\text{-}C_4H_9)_4$) and tetra-iso-propoxy titanium ($Ti(O\text{-}i\text{-}C_3H_7)_4$) were used as source precursors and O_2 was used as an oxidizing gas. The growth conditions have been described in detail elsewhere [9]. The growth rates calculated from the thicknesses of films deposited for 20 min were 6.7, 6.0 and 8.0 nm/min for Zr/Ti=0/100, 24/76 and 74/26, respectively. The orientation and composition were examined by X-ray diffraction (XRD) and energy-dispersive X-ray (EDX) analysis for films deposited for 20 or 40min, respectively. PZT island structures were prepared at deposition times from 5s to 7min. The surface morphology and cross-sectional structure of PZT island structures were characterized by scanning electron microscopy (SEM), atomic force microscopy (AFM) and TEM. Piezoresponse measurements were carried out using an SPM system shown in Fig.1 [8, 10-12]. Conductive cantilevers used in this study were made of Au-coated Si. The elastic constant and resonance frequency of the cantilever were 14-16N/m and 133-137kHz, respectively. The frequency and amplitude of the applied ac signal were 40kHz and 1.5-2.0 V_{pp} and the dc bias voltage was swept from -5 to 5V at 100mHz.

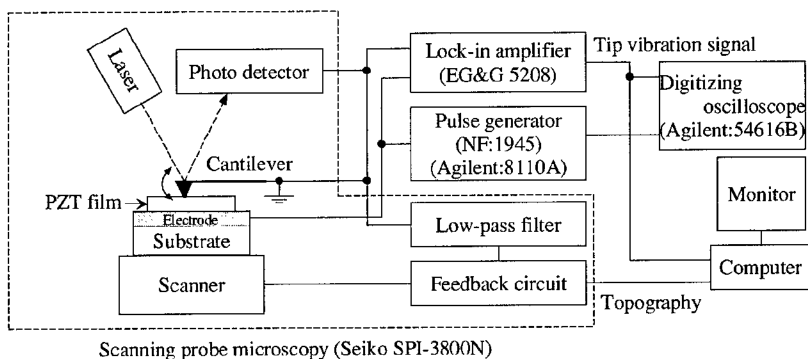

Figure 1 *A schematic diagram of our SPM system for piezoresponse measurements.*

RESULTS AND DISCUSSION

Figures 2-4 show AFM images of PZT island structures with Zr/Ti ratios of 0/100, 24/76 and 74/26, respectively. At the initial stage of MOCVD growth of PZT films, triangular-shaped PZT islands were observed independently of Zr/Ti ratios, as shown in Figs.2-4. The triangular shape directly reflected that PZT islands had (111)-orientated perovskite structure [5-8]. For a Zr/Ti ratio of 0/100, the length of the base of triangular islands increased from 50 to 160nm as the deposition time increased from 30s to 3min while the height increased from 35 to 70nm. At a deposition time of 7min, small islands coalesced into large islands. For Zr/Ti ratios of 24/76 and 74/26, coalescence of small islands with subsequent formation of continuous films were also observed as the deposition time increased. The width and height of islands deposited for 3min were 100 and 30nm for Zr/Ti = 24/76, and 80 and 20nm for Zr/Ti = 74/26, respectively. The width and height of islands at the same deposition time decreased as the Zr composition increased. This result corresponds to the fact that higher growth temperature is needed to crystallize Zr-rich PZT than for Ti-rich PZT. TEM observations revealed that these PZT islands had tetragonal or rhombohedral structures [7, 8].

To clarify whether PZT islands have ferroelectricity or not, piezoresponse measurements using SPM were taken for PZT island structures. In the piezoresponse measurements, the direction of spontaneous polarization can be determined by detecting the phase difference between the SPM tip vibration signal and applied ac voltage, when a small ac voltage is applied between a conductive cantilever and bottom electrode [8, 10-12]. The tip displacement corresponds to that of PZT surface caused by the piezoelectric effects. In addition, polarization reversal is directly evaluated by applying a dc bias voltage simultaneously.

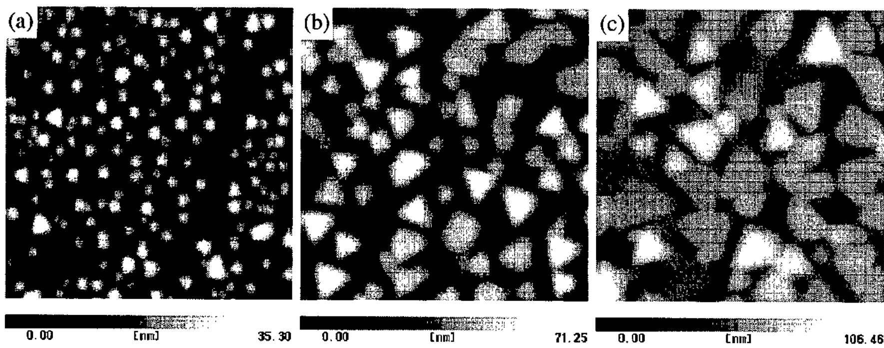

Figure 2 *AFM images of PZT (Zr/Ti=0/100) island structures deposited for (a) 30s, (b) 3min and (c) 7min. Scan area is 1x1μm.*

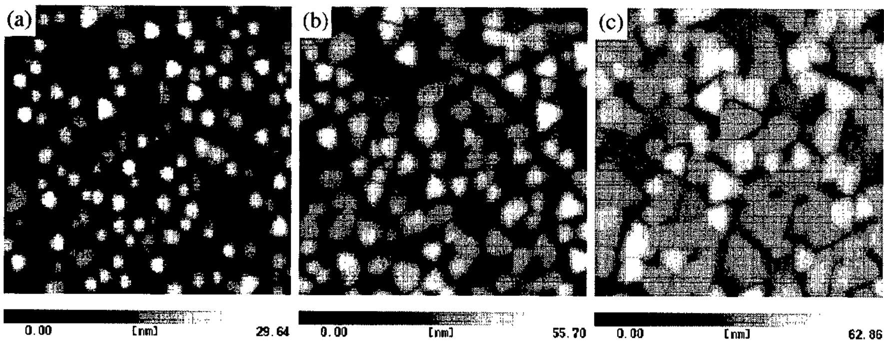

Figure 3 *AFM images of PZT (Zr/Ti=24/76) island structures deposited for (a) 1min, (b) 3min and (c) 7min. Scan area is 1x1μm.*

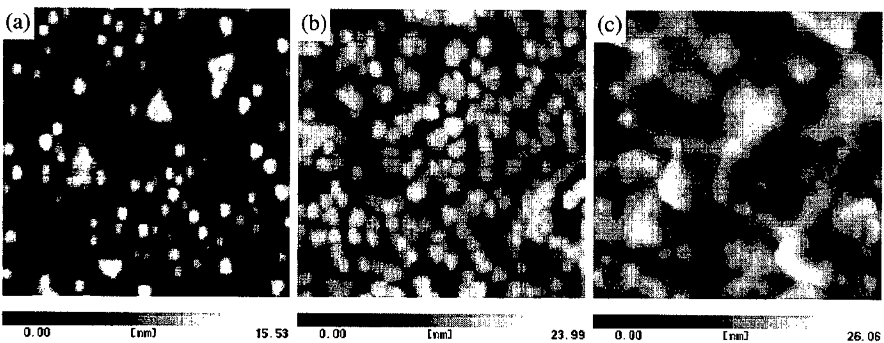

Figure 4 *AFM images of PZT (Zr/Ti=74/26) island structures deposited for (a) 1min, (b) 3min and (c) 7min. Scan area is 1x1μm.*

Fig.5 shows typical results of piezoresponse measurements as a function of dc bias voltage for PZT islands with various Zr/Ti ratios and deposition times. The measurements were carried out with the SPM tip fixed on the center of PZT islands. The phase difference of 0 and 180° correspond to the polarization upward and downward, respectively. The amplitude of piezoelectric vibration was calculated as a displacement per 1V, which was equivalent to d_{33} value. Both phase difference and amplitude showed hysteresis curves as the dc bias voltage changed from -5 to 5 V. These piezoresponse results directly indicate that PZT islands have ferroelectricity. In our experiments, the minimum width and height of the islands which showed ferroelectricity were 50 and 20nm, 70 and 30nm, and 70 and 8nm for Zr/Ti ratios of 0/100, 24/76 and 74/26, respectively. However, ferroelectricity observed in PZT island structures was very weak because coercive voltages of 1.5-2.0V were quite larger than expected values, 0.1V (if the height and coercive field were 20nm and 50kV/cm) and because the maximum value of displacement, 4-6pm/V, was much smaller than that measured in continuous films, 20-50pm/V, or reported values in bulk ceramics [13]. We think that this degradation of ferroelectricity is caused by an internal stress which was remained without relaxation in isolated islands.

The displacement curves of piezoresponce were dependent on the Zr/Ti ratios while no distinct dependence of the phase differnce was observed. In tetragonal PZT islands with Zr/Ti ratios =0/100 and 24/76, saturated curves were observed. On the other hand, in rhombohedral PZT islands (Zr/Ti=74/26), the displacement was not saturated and increased as the dc bias voltage increased. This difference in the displacement curves between tetragonal and rhombohedarl PZT islands is influenced by the size of islands and internal stress as well as the Zr/Ti ratio. Therefore, further investigation on the relationship between the size of PZT islands and domain structure within each island is now in progress.

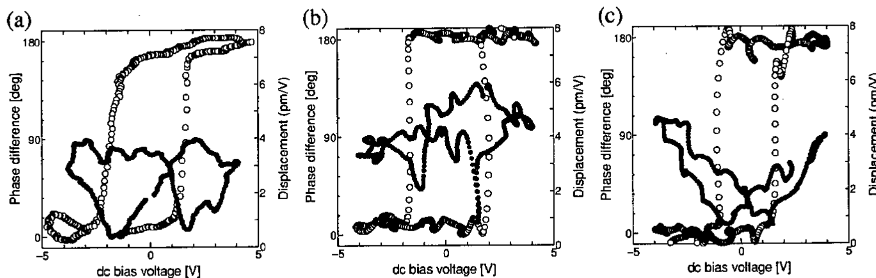

Figure 5 *Piezoresponse of PZT island structures. Zr/Ti ratios and deposition times are (a) 0/100 and 30s, (b) 24/76 and 3min and (c) 74/26 and 3min.Open and closed circles indicate phase difference and displacement, respectively.*

CONCLUSIONS

PZT island structures at the initial stage of MOCVD growth were investigated by piezoresponse measurements using SPM. From AFM observations, coalescence of small PZT islands with subsequent formation of continuous films were observed as the deposition time increased. The width and height of PZT islands at the same deposition time decreased as the Zr composition increased because higher temperature is needed for the crystallization of Zr-rich PZT than Ti-rich PZT. Piezoresponse measurements proved that PZT island structure had weak ferroelectricity. The displacement curves of piezoresponse were dependent on the Zr/Ti ratio. The minimum width and height of the islands which shows ferroelectricity were 50 and 20nm, 70 and 30nm, and 70 and 8nm for Zr/Ti = 0/100, 24/76 and 74/26, respectively. The minimum size which showed ferroelectricity is expected to be comparable with a capacitor size in gigabit-scaled NV-FeRAMs, and PZT thin films can be applied for such ultrahigh integrated NV-FeRAMs.

ACKNOWLEDGEMENTS

The authors thank Mr.K.Murakami for help with sample preparation. This work was partly supported by Grants-in-Aid for Scientific Research (B)(2)(12134207), (B)(2)(12450131), (C)(2)(12650348) and for Encouragement of Young Scientists (A)(11750265) from the Ministry of Education, Sports, Science and Culture, Research Grant from Himeji Institute of Technology, and the Japan Society for Promotion of Science (JSPS-RFTF96P00105).

REFERENCES

1. Y. Uemoto, *Oyo-Buturi*, **67**,1256 (1998). [in Japanese]
2. H. Fujisawa, S. Nakashima, K. Kaibara, M. Shimizu and H. Niu, *Jpn. J. Appl. Phys.*, 5392, **38** (1999).
3. M. Shimizu, S. Nakashima, K. Kaibara, H. Fujisawa and H. Niu, *Ferroelectrics*, **241**, 183 (2000).
4. M. Shimizu, H. Fujisawa and H. Niu, Mater.Res.Soc.Symp.Proc., *Mater.Res.Soc.Symp.Proc.*, **596**, 259 (2000).
5. M. Shimizu, M. Sugiyama, H. Fujisawa and T. Shiosaki, *Jpn. J. Appl. Phys.*, **33**, 5167 (1994).
6. M. Shimizu, M. Sugiyama, H. Fujisawa, T. Hamano, T. Shiosaki and K. Matsushige, *J. Crys. Growth*, **145**, 226 (1994).
7. H. Fujisawa, M. Shimizu, H. Niu, K. Honda and S. Ohtani, *Mater.Res.Soc.Symp.Proc.*, **596**, 321 (2000).
8. H. Fujisawa, K. Morimoto, M. Shimizu, H. Niu, K. Honda and S. Ohtani, *Jpn. J. Appl. Phys.*, **39**, 5446 (2000).
9. M. Shimizu, H. Fujisawa, M. Sugiyama and T. Shiosaki, *Integr. Ferroelectr.*, **6** (1995) 155.
10. T. Hidaka, T. Maruyama, M. Saitoh, N. Mikoshiba, M. Shimizu, T. Shiosaki, L. A. Wills, R. Hiskes, S. A. Dicarolis and J. Amano, *Appl. Phys. Lett.*, **68**, 2358 (1996).
11. A. Gruverman, O. Auciello and H. Tokumoto, *Appl. Phys. Lett.*, 3191, **68** (1996).
12. S. Hong, E. L. Colla, E. Kim, D. V. Taylor, A. K. Tagantsev, P. Muralt and N. Setter, *J. Appl. Phys.*, **86**, 607 (1999).
13. D. A. Berlincourt, C. Cmolik and H. Jaffe, *Proc. IRE*, **48**, 220 (1960).

Mat. Res. Soc. Symp. Proc. Vol. 655 © 2001 Materials Research Society

Fatigue in PZT Thin Films

V. Shur[1], E. Nikolaeva[1], E. Shishkin[1], I. Baturin[1], D. Bolten[2], O. Lohse[2], and R. Waser[2]
[1]Institute of Physics and Applied Mathematics, Ural State University,
51 Lenin Ave., Ekaterinburg 620083, Russia
[2]Institut fuer Werkstoffe der Elektrotechnik, RWTH Aachen, D-52056 Aachen, Germany

ABSTRACT

We have used the new approach to fatigue phenomenon for analysis of the switching current and C-V characteristic evolution during cycling in PZT thin films. It was shown that in accordance with theoretical predictions the rejuvenation stage precedes the fatigue one. We have demonstrated that fatigue behavior corresponds to the spreading of the internal bias field distribution function during ac switching.

INTRODUCTION

Suppression of switching charge by ac voltage cycling known as fatigue effect is one of the key problems impeding wide application of ferroelectric memory [1-9]. It was shown by direct observation that fatigue leads to arising and growth of non-switching regions ("frozen" domains) [8,9]. Recently we propose and investigate by computer simulation a new approach to explanation of fatigue kinetics based on self-organized evolution of spatially nonuniform internal bias field [10,11]. We suppose that domain kinetics during cycling is a self-organized process, as spatial distribution of the internal bias field depends on the previous domain kinetics and in turn defines the subsequent one. Analysis of this model by computer simulation predicts existence of initial rejuvenation stage with exponential increasing of the switching charge, which precedes the exponential charge decreasing during fatigue cycling [10,11]. In this paper we present the experimental testing of our theoretical predictions.

EXPERIMENT

The investigated $Pb(Zr_{0.2}Ti_{0.8})O_3$ thin films (100-200-nm-thick) were grown on $Pt/Ti/SiO_2/Si$ substrates by chemical solution deposition [7]. The films were deposited by a multi-layer spin-coating. They were pyrolized after each deposition step at 400°C and crystallized finally in O_2 at 700°C. X-ray diffraction patterns showed the films to be mainly [111] oriented. The Pt top electrodes were sputtered and the capacitor structures ($100 \times 100\ \mu m^2$) underwent a postanneal at 700°C in O_2 [7]. The fatigue measurements were carried out by applying a bipolar rectangular or triangular pulse train with 100% duty cycle and the amplitude $\mathbf{U_{cyc}} = 3 - 8$ V. The cycling frequency $\mathbf{f_{cyc}}$ ranged from 10 Hz to 1 MHz. The hysteresis loops (Fig. 1a) and dependencies of switching current on field (Fig. 1c) and on time (Fig. 1d) were measured in triangular waveform ($\mathbf{f} = 10 - 100$ Hz, $\mathbf{U} = 5 - 7$ V) after a certain number of switching cycles. Measurements and cycling have been done in temperature range $20 - 200^{O}$C using the aixACCT TF Analyzer 2000.

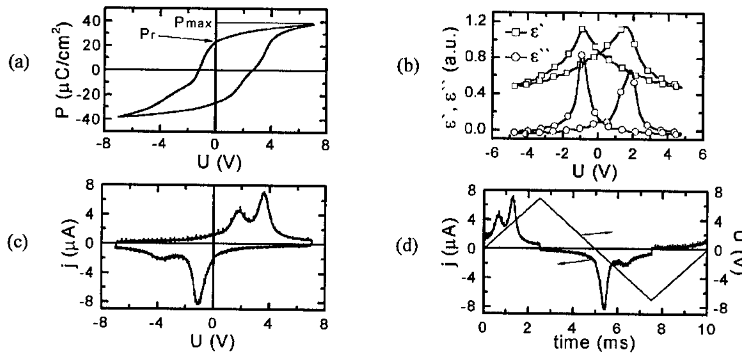

Figure 1. (a) Hysteresis loop, (b) voltage dependence of ε′ and ε″, (c) voltage dependence of switching current and (d) time dependence of switching current and applied voltage.

Reversible complex dielectric permittivity was measured applying additional high frequency weak ac field during switching. C-V measurements (Fig. 1b) were carried out at room temperature in triangular waveform with amplitude **U** = 5 V, switching frequency **f** = 10 Hz, modulation frequency $\mathbf{f_{mod}}$ = 10 kHz and modulation amplitude $\mathbf{V_{mod}}$ = 50 mV. Fatigue-induced evolution of hysteresis loops **P(U)** and switching currents **j(t)** and **j(U)**, so as both components of reversible dielectric permittivity during cycling ε′**(U)** and ε″**(U)** has been analyzed.

CYCLING IN RECTANGULAR PULSES

The switching charge dependence on the cycle number **N** demonstrates two stages of the process (Fig. 2). The first, rejuvenation stage corresponds to initial growth of remnant polarization. The second, fatigue stage manifests itself as conventional decrease of maximum and remnant polarization after long-time cycling.

Fatigue behavior at room temperature in the whole frequency range was found to be practically frequency independent, which is in accord with [7]. Only the numbers of switching cycles defines the polarization decrease. Such behavior allows us to accelerate the fatigue test in wide range of switching cycles number (from 10 to 10^8) by using the measurements at three subsequently increased frequencies (10 Hz, 3 kHz and 1 MHz) (Fig. 2b).

The measured dependence of the maximum switching charge (polarization) on **N** has been fitted according to our model [10,11] by the exponential decrease with two rate constants, which can be attributed to different mechanisms of internal bias field relaxation [13-15]

$$P_{max}(N) = P_\infty + P_{f1}\exp(-N/N_{f1}) + P_{f2}\exp(-N/N_{f2}) \qquad (1)$$

where $\mathbf{P_\infty}$ – limit of switching polarization for long-time cycling; $\mathbf{P_{f1}}$, $\mathbf{P_{f2}}$ – amplitudes of fatigue; $\mathbf{N_{f1}}$, $\mathbf{N_{f2}}$ – rate constants.

According to [10,11] the remnant polarization versus **N** data has been fitted by:

$$P_r(N) = P_{max}(N) - \Delta P_\infty - P_{rj}\exp(-N/N_{rj}) \qquad (2)$$

where $\mathbf{P_{rj}}$ – amplitude of rejuvenation; $\mathbf{N_{rj}}$ – rejuvenation rate constant, $\mathbf{\Delta P_\infty}$ – difference between switching polarization limit for $\mathbf{P_{max}}$ and $\mathbf{P_r}$.

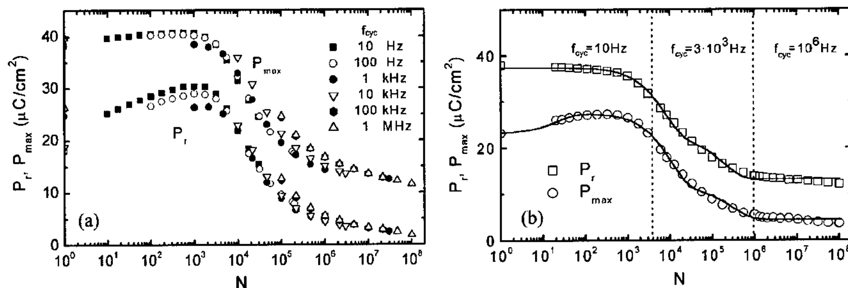

Figure 2. *Maximum and remnant polarization for cycling with varying frequencies fitted by equations (1) and (2). (a)* U_{cyc} *= 5 V,* U *= 5 V,* d *= 137 nm, (b)* U_{cyc} *= 6 V,* U *= 7 V,* d *= 205 nm.*

Essential change of the switching current shape was observed during cycling (Fig. 3a). It can be seen (Fig. 3b) that maximum current value $\mathbf{j_{max}}$ is extremely sensitive to the cycle number and its extremum corresponds to transition from rejuvenation stage to fatigue one.

We suppose that for switching in triangular pulses with low frequencies the polarization reversal can be considered as quasi-static switching in step-by-step increasing external field $\mathbf{E_{ex}(n)}$, where $\mathbf{n}$ is the step number. For spatially nonuniform internal bias field $\mathbf{E_b}$ the switching in the regions in which $\mathbf{E_{loc} = E_{ex}(n) + E_b > E_{th}}$ is finished before next external field increasing [12]. The whole area of the switched regions $\mathbf{\Delta A(n)}$ at each step (duration $\mathbf{\Delta t}$) determines the switching current at corresponding external field produced by applied voltage

$$j(n) = 2P_s \Delta A(n)]/\Delta t \qquad (3)$$

Thus time dependence of switching current is defined by the spatial distribution of internal bias field, which usually follows Gaussian [12]. The switching current during given cycle was fitted by sum of two Gaussians corresponding to areas with different sign of internal bias field

$$j(t) = A_1/w_1 \exp[-2(t-t_{c1})^2/w_1^2] + A_2/w_2 \exp[-2(t-t_{c2})^2/w_2^2] \qquad (4)$$

where $\mathbf{A_1}$ and $\mathbf{A_2}$ are proportional to the switching areas with different sign of internal bias field, $\mathbf{w_1}$ and $\mathbf{w_2}$ – dispersions of the internal bias field spatial distribution function, $\mathbf{t_{c1}}$ and $\mathbf{t_{c2}}$ are the moments when switching field approaches the value corresponding to maximum of the internal bias field distribution function.

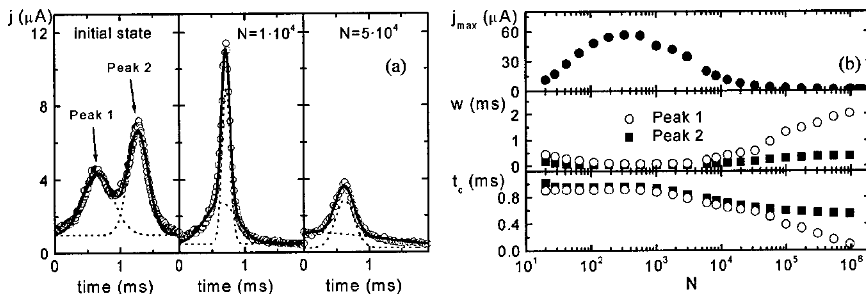

Figure 3. *(a) Switching currents for different number of switching cycles (*U_{cyc} *= 6 V,* U *= 7 V,* d *= 205 nm) and (b) behavior of the fitting parameters.*

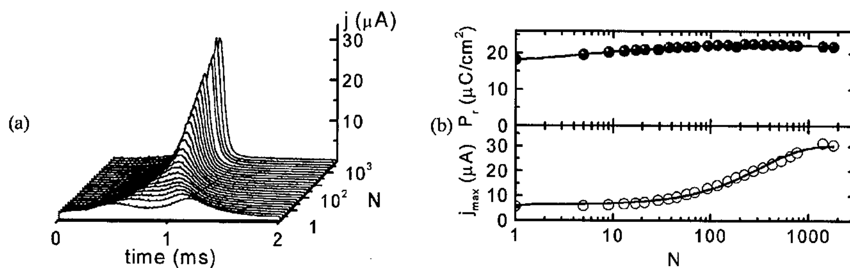

Figure 4. *(a) Evolution of current and (b) change of remnant polarization and current maximum during cycling* (U_{cyc} *= 5 V,* U *= 5 V,* d *= 137 nm).*

As all parameters in (4) are determined for the given cycle, the analysis of switching current change during cycling allows us to extract the information about the evolution of spatial distribution function of the internal bias field. The obtained decrease of the total switching area $\mathbf{A_1 + A_2}$ during fatigue cycling characterizes the increasing of the frozen domain area.

Essential shift of the distribution function maximum to lower fields is obtained during fatigue stage only. The observed essential increase of Gaussian dispersion $\mathbf{w}$ with cycling correlates with simulated smearing of internal bias field distribution function [10,11]. Therefore all obtained experimental results support our approach to fatigue phenomenon as spatially inhomogeneous dynamic imprint effect.

INVESTIGATION OF REJUVENATION STAGE

Detail investigation of rejuvenation stage was carried out by applying the triangular pulses used for hysteresis measurements. The change of switching current shape during rejuvenation stage is presented at Figure 4a.

The value of remnant polarization exponentially increases during rejuvenation stage (Fig. 4b) similar to that obtained for cycling in rectangular pulses (Fig. 2b). According to [10,11] the increase of the current maximum $\mathbf{j_{max}}$ (Fig. 4b) has been described by

$$j_{max}(N) = j_0 + j_1 \exp(-N/N_1) \qquad (5)$$

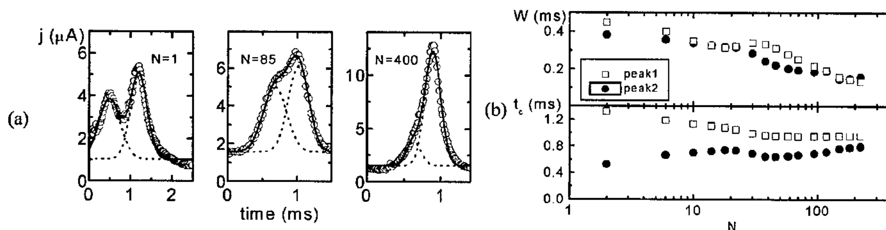

Figure 5. *(a) Fitting of switching current and (b) dependence of the fitting parameters on the cycle number.*

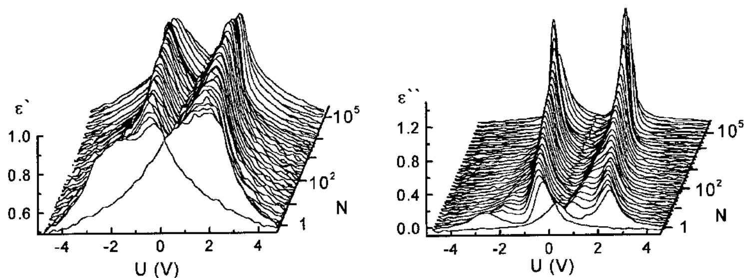

Figure 6. Evolution of the ε` and ε`` loops during cycling.

Detail analysis of the evolution of switching current shape during cycling at the rejuvenation stage (Fig. 5) demonstrates two main features. First, decreasing of Gaussian dispersions, which is due to the narrowing of the internal bias field distribution function. Second, converging of the distribution function maximums. Both features are correlated with the behavior predicted by our model [10,11].

C-V MEASUREMENTS

Reversible complex dielectric permittivity measured during cycling is very sensitive to the evolution of the domain structure. The shape of ε` and ε`` loops essentially changes (Fig. 6). It can be seen that behavior of ε`` is similar to that obtained for switching current.

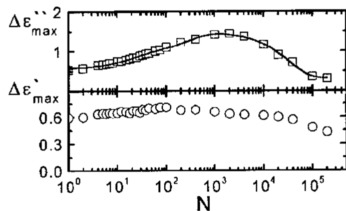

Figure 7. Amplitude variation during switching cycle of the complex dielectric permittivity components vs. cycle number.

The input of the mobile domain structure to dielectric permittivity has been characterized by the parameters $\Delta\varepsilon`_{max}$ and $\Delta\varepsilon``_{max}$ obtained as an amplitude of permittivity variation during the proper switching cycle. The dependence of $\Delta\varepsilon``_{max}$ (Fig. 7) on the cycle number demonstrates the same exponential behavior as obtained for the switching current data (Fig. 3b and 4b).

CONCLUSION

The new approach has been used for analysis of the switching current pulse and C-V characteristic evolution during cycling in PZT thin films. Rejuvenation and fatigue stages of the process have been revealed. It was shown that conventional fatigue stage always follows the

rejuvenation one. Switching current shape and current maximum value demonstrate essential sensitivity to cycling. The revealed evolution of spatially nonuniform distribution of internal bias field during periodical switching is an adequate characteristic of fatigue phenomenon. The evolution of the internal bias field can be attributed to competition of various mechanisms of the bulk screening of residual depolarization field [13-15]. All experimental data confirms the predictions of spatially inhomogeneous dynamic imprint model [10,11]. Detail analysis of the evolution of the switching current data and C-V characteristics for different fatigue cycling conditions will be published elsewhere.

ACKNOWLEDGEMENTS

The research was made possible in part by Programs "Basic Research in Russian Universities" (Grant No.5563) and "Priority Research in High School. Electronics" (Grant No. 03-03-29), by Grant No. 01-02-17443 of RFBR and by Award No.REC-005 of the U.S. Civilian Research & Development Foundation for Independent States of the Former Soviet Union (CRDF).

REFERENCES

1. H. Duiker, P. Beale, J. Scott, C. Paz de Araujo, B. Melnick, J. Cuchiaro, and L. McMillan, *J.Appl.Phys.*, **68**, 5783 (1990)
2. J. Lee, S. Esayan, A. Safari, and R. Ramesh, *Appl.Phys.Lett.*, **65**, 254 (1994).
3. E. Colla, D. Taylor, A. Tagantsev, and N. Setter, *Appl.Phys.Lett.*, **72**, 2478 (1998).
4. I. Stolichnov, A. Tagantsev, E. Colla, and N. Setter, *Appl.Phys.Lett.*, **73**, 1361 (1998).
5. V. Ya. Shur, S. D. Makarov, N. Yu. Ponomarev, I. L. Sorkin, E. V. Nikolaeva, E. I. Shishkin, L. A. Suslov, N. N. Salashchenko, and E. V. Kluenkov, *J.Kor.Phys.Soc.*, **32**, S1714 (1998).
6. J. F. Scott and M. Dawber, *Appl.Phys.Lett.*, **76**, 3801 (2000).
7. M. Grossmann, D. Bolten, O. Lohse, U. Boettger, R. Waser, and S. Tiedke, *Appl.Phys.Lett.*, **77**, 1894 (2000).
8. E. Colla, S. Hong, D. Taylor, A. Tagantsev, N. Setter, and K. No, *Appl.Phys.Lett.*, **72**, 2763 (1998).
9. A. Gruverman, O. Auciello, and H. Tokumoto, *Appl.Phys.Lett.*, **69**, 3191 (1996).
10. V. Ya. Shur, E. L. Rumyantsev, E. V. Nikolaeva, E. I. Shishkin, I. S. Baturin, M. Ozgul, and C.A. Randall, *Integrated Ferroelectrics*, **33**, 117 (2001).
11. V. Ya. Shur, E. L. Rumyantsev, E. V. Nikolaeva, E. I. Shishkin, and I. S. Baturin, *Appl.Phys.Lett.* (in press).
12. V. Ya. Shur, E. L. Rumyantsev, E. V. Nikolaeva, E. I. Shishkin, I. S. Baturin, and M. V. Kalinina, *Appl.Phys.Lett.* (to be published).
13. V. M. Fridkin, *Ferroelectrics Semiconductors*, (Consultants Bureau, New York and London, 1980).
14. V. Ya. Shur, in *Ferroelectric Thin Films: Synthesis and Basic Properties*, **10**, eds. C. A. Paz de Araujo, J. F. Scott, G. W. Taylor (Gordon and Breach, New York, 1996), p.153.
15. P. V. Lambeck and G. H. Jonker, *Ferroelectrics*, **22**, 729 (1978).

Mat. Res. Soc. Symp. Proc. Vol. 655 © 2001 Materials Research Society

Response of the Electric Field Gradient in Ion implanted $BaTiO_3$ to an External Electric Field

Marc Dietrich, Jörn Bartels[1], Manfred Deicher, Kristian Freitag[1], Vyacheslav Samokhvalov[2] and Sepp Unterricker[2]
Fachbereich Physik, Universität Konstanz, D-78457 Konstanz, Germany
[1]Institut für Strahlen- und Kernphysik, Universität Bonn, D-53115 Bonn, Germany
[2]Institut für Angewandte Physik, TU Bergakademie Freiberg, D-09596 Freiberg, Germany

ABSTRACT

Single crystalline, ferroelectric $BaTiO_3$ as material with the highest piezoelectric constants among the perovskites with ordered sublattices was implanted with $^{111}In(^{111}Cd)$. The electric field gradient at the Ti position was measured with perturbed γγ-angular correlation spectroscopy (PAC) while the crystal was exposed to an external electric field. A quadratic dependence could be observed: $\nu_Q(E) = (34.8(1) + 0.16(4)\ E/kV/mm + 0.080(2)\ E^2/kV^2/mm^2)$ MHz. Point charge model calculations reproduce the linear change of V_{zz}, but not the quadratic term. The polarizability of the host ions of $BaTiO_3$ is known to be nonlinear with respect to an electric field. The resulting quadratic shift of the electron density is reflected in the strength of the EFG.

INTRODUCTION

In solids, the electric field gradient (EFG) at a certain lattice site is determined mainly by the atoms in its nearest neighborhood, i.e. their electronic properties and the distances to each other. Therefore, variations of lattice constants lead to changes in EFG. Lattice constants change when the temperature is varied. Such studies have been performed for numerous materials with perturbed γγ-angular correlation spectroscopy (PAC) [1]. A few papers report on the response of the EFG on hydrostatic pressure [2] or on the bending angle of a single crystal [3].

Another way of applying uniaxial stress can be achieved by the inverse piezoelectric effect. In polar crystals lattice constants change or atoms are shifted when an electric field is applied externally resulting in an influence on the EFG at lattice sites. We have carried out experiments in order to observe these slight changes in $LiNbO_3$ with PAC recently. The measurements revealed only a tiny change of the EFG in dependence on the external electric field.

In this report we present further studies using a different material. The primary requirement for the success of such an experiment is a high piezoelectric constant of the material. Solids used as piezoelectric actuators with very high piezoelectric constants like $Sr_xBa_{1-x}NbO_3$ are not useful for PAC investigations because of the random occupation of the Ba sublattice by Ba and Sr atoms. This would result in a strongly damped spectrum since the probes are not exposed to an unique EFG. Therefore we have chosen $BaTiO_3$ as an ordered material with piezoelectric constants larger than those of $LiNbO_3$.

Calculations of EFG at lattice sites in $BaTiO_3$ with WIEN97 [4] using the FP-LAPW method will be presented. Since these first principles calculations are rather complex, we have chosen a

much more easy way of naive point charge model calculations [5] in order to simulate the behaviour of EFG under uniaxial strain.

EXPERIMENTAL DETAILS

$BaTiO_3$ crystallizes in the Perovskite structure and exhibits at room temperature a tetragonal ferroelectric phase. The single crystalline sample from 'Forschungsinstitut für mineralische und metallische Werkstoffe - Edelsteine/Edelmetalle - GmbH', Idar-Oberstein, had a size of 6 x 8 mm^2 and a thickness of 1 mm. The polar axis along c was perpendicular to the plane. The sample had been prepared from a crystal grown with 100 ppm Co in the melt for optoelectronics use. $BaTiO_3$ is very attractive as material for optical and holographic storage [6] and optical waveguides [7]. PAC studies in this material have been carried out with different nuclear probes for almost three decades, already [8-10].

We have implanted $^{111}In(^{111}Cd)$ at the isotope separator at Bonn university with an energy of 160 keV and a dose of 2.2×10^{13} cm^{-2} and a beam spot of 5 mm diameter. In order to remove the implantation damage the sample has been annealed for 2.5 h at 1700 K in air. The crystal was adjusted in a special Teflon holder to apply the electric field. The c-axis and consequently the symmetry axis of the EFG were oriented perpendicular to the detector plane. Aluminum electrodes with a diameter of 6 mm covered the implanted area. Transformer oil with a breakdown field strength of 6 kV/mm has been used for insulation. The breakdown field strength of the sample is much higher, about 40 kV/mm for nominally undoped $BaTiO_3$ [11].

The PAC technique [12] is sensitive to electric field gradients (EFG) present at the site of the probe atom $^{111}In(^{111}Cd)$. The EFG reflects the deviation the electron charge density from cubic symmetry. An EFG causes a hyperfine splitting of an excited state of the ^{111}Cd nuclei. The EFG is mainly described by the quadrupole coupling constant

$$\nu_Q = eQV_{zz}/h \quad (1)$$

(Q - nuclear quadrupole moment, V_{zz} - largest component of diagonalized EFG tensor). This quantity is measured by PAC and unique for a lattice site in defect free material. The fraction of probe atoms involved in this complex can be determined from the characteristic modulation of the PAC spectrum R(t). A small damping of the observed modulation due to the superposition of slightly different EFG caused by defects relatively far away from the probe atom is described by the width $\Delta\nu_Q$ assuming a Lorentzian distribution of these EFG. The PAC-measurements have been carried out at ambient temperature.

Calculations of EFG were performed with the WIEN97 implementation [4] of the Full-Potential Linearized-Augmented-Plane-Wave (FP-LAPW) method [13]. We worked in the GGA (generalized gradient approximation), in which recent progress has been made going beyond the LSDA (the local spin density approximation) by adding gradient terms of the electron density to the exchange-correlation energy or its corresponding potential [14]. For methodological purposes the unit cell is divided into non-overlapping spheres with radius R_{MT} (muffin-tin radius) and an interstitial region. The atomic spheres radii for $BaTiO_3$ were used as follows: $R_{MT}(Ba) = 2.3$ Å, $R_{MT}(Ti) = 1.7$ Å, $R_{MT}(O1) = 1.8$ Å and $R_{MT}(O2) = 2.0$ Å, respectively. We took for the parameter R_{Kmax}, which controls the size of the basis-set in these calculations, the value of 8.

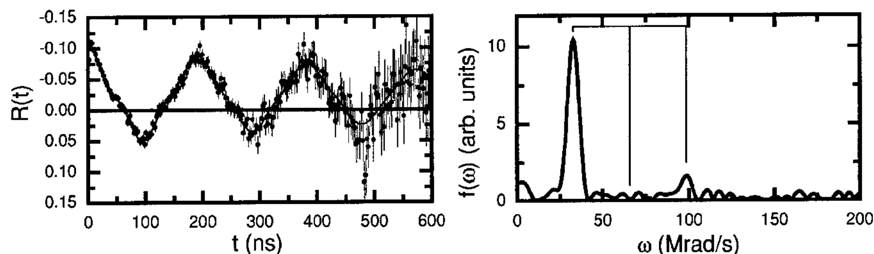

Figure 1. *PAC spectrum and its Fourier transform of* $^{111}In(^{111}Cd)$ *implanted into a* $BaTiO_3$ *single crystal. The sample has been annealed at 1700 K for 2.5 h. The c-axis has been oriented perpendicular to the detector plane.*

Integration in reciprocal space was performed using the tetrahedron method taking 500 k-points in the whole Brillouin zone. As convergence parameter the charge convergence criterion of 0.0005 was chosen. The value of 14 for G_{MAX} (the magnitude of the largest vector in charge density Fourier expansion) was used. The lattice parameters were taken from [15]: a = b = 3.9945 Å, c = 4.0335 Å, z(Ti) = 0.5153, z(O1) = -0.024, z(O2) = 0.4850.

Point charge model calculations have been carried out starting with same atomic positions [15]. The lattice contributions to the EFG at the Ti-site have been calculated. The deformation of the unit cell caused by the external electric field has been taken into account as changes in the lattice constants. The electric field along the c-axis causes a strain along both the c- and the a-axis. The relative changes for a field of 4 kV/mm are $\Delta a/a = 1.6\times10^{-4}$ and $\Delta c/c = -1.4\times10^{-4}$. The signs depend on the direction of the electric field with respect to the direction of the spontaneous polarization and are opposite to each other in any case.

RESULTS

The PAC spectrum and its Fourier transform of $^{111}In(^{111}Cd)$ in $BaTiO_3$ are shown in figure 1. 90(5) % of the probes are exposed to an axially symmetric EFG with the quadrupole coupling constant of $\nu_Q = 34.8(1)$ MHz and a distribution of $\Delta\nu_Q = 1.0(1)$ MHz. The second harmonic is not visible in the Fourier transform due to the special orientation of the crystal. A number of arguments indicate the substitution of $^{111}In(^{111}Cd)$ on the Ti-site [8]. One of these is the comparison of the measured EFG with those measured by NMR, which is host element specific, and with results of calculations. For this purpose, the largest component V_{zz} of the EFG at the Ba- and Ti-site in $BaTiO_3$ are summarized in table 1. With $^{111}In(^{111}Cd)$ a single EFG has been measured. The values for V_{zz} at the Ba- and Ti-sites have been calculated from the measured value of the EFG at the position of $^{111}In(^{111}Cd)$ according to

$$V_{zz,Ti} = (1-\gamma_\infty)_{Ti}/(1-\gamma_\infty)_{Cd}\,V_{zz,Cd} \quad (2)$$

($V_{zz,X}$ = largest component of EFG observed with atom X at a certain lattice site, $(1-\gamma_\infty)_X$ = Sternheimer factor for an ion of element X [16]). The value for $^{111}In(^{111}Cd)$ at the Ba-site is one

	lattice site	PAC $^{111}In(^{111}Cd)$	NMR [17]	Theory	Theory [18]	
				T = 0 K	T = 0 K	T = 296 K
V_{zz} in 10^{20} V/m²	Ba	(54.5(2))	4.35	5.6	2.97	6.00
	Ti	5.72(2)	6.82	3.1	0.59	6.85
	O1			8.9		
	O2			12.8		

Table 1. *Largest component V_{zz} of the electric field gradient at the Ba- and Ti-site in $BaTiO_3$. With $^{111}In(^{111}Cd)$ a single EFG has been measured which is expected to be the one at the Ti-site [8]. Nevertheless, the value that $^{111}In(^{111}Cd)$ at the Ba-site would give is written in brackets. More NMR results with ^{47}Ti, ^{49}Ti and ^{137}Ba have been compiled in [17]. Our theoretical approach with WIEN did not take into account lattice vibrations which is indicated as T = 0 K. The values taken from [18] have been calculated both without lattice vibrations and taking into account lattice vibrations (T = 296 K).*

order of magnitude higher than the results of both NMR and theories. Our theoretical approach with WIEN97 results in values that differ for the Ti-site by a factor of two and for the Ba-site by 30 % from the NMR-values.

The first harmonics in the Fourier spectra of measurements with electric field applied to the sample are drawn enlarged in figure 2. The electric field strength is defined as positive by connecting the non-implanted side of the crystal to the positive output of the high voltage supply. A shift of the peak to higher frequencies with increasing electric field strength is clearly visible. The corresponding quadrupole coupling constants in dependence on the electric field strength applied are shown in figure 3 for all PAC spectra recorded.
The fit to the experimental values results in the function

$$\nu_Q(E) = 34.8(1)\text{MHz} + 0.16(4)\frac{\text{MHz}}{\text{kV/mm}}\text{E} + 0.080(2)\frac{\text{MHz}}{(\text{kV/mm})^2}\text{E}^2 \quad (3).$$

DISCUSSION

The comparison of experimental and theoretical EFG in table 1 proves the substitution of $^{111}In(^{111}Cd)$ at the Ti-site as suggested in the literature [8]. Our theoretical approach with WIEN97 results in values that differ for the Ti-site by a factor of two and for the Ba-site by 30 % from the NMR-values. This may have two reasons. First, the EFG probably depends strong on the exact positions of the Ti- and O-ions in the unit cell. The calculated values may differ when using another set of atomic positions. Second, LMTO-calculations suggest a significant contribution of thermal fluctuation to the EFG [18]. WIEN97 does not take into account such lattice vibrations. Nevertheless, this contribution does not seem to be as strong as discussed in [18] since our values of the EFG differ less from the experimental ones than those calculated by LMTO without thermal fluctuations.

The linear change of the quadrupole coupling constant for $BaTiO_3$ is $\Delta\nu_Q/\Delta E = 0.16$ MHz/kV/mm. This is 10 times the value of 0.017 MHz/kV/mm observed for $LiNbO_3$. This has

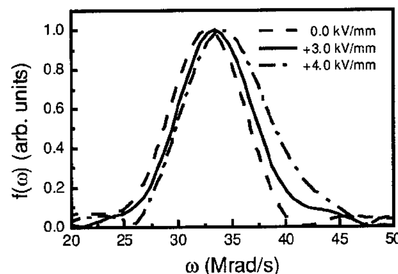

Figure 2. *Normalized Fourier transforms of PAC spectra recorded with $^{111}In(^{111}Cd)$ in $BaTiO_3$ for different externally applied electric field of 0.0 kV/mm, +3.0 kV/mm and +4.0 kV/mm indicated by the dashed, solid and dash dotted line, respectively.*

been expected looking into the piezoelectric constants. The piezoelectric strain constant d_{33} determines the strain in c-direction $S_{33} = d_{33}E_{33}$ of a Perovskite structure crystal with respect to the external electric field strength E_3 along c-axis. The strain constants are $d_{33} = 3.6\times10^{-11}$ C/N and 0.6×10^{-11} C/N for $BaTiO_3$ [19] and $LiNbO_3$ [20], respectively, and differ by a factor of 6.

The relative changes $\Delta\nu_Q/\nu_Q$ caused by the electric field strength of 1 kV/mm differ even more, by a factor of 40. The values are $\Delta\nu_Q/\nu_Q = 4.6\times10^{-3}$ ($BaTiO_3$) and 0.11×10^{-3} ($LiNbO_3$).

It turns out that the linear contribution can be simulated with point charge model calculations. The point charge model calculations result in a purely linear dependence of the EFG on the electric field strength. An electric field of 1 kV/mm causes a relative change of the quadrupole coupling constant of $\Delta\nu_Q/\nu_Q = 1\times10^{-2}$, twice the experimental value but the agreement is satisfactorily good.

The model does not propose a second order dependence. This may have two reasons. The first order effect of an external electric field is well studied concerning the influence on lattice constants. But only little information is available concerning the influence of an external electric

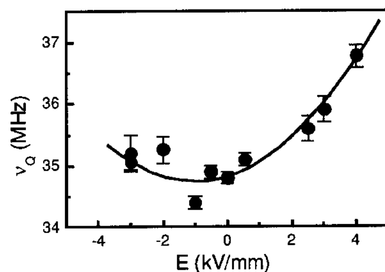

Figure 3. *Dependence of the quadrupole coupling constant ν_Q of $^{111}In(^{111}Cd)$ in $BaTiO_3$ on the externally applied electric field E. The solid line represents a fit of a second order polynomial to the values measured*

field on the atomic positions in the unit cell. One can imagine that the atoms are shifted relative to each other when a field is applied.

The polarizability of the host ions of $BaTiO_3$ is known to result in a quadratic shift of electron density with respect to an electric field strength carried by photons. When a static electric field is applied externally, the polarization occurs in a similar nonlinear way. The resulting quadratic shift of the electron density is reflected in the strength of the EFG.

CONCLUSIONS

We have shown the nonlinear dependence of the electric field gradient (EFG) at the Ti-site in $BaTiO_3$ on the strength of an external electric field. This effect is meant to reflect the nonlinear polarization of the electron shells. So, PAC spectrocsopy is feasible to be used for the investigation of the polarizability of electron shells in solids.

ACKNOWLEDGEMENT

We gratefully acknowledge the financial support of the Bundesministerium für Bildung und Forschung (03-DE5KO1-6, 03-DE5KO2-9).

REFERENCES

1. G.L. Catchen, W.E. Evenson and D. Alred, Phys. Rev., **B54**, R3679 (1996).
2. H.H. Rinneberg, G.P. Schwartz and D.A. Shirley, Hyp. Int., **3**, 97 (1977).
3. G. Marx and R. Vianden, Physics Letters, **A210**, 364 (1996).
4. P. Blaha, K. Schwarz and J. Luitz, WIEN97, (Techn. Univ. Wien 1999).
5. F.W. de Wette, Phys. Rev., **123**, 103 (1961).
6. E. Kratzig, F. Welz, R. Orlowski, V. Doormann and M. Rosenkranz, Solid State Comm., **34**, 817 (1980).
7. P. Moretti, P. Thevenard, G. Godefroy, R. Sommerfeld, P. Hertel and E.Krätzig, phys. stat. sol., **a117,** K85 (1990).
8. M. Uhrmacher, V.V. Krishnamurty, K.-P. Lieb, A. López-Garcia and M. Neubauer, Z. Phys. Chem., **206**, 249 (1998).
9. G.L. Catchen and R.L. Rasera, Ferroelectrics (UK), **120,** 33 (1991).
10. G. Schäfer, P. Herzog and B. Wolbeck, Z. Physik, **A257,** 336 (1972).
11. Landolt-Börnstein III/3, (Springer 1969).
12. G. Schatz, A. Weidinger, Nuclear condensed matter physics: nuclear methods and applications, transl. J.A. Gardner, (John Wiley & Sons, 1995).
13. E. Wimmer, H. Krakauer, M. Weinert and A.J. Freeman, Phys. Rev., **B24**, 864 (1981).
14. J.P. Perdew, S. Burke and M. Ernzerhof, Phys. Rev. Let., **77**, 3865 (1996).
15. H.D. Megaw, Acta Cryst., **15,** 972 (1962).
16. F.D. Feiock, W.R. Johnson, Phys. Rev., **187**, 39 (1969).
17. O. Kanert, H. Schulz, J. Albers, Solid State Comm., **91**, 465 (1994).
18. K.H. Weyrich, R.P. Madenach, Ferroelectrics, **111**, 9 (1990).
19. Landolt-Börnstein III/28a, (Springer, 1990).
20. Landolt-Börnstein III/16a, (Springer, 1981).

Mat. Res. Soc. Symp. Proc. Vol. 655 © 2001 Materials Research Society

SURFACE AND SIZE EFFECTS IN TGS, $NaNO_2$, AND DKDP NANOCRYSTALS

Juan D. Romero[1] , Luis F. Fonseca[1], Rafael Ramos[2], Manuel I. Marqués[3], Julio A. Gonzalo[3]
[1] Department of Physics, University of Puerto Rico, San Juan PR 00931-3343.
[2] Department of Physics, University of Puerto Rico, Mayaguez PR 00681
[3] Departamento de Física de Materiales C-IV. Universidad Autónoma de Madrid, Spain.

ABSTRACT

Monte Carlo simulations of some typical order-disorder ferroelectrics such as TGS, $NaNO_2$ and DKDP nanocrystals were studied using a Transverse Ising Model Hamiltonian with four-spins interactions. The microscopic parameters corresponding to this Hamiltonian were adjusted to fit the experimental polarization-temperature curves for each one of the materials in the bulk phase. Then the dependences of the ferroelectric-paraelectric phase transition temperatures, Tc, on the sizes of those crystals were studied with Monte Carlo simulations of the order-disorder system. We report a weak dependence of Tc on the size of the crystal (d) for these materials above d~6nm. The addition of surface effects showed that the expected low-temperature shift of Tc due to size effects, can be reverted.

INTRODUCTION

The great advances in nanostructures technology brought the researchers on the area of ferroelectrics to the necessity of studying the behavior of ferroelectric crystals as their dimensions are reduced to the order of a few nanometers. In particular, it is of main importance to understand the dependence of the ferroelectric-paraelectric phase transition temperature, Tc, on the size and on the surface conditions of the crystal. Many experimental and theoretical research have been done on this subject starting from the works by Känzig and co-workers [1,2] and Kneikamp and Heywang [3] reporting a dependence of the dielectric permitivity of $BaTiO_3$ ceramics on their grain size. Details of this kind of dependence are still under study [4] because there exist many contradictory results among the different experimental reports. For example, in the case of ferroelectric TGS films, Hadni and Thomas [5] observed that Curie temperature decreases with increasing thickness, but other measurements report the opposite behavior [6]. For particles, experiments showed that the transition temperature decreases with decreasing size [7], but the surface and size effects of well known materials are still not totally understood [8].

In our previous works [9, 10], we carried out Monte Carlo simulations using the Transverse Ising Model Hamiltonian with four-spin interactions to study the general behavior of ferrroelectric nanoparticles and films and the influence on this geometrically restricted configuration of changes in the surface microscopic parameters of the Hamiltonian. In some respects, we able to explain the possible reasons of the contradictory results reported by different authors, considering that the samples were prepared using different experimental procedures. Specifically, we started by obtaining the expected low-T shifting of T_C as the size of the particle is reduced and the associated change from first order to second order of the ferroelectric transition. However, our simulations shown that surface effects could drive T_C up and, if the magnitude of the surface interaction parameters become significantly larger than the internal values, the particle could spontaneously polarize its surface and its interior at different temperatures.

In this work we apply our simulation method to the case of some typical order-disorder ferroelectrics, in particular, Sodium Nitrite, $NaNO_2$; Deuterated Potassium Dihydrogen Phosphate, KD_2PO_4 (DKDP); and Triglycine Sulphate (TGS). We first introduce the formalism and explain how we determined the corresponding microscopic parameters of the Hamiltonian for each one of these materials. Secondly, we report the results of our simulations about the size dependence of Tc for each material and about the effects that can be anticipated when the experimental process for particle formation introduces significant microscopic differences between the surface and the interior of the particles. In the final section, we summarize our results and present conclusions.

THE MODEL AND THE MICROSCOPIC PARAMETERS

Monte Carlo simulations were carried out using the Metropolis algorithm and describing the system with a model Hamiltonian [11] that is a generalization of the DeGennes Hamiltonian of an Ising model in a transverse field, including four pseudospin interactions. We extended our calculations up to nearest neighbors interactions in a simple cubic pseudospin lattice. Under these conditions the hamiltonian reduces to:

$$H = -\Omega \sum_i S_i^x - \frac{1}{2} J \sum_{ij} S_i^z S_j^z - \frac{1}{4} J_4 \sum_{ijkl} S_i^z S_j^z S_k^z S_l^z$$

where Ω is the tunneling frequency, S_i^η are the x (η=x) and z (η=z) components of the pseudospin (PS) at lattice site *i*. *J* and J_4 are the two- and four-PS interaction coefficients, respectively.

The macroscopic polarization, P, is obtained from the configurational average of S^z from stabilized Monte Carlo sweeps (MCS). We used an Ultra Sparc 1 computer in which 10^4 MCS in a 5x5x5 lattice (N=5) takes approximately 15 seconds. We designed a numerical algorithm that stabilizes the initial configuration for a chosen initial temperature, and calculated the average $<S^z>$ at other temperatures by incrementing it by short intervals. We selected three times the correlation time as the criterion to choose the independent equilibrium configurations to be averaged [12]. For N<10 we averaged 10^4 equilibrium configurations and we chose 10^3 for larger lattices. T_c is obtained from the maximum of the electric susceptibility, χ, statistically expressed as [12]:

$$\chi = (1/k_B T)\left[< P^2 > - < P >^2 \right] \qquad \text{where,} \qquad P = (2\mu / a^3)\langle S^z \rangle$$

and μ is the elementary dipole moment of the unit cell and a is the lattice constant.

The microscopic parameters of each bulk material, *J* and J_4, were obtained by fitting the calculated T-dependence of P to the experimental data. Figure 1 shows the comparison between our simulations and the corresponding experimental data for TGS [13], $NaNO_2$ [13], and DKDP (88% D) [14]. The best *J* and J_4 are summarized in Table I, where k_B is the Boltzman constant. The ratio J_4/J is related with the sharpness of the phase transition. As can be seen from Table I, the smallest ratio is for TGS which shows a second order phase transition and the largest is for the case of DKDP where a clear first order transition can be observed. For all these materials, Ω~0.

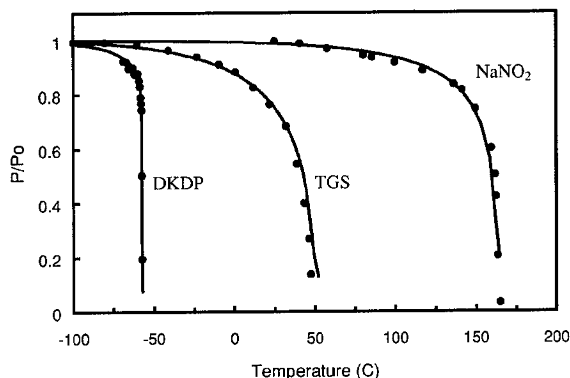

Figure 1. *Comparison between the experimental temperature dependence of the normalized macroscopic polarization (dots) and the simulations (line).*

Table I. The values of the microscopic bulk parameters for the three materials

	J/k_B (K)	J_4/k_B (K)	J/J_4
TGS	246.1	196.9	0.8
$NaNO_2$	257.3	643.2	2.5
DKDP (88%D)	98.0	490.1	5.0

SIZE EFFECTS

The above simulations for the bulk materials were run considering periodic boundary conditions at the "surface" of the pseudospin lattice. Numerical size effects were reduced by increasing the size of the periodically repeated lattice until reaching a convergent result for P. To study size effects on these materials, we eliminated the periodic boundary conditions from the "surface" of the lattice. In order to get the same bulk results but without the periodic boundary conditions, the size of the lattice was increased considerably. Starting from this lattice size, the number of lattice-cells was continuously reduced. The most significant effects were observed in the value of the critical temperature, T_c.. Figure 2 shows the dependence of T_c on the size of the crystal. As it is expected, T_c reduces as the size of the crystal is reduced in the three materials. In the figure, the critical temperature for each size was normalized by the corresponding bulk value. The size is reported as the number of cells (N) along one lattice axis, so that the volume of the crystal would be N^3a^3, where "a" is the lattice constant of the pseudospin cubic lattice.

As shown in figure 2, the size dependence of T_c for these materials is weaker than for displacive-type ferroelectrics like $BaTiO_3$ in which a size-driven shift of T_c is observed for particles with sizes below N~500 (or below N~120 for the case of $PbTiO_3$). In TGS, $NaNO_2$ and

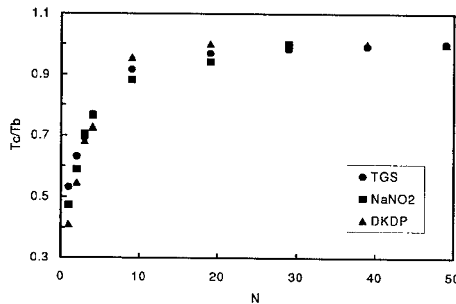

Figure 2. The dependence of Tc on the size of the crystal

DKDP, the changes in T_c are observed below N~40. In particular, TGS shows stronger size dependence (starting at N~40) and DKDP the weakest (starting at N~20). This critical N can be correlated with the characteristics of the bulk phase transition throughout the J_4/J ratio. The material with the sharper phase transition (and larger ratio) requires smaller sizes to start changing T_c. However, figure 2 also shows that $|T_b-T_c|$ (T_b is the bulk value of T_c) becomes larger in DKDP than in the other materials for very small particles (N<5). The temperature dependence of P changes from first order to second order type in the case of DKDP and $NaNO_2$ when the size of the particles is reduced. There is a continuous modification of this T-dependence of P as the size of the particles approaches zero and no critical size in which the ferroelectricity is destroyed can be observed in any of the three materials. This is consistent with other reports on the behavior of order-disorder ferroelectrics [15].

SURFACE EFFECTS

All the above simulations were carried out assuming that the microscopic conditions at the surface were identical to the conditions at the interior of the particles. However, significant changes can occur at the surface that will change the PS interaction coefficients. In order to study these effects for the three materials, we recalculated the T-dependence of P when the value of J and J_4 at the surface (J_S and J_{4S}) were different to the ones at the interior of the particle (as given in Table I). Figure 3 shows how the size dependence of T_c changes in DKDP when the two- and the four-PS surface interaction coefficients become weaker or stronger than the internal values. The legend indicates the value of the surface parameter that was increased or reduced with respect to the internal one. The dashed line was included as a reference corresponding to the case $J_S=J$ and $J_{4S}=J_4$. According to the simulations, T_c and the characteristics of the phase transition (first order- or second order-type) change because of the surface effects. As shown in Fig. 3, variations in the two-PS interaction coefficient is responsible of the bigger changes in the ferroelectric response. It is also observed that, increasing the magnitude of the surface parameters, the low-T shifting of T_c produced by the size effects can be reduced.

The strengthening of the surface ferroelectric interaction leads to a decoupling between the surface and the interior of the particle. In this situation, the surface can become ordered at higher temperature as compared to the interior. Figure 4 shows the ferroelectric behavior of a

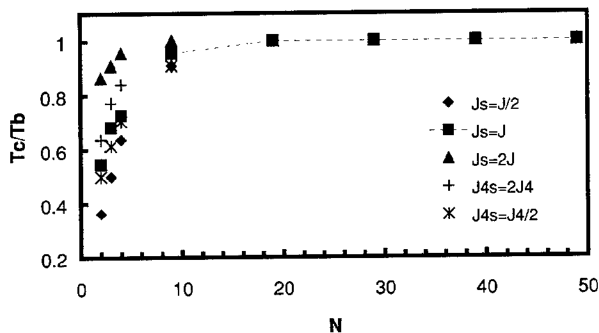

Figure 3. *Modification of the Tc behavior due to size effects in DKDP.*

DKDP particle with a size corresponding to N=30 and with J_S=4J. The T-dependence of P (total P, surface contribution to P, and internal contribution), as well as of the normalized susceptibility, clearly show two transitions. As observed from the figure, the higher temperature transition is related to the ordering of the surface and the lower temperature transition to the "delayed" ordering of the internal part of the particle as the temperature decreases [10].

The typical low-T shifting of T_c as the size of the particle is reduced can be reverted when the experimental conditions result in a large J_S/J ratio. Figure 5 shows the size-dependence of T_c for a DKDP particle with J_S/J=4 as compared with case of figure 2 (J_S=J). In this figure, a high-T shifting is observed when N was reduced due to the strong surface ferroelectric interactions. This effect has been experimentally observed in KDP particles [16]. For larger sizes one can distinguish between the size dependence of the "surface-T_c" (dashed line) and the "interior-T_c" (dotted line). This surface effect was also obtained in $NaNO_2$ and TGS with smaller J_S/J ratios.

Among other possible causes for size and surface effects is the action of a depolarization field. This effect was not considered in the above analysis. A microscopic model to study such effect which includes an electric field along z-direction will be presented elsewhere.

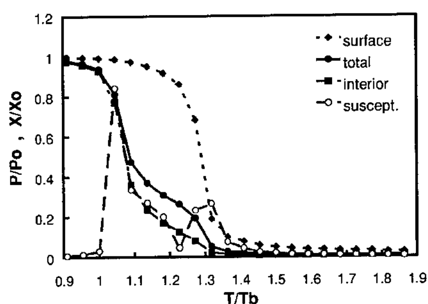

Figure 4.Surface and interior contributions to P for N=30 and J_S=4J.

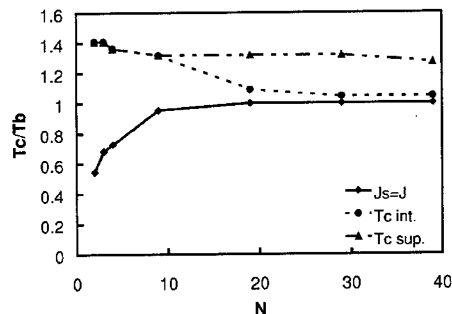

Figure 5. Surface and interior contributions to the size dependence of Tc when J_S=4J.

CONCLUSIONS

We studied size and surface effects in DKDP, $NaNO_2$ and TGS by performing Monte Carlo simulations of the ferroelectric response of the nanoparticles. We modeled the ferroelectric interaction with a Hamiltonian that considered up to four pseudospin interactions. The microscopic parameters were obtained by fitting the results of the average polarization with the experimental values reported for these materials. The obtained values of these parameters showed a good correspondence with the related thermodynamic phenomenological parameters [13, 14]. The better correspondence was obtained for the two-PS interaction coefficient. The expected low-T shifting of the critical temperature was obtained for the three materials when the sizes of the particles were reduced gradually. This shifting was related with a change from a first-order to a second-order phase transition behavior for the case of DKDP. Significant low-T shifting is obtained only for very small particles ($N<15$ or $d<6$nm) as compared with the perovskites where similar changes are observed for larger particles ($N\sim200$ or $d\sim80$nm) [17].

Surface effects are larger when the experimental conditions mainly affect the two-PS interaction coefficient. Strengthening of the ferroelectric interactions at the surface can revert the size effects commonly observed in the particles and the simulations confirm the contradictory experimental results reported for these materials. The three studied materials behave in a similar way and the effects depend on the J_4/J ratio.

ACKNOLWDEGMENT

We acknowledge helpful discussions with Dr. Brigita Urbanc. This work was supported by US ARO grant No. 41002-MS-DPS.

REFERENCES

1. A. Jaccard, W. Känzig, and M. Peter. Helv. Phys. Acta **26**, 521 (1953).
2. M. Anliker, H. R. Brugger, and W. Känzig. Helv. Phys. Acta **27**, 99 (1954).
3. H. Kneikamp and W. Heywang. Zeit. Angew. Phys. **6**, 385 (1954).
4. W. Y. Shih, W. Shih, and I. A. Aksay. Phys. Rev. **B50**, 15575 (1994).
5. A. Handi and A. Thomas. Ferroelectrics **59**, 221 (1984).
6. I. P. Batra and G. D. Silverman. Solid State Commum. **11**, 291 (1972).
7. K. Ishikawa, K. Yoshikawa, and N. Okada. Phys. Rev. **B37**, 5852 (1988).
8. K. Uchino, E. Sadanaga, and T. Hirose. J. Am. Ceram. Soc. **72**, 1555 (1989).
9. J. Romero and L. F. Fonseca. Mat. Res. Soc. Symp. Proc. **493**, 99 (1998).
10. J. Romero and L. F. Fonseca. Integrated Ferroelectrics **29**, 149 (2000).
11. Y. G. Wang, W. L. Zhong, and P. L. Zhang. Phys. Rev. **B53**, 11439 (1996).
12. H. Gould and J. Tobochnik, "Introduction to Computer Simulation Methods". University of California, Berkeley (Oxford University Press, New York, 1987), p. 573-583.
13. K. H. Hellwege, and A. M. Hellwege (eds.). "Landolt-Bornstein numerical data and functional relationships in science and technology".Vol. **III/16b**. Springer Verlag, 1982.
14. R. M. Hill and S. K. Ichiqui. Phys. Rev. **132**, 1603 (1963).
15. K.Sheshadri, R. Lahiri, P. Ayyub, S. Bhattacharya. J. Phys: Conden. Matter **11**, 2459 (1999).
16. E. V. Colla, A. V. Fokin, and Y. A. Kumzerov. Solid State Commun. **103**, 127 (1997).
17. W. L. Zhong, Y. G. Wang, P. L. Zhang, and B. D. Qu. Phys. Rev. **B50**, 698 (1994).

Mat. Res. Soc. Symp. Proc. Vol. 655 © 2001 Materials Research Society

Preparations and Characterizations of Epitaxial $SrBi_2Ta_2O_9$ Thin Films

Keisuke Saito[1], Masatoshi Mitsuya[2], Toshimasa Suzuki[3], Yuji Nishi[3], Masayuki Fujimoto[3], Masanori Nukaga[2], Isao Yamaji[1], Takao Akai[1] and Hiroshi Funakubo[2]

[1]Application Laboratory, Philips Japan Ltd.
7-35-1 Sagamiono, Sagamihara 228-0803, Japan
[2]Department of Innovative and Engineered Materials, Interdisciplinary Graduate School, Tokyo Institute of Technology
4259 Nagatsuta-cho, Midori-ku, Yokohama 226-8502, Japan
[3]Taiyo Yuden Co., Ltd., 5607-2 Nakamuroda, Haruna-machi, Gumma 370-3347, Japan

ABSTRACT

Epitaxial (001)-, (116)- and pseudo (103)-oriented $Sr_{0.35}Bi_{2.2}Ta_2O_9$ (SBT $_{(0.35/2.2/2.0)}$) films were successfully grown on (001), (110) and (111) $SrTiO_3$ substrates, respectively. High-resolution X-ray diffraction reciprocal space mapping (HRXRD-RSM) measurements and pole figure measurements clearly indicated that the (116)-oriented SBT $_{(0.35/2.2/2.0)}$ film consisted of two growth domains those c-axis are separated 180° apart in in-plane and pseudo (103)-oriented SBT film consisted of three growth domains those c-axis are separated 120° apart in in-plane. Moreover, lattice parameter measurements indicated that SBT films grew in fully relaxed state.

INTRODUCTION

Bismuth layer structured ferroelectric materials, such as $SrBi_2Ta_2O_9$ (SBT) and $Bi_4Ti_3O_{12}$ (BIT), have attractive attention for ferroelectric random access memory (FeRAM) application.[1] SBT, in particular, has been widely studied and recently, the FeRAM consisted of SBT capacitor has been commercially available. However, the character of SBT crystal in the form of thin film has not been fully understood yet. Therefore, it is important to investigate the physical properties including growth mechanism on crystalline substrate using epitaxial grade SBT film is highly desired. From Rietveld refinement using X-ray and neutron for SBT polycrystalline powder material, the lattice parameters and crystal symmetry of SBT crystal was identified.[2-4] The refined space group, $A2_1am$, indicates that the mirror plane exists parallel to a-b plane, therefore, the spontaneous polarization is expected not to exist along c-axis of SBT unit cell. This leads extensive interest on controlling the preferred orientation of SBT crystal. From the practical point of view, SBT film is prepared on fiber textured conductive bottom electrodes, such as Pt[1],

and IrO_x[5], and typically these bottom electrodes materials have (111) preferred orientation when those are grown on conventional oxidized (001) Si substrate. Recently, we reported that the SBT film grown on (111) preferentially oriented Pt bottom electrode grown by MOCVD has {103} preferred orientation.[6] We attributed the preferentially oriented SBT film growth to the local epitaxial growth between (111) oriented Pt bottom electrode and {103} SBT. In fact, the lattice mismatches between (111) Pt and (103) SBT are estimated to be 0.14% along [010] SBT and 4.5% along $[10\bar{3}]$ SBT and these rather small lattice mismatches are probably sufficient for promoting epitaxial growth or controlling the preferred orientation of SBT crystal. In the present study, we have prepared epitaxial SBT films that have three different orientation, (001), (116) and pseudo (103), on (001), (110) and (111) $SrTiO_3$ substrates, respectively, and epitaxial relations and growth mechanisms were investigated.

EXPERIMENTAL DETAILES

Epitaxial $SBT_{(0.35/2.2/2.0)}$ films were grown from two source materials, $Sr[Ta(O\cdot C_2H_5)_6]_2$ and $Bi(CH_3)_3$, by MOCVD at deposition temperatures of 750, 820 and 850°C on (001), (110) and (111) $SrTiO_3$ (STO) substrates, respectively. More detail growth conditions were published in the previous report[7] from our group. Epitaxial relations between the $SBT_{(0.35/2.2/2.0)}$ films and the STO substrates and lattice parameters of $SBT_{(0.35/2.2/2.0)}$ films were investigated employing high-resolution X-ray diffraction reciprocal space mapping (HRXRD-RSM[8]) technique using X'Pert-MRD system (Philips, Netherlands). The film compositions were characterized by PW 2404 wavelength dispersive X-ray fluorescence spectrometer (Philips, Netherlands). The film compositions were Sr/Ta=0.35 and Bi/Ta=1.1 for all of the films. Interfacial atomic configurations between $SBT_{(0.35/2.2/2.0)}$ films and STO substrates were characterized by transmission electron microscopy (TEM, Topcon 002B, Japan).

DISCUSSION

Figures 1(a)-1(c) show HRXRD-RSM results for the epitaxial $SBT_{(0.35/2.2/2.0)}$ films grown on (001), (110) and (111) STO substrates, respectively. The results show that *00l, hh<u>6h</u>* and *h0<u>3h</u>* diffraction spots are only laying along film surface normal direction and this indicates the SBT

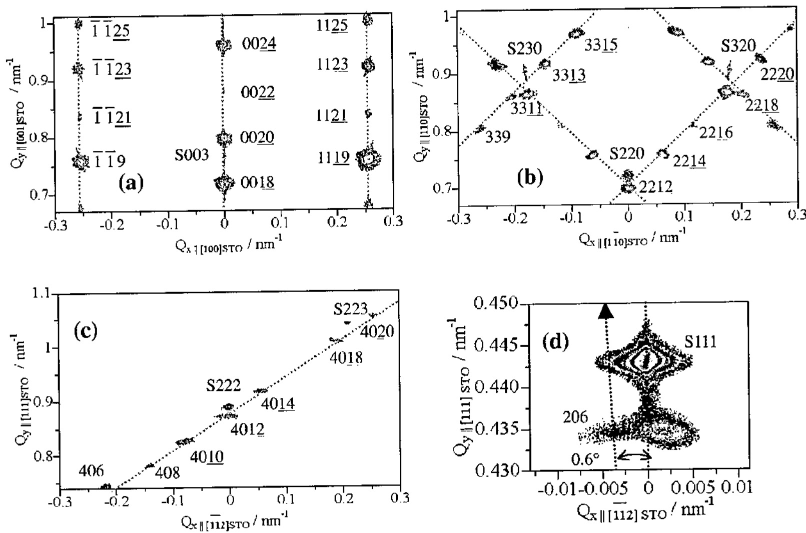

***Figure 1.** XRD-RSM results for epitaxial $Sr_{0.35}Bi_{2.2}Ta_2O_9$ films grown on (a) (001); (b) (110) and (c) (111) $SrTiO_3$; (d) magnification around (206) $Sr_{0.35}Bi_{2.2}Ta_2O_9$ / (111) $SrTiO_3$ substrate. S denotes substrate diffraction.*

$_{(0.35/2.2/2.0)}$ films have (001), (116) and pseudo (103) orientation. The magnification around *206* SBT/ *111* STO diffractions (fig. 1(d)) indicates that the *206* diffraction spot of SBT$_{(0.35/2.2/2.0)}$ tilted about 0.6 deg from [111] STO to [11$\bar{2}$] STO direction. This indicates that the SBT$_{(0.35/2.2/2.0)}$ film grown on (111) STO substrate has, strictly, (10$\underline{3.07}$) orientation. This is the reason why we call the SBT$_{(0.35/2.2/2.0)}$ film grown on (111) STO substrate as pseudo (103) orientation. The epitaxial relations between SBT$_{(0.35/2.2/2.0)}$ films and STO substrates were found as (001)[100] SBT ∥ (001)[110] STO, (116)[$\bar{1}\bar{1}$6] SBT ∥ (110)[$\bar{1}$10] STO and (103)[10$\bar{3}$] SBT ∥ (111)[11$\bar{2}$] STO for the SBT films grown on (001), (110) and (111) STO substrates, respectively. The lattice parameters of SBT$_{(0.35/2.2/2.0)}$ films were evaluated from several sets of HRXRD-RSMs and those were obtained as (a, b, c)= (0.552, 0.554, 2.500), (0.552, 0.554, 0.2496), (0.552, 0.553, 2.498) nm for (001), (116) and pseudo (103) oriented SBT$_{(0.35/2.2/2.0)}$ films, respectively. These obtained lattice parameters were almost matched to the reported values for SBT powder materials[2-4] and those indicates that the SBT$_{(0.35/2.2/2.0)}$ films were almost fully relaxed. Pole figure measurements for the (116) oriented and the pseudo (103) oriented SBT$_{(0.35/2.2/2.0)}$ films, shown in Fig. 2, indicate that the (116)-oriented SBT$_{(0.35/2.2/2.0)}$ film consisted of two growth domains those c-axis are separated 180° apart in in-plane and pseudo (103)-oriented

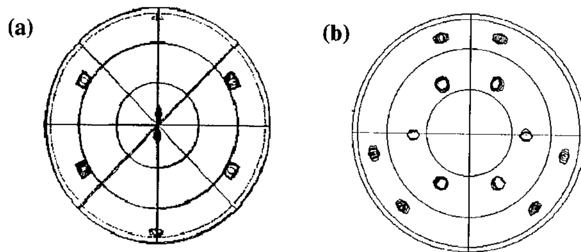

Figure 2. Pole figure measurements of SBT $_{(0.35/2.2/2.0)}$, (a) 115 diffraction of (116)-oriented SBT $_{(0.35/2.2/2.0)}$; (b) 113 diffraction of pseudo (103)-oriented SBT $_{(0.35/2.2/2.0)}$.

SBT $_{(0.35/2.2/2.0)}$ film consisted three growth domains those c-axis are separated 120° apart in in-plane. Finally, growth domain configurations of epitaxially grown SBT $_{(0.35/2.2/2.0)}$ films prepared on three differently oriented STO substrates were obtained as schematically shown in fig. 3.

TEM images are shown in Figs. 4. Figure 4(a) shows wavy shaped contrast. As characterized by Suzuki et al.[9], this is attributed to the stacking faults along c-axis of SBT $_{(0.35/2.2/2.0)}$ crystal and this was also observed in the other two films. In the case of SBT $_{(0.35/2.2/2.0)}$ film growth on (110) STO substrate, faceted (100) or (010) STO was observed as is shown in fig. 4(b) and the SBT $_{(0.35/2.2/2.0)}$ crystal seemed to directly grow on these faceted (100) or (010) planes. Moreover, this image clearly shows that the (116)-oriented SBT $_{(0.35/2.2/2.0)}$ film consisted of two growth domains those c-axis are separated 180° apart in in-plane and grain boundaries are introduced at an atomic step of faceted STO substrate surface. A lower magnification TEM image (not shown in here) for this (116) oriented SBT $_{(0.35/2.2/2.0)}$ film shows that the two growth domains are aligned alternatively and form mesh type of domain structure and the linear density

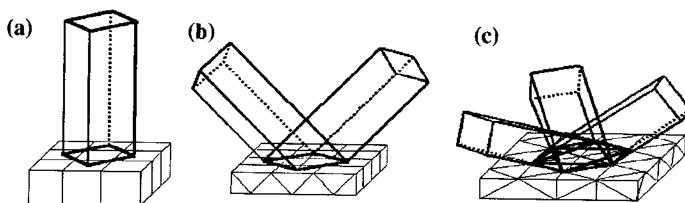

Figure 3. Schematic drawings of growth domain configurations of epitaxially grown SBT $_{(0.35/2.2/2.0)}$ films grown on (a) (001) STO; (b) (110) STO and (c) (111) $SrTiO_3$ substrates.

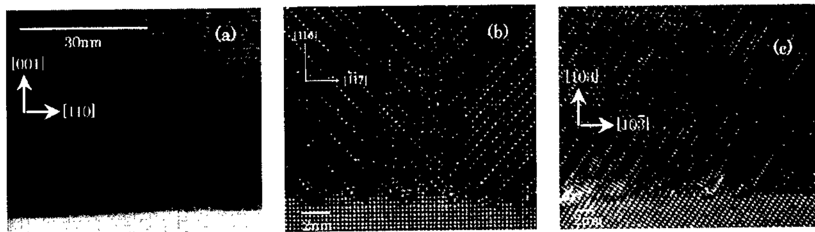

Figure 4. *High-resolution TEM images of (a) (001)-oriented; (b) (116)-oriented and (c) pseudo (103)-oriented $SBT_{(0.35/2.2/2.0)}$ films.*

of this growth domain boundary, in this case, was estimated as 0.019 nm^{-1}.

As indicated by HRXRD-RSM characterization, $SBT_{(0.35/2.2/2.0)}$ films grew on STO substrates incoherently. This growth mechanism of $SBT_{(0.35/2.2/2.0)}$ film is fairly different from $Pb(Zr_x,Ti_{1-x})O_3$ (PZT) case. PZT thin film is well known to release the growth strain introduced to the film during the film growth by forming multiple domain configurations. For example, Roytburd et al. reported that the tetragonal PZT film introduce mixed domain configurations, such as ...$a_1/a_2/a_1$..., ...$a_1/c/a_1$... etc depend on the valance between the magnitudes of the strain introduced by the lattice mismatches taking difference of thermal expansion coefficient between the PZT and the substrate into account and tetragonality strain of tetragonal PZT crystal.[10] This indicates that the controlling of preferred orientation of PZT crystal affects more severely on total polarization charge than SBT. Therefore, preferred orientation control is essential in the case of PZT. This difference between SBT and PZT is expected to bring an advantage for SBT in spatial uniformity of crystal orientation over a large wefer.

CONCLUSIONS

We succeeded in preparing epitaxial $Sr_{0.35}Bi_{2.2}Ta_2O_9$ ($SBT_{(0.35/2.2/2.0)}$) films with three different orientations, such as (001), (116) and (103.07) orientation, on (001), (110) and (111) $SrTiO_3$ substrates, respectively. (116)-oriented $SBT_{(0.35/2.2/2.0)}$ film shows two growth domains those c-axis are separated 180° apart in in-plane and TEM study shows that these domains are aligned alternatively and form mesh type of domain structure. On the other hand, (103.07)-oriented $SBT_{(0.35/2.2/2.0)}$ film shows the existence of three growth domains those c-axis are separated 120° apart in in-plane. Moreover, fairly small amount of residual strain in all of the $SBT_{(0.35/2.2/2.0)}$ films were ascertained by the lattice parameter measurements employing HRXRD-RSM technique and TEM observations show the existence of stacking faults along c-axis of $SBT_{(0.35/2.2/2.0)}$ crystals.

ACKNOWLEDGEMENTS

The author (KS) would like to thank Professor P. Fewster and N. Andrew of Philips Research Laboratory UK for their useful advices on HRXRD-RSM measurements. Also, the author (KS) would like to thank Dr. P. Munk of Philips Analytical Netherlands for his support for the present study.

REFERENCES

1. C. Araujo, J. D. Cuchiaro, L. D. MacMillan, M. C. Scott and J. F. Scott, Nature **374**, 627 (1995).
2. A. D. Rae, J. D. Thompson and R. L. Withers, Acta Crystallogr. **B48**, 418 (1992).
3. Y. Shimakawa, Y. Kubo, Y. Nakagawa, T. Kamiyama, H. Asano and F. Izumi, Appl. Phys. Lett. **74**, 1904 (1999).
4. The lattice parameters and the space group of SBT crystal are, a=0.5531, b=0.5535, c=2.4984 nm and $A2_1am$.
5. T. Eshita, H. Yamawaki, S. Miyagaki and Y. Arimoto, Integ. Ferroelectrics, **26**, 103 (1999).
6. K. Saito, M. Mitsuya, N. Nukaga, I. Yamaji, T. Akai and H. Funakubo, Jpn. J. Appl. Phys. **39**, 5489 (2000).
7. K. Ishikawa and H. Funakubo, Appl. Phys. Lett. **75**, 1970 (1999).
8. P. Fewster, J. Appl. Crystallogr. **24**, 178 (1991).
9. T. Suzuki, Y. Nishi, M. Fujimoto, K. Ishikawa and H. Funakubo, Jpn. J. Appl. Phys. **38**, 1261 (1999).
10. A. L. Roytburd, S. P. Alpay, L. A. Bendersky, V. Nagarajan and R. Ramesh, J. Appl. Phys. **89**, 553 (2001).

Mat. Res. Soc. Symp. Proc. Vol. 655 © 2001 Materials Research Society

Use of an External Electric Field to Convert the Paraelectric Phase to the Ferroelectric Phase in Ultra-thin Copolymer Films of P(VDF-TrFE)

[1]Matt Poulsen, [1]S. Adenwalla, [1]Stephen Ducharme, [2]V.M. Fridkin, [2]S.P. Palto, [2]N.N. Petukhova, and [2]S.G. Yudin
[1]Department of Physics and Astronomy and Center for Materials Research and Analysis, University of Nebraska, Lincoln, NE 68588
[2]Institute of Crystallography, Russian Academy of Sciences, 117333 Moscow, Russia

ABSTRACT

X-ray diffraction was used to probe the structural changes associated with the conversion of the paraelectric phase to the ferroelectric phase that results from the application of a large external electric field. The samples under study are ultrathin (150 to 250 Å) Langmuir-Blodgett films of the copolymer vinylidene fluoride (70%) with trifluoroethylene (30%) deposited on aluminum-coated silicon. Theta-2theta X-ray diffraction was used to measure the change in inter-layer spacing perpendicular to the film surface. Upon heating at zero external electric field, the crystalline films undergo a structural phase transition, at 100± 5°C, from the all-trans ferroelectric phase to the trans-gauche paraelectric phase. [1,2] Above the phase transition temperature, the non-polar paraelectric phase can be converted back to the polar ferroelectric phase, in a smooth continuous process, using a large external electric field (~1 GV/m). For example, at 100° C the ferroelectric phase first appears above 0.2 GV/m and increases steadily in proportion while the paraelectric phase decreases until complete conversion to the ferroelectric phase is achieved at approximately 0.6 GV/m.

INTRODUCTION

Ferroelectricity was first realized and identified by John Valasek in 1920, with the observation that the spontaneous polarization of Rochelle salt was reversible in the presence of an applied electric field. [3] Ferroelectric materials are analogous to ferromagnetic materials in that they both possess a net macroscopic dipole, a hysteresis effect, and a phase transition at a Curie temperature. At the Curie temperature, ferroelectric materials undergo a structural phase transition from a structure with net electric polarization, the ferroelectric phase, to a structure with no net polarization, the paraelectric phase. One family of ferroelectric materials are the copolymers of vinylidene fluoride with trifluoroethylene or P(VDF-TrFE). In the present study all films are composed of copolymers of 70% vinylidene fluoride with 30% trifluoroethylene. Using Langmuir-Blodgett deposition it is possible to obtain ultrathin (5→5000 Å) films of P(VDF-TrFE). We have investigated the effect an applied electric field has on the ferroelectric-paraelectric phase transition, using theta-2theta X-ray diffraction and dielectric measurements. We have shown that the application of a sufficiently large electric field causes the ferroelectric-paraelectric phase transition to be shifted to higher temperature. [4]

Sample Preparation

Solvent-cast and spin-coated films of PVDF and P(VDF-TrFE) have long been studied for their ferroelectric properties, however films made by these methods possess severe

limitations due to their polymorphous nature. [5] In order to obtain an increased degree of order and crystallinity, the Langmuir-Blodgett technique has been employed in the fabrication of ultrathin films of P(VDF-TrFE) 70:30 by our collaborators at the Institute of Crystallography in Moscow. In general, the Langmuir-Blodgett technique involves the deposition of one-molecule-thick layers, known as monolayers, onto a solid substrate, such as glass or silicon. By making a series of depositions it is then possible to build up any number of monolayers on each substrate. As a result, the Langmuir-Blodgett technique allows for precise nanoscale growth control on samples that possess a degree of order and crystallinity much higher than that obtained in thicker polymorphous films. [6] Samples made for this study ranged in thickness from 5 monolayers (25 Å) to 150 monolayers (750 Å). In the following study all samples were made using horizontal dipping (Langmuir-Schaefer variation) on a glass or silicon substrate coated with a 500 Å aluminum electrode. After LB deposition another layer of aluminum (500 Å) was evaporated onto the top of the copolymer film, creating a simple capacitor.

Sample Structure

Copolymer films of P(VDF-TrFE) can have several crystalline phases. The most interesting, and the focus of this research, are the β and α structures, which correspond to the ferroelectric and paraelectric phases respectively. [5,7,8] The ferroelectric phase possesses a net dipole moment, directed from the electronegative fluorine atoms to the relatively electropositive hydrogen atoms. In the ferroelectric phase the copolymer chains are in an all-trans (TTTT) conformation, as shown in figure 1a, with the copolymer chains packing in a quasihexagonal manner as depicted in figure 1c. While in the paraelectric phase the chains are in an alternating trans-gauche (TGTG*) conformation, as in figure 1b, packing in a manner such that alternating chains are anti-parallel, figure 1d, leaving the crystal structure with no net polarization.

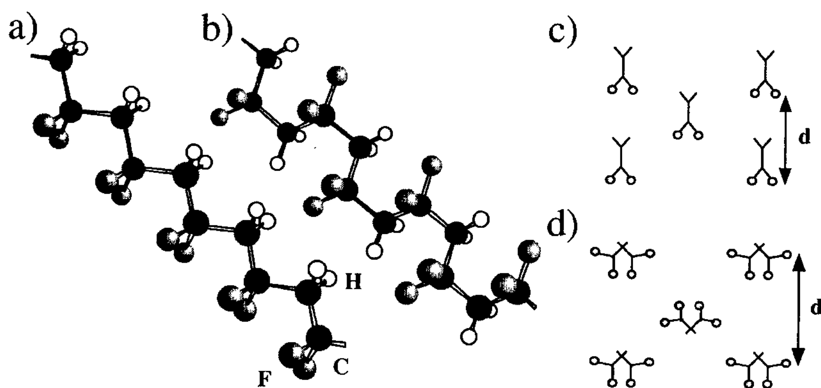

FIGURE 1. a) All-trans (TTTT) conformation of the ferroelectric β phase and b) trans-gauche (TGTG*) conformation of the paraelectric α phase found in PVDF; c) packing of polymer chains while in the ferroelectric phase (looking down the chains) and d) packing of chains while in the paraelectric phase.

EXPERIMENTAL

The properties of the Langmuir-Blodgett films of P(VDF-TrFE) were probed by two methods, capacitance measurements and X-ray diffraction measurements. Capacitance measurements were used to determine the dielectric constant, while X-ray diffraction measurements were used to measure the lattice spacing, where both properties are sensitive to changes in the crystal across the phase transition.

Near the phase transition temperature, it is known that due to the structural transition from the polar all-trans conformation to the non-polar trans-gauche conformation, there will be a large change in spontaneous polarization when crossing the phase transition temperature. [1] The dielectric constant will peak at the transition, where the polarization is most sensitive to changes in the temperature and the electric field. Therefore, measuring the temperature dependence of the capacitance allows one to measure the temperature dependence of the dielectric constant, which in turn allows for the qualitative understanding of the changes in spontaneous polarization of P(VDF-TrFE). A Hewlett Packard 4192A Impedance Analyzer was used to measure the a.c. capacitance and resistance of the P(VDF-TrFE) films as a function of temperature. Where a test frequency of 1 kHz was used, and the temperature was ramped at a rate of 1° C/minute.

Using theta-2theta X-ray diffraction, it is possible to measure the effects of elevated temperature and application of an external electric field on the crystal spacing along the direction perpendicular to the surface of the Langmuir-Blodgett films of P(VDF-TrFE), as indicated in figure 1c and figure 1d. Because the *d* spacing of the ferroelectric β phase and the paraelectric α phase are different, their relative proportions at any temperature or applied field could be calculated from the integrated intensities of their X-ray Bragg peaks. All X-ray diffraction measurements were made on a theta-2theta Rigaku diffractometer, with CuK_α radiation (wavelength = 1.542 Å).

RESULTS

Past structural measurements, performed on thicker polymorphous films of P(VDF-TrFE), fabricated using casting and solvent spin coating, have established the existence of thermal hysteresis in the lattice spacing near the ferroelectric-paraelectric phase transition. [9] In addition, structural and dielectric studies have also established the coexistence of the ferroelectric and paraelectric phases in ultrathin Langmuir-Blodgett films of P(VDF-TrFE) 70:30. [1,2] The observed metastability of phases near the phase transition temperature indicates the first-order nature of the ferroelectric-paraelectric phase transition. Ferroelectric theory also predicts that the structural and dielectric properties of P(VDF-TrFE) are dependent not only upon temperature but also on applied electric field. [1,3] Using the experimental methods described above we have investigated the electric-field dependence of the ferroelectric-paraelectric phase transition in ultrathin Langmuir-Blodgett films of P(VDF-TrFE).

Using capacitance measurements, Ducharme et al. have demonstrated that in the presence of an applied electric field the ferroelectric-paraelectric phase transition can be shifted to a higher temperature. [1] This behavior can be observed in figure 2, which shows results from an electric-field and temperature dependent capacitance study. According to prevailing models this shift is due to the interaction of the internal dipole of P(VDF-TrFE) with the applied electric field, which should stabilize the spontaneous polarization at higher temperatures. [3] The

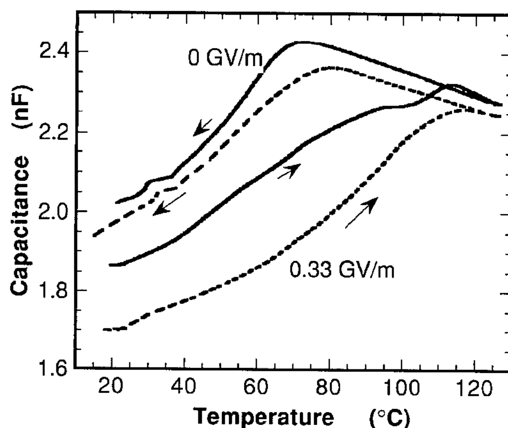

Figure 2. Capacitance measurements made at zero electric field (solid line) and with an applied of 0.33 GV/m (dotted line) made upon heating and cooling. (Adapted from Ref. 1. © 1998 by the American Physical Society, reprinted with permission.)

external electric field enhances the polar all-trans conformation compared to the non-polar trans-gauche conformation by requiring that an additional amount of thermal energy must be supplied in order to rotate the alternating monomer units by ± 60° and overcome the dipolar energy. As a result, the conversion of the ferroelectric phase to the paraelectric phase, and vice-versa, will occur at a higher temperature when an external electric field is present.

Electric-field dependent X-ray diffraction scans were performed at 100 °C. At this temperature, in the absence of an applied electric field, the copolymer is entirely in the paraelectric phase. The sample was first annealed at 120 °C for one hour to ensure that the copolymer had been entirely converted to the paraelectric phase and to improve the crystallinity of the copolymer film. After annealing, the film was then cooled back down to 100 °C for the X-ray diffraction measurements. While the sample temperature was maintained at 100 °C an external electric field was simultaneously applied using a d.c. voltage from a function generator. X-ray diffraction data was recorded at incremental steps of 2.5 volts, incrementing the electric field by 0.10 GV/m in the 25-nm thick films, up to a maximum of 0.70 GV/m.

Electric-field dependent Bragg diffraction scans at a fixed temperature for a 50-monolayer sample are shown in figure 3a. One can see that with zero electric field the copolymer was entirely in the paraelectric phase, represented by the peak at $2\theta = 18.2°$. As the applied electric field was increased from 0.0 GV/m to 0.2 GV/m there is little change in the observed X-ray diffraction scan; the sample remains entirely in the paraelectric phase. However, upon increasing the electric field to 0.4 GV/m one can see a dramatic change, with the appearance of an additional X-ray diffraction peak at $2\theta = 19.9°$, associated with the all-trans β phase, and a decrease in the intensity of the 18.2° diffraction peak, associated with the trans-gauche α phase. When the electric field was increased to 0.5 GV/m and then 0.6 GV/m the paraelectric peak progressively diminished in intensity while the ferroelectric peak simultaneously increases in intensity. This demonstrates the conversion of the trans-gauche

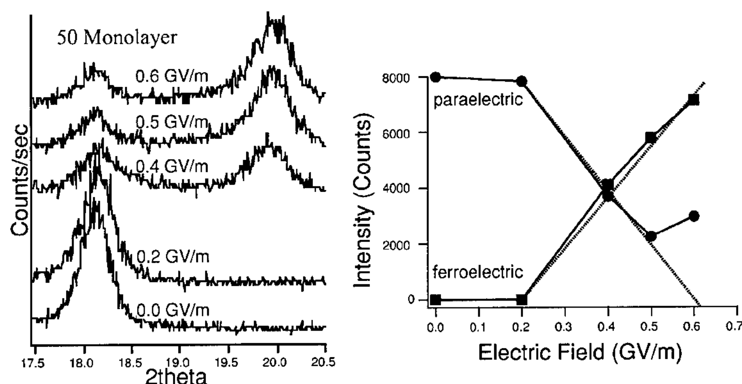

Figure 3. a) Electric-field dependent X-ray diffraction data, recorded at 100° C, with increasing electric field, from a 50 monolayer Langmuir-Blodgett film of P(VDF-TrFE); b) Electric field dependence of the integrated intensities for the paraelectric phase (circles) and the ferroelectric phase (squares).

paraelectric structure (figure 1a) to the all-trans ferroelectric structure (figure 1c) by the applied electric field.

In figure 3b the relative integrated intensities of the ferroelectric and paraelectric diffraction peaks from figure 3a have been plotted as a function of applied electric field with circles and squares representing the paraelectric and ferroelectric data respectively. Because the cross section of the X-ray beam was larger than the electrodes, it was necessary to subtract the contribution of the residual α phase, persisting in areas with no electrodes, from the intensities of the paraelectric peak. Summarizing the results of figure 3b, at low field there is no evidence of the ferroelectric phase at 100 °C, but at increasing field there was a gradual conversion of the trans-gauche paraelectric α phase to the all-trans ferroelectric β phase. The loss of the paraelectric phase is accompanied by creation of an equivalent amount of the ferroelectric phase; the electric field is converting one phase into the other phase. The region of paraelectric-ferroelectric coexistence, upon increasing field, extends from 0.20 GV/m to 0.60 GV/m, where full conversion from the paraelectric to the ferroelectric phase occurs at approximately 0.60 GV/m. The incongruous increase in the paraelectric intensity at 0.60 GV/m was likely caused by electrode degradation during the X-ray diffraction measurements. Inspection of the sample after the experiment revealed considerable electrode degradation.

CONCLUSION

In the preceding study we have demonstrated gradual conversion of the paraelectric phase to the ferroelectric phase by application of an external electric field in ultrathin Langmuir-Blodgett copolymer films of P(VDF-TrFE) 70:30. The X-ray diffraction studies have shown directly that, under the influence of an external electric field, the ferroelectric phase could exist at temperatures above the zero field phase transition temperature. These results are consistent with the picture of the VDF copolymers as ferroelectrics that possess a first-order phase transition.

REFERENCES

1) Stephen Ducharme, A.V. Bune, L.M. Blinov, V.M. Fridkin, S.P. Palto, A.V. Sorokin and S.G. Yudin, *Phys. Rev. B* **57**, 25 (1998).
2) Jaewu Choi, C.N. Borca, P.A. Dowben, A. Bune, M. Poulsen, S. Pebley, S. Adenwalla, and S. Ducharme, *Phys. Rev. B* **61**, 5760 (2000).
3) M.E. Lines and A.M. Glass, *Principles and applications of Ferroelectrics and Related Materials* (Clarendon, Oxford 1977).
4) Matt Poulsen, *Undergraduate Thesis*(University of Nebraska, Lincoln 2000).
5) V.V. Kochervinskii, *Russian Chemical Reviews* **65**, 865 (1996).
6) Michael Petty, *Langmuir-Blodgett Films* (Cambridge Press, New York 1996).
7) A. Lovinger, *Science* **220**, 1115 (1983).
8) K. Tashiro and H.S. Nalwa, *Ferroelectric Polymers,* (Marcel Dekker, New York, 1995), Chap. 2.
9) J.F. Legrand, *Ferroelectrics* **91**, 303 (1989).

Piezoelectric, Pyroelectric, and Optical Materials and Devices

Mat. Res. Soc. Symp. Proc. Vol. 655 © 2001 Materials Research Society

Ferroelectric and Piezoelectric Properties of Epitaxial $Pb(Yb_{1/2}Nb_{1/2})O_3$-$PbTiO_3$ Films

Takeshi Yoshimura and Susan Trolier-McKinstry
Materials Research Laboratory, The Pennsylvania State University,
University Park, PA 16802-4801, U.S.A.

ABSTRACT

$(1-x)Pb(Yb_{1/2}Nb_{1/2})O_3$-$xPbTiO_3$ (PYbN-PT, x=0.5) epitaxial films were grown on (001)$SrRuO_3$/(001)$LaAlO_3$ and (111)$SrRuO_3$/(111)$SrTiO_3$ substrates by pulsed laser deposition. (001)PYbN-PT epitaxial films with high phase purity and good crystalline quality were obtained for a wide range of deposition rates (60-90 nm/min) and temperatures (620-680 °C). (111)PYbN-PT films were also obtained at temperatures in the range of 600 °C to 620 °C. The ferroelectric and piezoelectric properties were investigated on both (001) and (111) PYbN-PT films. The remanent polarizations of (001)PYbN-PT and (111)PYbN-PT films were as high as 34 μC/cm^2 and 26 μC/cm^2, respectively. On (001)PYbN-PT films with a thickness of 900 nm, an e_{31} coefficient of -13 C/m^2 and an aging rate of 2.5% per decade were observed.

INTRODUCTION

Piezoelectric thin films have received considerable attention in recent years for their potential application to microelectromechanical systems (MEMS) such as microsensors and microactuators [1]. Since $Pb(Zr,Ti)O_3$ (PZT) exhibits attractive piezoelectric responses, PZT thin films have been widely studied [2-4]. However, the piezoelectric coefficients (d_{ij}) measured for PZT films are limited to those values typical of hard PZT ceramics.

Recently, it has been reported that single crystals of relaxor ferroelectrics-$PbTiO_3$ solid solutions such as $Pb(Mg_{1/3}Nb_{2/3})O_3$-$PbTiO_3$ (PMN-PT) and $Pb(Zn_{1/3}Nb_{2/3})O_3$-$PbTiO_3$ (PZN-PT) exhibit very large piezoelectric responses [5]. A piezoelectric d_{33} coefficient of 2500 pC/N has been observed for <001> oriented rhombohedral crystals, even though <111> is the polar direction. Furthermore, the response appears to be largely intrinsic. Therefore epitaxial films of relaxor ferroelectrics-$PbTiO_3$ solid solutions may also exhibit high piezoelectric responses [6]. Maria et al. [7] have reported that PMN-PT epitaxial films show enhanced piezoelectric coefficient relative to PZT films. In the present study, we focus on $(1-x)Pb(Yb_{1/2}Nb_{1/2})O_3$-$xPbTiO_3$ (PYbN-PT) epitaxial films. To compare with the piezoelectric properties of single crystals of relaxor ferroelectrics-$PbTiO_3$ solid solutions, (001) and (111) epitaxial PYbN-PT films were prepared. There are several reports concerning the synthesis and characterization of PYbN-PT bulk ceramics [8,9]. PYbN-PT with compositions in the range from x=0.2 to 0.49 exhibits relaxor ferroelectric behavior. Since PYbN-PT has the highest Curie point (~360 °C) near the morphotropic phase boundary (x~0.5) of the known relaxor ferroelectric-$PbTiO_3$ solid solutions, piezoelectric properties with good temperature stability can be expected. Although Bornand et al. [10-12] have reported on the growth and ferroelectric properties of PYbN-PT epitaxial films, to the best of the authors' knowledge, there are no reports about the piezoelectric properties of PYbN-PT films.

Experimental Procedure

To prepare (001) and (111) epitaxial PYbN-PT films, (001)$LaAlO_3$ and (111)$SrTiO_3$ single crystal wafers were used as the substrates. (Note that in this paper, the Miller indexes of all material are given in terms of a pseudocubic unit cell.) PYbN-PT films and $SrRuO_3$ bottom electrodes were prepared by pulsed laser deposition (PLD). The laser used was a KrF excimer laser (Lambda Physik Compex 102) with a 248 nm wavelength. $SrRuO_3$ bottom electrodes (200-300 nm thick) were deposited using stoichiometric $SrRuO_3$ ceramic targets (Target Materials Inc.). Details on the epitaxial growth of $SrRuO_3$ are given elsewhere [10,11,13]. To deposit PYbN-PT films, sintered ceramics of PYbN-PT with the 50:50 composition, including 25 wt% excess PbO, were used as targets. The excess PbO compensated lead loss in the films during growth. Oxygen and ozone gases were introduced to the deposition chamber using a commercial ozone generator (PCI). The specific deposition conditions of the $SrRuO_3$ bottom electrode and PYbN-PT films are given in Table I.

The crystalline phases and orientation of the films were evaluated by x-ray diffraction. θ-2θ scans and ω scans were conducted using a Scintag Pad V diffractometer. The ϕ scans for texture analyses were performed using an XPERT Phillips four circle diffractometer. Cu-Kα radiation was used in all cases.

For electrical measurement, circular Pt top electrodes (ϕ=0.1-0.6 mm) were sputtered on the film surface through a shadow mask. Low and high-field dielectric properties were measured using an impedance analyzer (HP4192A) or a Radiant Technologies RT66A standard ferroelectrics tester. The effective $e_{31(eff)}$ coefficients and their aging behaviors were characterized using a modification of the wafer flexure method described previously [14,15]. An effective $e_{31(eff)}$ coefficient, $e_{31(eff)}$=charge/strain was calculated from the resulting data assuming the Poisson's ration of 0.3. Prior to each test, samples were poled with a DC electric field (typically two or three times their coercive field) for 20 min. On all measurements of ferroelectric and piezoelectric properties, the electric field was applied to the top electrode.

Table I. Deposition conditions for $SrRuO_3$ and PYbN-PT epitaxial films.

	$SrRuO_3$	(1-x)PYbN-xPT
Temperature	730 °C	580-700 °C
Atmosphere	100% O_2	10% O_3-90% O_2
Pressure	200 mTorr	400 mTorr
Laser energy density	1.2 J/cm^2	1.5 J/cm^2
Laser frequency	10 Hz	3, 5 Hz
Number of laser shots	15000	2700
Target	Stoichiometric	x=0.5 25% excess PbO
Target to substrate distance	8 cm	4.5 cm

Results and discussion

Figure 1 shows a XRD θ-2θ pattern of a PYbN-PT film deposited at a substrate temperature of 660 °C and a laser frequency of 3 Hz on a (001)$SrRuO_3$/(001)$LaAlO_3$ substrate. The film showed

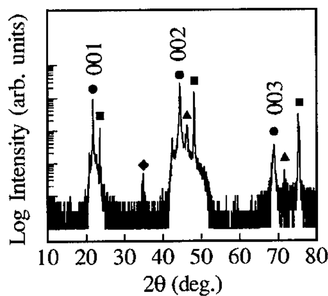

Figure 1. *XRD θ-2θ pattern of a PYbN-PT film deposited at a substrate temperature of 660 °C and a laser frequency of 3 Hz on a (001)$SrRuO_3$ /(001)$LaAlO_3$ substrate.(●) perovskite PYbN-PT, (■) $LaAlO_3$,, (▲) $SrRuO_3$, (◆) pyrochlore.*

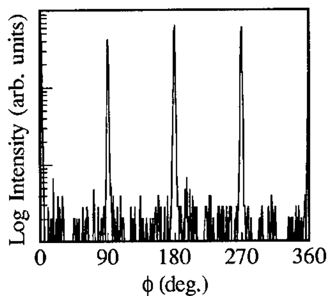

Figure 2. *ϕ scan of (303) for the (001)PYbN-PT film deposited at a substrate temperature of 660 °C and a laser frequency of 3 Hz.*

good (001) orientation. The full width at half maximum (FWHM) of the θ-2θ profile and rocking curve (ω scan) for PYbN-PT 002 were 0.15° and 0.49°, respectively. The former is limited by the instrument resolution. A small peak presented at 34.7° was corresponded to pyrochlore. The quantity of pyrochlore phase estimated from the ratio of the diffraction peak intensities of the pyrochlore phase (34.7°) to PYbN-PT (002) was <1%. Figure 2 shows a ϕ scan of the PYbN-PT (303) peak. There was no indication of misoriented grains in the plane. The heteroepitaxial growth of the PYbN-PT films on the substrates was confirmed by four equally spaced peaks separated by 90°.

To optimize the growth conditions, PYbN-PT films were deposited at various substrate temperatures and laser frequencies. The quantity of pyrochlore phase and FWHM of the θ–2θ profile and rocking curve for the films are shown in figure 3. The thickness of all films was 0.9 μm. The growth rates at laser frequencies of 3 Hz and 5 Hz were 60 nm/min and 90 nm/min,

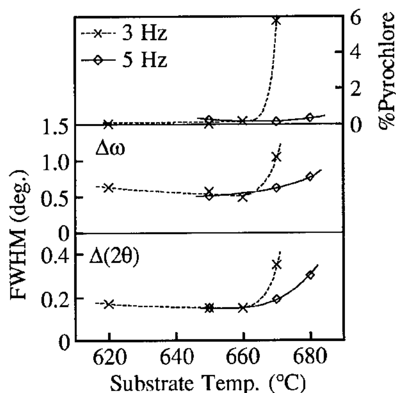

Figure 3. *The quantity of pyrochlore phase and FWHM of the θ-2θ profile and rocking curve (ω scan) of PYbN-PT (002) for films deposited at various temperatures and laser frequencies of 3 Hz and 5 Hz.*

respectively. (001) epitaxial PYbN-PT films were obtained up to 670 °C at 3 Hz. At 670 °C, however, the quantity of pyrochlore phase increased to 6%. The FWHM of the θ-2θ profile and rocking curve width also increased. Therefore, for growth with a 3 Hz laser frequency, perovskite PYbN-PT was favored up to 660 °C. On the other hand, (001)PYbN-PT films with <0.5% pyrochlore phase could be achieved for temperatures below 680 °C at 5 Hz. As compared to the growth conditions reported previously, PYbN-PT perovskite thin films with high phase purity were obtained for a wide range of deposition rates and temperatures at high deposition pressures (400 mTorr). The optimum temperature to grow perovskite PYbN-PT increases with increasing growth rate. These results indicate that Pb is volatile during the deposition. The pyrochlore phase appears due to Pb deficiency.

Figure 4 shows the polarization hysteresis loops for the (001)PYbN-PT films shown in figure 3. The films deposited at 650 and 670 °C showed the largest remanent polarization (P_r) at laser frequencies of 3 Hz and 5 Hz, respectively. The ferroelectric properties of the (001)PYbN-PT films were adversely affected by the pyrochlore phase, as the film deposited at 670 °C and 3 Hz showed a poor hysteresis loop. For PYbN-PT films with high phase purity, the coercive field increased with increasing of the growth temperature.

To obtain (111) epitaxial PYbN-PT films, the films were deposited on (111)$SrRuO_3$ /(111)$SrTiO_3$ substrates. Figure 5 shows XRD θ-2θ patterns of the films deposited at 3 Hz and various substrate temperatures. The thickness of these films and growth rate were 1.3 μm and 75 nm/min, respectively. For depositions at 580 °C, a diffraction peak corresponding to the pyrochlore phase was present at 49.1°. In this case, the pyrochlore phase was probably stabilized by low growth temperature rather than Pb deficiency. Although the optimum growth temperature for (001)PYbN-PT films was around 660 °C, the temperature for (111)PYbN-PT films was around 600 °C. Since the quality of (001)PYbN-PT films deposited on (001)$SrRuO_3$/(001)$SrTiO_3$ substrates at 660 °C were similar to that on (001)$SrRuO_3$/(001)$LaAlO_3$ substrates, the difference of the optimum growth temperature between (001)PYbN-PT films and (111)PYbN-PT films does not come from the difference of substrate material but from the difference of orientation. The polarization hysteresis loops for (001)PYbN-PT films are shown in figure 6. P_r of the film deposited at 600 °C was the largest.

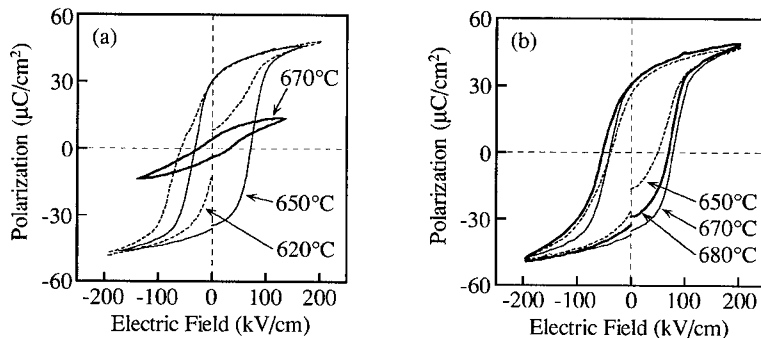

Figure 4. *Polarization hysteresis loops for (001)PYbN-PT films deposited at various temperatures and laser frequencies of (a) 3 Hz and (b) 5 Hz.*

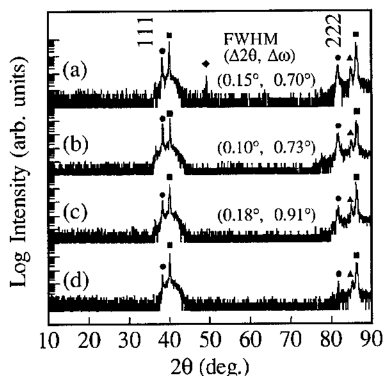

Figure 5. XRD θ-2θ patterns of PYbN-PT films deposited at various substrate temperatures on the (111)SrRuO$_3$/(111)LaAlO$_3$ substrates. (●) perovskite PYbN-PT, (■) SrTiO$_3$, (▲) SrRuO$_3$, (◆) pyrochlore. FWHM of the θ-2θ profile and ω scan for the PYbN-PT (111) are also shown.

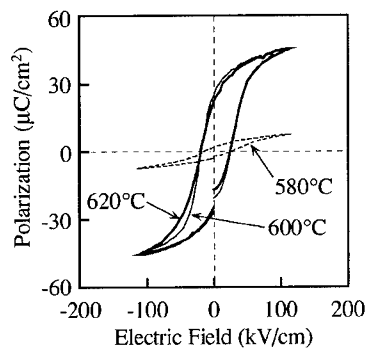

Figure 6. Polarization hysteresis loops for (111)PYbN-PT films deposited at various substrate temperatures.

The piezoelectric coefficient $e_{31(eff)}$ and its aging behavior were measured on the several films. The dielectric and piezoelectric properties of the (001) and (111)PYbN-PT films shown in figures 4 and 6 are summarized in Table II. The $e_{31(eff)}$ coefficients were asymmetric with poling direction. These asymmetric properties are due to the internal bias electric field of the films, because the hysteresis loops were also sifted along the electric field axis as shown in figure 4 [15,16]. When the hysteresis loops were shifted to the positive direction, the $e_{31(eff)}$ coefficients after poling with the top electrode negative were higher than those with the top electrode positive. The highest $e_{31(eff)}$ coefficient (-13 C/m^2) was obtained on the (001)PYbN-PT film deposited at 670 °C and 5 Hz after poling with an electric field of -167 kV/cm. The aging rate was 2.5% per decade. The $e_{31(eff)}$ coefficients for (111)PYbN-PT films were lower than those for (001)PYbN-PT films. This result is comparable to that previously reported for single crystal of relaxor-PT solid solutions.

Table II. The dielectric and piezoelectric properties of the (001) and (111)PYbN-PT films. ε_r: dielectric constant, Ep: poling field (kV/cm).

Orientation	Substrate Temperature	Laser Frequency	ε_r (at 1 kHz)	$e_{31(eff)}$	
(001)	620 °C	3 Hz	1100	-7.0 C/m^2 (Ep=167)	-2.8 C/m^2 (Ep=-167)
(001)	650 °C	3 Hz	800	-8.1 C/m^2 (Ep=167)	-11.0 C/m^2 (Ep=-167)
(001)	670 °C	5 Hz	800	-9.3 C/m^2 (Ep=167)	-13.0 C/m^2 (Ep=-167)
(111)	600 °C	3 Hz	1430	-2.6 C/m^2 (Ep=115)	-2.5 C/m^2 (Ep=-115)

Conclusions

The ferroelectric and piezoelectric properties of $Pb(Yb_{1/2}Nb_{1/2})O_3$ -$PbTiO_3$ (PYbN-PT) epitaxial films with a 50:50 composition were investigated. (001) and (111) PYbN-PT films with high quality and good ferroelectric properties were obtained on (001)$LaAlO_3$ and (111)$SrTiO_3$ substrates with $SrRuO_3$ bottom electrodes. For (001)PYbN-PT films, to deposit at higher substrate temperatures, higher growth rates are required due to Pb volatility. The piezoelectric coefficient ($e_{31(eff)}$) was measured by the wafer flexure technique. To the authors' knowledge, this is the first report of the piezoelectric properties of PYbN-PT films. (001)PYbN-PT films have higher piezoelectric coefficients ($e_{31(eff)}$) than (111)PYbN-PT films. An e_{31} coefficient of -13 C/m^2 and an aging rate of 2.5% per decade were observed for (001) PYbN-PT films with a thickness of 900 nm.

Acknowledgments

The authors are grateful to B. Jones and M. Angelone for their cooperation in the ceramic target synthesis and texture analyses, respectively. Support for this work was provided by the Office of Naval Research (U.S.) under Contract No. N00014-98-1-0527.

References

1. P. Muralt, J. Micromech. Microeng., **10**, 136 (2000).
2. P. Muralt, IEEE Transactions on Ultrasonics, Ferroelectrics, and Frequency Control, **47**, 903 (2000).
3. I. Kanno, S. Fujii, T. Kamada, and R. Takayama, Appl. Phys. Lett., **70**, 1378 (1997).
4. T. Tuchiya, T. Itoh, G. Sakai, and T. Suga, J. of the Ceramic Society of Jpn., **104**, 159 (1996).
5. S. E. Park and T. R. Shrout, J. Appl. Phys., **82**, 1804 (1997).
6. J. P. Maria, W. Hackenberger, and S. Trolier-McKinstry, J. Appl. Phys., **84**, 5147 (1998).
7. J. P. Maria, Ph.D. thesis, The Pennsylvania State University (1998).
8. T. Yamamoto and S. Ohashi, Jpn. J. Appl. Phys., **34**, 5349 (1995).
9. H. Lim, H. J. Kim, and W. K. Choo, Jpn. J. Appl. Phys., **34**, 5449 (1995).
10. V. Bornand and S. Trolier-McKinstry, Thin Solid Films, **370**, 70 (2000).
11. V. Bornand and S. Trolier-McKinstry, J. Appl. Phys., **87**, 3958 (2000).
12. V. Bornand, S. Trolier-McKinstry, K. Takemura, and C. A. Randall, J. Appl. Phys., **87**, 3958 (2000).
13. J. P. Maria, S. Trolier-McKinstry, D. G. Schlom, M. E. Hawley, and G. W. Brown, J. Appl. Phys., **83**, 4373 (1998).
14. J. F. Shepard Jr., P. J. Moses, and S. Trolier-McKinstry, Sens. Actuators A **71**, 133 (1998).
15. J. F. Shepard Jr., F. Chu, I. Kanno, and S. Trolier-McKinstry, J. Appl. Phys., **85**, 6711 (1999).
16. A. Kholkin, E. Colla, K. Brooks, P. Muralt, M. Kohli, T. Maeder, D. Taylor, and N. Setter, Microelectron. Eng. **29**, 261 (1995).

Mat. Res. Soc. Symp. Proc. Vol. 655 © 2001 Materials Research Society

Crystalline and electrical properties of ferroelectric silver niobate-tantalate thin films

Jung-Hyuk Koh [a], S.I. Khartsev [a], Alex Grishin [a], Vladimir Petrovsky [b]
[a] Condensed Matter Physics, Department of Physics, Royal Institute of Technology, Stockholm, S-100 44, Sweden;
[b] Department of Ceramic Engineering, University Missouri-Rolla, EMARC, Rolla, MO.

ABSTRACT

For the first time $AgTa_{0.38}Nb_{0.62}O_3$ (ATN) films have been grown on the $La_{0.7}Sr_{0.3}CoO_3$ (LSCO)/$LaAlO_3$ single crystal as well as onto $Pt_{80}Ir_{20}$ (PtIr) polycrystalline substrate. Comprehensive X-ray diffraction analyses reveal epitaxial quality of ATN and LSCO films on the $LaAlO_3$(001) substrate, while ATN/PtIr films have been found to be (001) preferentially oriented. Dielectric spectroscopy performed for ATN films and bulk ceramics in a wide temperature range 77 to 420 K shows the structural monoclinic M_1-to-monoclinic M_2 phase transition occurs in films at the temperature 60 °C lower than in ceramics. The tracing of the ferroelectric hysteresis *P-E* loops indicates the ferroelectric state in ATN films at temperatures below 125 K and yields remnant polarization of 0.4 $\mu C/cm^2$ @ 77 K. Weak frequency dispersion, high temperature stability of dielectric properties as well as low processing temperature of 550 °C make ATN films to be attractive for various applications.

INTRODUCTION

The great potential of high dielectric permittivity and low loss ferroelectrics as frequency agile materials, has recently attracted great attention. Such materials, when incorporated into devices, need to operate over wide bandwidths, handle high microwave power without breakdown, possess wide electrical tuning, and minimal loss. Perovskite $(Ba,Sr)TiO_3$ (BST) [1], $SrTiO_3$ (STO) [2], and $BaTiO_3$ (BTO) [3] films are considered to be the candidates for electrically tunable microwave components. A recent microwave-submillimeter-to-infrared spectroscopic study [4] has proved silver niobate-tantalate solid solutions $AgTa_xNb_{1-x}O_3$ (ATN) should also be regarded to the family of microwave ceramics.

A.Kania [5] has reported perovskite silver niobate-tantalate solid solutions show high dielectric permittivity and low loss tan δ in bulk ceramics, but to the best of our knowledge ATN has not been yet investigated in thin film form. One possible reason is the high volatility of the Ag component, which complicates ferroelectric thin film fabrication. In this paper, we report on highly crystalline ATN films deposited on LSCO/$LaAlO_3$ single crystal and onto $Pt_{80}Ir_{20}$ (PtIr) polycrystalline substrates, as well as results of comparative analyses of ATN bulk ceramics and thin film dielectric and ferroelectric properties. Fabricated ATN films exhibit high temperature stability and weak frequency dispersion of dielectric properties, dielectric permittivity about 500 and loss tan $\delta \sim 0.008$ at 100 kHz, electrical tunability $1-\varepsilon(56\ kV/cm)/\varepsilon(0) \sim 32\%$@77 K, and remnant polarization P_r (77 K) ~ 0.4 $\mu C/cm^2$.

EXPERIMENTAL PROCEDURES

A 248 nm KrF excimer laser was used to ablate stoichiometric LSCO and ATN ceramic targets. The processing parameters used to grow ATN and LSCO films are listed in the Table I. Optimized processing conditions have been found to be similar to fabricate ATN films both onto LSCO/$LaAlO_3$ single crystal and on the nicely polished PtIr polycrystalline substrate. To calibrate the deposition rate, shown in the Table I, LSCO and ATN films thickness was measured by α-step meter. X-ray diffraction (XRD) θ-2θ -scans, φ-scans and rocking curves were measured using an x-ray powder diffractometer *Siemens* D5000 with a Cu-K_α source. The temperature and frequency dependencies of dielectric characteristics were recorded using *Philips* PM6304 LCR meter with 30 mV rms signal voltage. 1 pC resolution electrometer circuit driven by 1 kHz triangular waveform signal and calibrated with the *Radiant Technology* RT66A pulsed tester has been employed to trace ferroelectric hysteresis loops. Silver 5×4 mm^2 and gold 2.4×10^{-3} mm^2 electrodes were made for ceramic bulk and ATN film capacitors, respectively. The corresponding accuracy of polarization measurements was 5 pC/cm^2 for bulk ceramic capacitor and 0.4 nC/cm^2 for film capacitor.

Table I. Processing conditions for $AgTa_{0.38}Nb_{0.62}O_3$ (ATN) and $La_{0.7}Sr_{0.3}CoO_3$ (LSCO) films.

Processing parameters	ATN	LSCO
Oxygen pressure (mTorr)	350	300
Substrate temperature (°C)	550	700
Target-to-substrate distance (mm)	50	55
Laser energy density (J/cm^2)	3-4	3-4
Laser repetition rate (Hz)	15	20
Deposition rate (Å/pulse)	0.45	0.175
Film thickness (μm)	0.4	0.4
Annealing oxygen pressure (Torr)	600	700
Annealing time (min)	20	20

RESULTS AND DISCUSSION

XRD data for the ATN films deposited onto PtIr substrates at different substrate temperatures ranged from 500 °C to 700 °C are shown Fig. 1. The ATN film prepared at substrate temperature 500 °C looks like x-ray amorphous. Appearance of strong ATN-001, 110, and 220 Bragg

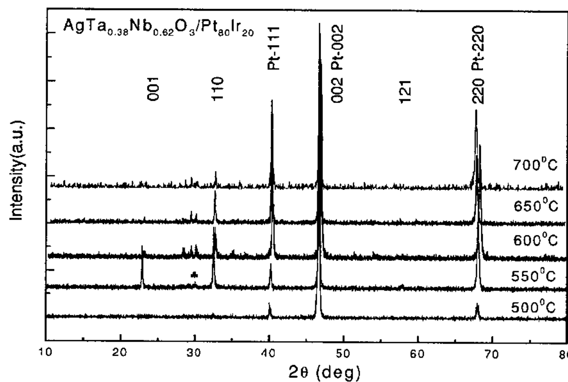

Fig 1. X-ray θ-2θ diffraction patterns of ATN on PtIr substrates deposited at different substrate temperatures from 500 °C to 700°C Symbol ♣ indicates Ag poor $Ag_2Nb_4O_{11}$ oxide (PDF card 21-1086).

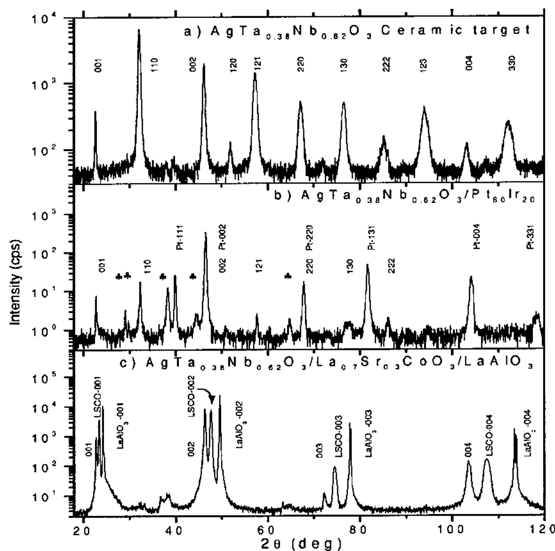

Fig. 2 XRD θ-2θ -scans for: **a)** ATN ceramic target; **b)** ATN onto polycrystalline PtIr substrate, and **c)** ATN /LSCO bilayer film onto $LaAlO_3$ single crystal. Symbols ♣ in **b)** indicate $Ag_2Nb_4O_{11}$ oxide.

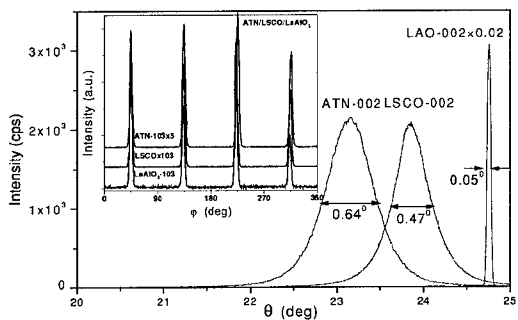

Fig. 3 XRD rocking curves (ω-scans) of ATN-002, LSCO-002, and $LaAlO_3$-002 for ATN/LSCO film grown onto $LaAlO_3$ single crystal. The insert shows φ-scans of off-normal (103) planes measured at oblique geometry.

reflections at substrate temperature of 550 °C indicate the crystallization of the perovskite ATN phase. Further increase of the temperature leads to the decomposition of perovskite phase to the Ag poor $Ag_2Nb_4O_{11}$ oxide (PDF card 21-1086).

XRD pattern of ATN ceramic target [Fig. 2(a)] shows perovskite structure with the lattice parameters $a = b = 3.921$ Å and $c = 3.933$ Å. ATN films grown on the $Pt_{80}Ir_{20}$ polycrystalline substrates [Fig. 2(b)] exhibit preferential *c*-axis orientation. The intensities of ATN-001 and 110 reflections are in the ratio of $I_{ATN-001} : I_{ATN-110} = 0.43$ while it is only of 0.057 for ATN ceramic target. Slight traces of $Ag_2Nb_4O_{11}$ oxide, identified in XRD pattern of ATN/PtIr film and marked by symbols ♣ in Fig.2(b), indicate Ag lost during PLD process on PtIr substrate. ATN and LSCO films grown onto $LaAlO_3$ single crystal [Fig.2(c)] have superior *c*-axis orientation with very narrow rocking curves shown in Fig. 3: FWHM = 0.64° and 0.47° for ATN and LSCO layer respectively. Four fold symmetry sharp φ-scans of ATN-103 (θ_{sam} = 57.76°, $2\theta_{det}$ = 76.87°), LSCO-103 (θ_{sam} = 57.82°, $2\theta_{det}$ = 79.00°), and $LaAlO_3$-103 (θ_{sam} = 58.33°, $2\theta_{det}$ = 79.86°) planes in the insert to Fig. 3 indicate

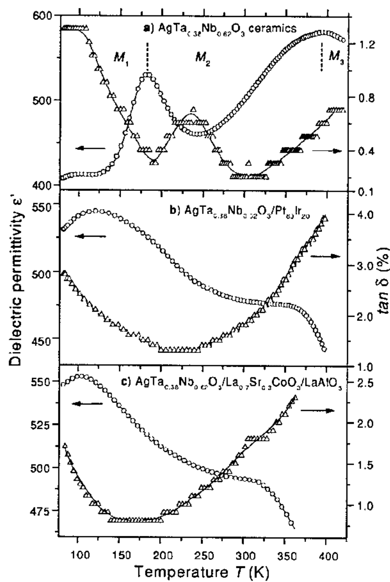

Fig 4 Temperature dependencies of the dielectric permittivity ε′ and the dissipation factor tan δ measured at 100 kHz in: **a**) ATN ceramics; **b**) ATN film onto PtIr substrate, and **c**) epitaxial ATN/LSCO/$LaAlO_3$ heterostructure. Supposed phase boundaries M_1-M_2-M_3 in ATN ceramics are shown in (**a**).

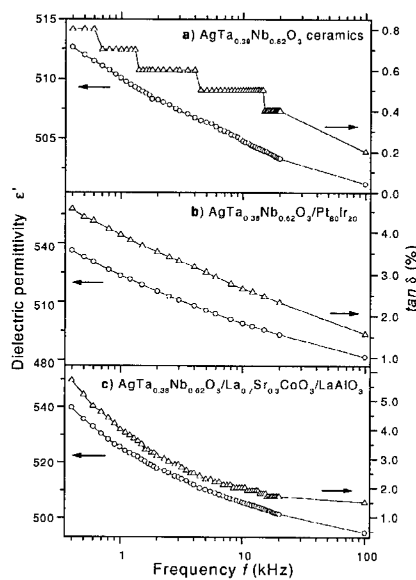

Fig. 5 Frequency dispersion of the dielectric permittivity ε′ and loss tan δ at room temperature in **a**) ATN ceramics; **b**) ATN/PtIr thin film, and **c**) epitaxial ATN/LSCO /$LaAlO_3$ heterostructure. The steps in tan δ plot (similar to Figs. 4**a** and 4**c**) are caused by limited (0.1 %) resolution of the LCR meter.

strong in-plane texture of ATN and LSCO films growing in epitaxial relationship with $LaAlO_3$ substrate. By combining XRD data from θ-2θ scan [Fig. 2(c)] and φ-scan (Fig. 3) the following lattice parameters have been obtained: for LSCO out-off-plane parameter c = 3.821 Å and in-plane parameters $a = b$ = 3.908 Å; for ATN film c = 3.924 Å, $a = b$ = 3.902 Å.

Temperature dependencies of dielectric permittivity ε′ and loss tan δ in films qualitatively reproduce those in ATN ceramics (refer Fig. 4). In a wide temperature range from 77 K to 420 K, ε′ (100 kHz) experiences moderate for ATN ceramics and much smaller for ATN films variations around the mean value of 500. In the bulk $AgTa_{0.38}Nb_{0.62}O_3$ ceramics two local maxima of $\varepsilon'(T)$ at 182 K and 394 K point out M_1-M_2 and M_2-M_3 structural phase transitions. In ATN/PtIr and ATN/LSCO films the M_1-M_2 transition, attributed to the ferro-

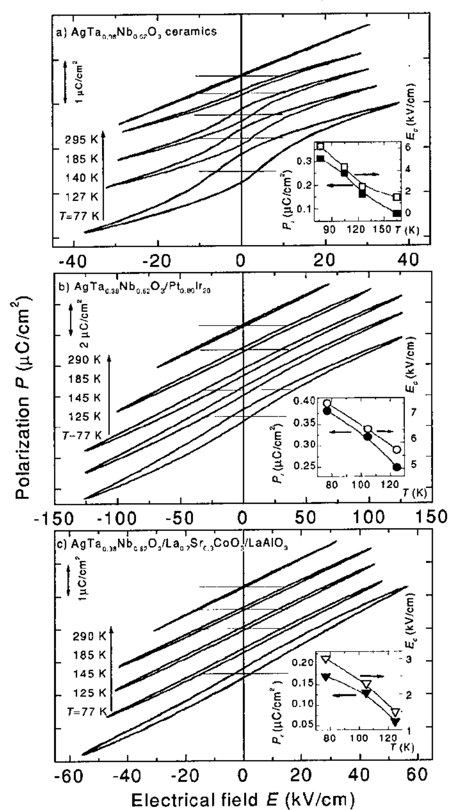

Fig. 6 Sequence of ferroelectric *P-E* hysteresis loops measured at various temperatures: **a)** ATN ceramics; **b)** ATN/PtIr thin film, and **c)** epitaxial ATN/LSCO/$LaAlO_3$ heterostructure. *P-E* loops are offset in vertical direction for clarity. Remnant polarization P_r and coercive field E_c vs temperature are shown in the insert.

antiferroelectric phase transformation, shows up with much broaden maximum than in ATN ceramics and shifts to lower temperature: 121 and 102 K respectively. The position of M_2-M_3 transition in ATN films is difficult to define. It displays itself by a slack shoulder on the high temperature wing of M_1-M_2 transition at 361 and 315 K in ATN/PtIr and ATN/LSCO film respectively. Although the processing conditions have been optimized to get LSCO resistivity as low as 1 mΩ·cm @ 300 K, nevertheless the resistivity increase at temperatures above 200 K causes an increase of loss tan δ.

The dielectric test performed at room temperature has revealed a weak frequency dispersion of ε′ (300 K) in frequency range 400 Hz-100 kHz: 2.4 % in ATN ceramics, 10.6 % in ATN/PtIr, and 8.7 % in ATN/LSCO film (Fig. 5). Both ε′ and tan δ monotonously decrease in the frequency range 400 Hz –100 kHz.

The resistivity of ATN/PtIr and ATN/LSCO films was around $6\text{-}8{\cdot}10^{11}$ Ω·cm at 30 kV/cm and 77 K and lowered ten times at room temperature. The maximum polarization in ATN films was achieved as low as 0.4 μC/cm² @ 77 K. Therefore, special precautions have been undertaken to eliminate inserted parasitic capacitance and inserted loss from LSCO counter electrode. To trace ferroelectric hysteresis loops, the electrometer circuit was driven by 1 kHz triangular waveform signal approaching to the pre-breakdown condition. To distinguish between the 'lossy capacitor' and ferroelectric response, *P-E* tracing has been performed in the frequency

range 50 Hz–5 kHz. The shape of *P-E* loop was found to be frequency independent. Although weak hysteresis of polarization was appearing already at $T \sim 190$ K, distinct *P-E* loops indicating the ferroelectric state are observed at temperatures lower those where the local maximum of the dielectric permittivity and anomalies of tan δ vs. T occur. In measured temperature range the averaged pyroelectric coefficient dP/dT was found to be 2.6, 2.7 and 2.3 nC/cm^2 K, while the measurements of the incremental polarizability $(\varepsilon-1)/4\pi = \partial P/\partial E$ yielded the electrical tunability $1 - \varepsilon(E_{max})/\varepsilon(0)$ of 70 %, 29 %, and 32 % in ATN ceramics, ATN/PtIr and ATN/LSCO films, respectively. The maximum polarization achieved by applying 30 kV/cm was found to be 1.92, 1.42, 1.24 μC/cm^2 @ 77 K and 1.27, 1.16, and 1.09 μC/cm^2 @ 195 K for ATN/LSCO/ $LaAlO_3$, ATN/PtIr thin film, and ATN bulk ceramic capacitors correspondingly. As shown in the insert to Fig. 6, the remnant polarization in ATN/PtIr film appeared to be higher while in ATN/LSCO film was lower than in ATN ceramics in whole temperature range 77-125 K.

SUMMARY AND CONCLUSIONS

In summary, ferroelectric $AgTa_{0.38}Nb_{0.62}O_3$ films have been pulsed laser deposited onto polycrystalline $Pt_{80}Ir_{20}$ substrate as well as onto $La_{0.7}Sr_{0.3}CoO_3/LaAlO_3$ single crystal from stoichiometric ceramic target. Fabricated films have been found to be single-phase, exclusively *c*-axis oriented on the $LaAlO_3$ single crystal, while preferentially *c*-axis oriented on the $Pt_{80}Ir_{20}$ polycrystalline substrate. Two anomalies in temperature dependencies of the dielectric permittivity ε' and loss tan δ indicate M_1-M_2 and M_2-M_3 structural phase transitions. Hysteresis of ferroelectric *P-E* loops indicates ferroelectric state in ATN films at temperatures below 125 K. Remnant polarization of 0.4 μC/cm^2 and electrical tunability as high as 32% @ 77K, tan δ (100 kHz) as low as 0.008, and high temperature stability of the dielectric properties promise new silver niobate-tantalate films for various applications.

We are thankful to Dr. Antoni Kania for supplying the dense $AgTa_xNb_{1-x}O_3$ ceramic targets and to Dr. J. Petzelt, who drawn our attention to microwave properties of this ceramics.

ACKNOWLEDGMENT

This research was funded by the Swedish Agency NUTEK.

REFERENCES

1. H.H. Feng, C.L. Chen, Appl. Phys. Lett. **75**, 412 (1999).
2. H.C. Li, W. Si, A.D. West, X.X. Xi, Appl. Phys. Lett. **73**, 190 (1998).
3. B.H. Hoeman, G.M. Ford, Appl.Phys.Lett. **73**, 2248 (1998).
4. A.A. Volkov, B.P. Gorshunov, G. Komandin, W. Fortin, G.E. Kugel, and J. Grigas, J. Phys.: Condens. Matter **7**, 785 (1995).
5. A. Kania, Phase Transitions, **3**, 131 (1983).

Mat. Res. Soc. Symp. Proc. Vol. 655 © 2001 Materials Research Society

Dielectric and Piezoelectric Properties of PZT 52/48 Thick Films with (100) and Random Crystallorgraphic Orientation

Q. F. Zhou, E. Hong, R. Wolf, and S. Trolier-McKinstry
Materials Research Laboratory, The Pennsylvania State University,
University Park, PA 16802

ABSTRACT

Ferroelectric $Pb(Zr_{1-x}Ti_x)O_3$ (PZT) films have been extensively studied for active components in microelectromechanical systems. The properties of PZT films depend on many parameters, including composition, orientation, film thickness and microstructure. In this study, the effects of crystallographic orientation on the dielectric and transverse piezoelectric properties of $Pb(Zr_{0.52}Ti_{0.48})O_3$ (PZT 52/48) films are reported. Crack free random and highly (100) oriented PZT(52/48) films up to ~ 7 μm thick were deposited using a sol-gel process on Pt (111)/Ti/SiO_2/Si and Pt(100)/SiO_2/Si substrates, respectively. The dielectric permittivity (at 1kHz) for the (100) oriented films was 980-1000, and for the random films ~ 930-950. In both cases, tanδ was less than 0.03. The remanent polarization (~ 30 $\mu C/cm^2$) of random PZT films was larger than that of (100) oriented PZT films. The transverse piezoelectric coefficient ($d_{31(eff)}$) of PZT films was measured by the wafer flexure method. The $d_{31(eff)}$ coefficient of random PZT thick films (-80pC/N) was larger than that of (100) oriented films (-60pC/N) when poled at 80 kV/cm for 15 min.

INTRODUCTION

Recently, there has been an increasing interest in ferroelectric lead zirconate titanate (PZT) films because of their wide range of applications in microelectronics, microelectromechnical systems (MEMS) and ultrasonic imaging. Potential applications include membrane sensors [1], micro-accelerometers [2] and micro-motors [3]. In general, these devices are based on films of thicknesses less than 1 μm. However, applications based on piezoelectric films are not limited to the realm of microdevices, and some potential applications require more thick films that have large piezoelectric coefficients and high energy densities. Therefore, PZT thick films are of interest.

There are a number of groups which have successfully fabricated PZT system thick films. Tsuzuki et al. [4] prepared PLZT thick films by multiple electrophoretic deposition and sintering processing. Sayer et al. [5] have reported the thick PZT ceramic coating using a sol-gel based ceramic-ceramic 0-3 composites. Cross et al. [6] prepared the PZT thick films by modified sol-gel process using acetic acid route. Milne et al. [7] also fabricated the PZT thick films using titanium diisopropoxide biacetylacetonate as raw materials. However, preparing thick uniform PZT films with large area by the sol-gel technique is still challenging due to cracking that results from large stresses between the substrate and film.

In this paper, crack-free sol-gel PZT thick films with the morphotropic phase boundary (MPB) composition of $Pb(Zr_{0.52}Ti_{0.48})O_3$ (PZT 52/48) were deposited on Pt(111)/Ti/SiO_2 and Pt (100)/SiO_2/Si substrates, respectively. The dielectric and piezoelectric properties of PZT films with different orientation were investigated.

EXPERIMENTAL PROCEDURES

The sol-gel PZT solutions were prepared using 2-methoxyethanol (2-MOE) as the solvent. Initially, lead acetate trihydrate was dissolved in 2-methoxyethanol at 80 °C, then refluxed at 115 °C for 1hr under Ar. The water of hydration was distilled at 115 °C under vacuum (~130 mbar). Appropriate quantities of zirconium n-propoxide and titanium iso-propoxide were stirred in 2-MOE at 25°C. Upon completion of the dehydration step, the rotary flask containing the lead acetate complex was cooled well below 100°C and the zirconium and titanium precursors were added. This mixture was refluxed for 2 hr at 120°C. To compensate for lead volatilization during film heat treatments, 20mol% excess lead was added to the solutions.

Following the reflux step, the solution was distilled at 120°C again with the aid of vacuum. The mixture was allowed to cool to room temperature, and 22.5 vol% acetylacetonate (2,4 pentanedione) was introduced while stirring, which acted as a chelating agent to prevent solution hydrolysis in the presence of atmospheric moisture. 2-MOE was added to achieve a final solution with 0.75 molar concentration.

The solution was deposited onto platinized silicon substrates [Pt(111)/Ti/SiO_2/Si, Nova Electronics; Pt(100)/SiO_2/Si, Inostek Inc.] by spin-coating at 1500 rpm for 30 seconds on a photoresist spinner. After deposition, each layer was subjected to a two-stage pyrolysis sequence to drive out solvent and decompose organic compounds. A 1 minute heat treatment at 300°C was immediately followed by one at 450°C (1 minute). The amorphous layer was then crystallized to phase-pure perovskite at 700°C for 30 seconds using rapid thermal annealing (RTA). Every layer thickness is about 0.2 μm. Thicker PZT films were fabricated by repeating this procedure to achieve the desired film thickness [8]. Platinum top electrodes with diameters of 1.5 mm were sputter deposited and then annealed at 700°C for 20 seconds by RTA prior to electrical characterization.

The structure of the PZT films was examined using a Scintag x-ray diffractometer (XRD) with Ni filtered CuKα radiation. The x-ray diffraction (XRD) patterns were recorded at a rate of 1°/min in the 2θ range of 20°-60°. The thickness of the films was measured using a surface profiler (Tencor Instruments). The morphology of the films was observed using a scanning electron microscope (SEM; Hitachi, S-3500N) and atomic force microscope (AFM, Digital Instruments Nanoscope). The dielectric permittivity was measured using an impedance analyzer (HP4194A, Hewlett-Packard) with an oscillation amplitude of 30 mV. High field hysteresis properties were characterized using a RT66A (Radiant Technology, Albuquerque, NM) ferroelectric test system. The transverse piezoelectric (d_{31}) coefficients of the films were characterized using a modification of wafer flexure method described previously [9]. The aging rate of the d_{31} coefficients was measured after the poling field was removed.

RESULTS AND DISCUSSION

Figure 1 shows the XRD patterns of 0.45 μm to 7 μm PZT thick films deposited on (111)-Pt(120nm)/Ti(20nm)/Si(200nm)/ substrates heated at 700°C for 30 seconds. It can be seen that highly (111) preferred orientation occurs in PZT films with thicknesses less than 1.2 μm as shown in figure 1(a) and 1(b). At these thicknesses, orientation is strongly affected by the (111)

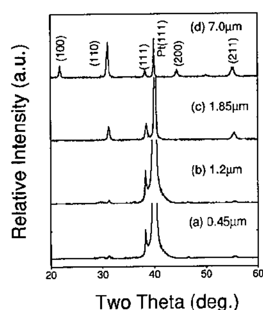

Figure 1. XRD patterns of the sol-gel derived PZT 52/48 films deposited on Pt(111)/Ti/SiO$_2$/Si substrates with different thickness (a) 0.45 μm, (b) 1.2 μm, (c) 1.85 μm and (d) 7.0 μm

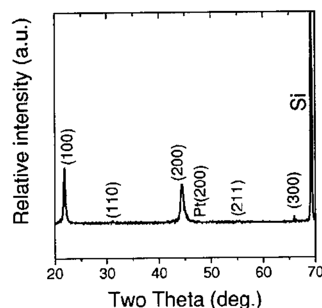

Figure 2. XRD patterns of sol-gel derived 7.3 μm PZT 52/48 film deposited on Pt (100)/SiO$_2$/Si substrates

Pt/Ti electrodes. However, the intensity of the (111) perovskite peak decreases with increasing thickness from 1.8 μm to 7.0 μm as shown in figure 1(c) and 1(d). That is, for this processing route, on (111)-oriented electrodes PZT films approach random orientation with increasing thickness. This may come from a mismatch between every layer during sol-gel deposition. Figure 2 shows the XRD patterns of 7.3 μm PZT thick films deposited on (100)-Pt(150nm)/SiO$_2$(300)nm/Si substrates. These films have highly (100) preferred orientation, suggesting nucleation dominated by the oriented Pt electrode. Only very small (110) and (211) peaks were observed in figure 2.

Figure 3 shows SEM pictures of random and (100) oriented PZT films. The cross sectional view of the films shows that the thickness was over 7 μm, every layer corresponds to one crystallization step, and grains are approximately equi-axed. Figure 4 shows AFM surface images of random and (100) oriented PZT films. From figure 4(a) it is seen that the (100)

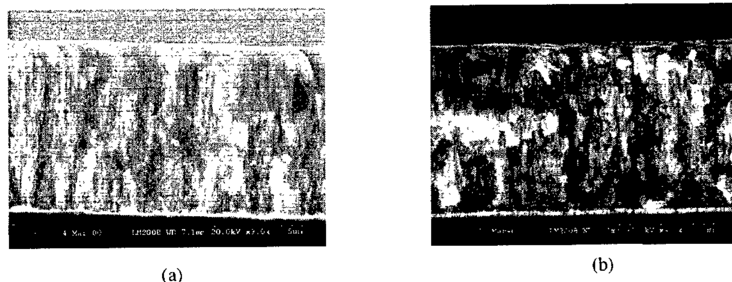

(a) (b)

Figure 3. SEM cross sectional views for sol-gel derived PZT films (a) (100) oriented film and (b) random film

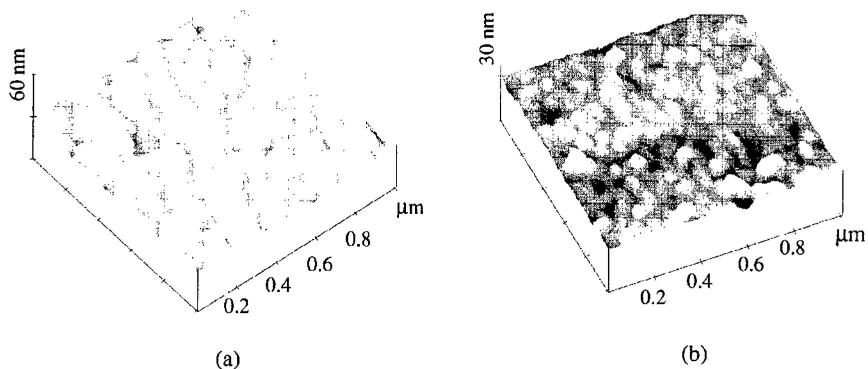

Figure 4. AFM images of surface sol-gel derived PZT (a) (100) oriented film and (b) random film

oriented film consisted of large grains with grain sizes ranging from 100 nm to 130 nm. Random PZT films consisted of uniform small grains as shown in figure 4(b), an average grain size of about 80 nm. The difference in grain size may stem either from the difference in the nucleation rate of films for the two different electrode orientations or from differences in the electrode grain sizes.

The frequency dependence of dielectric permittivity at room temperature for the random and (100)-oriented films is shown in figure 5(a) and (b). It can be seen that the dielectric constant (~985) of the (100) oriented film at 1 kHz was slightly higher than that (~950) of the random film. In both cases, the dielectric loss of the films was below 0.03 at 1kHz (room temperature).

The ferroelectric hysteresis loops of random and (100) oriented PZT 52/48 thick films are

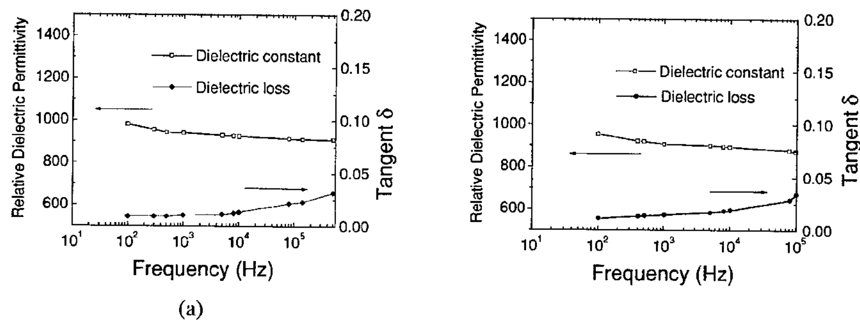

Figure 5. Frequency dependence of dielectric permittivity and loss at room temperature for PZT films (a)(100) oriented and (b) random films

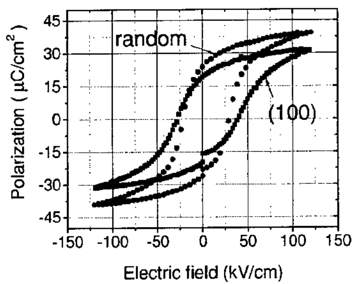

Figure 6. Polarization as a function of electric field for random and (100) oriented PZT 52/48 thick films

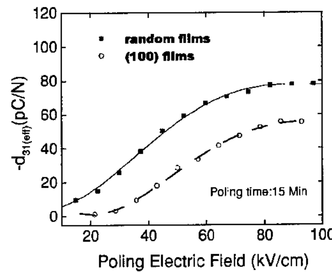

Figure 7. The d_{31} coefficient of random and (100) oriented PZT thick film with different poling electric field for 15 Min

shown in figure 6. The remanent polarization (P_r) in the random films is about 30 μC/cm^2 for E_{max} = 180 kV/cm, and the saturation polarization (P_s) is over 40 μC/cm^2. When compared for the same field level the P_r and P_{max} of random PZT films are larger than those of (100) oriented PZT films shown in figure 6.

The d_{31} coefficients of the films were characterized using a modification of the wafer flexure technique [10]. The effective piezoelectric coefficient $d_{31(eff)}$ of the films can be determined by the stress-strain relationship using plate theory [11]. The in-plane stress (σ_1) of the films generated by a pressure difference in the cavity is,

$$\sigma_1 = E\,\varepsilon / 1\text{-}\nu, \qquad (1)$$

where E is the Young's modulus of the film (Young's modulus of PZT films is 101GPa), ν the Poisson's ratio of the sample (~1/3), and ε the in-plane strain in the sample mounted on the stress rig measured with a strain gauge.

Supposing that the biaxial stress (σ_{tot}) is the same for the perpendicular direction on the sample surface,

$$\sigma = \sigma_1 + \sigma_2, \qquad (2)$$

$d_{31(eff)}$ can be obtained by

$$d_{31(eff)} = Q / 2\sigma_1 A, \qquad (3)$$

where Q is the charge, and A the area of top electrode. Figure 7 shows the $d_{31(eff)}$ coefficient of random and (100) oriented PZT thick film with different poling electric fields (the poling time was 15 minutes). The $d_{31(eff)}$ increased as the poling field approached the coercive field of the film, and then saturated at a poling field of about three times the coercive field. The random PZT films had a larger piezoelectric coefficient (-80 pC/N) compared to the (100) oriented films (-60 pC/N). It is suggested that this is due to the larger intrinsic contribution for piezoelectric properties in random PZT films which showed larger remanent polarizations than (100) oriented films (see figure 6).

The aging rates of the transverse piezoelectric coefficient for random and (100)- oriented PZT films were also measured using the wafer flexure technique. The $d_{31(eff)}$ coefficients were monitored at regular intervals after poling at 80 kV/cm for 15 minutes, and normalized $d_{31(eff)}$ were plotted versus the logarithm of time. The aging rates were then obtained from the slopes. The aging rate of the random PZT film was about 4.2% / decade, and (100) oriented films was about 9% / decade. In addition, it was found that the $d_{31(eff)}$ coefficients is different when top electrode connect positive or negative during poling, detail results will be reported.

CONCLUSIONS

Random and (100) oriented PZT (52/48) films up to ~ 7 μm thick were fabricated using a modified sol-gel process on Pt (111)/Ti/SiO_2/Si and Pt (100)/SiO_2/Si substrates, respectively. The dielectric permittivity (at 1kHz) of the (100)-oriented films was slightly higher than that of the random films. In both cases, the dielectric loss was less than 0.03. However, the remanent polarization of random PZT films was larger than that of (100) oriented PZT films. The transverse piezoelectric coefficient ($d_{31(eff)}$) of random PZT thick films was also larger than that of (100)-oriented films when poled at 80 kV/cm for 15 min. The aging rates of PZT films was in the range of 4-9% per decade.

ACKNOWLEDGMENTS

Support from the office of Naval Research is gratefully acknowledged.

REFERENCES

1. D. L. Polla, SPIE, **24**, 3046(1997).
2. K. R. Udayakumayer, J. Chen, K. G. Brooks, L. E. Cross, A. M. Flynn, and D. J. Erlich, Mat. Res. Soc. Sym. Proc. **49**, 243(1991).
3. H. Van Lintel, F. Vander Pohl and S. Boustra, Sensors and Actuators A **153**, 15(1988).
4. S. Sugiyama, A. Takagi and K. Tsuzuki, Jap. J. Appl. Phys., **30**, 2170(1991).
5. D. A. Barrow, T. E. Petroff and M. Sayer, Surface and Coating Technology, **76**, 113(1995).
6. H. D. Chen, K. R. Udayakumar, C. J. Gaskey and L. E. Cross, J. Am. Ceram. Soc., **79**, 2189(1996).
7. R. Kurchania and S.J.Milne, J. Mater. Res., **14**, 1852(1999).
8. Q. F. Zhou, H. L. W. Chan and C. L. Choy, Thin Solid Films, **375**, 95(2000).
9. J. F. Shephard Jr., F. Xu, I. Kanno, and S. Trolier-McKinstry, J. Appl. Phys., **85**, 6711(1999).
10. J. F. Shepard, Jr., P. J. Moses, and S. S.Trolier-McKinstry, Sensors and Actuators A **71**, 133(1998).
11. S. Timoshenko and S. Woinowsky-Krieger, Theory of Plates and Shells (McGraw Hill Inc, New York 1959).

Mat. Res. Soc. Symp. Proc. Vol. 655 © 2001 Materials Research Society

Piezoresponse measurement and imaging of electromechanical PZT and PZN-BT thin films

C. Morros, M.H.Corbett, G. Catalan, J.M. Gregg and R.M. Bowman
Condensed Matter Physics & Materials Science Research Division,
School of Mathematics & Physics,
Queen's University of Belfast
Belfast BT7 1NN UK

ABSTRACT

Pulsed laser deposition (PLD) was used to growth thin films of lead zirconium titanate (PZT) and lead zinc niobate-barium titanate (PZN-BT). The PZT films were prepared from commercial PZT-5H ceramic target and the PZN-BT made from target made using a modified Columbite method. The PZT films had dielectric constants of 300 and loss of 0.03 at 10kHz, whilst for the PZN-BT films they were 350 and 0.03 respectively at 300K. Hysteresis measurements confirmed their switching properties

A piezoresponse microscope based on a modified atomic force microscope was developed to determine electromechanical response at a sub-micrometer resolution. The PZT films yielded d_{33} ~100pm/V. Mapping measurements on the PZT demonstrated local switching of individual grains. First measurements of piezoresponse of PZN-BT yielded values in the region 150-200 pm/V.

INTRODUCTION

Recently there has been great interest in thin film applications of electroceramics, for example for high frequency ultrasound imaging of tissue [1]. This has resulted in effort to prepare and characterise electroceramic materials and their responses at the micron and sub-micron level. Conventional methods such as laser Doppler interferometry are of little use, particularly with the potential for small sample geometry's in thin films. Recently, piezoresponse imaging (a generic term to describe scanning probe microscope based electromechanical measurement) has been developing particularly with lead zirconium titanate (PZT) films [2,3]. Much of the work is stimulated by applications of PZT for memory and electronics application.

In this paper we describe the development of our piezoresponse microscope and demonstrate its functionality by measurement of the properties of routine PZT thin films. Due to the difficulty of synthesis, a small number of groups have access to high quality elecrostrictive thin films such as lead magnesium niobate (PMN) and lead zirconium niobate (PZN) of interest in next generation transducer and actuator applications. Therefore, few if any, investigations by piezoresponse on these systems have been reported. In this paper we report for the first time the electromechanical response of $Pb(Zn_{1/3}Nb_{2/3})O_3$-$BaTiO_3$ (PZN-BT) films using piezoresponse techniques.

EXPERIMENT

PZT thin film growth

The thin films were prepared by standard pulsed laser deposition. A $SrRuO_3$ conducting lower electrode is grown on the substrate prior to the growth of the electroceramic thin film. This takes place at 800 °C and the $SrRuO_3$ is typically 150 nm thick.

For PZT growth we used a 1" diameter polycrystalline ceramic disc cut from a rod of commercial PZT-5H (Morgan-Matroc). The films were prepared using conditions similar to our protocols for other lead based compounds [4]. The PZT films discussed below were deposited at a temperature of 600 °C. The pressure during deposition was 0.25 mbar of flowing oxygen. Deposition times varied but typically 15 minutes at a laser repetition rate of 10 Hz and energy density of ~ 2.5J/cm^2 yielded a film of around 400 nm thickness. On completion of the PZT deposition substrate temperature was raised to 615 °C oxygen pressure ramped to 900 mbar. The film was then annealed for one hour at these conditions to ensure complete oxygenation. Without this anneal the electroceramic thin films typically exhibit high dielectric loss [5].

X-ray diffraction confirms that the films grow in a high oriented state with respect to the substrate. Compositional measurements indicate good stoichiometry.

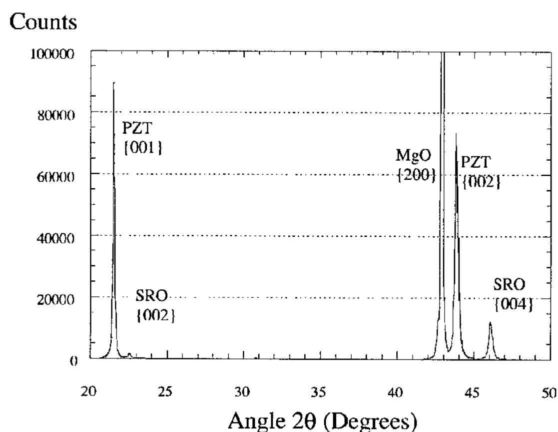

Figure 1. θ-2θ scan of a {100}MgO/$SrRuO_3$/PZT thin film structure

The dielectric performance of PZT films were determined at room temperature using a HP 4263B LCR meter and a Radiant Technologies Precision Workstation. Small gold contact pads were thermally evaporated on the top of the PZT film and the two capacitors in series model was assumed. Dielectric constant were typically 300-400 at 10 kHz and the dielectric loss (tan δ) was 0.01. Hysteresis loops (Figure 2) confirmed the quality of the PZT thin films.

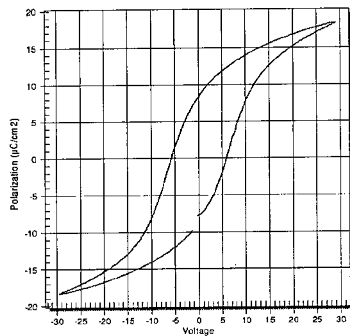

Figure 2. Polarisation hysteresis loop of a 400 nm thick PZT thin film grown at 600 °C

PZN-BT thin film growth

The 20%{$Pb(Zn_{1/3}Nb_{2/3})O_3$} - 80%{$BaTiO_3$} films (0.2PZT-0.8BT) were prepared from a target made using a modified Coulombite method [4] whose first stage pre-fires weighted stoichiometric amounts of ZnO and Nb_2O_5, with 1% excess ZnO. In the second stage PbO and $BaTiO_3$ are added and the mixture is re-fired and then pressed and sintered in air to form the target. The target composition was confirmed by microprobe measurement.

The films and capacitor structures were grown in the same way as described above. In this case the 0.2PZN-0.8BT layer was deposited at 600 °C, in 0.25 mbar of oxygen, followed by an anneal in 900 mbar oxygen at 615 °C, for one hour.

Dielectric characterisation of the 0.2PZN-0.8BT showed relaxor behaviour with dielectric constant of ~350 and tan δ of ~0.03 at 10kHz in room temperature.

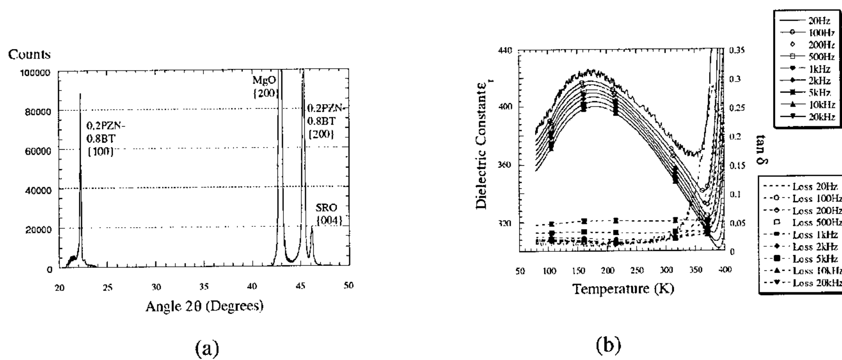

Figure 3. (a) θ-2θ scan of a {100}MgO/$SrRuO_3$/0.2PZT-0.8BT thin film structure, (b) temperature dependence of dielectric constant and loss at various frequencies

Piezoresponse microscope

The piezoresponse microscope is constructed around a Digital Instruments Nanoscope E atomic force microscope, in manner similar to several groups in the literature [2,3]. Briefly, the microscope is operated in contact mode and the external driving signal from a HP 33120A source is supplied to the sample via contact made to either the lower electrode or the Au upper contacts. The oscillations induced in the microscope tip by the vibration of the thin film surface are measured in a phase–locked loop using a EG&G 5209 lock-in amplifier. In most of the experiments reported a conducting Pt/Ir coated Si tip is used; it has a spring constant of 0.28 N/m and a resonant frequency greater than 60 kHz. A schematic diagram of the microscope is illustrated in Figure 5.

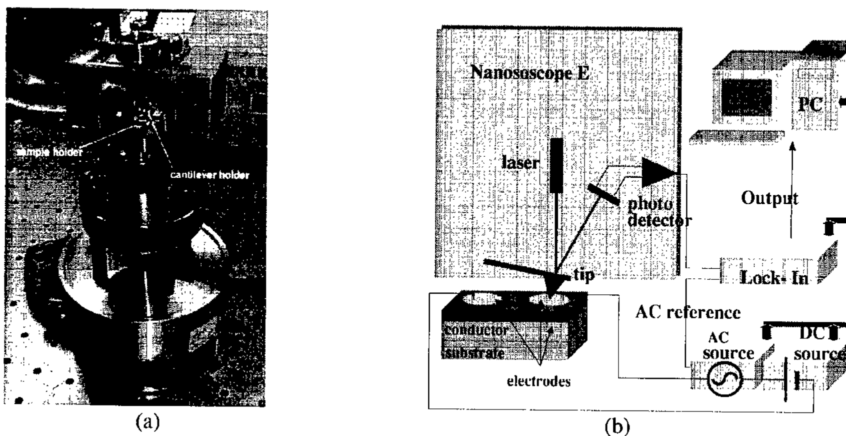

Figure 4. (a) Photograph of the Nanoscope E AFM head, (b) block diagram of the microscope and ancillary instrumentation.

RESULTS

Piezoresponse of PZT films

Measured d_{33}-V loops on the electrodes of the PZT film are plotted in Figure 5. Different behaviour is observed on each electrode and experiments not reported here show that there is some variation in the measured d_{33} values on the same electrode.

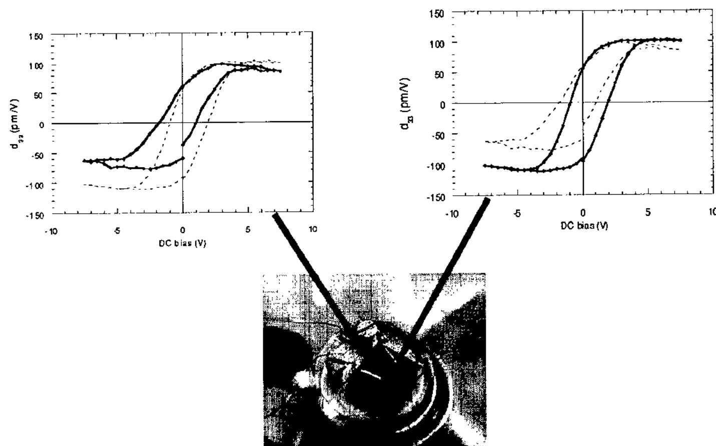

Figure 5. Piezoresponse loops taken on the Au contacts as indicated in the photograph. The dashed lines in the graphs is the loop measured on the other electrode for comparison.

Piezoresponse scanning images were also obtained with the PZT thin film. Figure 6 shows the topography and piezoresponse images acquired simultaneously. The piezoresponse images were obtained using a 3 V_{RMS} and 10 kHz voltage with a conducting tip acting as the upper electrode and the $SrRuO_3$ as the lower electrode in the capacitor. After the scan, the tip was kept on the position marked with a cross and a dc voltage level of 25 V was applied for 5 s. The scanning was resumed with the dc voltage reset to zero. The result of the poling is shown in Figure 6(b). Comparison of between Figures 6 (a) and (b) shows the reversing of the piezoresponse signal corresponding to the grain being poled. Note that switching has changed some of the neighbouring grains as well.

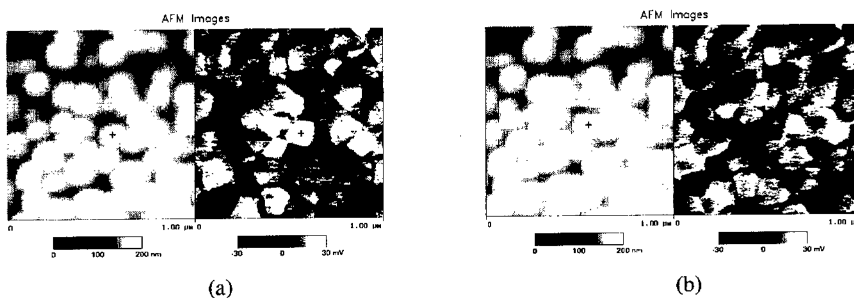

Figure 6. (a) Topography and piezoresponse of a PZT film and (b) after applying 25V at the position + for 5 seconds.

Piezoresponse of PZN-BT

The electromechanical response of the 0.2PZN-0.8BT film was measured using piezoresponse. In this case a Si_3N_4 tip was located on the gold electrode of the capacitor. Then a 1 V_{RMS} 10 kHz signal was applied and the deflection monitored as a function of applied field. The results are shown in Figure 7. A maximum response of ~180 pm/V was obtained.

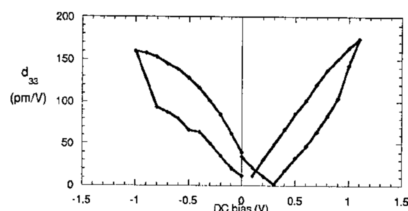

Figure 7. Piezoresponse of a PZN-BT films measured on a Au electrode in a capacitor structure.

DISCUSSION

PZT d_{33} loops measured on both electrodes have magnitudes in agreement with the results reported [2]. Reversing of the piezoresponse signal indicates that polarisation has been reversed accordingly. In Figure 6 we note that a "black" grain in contact with the grain being poled is switched to "white" whereas the sense of the poling was "white-to-black". Such effect could be the result of induced polarisation reversing due to domain interaction. Further investigation of the the switching observed and its relation to the in-plane mineralogy and surface topography of the film is required. Electromechanical response of 0.2PZN-0.8BT films has been measured and has been reported for the first time. The results show hysteresis in d_{33} behaviour.The d_{33max} values obtained are about one order of magnitude lower than those reported on related composite PZN-PT in bulk single crystal form [6]: $d_{33\ max}$ ranged from ~1100 pm/V (PZN) up to ~2500 (0.92PZN-0.08PT) in <001> oriented rhombohedral crystals. Closer values were reported [7] on thin film 0.9PMN-0.1PT: d_{33max} ~65 pm/V measured with AFM, in agreement with the interferometer measurements on thin film PMN [8] yielding d_{33max}~62 pm/V.

REFERENCES

1. E.P.Papadakis (ed.) *Ultrasonic Instruments and Devices*, Academic Press, (1999).
2. C.S.Ganpule, A.Stanishevsky, S.Aggarwal, J.Melngailis, E.Williams, V.Joshi and C.Paz de Araujo, *Appl.Phys.Lett.* 75, 3874-3876 (1999).
3. A.Gruverman,O.Auciello,R.Ramesh & H.Tokumoto, *Nanotech.* **8**, A38-A43 (1997).
4. M.Corbett,G.Catalan,R.M.Bowman & J.M.Gregg, *J. Mater. Res.* **14**, 2355-2358 (1999).
5. G.Catalan,M.Corbett,R.M.Bowman & J.M.Gregg, *Appl.Phys.Letts.* **74**, 3035-3037 (1999)
6. 6. Seung-Eek Park & Thomas R. Shrout, *J.Appl.Phys.* **82** 1804-1811 (1997).
7. 7. V.Nagarajan, S.P.Alpay, C.S.Ganpule, B.K.Nagaraj, S.Aggarwal, E.D.Williams, A.L.Roytburd & R.Ramesh, *Appl. Phys. Letts.* **77** 438-440 (2000).
8. 8. Z.Kighelman,D.Damjanovic,A.Seifert,L.Sagalowicz & N.Setter, *Appl. Phys. Letts.* **73** 2281-2283 (1998).

Mat. Res. Soc. Symp. Proc. Vol. 655 © 2001 Materials Research Society

A DIELECTRIC BOLOMETER BEHAVIOR OF BST THIN FILM PREPARED BY METAL-ORGANIC-DECOMPOSITION WITH EXCELLENT REPRODUCIBILITY IN THERMAL CYCLING TEST

Minoru Noda, Hong Zhu, Huaping Xu, Tomonori Mukaigawa, Kazuhiko Hashimoto and Masanori Okuyama, Osaka Prefecture Super-Eye-Image-Sensor (SEIS) Project, Osaka, JAPAN.

ABSTRACT

We have proposed a new type of simple detector pixel circuit and device structure for application of dielectric bolometer mode (DB) of infrared (IR) image sensor. The DB mode has merits such as uncooled room temperature operation, chopperless, low power dissipation, and high-sensitivity. A stable $Ba_{1-x}Sr_xTiO_3$ (BST) thin film has been successfully developed as a dielectric bolometer material for IR detector by Metal-Organic-Decomposition (MOD) method. The film was prepared on both $Pt/Ti/SiO_2/Si$-bulk and $Pt/Ti/NSG/Si_3N_4/SiO_2$ membrane structures, where an IR light is detected at the membrane as a change in dielectric constant (ε). So, the important issue for realizing a reliable IR sensor with high-sensitivity has been achieved to have a good thermal stability in ε against change in the detector temperature. XRD patterns and D-E hysteresis curves were measured and revealed that the BST film has a good perovskite structure and shows an adequate ferroelectric loops, especially for final annealing temperature higher than 700℃. Temperature Coefficient of Dielectric constant (TCD), which decides the IR sensitivity, of the MOD made BST film is about 1 %/K. The reproducibility in ε, namely IR detector capacitance, was found to be very good in temperature ranging from about 10 to 80 ℃ within a relative change of 2 %. Finally, the stabilities in both the temperature dependence of ε and the output level have been obtained with a fairly large IR detectivity, where voltage sensitivity(R_v) and specific detectivity(D^*) were about 1.2 kV/W and 2.9e8 cmHz $^{1/2}$/W, respectively.

1. INTRODUCTION

Recently, development of highly-sensitive, low-cost, uncooled thermal detectors or imagers has increasingly become a mainstream activity in the field of infrared (IR) sensing[1]. In order to close the performance gap by attaining the ultimate noise-equivalent-temperature-difference (NETD) about 5mK set by uncooled thermal detection mechanism[2], various new monolithic schemes have been envisioned to integrate advanced sensor material processes and micromachining techniques with existing on-chip Si-readout technology. Especially dielectric bolometer (DB) using ferroelectric film is very advantageous due to its chopperless operation, high-sensitivity like pyroelectric mode and low power operation, to fabricate an excellent IR imager.

This paper deals with 1) BST thin film for DB mode detector prepared by Metal-Organic-Decomposition, 2) electrical properties of BST thin film capacitor as a DB mode detector, featuring reproducibility of temperature dependence of BST capacitance after thermal cycling, and 3) resultant IR response in the detector.

2. DETECTOR PIXEL STRUCTURE OF DB MODE

Figures 1(a) and (b) show our developed detector pixel circuit and its device structure at an IR-detecting capacitor, where the circuit operation was described in detail elsewhere[3]. A main operation in the dielectric bolometer-type detector is as follows, 1)when temperature of ferroelectric material in the detecting capacitor is increased compared to the other reference capacitor, its dielectric constant changes and therefore its capacitance becomes changed, 2)the change in the capacitance is detected as a voltage change, which is amplified through some operational amplifiers. As one of the DB mode detector circuit, the serially-connected capacitor-capacitor circuit was selected because its simple configuration is very effective in reducing its pixel size and then increasing the pixel density in an Uncooled Focal Plane Array (UFPA). A source-follower output buffer was also added to the output stage in the detector pixel circuit in order to reduce output impedance, therefore resulting in noise reduction.

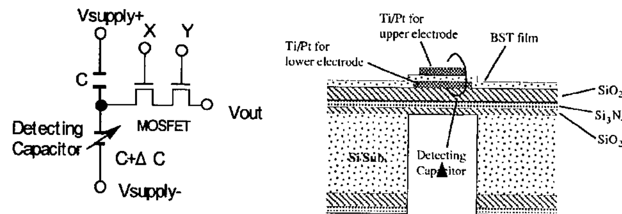

Figures 1. (a) Detector pixel circuit and (b) its device structure at an IR-detecting capacitor.

3. PREPARATION OF BST THIN FILM BY MOD

Metal-Organic-Decomposition (MOD) solutions of 0.06 M (mol/liter) with Ba/Sr ratio of 75/25 have been used to prepare BST film. The precursor solution was prepared by complex of barium carboxylate($Ba(COOH)_2$), strontium carboxylate($Sr(COOH)_2$) and titanium alcoholate($Ti(OR)_n$), which were from Kojundo Chemical Laboratory Co. Ltd. The deposition process and parameter is listed in Table I. A typical process to make BST film is to spin-coat the solution on the micromachined Si wafer at 4000 rpm, 20 seconds at first; then the film is baked on hot plate at 150 °C for 10 minutes to remove the solvent; and then the film is given a pyrolysis heat treatment in a silica tube furnace at 470 °C for 30 minutes in air to remove the residual organics and promote chemical reaction. All the three processes were repeated several times until the desired thickness of the film is obtained. Finally, the film with certain thickness is annealed in the furnace in air at 600-800°C for 5 to 60 minutes to make the thin film become crystallized. Usually a 10-layer BST film is deposited with a thickness about 400 nm. The bulk substrate material of $Pt/Ti/SiO_2/Si$ is used to find the best condition to deposit BST film. The micromachined Pt/Ti/NSG(Non-doped Silicate Glass)/$Si_3N_4/SiO_2/Si$ chip is used to fabricate the sensor. The ferroelectric properties of the BST film are measured with RT6000 System(Radiant Technologies Co.).

1. Spin coating	500 rpm 5 sec,
	2000~4000 rpm, 20 sec
2. Drying	150 ℃, 10 min.
3. Prebaking	470 ℃, 30 min.
4. Final annealing	600 ~ 800 ℃, 5~60 min.

Table I. Process and parameters of MOD.

4. CRYSTALLINE AND FERROELECTRIC PROPERTY OF BST THIN FILM

A good BST film should have a smooth surface and should have no macro- or micro-cracks for capacitor fabrication. A smooth surface is very important to the later process in the sensor fabrication as the upper Pt/Ti electrode is directly deposited and patterned on the BST surface. What is more, cracks in BST film will have serious effects on the electrical property. The surfaces of the BST films deposited at different spin-coating rates and under different final annealing temperatures have been observed under optical microscope and all the samples are prepared on bulk material of $Pt/Ti/SiO_2/Si$ substrate. It was found that the films spin coated at 2000 rpm all have macro-cracks even though they are annealed at different temperatures of 600, 700 and 800 ℃. This is because each layer of the film spin coated at 2000 rpm is thick and this makes the final film have high internal stress during the final high temperature annealing process. The surface of the BST films spin coated at 3000 and 4000 rpm, on the other hand, are good and no macro-crack is observed. Therefore, the film deposited at low spin coating rate tends to have crack on the substrate, so the film should be deposited at a high spin coating rate. Between 3000 rpm and 4000 rpm spin coating rate, 4000rpm is preferred as it gives a thinner thickness of each layer.

Figure 2 shows the X Ray Diffraction (XRD) patterns of BST films spin-coated at 4000rpm annealed for 1 hour at 600, 700 and 800 ℃, respectively. Depending on the precursors a Ba-Ti-O-carbonate phase is possible to be seen in XRD charts as intermediate phase. It is estimated from the chart BaO_x especially BaO or $BaCO_3$ phases are existed. BST film annealed at 600 ℃ shows the broad BaO_x peak, but does not show any perovskite BST (101) and (110) peaks, which shows that the BST crystalline is not formed at 600 ℃. Films annealed at 700 and 800 ℃ show perovskite BST (101) and (110) peaks dominating pattern, which

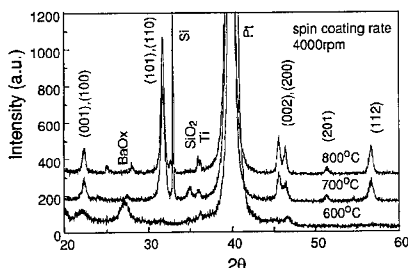

Figure 2. XRD patterns of BST films spin-coated at 4000 rpm annealed at different temperatures for 1 hour.

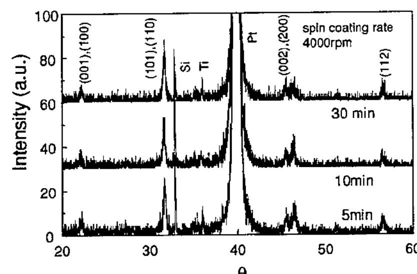

Figure 3. XRD patterns of BST films spin-coated at 4000 rpm annealed at 800 ℃ with different annealing time.

shows the film becomes crystallized at these temperatures. The film annealed at 800 °C seems to have a large and better crystalline than that annealed at 700 °C, as its (101) and (110) peaks have higher intensities and are sharper than those of (101) and (110) peaks annealed at 700 °C. From the XRD results, it is clarified that the best condition to anneal the BST film is more than 700 °C.

Figure 3 shows the XRD patterns of the films spin coated at 4000 rpm and annealed at 800 °C for 5, 10 and 30 minutes, respectively. The three films all have almost the same XRD pattern. In the case of the film annealed for 5 minutes, the main peak of BST can be seen clearly, which means that the film has become crystallized. It seems that the annealing temperature is more important than annealing time. At a proper temperature, even a short time annealing is enough to make the film become crystallized.

Figure 4 shows the surface micrograph of BST film observed by Atomic Force Microscope (AFM). The

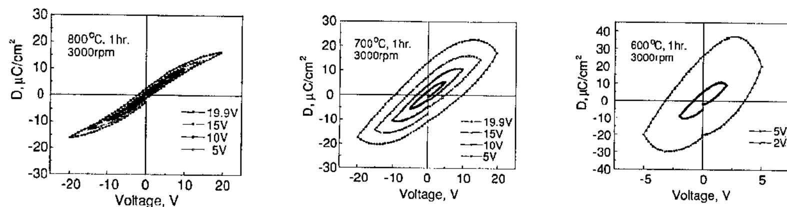

Figure 5. Hysteresis loops of BST film spin coated at 3000 rpm annealed for 1 hour with different annealing temperatures.

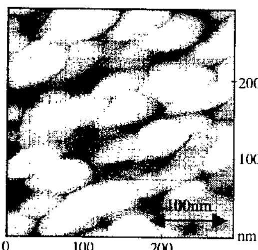

Figure 4. AFM image of the BST film spin coated at 4000 rpm annealed at 800 °C for 1 hour.

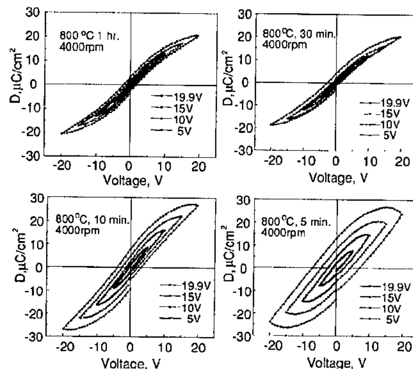

Figure 6. Hysteresis loops of BST film spin coated at 4000rpm annealed at 800°C temperature with different annealing time.

grain size of film spin-coated at 4000 rpm, annealed at 800 °C for 1 hour is not large, and in the range from 50 to 80 nm. Observed from a three dimensional view, the surface of the film is very smooth and the roughness is about 10 nm.

Figure 5 shows the hysteresis loops of BST film spin-coated at 3000rpm annealed for 1 hour at different temperatures. The films annealed at 800 and 700 °C can withstand 20 V bias, while the film annealed at 600 °C can only withstand 5 V bias. The best loop among them is the one annealed at 800 °C, a slim sloop, while a fat loop when annealed 700 °C. The film annealed at 600 °C almost shows a leak loop. Considered

from the XRD patterns of the films annealed at different temperatures in Fig. 1, the BST crystalline almost has not formed when the film is annealed at 600 ℃. The films annealed at 800 and 700 ℃ almost have the same XRD pattern, showing clear perovskite BST peaks, but their hysteresis loops are quite different from each other. This indicates that the microstructure has great effects on the electrical property of the BST film.

Figure 6 shows the hysteresis loops of BST film spin-coated at 4000rpm annealed at 800 ℃ with different annealing time. The four kinds of films all can withstand 20 V bias. The loops of the films annealed for 60 and 30 minutes are almost the same, a slim loop showing typical ferroelectric characteristics in both cases. The loops of the films annealed for 10 and 5 minutes are not as good as those annealed for 60 and 30 minutes, both showing a fat loop. The loop of the film annealed for 10 minutes is better than that annealed for 5 minutes. Then it seems that the ferroelectric property of the film annealed for long time is better than that annealed for short time. This is probably because that long time annealing tends to result in grain growth and resultant larger grain size of the film. From the XRD pattern in Fig. 2, we can see that the films annealed for 30, 10 and 5 minutes almost have the same kind of XRD pattern, but their hysteresis loops are quite different from each other. Therefore, we should say that the microstructure of the film has great effects on the ferroelectric property of BST film. Many papers have reported that the ferroelectric properties have great connection with the grain size of the film [4]. And that BST film with large grain size tends to have better ferroelectric property. Considering that long time annealing tends to show a BST film with large grain size, annealing time of 60 minutes is preferred.

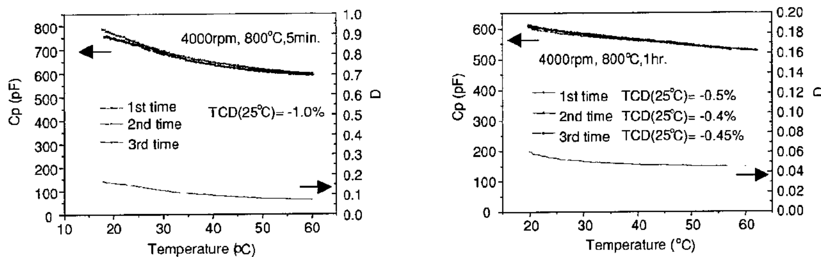

Figures 7. Capacitance in IR sensing capacitor vs. temperature with final annealing time of 5(a) and 60(b) minitues, respectively.

5. THERMAL CYCLING TEST IN TEMPERATURE DEPENDENCE OF BST CAPACITOR

To realize a high-sensitivity and practical usability in the DB-mode IR sensor, it is quite serious issue to have a stable and reproducible temperature dependence of capacitance in IR sensing capacitor after thermal cycling. We have measured, therefore, a number of the dependence using the above BST preparation conditions. Figures 7(a) and (b) show the capacitance in IR sensing capacitor vs. temperature with final annealing time of 5 and 60 minitues, respectively. For annealing time of 5 min. in Fig.7(a), it is found that the capacitance is monotonously decreased with the temperature for the measured temperature range and temperature dependence of dielectric constant(TCD) is about 1%/K. And that dielectric loss (D) is in the range between about 0.1 to 0.05. The difference in the C-T curves against the thermal cycling is fairly small,

although the curve seems to be more stablized after the first cycling. The most important point is that the difference in the TCD, namely the gradient of the curve, should be low against the thermal cycling around room temperature. For annealing time of 60 min. in Fig.7(b), on the other hand, the situation is almost the same as the former case but the stability against the thermal cycling seems to be better than the former within a relative change of 2%, although the TCD itself is smaller than the 1%/K. It is estimated that this is due to smaller dielectric loss (D), ranging from about 0.055 to 0.045, and film degradation by leakage is more suppressed than the former. Therefore, we have selected the latter annealing time of 60 minitues for IR sensor fabrication from the viewpoint of the TCD stability against the thermal cycling.

7. IR RESPONSE OF DETECTOR PIXEL

Figure 8 shows an IR response of a fabricated detector pixel with the MOD BST film. An IR chopping is used in order to make clear the difference between with and without IR irradiation, although the chopping is principally unecessary in the DB mode. It is found from the figure that the voltage sensitivity (R_v) and specific detectivity (D*) are about 1.2 kV/W and 2.9e8 cmHz $^{1/2}$/W, respectively, with noise voltage (V_n) of 100 nV. These values are fairly competitive with the state-of-the-art performance of the other type uncooled IR sensors[1,2].

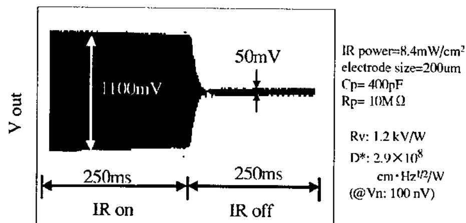

IR power=8.4mW/cm²
electrode size=200um
Cp= 400pF
Rp= 10MΩ

Rv: 1.2 kV/W
D*: 2.9×10⁸ cm·Hz¹ᐟ²/W
(@Vn: 100 nV)

Figure 8 IR response of a fabricated detector pixel with the MOD BST film.

CONCLUSIONS

A $Ba_{1-x}Sr_xTiO_3$ ferroelectric thin film for detector pixel of uncooled infrared (IR) image sensor was prepared and investigated by using MOD. Their electrical characteristics such as temperature dependence of capacitance and insulation are very good from the viewpoints of stability against thermal cycling. The MOD film was applied to our proposed DB mode of IR detector. Finally, the DB-mode operation in the detector pixel was confirmed on the integrated device structure, and the resultant voltage sensitivity (R_v) and specific detectivity (D^*) were observed to be about 1.2 kV/W and 2.9e8 cmHz $^{1/2}$/W, respectively. It is concluded that the BST film is sufficiently applicable to uncooled DB mode IR sensor fabrication.

REFERENCES

1. R. S. Balcerak: Proc. SPIE, **3698**, 110-118 (1999).
2. P. W. Kruse and D. D. Skatrud: Semiconductors and Semimetals 47, (San Diego: Academic Press, 1997).
3. M. Noda, K. Hashimoto, R. Kubo, T. Mukaigawa, H. Xu and M. Okuyama, Sensors and Actuators A, **77**, 39-44 (1999).
4. H.-F. Cheng, J. Appl. Phys. **79**, 7965-7971 (1996).

Mat. Res. Soc. Symp. Proc. Vol. 655 © 2001 Materials Research Society

Sol-Gel Derived Pyroelectric Barium Strontium Titanate Thin films for Infrared Detector Applications

Jian-Gong Cheng, Jun Tang, Shao-Ling Guo, Jun-Hao Chu
National Laboratory for Infrared Physics, Shanghai Institute of Technical Physics, Chinese Academy of Sciences, Shanghai 200083, China

ABSTRACT

$Ba_{0.8}Sr_{0.2}TiO_3$ thin films that are suitable for infrared detector applications have been prepared with a sol-gel process using a highly diluted precursor solution. Columnar structure with grain size close to 200 nm was obtained with layer-by-layer homoepitaxy due to a very small thickness of individual layer. The measured pyroelecrtic coefficient is larger than 3.1×10^{-4} C/m^{2}K at the temperatures ranging from 10 to 26 °C and reaches the maximum value of 4.1×10^{-4} C/m^{2}K at 16.8 °C. The infrared detectivity of 4.6×10^7 cmHz$^{1/2}$W^{-1} has been obtained at 19 °C and 10 Hz in the $Ba_{0.8}Sr_{0.2}TiO_3$ films deposited on thick (500 μm) platinum coated silicon substrates. The better infrared response can be expected by the improvement in the thermal isolation of pyroelectric element and the electrode materials.

INTRODUCTION

Barium strontium titanate (BST) has been extensively studied for advanced dynamic random access memory (DRAM) and uncooled infrared detector applications [1, 2], due to its high dielectric constant and composition dependent Curie temperature (from 30 to 400 K). Thin films of BST have been prepared by many growth techniques, such as rf-magnetron sputtering, laser ablation, metalorganic chemical vapor deposition [3-5], and sol-gel process [6-8]. Compared to other deposition methods, sol-gel process offers some advantages, such as homogeneity, stoichiometry control, and the ability to coat large and complex area substrates. However, the sol-gel derived BST films always fail to display pronounced ferroelectric hysteresis loops [6-8], which makes it unsuitable for infrared detector applications. In this paper, we report on the deposition of pyroelectric $Ba_{0.8}Sr_{0.2}TiO_3$ thin films that are suitable for infrared detector applications by a sol-gel process using a 0.05M solution precursor.

EXPERIMENTAL DETAILS

The starting materials were barium acetate, strontium acetate and titanium butoxide. Barium acetate and strontium acetate were mixed in a ratio of Ba/Sr of 4/1, and then dissolved into heated acetic acid. This was followed by an addition of equimolar amounts of titanium butoxide stabilized by appropriate acetylacetone under constant stirring. The mixture was then filtrated as

the stock solution. The coating solution of 0.05 M was prepared by diluting the stock solution with acetic acid. The $Ba_{0.8}Sr_{0.2}TiO_3$ films were deposited on $Pt/Ti/SiO_2/Si$ substrates by spin coating of the 0.05 M solution at 6000 rpm for 40 s. After coating of each layer, the films were given a pyrolysis heat treatment at 350 °C for 5 min to remove residual organics, and then annealed at 750 °C for 10 min in air. The average thickness of a single-coated as-annealed layer, measured by an ellipsometer, was found to be about 8 nm. The desired film thickness of approximately 800 nm was achieved by repeating the spin-coating and heat-treating cycles.

The structure of the films was analyzed with X-ray diffractometry (XRD; Model D5000, Siemens, Karlsruhe, Germany). The microstructure was observed using field emission scanning electron microscopy (FE-SEM; Model XL30 FEG, Philips, Eindhoven, the Netherlands). The electrical measurements were performed on the films in metal-ferroelectric-metal (MFM) configuration. Pt dots with an area of 3.4310^{-3} cm^2 were evaporated through a mask on the films to form metal-ferroelectric-metal (MFM) capacitors. The temperature dependence of dielectric constant was obtained with an HP4284 LCR meter (Hewlett-Packard, Palo Alto, CA). The pyroelectric coefficient p in the $Ba_{0.8}Sr_{0.2}TiO_3$ thin films was measured by a direct technique initially used by Byer and Roundy [9]. Prior to the measurement of p, the sample was poled at 9 V for 15 min at room temperature. The variation of spontaneous polarization produces a displacement current I parallel to the polar axis given by

$$I=A\,p(\mathrm{T})\frac{dT}{dt}, \qquad (1)$$

where p(T) is the pyroelectric coefficient evaluated at temperature T, $\frac{dT}{dt}$ is the temperature change rate, and A is the area of the top electrode. In the direct measurement technique, the device is mounted on a copper block and resistively heated (or cooled) at a constant rate. The pyroelectric current I was measured using a Keithley Model 6517 Electrometer. A temperature change rate of 3 °C per minute was used in our measurement. The infrared response characterization was performed on the $Ba_{0.8}Sr_{0.2}TiO_3$ film capacitors with the dynamic method suggested by Chynoweth [10]. A 500 K blackbody with a chopping frequency of 10 Hz was used as the infrared radiation source. The pyroelectric response produced by the small temperature oscillations in the specimen was monitored with a digital HP54540A oscilloscope through a voltage amplifier with an amplification of 6000 and a bandwidth of 1 Hz. A poling procedure was also applied to the devices before the measurements in order to improve the alignment of the ferroelectric domains.

DISCUSSION

XRD analyses revealed a tetragonal perovskite lattice with a distortion of 1.009 for the $Ba_{0.8}Sr_{0.2}TiO_3$ films. FE-SEM investigation showed that the films exhibited columnar grains with a diameter of 100 to 200 nm, which is attributed to the columnar growth of the films derived

from highly diluted solution. The detailed discussion was reported in our other papers [11,12].

Fig. 1 shows the temperature dependence of the dielectric properties for the $Ba_{0.8}Sr_{0.2}TiO_3$ thin films. The dielectric constant (ε_r) was calculated from the capacitance, which was measured at 1kHz and zero bias with a HP4284A LCR meter. The temperatures for the dielectric constant measurement ranged from –30 to 35 °C. As the temperature increased from –30 to –9 °C, the dielectric constant increased slowly from 560 to 590. The dielectric peak at about –9 °C corresponds to the orthorhombic-tetragonal phase transition; as the temperature increased from 4 to 25 °C, the dielectric constant increased drastically from 592 to 754. The dielectric peak at about 25 °C corresponds to the tetragonal-cubic phase transition. Compared to $Ba_{0.8}Sr_{0.2}TiO_3$ bulk ceramics, the orthorhombic-tetragonal phase transition for the sol-gel derived $Ba_{0.8}Sr_{0.2}TiO_3$ thin films shifted to the higher temperatures, while the tetragonal-cubic phase transition shifted to the lower temperatures. These unusual properties are likely to be related to the small grain size [13]. The dissipation factor (tanδ) was less than 2% in the temperatures ranging from –30 to 35 °C and showed two peaks located at about –9 °C and 25 °C, respectively.

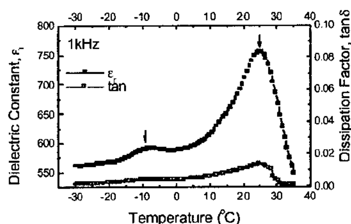

Figurer 1. *Temperature dependence of the dielectric constant and dissipation factor for the* $Ba_{0.8}Sr_{0.2}TiO_3$ *thin films.*

Fig. 2 gives the temperature dependence of the pyroelectric coefficient, *p*-T. The measured pyroelectric coefficient was larger than 2.0×10^{-4} C/m²K at the temperatures ranging from 5 to 30 °C and reached the maximum value of 4.1×10^{-4} C/m²K at 16.8 °C, which is about twice the value of pyroelectric coefficient of lithium tantalate ($LiTaO_3$) single crystal that is currently used for infrared detector applications [2].

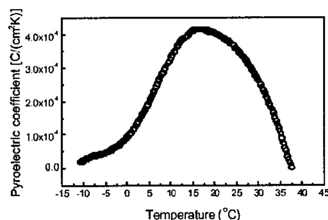

Figure 2. *Temperature dependence of the pyroelectric coefficient for the* $Ba_{0.8}Sr_{0.2}TiO_3$ *thin films*

A useful comparative figure of merit used in comparing pyroelectric materials is defined as

$$F_D=p/c(\varepsilon_0\varepsilon_r\tan\delta)^{1/2} \qquad (2)$$

where ε_0 is the permittivity of vacuum space, p, c, ε_r and $\tan\delta$ are pyroelectric coefficient, volume specific heat, dielectric constant and dissipation factor of the pyroelectric materials, respectively. From the known bulk volume specific heat value $c=2.5\times10^6$ J/m^{3}K and the measured ε_r and $\tan\delta$ shown in Fig.1, the estimated figure of merit at various temperatures for the $Ba_{0.8}Sr_{0.2}TiO_3$ film is shown in Fig. 3. The maximum of the value of F_D for the $Ba_{0.8}Sr_{0.2}TiO_3$ film is about 3.9×10^{-5} Pa$^{-1/2}$ at 32 °C. Compared to $LiTaO_3$ single crystal ($F_D=4.9\times10^{-5}$ Pa$^{-1/2}$), the prepared $Ba_{0.8}Sr_{0.2}TiO_3$ film showed a less lower figure of merit, because of its high dielectric constant. However, for the thermal imaging applications, small area elements imply a need for high dielectric constant, to obtain good capacitance matching [2]. So the $Ba_{0.8}Sr_{0.2}TiO_3$ films deposited on $Pt/Ti/SiO_2/Si$ substrates from a 0.05M solution are more suitable for the thermal imaging applications than $LiTaO_3$ single crystal, especially for 'integrated' detectors.

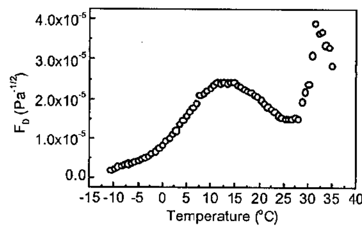

Figure 3. *Temperature dependence of the figure of the merit for the $Ba_{0.8}Sr_{0.2}TiO_3$ thin films*

Fig. 4 shows the pyroelectric response voltage *vs* the radiation time, V_s-t, which was obtained at a chopping frequency of 10 Hz under a temperature of 19 °C and a wet of 58%. From this figure, it can be seen that the response voltage was modulated by the chopped blackbody radiation at a frequency of 10 Hz. This demonstrated that the response signal resulted from the pyroelectric properties in the $Ba_{0.8}Sr_{0.2}TiO_3$ thin films, instead of trapped charge release. If the signal was caused by trapped charge release, one can not explain the fact that the response signal shows an oscillating waveform with almost constant amplitude and the same frequency as chopping [10].

The incident energy flux can be calculated from the equation:

$$\Phi_s=\frac{\sigma\left(T_b^4-T_0^4\right)A_bA_d}{2\sqrt{2}\pi L^2}, \qquad (3)$$

where Φ_s is the blackbody radiation energy, i.e. the incident energy flux. T_b is the temperature of blackbody. T_0 is the ambient temperature. A_b is the area of emission aperture of the blackbody. A_d is the area of the pyroelectric element. L is distance between the pyroelectric

element and the emission aperture. σ is Stefan constant (5.67×10^{-12} $Wcm^{-2}K^{-4}$). In our experiment, T_b=500 K, T_0=292 K, $A_b=\pi/4$ cm^2, $A_d=3.4\times10^{-3}$ cm^2, and L=16 cm. So Φ_s is about 3.6×10^{-7} W. The measured pyroelectric response voltage (V_s) and the noise voltage (V_n), shown in figure 4, were used to calculate a normalized detectivity D^*, which is defined as

$$D^*=\frac{V_s}{V_n}\bullet\frac{\sqrt{A_d\Delta f}}{\Phi_s}, \tag{4}$$

Where V_s is pyroelectric response voltage, V_n is noise voltage, and Δf is the amplifier bandwidth. The D^* value of 292 K and 10 Hz is about 4.6×10^6 $cmHz^{1/2}W^{-1}$. The relatively low value of D^* in the $Ba_{0.8}Sr_{0.2}TiO_3$ films deposited on thick (500 μm) platinum coated silicon substrates should be mainly attributed to the high reflectivity of the top electrode of Pt and the high thermal conductivity and the high heat capacity of the device duo to the thick substrate. In addition, the wet ambience also reduces the D^* value due to the increasing of the thermal noise of the device. Improvements in the quality and design of the sol-gel derived $Ba_{0.8}Sr_{0.2}TiO_3$ film infrared detector are under consideration and are expected to greatly increase the performance.

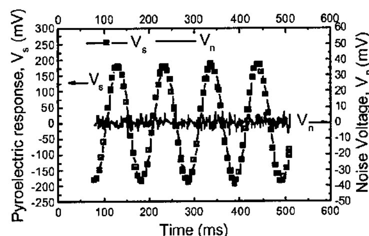

Figure 4. *The pyroelectric response voltage vs the radiation time for the $Ba_{0.8}Sr_{0.2}TiO_3$ thin film capacitors with a top electrode area of 3.4×10^{-3} cm^2.*

CONCLUSIONS

Quality $Ba_{0.8}Sr_{0.2}TiO_3$ thin films have been fabricated by a sol-gel process using a highly diluted precursor solution. A columnar structure with grain size close to 200 nm was obtained with layer-by-layer homoepitaxy due to a very small thickness of individual layer. Two dielectric peaks in the dielectric constant-temperature curve were measured at about –9 °C and 25 °C, respectively. The measured pyroelectric coefficient was larger than 2.0×10^{-4} C/m^2K at the temperatures ranging from 5 to 30 °C and reached the maximum value of 4.1×10^{-4} C/m^2K at 16.8 °C. The infrared detectivity of 4.6×10^6 $cmHz^{1/2}W^{-1}$ has been obtained at 19 °C and 10 Hz in the $Ba_{0.8}Sr_{0.2}TiO_3$ films deposited on thick (500 μm) platinum coated silicon substrates. The better infrared response can be expected by the improvement in the thermal isolation of pyroelectric element and the electrode materials.

ACKNOWLEDGMENTS

This work is supported by the Climbing Project and National Natural Science Foundation of China (69738020).

REFERENCES

1. G. W. Dietz, M. Schumacher, R. Waser, S. K. Streiffer, C. Basceri, A. I. Kingon, *J.Appl.Phys.*, **82**, 2359(1997).
2. R. W. Whatmore, P. C. Osbond and N. M. Shorrocks, *Ferroelectrics,* 76, 351(1987).
3. C. M. Chu, P. Lin, *Appl. Phys. Lett.*, **70**, 249(1997).
4. S. Yoon, J. Lee, A. Safari, *J. Appl. Phys.*, **76**, 2999(1994).
5. C. S. Chern, S. Liang, Z. Shi, S. Yoon, A. Safari, P. Lu, B. H. Kear, B. Goodreau, T. Marks, S.Hou, *Appl. Phys. Lett.*, **64**, 3181(1994).
6. D. M. Tahan, A. Safari, L. Klein, *J. Am. Ceram. Soc.*, **79**, 1593(1996).
7. B. A. Baumert, L-H.Chang, A. Matsuda, C. Tracy, N. Cave, R. Gregory, and P. Fejes, *J. Mater. Res.,* **13**, 197(1998).
8. R. W. Schwartz, P. G. Clem, and J. A. Voigt *et al*, *J. Am. Ceram. Soc.* 82, 2359(1999).
9. R. L. Byer and C. B. Roundy, *IEEE Trans. Sonics & Ultrsonics* **SU-19**, 333(1972).
10. A. G. Chynoweth, *J. Appl. Phys.* 27, 78(1956).
11. Jian-Gong Cheng, Xiang-Jian Meng, and Biao Li , *Appl. Phys. Lett.* **75**, 2132(1999).
12. Jian-Gong Cheng, Xiang-Jian Meng, and Jun Tang , *Appl. Phys. Lett.* **75**, 3402(1999).
13. Lei Zhang, Wei-Lie Zhong, Chun-Lei Wang, Pei-Lin Zhang, Yu-Guo Wang, *J. Phys. D: Appl. Phys.* **32**, 546(1999).

Mat. Res. Soc. Symp. Proc. Vol. 655 © 2001 Materials Research Society

A Modified SBN System for Pyroelectric Sensors

H. Amorín[1], F. Guerrero[2], J. Portelles[1], M. Venet[1], A. Fundora[1] and J. M. Siqueiros[3]

[1] Facultad de Física - Instituto de Materiales y Reactivos, Universidad de la Habana, Vedado, La Habana 10400, Cuba.
[2] Facultad de Ciencias Naturales, Universidad de Oriente, Santiago de Cuba 90500, Cuba.
[3] Centro de Ciencias de la Materia Condensada, UNAM, Apartado Postal 2681, Ensenada, B.C., México, 22800.

ABSTRACT

The Thermally Stimulated Depolarization Current (TSDC) and pyroelectric properties of the modified SBN ferroelectric ceramic system were studied for different lanthanum and titanium doping concentrations. The TSDC measurements show the pyroelectric peak for all compositions while a second smaller peak at higher temperature, possibly associated to induced vacancy-impurity dipoles, is also observed in all cases. The second peak contribution was experimentally and mathematically eliminated to determine the remanent polarization and pyroelectric coefficient, both associated only to permanent ferroelectric dipoles. The figures of merit for sensor devices are determined for all compositions and compared with those of other pyroelectric systems. The $La_{0.03}Sr_{0.255}Ba_{0.7}Nb_{1.95}Ti_{0.05}O_{5.975}$ sample, in particular, has excellent pyroelectric response, making this material very suitable for pyroelectricity-derived applications.

INTRODUCTION

To select a material for pyroelectric sensors three different criteria have been used in the literature [1-2], each one with an associated figure of merit [3-4]: 1) The voltage response defined as $F_V = \frac{p}{C\,\varepsilon_o\,\varepsilon}$ where the pyroelectric voltage response is to be maximized. 2) The detectivity $D = \frac{p}{C\sqrt{\varepsilon_o \varepsilon \tan\delta}}$ where the signal to noise ratio of the pyroelectric detector is to be maximized and 3) the current response $F_I = \frac{p}{C}$, used to characterize detectors in the transverse mode where a fast response and a wide bandwidth are needed. In the latter expressions, p is the pyroelectric coefficient; C is the volume specific heat, ε the dielectric permittivity and $\tan\delta$ the dielectric losses of the material.

Among the ferroelectric materials with outstanding properties, niobate crystals with tungsten-bronze structure, like the $Sr_xBa_{1-x}Nb_2O_6$ (SBN) system, stand out [1,5]. Their high pyroelectric and electro-optic coefficients and low dielectric permittivity characterize these materials [5]. SBN solid solutions have been selected for a number of technological applications such as pyroelectric detector [6], and electro-optic [7], photorefractive [8] and acoustic surface wave (SAW) devices [9].

Defects such as vacancies and impurities strongly affect the material property [10]. It is seen, for instance, that the transition temperature takes lower values as the concentration of vacancies and/or dopants increase as opposed to the case where all the crystallographic sites are completely occupied [11]. Rare earth doping of the SBN system will lead to lower Tc and improve dielectric and pyroelectric properties at room temperature [12-13]. Specifically, lanthanum doping will produce a very stable polarized material at room temperature [14].

In the SBN system, as well as in all tungsten-bronze niobates, the B site cation (niobium in this case) is the ferroactive ion [15]. A strong effect is to be expected in the material properties when Nb is substituted by Ti, not only because the ferroactive ion is being partially substituted but also because a 4+ valence ion (Ti) is replacing a 5+ valence ion (Nb) [16]. Vacancies in the oxygen sites must then appear to maintain charge neutrality increasing the number of defects in the structure leading to a decrease in the transition temperature of the material [17-18].
In previous reports the influence of small amounts of lanthanum in SBN ceramics has been studied [19-21]. In this work, the pyroelectric properties of the $Sr_{0.255}La_{0.03}Ba_{0.7}Nb_{2-y}Ti_yO_{6-y/2}$ (LSBNT) ceramic system are studied with the purpose of evaluating its properties for pyroelectric detection devices.

EXPERIMENTAL PROCEDURE

The raw materials $BaCO_3$, $SrCO_3$, La_2O_3, Nb_2O_5 and TiO_2 with high purity grade (> 99.9 %) were used to prepare the $Sr_{0.255}La_{0.03}Ba_{0.7}Nb_{2-y}Ti_yO_{6-y/2}$ (LSBNT) ceramic system. To examine the influence of titanium content on the properties of the sintered material for $y = 0.01$ (LSBNT1), 0.03 (LSBNT3), 0.05 (LSBNT5) and 0.1 (LSBNT10); the powders were prefired for 2 hours at 1100ºC and then uniaxially die-pressed at 612 Mpa, into 10 mm in diameter disks. Finally, the samples were sintered for 5 hours at 1250ºC.

To measure the TSDC, silver paste was deposited on the flat faces of the samples as electrodes and polarized afterward using a dc voltage. The samples were heated up to poling temperature (T_p) and a dc bias (V_p) was then applied. After 30 minutes, the samples were let to cool down, in the presence of an external electric field, down to ambient temperature, where the bias voltage is turned off. The polarization electric field varied from 10 to 20kV/cm. The polarization state of the material was studied through the measurement of the TSDC by means of the Static Charge Integration Method, using a PHILIPS PM2525 multimeter with a sensitivity of 0.1nA. The samples were studied in a temperature range between room temperature and 250ºC, registered with a Chromel-Alumel thermocouple and a YFE 2503 multimeter. The heating ratio was 6ºC/min.

RESULTS AND DISCUSSION

The curves showing the dependence of the thermally stimulated current with temperature for samples of LSBNT1 and LSBNT3, polarized at different fields, are presented in figure 1, where two peaks are observed for both samples. The highest peak is related to the pyroelectric current originated from the polarization of the ferroelectric domains since it appears in the same temperature range as the permittivity maximum [18]. The height of this peak will increase very slightly with the polarization field due to the increase in the domain orientation.

The second peak, of lower intensity, is located at 200ºC approximately and grows with the polarization field. This peak, however, is associated either to induced dipoles or to motion of charge. Usually, injected charge motion takes place at higher temperatures for these materials [19,23]. As a matter of fact, some measurements were performed at temperatures above 200ºC and negative values of the current were obtained that were associated to inject charge motion [19]. Moreover, since LSBN ceramics do not presents this second peak in pyroelectric measurement [19], it is evident that its presence is associated to the inclusion of titanium in the system.

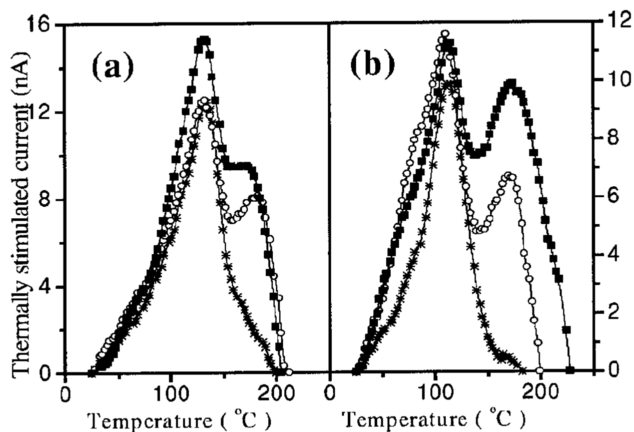

Figure 1. *Curves of thermally stimulated current for samples a) LSBNT1 and b) LSBNT3 polarized at (*) 10kV/cm, (O) 15kV/cm and (■) 20kV/cm.*

In the system under study, the vacancy concentration is increased by the substitution of ions of different valence, that is, Ti^{4+} by Nb^{5+}. To maintain charge neutrality, vacancies must exist in the A sites of the tetragonal tungsten bronze (TTB) structure as well as in the oxygen sites [16]. These vacancies can form, together with the added impurities, induced dipoles of the vacancy-impurity type, which may be oriented under the action of a strong electric field and that will contribute to the thermally stimulated current giving rise to a peak in the current *vs* temperature measurements. In our case, the second peak does not change position with the increment in the titanium concentration.

Measurements are now being performed to elucidate the true source of this second peak. The applied method is able to eliminate the pyroelectric contribution and determine the activation energy associated to the mechanism involved in this second peak. The results will be the subject of a future publication.

Figure 2 shows the pyroelectric current, remanent polarization (P_r) and pyroelectric coefficient (p) curves as functions of temperature for samples of different compositions and previously polarized at 20kV/cm. In this case the second peak contribution was mathematically subtracted to obtain the true remanent polarization from the ferroelectric domains contribution. For this purpose, the second peak was fitted by a Gaussian function and removed from the original depolarization current curve.

In the three sets of curves, a decrease in each of those variables with the titanium content may be observed, evidencing that titanium doping lowers the total dipole moment per unit volume of the material. A decrease in the temperature corresponding to the maximum value of the pyroelectric coefficient (T_p) with titanium content is also noted and is reported in Table 1, together with the values of the temperature of the maximum permittivity (T_ε) obtained from the thermoelectric analysis measurements [18]. All the relevant properties characterizing the pyroelectric effect in the studied samples are collected in Table 1.

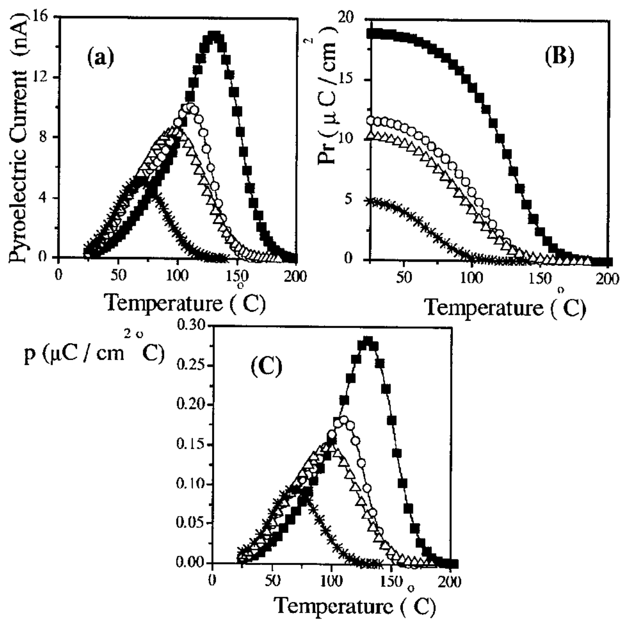

***Figure 2**. Curves of a) pyroelectric current, b) remanent polarization (P_r) and c) pyroelectric coefficient (p), for LSBNT1 (■), LSBNT3 (O), LSBNT5 (Δ) and LSBNT10 (✻) samples, previously polarized at 20kV/cm.*

Table 1. Magnitudes of the relevant properties characterizing the pyroelectric behavior of the LSBNT system for different titanium content. I_p is the maximum pyroelectric current, P_r is the remanent polarization, p is the maximum pyroelectric coefficient, T_p is the temperature of maximum pyroelectric current, and T_ε the temperature of maximum permittivity [18].

Sample	I_p (nA)	P_r (μC/cm²)	p (μC/cm² ºC)	T_p (ºC)	T_ε (ºC)
LSBNT1	14.8	18.9	0.28	131	154
LSBNT3	10.1	11.6	0.18	110	139
LSBNT5	8.4	10.3	0.15	95	120
LSBNT10	5.2	4.8	0.09	69	79

The figures of merit F_v, D and F_I, for several materials used as pyroelectric sensor are presented in Table 2. Also included are the corresponding values for LSBNT1 and LSBNT5 samples at 50ºC. For LSBNT5 sample, the results compare well with those reported for doped/undoped SBN single crystals [13] and PZT ceramics [24], the latter could be taken as a standard material for pyroelectric detection.

Table 2. Figures of merit (Fv, D and F_I) and other parameters for different ferroelectric materials at room temperature and for LSBNT1 and LSBNT5 at 50°C. p is the pyroelectric coefficient, ε is the dielectric permittivity, Tanδ represents the dielectric losses and C is the volume specific heat.

Sample	Fv (Vm^2/J)	D ($10^{-5}m^{3/2}/J^{1/2}$)	F_I (10^{-10} m/V)	p (10^{-4} C/m^2 °C)	ε	Tanδ	C (10^6 J/m^3 °C)
SBN50§	0.07	7.8	2.5	0.06	400	0.003	2.3
La:SBN§	0.03	4.8	4.5	11.7	1630	0.006	2.6
LSBNT1	0.03	0.6	1.2	2.8	480	0.085	2.3
LSBNT5	0.03	1.6	2.4	5.3	1010	0.024	2.2
PZT†	0.06	1.5	5.8	3.8	290	0.003	2.5

§ S. T. Liu et al. [13].

† S. Bauer et. al. [24].

CONCLUSIONS

The Thermally Stimulated Depolarization Current of the $La_{0.03}Sr_{0.255}Ba_{0.7}Nb_{2-y}Ti_yO_{6-y/2}$ ceramic system was studied, presenting two peaks in the temperature interval from room temperature to 200°C for all compositions. The more intense peak was found at lower temperatures and was associated to the pyroelectric current. The second one, at higher temperatures, was less intense and possible associated to induced vacancy-impurity dipoles. The pyroelectric current, pyroelectric coefficient and remanent polarization values decreased with titanium concentration in pyroelectric measurements. The figures of merit for the $La_{0.03}Sr_{0.255}Ba_{0.7}Nb_{1.99}Ti_{0.01}O_{5.995}$ and $La_{0.03}Sr_{0.255}Ba_{0.7}Nb_{1.95}Ti_{0.05}O_{5.975}$ systems were obtained and compared with those reported in the literature for other ferroelectric materials. The results show that the $La_{0.03}Sr_{0.255}Ba_{0.7}Nb_{1.95}Ti_{0.05}O_{5.975}$ ceramic is a good candidate for pyroelectric sensor devices.

ACKNOWLEDGMENTS

One of the authors, Harvey Amorín, acknowledges the Latin-American Center of Physics (CLAF, Rio de Janeiro-Brazil) and the International Center for Theoretical Physics (ICTP, Trieste-Italy), for financial support. This work has been partially supported by CoNaCyT-México, through grant No. 33586E and by DGAPA-UNAM grant No. IN104000.

REFERENCES

1. Lines M. E. and Glass A. M., "Principles and Applications of Ferroelectric and Related Materials", (Clarendon Press, Oxford, 1977).
2. Liu S. T. and Long D., "Proceeding of the IEEE, Devices and Application", **66** (1978) 14.
3. Whatmore R. W., *Ferroelectrics*, **118** (1991) 241.
4. Putley E. H., "The Pyroelectric Detector", Ed. Academic Press, New York (1970).
5. Yuhuan Xu, "Ferroelectric Materials and their Applications", Elsevier Science Publishers B. V., North-Holland (Los Angeles, USA, 1991).
6. Glass A. M., *J. Appl. Phys.*, **40** [12] (1969) 4699.
7. Lenzo P. V., Spencer E. G. and Ballman A. A., *Appl. Phys. Lett.*, **11** [1] (1967) 23.
8. Neurgaonkar R. R. and Cory W. K., *J. Opt. Soc. Am. B: Opt. Phys.*, **3** [2] (1986) 274.

9. Neurgaonkar R. R., Kalisher M. H., Lim T. C., Staples E. J. and Keester K. L., *Mater. Res. Bull.*, **15** [9] (1980) 1235.
10. Subbarao E. C. and Shirane G., *J. Chem. Phys.*, **32** (1960) 1846.
11. Umakantham K., Chandramouli K., Nageswara Rao G. and Bhanumathi A., *Bull. Mater. Sci.*, **19** [2] (1996) 345.
12. Nagata K., Yamamoto Y., Igarashi H. and Okazaki K., *Ferroelectrics*, **38** (1981) 853.
13. Liu S. T. and Maciolek R. B., *J. Electron. Mater.*, **4** [1] (1975) 91.
14. Liu S. T. and Bhalla A. S., *Ferroelectrics*, **51** (1983) 47.
15. Jamieson P. B., Abrahams S. C. and Bernstein J. L., *J. Chem. Phys.*, **48** [11] (1968) 5048.
16. Amorín H., Portelles J., Guerrero F., Siqueiros J., *Revista Mexicana de Física*, **44** [3] (1998) 217.
17. Ravez J., Debadie M., Von der Mühll R. et Hagenmuller P., *J. Solid State Chem.*, **16** (1976) 423.
18. Amorín H., Portelles J., Guerrero F., Fundora A., Siqueiros J., *J. of Electroceramics* **3**, 371 (1999).
19. Amorín H., Guerrero F., Portelles J., González I., Fundora A., Siqueiros J. and Valenzuela J., *Solid State Comm.*, **106** [8] (1998) 555.
20. Guerrero F., Portelles J., González I., Fundora A., Amorín H., Siqueiros J. and Machorro R., *Solid State Comm.*, **101** [6] (1997) 463.
21. Guerrero F., Portelles J., Amorín H., Fundora A., Siqueiros J. and Hirata G., *J. Europ. Ceram. Soc.*, **18** [7] (1998) 745.
22. Jaffe A. and Cook W., "Piezoelectric Ceramics", Academic Press (London and New York, 1971).
23. Peláiz A., Calderón F., Pérez O., Santos J. and González I., *High Temp. High Press.*, **30** (1998) 179.
24. S. Bauer and B. Ploss, *J. Appl. Phys.*, **68** [12] (1990) 6361.

Mat. Res. Soc. Symp. Proc. Vol. 655 © 2001 Materials Research Society

Sensing Properties of $Ba_{1-x}La_xNb_yTi_{1-y}O_3$ (x=0.25%, y=0.25%) Thin-Film on SiO_2/Si Substrate

B. Li , P. T. Lai, G. Q. Li [1], S. H. Zeng[1] , M. Q. Huang[1]
Department of Electrical and Electronic Engineering, the University of Hong Kong,
Pokfulam Rd., Hong Kong
[1]Department of Applied Physics, South China University of Technology,
Guangzhou, China

ABSTRACT

Barium lanthanum titanate-niobate ($Ba_{1-x}La_xNb_yTi_{1-y}O_3$) film deposited on a SiO_2/Si substrate by the argon ion-beam sputtering technique has been used to fabricate a thin-film resistor and a metal-insulator-semiconductor (MIS) capacitor by standard integrated-circuit technology. Measurements show that the film resistor has superior sensitivity for visible light and a thermal sensitivity within the range 28~400 °C, while the MIS capacitor is highly sensitive to relative humidity. The optical absorption spectrum of the film has been measured and the bandgap of the film determined. The effects of test frequency on the impedance of the film resistor at various temperatures and on the humidity-sensitive characteristics of the MIS capacitor have been investigated.

INTRODUCTION

With the progress of automatic control applications, the need for miniaturized, intelligent and programmable sensors has become important issue. To achieve these goals, exploiting thin-film sensors on silicon substrates is always the target of investigations. Therefore, desirable sensing thin-film materials have been actively sought. Perovskite-type oxides (ABO_3) attract much attention in recent years because these oxide are not only used as high-permittivity dielectric in non-volatile memory, but also can be used as sensing materials, moreover, sensing properties of these oxides may be modified by appropriate combination of cationic constituents. Our previous works [1,2] have found that even though both $Ba_{1-x}La_xTiO_3$ and $SrNb_xTi_{1-x}O_3$ thin film have photo-, thermal and humidity sensitivity characteristics, photo sensing characteristics is better in La-doped film and thermal sensing characteristics is better in Nb-doped film. Therefore, in this work, $Ba_{1-x}La_xNb_yTi_{1-y}O_3$ (x=0.25%, y=0.25%) thin-film is proposed with a view to achieving better photo, thermal and humidity sensing properties.

EXPERIMENTS

Figure 1 shows the structure of the sensor, consisting of a thin-film resistor, and a metal-insulator-semiconductor (MIS) capacitor. This multi-function thin-film micro-sensor was fabricated on n/n^+ type (111) silicon epitaxial wafer with a 0.3~0.6 Ωcm resistivity. A SiO_2 layer with a thickness of 10 nm was grown by thermal oxidation at 900 °C for 25 min. 0.5 μm of $Ba_{1-x}La_xNb_yTi_{1-y}O_3$ film was deposited on the oxide layer by argon ion-beam sputtering equipment at room temperature under a vacuum of 1.33 mPa. High-purity aluminum and gold were then

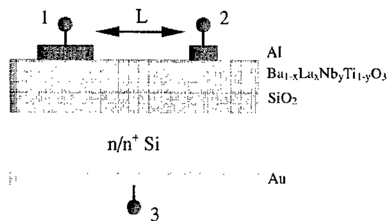

Figure1. *Cross section of the sensor device. 1 and 2 are the electrodes of thin-film resistor with length L (0.05 mm) and width W (2 mm); 1 and 3 are the electrodes of MIS capacitor (effective area of upper electrode is 0.55 mm^2).*

evaporated respectively onto the $Ba_{1-x}La_xNb_yTi_{1-y}O_3$ film and the back surface of the wafer to form electrode and ohmic contact. Finally, post-metallization annealing was done at 400 °C for 15 min in nitrogen to make a good contact, meantime and adjust the grain and the porosity of the sputtered thin-film. Dice of the wafer were attached to headers for subsequent testings.

Current-voltage (I-V) and resistance-temperature (R-T) measurements on the resistor at various visible-light intensities (0~1800 lux) and temperature (28 °C~400 °C) were carried out with a d.c. power supply, while the current of the MIS capacitor versus relative himidity (RH) (12%~92%) was measured by an a.c. power supply. Moreover, the frequency effects on the impedance of the film resistor and the current of the MIS capacitor were investigated over a range of 20 Hz~2 MHz. Different RH levels were achieved by closed chambers containing different standard saturation salt solutions.

The deposited film is believed to be a ceramic polycrystalline material as the target material [3, 4], because the substrate was not heated during film deposition and low temperature was used for post-deposition annealing. Hence, a single crystal or a glass structure should not form. Meanwhile, the deposited film should be an n-type semiconducting material, because with nearly the same atomic radius between La^{3+} (0.0122 nm) and Ba^{2+} (0.0143 nm), and between Nb^{5+} (0.069 nm) and Ti^{4+}(0.064 nm), donor levels can be formed in the bandgap by partial substitutions of Ba^{2+} by La^{3+} and Ti^{4+} by Nb^{5+} in the target material. Moreover, since the substrate was not heated during film deposition and a low temperature was used for post-deposition annealing, single crystal or glass structure should not form in the deposited film. The chemical composition of the film was examined by Auger electron spectroscopy (AES) and the composition of La and Nb was found to be about 0.25% respectively.

RESULTS AND DISCUSSION

Figure 2 shows the current of the film resistor versus visible-light intensity at 30 °C. The film is highly sensitive to light intensity and presents a reasonably good linearity. For a test voltage V_t of 1 V, the current increases by 29.4% and 400% when light intensity increases from 0 to 100 and 1000 lux respectively. More importantly, the operating voltage can be as low as 1 V, as compared to 3 V for $Ba_{1-x}La_xTiO_3$ film , and 10 V for $Sr_{1-x}La_xTiO_3$ film. Therefore, this

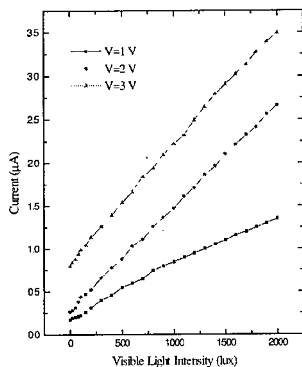

Figure 2. Current of thin-film resistor (L = 0.05 nm, W = 2 mm) vs. visible-light intensity at various test voltages (Vt) (V_t is in r.m.s. value).

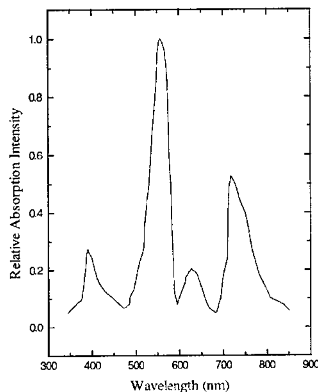

Figure 3. Relative absorption intensity of film vs. wavelength of light (light-source energy is the same for various wavelengths).

material has great potential in a multitude of photoconductor applications requiring low power levels.

The absorption spectrum of the film in Figure 3 shows that the intrinsic absorption peak is at a wavelength of 557 [μm] and the long-wave cut-off is at 595 [μm]. Hence, the bandgap is 2.15 eV, which is smaller than the value for $BaTiO_3$ (2.64 eV). The intrinsic absorption cut-off shifts towards the long-wave region, possibly due to La-doped and Nb-doped atoms because the

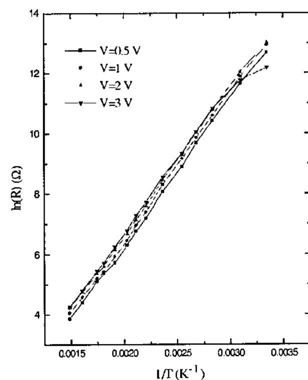

Figure 4. The resistance of the thin-film resistor vs. temperature at various test voltages (V_t) under light, -tight conditions.

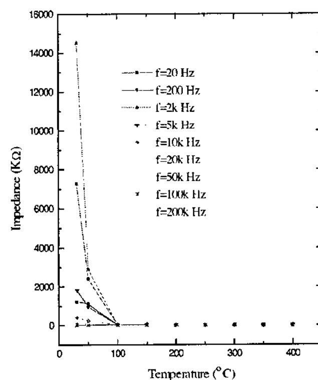

Figure 5. Impedance of thin-film resistor (L =0.05 mm W = 2 mm) vs. temperature at various test frequencies (f) under light-tight conditions.

average atomic number of $Ba_{1-x}La_xNb_yTi_{1-y}O_3$ is higher than $BaTiO_3$ and hence the effective bandgap is reduced, which is usually the case for III-V compound semiconductors [5]. The lower absorption peaks within the wavelength region 0.6-0.77 μm should be related to extrinsic absorption by impurities and defect energy levels.

The ln(R)-T characteristics of the film resistor (under light-tight conditions) shown in Figure 4 exhibit a negative temperature coefficient (NTC) and have good linearity and high sensitivity. The temperature coefficient of the film at 30 °C is $-5.22\%°C^{-1}$ under a test voltage of 1 V, which is similar to that of $SrNb_xTi_{1-x}O_3$ film ($-4.36\%\ °C^{-1}$) [1], and higher than that of $Ba_{1-x}La_xTiO_3$($-1.61\%°C^{-1}$) [2] and $Sr_{1-x}La_xTiO_3$ ($-1.73\%°C^{-1}$) [6]. The effect of test frequency on the impedance (Z) of the film resistor at different temperatures is depicted in Figure 5. Z decreases with frequency because of parasitic capacitance associated with the MIS structure underneath the film resistor. At higher frequencies, the capacitive effect gets more severe, overwhelming the temperature effect. Further measurements reveal that the current through the MIS capacitor under d.c conditions is hardly affected by temperature and light intensity. Therefore the thermal sensitivity and photosensitivity of the film resistor are only due to the properties of the $Ba_{1-x}La_xNb_yTi_{1-y}O_3$ film.

The influence of relative humidity on the a.c current of the MIS capacitor is shown in Figure 6. When RH changes from 12% to 92%, the current increases by about 194% under a test voltage of 500 Hz and 4 V at 30 °C. The curves possess a hysteresis loop as the RH changes from low to high and then back to low, and the maximum hysteresis is about 4%. The higher the test voltage, the smaller is the hysteresis loop, possibly because Joule heating accelerates evaporation of water. The response time of humidity sensitivity of the MIS capacitor is shown in Figure 7. As RH changes from 12 to 92 % and then back, the adsorption and desorption response times are only about 8 s and 12 s respectively, (120 s and 150 s for $Sr_{1-x}La_xTiO_3$, 15 s and 10 s for $SrNb_xTi_{1-x}O_3$, 4.5 s and 5 s for $Ba_{1-x}La_xTiO_3$). The shorter response times of the film indicate its physisorption is more dominant than that in other films.

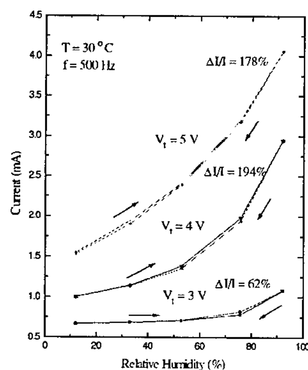

***Figure 6**. Current of MIS capacitor vs. relative humidity at various test voltages (Vt): (→) RH changes from12% to 92%; (←) RH changes from 92% to 12% .*

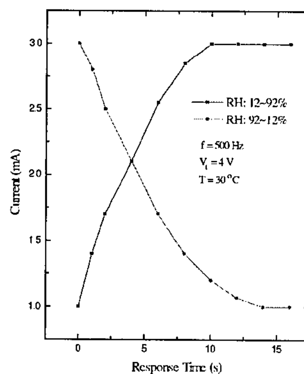

***Figure 7**. The change in current of the MIS capacitor as the RH changes from 12 to 92% and then back (for both cases, the RH change occurs at time = 0)*

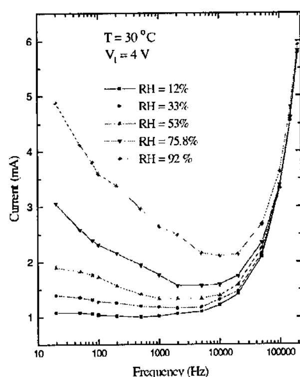

Figure 8. *Influence of test frequency on humidity-sensitivity characteristics of MIS capacitor.*

The effects of frequency on the current of the MIS capacitor are shown in Fig. 8, with the current exhibiting a valley between 20 Hz and 10^5 Hz. Based on a simple parallel resistor-capacitor circuit model, the current valley should be due to a combined effect of frequency increase and dielectric-loss increase on the impedance of the MIS capacitor [1]. On the other hand, as RH changes from 12% to 92%, a large current change (≥ 100%) can be achieved over a wide frequency range of 20 Hz to 2×10^4 Hz, which is similar to $Ba_{1-x}La_xTiO_3$ film and $SrNb_xTi_{1-x}O_3$ film (20~10^5 Hz), and wider than that of the $Sr_{1-x}La_xTiO_3$ film (10^2~5×10^2 Hz), implying that this device can be applied to a wider range of operating frequency.

CONCLUSIONS

A new microsensor consisting of a thin-film resistor and a MIS capacitor is developed by depositing barium lanthanum titanate-niobate ($Ba_{1-x}La_xNb_yTi_{1-y}O_3$) thin-film on SiO_2/Si substrate. The thin-film resistor has good sensitivity for visible light and good thermal sensitivity within the temperature range of 28~400 °C. The MIS capacitor is sensitive to relative humidity (RH), with a 194% change of current for a humidity change from 12% to 92% RH at a test voltage of 500 Hz and 4 V, and with short response times of 8 s and 12 s for adsorption and desorption of water vapor respectively. Frequency effects on humidity sensitivity performances also demonstrate that this device can be applied to a wide range of operating frequencies. Therefore, $Ba_{1-x}La_xNb_yTi_{1-y}O_3$ sputtered thin-film is a promising material for multi-sensing devices, and the batch-fabricated devices are the strongest contender in microprocessor-controlled applications, because they are cost-effective and compatible with existing IC fabrication technologies.

ACKNOWLEDGEMENTS

This work was partially supported by RGC research Grant, Hong Kong, CRCG Research Grant, the University of Hong Kong and a Sci-Tech Committee Grant of Guangdong, China.

REFERENCES

[1] G. Q. Li, P. T. Lai, S. H. Zeng, M. Q. Huang and B. Li, A new thin-film humidity and thermal micro-sensor with $Al/SrNb_xTi_{1-x}O_3/SiO_2/Si$ structure, *Sensors and Actuators A*, **75**, 70 (1999).

[2] B. Li, P. T. Lai, G. Q. Li, S. H. Zeng and M. Q. Huang, A new multi-function thin-film microsensor based on $Ba_{1-x}La_xTiO_3$, *Smart Materials and Structure*, **9**, 498 (2000).

[3] T.Seiyama, N. Yamazoe and H. Arai, Ceramic humidity sensors, *Sensors and Actuators*, **4** 85 (1983).

[4] R. H. Bube, *Photoelectronic Properties of Semiconductors*, Cambridge University Press, (1992) pp. 189.

[5] B. R. Nag, *Electron Transport in Compound Semiconductors*, Springer, Berlin, 1980.

[6] G. Q. Li, P. T. Lai, S. H. Zeng, M. Q. Huang and Y. C. Cheng, Photo-, thermal and humidity sensitivity characteristics of $Sr_{1-x}La_xTiO_3$ film on SiO_2/Si structure, *Sensors and Actuators A*, **63**, 223 (1997).

Mat. Res. Soc. Symp. Proc. Vol. 655 © 2001 Materials Research Society

The Physics of Electric Field Effect Thermoelectric Devices

V. Sandomirsky, A. V. Butenko, R. Levin[1] and Y. Schlesinger
Department of Physics, Bar-Ilan University, Ramat-Gan 52900, Israel
[1]The College of Judea & Samaria, Ariel 44837, Israel

ABSTRACT

We describe here a novel approach to the subject of thermoelectric devices. The current best thermoelectrics are based on heavily doped semiconductors or semimetal alloys. We show that utilization of electric field effect or ferroelectric field effect, not only provides a new route to this problem, bypassing the drawbacks of conventional doping, but also offers significantly improved thermoelectric characteristics. We present here model calculation of the thermoelectric figure of merit in thin films of Bi and PbTe, and also discuss several realistic device designs.

INTRODUCTION

Application of an electric field (Electric Field Effect - EFE) to a capacitor structure of the type Gate-Dielectric-Semimetal (or non-degenerate semiconductor), or Gate-Ferroelectric-Semimetal injects, into the semimetal or semiconductor sample, charge carriers which are distributed among the electron and hole bands. Depending on the field polarity, the number of carriers of the corresponding sign increases, while the number of carriers of the other sign diminishes. This is connected with the change of the electron (η_e) and the hole (η_h) Fermi levels with an applied electric field, i. e. $\eta_e=\eta_e(E)$ and $\eta_h=\eta_h(E)$. Increasing the electric field can result in zero concentration of the corresponding charge carrier type. A further increase of the electric field results in a further increase of the introduced carriers and hence of the conductivity. It follows from the above argument that all the thermoelectrical effects (the state-of-art of the field has been recently presented by Mahan [1]), such as Peltier, Seebeck, Nernst etc are strongly dependent on the magnitude of the electric field. Thus, the EFE offers a novel, controllable and more effective route to thermoelectricity. In the following we will term this sort of thermoelectrics by EFE-TE.

In following we analyze in detail the electric field dependence of the Seebeck effect (see also [2]). One can show that the Seebeck effect is expressed by the formula

$$S = S_p - S_n, \tag{1}$$

where

$$S_p = \frac{k_B}{e}\frac{\langle \sigma_p s_p \rangle}{\langle \sigma_p + \sigma_n \rangle}; \quad S_n = \frac{k_B}{e}\frac{\langle \sigma_n s_n \rangle}{\langle \sigma_p + \sigma_n \rangle}. \tag{1'}$$

Here σ_p and σ_n are the hole and the electron conductivities, s_p and s_n are the hole and the electrons related Seebeck coefficients, < > denotes averaging over the sample thickness. The later is needed because of the inhomogeneous electric field in sample (the larger the dielectic constant ε the larger the characteristic screening length L_s, determining the rate of the exponential decrease of the field in the sample).

In absence of electric field (E=0), S_n and S_p are of comparable magnitude, therefore S is smaller than each of the above quantities. For a certain value of the mobilities, S_p could equal S_n and therefore S=0. It should be noted (Eq. 1') that S depends on the electric field via the field dependence of σ (due to a change of carrier concentration with E) and the field dependence of $s_{n,p}$ (via the dependence of the Fermi energies on E) according to

$$s_k = \left[\frac{(\frac{5}{2}+\lambda)F_{\frac{3}{2}+\lambda}}{(\frac{3}{2}+\lambda)F_{\frac{1}{2}+\lambda}} - \eta_k \right], \qquad (2)$$

where

$$\eta_k = \frac{(\varepsilon_F)_k}{k_B T}; \qquad F_i = \int_0^\infty \frac{x^i dx}{1+exp(x-\eta)}.$$

Here λ is the exponent in the energy dependence of the scattering relaxation time $\tau (\tau \propto \varepsilon^\lambda)$, η_k is the reduced Fermi level (index k indicating the hole or the electrons related quantities), and F_i is the Fermi integral ($i = {}^1/_2 + \lambda$ or ${}^3/_2 + \lambda$).

The unique characteristic of the method we propose here, lays in its ability to dynamically optimize and vary the thermoelectric behavior of the system (by varying the applied electric field magnitude and polarity) under a variety of conditions.

TEST-CASE CALCULATIONS

a. *Bi films.*

The curves of Fig. 1 were calculated assuming a value of film thickness L=100 Å, and temperature T=300 K. It should be noted that the detailed shape of the curve in Fig. 1 (in particular, via the energy dependence of the mobilities) depends also on the particular scattering mechanism (e.g. scattering by defects, ionized impurities, acoustic and/or optical phonons etc).

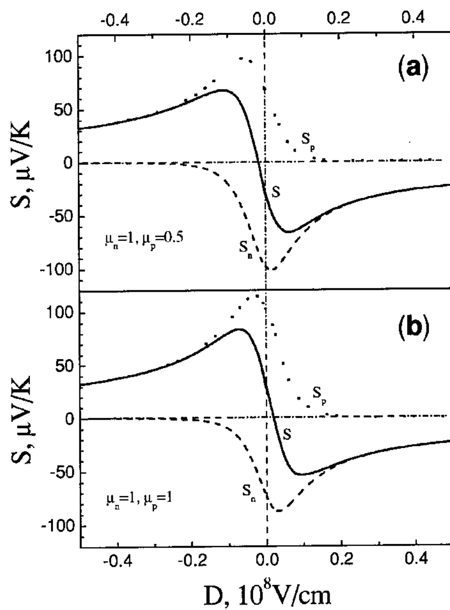

Figure 1.

The total, S, and the partial (S_p due to holes an S_n due to electrons) Seebeck coefficients as a function of the electric displacement D.
(a) - mobilities μ_n=1, μ_p=0.05 m^2/Vsec
(b) - mobilities μ_n=1, μ_p=1 m^2/Vsec

The curves have been calculated assuming only electron-acoustic phonon scattering.

With increasing positive polarity (for definiteness) the hole concentration, and therefore also S_p goes to zero. At the same time $|S_n|$ goes through a maximum and then falls with increasing E (because of the increase of η with E). A similar behavior (with the roles of electrons and holes interchanged) is obtained for negative E. This is demonstrated in Fig. 1 by the two extrema of $S(D)$ (D is the electrical displacement) at $D_{m,pos}$ and $D_{m,neg}$.

The quality of the thermoelectric behavior is usually characterized by the dimensionless, sample averaged, figure of merit [2, 3]

$$M = \frac{\langle \sigma S \rangle^2}{\langle \sigma \rangle \kappa} T, \qquad (3)$$

where σ is the electrical conductivity.

The electric field dependence of M is shown in Fig. 2. The two maxima of M are related to the two extrema of S (see Fig. 1). They appear at slightly shifted values of E, due to the monotonical field dependence of σ. It follows thus, that (together with the field variation of the thermoelectric quantities described above) also a strong field dependence of M should be observed. This leads to the possibility that thin Bi films (which are not good thermoelectrics) can actually attain a high M under electric field conditions.

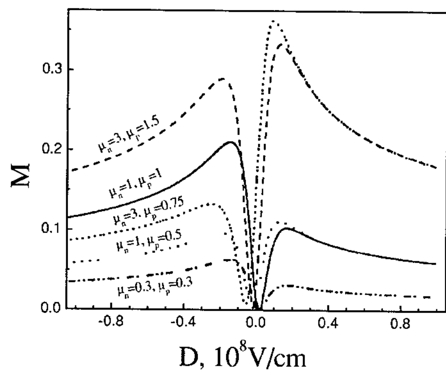

Figure 2.

The sample averaged figure of merit, for different combinations of the electron and hole mobilities, as a function of the electric displacement D.

The curves have been calculated assuming only electron-acoustic phonon scattering.

b. *PbTe film.*

The currently typical thermoelectrics are the, narrow gap, doped semiconductors $A_{IV}B_{VI}$ such as Bi_2Te_3, PbTe etc. Fig. 3 shows the calculation results of the maximum value of $M(D)$, for PbTe, as a function of film thickness L. The range of film-thickness L<700 Å was chosen so that $L \leq L_s$ (the screening length), assuring a reasonable homogeneity of the electric field over the sample thickness.

The present "worst case" calculations are based upon an assumed value of mobility $\mu = 0.05$ m^2/Vsec (a typical value determined by the current thin film preparation methodology) and assuming electron-acoustic phonon scattering mechanism only. Even so, despite the low mobility and the unfavorable energy dependence of τ ($\tau_{e\text{-}ph} \propto \varepsilon^{-0.5}$), the calculated figure of merit for PbTe under the electric field effect, reaches a considerably high value $M \geq 2$ for a thin (L<120 Å) film, see Fig. 3. In analogy with the technological advances

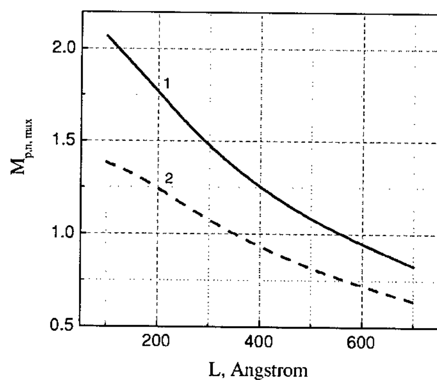

Figure 3.

The maximum sample averaged figure of merit $M(E)$ for thermoelectric layer of
(1) - negative polarity (p-type)
(2) - positive polarity (n-type)
as a function of film thickness L.

in Bi film preparation methods [4], we expect a similar improvement in the PbTe system, resulting in a higher mobility (actually, a value of $\mu = 0.2$ m^2/Vsec, at room temperature, has been reported just now [5]). Moreover, it is noteworthy that, in general, for a given value of mobility, $M(E)$ will be significantly higher when other scattering mechanisms (besides electron-acoustic phonon scattering) are involved.

EFE-TE DEVICE STRUCTURAL CONFIGURATIONS

The analysis and calculations, outlined in the previous sections, have been carried out assuming the simplest model structure (a parallel plate capacitor, comprising of a metallic gate, a dielectric layer and a semimetal or semiconductor film). However, it is clear that more complex structures can be developed for higher efficiency and/or for specific purposes. In the following we describe shortly several of the configurations currently studied, both experimentally as well as theoretically.

a. *p-n thermoelement.* This two-arm structure, shown in Figure 4, is obtained by replacing the metallic gate by a second layer of thermoelectric material. This device exploits the electric field effect mechanism, causing the negative polarity thermoelectric layer to become an n-type semimetal (or semiconductor) and, at the same time, the positive polarity layer to become p-type. This structure thus serves as a controllable thermoelectric analogue of the standard p-n element. The device can be optimized choosing different thermoelectrics for each arm.

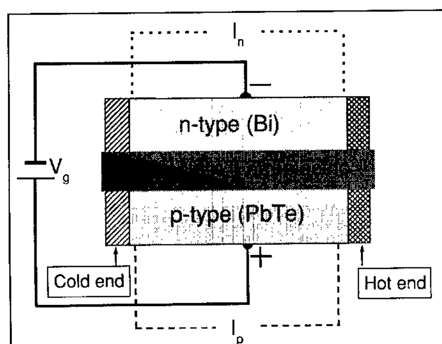

Figure 4.

The two-arm p-n thermoelement.

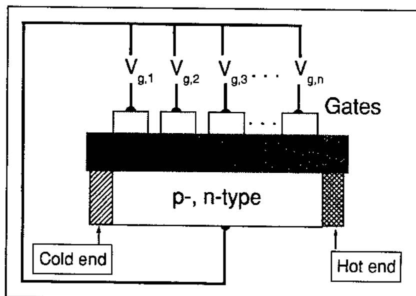

Figure 5.

The sectioned gate EFE-gradient thermoelement.

b. *EFE gradient thermoelectric device.* In this device, shown in Figure 5, a sectioned gate configuration or a resistive gate, create the conditions analogous to the gradient doping in conventional thermoelectrics. It should be emphasized that in the EFE-TE case the gradient can be dynamically varied, thus offering an active device.

c. *A split-gate Peltier cooler/heater device.* Here, as shown in Figure 6, opposite polarity voltage is applied to the two sections of the split gate thus creating a p-n junction. In such way, the direction of current determines whether the p-n junction absorbs or emits heat.

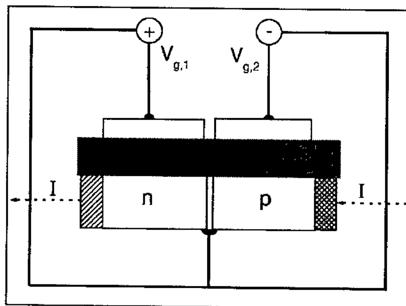

Figure 6.

The split-gate Peltier cooler/heater.
Cooling or heating functions are determined by the direction of the current.

REFERENCES

1. G. D. Mahan, *Solid State Physics,* **51**, eds. H. Ehrenreich and F. Spaepen, Academic Press (1998).
2. V. Sandomirsky, A. V. Butenko, R. Levin and Y. Schlesinger, submitted to J. of Appl. Phys. (2001)
3. Film Thermoelements: Physics and Application, ed. N. S. Lidorenko, Nauka, Moscow (1985) in Russian.
4. F. Y. Yang, Kai Liu, Kimin Hong, D. H. Reich, P. C. Searson, C. L. Chien, Y. Leprince-Wang, Kui Yu-Zhang and Ke Han, Phys. Rev. B, 61, 6631 (2000); C. L. Chien, F. Y. Yang, Kai Liu and D. H. Reich, Journal of Appl. Phys., 87, 4659 (2000).
5. Z. Dashevsky, private communication.

Thin Film Processing

Mat. Res. Soc. Symp. Proc. Vol. 655 © 2001 Materials Research Society

ELECTROPHORETIC DEPOSITION OF FERROELECTRIC COMPOSITES FOR APPLICATIONS IN ELECTRONIC SCANNING SYSTEMS.

E. Ngo, P.C. Joshi, M. W. Cole, C. W. Hubbard
Army Research Laboratory
Weapons and Materials Directorate
Attn: AMSRL-WM-MC; Building 4600
Email: engo@arl.mil
Aberdeen Proving Ground, MD 21005, U.S.A.

ABSTRACT

We have investigated the electrophoretic deposition (EPD) as a low cost and conformal method of fabricating barium strontium titanium (BST) based composite thick films. The films were deposited at a controlled rate on platinum substrate in acetone-based slurry under electric bias. Acetone-aerosol OTS surfactant dispersion was used as dispersive medium. Conformal BST based thick films of 10-80 μm were obtained. The dielectric constant and dielectric loss factor of $Ba_{0.60}Sr_{0.40}TiO_3$ and $Ba_{0.60}Sr_{0.40}TiO_3$ – 20wt% compositions were 603.3 and 0.029 and 327.0 and 0.002, respectively. The low frequency electronic properties of the electrophoretic films were also compared with those of the bulk BST ceramics. In addition, the optical and the structural properties of the films are also discussed. The various techniques employed include x-ray diffraction, SEM and surface profilometer.

I. INTRODUCTION

$Ba_{(1-x)}Sr_{(x)}TiO_3$ (BST) is a continuous solid solution between barium titanate and strontium titanate over the entire range of concentration. The Curie temperature of $Ba_{(1-x)}Sr_{(x)}TiO_3$ decreases linearly with increasing strontium titanate concentration. As a result, the transition temperature and, hence, the electrical and optical properties of $Ba_{(1-x)}Sr_{(x)}TiO_3$ can be tailored over a broad range to meet the requirements of various electronic applications. It has been reported that barium strontium titanate based composite materials, $Ba_{(1-x)}Sr_{(x)}TiO_3$-MgO, posses significantly reduced dielectric constant and dielectric loss compared to that of pure $Ba_{(1-x)}Sr_{(x)}TiO_3$.[1] These BST-MgO bulk composite materials have also demonstrated excellent dielectric loss and dielectric tunability characteristics at X-band and K-band frequencies. By optimizing the Ba/Sr ratio and MgO content, the Curie temperature can be shifted below the room temperature making the material paraelectric under normal operating conditions. [2] The non-linearity of the dielectric properties with respect to applied DC voltage makes these composite materials attractive for tunable microwave devices particularly for phased array antenna. In addition, a decrease in T_c below room temperature reduces the dielectric loss due to disappearance of the ferroelectric hysteresis.

Electrophoretic deposition (EPD) is a simple, cost effective and conformal method of depositing thick films. The deposition occurs in a solution under bias. This phenomenon occurs due to the charge on the surface of the particle that is attracted to the opposite polarity on the surface of the

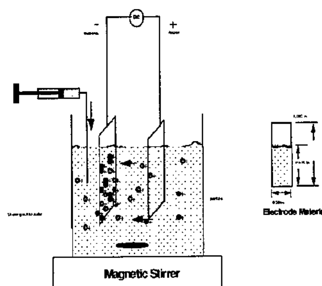

Figure 1. Basic schematic of electrophoretic deposition.

substrate.[3] Therefore, in an effort to optimize deposition, the effects of particle surface potential, particle size, and suspension conditions must be investigated. This investigation outlines some of the initial findings and compares the results with those obtained for bulk BST material.

II. EXPERIMENTAL

Ceramic processing

Raw materials were obtained from FERRO Corp, PenYan NY. In this study, the compositions fabricated were pure $Ba_{(0.6)}Sr_{(0.4)}TiO_3$ and $Ba_{(0.6)}Sr_{(0.4)}TiO_3$-20 wt% MgO. The ceramic has been processed using standard solid state methods. The mixture was ball milled in ethanol using alumnia grinding media for about 24 hours and, subsequently,

air dried. The powder is then calcined at 1100 °C for 2 hours. After calcination, 3 wt % of organic binder (Rohm and Hass Company, product Rhoplex B-60A, an aqueous emulsion of acrylic polymer) was added to improve green body strength and permit sample fabrication. The mixture was then ball milled for about five hours and air-dried. The powder was uniaxially cold pressed at a pressure of approximately 6000 psi into pellet form. The pellets were sintered at a temperature of 1350 °C. For low frequency dielectric characterization, the materials were machined to approximate 1mm in thickness and silver electrodes on both sides by screen-printing to form metal-insulator-metal (MIM) capacitors. The dielectric measurements were conducted by using HP4194A Impedance/Gain-Phase Analyzer.

Electrophoretic Processing

The initial processing procedure is similar to the ceramic processing discussed earlier. Immediately after calcining, the materials were mixed and ball milled to obtain an average particle size of 0.5 micron. Sedigraph particle analyses (via Sedigraph 5100) confirmed the particle size distribution. The materials were then processed, calcined, and deposited by the electrophoretic deposition method. Figure 1 shows the schematic diagram of the EPD process. Electrophoretic deposition was performed in a acetone base slurry mixed with OTS-surfactant as a reactive agent media. The magnetic stirrer was set steady at 150 rpm to reduce particle sedimentation. Two Pt substrates were immersed into the solution, separated approximately 1 cm apart. The films were deposited for 2, 4, and 6 minutes to analyze the effect of deposition time on the film thickness. The deposited films were placed in a saturated acetone bath to slow down the drying process. This process step is crucial to avoid rapid drying which can cause micro-cracks in the green body,

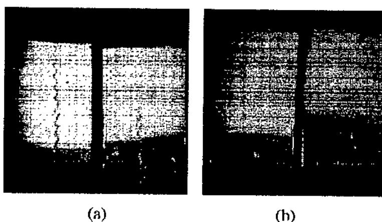

(a) (b)
Figure 2. SEM micrographs of (a) $Ba_{(0.6)}Sr_{(0.4)}TiO_3$ - 20 Wt% MgO films deposited by EPD, (b) Reverse side shows uniform and conformal film on both sides.

III. RESULT AND DISCUSSION

which further degrade film quality during sintering. Figure 2 shows the surface features of $Ba_{(0.6)}Sr_{(0.4)}TiO_3$-20 wt% MgO thick film deposited on Pt substrates. The SEM micrographs clearly show that the films were highly uniform and conformal. The films were sintered at slow ramp rate of about 1^0C/minute to 1250 °C with a dwell for 2 hours. The film quality was strongly influenced by the ratio of acetone to aerosol OT-S surfactant. At an an applied *dc* bias of 100V, the pure $Ba_{(0.6)}Sr_{(0.4)}TiO_3$ powder was barely deposited on the cathode in the acetone solution. The addition of aerosol was necessary to deposit films. Even a small concentration of OT-S surfactant caused the $Ba_{(0.6)}Sr_{(0.4)}TiO_3$ to be easily deposited in a uniform and conformal fashion on the Pt cathodes. The acetone to aerosol ratio was optimized (100:1) to obtain highly dense thick films with uniform surface morphology. The film thickness increased rapidly in the first minute of deposition then decreased and ultimately stopped at around 6 minutes. The as-deposited green films were dried in an acetone-saturated chamber at room temperature for 30 minutes and sintered at 1250 °C for 2 hours. This step was used to mitigate micro cracking, which occurs during the drying process. X-ray diffraction (XRD) patterns of $Ba_{(0.6)}Sr_{(0.4)}TiO_3$ and $Ba_{(0.6)}Sr_{(0.4)}TiO_3$-20 wt% MgO were used to identify the crystalline phases. Figure 3 displays the XRD patterns of the bulk and EPD thick films and confirms that the bulk and EPD films possess identical stoichiometry and crystallinity.

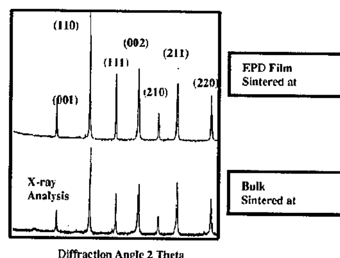

Figure 3. Illustrated the XRD pattern of bulk and thick film deposite by EPD.

Furthermore, FT-Raman spectroscopy substantiated that the optica and structural properties of the thick films are similar to those of th corresponding bulk ceramics. The Raman shifts peak for both of th bulk and films were at around 2000^{cm-1}. The results suggest that n selective ablation of any of the species had occurred since there is n drastic alteration of the composition in a way that will be reflected i the behavior of the material. The film thickness, measured using surface profilometer, was adjusted by changing deposition time. Th 10-80 μm thick films were

	$Ba_{0.60}Sr_{0.40}TiO_3$		$Ba_{0.60}Sr_{0.40}TiO_3$-20Wt% MgO	
	Bulk	EPD Films	Bulk	EPD Films
Dielectric Constant	5160.64	603.30	1068.43	327.00
Loss	0.009	0.029	0.002	0.002
Tunability %	56.70	17.34	15.80	8.00

Table I. Electronic Properties of $Ba_{0.60}Sr_{0.40}TiO_3$ and $Ba_{0.60}Sr_{0.40}TiO_3$ -20Wt% MgO Thick Film Deposited by EPD Method.

used in the present study. The dielectric properties of the films were measured in terms of the dielectric constant (ε_r), loss tangent (tan δ), and tunabiltiy ($\Delta C/C_o$) at 2V/μm. The small signal dielectric measurements were conducted at 1 MHz on (metal-insulator-metal) MIM capacitors by applying an alternating current *ac* signal of 10 mV amplitude. Platinum electrodes were sputter deposited through a shadow mask on the top surface of the films to form MIM capacitors. Table I show the properties of $Ba_{(0.6)}Sr_{(0.4)}TiO_3$ and $Ba_{(0.6)}Sr_{(0.4)}TiO_3$-20 wt% MgO thick film deposited by EPD. The dielectric constant of the EPD films were significantly reduced, as shown in Fig. 4, compared to bulk materials due to the decreased film density and finer grain structure.

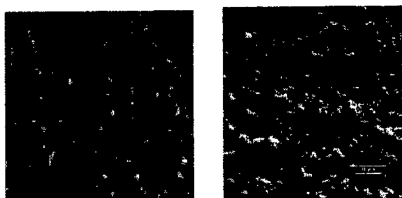

Figure 4. SEM micrographs of (a) bulk ceramic sintered at 1350 °C of $Ba_{(0.6)}Sr_{(0.4)}TiO_3$-20 wt% MgO and (b) EPD thick film sintered at 1250 C^0 for 2 hours.

IV. CONCLUSION

This work investigated electrophoretic deposition (EPD) of conformal films of undoped BST and Mgo-BST composite. The compositions are well represented in earlier literature. Our results demonstrate that the material properties of the EPD thick films parallel those of the bulk BST based ceramics. Both of the pure $Ba_{(0.6)}Sr_{(0.4)}TiO_3$ and $Ba_{(0.6)}Sr_{(0.4)}TiO_3$-20 wt% MgO composite EPD films exhibited good structural properties and dielectric constant. The dielectric constant, dielectric loss factor and tunability of $Ba_{0.60}Sr_{0.40}TiO_3$ and $Ba_{0.60}Sr_{0.40}TiO_3$ – 20wt% compositions were 603.3, 0.029, 17.34% and 327.0, 0.002, 8.0%, respectively. The enhanced dielectric properties of $Ba_{(1-x)}Sr_{(x)}TiO_3$-20Wt% MgO composite thick film compared to pure BST thick film, suggest that they are suitable for integrated capacitor and tunable microwave applications.

Reference:

1. Babbit, R.W, Koscica, T.E., and Drach, W.E., Microwave J., **35**, 63 (1992).
2. P.C. Joshi and M. Cole, Mat. Res. Soc. Symp. Proc., Spring 2000 (to be published).
3. P. Sarkar and P. S. Nicholson, J. Amer. Ceram. Soc. **79**, 1987 (1996).

Mat. Res. Soc. Symp. Proc. Vol. 655 © 2001 Materials Research Society

GROWTH AND CHARACTERIZATION STUDIES OF $ABi_2Ta_2O_9$ (A = Ba, Sr and Ca) FERROELECTRIC THIN FILMS

R. R. Das, W. Pérez, R. J. Rodríguez, P. S. Dobal, R. S. Katiyar and S.B. Krupanidhi*
Department of Physics, University of Puerto Rico, San Juan PR 00931-3343
* Materials Research Center, Indian Institute of Science, Bangalore- 560012, India

ABSTRACT

Thin films of ferroelectric $ABi_2Ta_2O_9$ bismuth-layered structure, where A = Ba, Sr and Ca, were prepared by pulsed laser deposition technique on $Pt/TiO_2/SiO_2/Si(100)$ substrates. The influence of substrate temperature between 500 to 750°C, and oxygen partial pressure 100-300 mTorr, on the structural and electrical properties of the films was investigated. The films deposited above 650°C substrate temperature showed complete Aurivillius layered structure. Films annealed at 750°C for 1h in oxygen atmosphere have exhibited better electrical properties. Atomic force microscopy study of surface topography shows that the films grown at lower temperature has smaller grains and higher surface roughness. This paper discusses the pronounced influence of A-site cation substitution on the structural and ferroelectric properties with the aid of Raman spectroscopy, X-ray diffraction and electrical properties. The degradation of ferroelectric properties with Ba and Ca substitution at A-sites is attributed to the higher structural distortion caused by changing tolerance factor. A systematic proportionate variation of coercive field is attributed to electronegativity difference of A-site cations.

INTRODUCTION

Ferroelectric thin films of several compositions have received major attention for their place in nonvolatile memory technology [1,2]. The reliable operation of the devices after switching for 10^{10}-10^{12} electric cycles, became a major issue, as most of the compositions experienced fatigue. This prompted the community to quest for newer materials which can withstand the challenges of fatigue. Aurivillius compounds of Bi-layered series received significant attention due to their stable operation potential, beyond 10^{10} switching cycles [2,3]. The Bi-layered compounds assume the formula, $(A_{n-1}B_nO_{3n+1})^{2-}(Bi_2O_2)^{2+}$, where A is twelvefold coordinated and B is sixfold coordinated cations, in which the lattice structure composed of n-number of $(A_{n-1}B_nO_{3n+1})^{2-}$ unit cells sandwiched between $(Bi_2O_2)^{2+}$ slabs along pseudo-tetragonal c-axis [4]. $SrBi_2Ta_2O_9$ (SBT) and $SrBi_2Nb_2O_9$ (SBN) are most popularly studied compound. In the present study, the A-site cations are substituted by Ba and Ca to compare their behavior with the established SBT. Paper describes the results of phase evolution, structural and electrical properties of PLD growth films of SBT, $BaBi_2Ta_2O_9$ (BBT) and $CaBi_2Ta_2O_9$ (CBT), with variation of process parameters such as substrate temperature, ablation pressure and annealing temperatures.

EXPERIMENTAL

Polycrystalline BBT, SBT and CBT thin films were grown on $Pt/TiO_2/SiO_2$ /Si substrates by pulsed laser ablation technique using a KrF (λ = 248nm) excimer laser at a pulse repetition

rate of 5 Hz and focused to a fluence of 2.5-3.0 J/cm^2. The substrates were cleaned by acetone, in ultrasonic cleaned for 3 min followed by rinsing in isopropyl alcohol. The distance between the target and substrate was maintained at 5cm during deposition. Ceramic target of 3.5 cm diameter with 15% excess bismuth was prepared by conventional powder processing method. Appropriate amount of oxide raw materials are ball milled for 24h. The mixed powders were calcined at 800°C for 24h and then pressed to pellet at 15MPa followed by sintering at 1050 °C for 8h in order to achieve highly densified target. The complete phase formation of the targets was confirmed by x-ray diffraction [5]. During deposition, the substrate temperature was varied from 500°C to 700°C with oxygen pressures varying between 100-300 mTorr to maintain better stochiometry of the film. The base pressure was dropped to 5×10^{-6} Torr before ablation. The phase formation and crystallographic orientations of as grown and annealed films were identified by Siemens D5000 X-ray diffractometer using Cu Kα radiation with Ni-filter. The microstructure of the as-deposited films was observed by atomic force microscopy (AFM, Nanoscope IIIa, Digital instruments). Room temperature micro-Raman spectra of the films were obtained by a spectrometer with triple monochromator (Jobin Yvon T6400) in a back scattering geometry. The spectra were excited with an Ar-ion laser operating at a wavelength of 514.5 nm. Thickness of the films were estimated by using filmetrix F 20. 500μm gold dots were deposited on the films as the top electrode using DC magnetron sputtering. The frequency dependent dielectric permittivity and tangent loss were studied from 1 kHz to 1 MHz with an oscillating voltage of 100 mV. The P-E hysteresis loops were measured using ferroelectric tester RT 6000 HVS (Radiant Tech.) at virtual ground mode.

RESULTS and DISCUSSIONS

Due to the dielectric anisotropy and uniaxial polarization characteristics of bismuth layer compounds, it is well established that layered perovskites are highly sensitive to process parameters. A number of reports have confirmed the stochiometry and orientation dependence of polarization in the Aurivillius series [1-3,6]. Growth sequence of polycrystalline BBT films deposited by varying substrate temperatures from 600-750°C at 100 mTorr ablation pressure is illustrated in Figure 1. Indexing of diffraction patterns has been done according to Lu et al [7]. It is clearly observed that the phase formation starts from 600°C. The broadening of the high intensity (115) reflection at 29° of the film grown at 600°C could be due to lattice mismatch and thermal stress between the film and the substrate. Second phases of Ta_2O_5, Bi_2O_3 and $BaTa_2O_6$ were identified in the films above substrate temperature of 700 °C which is attributed to re-evaporation of bismuth oxide at higher temperature due to volatility of Bi.

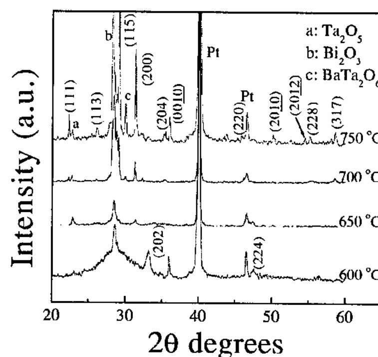

***Figure 1:** X-ray diffractograms of as grown BBT films.*

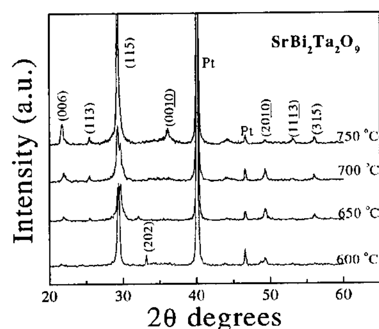

Figure 2: X-ray diffraction patterns of SBT films.

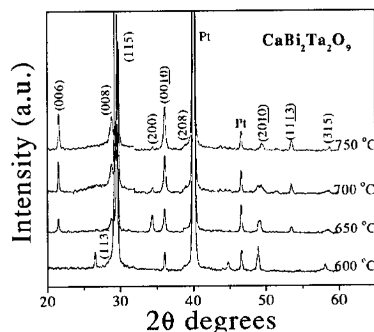

Figure 3: X-ray diffractograms of CBT films at different growth temperatures.

Fig.2 shows the phase evolution of SBT films deposited under 100mTorr oxygen pressure and different substrate temperatures. All films are polycrystalline in nature starting from 500°C. The splitting of (115) diffraction lines of the film grown at 650 and 700°C substrate temperature established the orthorhombic crystal structure of the SBT at room temperature. The broadening of the most intense diffraction line (115) at lower temperature is attributed to the presence of finer grains during growth.

Systematic variation of phase formation and orientation with growth temperature of as grown CBT films at 100 mTorr oxygen pressure are shown in Figure 3. Preferential orientation along c-axis, confirmed by the strong diffraction lines (0010), (006) and (008), increases with increase in substrate temperature. A systematic shift of most intense (115) reflection, with temperature, towards higher diffraction angle could be due to thermal stress during the growth of the films. It may also be noticed that oxygen pressure has pronounced influence on the orientation of CBT films. Higher oxygen pressures (~200mtorr) enhance the nucleation of grains with better stochiometry and higher surface energy which tend to orient the grains along the polarization axis [8].

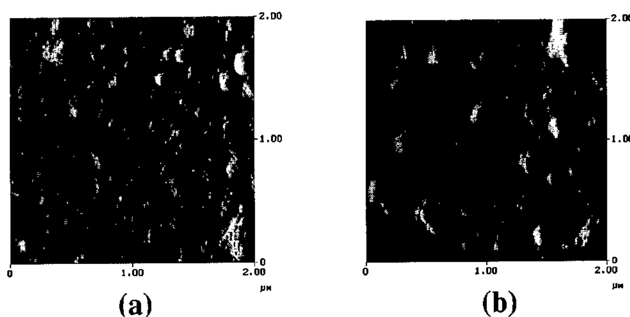

Figure 4: Typical AFM micrographs of as grown CBT films at (a) 500 °C and (b) 650 °C.

The effect of substrate temperature on surface topography of the as-grown films were analyzed by AFM using tapping mode with amplitude modulation. The growth pressure during ablation was maintained at 100 mTorr. It was observed from microstructure (Fig.4) that the grain size is directly influenced by the growth temperature. Films at a lower temperature (500°C) have relatively lower grain size (~ 24 nm) compared to that at higher temperature 650°C (~ 100 nm). The surface roughness is also comparatively larger in the films deposited at lower temperature. This behavior could be due to the increase in adatom mobility and surface energy of the ablated species to form lager grains at higher temperature. Other films ablated from SBT and BBT targets show similar kind of variation in morphology with temperature.

Room temperature micro-Raman spectra of $ABi_2Ta_2O_9$ (ABT) films were studied in order to understand the phase evolution and internal lattice vibrations of the A-site substituted layered perovskites. In all materials, it was observed that the films grown above 700°C substrate temperature had the characteristic features of bulk ceramic sample. Fig 5 shows the Raman spectra of as grown CBT, BBT films deposited at the substrate temperature of 750°C, and the SBT film deposited at 700°C and post annealed at 800°C for 1h. During the deposition the ablation pressure of all films was maintained at 100mTorr. The inset figure (Fig.5) shows the tolerance factor dependence of E_g (53 cm^{-1}) and A_{1g} (163 cm^{-1}) optical modes. Bulk results showed that the soft mode is sensitive to the substitution at A-site from Ca to Ba in ABT series, reported by Kojima [9]. We also observed similar kind of behavior in the films. With increasing ionic radii from Ca (1.0 Å) to Sr (1.1 Å) and Ba (1.4 Å) in these materials, the frequency of A_{1g} mode decreases from 60.5 to 57 and 54 cm^{-1}, while E_g mode frequency decreases from 164 to 162 and 153 cm^{-1}. A-site cation does not participate for symmetric stretching of O-Ta-O octahedral chains at a frequency of 830cm^{-1} known as breathing mode. However, the increase of this mode frequency could be associated with the mass and ionic radii differences of cations that influences the force constants of neighboring ions inside the layered perovskite unit cell ATa_2O_7, because of twelve fold coordinated nature of A-site cation. The broadening of 827 cm^{-1} peak with another extra mode at 926cm^{-1} of BBT film might be due to the presence of impurity phases present in the films at higher growth temperature as observed through x-ray diffraction. Most of the intense peaks are broadened in comparison to bulk results, which is attributed to thermal stress between the film and the substrate during high temperature growth process. According to neutron diffraction results of Shimakawa et al [10], the presence of Ca at A-sites of SBT will increase the orthorhombic structural distortion due to lattice mismatch between AO and TaO_2 planes, which could be the second possible reason for the decrease of optical phonon modes which are characteristics of ferroelectric properties in these materials.

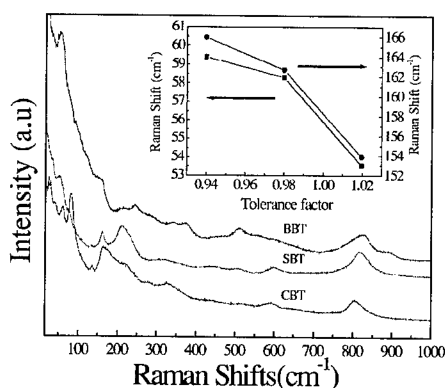

Fig. 5: Room temperature micro-Raman spectra of $ABi_2Ta_2O_9$ films.

Figure 5(a) shows the typical hysteresis loops of BBT films grown at a substrate temperature at 650°C and ablation pressure of 200mTorr. The measured maximum polarization (P_m), remanent polarization (P_r) and coercive field (E_c) values at an applied field 180 kV/cm were 16.3 μC/cm², 3.8 μC/cm² and 23 kV/cm, respectively. Poor ferroelectric properties of BBT films deposited at higher substrate temperature (≥700°C) were also observed and might be due to the presence of secondary phases as described in Fig1.

Well saturated polarization of SBT films grown at substrate temperature 700°C and annealed at 650°C are shown in Fig 5(b). Values of maximum polarization (P_m ~ 12.75 μC/cm²), remanent polarization (P_r ~ 4.5μC/cm²) and coercive field (E_c ~ 68kV/cm) are obtained at an applied field 300kV/cm. Annealing at lower temperature might help to release the growth stress at higher substrate temperature. It was also noticed that higher in-situ growth temperature of SBT films leads to preferential orientation along c-axis. The results are consistent to reported values of SBT films prepared by other techniques [11].

Ferroelectric hysteresis properties of 470nm thick polycrystalline CBT films deposited at 650°C and annealed at 750°C are illustrated in Fig 5(c). The measured values of remanent polarization (P_r) and coercive field (E_c) at an applied field of 277 kV/cm are about 2.3 μC/cm² and 112 kV/cm, respectively. There is negligible degradation (< 5%) of polarization after fatigue even above 10^{10} electric cycles at 500 kHz and 150kV/cm. This results infer that the ferroelectric properties of Bi-layered compounds are highly influenced by A-site cations. Polarization values obtained from BBT and CBT are lower than the measured values of SBT. These results can be linked to orientation of the films or due to change in tolerance factor of individual perrovskite unit cells in different A-site substituted compounds. However, a systematic change in coercive field with variation from Ba to Ca was observed. The higher electronegativity of Ca might be responsible for higher coercive field in CBT.

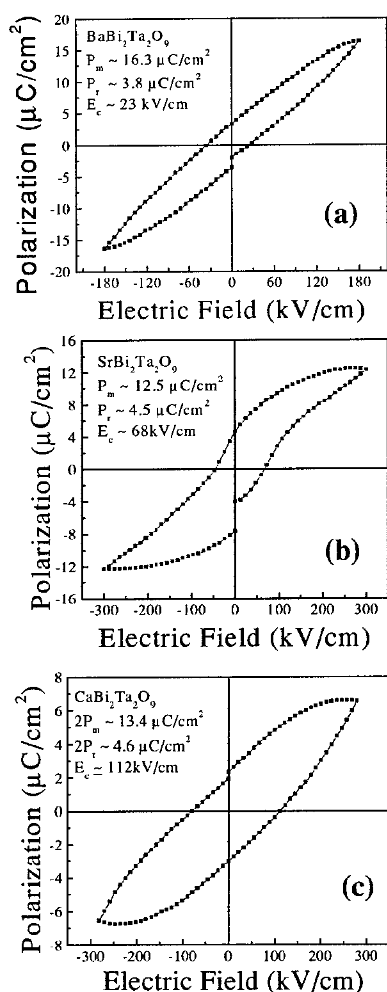

Fig 6: *Typical hysteresis loops of (a) BBT, (b) SBT and (c) CBT films*

Table 1: *Dielectric properties of ABT compounds*

	Growth Temperature (°C)	Annealing Temp.(°C)	ε	tanδ
CBT	600	750	116	0.016
SBT	500	750	237	0.033
BBT	600	750	88	0.003

The highest dielectric properties obtained for different compounds measured at 100 kHz from the films grown at different conditions are shown in Table 1. The highest dielectric constant is obtained in SBT, whereas there is a negligible dissipation factor in case of BBT films deposited at 600°C substrate temperature. It was observed in the present work, that the incipient growth temperature, even after annealing, influences the final orientation of film. A close correlation was observed between the orientation of film and the dielectric constant. More systematic studies are in progress in this direction.

CONCLUSION

$ABi_2Ta_2O_9$ thin films are successfully grown on platinized silicon substrates using PLD technique. X-ray diffraction studies showed that films crystallize at substrate temperature above 500°C, whereas Raman spectra confirmed the Bi-layer perovskite formation at growth temperature above 650°C. Increase of garin size with lower surface roughness at higher substrate temperature is examined by AFM. The decrease of lowest optical phonon modes E_g and A_{1g} at 53 and 164 cm^{-1} with increase of tolerance factor is attributed to the increase of mass of A-site cation which influences the force constant of neighbouring ions. Substitution Ba and Ca at A-site of SBT did not improve the remanent polarization. The dielectric constant and dissipation factors obtained for this series of compounds is consistent with the reported values.

ACKNOWLEDGEMENT

This work is supported in parts by DAAG55-98-1-0012, NASA-NCC5-518 and NSF-DMR 9801759 grants.

REFERENCES

1. J. F. Scott, Ferroelectrics Review, **1,** 1 (1998).
2. J. F. Scott and C.A. Paz de Araujo, Science **246,** 1400 (1989).
3. S.B.Desu and D.P. Vijaya, Mat. Sci. Eng. **B 32**, 75 (1995).
4. E.C. Subbarao, J. Phys. Chem. Solids, **23**, 665 (1962).
5. J. Lee, H. Kim, H. Kwon and Y. Jeong, Appl. Phys. Lett., **73**, 166 (1998).
6. T. Chen, T. Li, X. Zhang and S.B. Desu, J. Mat. Res. **12**, 1569 (1997).
7. C. Lu and B. Fang, J. Mat. Res. **13**, 2262 (1998).
8. R.R. Das, W.Perez, S.B. Krupanidhi and R.S. Katiyar, (to be published).
9. S. Kojima, J. Phys.: Condens Matt.,**10**, L327 (1998).
10. Y. Shimakawa, Y. Kubo, Y. Nakagawa, S. Goto, T. Kamiyama, H. Asano and F.Izumi, Phys. Rev., **B 61**, 6559 (2000).
11. N. Nukaga, K. Ishikawa and H. Funakubo, Jpn. J. Appl. Phys., **38**, 5428 (1999).

Mat. Res. Soc. Symp. Proc. Vol. 655 © 2001 Materials Research Society

Ferroelectric and Fatigue Properties of Alkoxy-Derived $CaBi_2Ta_2O_9$ Thin Films

Kazumi Kato[1,2], Kazuyuki Suzuki[1], Kaori Nishizawa[1], Takeshi Miki[1]

[1]National Industrial Research Institute of Nagoya, 1 Hirate-cho, Kita-ku, Nagoya 462-8510, Japan, kzmkato@nirin.go.jp

[2]Frontier Collaborative Research Center, Tokyo Institute of Technology, 4259 Nagatsuda-cho, Midori-ku, Yokohama 226-8503, Japan

ABSTRACT

$CaBi_2Ta_2O_9$ (CBT) thin films were successfully prepared on Pt-passivated quartz glass substrates using a triple-alkoxide solution. The thin film crystallized to a single phase of perovskite at 750°C via a mixture of fluorite and perovskite phases. The 750°C-annealed thin film showed random orientation and consisted of fine grains with a diameter of about 80 nm. The dielectric constant and loss factor were 124 and 0.04, respectively, and were constant in the frequency range of 10 kHz to 1 MHz. The thin film exhibited P-E hysteresis loops at relatively high voltages. The remanent polarization and coercive electric field were 6.9 $\mu C/cm^2$ and 170 kV/cm at 13 V, respectivey. The fatigue behaviors against various electric pulse sequences were examined. The polarization did not change when the pulse width was short such as 10^{-6} s, however, it increased gradually with number of switching cycles when the pulse width was relatively long such as 10^{-3} s.

INTRODUCTION

CBT is a member of Bi-based layer-structured perovskite compounds such as $SrBi_2Ta_2O_9$ (SBT) and $SrBi_2(Ta, Nb)_2O_9$ (SBTN) [1], for which there has been much research on their potential for nonvolatile random access memory application [2]. Compared with SBT and SBNT ceramics, the dielectric constants were reported to be low for CBT ceramics [3]. Therefore, the CBT thin film is considered to be a good candidate for application to nonvolatile ferroelectric memory with the metal-ferroelectric(-metal)-insulator field effect transistor (MF(M)ISFET) structure. For such memory, the ferroelectric thin film needs to have not a high remanent polarization but only sufficient polarization to modulate the FET channel conductivity. It is important for the ferroelectric thin film to have a low dielectric constant in order to reduce charge injection from the semiconductor.

In our previous works, CBT thin films were successfully synthesized by using a triple alkoxide solution [4-6]. The triple alkoxide was found to be a key material not only for the synthesis of SBT and $SrBi_2Nb_2O_9$ (SBN) ferroelectric thin films [7-13] but also for the synthesis of CBT thin films. It was because the arrangement of metals and oxygen in the triple alkoxide molecules was identical to sublattices of SBT, SBN and CBT perovskite crystals. As a result, the activation energy for crystallization was lowered. In the present study, characteristics of the microstructure and surface morphology of the alkoxy-derived CBT thin films on Pt-passivated glass substrates under and over the ferroelectric phase transition were investigated. The dielectric and ferroelectric properties were addressed. Additionally, dependence of fatigue behaviors on electric pulse sequences was examined.

EXPERIMENTAL DETAILS

Ca metal was dissolved in anhydrous ethanol as a solvent and heated at 78°C for 1 h. Bismuth triethoxide ($Bi(OC_2H_5)_3$) was added to the Ca alkoxide solution, and the mixture was heated at 78°C for 2 h. Then, tantalum tetraethoxide ($Ta(OC_2H_5)_5$) and diethanolamine ($NH(C_2H_4OH)_2$) were added, and the solution was heated at 78°C for 1 h. The atomic ratio of the metals, Ca : Bi : Ta, was 1 : 2 : 2. The molar ratio of diethanolamine to the triple alkoxide was 3 : 1. The aforementioned procedure was conducted in dry nitrogen flow. For partial hydrolysis, water was added to the triple alkoxide solution in a molar ratio of 1:18 (water : triple alkoxide) and the solution was then stirred for 1 h at room temperature. The concentration of the hydrolyzed triple alkoxide solution was 0.025 M. Thin films were deposited on substrates by spin coating the hydrolyzed triple alkoxide solution. Pt-passivated quartz glass ($Pt(111)/SiO_2$) was used as a substrates. Each layer was deposited in two steps of 1000 rpm for 3 s and 3000 rpm for 30 s. The as-deposited thin films were dried at 150°C, calcined at 350°C for 10 min in air, and then heated by rapid thermal annealing in oxygen flow. Film thickness was increased to 300 nm by repeating the spin coating and rapid thermal annealing processes.

The crystalline phase and the crystallinity of the thin films and powders were identified by using X-ray diffraction (XRD) measurements using Cu Kα radiation. The acceleration voltage and current were 40 kV and 40 mA, respectively. The microstructure and surface topography of the thin films were observed using a field emission scanning electron microscopy (FESEM) and an atomic force microscope (AFM), respectively. Prior to electrical measurements, circular Pt electrodes of 500 μm diameter were deposited by r. f. sputtering, which was followed by annealing at 700°C for 60 min. Dielectric and ferroelectric properties were measured using a multifrequency LCR meter (HP 4275A) and a Radiant Technologies ferroelectric test system (RT6000S) at room temperature, respectively.

RESULTS AND DISCUSSION

Figure 1 shows XRD profiles of 650°C- and 750°C-annealed CBT thin films on Pt-passivated quartz glass. The 650°C-annealed thin film consisted of a mixture of ferroelectric perovskite and non-ferroelectric fluorite phases. However, the 750°C-annealed thin film consisted of only a single phase of ferroelectric perovskite and showed random orientation. Figures 2 (a) and 2 (b) show AFM images of the surface topography of 650°C- and 750°C-annealed CBT thin films on Pt-passivated quartz glass, respectively. The 650°C-annealed thin film consisted of both large and small grains with diameters of about 200 nm and less than 100 nm, respectively. In contrast, 750°C-annealed thin film consisted of uniform fine grains of which the diameter was about 80 nm. The surface characteristic of ferroelectric CBT thin films was fairly different from that of SBT thin films, which consisted of elongate and anisotropic grains and thereby, the surface were relatively rough. The flat surface and isotropic grains of CBT thin films were considered to prefer for application to the integrated systems. Figures 3 (a) and 3 (b) show SEM cross-section photographs of 650°C- and 750°C-annealed CBT thin films on Pt-passivated quartz glass. No remarkable change was observed.

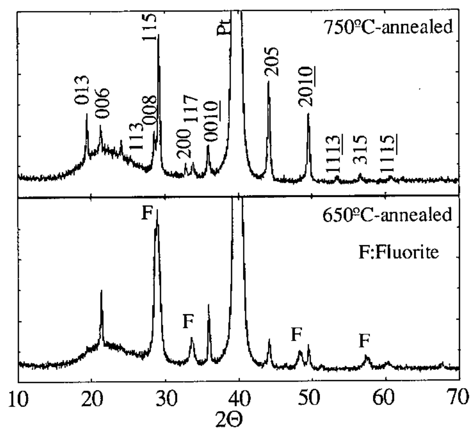

Figure 1. *XRD profiles of 650°C- and 750°C-annealed CBT thin films on Pt-passivated quartz glass [6].*

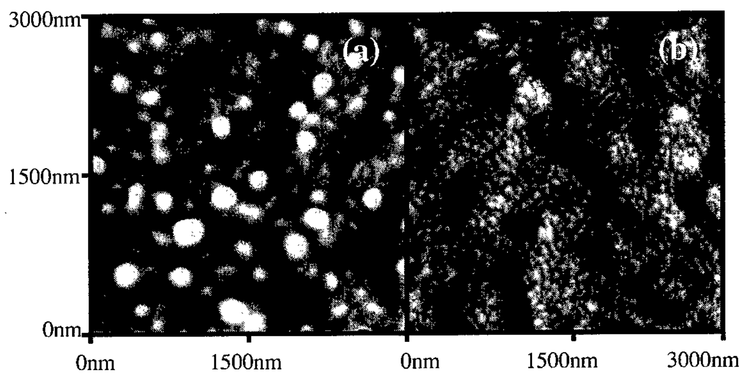

Figure 2. *AFM images of (a) 650°C- and (b) 750°C-annealed CBT thin films on Pt-passivated quarts glass.*

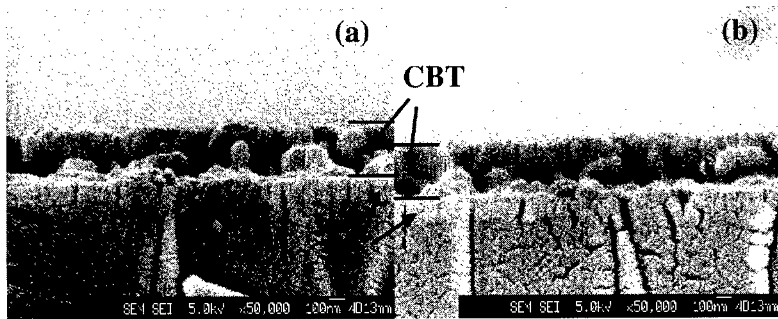

Figure 3. *SEM photographs of edge-profiles of (a) 650°C- and (b) 750°C-annealed CBT thin films on Pt-passivated quartz glass.*

Both thin films consisted of fine grains which had isotropic shape and several grains stacked along the out-of plane direction.

Figure 4 shows the frequency dependence of dielectric constants and loss factors for 750ºC-annealed CBT thin films on Pt-passivated quartz glass. The dielectric constant and loss factor were constant in the frequency range of 10 kHz to 1 MHz, and were about 120 and 0.04, respectively. Figure 5 shows *P-E* hysteresis loops of the CBT thin films on Pt-passivated quartz glass. The loops were not saturated at lower applied voltages such as 5 V but saturated at high voltages such as 11 V and 13 V. The remanent polarization (P_r) and the coercive electric field (E_c) at 13 V were 6.9 μC/cm^2 and 170 kV/cm, respectively. Figures 6 (a) and 6 (b) show changes of polarization, when the sequent electric pulses with the width of 1 x 10^{-6} s and voltages of 5 V and 10 V, respectively, were applied. The polarization did not show change after 2 x 10^{10} switching cycles at 5 V, however, it showed a decrease after 7 x 10^9 switching cycles at 10 V. The results indicated that the CBT thin film showed minimal fatigue when cycled at the voltage lower than its saturation voltage. Figures 7 (a), 7 (b) and 7 (c) show changes of polarization, when the sequent electric pulses with the width of 10^{-5} s, 10^{-4} s and 10^{-3} s, respectively, and the voltage of 10 V. Although the behavior was not significant for the width of 10^{-5}s, the polarization gradually increased with switching cycles when the pulse width was longer such as 10^{-4} s and 10^{-3} s. The similar behavior had been previously observed for SBT thin films [14], and was considered to be due to release of pinned domains in the thin films by the applied pulse with extended width. The polarization decreased after 2 x 10^9 and 7 x 10^8 switching cycles for the applied pulse with width of 10^{-5} s and 10^{-4} s, respectively.

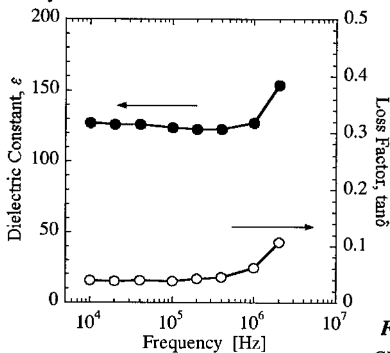

Figure 4. *Dielectric properties of 750ºC-annealed CBT thin film.*

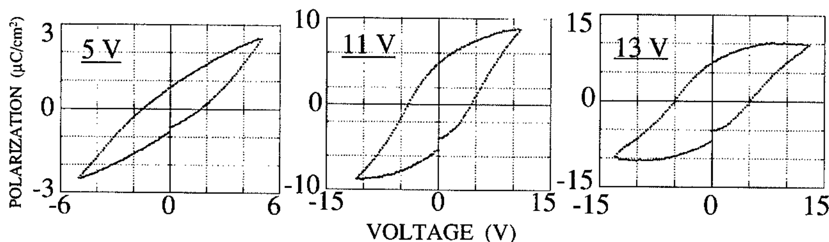

Figure 5. *P-E hysteresis loops of 750ºC-annealed CBT thin film at various applied voltages.*

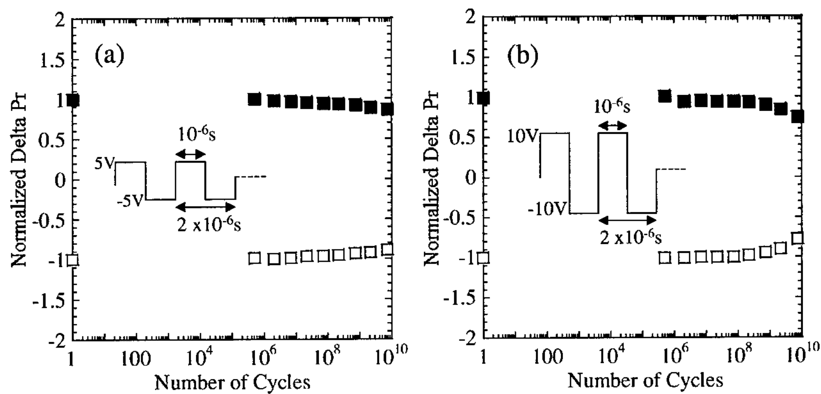

Figure 6. *Changes of polarization of CBT thin films when bipolar pulses with width of 10^{-6} s and voltages of (a) 5 V and (b) 10 V were applied.*

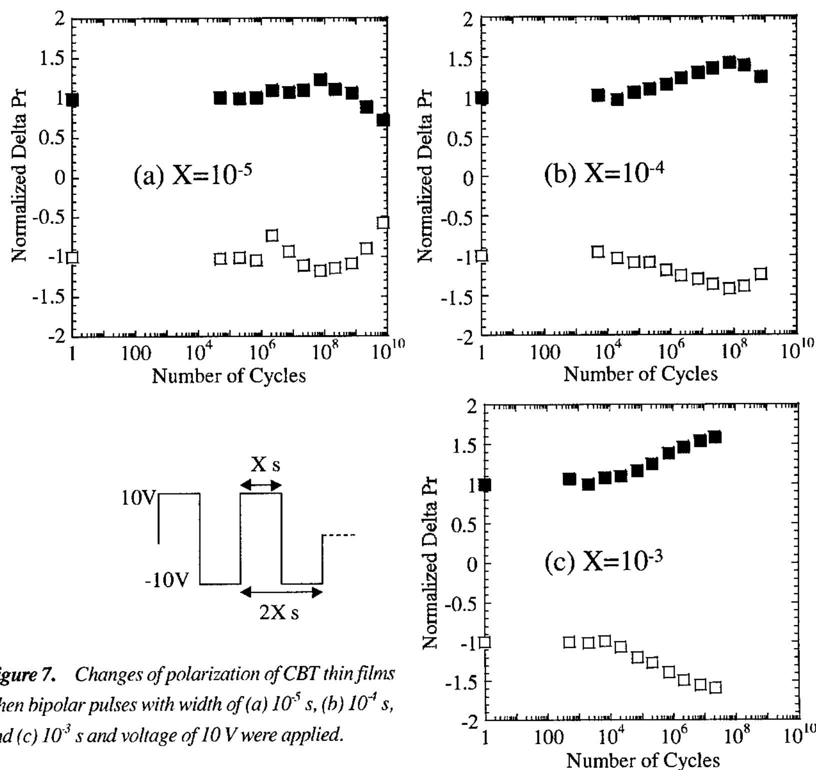

Figure 7. *Changes of polarization of CBT thin films when bipolar pulses with width of (a) 10^{-5} s, (b) 10^{-4} s, and (c) 10^{-3} s and voltage of 10 V were applied.*

CONCLUSION

CBT thin films were successfully prepared on Pt-passivated quartz glass substrates using a triple-alkoxide solution. The thin film crystallized to a single phase of perovskite at 750°C via a mixture of fluorite and perovskite phases. The 750°C-annealed thin film showed random orientation and consisted of isotropic fine grains with a diameter of about 80 nm. The flat surface was preferred for application to the integrated systems. The dielectric constant and loss factor were 124 and 0.04, respectively, and were constant in the frequency range of 10 kHz to 1 MHz. The thin film exhibited P-E hysteresis loops at relatively high voltages. The remanent polarization and coercive electric field were 6.9 $\mu C/cm^2$ and 170 kV/cm at 13 V, respectively. The polarization did not change after 2 x 10^{10} cycles of switching with the pulse width of 10^{-6} s and voltage of 5 V. However, it increased gradually with number of switching cycles when the pulse width was relatively long such as 10^{-4} s and 10^{-3} s with the applied voltage of 10 V.

ACKNOWKEDGMENTS

The authors acknowledge the financial support by the Industrial Science and Technology Frontier (ISTF) Program promoted by AIST, MITI, Japan.

REFERENCES

1. I. G. Ismailzade, *Bull. Acad. Sci. USSR, Phys. Ser.*, **24**, p. 1,201 (1960).
2. C. A-Paz de Araujo, J. D. Cuchiaro, L. D. McMillan, M. C. Scott and J. F. Scott, *Nature*, **374**, p. 627 (1995).
3. G. A. Smolenskii, V. A. Isupov and A. I. Agranovskaya, *Sov. Phys. Solid State*, **3**, p. 651 (1961).
4. K. Kato, *Mat. Res. Soc. Symp. Proc.*, **596**, p. 167 (2000).
5. K. Kato, K. Suzuki, K. Nishizawa and T. Miki, *J. Appl. Phys.*, **88**, p. 3,779 (2000).
6. K. Kato, K. Suzuki, K. Nishizawa and T. Miki, *Jpn. J. Appl. Phys.*, **39**, p. 5,501 (2000).
7. K. Kato, C. Zheng. S. K. Dey and Y. Torii, *Integr. Ferroelectr.*, **18**, p. 225 (1997).
8. K. Kato, J. M. Finder, S. K. Dey and Y. Torii, *Integr. Ferroelectr.*, **18**, p. 237 (1997).
9. K. Kato, C. Zheng, J. M. Finder, S. K. Dey and Y. Torii, *J. Am. Ceram. Soc.*, **81**, p. 1,869 (1998).
10. K. Kato, *Integr. Ferroelctr.*, **22**, p. 13 (1998).
11. K. Kato, *Jpn. J. Appl. Phys.*, **37**, p. 5,178 (1998).
12. K. Kato, *Integr. Ferroelctr.*, **26**, p. 243 (1999).
13. K. Kato, *Jpn. J. Appl. Phys.*, **38**, p. 5,417 (1999).
14. T. Nishida, M. Takaoka, S. Okamura and T. Shiosaki, *Abstract of 12 th Int. Symp. Integr. Ferroelectr.*, p. 57 (2000).

Mat. Res. Soc. Symp. Proc. Vol. 655 © 2001 Materials Research Society

Hydrothermal Fabrication of Barium Strontium Titanate Ceramics for High-Frequency Wireless Communication Networks

K. Zelonka[1], M. Sayer[1], H. Hammad[2] and A.P. Freundorfer[2]
[1] Department of Physics, [2] Department of Electrical Engineering,
Queen's University, Kingston, ON, K7L 3N6, CANADA.

ABSTRACT

Thin films of barium strontium titanate are fabricated on alumina by a hydrothermal method. Crystalline films are produced at temperatures as low as 60°C. The relative dielectric permittivity of films with the composition $Ba_{0.15}Sr_{0.85}TiO_3$ lies in the range between 150 and 220 for low frequencies (100 kHz to 1 MHz), decreasing with frequency. The loss tangent for the films increases from 0.05 to 0.15 over the same frequency range. Relative concentrations of barium and strontium in the film are controllable through the hydrothermal reaction conditions. The surface microstructure of the films is examined.

INTRODUCTION

The demand for communication via wireless networks is necessitating the design of novel signal transfer technologies. Integration of these devices on a large scale requires that they be made inexpensively. This demands that components be small and easy to produce. On-chip fabrication of the device components is the most direct method of obtaining small, inexpensive devices.

In order for on-chip fabrication to be feasible, however, each step in the process must maintain the products previously produced. In the case of devices to be fabricated on GaAs, the substrate itself limits the process. Upper process temperatures are limited to 200°C on GaAs substrates. Such a low upper temperature limit precludes use of conventional fabrication techniques to deposit ceramic structures.

In this paper we examine hydrothermal processing as a novel technique that allows ceramics to be deposited at temperatures below 200°C, and is thus compatible with technologies to be fabricated on GaAs. In particular, we examine the deposition of barium strontium titanate by the hydrothermal method. $Ba_{1-x}Sr_xTiO_3$ (BST) is selected due to its high relative permittivity and low loss tangent. These characteristics are favourable for the production of dielectric grating antennae with small physical dimensions and large bandwidth.

EXPERIMENTAL DETAILS

Hydrothermal BST films are currently fabricated on alumina. The precursor titanium layer is deposited via RF sputtering in argon from a 10cm diameter titanium target. This metal layer is reacted chemically to form the BST ceramic.

The reactant solution is prepared by dissolving $Ba(OH)_2{\cdot}8H_2O$ and $Sr(OH)_2{\cdot}8H_2O$ in deionized water. This solution is placed in a Teflon beaker, and the sample (secured in a Teflon holder) is lowered into the solution. The beaker is then placed into and sealed in an autoclave. Pressure inside the apparatus is the autogenous pressure of the solution at the reaction temperature. For the solutions used, this pressure (~ 1 MPa for processing at 180°C) is very

close to the vapour pressure of water at the reaction temperature. The reaction temperature of 60°C to 200°C is controlled by an external heater.

After processing, the solution is allowed to cool to room temperature inside the sealed autoclave. The samples are then removed and rinsed under deionized water, and dried in air.

RESULTS AND DISCUSSION

The BST films produced by the hydrothermal method appear dark and lustrous, displaying brilliant colours depending on film thickness. The thickness of the ceramic films under these reaction conditions depends only on the thickness of the initial titanium layer. BST films are currently produced with a thickness of 0.5 microns, from a titanium layer of the same thickness.

Film Composition and Stoichiometry

Control of the ratio of barium to strontium in BST is essential to fabrication of a good dielectric. This ratio controls whether BST behaves as a ferroelectric or paraelectric material at room temperature [1]. For room temperature applications where the paraelectric regime is favoured, the composition $Ba_{0.7}Sr_{0.3}TiO_3$ has been determined to be optimal [1]. This composition gives the highest relative permittivity. This is the desired result for our intended applications. Composition of the BST films produced hydrothermally has been determined by nuclear atomic absorption.

To determine the relationship between barium and strontium concentrations in the reactant solution and the relative amounts incorporated into the film, the concentration of $Sr(OH)_2{\cdot}8H_2O$ in solution is held constant at 0.5M, and the concentration of $Ba(OH)_2{\cdot}8H_2O$ is varied as 0.1M, 0.25M and 0.5M. Films are processed for 8 hours at 180°C.

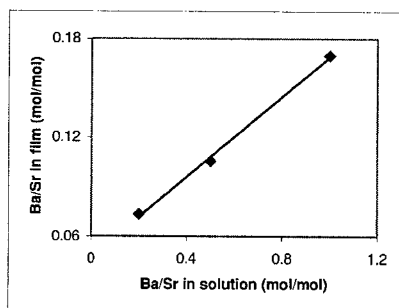

Fig. 1: Relationship between relative concentrations of Ba and Sr in reactant solution to that in hydrothermal BST film.

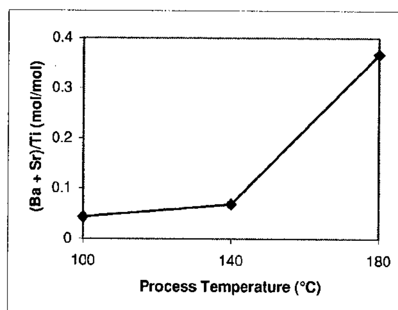

Fig 2: Variation of BST film stoichiometry with reaction temperature.

Figure 1 shows that there is an approximately linear relationship between the ratio of barium to strontium in the solution to that in the final film, over the range studied. It is expected that by

controlling the relative concentrations of precursors in the reactant solution, the ratio of barium to strontium in the film can be controlled over the entire range of solid solution.

The effect of process temperature on film stoichiometry is examined in Figure 2. Solution concentrations are held constant for both $Sr(OH)_2 \cdot 8H_2O$ and $Ba(OH)_2 \cdot 8H_2O$, at 0.5M. The process time is held constant at 8 hours. The film composition more closely approaches the stoichiometric composition $Ba_{1-x}Sr_xTiO_3$ for higher process temperatures. Deviation from stoichiometry is still significant, however.

X-ray Analysis

Glancing angle X-ray analysis (Cu Kα radiation) using an incidence angle of 2° is used to confirm the crystallinity of the films produced. Films produced at temperatures as low as 60°C exhibit characteristic BST peaks. It is possible to produce films that are well crystallized with no residual titanium peaks evident. With a higher concentration of reactant ions in the solution, the reaction to convert Ti to BST is more strongly driven to promote ceramic production. Thus, the film shows pure BST in a shorter reaction time.

The peak near 52° in Figure 3 is shifted in the spectrum for the sample processed for 3 hours, and is a BST peak, not a peak due to residual titanium.

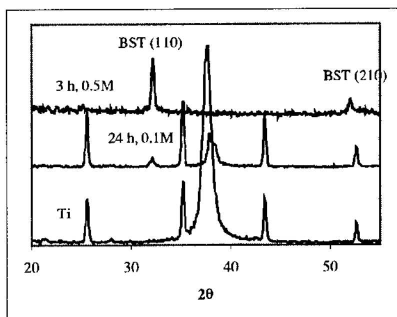

Fig. 3: Formation of BST from Ti with different solution concentrations, at 180°C. Bottom trace: Ti substrate, middle trace: a 0.1M solution processed for 24h, top trace: a 0.5M solution processed for 3h.

Surface Morphology

The surface of the BST films fabricated are studied using scanning electron microscopy. The surfaces tend to have a layer of grains that are not densely packed on top of a dense substructure. All films shown are processed in a solution with $Sr(OH)_2 \cdot 8H_2O$ and $Ba(OH)_2 \cdot 8H_2O$ at a concentration of 0.1M.

No variation in surface morphology is seen with change of process time. Films processed at 140°C and above have spherical grains of relatively constant diameter of approximately 0.3 microns. At 100°C process temperature, large grains with diameters up to 0.7 microns are evident. Below 100°C, few surface grains are apparent.

A strong grain size effect has been reported in the electrical properties of BST [2]. This includes a maximum in relative permittivity in films with 1 μm grain size.[2]. Thus, BST fabricated hydrothermally at temperatures near 100°C rather than at higher temperatures may have favourable electrical behavior, such as a higher relative permittivity.

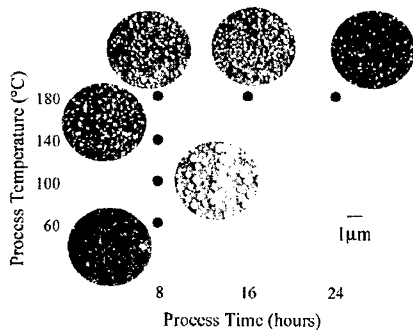

Fig. 4: Variation of surface microstructure of hydrothermally fabricated BST thin films with process time and process temperature.

Electrical Characterization

The electrical properties of BST films at low frequencies (1MHz) are determined through parallel capacitance measurements. A platinum layer is deposited on the alumina substrate prior to deposition of the precursor titanium layer. The BST film is then fabricated as above. Reaction temperature is 180°C, and the concentration of both $Sr(OH)_2{\cdot}8H_2O$ and $Ba(OH)_2{\cdot}8H_2O$ in the solution is 0.5M. Gold top electrodes are evaporated onto the surface of the BST.

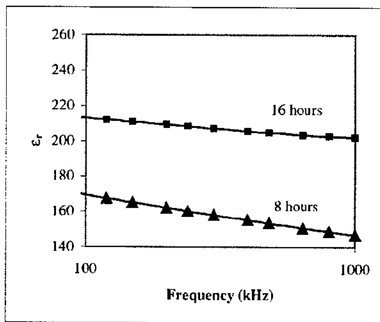

Fig 5: Variation of relative dielectric constant of hydrothermally fabricated BST thin films with frequency. Ba:Sr = 0.15:0.85 in film.

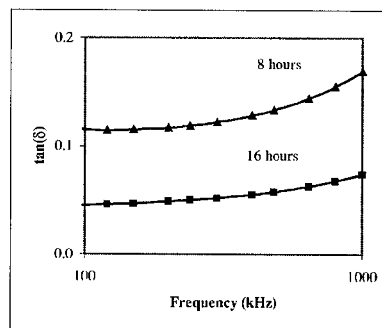

Fig 6: Variation of loss tangent of hydrothermally fabricated BST thin films with frequency. Ba:Sr = 0.15:0.85 in film.

A decrease in relative permittivity and an increase in loss tangent with increase in frequency are found. Values for these parameters are consistent with values reported elsewhere [3]. The ratio Ba:Sr is 0.15:0.85 in these films. With an increased concentration of barium in the films to the 0.7:0.3 Ba:Sr region, an associated increase in the relative permittivity is expected. Figures 5

and 6 show that a longer process time leads to an improvement in film characteristics. This may be associated with an increase in the molar ratio (Ba+Sr)/Ti. For the film processed for 8 hours, (Ba+Sr)/Ti = 0.37. For the film processed for 16 hours, (Ba+Sr)/Ti = 0.77.

CONCLUSIONS

The characteristics of BST films fabricated by the hydrothermal method depend strongly on the reaction conditions, including reaction time, temperature, concentration of reactants, and thickness of the initial titanium layer. The characteristics of interest in the final film can be controlled more or less independently via alteration of separate reaction conditions. Thus, it is expected that it is possible to produce a BST film with virtually any tailored set of characteristics, with respect to film thickness, Ba/Sr ratio (and thus electrical characteristics), and (Ba+Sr)/Ti ratio. Hydrothermal processing is a promising new method for fabrication of thin film BST at low temperatures.

REFERENCES

1. B.A. Baumert, L-H. Chang, A.T. Matsuda, and C.J. Tracy, *J. Mat. Res.* 13, 197 (1998)
2. L. Zhang, W.L. Zhong, C.L. Wang, P.L. Zhang, Y.G. Wang, *Phys. Stat. Sol. (a)* 168, 543 (1998)
3. C. Cho, E Shi, M. Jang, S. Jeong, and S. Kim, *Jpn. J. Appl. Phys.* 33, 4984 (1994)

Mat. Res. Soc. Symp. Proc. Vol. 655 © 2001 Materials Research Society

Electrical Characteristics of Chemical Solution Deposited Nd^{3+} Doped PZT (53/47) Thin Films in Planar Electrode Configuration

S.B. Majumder, B. Perez, B. Roy, A. Martinez, and R.S. Katiyar
PO Box 23343, Department of Physics, University of Puerto Rico
San Juan, PR 00931, USA

ABSTRACT

Electrical characteristics of ferroelectric thin films in planar electrode configuration are important to characterize these materials for their applications in micro electro mechanical (MEM) and tunable microwave devices. In the present work we have prepared polycrystalline $Pb_{1-3x/2}Nd_x(Zr_{0.53}Ti_{0.47})O_3$ (x = 0.0 to 10.0 at %) thin films on platinized silicon substrate by chemical solution deposition (CSD) technique. The films were characterized in terms of their dielectric and ferroelectric properties by depositing planar interdigital finger electrodes on the surface of the films by electron beam lithography. The capacitance and loss tangent of undoped and 4 at % Nd doped PZT films measured at 100 kHz were found to be 138 pF, 0.033 and 95 pF, 0.019 respectively. Saturated hysteresis loops were obtained in undoped PZT film by applying 100 V across 10 μm electrode separation. Nd doped PZT films on the other hand, electrically shorted at comparatively lower voltage. The electrical characteristics of these films are correlated with their phase formation behavior and microstructural features.

INTRODUCTION

Smart materials can sense and accordingly respond to a variety of external stimuli such as pressure, electric and magnetic fields, temperature, nuclear radiation etc. Devices made of smart materials such as actuators and sensors are integral part of a smart system. The family of smart material include piezoelectric and electrostrictive materials, polymers, shape memory alloys, electro-rheological fluids, optical fibers etc. Among these materials piezoelectric materials are attractive for the design of smart devices due to large strain yield, high response speed, reasonable electro-mechanical efficiency, inexpensive and light weight and they can be easily shaped, bonded or embedded in a variety of surfaces [1].

Piezoelectric materials are non-centrosymmetric and posses permanent electric dipole. Due to direct piezoelectric effect the piezoelectric material can generate electrical charge (voltage) when an external stress is applied to it. On the other hand, due to the converse piezoelectric effect the piezoelectric materials are strained when an external electrical field is applied to it. Sensors and actuators are fabricated exploiting the direct and converse piezoelectric effect respectively. Utilizing bulk piezoelectric materials cantilever mounted (unimorph / bi-morph), multi-layer, and Moonie type actuators have been designed. Irrespective of the adopted design in all the piezo-actuators the characteristic parameters are (i) degree of displacement, (ii) magnitude of the generative force and (iii) response speed (resonance frequency). For efficient actuator performance large possible generative displacement and force are desired.

A bending actuation mechanism is an effective way to achieve large displacement in piezo-actuator design. Bimorph and unimorph are typical bending actuator designs. When the actuator is driven with electrical field the piezo transverse strain is converted to large bending

displacement in the perpendicular direction of the applied field due to the constrain of each component in the actuator structure. The material parameter of interest in this design is d_{31}, where the field is applied in 'z' direction and the generated strain is in 'x' direction. Since the d_{33} and k_{33} (electro-mechanical coupling coefficient) are almost two times larger than that of d_{31} and k_{31} values, strong advantages exist for unimorph bending actuators with a transversely polarized PZT layer which can be driven electromechanically through the piezo d_{33} mode rather than conventional d_{31} mode [2]. In d_{33} mode both the measured strain and the direction of applied field are along the surface of the piezo layer. For practical devices, such as micro-machined unimorph diaphragm pressure sensors, transverse polarization configuration will be more attractive as in this case the thickness of the diaphragm and the electrode spacing are independent variables. Since the low capacitance of the unimorph structure matches well with the field effect transistor input capacitance, a higher voltage sensitivity is expected in transverse design as compared to the conventional longitudinal mode design utilizing d_{31} parameter. In thin film form many micro-machined unimorph transducers for various MEMs devices have been developed by combining silicon micro-electronics technology and on chip ferroelectric PZT thin films [3].

However, little effort has so far been attempted to fabricate transverse actuator structure [4]. As a first step, towards producing d_{33} mode unimorph bending transducers on Si substrates, one should characterize the dielectric and ferroelectric properties for transverse fields generated from IDT surface electrodes. This work is one of the few attempts to characterize PZT films in transverse field direction. Addition of donor dopants have found useful in increasing the polarization and reducing the leakage current density. In this work we have prepared $Pb_{1-x}Nd_x(Zr_{0.53}Ti_{0.47})O_3$ (x = 0.0 to 10 at%) to study the effect of Nd impurity ions on the phase formation behavior, surface morphology , ferroelectric and dielectric characteristics on PZT thin films.

EXPERIMENTAL

$Pb_{1-3x/2}Nd_x(Zr_{0.53}Ti_{0.47})O_3$ (x = 0.0 to 10 at%) thin films were deposited on platinized silicon substrates by a CSD technique. To prepare the precursor sol, lead acetate was dissolved in acetic acid and refluxed at 110° C to dehydrate the water of crystallization. Separately inside a moisture controlled glove box Ti – isopropoxide and Zr –n- propoxide were codissolved in acetic acid. The acetic acid serves as chelating agent and reduces the moisture sensitivity of the alkoxides. The double alkoxide solution was mixed with Pb acetate solution at 90°C through continuous stirring. Finally stoichiometric amount of Nd- nitrate dissolved in methoxy-ethanol was mixed into the complex Pb-Zr-Ti sol through continuous stirring to prepare Nd doped PZT precursor parent sol. The parent sol had a strength about 1 ML^{-1}. The parent sol was diluted to a strength of 0.3 ML^{-1} with the addition of acetic acid and used as coating sol. The coating solution was spun coated on cleaned platinized silicon wafer and just after deposition and heated at 600°C for 5 min in flowing oxygen for organic removal as well as nucleation of perovskite phase directly from the as deposited amorphous phase. The coating and firing sequence was repeated for 10 times to obtain films about 0.5 μm thick. Finally the films were annealed at 700°C for 1 h in flowing oxygen ambient for crystallization.

The interdigitated capacitors were fabricated using e-beam lithography followed by metallization and lift-off processes. To facilitate the lifting-off process, a bilayer of the e-resist was used. A layer of positive lower molecular weight e-beam resist (495K PMMA C2) was spun onto the film surface and baked. A second layer of higher molecular weight (950K PMMA 2%)

e-resist was then spun onto the first e-resist layer and baked. The total resist thickness obtained was approximately 4400Å. The pattern was then exposed on the sample using a JEOL JSM-840A controlled by PC running JC Nabity's NPGS software [5]. After developing the exposed resist, aluminum contacts were deposited onto the samples followed by a lift-off process. The flow diagram of the IDT electrode fabrication is shown in Fig.1. It was found that the thickness of PMMA polymer layers control the e-beam energy doses and the deposited aluminum thickness should be roughly 1/3rd to that of polymer thickness for optimum electrode quality.

RESULTS AND DISCUSSION

Phase Formation Behavior

The doped and undoped PZT films crystallized into a rhombohedral structure of perovskite phase. Up to 4 at% Nd doping, the films have only perovskite phase (Fig.2), however, with further increase in Nd %, the paraelectric pyrochlore phase coexisted with the perovskite phase. Nd^{3+} replaces Pb^{2+} at the A site and to maintain the charge neutrality, it introduces Pb vacancies in the lattice. It is well known that the as-deposited amorphous PZT transforms to perovskite phase through the formation of an intermediate oxygen deficient $A_2B_2O_{7-x}$ pyrochlore phase during a conventional annealing process [6]. The increase in dopant concentration leads to increasing Pb deficiency and tends to stabilize part of the intermediate pyrochlore phase. The perovskite ratio is determined using the following relation

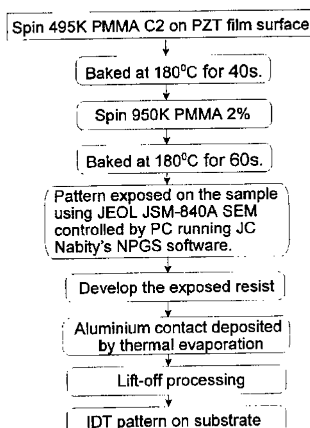

Figure 1 Flow diagram of IDT fabrication by e- beam lithography technique

Perovskite ratio % =
$I_{perovskite}/(I_{perovskite}+I_{pyrochlore})\ X\ 100$,

where $I_{perovskite}$ and $I_{pyrochlore}$ represent the integrated peak areas for the 100 % diffraction peaks for the perovskite and pyrochlore phases respectively. It was found that the perovskite phase fraction reduces with the increase in dopant concentration beyond 5% Nd doping. The calculated lattice parameter of Nd doped PZT films, decreases monotonically up to 8 at % of doping. Substitution of A site (contains Pb ion) with an ion having smaller ionic radii (i.e Nd) than the host ion will lead to the shrinkage of lattice parameter hence, as observed the lattice parameter should reduce with the increase in Nd content.

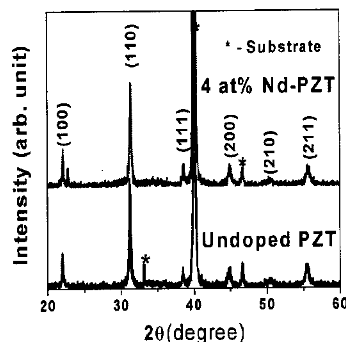

Figure 2 X-ray diffractograms of undoped and 4 at% Nd doped PZT thin films

Surface Morphology

Figure 3 shows the AFM micrographs of undoped, 4 at%, 6 at%, and 8 at % Nd doped PZT thin films. The undoped film has a smooth and homogeneous microstructure with an average grain size about 200 nm. The average grain size is slightly reduced in 4 at % Nd doped film however, it reduces drastically with further Nd addition as shown in Fig 3 (c) and 3 (d). Overall, all the films showed uniform grain size distribution and surface conditions, within the present annealing conditions. The surface roughness of the undoped PZTfilm was 2.1 nm and it increased systematically with Nd addition and thus the surface roughness 8 at% Nd doped PZT film was ≈ 8.2 nm. From the observed microstructures of the films it is clear that the grain sizes are inversely proportional to the amount of Nd content. Introduction of Nd into the PZT lattice causes the increase in Pb vacancy concentration. To maintain the charge neutrality, vacancies could also be introduced at B site as well. The lead vacancy concentration is increased with the increase in Nd content which in turn stabilizes the intermediate pyrochlore phase [6]. Most likely the Nd rich pyrochlore phase is localized at the grain boundary region and if the grain boundary is surrounded with PZT substituted with Nd^{3+} ions, vapor pressure of PbO might be decreased and in that case as observed grain growth is inhibited. The pyrochlore phase at the grain boundary for PZT doped with higher Nd content (> 4 at %) was difficult to be observed in AFM micrographs and TEM investigations are underway to observe the distribution of the pyrochlore phase in the Nd doped PZT thin films.

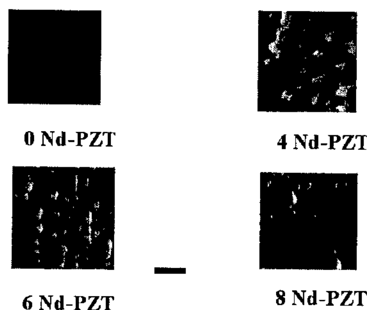

Figure 3 AFM micrographs of Nd doped PZT thin films. The length of the bar is 0.25μm.

Electrical Properties

Figure 4 shows the e-beam lithography fabricated IDT pattern on PZT thin films about 1 μm thick. About 5 identical IDT electrode patterns were deposited on each sample and the electrical data reported are the average of the respective measurement data on these five electrodes. Each IDT contains 15 fingers of length 100 μm and separated by 10μm.

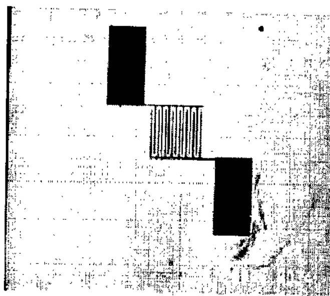

Figure 4 SEM micrograph of IDT pattern deposited by e-beam lithography

Figure 5 (a) and 5 (b) depict the capacitance vs frequency response of undoped and

4 at % Nd doped PZT films. It may be seen that the capacitance shows a frequency dependence, while the dispersion behavior tended to reduce with increasing Nd content. At low frequencies, the dispersion in capacitance is normally due to space charge accumulation, while at higher frequencies, the grain-grain boundary capacitance interference becomes mostly responsible. It may also be realized from Fig. 5 (a) that the dielectric constant reduces with increasing Nd content. Such behavior may be attributed to the following :

(a) Presence of pyrochlore phase , which may go undetected in XRD, with increasing Nd content which offers a relatively lower dielectric constant in series with the perovskite phase. Such combination effectively reduces the total dielectric constant.

(b) Reduced grain size with increasing Nd content , as seen from the AFM micrograph in Fig. 4. It is generally observed in ferroelectric ceramic materials such as PZT, $BaTiO_3$ etc that the dielectric constant is sensitive to grain size and is extrinsically influenced [7]. The observed dielectric behavior in the present case may be found consistent with these reports.

The variation of tan δ with frequency at different dopant concentrations is shown in Fig. 5 (b). It may be realized that the dielectric loss reduces with increasing Nd concentration, which may be associated with reduced oxygen vacancies. It is also worth mentioning that the pyrochlore phase material is more insulating in nature The presence of even minute amount of pyrochlore phase fraction may also contribute to reduced dielectric losses.

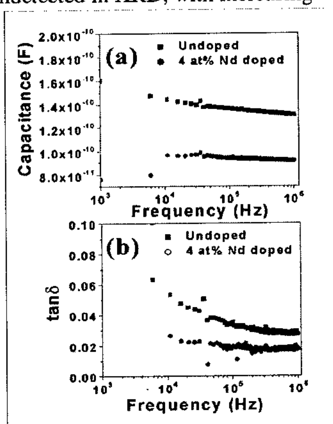

Figure 5 Frequency dispersion of (a) capacitance and (b) loss tangent of undoped and 4 at% Nd doped PZT thin films

Figure 6 shows the electrical hysteresis between the induced charge and the applied voltage of undoped and 4 at % Nd doped PZT thin films. As shown in the figure, saturated hysteresis loops are obtained in both undoped and doped PZT thin films. However, the Nd doped film withstand less voltage as compared to the undoped one. This could be due to rougher surface of the doped film as compared to the undoped film. The charge vs voltage data can be converted to a polarization vs electric field scale, assuming that the area switched is the product of the length of the electrode fingers and film thickness and the electric field is uniform across the electrode gap [4]. However, the calculated values are not very accurate as the fringing field associated at the end of each finger electrode would affect the polarization and electric

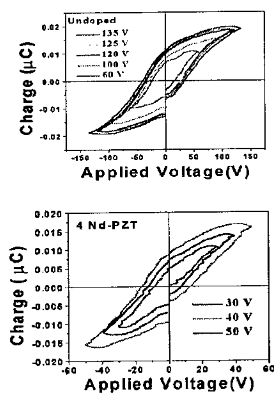

Figure 6 Hysteresis loops of PZT thin films

field values. However, the approximate remnant polarization (P_r) in the range of 20-30 μC /cm^2 and the coercive field (E_c) in the order of 40-50 kV/cm are close to the corresponding values of undoped PZT deposited on platinized silicon substrate where the hysteresis measurement was performed applying electric field across the thickness of the film. It was observed that the polarization reduces moderately up to 4 at % Nd content. As mentioned earlier, considering the effect of ionic radius, the lattice parameter shrinks with the addition of Nd. Polarization in the ferroelectric perovskite lattice is contributed by the displacement of higher valence B site cations along the polar axis from their position in the paraelectric phase. The contraction of lattice parameter is probably accompanied by a decrease in the rattling lattice space available for B site cations and therefore the dielectric constant and the polarization values decrease moderately up to 4 at % Nd doping.

CONCLUSIONS

In the present work undoped and Nd doped PZT (53/47) thin films were prepared on platinized silicon substrate by chemical solution deposition technique. Process methodology for the fabrication of IDT electrode by e-beam lithography has been optimized. The symmetric hysteresis loops measured by using IDT electrodes on the surface of the undoped and Nd doped PZT thin film suggest excellent transverse coherence in the films. Work is in progress to study the fatigue, retention and leakage current characteristics of these films.

Acknowledgment

This work was supported in parts by the grants : NSF-DMR-9801759, NASA-NCC5-518 and DAAG55-98-1-0012. Thanks are due to Mr. A.L. M. Cruz for the AFM measurements and MCC for providing the XRD facilities.

REFERENCES

1. Q.M. Wang, Q. Zhang, B. Xu, R. Liu, and L.E. Cross, *J. Appl. Phys.* **86**, 3352, (1999).
2. V.D. Kugel, S. Chandran, and L.E. Cross, *Appl. Phys. Lett.* **69**, 2021, (1996).
3. D.L Polla and L.F. Francis, *MRS Bull.* **21**, 59, (1996).
4. B. Xu, Y. Ye, L.E. Cross, J.J. Bernstein, and R. Miller, *Appl. Phys. Lett.*, **74**, 3549, (1999)
5. J.C. Nabity and M.N. Wybourne; *Rev.Sci. Instrum.* **60** (1), 27, (1989).
6. S.B. Majumder, D.C. Agrawal, Y.N. Mohapatra, and V.N. Kulkarni, Integr. Ferroelectr. **9**, 271, (1995).
7. N. Tohge, S. Takahashi, T. Minami, J. Am. Ceram. Soc. **74**, 67, (1991).

Piezoelectric Materials, Capacitors, and Novel Devices

Mat. Res. Soc. Symp. Proc. Vol. 655 © 2001 Materials Research Society

OXIDE FILMS FOR INTEGRATED CAPACITORS IN THIN FILM FUNCTIONAL MODULES

M. Klee*, D. Wissen*, W. Keur**, R. Kiewitt*, D. Bausen*, P. Lok***,
* Philips GmbH Forschungslaboratorien Aachen, Weißhausstr. 2, 52066 Aachen, Germany, mareike.klee@philips.com
** Philips Research Laboratories Eindhoven, P.O. BOX
*** Philips Discrete Semiconductors, Nijmegen

ABSTRACT

Single oxide films as well as complex oxide films are intensively studied for multi-chip modules with integrated passive functions. In this paper the processing and properties of oxide films such as Ta_2O_5, TiO_2, Nb_2O_5, Ta_2O_5-Al_2O_3, Ta_2O_5–Nb_2O_5 as well as complex oxide films such as $BiNbO_4$ and $Ba_{1-x}Sr_xTiO_3$ films will be discussed with respect to their integration into thin film functional modules.

INTRODUCTION

Ceramic oxide films are a revolution in the electro-ceramic industry. The integration of ferroelectric thin films into semiconductor processes is the basis for a new class of memories such as ferroelectric non-volatile memories (FERAMs). The high performance of oxide films, which has been achieved in the last years as well as the progress in integration technologies offers high density functional modules [1-11]. To apply oxide thin films in miniaturised and integrated high performance devices, thin films have to be tuned with respect to their special applications. In the following, the processing and the electric properties of oxide thin films will be discussed, especially, with respect to their dielectric properties in integrated capacitors.

HIGH PERFORMANCE FUNCTIONAL MODULES

For high functionality portable electronic systems such as mobile communication and wireless data transfer systems, new product concepts are requested, that enable the integration of passive functions (capacitors, resistors, inductors) with active functions into high performance multifunctional modules. Various concepts are developed:

- Thick Film Technologies
- Ceramic Co-firing Processes (MCM-C)
- Laminate Technologies (MCM-L)
- Thin Film Multi-chip Modules (MCM-D)

Thin film functional modules with a planar integration of e.g matching circuits, filtering circuits next to active functions such as amplifying stages. on top of Si or Al_2O_3 are on the market. To achieve a high degree of integration also three-dimensional integrated modules have been demonstrated, see ref. [1].

Dielectric thin films with a temperature coefficient of the capacitance of ± 60 or ± 30 ppm/K

For applications such as integrated matching circuits, thin film capacitors are requested, that show a very stable capacitance over a large temperature range. Thin film capacitors have to be developed that offer a temperature stability of the capacitance of ± 60 or ± 30 ppm/K, if

heated up from –55°C up to 125°C (so called COH or COG specifications). One dielectric thin film material with a temperature coefficient of the capacitance of ± 30 ppm/K, is SiN(H). SiN(H) with a relative permittivity of 6.5 gives limitations in the integration of large capacitance values.

Thin films in the systems Ta_2O_5, TiO_2, Nb_2O_5, Ta_2O_5-Nb_2O_5, Ta_2O_5-Al_2O_3

To achieve integrated capacitors with high capacitance density and stable temperature characteristic of the capacitance, we investigated various oxide films in the systems Ta_2O_5, TiO_2, Nb_2O_5, Ta_2O_5-Nb_2O_5, Ta_2O_5-Al_2O_3. Cava et al. [12-14] studied ceramics in the systems Ta_2O_5-Al_2O_3, Ta_2O_5-SiO_2, Ta_2O_5-TiO_2, Ta_2O_5-Nb_2O_5. For polycrystalline $(Ta_2O_5)_{1-x}(Al_2O_3)_x$ ceramics with x = 0.05-0.2 an enhanced dielectric constant of approx. 40 for x=0.1 compared with pure Ta_2O_5 (ε_r approx. 25-30) is reported. Moreover the temperature coefficient of the relative permittivity could be greatly suppressed in the Al_2O_3 substituted materials. A relative permittivity of 30-40 and a temperature coefficient of less than 20 ppm/K has been found in the temperature range of –40°C up to +100°C for $0.05<x<0.07$. With the doping of Ta_2O_5 with Al_2O_3 the positive temperature coefficient of + 250 ppm/K has been shifted to negative values of –5 ppm/K up to –40 ppm/K. X-ray powder diffraction analysis reported by Cava et al. [12] stated for ceramics with $0<x<0.075$ a solid solution of Ta_2O_5-Al_2O_3. For $0.075<x<0.2$ a solid solution phase of Ta_2O_5-Al_2O_3 as well as $AlTaO_4$ are present. Desu et al. [15] processed Al_2O_3 doped Ta_2O_5 thin film by spin-on processing. They report for $(Ta_2O_5)_{0.9}(Al_2O_3)_{0.1}$ films a relative permittivity of 42.8 and a temperature coefficient of 20 ppm/K.

In this paper we report the processing and properties of Ta_2O_5, TiO_2, Nb_2O_5 as well as Ta_2O_5-Al_2O_3 and Ta_2O_5–Nb_2O_5 thin films. Layers with a thickness of 400 nm - 800 nm have been processed by means of sol-gel techniques on top of Si wafers with a Ti/Pt electrode (see Table 1). Amorphous films are grown at temperatures of 300-600°C; crystalline films are formed at temperatures of 650-750°C. The characterisation of thin film capacitors with sizes of 1 mm^2 revealed in accordance with the bulk ceramics for amorphous Ta_2O_5 films a relative permittivity of 21 and dielectric losses of 0.12 % (measured at 0.1V, 1 KHz). Crystalline Ta_2O_5, Nb_2O_5 show relative permittivities of 35 and 73 and dielectric losses of 0.4-0.7% (measured at 0.1 V, 1KHz). The TiO_2 layers with the anatase phase revealed relative permittivities of 75 and dielectric losses of 0.1%. With these oxides, relative permittivities, which are factors of 5-10 larger than SiN(H) are achieved. However, very strong temperature coefficients of the permittivities compared with SiN(H) are found. For crystalline Ta_2O_5 films a temperature coefficient of +210 ppm/K, measured at 100 kHz (see Fig. 4) was determined. For Nb_2O_5 films a temperature coefficient of + 480 ppm/K (measured at 100 kHz) and for TiO_2 films a temperature coefficient of - 750 ppm/K (measured at 100 kHz) was found. To tune thin oxide films with respect to their temperature stability of the capacitance, we studied films in the system $(Ta_2O_5)_{1-x}(Al_2O_3)_x$ with x=0.03-0.1 Amorphous films with a dense morphology (see Figure 1a) are processed on top of Pt (111) electrodes at temperatures of 600-650°C. Un-doped as well as doped Ta_2O_5 films with x=0.05-0.1 show relative permittivities of 21-15 (see Table 1). The dielectric losses, measured at 0.1 V, 1 KHz are in the order of 0.1-0.3 %. Measurements of the temperature dependence of the capacitance from –55°C up to + 125°C (100 KHz, 0.1 V), revealed for the amorphous $(Ta_2O_5)_{1-x}(Al_2O_3)_x$ with x=0.0-0.1 temperature coefficients of +65 ppm/K (Ta_2O_5), + 68 ppm/K ($(Ta_2O_5)_{1-x}(Al_2O_3)_x$ x=0.05), + 85 ppm/K ($(Ta_2O_5)_{1-x}(Al_2O_3)_x$ x=0.1) (see Fig. 2). These amorphous films are slightly out of the ± 60 ppm/K specification.

Table 1 Dielectric properties of amorphous and crystalline $(Ta_2O_5)_{1-x}(Al_2O_3)_x$ films with x=0.0-0.1

Material	crystallinity	ε_r 0.1 V/ 1 KHz	tanδ % 0.1 V 1 KHz	TCC ppm/K
Ta_2O_5	amorphous	21	0.12	see Fig. 2
$Ta_2O_5)_{0.95}(Al_2O_3)_{0.05}$	amorphous	21	0.3	"
$(Ta_2O_5)_{0.9}(Al_2O_3)_{0.1}$	amorphous	15	0.1	"
Ta_2O_5	crystalline	35	0.7	see Fig. 4
$(Ta_2O_5)_{0.97}(Al_2O_3)_{0.03}$	crystalline	39	0.5	"
$(Ta_2O_5)_{0.95}(Al_2O_3)_{0.05}$	crystalline	38	0.8	"
$(Ta_2O_5)_{0.945}(Al_2O_3)_{0.055}$	crystalline	40	0.3	"
$(Ta_2O_5)_{0.93}(Al_2O_3)_{0.07}$	crystalline	39	0.3	"
$(Ta_2O_5)_{0.9}(Al_2O_3)_{0.1}$	crystalline	38	0.3	"

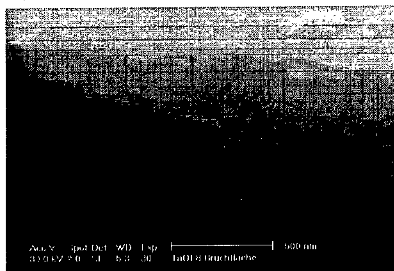

Figure 1a Amorphous $(Ta_2O_5)_{1-x}(Al_2O_3)_x$ x=0.1, grown on top of Si/SiO$_2$/Ti/Pt substrates

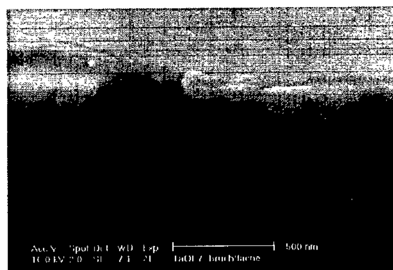

Figure 1b Crystalline $(Ta_2O_5)_{1-x}(Al_2O_3)_x$ x=0.1, grown on top of Si/SiO$_2$/Ti/Pt substrates

For crystalline Ta_2O_5 films, firing temperatures of 700°C were applied. Al_2O_3 doping increases the crystallisation temperature to 750°C for $(Ta_2O_5)_{1-x}(Al_2O_3)_x$ films with x=0.1 SEM investigations of un-doped and doped Ta_2O_5 films show for the crystalline films a columnar growth on top of the Pt(111) electrodes (see Fig. 1b). The crystalline $(Ta_2O_5)_{1-x}(Al_2O_3)_x$ films revealed the orthorhombic low temperature phase. A shift of the X-ray diffraction lines was obtained for $(Ta_2O_5)_{1-x}(Al_2O_3)_x$ films with x=0.03-0.1 compared with the pure Ta_2O_5 films, demonstrating the formation of a solid solution in $(Ta_2O_5)_{1-x}(Al_2O_3)_x$ films (see Fig. 3). Striking is, that the $(Ta_2O_5)_{1-x}(Al_2O_3)_x$ films with x=0.03-0.1, show a splitting of the (002) and (003) lines. This indicates the formation of a slightly monoclinic distorted lattice in the $(Ta_2O_5)_{1-x}(Al_2O_3)_x$ films.

Measurements of the relative permittivity (1 KHz, 0.1V) showed for the Al_2O_3 doped Ta_2O_5 thin films relative permittivities of 38-40 and dielectric losses of 0.3-0.8 % (see Table 1). Measurements of the capacitance (at 100 KHz, 0.1 V) as a function of temperature have been carried out for crystalline $(Ta_2O_5)_{1-x}(Al_2O_3)_x$ films with x=0.0-0.1 (see Figure 4). In accordance with the bulk ceramics [12] we found for crystalline Ta_2O_5 films a temperature coefficient of + 210 ppm/K.

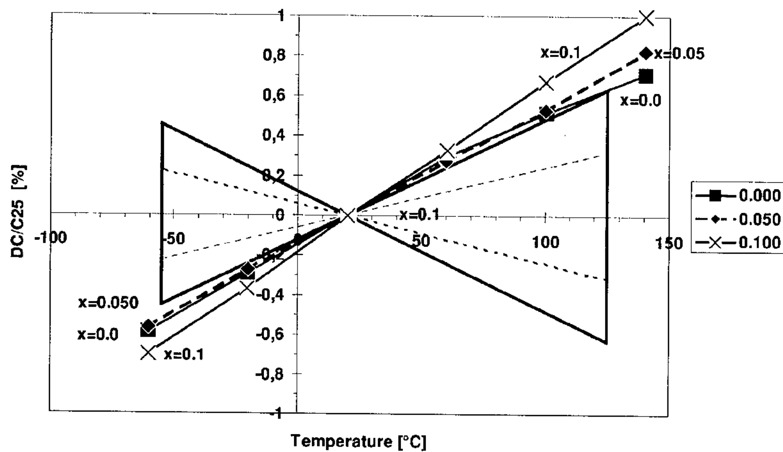

Figure 2 Relative capacitance as a function of temperature for amorphous $(Ta_2O_5)_{1-x}(Al_2O_3)_x$ films with x=0.0-0.1. Measurement frequency 100 KHz. In the figure the ± 60 ppm/K (black line) and ± 30 ppm/K (dashed line) specifications are included.

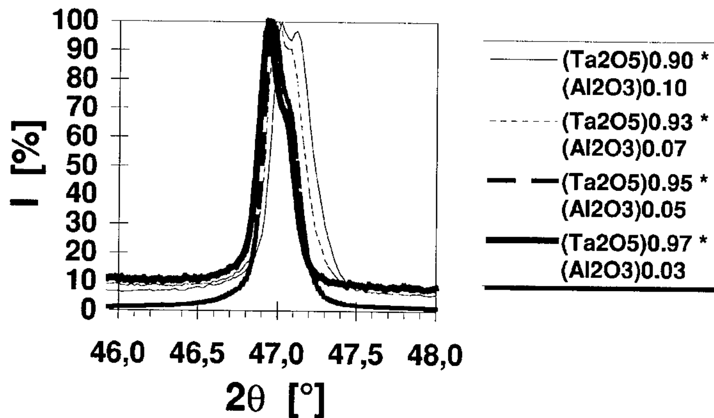

Figure 3 X-ray diffraction patterns for the (002) lines of crystalline $(Ta_2O_5)_{1-x}(Al_2O_3)_x$ films with x=0.03-0.1.

Doping of the Ta_2O_5 films with Al_2O_3 (x=0.03), suppresses the temperature coefficient down to approx. + 74 ppm/K. For an Al_2O_3 doping level of x=0.055 the $(Ta_2O_5)_{1-x}(Al_2O_3)_x$ films achieved a temperature coefficient of the capacitance better than ± 30 ppm/K. Doping of $(Ta_2O_5)_{1-x}(Al_2O_3)_x$ films with Al_2O_3 x=0.07- 0.1 shifts the temperature coefficient of the capacitance in the negative range. For $(Ta_2O_5)_{1-x}(Al_2O_3)_x$ films with x=0.1 a temperature coefficient of – 134 ppm/K was measured. A plot of the temperature coefficients of crystalline $(Ta_2O_5)_{1-x}(Al_2O_3)_x$ films as a function of the Al_2O_3 doping x is shown in Figure 5 and revealed a slope of approx. – 3306 ppm/K per Al doping x.

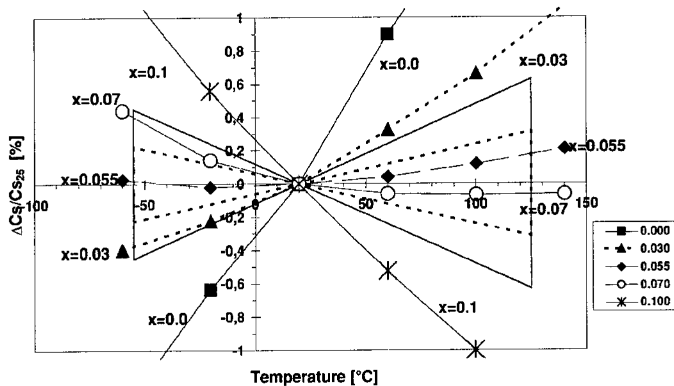

Figure 4 Relative capacitance as a function of temperature for crystalline $(Ta_2O_5)_{1-x}(Al_2O_3)_x$ films with x=0.0-0.1. Measurement frequency 100 KHz. In the figure the specifications with ± 60 and ± 30 ppm/K are included.

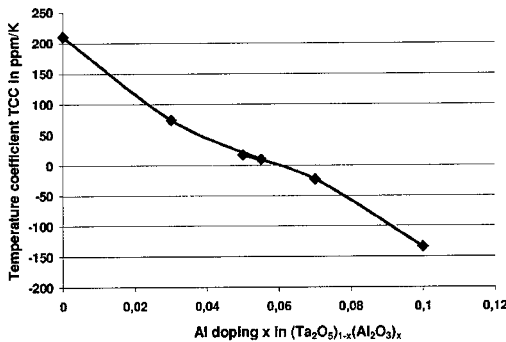

Figure 5 Temperature coefficient TCC as a function of Al doping for crystalline $(Ta_2O_5)_{1-x}(Al_2O_3)_x$ films with x=0.0-0.1 (measurements taken at 100 KHz).

Measurements of the current density as a function of the electrical field for metal-insulator-metal structures have been carried out for $(Ta_2O_5)_{1-x}(Al_2O_3)_x$ films. Voltage steps have been applied to the samples and the current was measured as a function of time. The experiments have been carried out at room temperature for 10 s up to 60 s. In Figure 6 the current densities measured after 10 s are given as a function of the electric field for amorphous and crystalline $(Ta_2O_5)_{1-x}(Al_2O_3)_x$ with x=0.1. For amorphous films, the current density is below $5*10^{-10}$ A/cm^2 for electrical fields up to 1 MV/cm. Above 3 MV/cm a strong increase of the current density has been measured. The crystalline $(Ta_2O_5)_{1-x}(Al_2O_3)_x$ films show a current density below 10^{-9} A/cm^2 only up to fields of 100 kV/cm. A strong increase of the current density is observed at much lower electrical fields of 300 kV/cm.

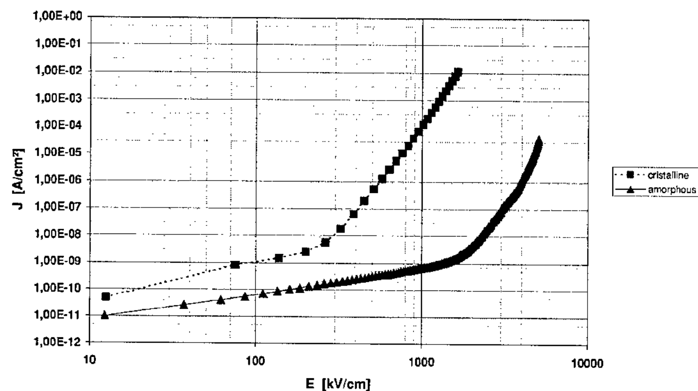

Figure 6 Current density as a function of field for amorphous and crystalline $(Ta_2O_5)_{1-x}(Al_2O_3)_x$ films with x=0.1 (measurements taken at room temperature after 10 sec).

$BiNbO_4$ thin films with V and Cu doping

Dielectric materials with high capacitance densities and low temperature coefficient of capacitance can also be found in complex oxides used in microwave applications. In ceramics, numerous microwave materials with complex compositions and relative permittivities of 17-80 are applied. In the last years, there has been a focus in microwave ceramics that can be processed with highly conductive metals such as Cu or Ag. One attractive low-temperature co-fired ceramic is $BiNbO_4$, which can be sintered at temperatures of 875-975°C, if V_2O_5 is added as sintering aid, see ref. [16, 17]. This microwave material shows a relative permittivity of 43-44, a Q-factor of 2000-4000 at 1 GHz and a temperature coefficient of the resonance frequency of 3-20 ppm/K. Investigations by C. Yang [17] on $BiNbO_4$ ceramics have shown that V_2O_5 doping in the order of 0.1-0.9 wt% shifts the temperature coefficient of the resonance frequency to positive values, whereas CuO doping shifts the temperature coefficient of the resonance frequency to negative values. Thin films in the system Bi-Nb-O are reported by S. Chattopadhyay et al. [18], who make use of a pulsed laser deposition technique. W. Ren et al. [19] studied bismuth pyrochlore films in the system Bi-Zn-Nb-O, by means of sol-gel processes.

We investigated thin films $BiNbO_4$ with V-doping and Cu-doping by a modified sol-gel processing. Films with 1-2 at% V or 1-2 at % Cu as well as a mixed doping with 1-2 at% V and 1-2 at% Cu were deposited on top of Si/SiO_2 substrates with a Ti/ Pt (111) electrode. 30-50 nm thick $BiNbO_4$ films doped with V and Cu and fired at 700°C grow on top of Pt(111) in the triclinic β- $BiNbO_4$ phase (see Figure 7). The triclinic β- $BiNbO_4$ phase with the lattice constants a=0.771 nm, b=0.555 nm, c=0.797 nm, α=89°, β=77°, γ=87° is the high temperature phase and forms in ceramics irreversibly at temperatures above 1020°C. Bulk ceramics sintered at temperatures of 880-960°C form the low temperature α- phase, which is closely related to the stibiotantalite ($SbTiO_4$) phase with an orthorhombic lattice and the lattice constants a=0.5673 nm, b=1.1714 nm, c=0.4978 nm. The low processing temperature of 700°C applied for our thin V, Cu doped BiNbO4 suggest the formation of the orthorhombic phase. The crystallisation of the triclinic high temperature phase in very thin films might be explained by a surface nucleation on top of the Pt(111) electrode. This hypothesis has been confirmed by processing of 0.56 μm thick films on top of Pt (111) electrodes at 700°C. The approx. 0.5 μm thick films

crystallise in the orthorhombic low temperature $BiNbO_4$ phase at a temperature of 700°C (see Figure 8).

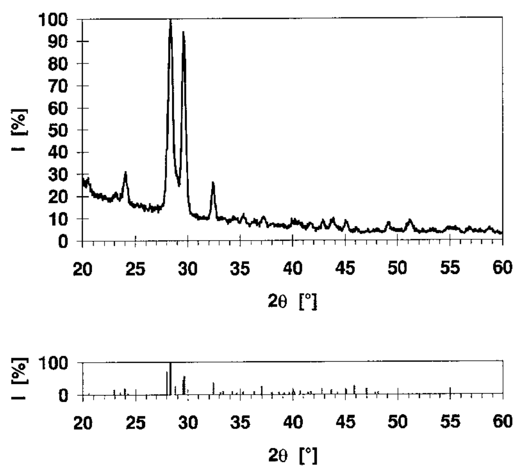

Figure 7 X-ray diffraction pattern of a triclinic $BiNbO_4$ film with V and Cu-doping, grown on top of a Pt (111) electrode. For comparison the powder diffraction pattern of the triclinic ß-phase from the JCPDS data (No. 16-0486) is given.

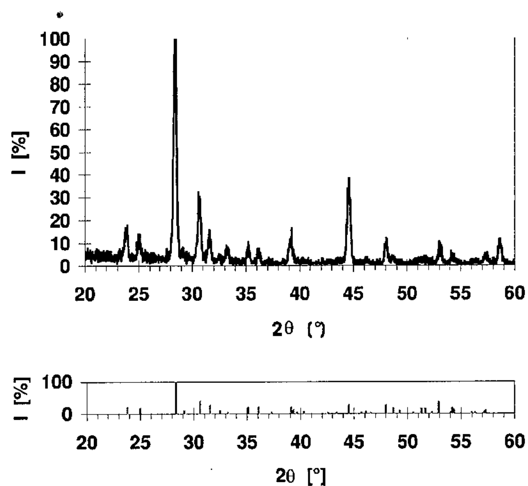

Figure 8 X-ray diffraction pattern of an orthorhombic $BiNbO_4$ film with V and Cu-doping. For comparison the powder diffraction pattern of the orthorhombic α-phase from the JCPDS data (16-0295) is given.

We assume that processing of thicker layers results in a bulk nucleation and the formation of the low temperature orthorhombic $BiNbO_4$ phase. The orthorhombic $BiNbO_4$ films with V- and Cu-doping grow with a dense morphology on top of $Si/SiO_2/Ti/Pt$ substrates.

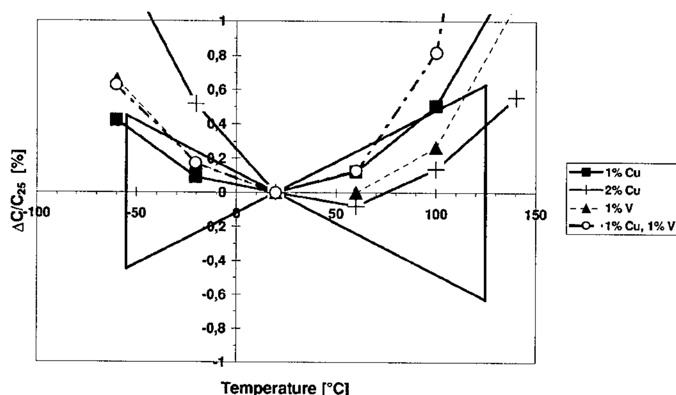

Figure 9 Relative capacitance as a function of temperature for orthorhombic $BiNbO_4$ films with V/ Cu doping. Measurement frequency 100 KHz. In the figure the specification with ± 60 ppm/K is included.

Measurements of the capacitance and the dielectric losses revealed for the V-doped, the Cu-doped and the V and Cu co-doped $BiNbO_4$ films relative permittivities of 50-58 and dielectric losses of 0.03-0.3% (measured at 1 KHz, 0.1 V). The $BiNbO_4$ films with 1 at % Cu doping achieve in the temperature range of –55°C up to 100°C a temperature coefficient of ± 60 ppm/K (see Figure 9). Higher Cu doping (2 at % Cu) gives rise to a negative shift, as reported for bulk ceramics so that films with 2% Cu show a variation of the relative capacitance of ± 60 ppm/K from 25°C up to 125°C. For $BiNbO_4$ films with 1 at % V doping, the capacitance does not deviate from the room temperature values more than ± 60 ppm/K for the temperature range of –35°C up to 110°C. Adding 1 at% V and 1 at% Cu to $BiNbO_4$ films results in films with a variation of the relative capacitance of ± 60 ppm/K in the temperature range of –40°C up to +70°C.

Dielectric thin film with a stability of the capacitance of ± 15% from –55°C up to 125°C

To integrate functions such as filters into thin film functional modules, capacitors of a few hundred pF up to tens of nF have to be realised. Here especially the lead-based systems such as PZT play an important role see ref. [1,5,9]. These material systems have been intensively studied [5] and will not be reviewed. We will discuss the performance of earth-alkaline titanate films for these applications.

$Ba_{1-x}Sr_xTiO_3$ thin films with x=0-0.3

$Ba_{1-x}Sr_xTiO_3$ thin films with x=0-0.3 have been processed on top of Si and Al_2O_3 substrates with a thickness of 100-500 nm. A modified sol-gel process has been applied, see ref.

[5]. Ti/Pt electrodes have been deposited underneath the dielectric layers by sputtering. Figures 10a, b demonstrate the dense and homogeneous microstructure, which could be achieved for $Ba_{1-x}Sr_xTiO_3$ thin films on top of Si as well as Al_2O_3 substrates. Measurements of the capacitance and dielectric losses revealed for the $Ba_{1-x}Sr_xTiO_3$ films grown on top of ceramic substrates in accordance with the films grown on top of Si, relative permittvities of 360-660 and dielectric losses of 0.6-0.8% (measured at 0.1 V/ 1KHz). The larger relative permittivities of 660 are found for the thicker films with d=0.3-0.5 μm.

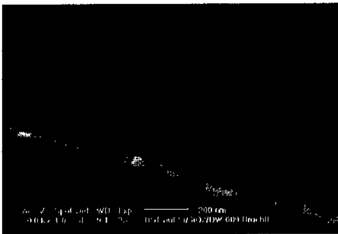

Figure 10a $Ba_{0.7}Sr_{0.3}TiO_3$ films grown on top $Si/SiO_2/Ti/Pt$ substrate;

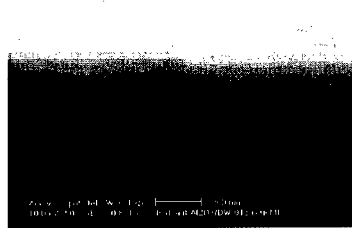

Figure 10b $Ba_{0.7}Sr_{0.3}TiO_3$ films grown on top $Al_2O_3/Ti/Pt$ substrate;

The temperature stability of the capacitance of $Ba_{1-x}Sr_xTiO_3$ thin films grown on top of Si and Al_2O_3 substrates was studied as a function of Sr-doping. As can be derived from Figure 11, pure $BaTiO_3$ thin films grown on top of Al_2O_3 substrates fulfil by far the X7R specification ((C-C_{25}/C_{25})*100 achieves ± 15% from –55°C up to 125°C). The variations of the capacitance at –55°C up to 125°C are for our $BaTiO_3$ thin films less than 7%. A flat curve is observed with a broad maximum at approx. 60°C. The curve shows a shift of the maximum by approx. 65°C to lower temperatures compared with $BaTiO_3$ bulk ceramics. Investigations of $Ba_xSr_{1-x}TiO_3$ thin films grown by sputtering on top of MgO (100) / Pt (100) substrates by Abe et al. [20] revealed that a strong elongation of the c-axis in $Ba_xSr_{1-x}TiO_3$ films, caused by an lattice mismatch between Pt and $Ba_xSr_{1-x}TiO_3$ shifts the Curie point of the films by more than 150°C to higher temperatures compared with the bulk ceramics.

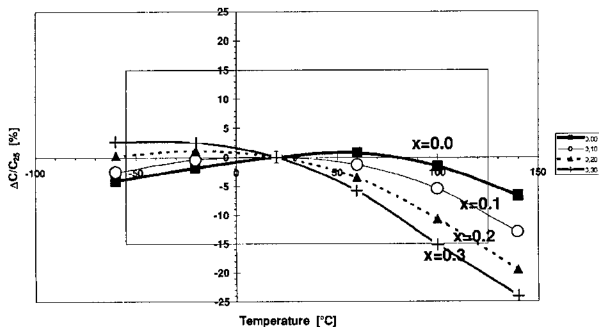

Figure 11 Relative capacitance as a function of temperature for $Ba_{1-x}Sr_xTiO_3$ films grown on top of Al_2O_3 substrates. Temperature range –55°C - + 125°C, measurement frequency 1 KHz. In the figure the X7R specification is included.

Our polycrystalline $BaTiO_3$ thin films, grown on top of Al_2O_3 ceramics, experience quite different stress conditions, which result in a shift of the broad maximum to lower temperatures. This holds for the pure $BaTiO_3$ films, where a shift of approx. 65°C to lower temperatures is observed as well as for Sr-doped $BaTiO_3$ thin films (see Fig. 11). Solid solutions of $Ba_{1-x}Sr_xTiO_3$ bulk ceramics show a Curie point shift of approx. 4° per at% Sr. A similar behaviour has been found in our thin films. The broad maximum of $BaTiO_3$ thin films at 60°C, is shifted to approx. room temperature for 10 at% strontium doping, to –10°C - –20°C for 20 at% Sr doping and to –40°C - –50°C for 30 at % Sr doping (see Fig. 11). Due to the broad maximum at +60°C for the pure $BaTiO_3$ thin films grown on top of Al_2O_3 substrates and the shift of the maximum by approx. 4° per at% Sr in $Ba_{1-x}Sr_xTiO_3$ thin films, only the $Ba_{1-x}Sr_xTiO_3$ with x=0.0 and 0.1 fulfil the X7R specification. The $Ba_{1-x}Sr_xTiO_3$ films with x=0.2 fall out of the specification above 120°C. Films with x= 0.3 show only in the temperature range –55°C up to 100°C a deviation of the capacitance from the room temperature value of +5% up to –15%.

To determine the quality of $Ba_{1-x}Sr_xTiO_3$ films, grown on top of Al_2O_3 substrates we investigated the current density of the thin films as a function of the electrical field. Voltage steps have been applied and the current has been taken after 1000 s. Measurements have been performed at room temperature as well as at 165°C. Figure 12 shows the current density of $Ba_{0.7}Sr_{0.3}TiO_3$ films grown on top of Al_2O_3 substrates as a function of the applied field. Low current densities of < 10^{-9} A/cm² were observed up to fields of 100 kV/cm. With increasing field an increase of the current density is found. The $Ba_{1-x}Sr_xTiO_3$ films, grown on top of Al_2O_3 substrates, show current densities which are comparable to the data reported for films grown on top of Si-substrates by e.g. CVD processes.

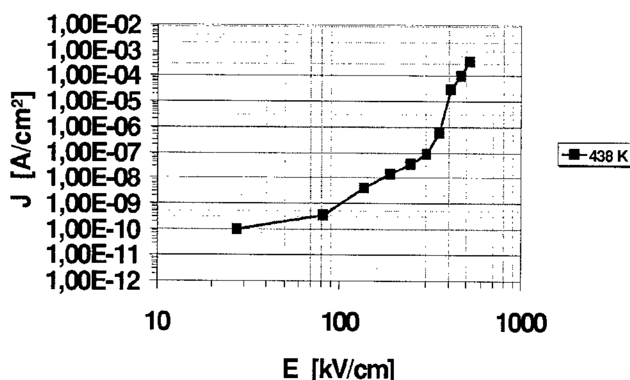

Figure 12 Current density as a function of field for a $Ba_{0.7}Sr_{0.3}TiO_3$ film grown on top of an Al_2O_3 substrate with Ti/Pt electrode (measurement taken at 165°C after 1000 s).

CONCLUSIONS

High performance oxide thin films have relevance for integrated capacitors in complex functional modules. Thin films in the systems Ta_2O_5, TiO_2, Nb_2O_5, Ta_2O_5-Al_2O_3, Ta_2O_5–Nb_2O_5, $BiNbO_4$, $Ba_{1-x}Sr_xTiO_3$ have been processed by sol-gel and modified sol-gel techniques. Metal-insulator-metal structures have been processed on top of Si and Al_2O_3 substrates and the thin films were studied with respect to their performance for integrated capacitors. Crystalline Ta_2O_5, TiO_2 and Nb_2O_5 films offer relative permittivities of 39-75. Doping of Ta_2O_5 thin films

Mat. Res. Soc. Symp. Proc. Vol. 655 © 2001 Materials Research Society

Thin Film Superlattices of Lead Based Relaxors

M. H. Corbett, J. M. Gregg, R. M. Bowman
Condensed Matter Physics and Material Science Division,
Department of Pure and Applied Physics, Queen's University Belfast,
University Road, Belfast, BT7 1NN, UNITED KINGDOM.

ABSTRACT

Thin film capacitor structures in which the dielectric is composed of superlattices of the relaxors $[0.2Pb(Zn_{1/3}Nb_{2/3})O_3 - 0.8BaTiO_3]$ and $Pb(Mg_{1/3}Nb_{2/3})O_3$ have been fabricated on MgO {100} substrates by Pulsed Laser Deposition. Structural studies show dielectrics to be 100% perovskite, with strong chemical distinction between individual relaxor layers. The dielectric properties of the superlattices were investigated as a function of periodicity. Significant enhancement of the dielectric constant was observed in relatively fine-scale superlattices, consistent with previous studies. However, unlike previous work, in these relaxor superlattices dielectric enhancement is not associated with increased loss. Rather tan δ is low across the entire superlattice series. Polarisation measurements as a function of temperature suggest that the observed enhancement in dielectric constant is associated with the onset of coupled behaviour. The thickness of the individual layers in the superlattice at which coupled *functional* behaviour becomes apparent is ~10nm and is comparable to that found in literature for coupled *structural* behaviour.

INTRODUCTION

An enhancement of the dielectric constant of thin film ferroelectrics is believed to be obtainable if two or more materials are multi-layered together in a fine superlattice structure [1,2]. Experimental work has shown this to be the case [3-6]. However the degree of observed enhancement and the scales of superlattice periodicity at which enhancement occurs are inconsistent across the literature. Recent work has noted that such increased dielectric constants can be correlated to the onset of significant Maxwell-Wagner effects rather than any co-operative dielectric interaction [7], and modelling has shown that all the novel features displayed by ferroelectric superlattices can be generated by Maxwell-Wagner considerations [11]. The implication is that increased defect-related transport, rather than dielectric interactions between nanolayers, is responsible for the enhancements experimentally observed.

In spite of this, work on the structural phase transformation behaviour in $KTaO_3/KNbO_3$ superlattices [8] indicates that genuine coupled behaviour can occur at fine layer thicknesses. To date though, such inter-layer coupling has not been clearly manifested in functional properties.

In an attempt to observe coupled functional behaviour in superlattices without interference from Maxwell-Wagner effects, the authors have studied thin film capacitor structures in which the dielectric is composed of superlattices of two relaxor electroceramics $[0.2Pb(Zn_{1/3}Nb_{2/3})O_3 - 0.8BaTiO_3$ (0.2PZN-0.8BT) and $Pb(Mg_{1/3}Nb_{2/3})O_3$ (PMN)]. This paper presents results from the study and their interpretation.

EXPERIMENTAL DETAILS

Superlattices of (0.2PZN-0.8BT / PMN) with $SrRuO_3$ (SRO) lower electrodes were fabricated by Pulsed Laser Deposition on polished single crystal {100} MgO substrates. The SRO electrode was deposited for 30 minutes in 0.15mbar O_2 at 800°C and then allowed to cool naturally at this gas pressure to a temperature of 630°C. Superlattices of 0.2PZN-0.8BT and PMN were then deposited with 0.2PZN- 0.8BT as the bottom layer. Deposition time was ~ 30 minutes with laser repetition rate 10Hz and fluence at the target of ~ 1.7 J/cm^2. Total dielectric film thickness was maintained at ~ 600nm. After deposition, the films were annealed *in situ* at 625°C in 900mbar O_2 for 1 hour. Au top electrodes (~2mm^2) were then deposited by thermal evaporation through a hard mask.

X-ray diffraction scans were performed on a Siemens D5000 x-ray diffractometer. Cross-sectional transmission electron microscopy was performed on a FEI Philips Tecnai F20 with a High Angle Annular Dark Field (HAADF) detector and energy dispersive x-ray capability for chemical analysis. Dielectric constant, loss and polarisation measurements as a function of temperature were carried out in an Oxford Instruments cryostat with heating rates maintained using a Lakeshore 330 Temperature Controller. Dielectric data was obtained with an HP4284A LCR meter using an a.c. measuring voltage of 20mV(~0.17 kV/cm).

Polarisation loops were measured using a Radiant Technologies RT6000 Precision Workstation every 2K between 100K and 250K at a heating rate of 0.5K/min.

RESULTS AND DISCUSSION

Figure 1 shows a θ-2θ x-ray diffraction scan from one of the capacitor structures before the addition of Au top electrodes. The dielectric is perovskite (no pyrochlore peaks evident) with strong in-plane orientation $\{001\}_{perovskite} \| \{100\}_{MgO}$. Successful superlattice fabrication is illustrated by the occurrence of satellite peaks around the $\{200\}_{perovskite}$ Bragg reflection, the separation of which allowed superlattice periodicities to be calculated. Figure 2 shows a cross-sectional STEM image (using HAADF) along with an EDX line-scan perpendicular to the substrate showing that individual layers are reasonably chemically distinct. TEM investigation highlighted the difference in the deposition rates of 0.2PZN-0.8BT and PMN layers with the former being ~1.5 times thicker than the latter.

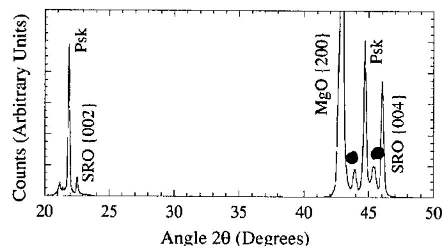

Figure 1. *θ-2θ x-ray diffraction scan of a 60 layer (0.2PZN-0.8BT, PMN) / SRO/ MgO film showing pure perovskite (Psk) phase with superlattices peaks marked by ●.*

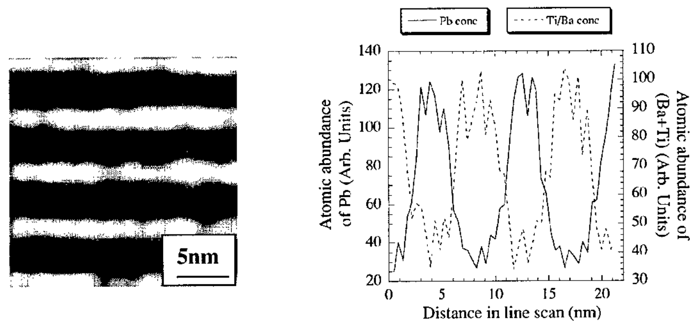

Figure 2. *HAADF and EDX scans of a section of the 120-layer (0.2PZN-0.8BT, PMN) superlattice showing distinct layers with little chemical mixing.*

The behaviour of the dielectric constant and loss tangents of the various superlattices are shown in figure 3 as a function of temperature. All superlattices exhibit excellent relaxor behaviour with frequency dispersion around and below T_m and losses less than 0.1 up to 100kHz at all temperatures. For decreasing periodicity there is a general increase in ε' and a reduction in T_m. This T_m decrease is reminiscent of the reduction of T_c modelled by Wang *et al.* [9] for ferroelectric superlattices. Here, T_m decreases from around 250K for the bilayer, to 160K for the 360 layer superlattice (100Hz values).

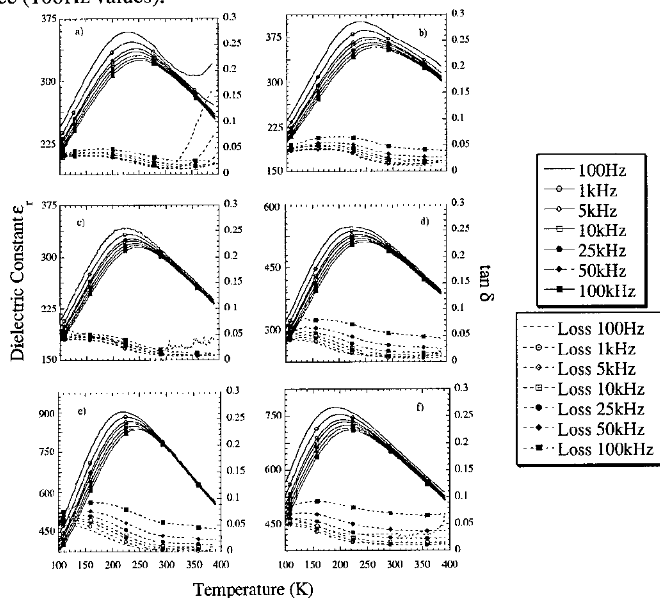

Figure 3. *Dielectric constant measurements for a) 2-layer b) 10-layer c) 30-layer d) 90-layer e) 120-layer f) 360-layer superlattices. Total thickness is maintained at 600nm.*

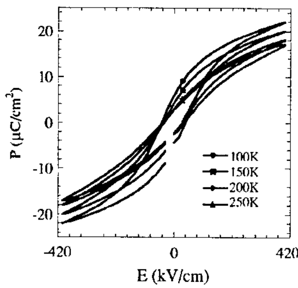

Figure 4. *Polarisation loops for the 180-layer superlattice for temperatures 100K, 150K, 200K and 250K.*

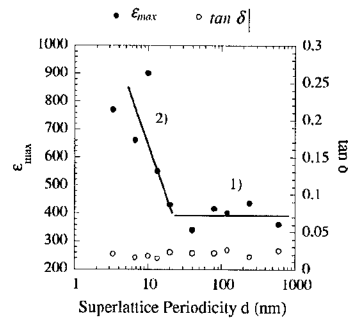

Figure 5. *Dielectric maxima and corresponding losses against superlattice periodicity for 1kHz. 1) uncoupled region 2) coupled region*

Saturated polarisation loops required high fields (of the order of 400kV/cm) and showed a trend of decreasing polarisation on increasing temperature as in figure 4. There was non-zero spontaneous polarisation observable at temperatures well above the expected freezing temperatures (even beyond T_m) for all films. This is in agreement with previous polarisation loop studies of spontaneous polarisation in single crystal PMN [10].

Figure 5 shows the dielectric maxima and corresponding losses against superlattice periodicity d at 1kHz. Clearly, there is a dramatic enhancement in the dielectric constant as the periodicity of the superlattice decreases, consistent with previous work on ferroelectric superlattices ($PbZrO_3$ / $PbTiO_3$ [4] and $BaTiO_3$ / $SrTiO_3$ [5]). In contrast to previous work, however, the dielectric enhancement is not associated with any increase in tan δ (consistently less than 0.03 for all periodicities). Previous interpretations of dielectric enhancement being a result of Maxwell-Wagner behaviour [11] are therefore inappropriate.

Similar functions to that shown in figure 5 have been predicted by Qu *et al.* [1] and Shen and Ma [2] for ferroelectric superlattices, assuming that as layer periodicity decreases, size effects force spontaneous depolarisation to occur, with associated anomalies at critical single layer thicknesses (effectively size-induced ferroelectric-paraelectric transitions). It is tempting to interpret the results presented here in terms of these models. However, the increase in dielectric constant with decreasing periodicity in our relaxor superlattices is associated with an *increase* in the spontaneous polarisation (figure 6). The size-induced depolarisation models are therefore not relevant either.

In an attempt to rationalise the dielectric enhancement experimentally, the polarisation behaviour of the superlattices as a function of temperature was analysed in detail. Figure 7 illustrates the behaviour of $-\frac{dP_r}{dT}$ against T for the superlattice structures. As can be seen, in coarse superlattices two anomalies in the gradient of remnant polarisation with temperature occur, suggestive of two distinct events. It is suspected that they correspond to freezing (or melting) events, and in this respect the fact that the higher temperature anomaly occurs at ~ 215K (~ the freezing temperature of single-crystal PMN) is particularly worthy of note. For fine-scale superlattices with periodicities less than ~ 20nm, the double anomaly behaviour changes to a

single anomaly (figure 7c and d), and this is strongly associated with the onset of progressive dielectric enhancement on further periodicity decrease.

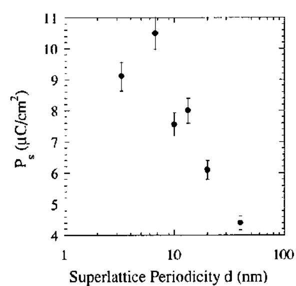

Figure 6. P_s at 180K extrapolated from hysteresis loops for superlattice periodicities of 40nm and less

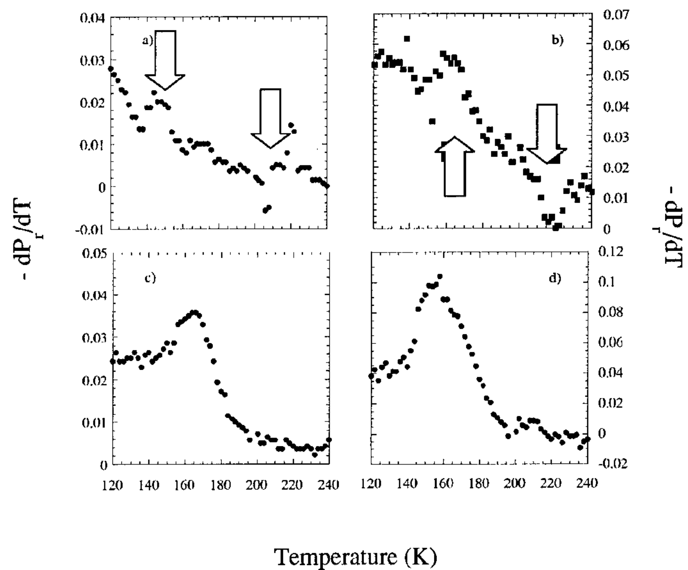

Figure 7. -dP_r / dT v T plots for a) 2-layer b) 15-layer c) 60-layer d) 360-layer superlattices. Anomalies in a) and b) are marked.

On this basis, we suggest that the dielectric behaviour illustrated in figure 5 can be broadly divided into two regions, as indicated by the solid lines:

1) a region of negligible layer coupling at coarse superlattice periodicities, where two independent relaxor freezing temperatures occur and
2) a region of strong layer coupling at medium to fine superlattice periodicities where a single freezing event occurs.

It is interesting that the periodicity associated with the apparent onset of coupled functional behaviour corresponds to a PMN thickness of 8nm and 0.2PZN-0.8BT thickness of 12nm. Specht *et al.* [12] postulated similar structural coupling behaviour in $KTaO_3$ / $KNbO_3$ superlattices and proposed a coupling length of around 7nm. It therefore appears that functional coupling in relaxor superlattices correlates well to a structural coupling in previous studies.

CONCLUSIONS

Superlattices of 0.2PZN-0.8BT and PMN have successfully been fabricated by Pulsed Laser Deposition and show a real dielectric enhancement on decreasing layer thickness. This enhancement cannot be successfully attributed to either Maxwell-Wagner effects, or thickness-induced depolarisation. Analysis of the remnant polarisation as a function of temperature shows a difference between coarsely layered superlattices, where two anomalies can be seen, and fine-scale superlattices, where only a single anomaly is observed. The onset of a single anomaly correlates to the onset of dielectric enhancement, and it is therefore suspected that the enhancement is associated with a change from non-coupled to coupled dielectric behaviour. The individual layer coupling length is similar to that proposed in previous crystallographic studies on ferroelectric superlattices.

ACKNOWLEDGMENTS

The authors acknowledge the financial support of DHEFTE, the EPSRC and the Royal Society, and the help from Jordi Romero, Mike Higgins, Paddy Gaffkin and Steve McFarland.

REFERENCES

[1] B. D. Qu, W. L. Zhong and R. H. Prince, *Phys. Rev. B*, **55**, 11218 (1997)
[2] J. Shen and Y. Ma, *Phys. Rev. B*, **61**, 14279 (2000)
[3] A. Erbil, Y. Kim and R. A. Gerhardt, *Phys. Rev. Lett*, **77**, 1628 (1996)
[4] I. Kanno, S. Hayashi, R. Takayama and T. Hirao, *Appl. Phys. Lett.*, **68**, 328 (1996)
[5] H. Tabata, H. Tanaka and T. Kawai, *Appl. Phys. Lett.*, **65**, 1970 (1994)
[6] B. D. Qu, M. Evistigneev, D. J. Johnson and R. H. Prince, *Appl. Phys. Lett.*, **72**, 1394 (1998)
[7] D. O'Neill, R. M. Bowman and J. M. Gregg, *Appl. Phys. Lett.*, **77**, 1520 (2000)
[8] H-M. Christen, E. D. Specht, D. P. Norton, M. F. Chisholm and L. A. Boatner, *Appl. Phys. Lett.*, **72**, 2535 (1998)
[9] X-G. Wang, N-N. Liu, S-H. Pan and G-Z. Yang, *Phys. Lett. A*, **267**, 434 (2000)
[10] V. Bokov and I. E. Myl'nikova, *Soviet Physics-Solid State*, **3**, 613 (1961)
[11] G. Catalan, D. O'Neill, R. M. Bowman and J. M. Gregg, *Appl. Phys. Lett.*, **77**, 3078 (2000)
[12] E. D. Specht, H-M. Christen, D. P. Norton and L. A. Boatner, *Phys. Rev.Lett.*, **80**, 4317 (1998)

Mat. Res. Soc. Symp. Proc. Vol. 655 © 2001 Materials Research Society

Macroscopic Actuators Using Thick Piezoelectric Coatings

M. Sayer[1], G.R. Lockwood[1], T.R. Olding[1], G. Pang[1], Lester M. Cohen[2], W.Ren[3] and B.K.Mukherjee[3]
[1]Department of Physics, Queen's University, Kingston, ON, K7L 3N6, Canada
[2]Smithsonian Astrophysical Observatory, 60 Garden St. Cambridge, Mass. 02138, USA
[3]Department of Physics, Royal Military College of Canada, Kingston, ON, K7K 7B4, Canada

ABSTRACT

Large scale actuated structures often require piezoelectric elements in the thickness range 10-50μm. For manufacturing purposes, the chemical solution deposition of sol gel composites can create such structures using methods compatible with semiconductor fabrication technology. The piezoelectric characteristics of structures fabricated by patterning methods based on the lapping and dicing of bulk ceramic, spray coating and laser machined and micromolded sol gel composites are compared. Laser interferometer measurements on PZT/PZT composites give d_{33} = 200 pC/N and d_{31} = 24 pC/N. The design and fabrication of large area voltage actuated mirrors and annular and linear ultrasonic arrays in the frequency range of 50 MHz are demonstrated.

INTRODUCTION

MEMS (micro-electro-mechanical systems) technology incorporates electromechanical actuation into structures micromachined into silicon having dimensions on the scale of 1-20μm [1]. The piezoelectric or electrostrictive actuating element has a thickness compatible with this scale, e.g. 0.5-3μm. Such elements may be created by chemical solution deposition (sol gel or metallorganic decomposition), physical sputtering or pulsed laser deposition.

An important class of larger actuated structures exist in which either the desired properties result from the dimensions of the structure, or in which forces need to be applied to structures having large size or complex geometry [2]. These macroscopic applications generally require a film thickness in the range 20 to 200μm and include mechanical resonators, large area structures on metal and glass, complex surfaces such as optical fiber and systems which require multi-element actuation. In these applications, actuation has generally been accomplished using strategically placed bulk discrete ceramic elements [3]. Examples of such structures are ultrasonic and surface acoustic wave transducers and arrays, unimorph and bimorph actuators, ink jet printer heads and active damping systems. Common problems in the implementation of such devices are the cost and complexity of assembly, the method of interconnection and the incorporation of external circuitry, and limited opportunities for batch fabrication. In this paper we discuss the application of sol gel composites to this problem, use interferometer methods to show comparative performance characteristics with respect to bulk ceramics, and illustrate device design by specific examples.

MATERIAL FABRICATION AND CHARACTERIZATION

Sol gel composite coatings are prepared by depositing a suspension of a powder in a sol gel solution on a substrate and firing [4,5]. Fabrication of large area coatings is simple and low cost using dip, spray, screen or spin coating over areas up to m^2. The solutions may be employed

within molding or screen printing technologies. The sol gel derived phase acts to bind the powder phase internally between grains and also to bind the overall coating to the substrate. The temperature of fabrication is that required to process the sol gel phase, with the powder phase acting to enhance the crystallization of the amorphous sol gel derived phase at a given process temperature. This leads to process temperatures from 400°C to 750°C depending on the sol gel.

Some consequences are inherent in sol gel composite coatings which intrinsically have three phases: powder/sol gel derived phase/porosity. First, the composite is not sintered and does not achieve a temperature where solid state diffusion between the phases occurs. The inter-particle bonding is chemical in nature and is determined by the bond linkages at the powder surface [6] or by the chemical formation of bonding phases at the interfaces. Second, since the formation of the sol gel phase involves the drying and firing of a solution which is 30-50% molar solids, substantial shrinkage of this phase is inevitable. Thus sol gel composite coatings have a density of <100%. Enhancement of this density requires specific consideration of the packing of the powder and/or physical fabrication techniques which are designed to optimize the density. Such techniques include a small powder size to facilitate particle packing and back filling of porosity using pure sol gel layers. Advantages of the microstructure include good mechanical toughness because of effective crack inhibition at the interfaces between the powder grains, and good mechanical/electrical inter-particle coupling because of similar or complementary mechanical or electrical properties between the powder and the sol gel derived phase.

For piezoelectric purposes, the lead zirconate titanate (PZT) system has shown satisfactory performance [7,8]. The primary powder phase is generally a pre-calcined sub-micron (mean particle size d_{mean} around 1μm) size powder with good piezoelectric characteristics. A mixture of particle sizes can also be of value for some powders. PZT-5 type powders with a medium coercive field are generally of value. Selection from commercial powders has to be undertaken with care since the required powder properties derive from a judicious compromise between a calcination temperature that generates good piezoelectric characteristics *within the powder* without undue particle size growth. This is followed by a milling schedule that reduces the particle size range without appreciably compromising piezoelectric strength. Not all PZT powders from commercial sources obey these criteria since manufacturers normally expect that further sintering will develop the final piezoelectric characteristics. An acetic acid based sol gel [9] suspension having 50wt% solids at a molar ratio of 50wt%powder/50wt%sol gel solution provides acceptable bonding in the sol gel derived phase on firing. Enhanced mechanical strength may be provided by the addition of up to 10wt% of an acetic acid based alumina sol gel. In order to create a solution for deposition of coatings, the powder is suspended in the sol gel solution using ultrasonic mixing for periods of several hours. While dip or spin coating may be used for application to a substrate, spray coating using a high quality air gun has been found to be most effective for the deposition of a fired thickness of 5-10μm/coat over a wide range of areas. In a representative process, following deposition, the film is first dried at 70°C for 5 min, fired at 450°C for 5min and then annealed at 600ºC for 5 min. Multiple coatings then allow the build up of a desired thickness from 100 to 200μm depending on the substrate. A final capping layer of a sol gel layer containing no powder completes the deposition. A pure sol gel layer after every 3-5 composite layers can also enhance the internal density.

In routine measurements on metal substrates, the film thickness is measured using a Positector 6000 magnetic probe. This is checked by cross-sectional scanning electron micrographs. A representative surface roughness for a 50μm thick film with a pure sol gel capping layer measured by a Rank Talystep profileometer is ± 2.0 μm. While this is acceptable

for electrodes for many macroscopic purposes, for patterned electrodes or structures utilizing photolithography, removal of about 10μm from the surface using a fine lapping maching (e.g. a Logitech MP6) is sufficient to give a surface roughness of ± 0.2 μm. Substrates can include Ti/Pt coated silicon, stainless steel, steel or aluminum plates, and metallised optical fibre. The relatively low process temperature minimizes oxidation of the substrate surface during preparation. Following deposition, upper electrodes of aluminum, gold or platinum are applied by vacuum evaporation or sputtering and the samples are poled using poling fields of 6-8V/μm applied for 10min in air. In the work reported in this paper the poling temperature was 20°C.

A particular interest in this paper has been to establish the low frequency characteristics of piezoelectric coatings created under conditions that may be regarded as routine fabrication. Direct piezoelectric measurements of d_{33} on composite coatings about 50μm in thickness prepared on 1.59 mm thick steel and 550μm silicon substrates using an electrode area of ~0.75cm^2 have been made using a Zygo ZMI 2000 laser doppler interferometer. Small sections of aluminized silicon wafers were affixed to the front surface of the sample using rubber cement to create the necessary reflectivity. Voltages applied during the measurement ranged from 20-200V p-p. d_{33} was measured from the change in thickness (Δt) of the coating with applied voltage such that $\Delta t = d_{33}V$. d_{31} was measured by the deflection of the end of a unimorph strip consisting of a 43μm thick PZT/PZT coating on a AISI302 stainless steel strip 75μm thick having an elastic modulus of 2 x 10^{11} N/m^2 [10,11]. The measurements were made at a frequency of 10Hz. Linear corrections were made to the response to account for the ratio of the area of the electrodes to that of the piezoelectric and the position of the mirror on the beam. Additional piezoelectric and elastic measurements were made from the high frequency dielectric response and use of the thin film module in the Piezoelectric Resonance Analysis Program (PRAP) [12,13]. In the above calculations, the elastic compliance for the PZT/PZT film on steel was 6 x 10^{10} N/m^2. Values of d_{31} at 10 Hz were computed from the expression for the displacement x (L) of the end of a cantilever of length L by a piezoelectric coating of thickness t [11].

$$x(L) = d_{31}V\left[\frac{L}{t_{PZT}}\right]^2 Z(a,k) \qquad 1)$$

where a is the ratio of the elastic moduli of the substrate and the PZT coating, and k is the ratio of substrate thickness to PZT thickness.

$$Z(a,k) = \frac{3ak(1+k)}{1+a^2k^4+2a(2k+3k^2+2k^3)} \qquad (2)$$

RESULTS

1. Coating Structure and Properties

Figure 1 shows a) optical and b) scanning electron micrographs of a cross-sections of a sol gel composite PZT/PZT coating 45μm thick deposited on a 75μm stainless steel cantilever

substrate (b). Figure 1c) compares the fine grain structure of the composite with large grains observed in a lapped ceramic sample of PZT-5H.

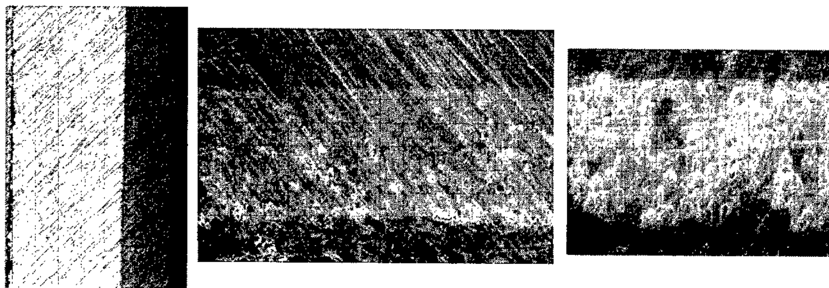

a) 75μm 45μm b) 45μ m thick composite c) 45μm thick ceramic

Figure 1. *a) optical micrograph of a polished stainless steel-PZT/PZT sol gel gel composite, b)scanning electron micrograph of a PZT/PZT composite coating, c) large grain structure in a lapped PZT-5H ceramic.*

By comparison with the lapped ceramic, some of the porosity inherent to sol gel composites is evident in the cross-section shown in Fig.1 b). Figs. 1 b) and 1 c) shows that the sol gel composites have a much finer grain structure compared to the well sintered ceramic. Excellent adhesion occurs between the ceramic and the underlying metal and no cracking occurs across the face of the coating.

Using the Zygo laser interferometer for 45 μm coatings on 1.59 mm thick steel with an upper circular electrode of aluminum 10 mm in diameter, the actuator was driven in d_{33} mode by 200V p-p applied from a power amplifier driven by a waveform synthesizer. The peak to peak surface amplitudes at frequencies of 10 Hz and the calculated values of d_{33} are summarized in Table I. The PZT/PZT composite showed a d_{33} = 200 pC/N which was consistent across a number of samples. This is about two thirds of the value generally expected for bulk PZT ceramic. The d_{33} values for PZT/alumina composites were significantly smaller at d_{33}=90 pC/N. Qualitatively the alumina coating was mechanically softer than that using the PZT sol gel. During poling the leakage current was significantly higher.

Table I. *d_{33} measurements for 40μm thick PZT and alumina based sol gel composites on steel.*

Composite	Voltage (p-p)	Amplitude (mm)	d_{33} (pC/N)
PZT/PZT	200	0.04	200
PZT-alumina	200	0.018	90

Unimorph d_{31} measurements of coatings prepared on one side of a stainless steel cantilevers required significantly lower excitation voltages in the range of 20V p-p. Since the cantilevers could be excited into large amplitude oscillations at a resonant frequency determined by the dimensions and modulus of the stainless steel substrate, care was taken to make d_{31} measurements at a frequency much below resonance. 10 Hz was again acceptable. The deflection of the cantilever (x(L)) at the mirror position and the computed value of d_{31} for each unimorph is summarized in Table II. The elastic modulus of the coatings was estimated at 6 x 10^{10} N/m^2 [12,13].

Table II. *d_{31} measurements for 45μm thick PZT/PZT on 75μm AISI302 thick stainless steel. The bracketed figure in the first column is the effective length of the unimorph set by the mirror position. The ratio of the elastic moduli for the steel substrate and the PZT is 3.33.*

Sample length (mm)	Voltage (p-p)	Amplitude (mm)	d_{31} (pC/N)
10 (7)	20	2.92	31
10 (7.5)	20	3.85	35
18 (15.5)	20	6.0	13
26 (22)	20	16.2	17

In order to demonstrate the variability for different unimorphs individual data is shown. The range of values of d_{31} is considerably larger than for d_{33} measurements. This may reflect a stronger effect of the nature and the distribution of porosity for d_{33} actuation. The average value of the magnitude of $d_{31} = 24$ pC/N is roughly 30% of that generally expected for bulk PZT ceramic. The value is an even smaller ratio of the value of d_{31} expected for the constituent powder. Based on these direct measurements, magnitudes of $d_{33} = 200$ pC/N and $d_{31} \sim 24$ pC/N for the PZT/PZT composite can be regarded as a good design values for representative processing. The PZT/PZT sol gel composite coatings were prepared by standard methods using powders and sol gels with which we have had significant experience. With the possible exception of further studies of poling efficiency as a function of temperature and time, and improved electrodes based on platinum rather than aluminum, the values for d_{33} and d_{31} (30-50% of bulk ceramic values) are realistic estimates of the piezoelectric activity. The advantage of sol gel composite coatings lies not in the magnitude of the response achievable, but in their potential as a manufacturable technology which may be used if the response achieved is acceptable.

2. Unimorph Actuation at Resonance

The response of the unimorph system to higher frequencies demonstrates the capacity of the PZT/PZT coating to stimulate large systems at resonance [10]. Figure 2 shows the set of unimorphs used in the above d_{31} measurements. The curvature of each element after processing is a result of differential thermal contraction between the steel and the ceramic coating during cooling from the processing temperature of 600°C. In practice, a bimorph design would avoid this problem. Fig. 2a) illustrates the resonant response of several mm for the largest unimorph on a spray coated set of cantilevers when driven by 20Vp-p. Figure 2b) shows the vibration

amplitude as a function of frequency. The resonant frequency of the different oscillators varies as 1/length^2. The measurements were made by the Zygo interferometer at frequencies away from resonance and were extrapolated through the maximum because the capture range of the interferometer was exceeded for these amplitudes.

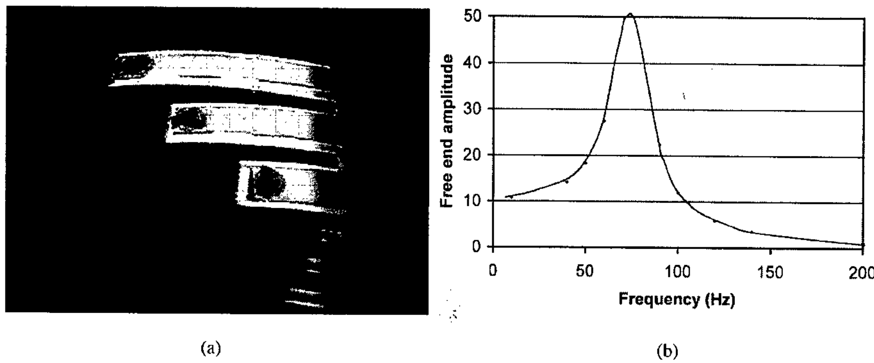

(a) (b)

Figure 2. a) The resonant response of a 75μm thick stainless steel/45μm PZT/PZT composite coating in a unimorph structure. The largest element is 26mm in length and is excited at a frequency of 75Hz. The resonant frequency varies as 1/length^2. b) the amplitude as a function of frequency. The curvature results from differential thermal contraction during cooling from the processing temperature.

3. Piezooptics - Voltage Variable Curvature Mirrors

Fine control over the radius of curvature of large diameter mirrors can be implemented by the d_{31} response of a piezoelectric coating on the back surface of the mirror.

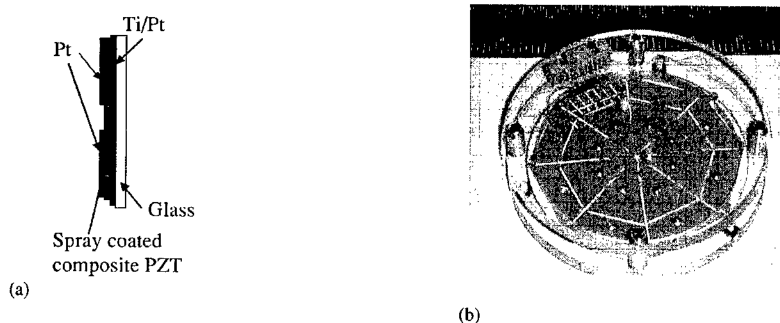

(a) (b)

Figure 3: Large area piezoelectric coatings formed by spray coating of sol gel composites on Ti/Pt coated glass plates 10 cm in diameter. a) basic design showing that the upper or back electrode is segmented to provide local control of the surface configuration. b) implemented device.

Figure 3(a) shows the desired structure of an element of a mirror, while Figure 3(b) shows its implementation in terms of sol gel composites. The mirror was formed of a 10cm diameter glass plate with a 200Ti/2000A Pt coating prepared initially both as a rear surface mirror and as the lower electrode for the piezoelectric coating. The actuating element was formed by a five-layer deposition of a 50 μm thick PZT/PZT sol gel composite spray coated on the platinum electrode. A segmented upper electrode was created by the sputtering of Ti/Pt through a mask. Contact to each segment was made using conducting silver epoxy.

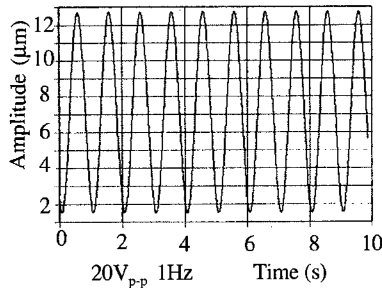

Figure 4: *Response of the centre of the mirror as measured using the Zygo interferometer.*

The response of the center of the plate to a 20Vp-p voltage applied to all segments connected in parallel was of the order of 12 μm as measured using the Zygo interferometer. In this application the quality of the front surface mirror is of crucial importance. In a multi-layer deposition, care has to be taken to protect the front glass surface from chemical degradation during the spraying and firing processes.

4. High Frequency Ultrasonic Arrays.

Pulsed ultrasound at frequencies from 10 - 150 MHz has a penetration distance in aqueous media of cms down to a few mms respectively. Focused ultrasonic imaging at this frequency may be accomplished by multi-element transducers arranged as annular, one or two dimensional arrays. Such arrays are illustrated in Figure 5.

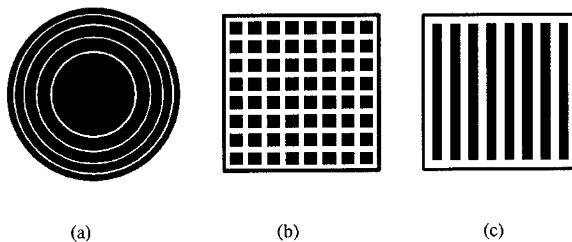

Figure 5: *Types of ultrasonic arrays used for high frequency ultrasound a) annular, b) two dimensional c) one dimensional or linear arrays*

The implementation of such arrays is currently at the technical limit of transducer design. The reason for this is illustrated by the design requirements noted in Table III and Figure 6 . These include the need for a matching layer to optimise the acoustic impedance Z to facilitate the transmission of ultrasound into the medium (usually water), an acoustically absorbing backing layer to minimize back transmission into the support, and element dimensions which not only generate the appropriate ultrasound frequency in the d_{33} direction but also minimize unwanted d_{31} modes perpendicular to the transmission direction. A kerf filler may be introduced between the elements to eliminate such modes.

Table III: *Design parameters for a 50MHz linear array*

Dimensions	Design Constraints	Typical Values
Element Spacing	Spacing < λ_w Linear Array, Spacing < $\lambda_w/2$ Phased Array λ_w - wavelength in water (Grating Lobes)	Spacing = 30 μm
Piezoelectric Thickness	Thickness = $0.5\lambda_{piezo}$ (half wavelength resonance)	Thickness = 45 μm
Element Aspect Ratio	Width/Height < 0.6 (Lateral Modes)	Width = 18 μm Aspect Ratio = 0.4
Matching Layer	Matching Layer Thickness ~ $\lambda_m/4$ λ_m - wavelength in matching layer Mechanical Impedance Z_m $Z_m = (Z_{peizo} Z_{water})^{1/2}$	Thickness = 10 μm Z_m = 7 MRayls
Backing Layer	High loss > 0.5 dB/mm/MHz Mechanical Impedance Z_b $0 < Z_b < Z_{peizo}$ $Z_b = 0$ Maximum Efficiency, $Z_b = Z_{peizo}$ Maximum Bandwidth	Thickness = 1 mm Z_b = 14 MRayls

The table shows that the transducer dimensions are in the range of 30-50μm. Current transducers are individually fabricated by painstaking mechanical shaping of bulk ceramics. Achieving array transducers with up to 256 elements therefore presents a formidable task. Sol gel composite coatings provide a potential route to implement such transducers using batch fabrication methods compatible with those used in the semiconductor industry.

Sol gel composites provide a method of implementing multilayer coatings (e.g. matching layer, active piezoelectric coating , electrodes and backing layer on a substrate compatible with 4" or 6" semiconductor processing. Appropriate lapping at intermediate stages can be carried out to define the necessary thicknesses of each layer. Patterning can take place by either a subtractive (e.g. laser machining) or additive (e.g. photolithography and micromolding) process. Interconnections with external circuitry and/or integration with microelectronics can occur through multi-layer ceramic module technology. Subtractive fabrication methods based on laser

machining of sol gel composites have been discussed elsewhere [2,7]. This paper describes progress in additive design based on micromolding of PZT/PZT sol gel composites using SU-8 photoresist. Fig. 7a) shows the basic principle of micromolding.

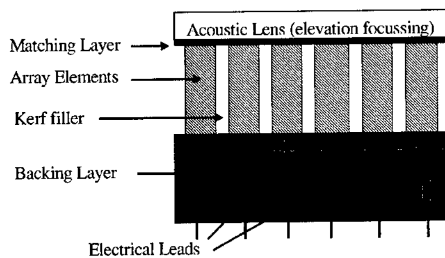

Figure 6: *Illustration of the components of a high frequency array transducer to be used for ultrasonic imaging. The total number of elements may be up to 256.*

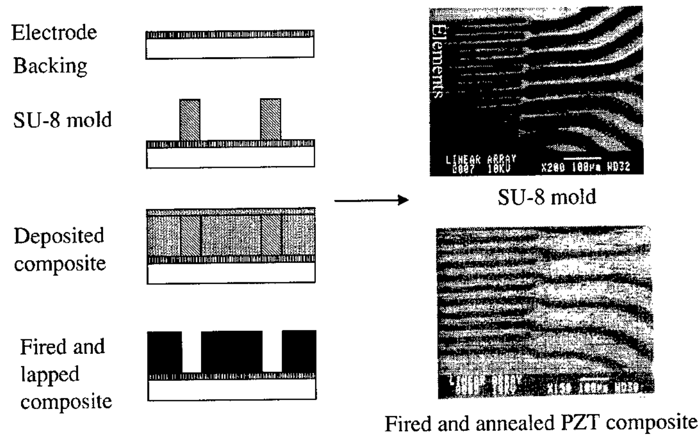

Figure 7: *a) Illustration of procedures to fabricate an array device using SU-8 based micromolding. b) upper picture - and SU-8 mold, c) lower picture - an unlapped fired device structure.*

A lower platinum electrode is formed on a silicon substrate by standard procedures. Thick photoresist procedures based on SU-8 photoresist [14] and a Karl Suss MA-6 mask aligner are implemented to create a deep mold 25-100μm thick for filling by a sol gel composite slurry by spray coating. In initial experiments based on UV-LIGA procedures [1] an intermediate nickel model was formed by electroplating. However, experiments showed that the SU-8 photoresist maintained its shape integrity up to the temperature of 450°C required to dry and fire the sol gel composite. After lapping of the ceramic to the required thickness, subsequent annealing at

600°C served to both crystallize the sol gel phase of the ceramic and burn out the photoresist mold. Connection procedures can then be implemented to form the interconnections. Results for sections of a design previously implemented using laser machining [2,7] are shown in Fig. 7 b) and 7 c). Fig 7 b) is an SU-8 mold while Fig. 7 c) shows an unlapped ceramic after molding and firing.

In current experiments, this procedure has been implemented for electroded coatings on 10cm silicon wafers which have then been lapped using a Logitech MP6 lapping machine. Lapped devices up to 40μm in thickness have been created as shown in Figure 8 a) and 8 b). Techniques to create the upper patterned electrodes are now being evaluated.

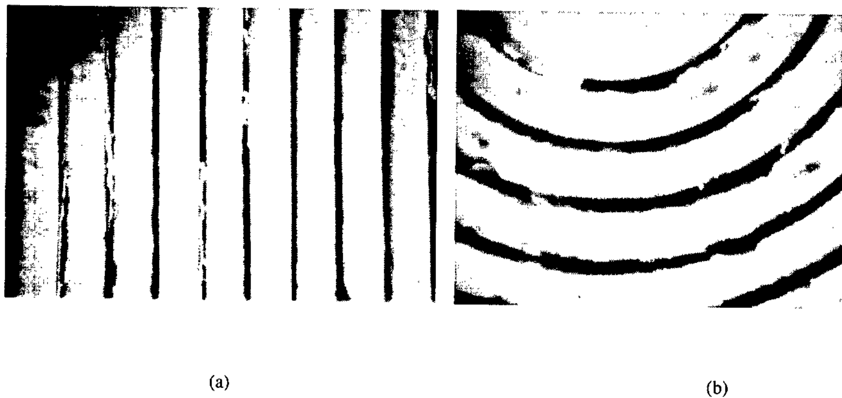

(a) (b)

Figure 8: PZT/PZT micromolded sol gel composites using an SU-8 mold. Both pictures show some residual SU-8 within the channels. a) line pattern 30μm wide and <10μm in spacing b) annular pattern 50μm wide and 25μm spacing.

SUMMARY AND CONCLUSIONS

Sol gel composite coatings provide a manufacturable technique to create piezoelectric coatings for the actuation of large area or complex geometry devices. The achievable thickness is beyond that available through conventional methods of chemical solution deposition. The piezoelectric properties are inherently reduced in the unsintered composite material so that a necessary question is whether the material will serve for the intended purpose. A purpose of this paper has been to establish the piezoelectric coefficients for coatings manufactured under easily reproducible conditions. The magnitudes of d_{33} =200 pC/N and d_{31} = 24 pC/N are roughly two thirds and one third respectively of that generally expected for bulk PZT ceramic with d_{31} showing a higher variability between measurements.

ACKNOWLEDGEMENTS

This work has been carried out under a Strategic Grant to M.Sayer and G.R.Lockwood awarded by the Natural Sciences and Engineering Research Council of Canada. Thanks are due to the United States Office of Naval Research for provision of the Zygo Interferometer to

B.K.Mukherjee and W.Ren. The voltage actuated mirrors were fabricated under Contract # SO0-61869 funded by the Smithsonian Astrophysical Observatory. Assistance with micromolding technology and substrates were provided by Gennum Corporation, Burlington, ON. The use of photolithographic facilities and assistance with SU-8 molding by Dr. Margaret Buchanan of the Institute of Microstructural Sciences at the National Research Council of Canada is acknowledged. Assistance in scanning electron microscopy from Mr. Joel Reid is appreciated. Some work on unimorphs was accomplished in a collaborative project with Mr. K.Tontch and Dr. R.Waser of RWTH Aachen University of Technology D-52056 Germany

REFERENCES

1. M.Madou, *Fundamentals of Microfabrication,* (CRC Press, 1997) pp 145-
2. M.Sayer, M.Lukacs, T.Olding, G.Pang, L.Zou and Y.Chen, Mat. Res. Soc. Symp. Proc. 541, 599 (1999)
3. S.Zhou, C. Liang and C.A.Rogers, J. Intel. Mater. Syst. and Struct. 6, 733 (1995)
4. D.A.Barrow, T.E.Petroff, R.Tandon and M.Sayer, *J. Appl. Phys.* 81, 876 (1997)
5. D.A.Barrow, T.E.Petroff and M.Sayer, *U.S.Patent* #36573 (2000)
6. T.E.Petroff, S.Hesp and M.Sayer, *Ceram. Trans. 41*, eds L.M.Levison and S.I.Hirano, the American Ceramic Society, Westerville, OH, 1994, p337
7. M.Sayer, M.Lukacs, G.Pang, L.Zou, Y.Chen and C.K.Jen, in *Piezoelectric Materials: Advances in Science, Technology and Applications*, eds C.Gallassi, M.Dinescu, K.Uchino and M.Sayer, (Kluwer, 2000) pp. 249-260
8. D.A.Barrow, O. Lisboa, C.K.Jen and M.Sayer, *J. Appl. Phys.* 79, 3323 (1996)
9. T.R.Olding, B.Leclerc and M.Sayer, Integ. Ferroelect. 26, 225 (1999)
10. These structures were laser machined in a joint project with K.Tontch and R.Waser
11. Q-M Wang, X-H Du, B.Xu and L.E.Cross, IEEE Trans. Ultrason. Ferroelect. and Freq. Cont 46, 638 (1999) (1978)
12. M.Lukacs, T.R.Olding, M.Sayer, R.Tasker and S.Sherrit, J. Appl. Phys. 85, 2835 (1999)
13. Piezoelectric Resonance Analysis Program, http://www.canlink.com/tasi/tasi.html, TASI Technical Software, Kingston, Ontario, Canada (1998)
14. Microlithography Chemical Corporation Corp., 1254 Chestnut St. Newton, MA 02164-1418, http://www.microchem.com

Mat. Res. Soc. Symp. Proc. Vol. 655 © 2001 Materials Research Society

High Frequency Thin Film Acoustic Ferroelectric Resonators

Paul Kirby[a], Qing-Xin Su[a], Eiju Komuro[b], Masaaki Imura[b], Qi Zhang, and Roger Whatmore[a]
[a]Nanotechnology and Microsystems group, School of Industrial and Manufacturing Sciences, Cranfield University, Cranfield, Bedford, MK43 0AL, UK
[b]Telecom Technology Development Centre, TDK Corporation, 2-15-7, Higashi-Ohwada, Ichikawa-shi, Chiba, 272-8558 Japan

ABSTRACT:

Both ZnO and PZT Thin Film Bulk Acoustic Resonator filters were fabricated, tested and modeled in this study. The development of an accurate Mason model allows the effect of particular parasitic components on the microwave s-parameters in the region of the series and parallel resonances to be identified. The parasitic components that limit the performance of our ZnO and $PbZr_{0.3}Ti_{0.7}O_3$ Thin Film Bulk Acoustic Resonator filters are analysed. From an analysis of $PbZr_{0.3}Ti_{0.7}O_3$ Thin Film Bulk Acoustic Resonator measurements values for the longitudinal acoustic velocity and electromechanical coupling coefficient can be derived. Measured $PbZr_{0.3}Ti_{0.7}O_3$ Thin Film Bulk Acoustic Resonator filter responses confirm that the larger electromechanical coupling coefficients in this material compared to ZnO give wider filter band-widths.

INTRODUCTION:

There is a great commercial interest in decreasing the size of microwave 1-3 GHz filters to allow more functions to be incorporated in future mobile phones [1]. Presently there are two types of filters being developed to meet this need, ceramic filters based on electromagnetic modes and acoustic filters. The typical dimensions of both types of microwave filters are similar to the wavelength at the operating frequency. By using the piezoelectric effect to generate acoustic modes wavelengths and dimensions can be reduced by about four orders of magnitude compared to electromagnetic modes.

There are two types of acoustic filters considered contenders for future generations of mobile phones, both based on piezoelectric materials: surface acoustic wave (SAW) devices and Thin Film Bulk Acoustic Resonators (FBAR). The piezoelectric effect has been widely used in bulk acoustic resonators, such as single crystal quartz for many years. Recently by careful thinning or etching the quartz plate operation up to 200 MHz can be achieved but the low acoustic velocity of quartz and the resulting fragility of thinned substrates means that this technology cannot progress to higher frequencies. In SAW devices that direction of propagation is in the plane of the wafer while for FBAR it is perpendicular to a substrate surface. For FBAR operation the piezoelectric film thickness must be of the order of the acoustic wavelength at the desired operating frequency. In this paper we compare two candidate thin film piezoelectric materials, ZnO and $PbZr_{0.3}Ti_{0.7}O_3$ (PZT) that have different acoustic properties. Although there has been considerable previous work on ZnO FBAR [2] and ZnO FBAR filters [3] there has only been a few reports on PZT FBARs [4]. In particular, the electromechanical coupling coefficients

of the two materials are very different. The higher values of electromechanical coefficient of PZT compared to ZnO should allow wider band-width filters to be fabricated.

In FBAR devices the electrical and crystallographic quality of the piezoelectric thin film is often determined by the structure of the layer on which growth takes place. ZnO thin films with the desired C-axis orientation can be grown on Au and Al [5]. For PZT the situation is more constrained since the only metal on which high quality material can be grown is platinum [6]. Unfortunately Pt has low conductivity compared to Al and Au so higher electrode parasitic resistance effects could result.

EXPERIMENT

A schematic cross-section of the FBARs fabricated is shown in Figure 1. The thin film membrane is created by wet etching away the silicon. For both ZnO and PZT FBARs a Si_3N_4

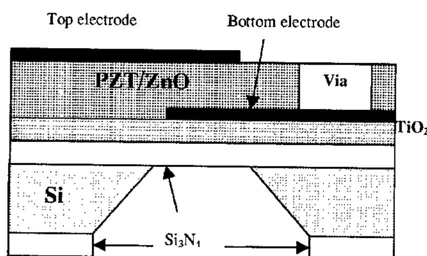

Figure 1. Schematic cross-section of ZnO and PZT FBAR

(200 nm) layer served as a support membrane. PZT layers deposited on Si_3N_4 were found to have poor surface morphology, including cracks, so a thin layer (50nm.) of TiO_2 layer was inserted between the Si_3N_4 and PZT to avoid this cracking. The TiO_2 was formed by the oxidation of titanium. The sputtered metal layers were 100 nm thick. For the RF sputtered ZnO films used in this study only one orientation, C-axis perpendicular to the substrate, was observed by X-Ray diffraction. A sol gel preparation route [6] was used for the PZT films. For the FBAR configuration adopted, both ZnO and PZT layers were processed as blanket layers and the only patterning required for these layers was the opening of large contact hole areas using wet etching to allow access of the microwave probes. ZnO FBAR structures were prepared with Cr/Au electrodes while Pt was used for PZT FBARs.

MODELLING

One dimensional models were used to model the impedance data measured on fabricated FBARs. The full model used for the membrane supported FBAR structure is shown in figure 2. The piezoelectric layer is represented by one electrode and two acoustic ports. Multi-layers are taken into account by linking the acoustic ports in series. The non-piezoelectric electrode and support layers simply consist of acoustic ports. The terminations at the surface are simple

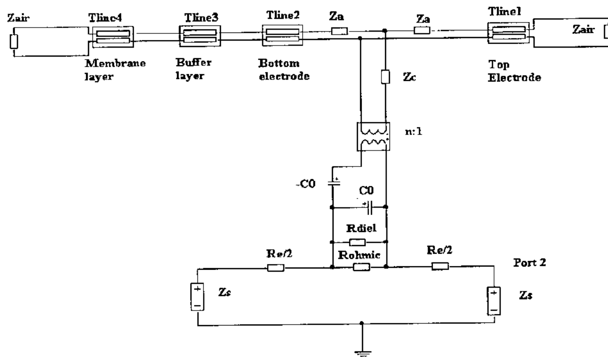

resistors with values equal to the radiation impedance of the surrounding medium, which is equivalent to ~400 ohms for air.

Additional components have been added to account for the non-ideal properties of the piezoelectric layer and electrodes. R_{diel} represents the dielectric loss, which can be frequency dependent, placed in parallel with the clamped capacitance of the device. The R_{ohmic} term is included to model conduction losses due to free carriers in the piezoelectric material. Electrode resistances are represented by $R_{e/2}$.

It is possible to use different regions of the resonance curves to identify the effects of different loss mechanisms. Figure 3a and 3b shows the modelled S-parameters of a single FBAR when the electrode resistance and the dielectric loss in the piezoelectric material is varied. Platinum has about five times the resistivity of gold [7]. The effect of lowering the electrode resistance is to reduce the magnitude of S_{11} at series resonance frequency, S_{11min}, but has little effect on the S_{21} response, as shown in figure 3a. It is expected that a change in the acoustic loss of the piezoelectric material will have the same effect. Changes in the dielectric loss are observed as changes in the depth of the parallel resonance of S_{11} and S_{21}. A lower dielectric loss increases

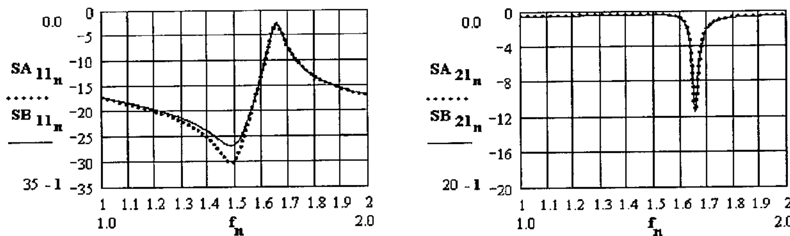

Figure 3(a). Modelled S-Parameters versus frequency (1-2 GHz) for Pt (SA_{11} and SA_{21}) and Au (SB_{11} and SB_{21}) electrodes.

the depth of the S_{21} response and reduces the insertion loss of S_{11}, as shown in figure 3b. Changes in the resistivity of the piezoelectric material has similar effects. Higher resistivity dielectric films will increase the depth of the S_{21} response and reduce the insertion loss of S_{11}. It

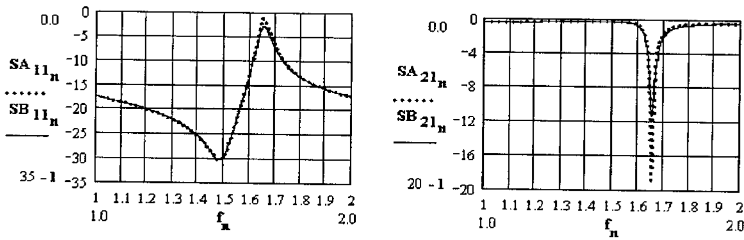

Figure 3(b). Modelled S-Parameters versus frequency (1-2 GHz) for a dielectric loss of 1% (SA_{11} and SA_{21}) and 4% (SB_{11} and SB_{21}).

is very difficult to distinguish between the effects of dielectric and resistivity losses. However, it is likely that the main loss mechanism is dielectric loss for PZT and DC loss for ZnO FBAR.

Figure 4 shows that by using the Mason model of figure 2, good agreement can be achieved between measured and modeled data. This gives confidence that the derived component values can be used to design filters. Although literature reports on the dielectric loss of ZnO thin films

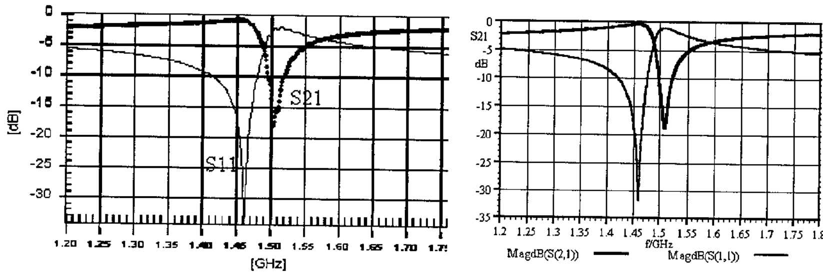

Figure 4. Comparison of measured (left) and modelled S-Parameters for a ZnO FBAR

are limited, our own measurements at lower frequency (100kHz) suggest that the loss is very low. We believe therefore that the limited depth of the parallel resonance (in S21) measured in our material can be improved by increasing the ZnO dc resistivity, as mentioned above. This is also suggested by the insertion loss of the S_{11} parameters at parallel resonance being less than 3 dB. Figure 3(b) shows that the parallel insertion loss increases with increasing dielectric loss.

Figure 5 shows recorded S-parameters from a fabricated PZT FBAR having an area of 45 μm^2. The PZT was poled at high temperature prior to etching the silicon substrate. The parallel resonance S11 insertion loss measured for PZT is greater than for ZnO FBAR. We associate this with the relatively high dielectric loss (~1-3%) observed in sol gel prepared thin film PZT layers. We believe that dielectric losses currently limit the performance of our PZT FBARs.

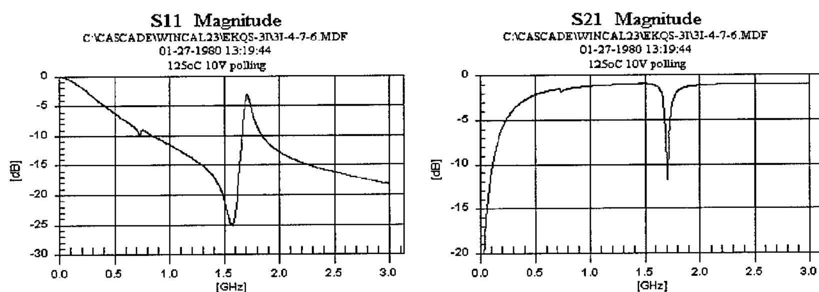

Figure 5. S-Parameters versus frequency of a PZT FBAR

The material properties deduced from analysis of ZnO and PZT FBARs measurements are shown in table 1. The deduced electromechanical coefficients for both materials are very close to bulk material values.

Table 1. Material parameters deduced from ZnO and PZT FBARs

	ZnO	PZT
Elecromechanical Coupling Coefficient, κ_t^2	7%	19.8%
Q-values	350	54
Acoustic velocity (m/s)	6340	4500

FBAR FILTERS

Based on the analysis of measured impedance data obtained from single FBAR structures we have designed ZnO and PZT FBAR ladder filters. For a ZnO FBAR ladder filter having two series and two parallel FBAR elements the measured behaviour is to close to the modelled performance. A pass-band insertion loss of 3-4dB was measured with out of band rejection better than 25 dB. A 3dB band-width of 60 MHz was measured.

The designed performance and measured response for a 2x2 PZT filter is shown in figure 6. The measured insertion loss is ~6.5 dB compared to the predicted 2.5dB. This difference is thought to be due to the difference from the designed thickness of the series and parallel FBAR that make up the ladder filter. Another contribution will be the losses that arise from the

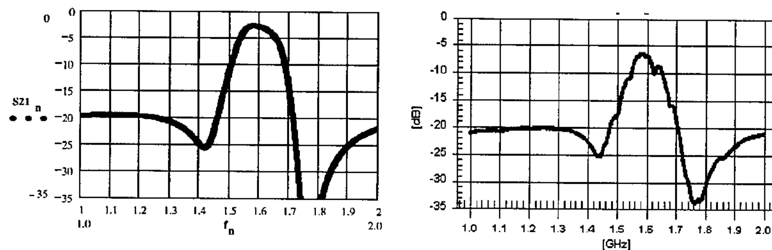

Figure 6. Measured (right) transmission coefficients for a 2/2 PZT FBAR compared to design (left). The PZT was poled with 10 volts applied at 125 °C.

presence of spurious modes that are present in small area PZT FBARs. A 3 dB band-width of 100 MHz was measured consistent with the high electromechanical coupling coefficient.

CONCLUSIONS

This study has shown that the large electromechanical coefficient expected in PZT thin films leads to large separation between the series and parallel resonances in single FBARs and wide band-width FBAR filters. By inclusion of electrode resistances, piezoelectric dielectric loss and dc resistivity components within a Mason model it is possible to identify their influence on the microwave responses. For ZnO FBAR filters improved performance will result from the development of ZnO with higher resistivity while for PZT material with lower dielectric loss is required.

REFERENCES

1. K.M.Lakin, G.R. Kline, K.T.McCarron, IEEE Trans. Microwave Theory and Techniques, vol. 43 (12), Dec. 1995.
2. Y. Miyasaki, S. Hoshino, S. Takahashi, 1987 Ultrasonics Symposium, 385-393.
3. L. Mang, F. Hickernell, R.Pennell, T.Hickernell, 1995 IEEE MTT-S Digest, 887-890
4. A. Yamada, C.Maeda, T.Sato, T.Umemura, F.Uchikawa, K.Misu, S.Wadaka, Integrated Ferroelectrics, vol 22, p353-361 (1998)
5. Y.Yoshino, S.Iwasa, H. Aoki, Y.Deguchi, Y.Yamamoto, K.Ohwada, Mat. Res. Soc. Proc. Vol.441, 241-246 (1997).
6. Z.Huang, Q.Zhang and R.W.Whatmore, J. Applied Physics, 85(10), 7355-7361, (1999)
7. C.T.Lynch, Handbook of Materials Science, vol. 1 General Properties, CRC, Cleveland (1974).

Mat. Res. Soc. Symp. Proc. Vol. 655 © 2001 Materials Research Society

Preparation and Characterization of $(Bi,La)_4Ti_3O_{12}$ Films by the Sol-Gel Technique

Eisuke Tokumitsu, Takeaki Isobe, Takeshi Kijima[1] and Hiroshi Ishiwara[1]
Precision and Intelligence Laboratory,
[1]Frontier Collaborative Research Center
Tokyo Institute of Technology
4259 Nagatsuta, Midori-ku, Yokohama 226-8503, Japan

ABSTRACT

$(BiLa)_4Ti_3O_{12}$ (BLT) films have been fabricated by the sol-gel technique and characterized. It is shown that the partially replacing Bi with La can promote the crystallization, hence can reduce the crystallization temperature of the film. It is also demonstrated that crystalline orientations of sol-gel derived ferroelectric BLT films can be controlled by the growth conditions.

INTRODUCTION

Recently, ferroelectric materials have attracted much attention for non-volatile memory applications. There are two types in ferroelectric memories (FeRAMs) : one is conventional capacitor-type FeRAM [1] and the other is transistor-type FeRAM using ferroelectric-gate FETs [2-3] where the ferroelectric thin film is used as a gate insulator. Since the memory cell of the so called 1T1C type FeRAMs consists of one MOSFET and one ferroelectric capacitor and we have to reduce the size of these devices for high-density implementation, a large remanent polarization Pr of the ferroelectric films is desirable. On the other hand, transistor-type FeRAMs, the remanent polarization of the ferroelectric film as a gate insulator should match the charge which can control the channel conductivity of FETs [4,5]. The induced charge per unit area by the gate insulator, Q/S, can be calculated as $Q/S=\varepsilon E$, where ε and E indicate dielectric constant of the gate insulator and applied electric field, respectively. For example, the maximum charge induced by SiO_2 is 3.5 $\mu C/cm^2$, if we assume that the maximum electric field (breakdown field) is 10 MV/cm and that the relative dielectric constant of SiO_2 is 3.9. On the other hand, the remanent polarization of well-known ferroelectric materials, $Pb(Zr,Ti)O_3$ (PZT) and $SrBi_2Ta_2O_9$ (SBT) films are from 30 to 50 $\mu C/cm^2$ and about 10 $\mu C/cm^2$, respectively. These values are much larger than the maximum charge which can be induced by SiO_2. This means that even if we have a good ferroelectric film with large remanent polarization, we cannot use the entire polarization to control the channel conductivity of metal-oxide-semiconductor (MOS)-FETs but can use only a small part of the polarization, namely a small minor loop. In such a case, the obtainable memory window, which is given by 2 V_C, will become small, because the coercive voltage, V_C, of the minor loop is smaller than that of the saturated P-E hysteresis loop. Hence, small or moderate remanent polarization is required for the ferroelectric films in transistor-type FeRAM applications.

In this work, we have characterized $(Ba,La)_4Ti_3O_{12}$ (BLT) films [6] prepared by the sol-gel technique. From the analogy of $Bi_4Ti_3O_{12}$ [7,8], the BLT may have large anisotropy in electrical properties. Hence, the control of crystalline orientation is important to obtain the desired electrical properties

EXPERIMENTAL

$Pt/Ti/SiO_2/Si$ structures were used as substrates. First, BLT solution was spin-coated and dried at 180 °C for 5 min. Then, the pre-annealing was performed at 350-650 °C in the oxygen ambient. After repeating the above process for typically four times, we crystallized the sample at 650, 700, or 750 °C in oxygen ambient. Next, the Pt top electrodes were vacuum evaporated and the samples are annealed again at the crystallization temperature for 10 min.. The thickness of the fabricated BLT films was 150-200 nm. The crystalline properties of the samples were characterized by X-ray diffraction (XRD), scanning electron microscope (SEM). Polarization – electric-field (P-E) and current – voltage (I-V) characteristics were measured to evaluate electrical properties.

RESULTS AND DISCUSSION

We first examined the crystalline quality and electrical properties of the BLT films by changing excess Bi amount in the source solution. Source solution with excess Bi is commonly used in the sol-gel technique to fabricate Bi-layered ferroelectrics such as $SrBi_2Ta_2O_9$ (SBT)

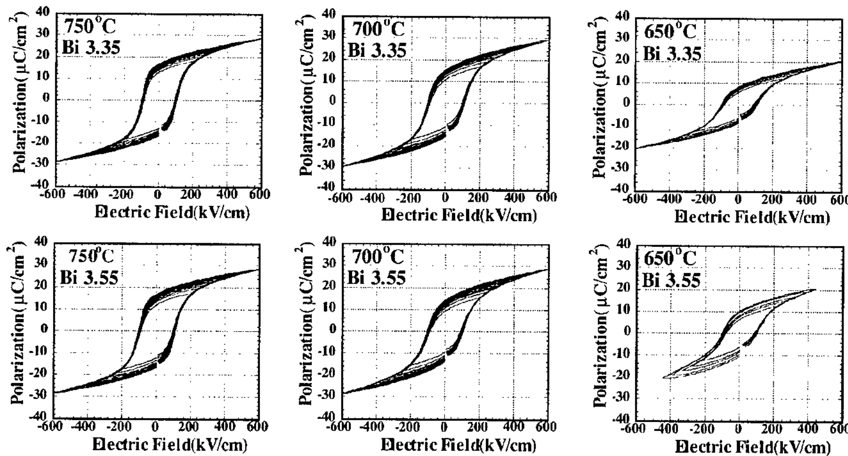

Figure 1. P-E hysteresis loops of the BLT films. Bi composition in the source solution is 3.35 or 3.55 and La composition is fixed at 0.75.

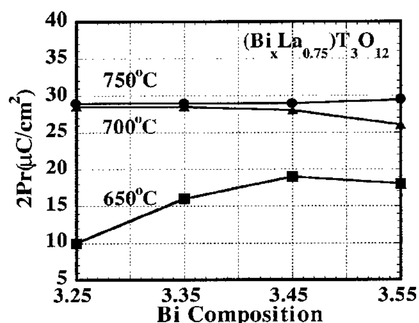

Figure 2. *Remanent polarization ($2P_r$) as a function of Bi composition*

films. In this experiment, the La composition was fixed at 0.75 and the Bi compositions was varied from 3.25 to 3.55. This means that the total amount of both Bi and La was varied from 4.0 (stoichiometric composition) to 4.3. It was found from the XRD measurements that the diffraction peaks from (001) and (117) crystallites can be seen and that randomly-oriented BLT films were obtained in this experiment. Figure 1 shows P-E hysteresis loops of the BLT films derived from the solution with Bi compositions of 3.35 and 3.55. Excellent P-E hysteresis loops can be obtained when the crystallization temperatures are above 700 °C. Remanent polarizations, P_r, are as large as 15 $\mu C/cm^2$ for the films grown at more than 700 °C. On the other hand, when the samples are annealed at 650 °C, the hysteresis loops become small and the remanent polarization is reduced to less than 10 $\mu C/cm^2$. The coercive field, E_C, are about 100 kV/cm and insensitive to the crystallization temperature. Figure 2 shows the observed remanent polarization ($2P_r$) as a function of Bi composition with varying the crystallization temperature. When the crystallization temperatures are higher than 700 °C, there is little

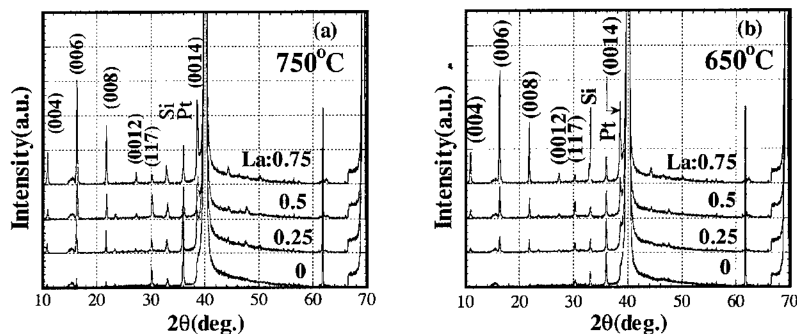

Figures 3. *X-ray diffraction patterns for the BLT films prepared at (a) 750 and (b) 650 °C.*

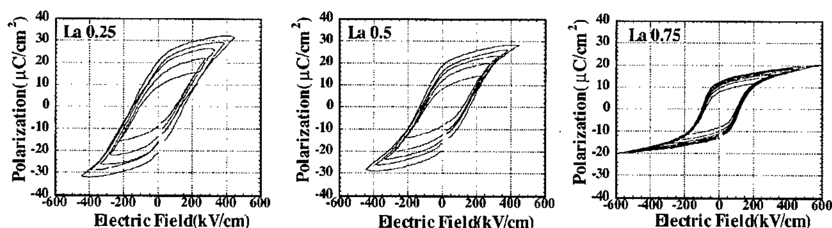

Figure 4. P-E hysteresis loops of the BLT films when the La composition is varied from 0.25 to 0.75.

dependence of the remanent polarization on the Bi composition, while the Bi content of 3.35-3.45 is optimum to obtain large remanent polarization when the annealing temperature is 650 °C.

Next, we varied the La composition in the source solution from 0 to 0.75. Total amount of Bi and La is fixed at 4.3. Figures 3 (a) and (b) show X-ray diffraction patterns for the BLT films prepared at 750 and 650 °C, respectively. It is worth noting that the diffraction peak intensities from (001) and (117) crystallites increase with La composition. Especially when the crystallization temperature is 650 °C, if no La is added, namely $Bi_4Ti_3O_{12}$, only small broad diffraction peak from (117) can be observed. This means that the 650 °C is not high enough to crystallize the $Bi_4Ti_3O_{12}$ film. On the other hand, by increasing the La content to 0.75, large and sharp diffraction peaks appear at both (001) and (117) positions. These results suggest that although the mechanism is not clear at present, the partial replacement of Bi with La in the BLT enhances the crystallization of the film. Therefore, BLT film can be crystallized at lower temperatures than $Bi_4Ti_3O_{12}$ film.

P-E hysteresis loops of BLT when the La composition is varied from 0.25 to 0.75 is shown in figure 4. The crystallization temperature is 750 °C. It is found that the P-E hysteresis loop can be improved as the La composition is increased to 0.75. This corresponds to the enhanced crystalline quality of the film with high La composition.

Finally, we demonstrate that the crystalline orientation of the BLT film can be controlled by the pre-annealing temperature. The XRD patterns for BLT films, crystallized at 750 °C, are shown in figure 5 when the pre-annealing temperature is 450 or 550 °C. When the pre-annealing temperature is 550 °C, the largest diffraction peak is from (117) crystallites and the peak intensities of (006) and (008) are small. On the other hand, when the pre-annealing temperature is reduce to 450 °C, the large and sharp diffraction peak can be observed at (006) and (008), and the (117) peak intensity becomes very small. Note that such a difference in crystalline orientations depends on the pre-annealing temperature and the crystallization temperature for both samples are same. For randomly oriented $Bi_4Ti_3O_{12}$ films, the (006)/(117) peak intensity ratio should be 0.14. Since the (006)/(117) peak intensity ratio of the BLT film with a pre-annealing temperature of 450 °C shown in this figure is 6.13, the film mainly consists of (001)-oriented BLT crystallites. On the other hand, for the BLT film when the pre-annealing was performed at 550 °C, the (006)/(117) peak intensity ratio is 0.11, which is close to the ratio

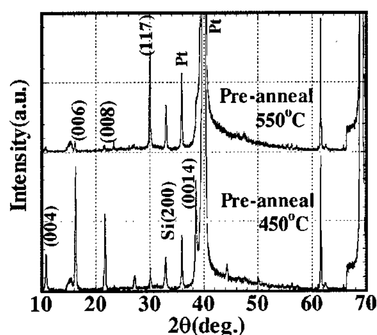

Figure 5. XRD patterns of BLT films, crystallized at 750 °C, when the pre-annealing temperature is 450 or 550 °C.

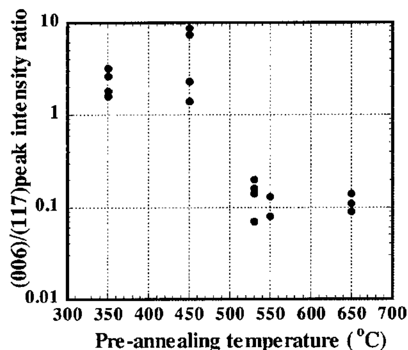

Figure 6. (006)/(117) peak intensity ratio as a function of the pre-annealing temperature.

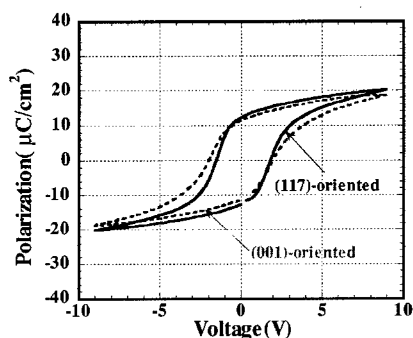

Figure 7. P-E hysteresis loops of (001) and (117)-oriented BLT films.

for randomly oriented $Bi_4Ti_3O_{12}$.

To clarify the effect of pre-annealing temperature on the crystalline orientations of the BLT films, (006)/(117) peak intensity ratios of the XRD patterns for the various BLT films are plotted in figure 6 as a function of pre-annealing temperature. The data obtained for the BLT films crystallized at both 700 and 750 °C are plotted in this figure. It is clearly found that when the pre-annealing temperature is lower than 450°C, the (001) crystallite is dominant. On the other hand, when the pre-annealing temperature is higher than 550 °C, the films contain (117) crystallites and must be close to randomly oriented BLT films. Although the mechanism for the final film orientation difference due to the pre-annealing temperature is not fully understood, it is considered that the random nucleation is enhanced at high pre-annealing temperature, which results in the randomly oriented, or weakly (117)-oriented BLT films. On the other hand, when

the pre-annealing temperature is lower than 450 °C, it is supposed that the (001)-oriented nuclei are preferentially formed, which produces the (001)-oriented BLT films.

P-E hysteresis loops of (117) and (001)-oriented films are shown in figure 7. A remanent polarization of 12 $\mu C/cm^2$ is obtained for the (117)-oriented BLT film. On the other hand., the remanent polarization of the (001)-oriented BLT film is slightly smaller. However, the observed difference in remanent polarization between (001)- and (117) oriented BLT films is not so large as expected from the electrical properties of $Bi_4Ti_3O_{12}$. In $Bi_4Ti_3O_{12}$, the remanent polarizations are 50 and 4 $\mu C/cm^2$ along a- and c- axes, respectively. The observed modest property anisotropy may be partly because the (117)-oriented BLT films examined in this work are close to the randomly oriented films.

CONCLUSION

Ferroelectric BLT films have been fabricated by the sol-gel technique and characterized. It was found that the excess Bi is necessary to obtain good electrical properties especially at low temperatures. It has been demonstrated that the crystallization can be enhanced by partially replacing Bi atoms with La atoms and that good electrical properties can be obtained for BLT films when La composition is 0.75. It has been also demonstrated that the crystalline orientations of the BLT films depends on the pre-annealing temperature. From these experimental results, ferroelectric BLT is one of the most promising materials for FeRAM applications.

ACKNOWLEDGMENT

This work was performed under the auspices of the R&D Projects in Cooperation with Academic Institutions (Next-Generation Ferroelectric Memory) supported by NEDO (New Energy and Industrial Technology Development Organization in Japan) and managed by FED (R&D Association for Future Electron Devices).

REFERENCES

1. J. T. Evans and R. Womack, *IEEE J. Solid State Circuits*, **23**, 1171 (1988).
2. I. M. Ross, *U. S. Patent 2791760* (1957).
3. J. L. Moll and Y. Tarui, *IEEE Trans. Electron Devices*, **ED-10**, 338 (1963).
4. E. Tokumitsu, G. Fujii and H. Ishiwara, *Appl. Phys. Lett.*, **75**, 575 (1999).
5. E. Tokumitsu, G. Fujii and H. Ishiwara, *Jpn. J. Appl. Phys.*, **39**, 2125 (1999).
6. B. H. Park, B. S. Kang, S. D. Bu, T. W. Noh, J. Lee and W. Jo, *Nature*, **401**, 682 (1999).
7. R. E. Newnham, R. W. Woffe and J. F. Dorrian, *Mat. Res. Bull.*, **6**, 1029 (1971).
8. T. Kijima and H. Matsunaga, *Jpn. J. Appl. Phys.*, **38**, 2281 (1999).

Mat. Res. Soc. Symp. Proc. Vol. 655 © 2001 Materials Research Society

Theoretical and Experimental Studies on Retention Characteristics of Metal-Ferroelectric-Insulator-Semiconductor and Metal-Insulator -Ferroelectric-Insulator-Semiconductor Structures

Masanori Okuyama, Mitsue Takahashi, Kazushi Kodama, Toshiyuki Nakaiso and Minoru Noda
Area of Materials and Device Physics, Department of Physical Science,
Graduate School of Engineering Science, Osaka University, Toyonaka, Japan

ABSTRACT

Retention characteristics of Metal-Ferroelectric-Insulator-Semiconductor(MFIS) and Metal-Insulator-Ferroelectric-Insulator-Semiconductor(M-I-FIS) structures have been investigated both theoretically and experimentally. The simulated time dependence of capacitance for the MFIS has indicated that reducing currents through the ferroelectric and the insulator layers improves the retention characteristics more effectively than choosing the insulators with larger dielectric constants. The M-I-FIS structure has been studied in order to reduce the charge injection between the metal and the ferroelectric layer in the MFIS. The simulations have indicated that the M-I-FIS can provide much longer retention time than the original MFIS, although the experimental retention time of the M-I-FIS have almost the same as that of the MFIS.

INTRODUCTION

Metal-Ferroelectric-Insulator-Semiconductor (MFIS) has been attracting much attention as one of favorable structures for a practical use in FET-type nonvolatile memories. The structure is regarded as a useful memory with nondestructive readout operation, which follows a good scaling-down rule. However, only a few ferroelectric gate FET memories have shown long retention times so far[1, 2], while many other MFS and MFIS structures have still shown short retention times. These structures cannot avoid currents in the ferroelectric and the insulator layers, which are caused by several factors such as ion drifts, thermal- and field- induced relaxation of polarization and carrier conduction induced by an intrinsic depolarization field which has the opposite direction to the ferroelectric spontaneous polarization. These currents are supposed to make retention characteristics worse. In this article, time dependence of capacitance has been simulated for an MFIS structure on the assumption that the current through the ferroelectric layer increases charges injected into the interfacial region between the metal and the ferroelectric layers and compensates the field imposed on the layer. The simulation has reproduced well our previous experimental data[3], which indicates the validity of our model. In order to improve retention characteristics of the MFIS by reducing the current from the top electrode metal, we have studied the effect of preparing a thin insulator layer under the metal on the retention time. This structure called as a Metal-Insulator-Ferroelectric-Insulator-Semiconductor (M-I-FIS) has been investigated both theoretically and experimentally.

ANALYSIS

Process of retention loss has been simulated by solving numerically several electrodynamic simultaneous equations such as a current continuity equation, a voltage-drop equation for each layer in the structures and Gauss's law for both the ferroelectric and the insulator layers[4]. The current density has been defined as $J_f(E_f, t)$ through the ferroelectric layer which is dependent on the applied field E_f and time t, and as $J_i(E_i)$ through the insulator layer which is dependent only on the applied field E_i. The effect of the $J_i(E_i)$ and $J_f(E_f, 0)$ on the retention time have been calculated for an MFIS. In this paper, retention time has been defined as time to show a half of the initial capacitance when the measurement is started. In order to simulate the retention characteristics of an MFIS structure, we used d_f=400nm as the ferroelectric layer thickness, d_i =10nm as the insulator thickness, V_{fb} =0V as the flatband voltage, ε_f =50 as the dielectric constant of the ferroelectric layer, ε_i =3.9 as the dielectric

constant of the insulator layer and T =300K as the temperature. In order to study M-I-FIS structures, additional insulator layers of ε_i =3.9 with various thickness have been assumed to be prepared on the FIS. The field-dependent polarization for the ferroelectric layer has been assumed to show hysteresis loops modeled by Miller[5]. We assumed the p-type silicon substrate with a uniform doping concentration of N_a =10^{15}cm^{-3}, a value for spontaneous polarization of P_s =1.2μC/cm^2, a remanent polarization of P_r =1.0μC/cm^2 and a coercive field of E_c =50kV/cm. The software *mathematica 4.0* was used for these calculations.

EXPERIMENTAL

$SrBi_2Ta_2O_9$ (SBT) thin film was prepared on a substrate by Pulsed Laser Deposition(PLD) method in O_2 atmosphere. A pulsed ArF-excimer laser with a wavelength of 193nm was used to deposit the films. The repetition frequency was 5Hz, and the laser fluency was from about 2 to 3J/cm^2. The target was a ceramic disk of stoichiometric SBT. The substrate was SiO_2/n-Si(100). The thickness of the SiO_2 layer was 27nm from the capacitance of the substrate with Al top electrode when the dielectric constant of the SiO_2 was assumed to be 3.9. The distance between the target and substrate was 20mm. During the deposition, the temperature of the substrate was 500℃ measured by thermocouple, and the O_2 pressure was 0.3Torr. The thickness of the SBT film was from about 400 to 600nm measured by a profiling analyzer (Dektak^{3}ST, SLOAN TECHNOLOGY).

In order to make an M-I-FIS structure, MgO film was prepared on the SBT film by the PLD method in O_2 atmosphere. The target was a pressed disk made from MgO powder. The distance between the target and the SBT/SiO_2/n-Si plate was 25mm. The deposition temperature and pressure were 500℃ and 0.01Torr, respectively.

The chamber was evacuated to 5×10^{-6}Torr before every deposition. After the deposition, the sample was cooled down to room temperature in the chamber, and then moved into a tube furnace to anneal at 600℃ in O_2 atmosphere for 20 minutes. An array of Al dots of diameter 250 μm ϕ was deposited as top electrodes by evaporation. The backside electrode was formed by evaporation of AuSb.

Physical properties of the films were characterized using x-ray diffraction(XRD), scanning electron microscopy(SEM) and atomic force micorscopy(AFM) techniques. Voltage dependent capacitance was evaluated using C-V plotter(HEWLETT PACKARD 4280A) at 1MHz. The sweeping rate of the applied gate voltage was 0.2V/sec.

RESULTS AND DISCUSSION

Retention time dependent on $J_i(E_i)$ has been investigated when $J_f(E_f, t)$ is assumed to be the same as reported before[3](Figures 1(a), (b)). A proportional parameter A, which is expressed as $J_i(E_i)=AJ_{i0}(E_i)$(inset in Figure 1(b)), has been defined to describe how much current is flowing through the insulator layer. $J_{i0}(E_i)$ is the current density which is negligibly

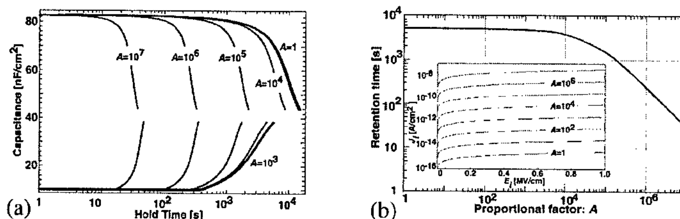

Figures 1 (a)Calculated time dependent capacitance of MFIS(F: ε_f=50, d_f=400nm / I: ε_i=3.9, d_i=10nm) for various currents through the insulator defined as $J_i=AJ_{i0}(E_i)$. The current through the ferroelectric layer was assumed to be the same as reported before[3].The calculated results for $A=10^3$ and A=1 show almost the same curves with each other. (b) Calculated retention time dependent on the proportional factor A used in (a). The inset shows the modeled current J_i dependent on the applied fields.

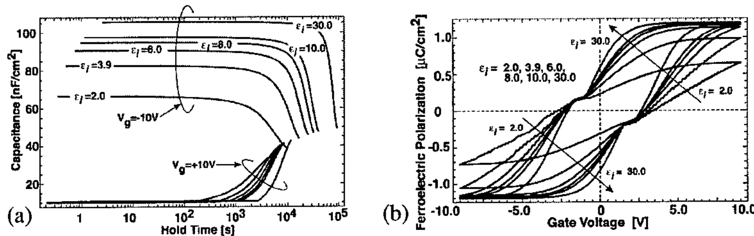

Figures 2 (a)Calculated time dependent capacitance of MFIS(F: ε_f=50, d_f=400nm / I: d_i=10nm) for various ε_i. The current through the ferroelectric and the insulator layer were assumed to be the same as reported before[3]. (b) Calculated ferroelectric polarization in the MFIS dependent on the applied gate voltage for various ε_i from 2.0 to 30.0.

small compared to $J_f(E_f, t)$[3]. When $A<10^3$, time dependent capacitance for the modeled MFIS has shown rapid convergence upon the curve for A=1 which agreed well with our experimental results[3]. However, Figure 1(b) shows that in cases of $A>10^4$, retention time decreases as A increases, while currents for $A<10^3$ exhibit almost the constant maximum retention time of 5×10^3 sec. This result implies that $J_i(E_i)$ less than a given value for $A<10^4$ does not affect very much on the retention time, however, when $J_i(E_i)$ becomes larger than the value, seriously worse retention characteristics will be observed.

Retention characteristics for various ε_i have been also simulated(Figure 2(a)). When a negative gate bias voltage has been applied to write data, the curves of time dependent capacitance are sensitive to the values of ε_i. However, the curves for a positive gate bias have not shown much difference with each other for various ε_i (Figure 2(a)). On the other hand, Figure 2(b) has shown that the ferroelectric hysteresis loops become upright gradually as ε_i increases. These results indicate that selecting the insulator of large ε_i in an MFIS is very effective to lower the operation voltage, but not enough to obtain long retention time.

When $J_f(E_f, 0)$ increases, retention time has also shown a downward tendency (Figures 3(a), (b)). Very small current through the insulator layer for the parameter A =1 discussed above has been assumed to investigate the effects of $J_f(E_f, 0)$. Time dependence of current through the ferroelectric layer has been assumed to be as $J_f(E_f, t)= J_f(E_f, 0)\, t^{-0.52}$, where $J_{f0}(E_f, 0)$ was experimentally obtained[3]. Another proportional parameter B has been defined as $J_f(E_f, 0)=BJ_{f0}(E_f, 0)$ to describe how much current is flowing through the ferroelectric layer. The parameter B has been decided to be 1, as the time dependent capacitance for the modeled MFIS reproduce the experimental results well. As shown in Figure 3(b), currents for $B<10^{-3}$ exhibit almost the maximum constant retention time of 3×10^8 sec. This result implies that $J_f(E_f, 0)$ less than a given value for $B<10^{-3}$ does not affect very much on the retention time,

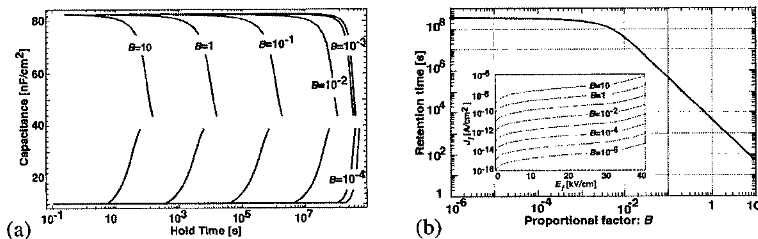

Figures 3 (a) Calculated time dependent capacitance of MFIS(F: ε_f=50, d_f=400nm / I: ε_i=3.9, d_i=10nm) for various current densities through the ferroelectric defined as $J_f=B\cdot J_f(E_f, 0)$. The current through the insulator layer was assumed to be for A=1 in Figure 1(b). The calculated results for $B<10^{-3}$ show almost the same curves with each other. (b) Calculated retention time dependent on the proportional factor B used in (a). The inset shows the modeled current J_f dependent on the applied fields E_f for various B.

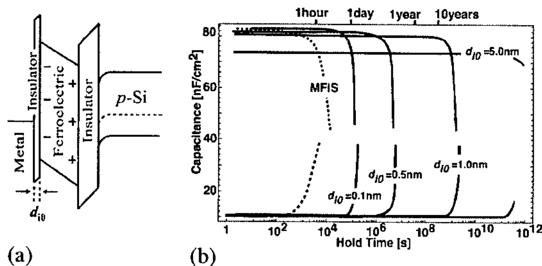

Figures 4 (a) Simplified band diagram for an M-I-FIS structure, which includes an additional insulator layer with the thickness of d_{i0}.
(b) Calculated capacitance dependent on hold time for the M-I-FIS structure. Note that the structure for d_{i0}=0nm is regarded as an MFIS.

however, if $J_f(E_f, 0)$ becomes larger than the value, much worse retention characteristics will be observed.

Rapid decrease in retention time shown in Figure 3(b) implies a decrease of current through the ferroelectric layer results in much progress in retention time. In order to decrease the current through the ferroelectric layer, two ways can be proposed in designing a structure of an MFIS. One way is to choose a top electrode metal with larger work function. The other is to insert a thin insulator film between the top electrode metal and the ferroelectric layer. The latter has been studied theoretically by forming a Metal-Insulator-Ferroelectric-Insulator-Semiconductor (M-I-FIS) (Figure 4(a)). The insulator between the metal and the ferroelectric layers should be much thinner than that between the ferroelectric and the semiconductor layers so as not to reduce the potential applied on the ferroelectric layer. Device characteristics of the M-I-FIS have also been investigated by applying our physical model discussed above. In order to operate the simulation, current through the insulator layer on the silicon substrate has been assumed for A=1 (Figure 1(b))and ε_i =3.9 (Figure 2(a), (b)) and current through the ferroelectric layer for B=1 given in Figure 3(b). An additional SiO_2 thin layer with each thickness of d_{i0}= 0.1, 0.5, 1.0 and 5.0nm was assumed to be formed between Al and SBT layers in the MFIS structure of Al/SBT/SiO_2/Si. A tunneling current has been assumed through the insulator layer as well as the Schottky and the Fowler-Nordheim emission. The current through a trapezoidal potential of the additional thin SiO_2 layer has been modeled as follows[6]:

$$J_i = \alpha E_i d_i \cdot \exp(-\frac{2d_{i0}}{\hbar}\sqrt{\varphi m}) \ , \qquad (1)$$

where $\hbar$ is the Planck's constant, φ is work function difference for the M-I system and m is the electron mass, respectively. The parameter α is a proportional factor which has been determined to normalize roughly curves for the M-I-FIS with d_{i0}=0.1nm by the curves for the MFIS. In this rough estimation, we used φ = 3.2eV for the system of Al/SiO_2 and the mass of m=9.11×10^{-31}kg for a free electron.

Results of the calculations are given in Figure 4(b). M-I-FIS structures have exhibited much better retention characteristics than the original MFIS. When d_{i0}=1.0nm is assumed, the

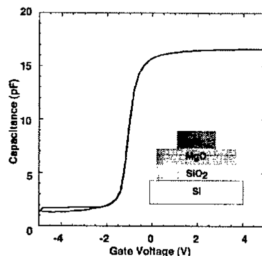

Figure 5 C-V characteristics of Al/MgO/SiO_2/Si/AuSb diode.

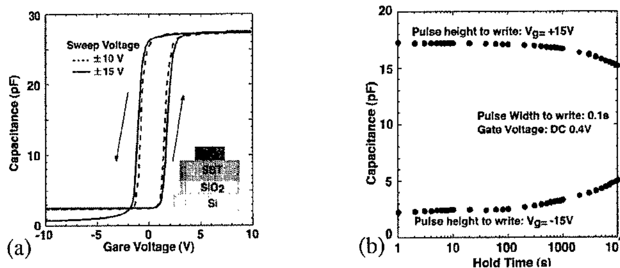

Figures 6 (a) C-V and (b) Retention characteristics of $Al/SBT/SiO_2/Si/AuSb$ structure.

calculation indicates that the retention time will be over 10 years. In the case of d_{i0}=5.0nm, the M-I-FIS is expected to show much longer retention time than 10 years, however as shown in the Figure 4(b), the initial capacitance difference between the states written by positive and the negative gate voltages becomes smaller. This is because the thicker d_{i0} makes the total capacitance smaller for the M-I-FIS.

The M-I-FIS structure has been also studied experimentally. At first, a structure of $MgO/SiO_2/Si$ has been examined. An XRD pattern has clearly shown the (200)-MgO peak for the as-deposited MgO surface. Then a characteristic of capacitance dependent on applied voltage(C-V) has been studied for $Al/MgO/SiO_2/Si/AuSb$ structure(Figure 5). No hysteresis loop has been shown for the structure which indicates that charge injection into the insulator layers is negligible. At second, a structure of $SBT/SiO_2/Si$ has been produced and studied on its surface morphology using AFM. No serious damage has been observed on the SBT surface. The mean roughness of 4.4nm and the maximum height of 29nm were obtained. Counterclockwise hysteresis loops have been clearly observed for C-V characteristics of the $Al/SBT/SiO_2/Si/AuSb$ structure (Figure 6(a)). The C-V hysteresis loops have been spread almost symmetrically over the vertical axis for the zero voltage. Memory window of about 2.8V at the sweeping voltage from Vg= −15V to +15V(Figure 6(a)) and a retention time of 10^4sec. (Figure 6(b)) have been obtained.

At last, an M-I-FIS structure of $Al/MgO/SBT/SiO_2/Si/AuSb$ has been fabricated. Memory window of about 1.0V at the sweeping voltage from Vg= −15V to +15V(Figure 7(a)) and a retention time over 10^4sec.(Figure 7(b)) have been obtained. The retention characteristic seems slightly but not much improved as compared to that of the $Al/SBT/SiO_2/Si$ structure(Figure 6(b)). By using an AFM technique for the top MgO layer of the structure, the mean roughness of 3.3nm and the maximum height of 31nm have been obtained, although a SEM image has not shown serious damages(Figure 8). Improvement of the surface morphology on the insulator layer is expected to make the retention time longer.

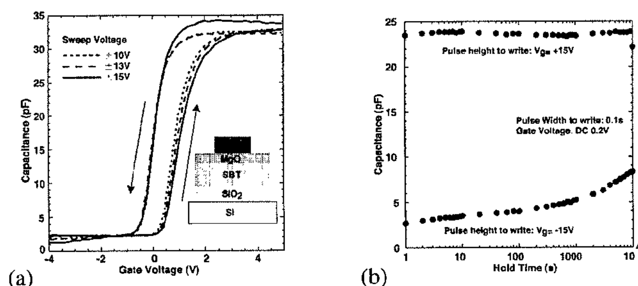

Figures 7 (a)C-V and (b)Retention characteristics of $Al/MgO/SBT/SiO_2/Si/AuSb$ structure.

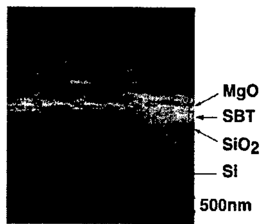

Figure 8 SEM image of a cross section of $MgO/SBT/SiO_2/Si$ structure.

SUMMARY

A simple model has been used to investigate retention characteristics of an MFIS structure by considering effects of currents through the insulator and the ferroelectric layers. The simulations for the MFIS have indicated that the retention characteristics can be severely degraded when currents through the insulator and the ferroelectric layers flow more than certain values. In order to decrease the charges injected between the metal and the ferroelectric layers, the physical model for the MFIS have been modified and applied to an M-I-FIS structure. The calculation has indicated that inserting a thin insulator film can be very effective to provide much longer retention time than the original MFIS. The M-I-FIS structure has been also studied experimentally, however, such a long retention time as predicted by the simulation has not been obtained so far. It is supposed partly because the rough surface of the insulator under the top electrode has still induced current into the ferroelectric layer.

ACKNOWLEDGMENTS

This study was partially supported by grants from Semiconductor Technology Academic Research Center (STARC), ROHM CO. LTD. and a Grant-in-Aid for Scientific Research from the Ministry of Education, Science and Culture, in Japan (No.12134205).

REFERENCES

1. E. Tokumitsu, G. Fujii and H. Ishiwara, *Appl. Phys. Lett.* 75, 575, 1999
2. S. Xiong and S. Sakai, *Appl. Phys. Lett.* 75, 1613, 1999
3. M. Okuyama, H. Sugiyama, T. Nakaiso and M. Noda: to be published in the Journal of Integrated Ferroelectrics, 2000.
4. M. Takahashi, H. Sugiyama, T. Nakaiso, K. Kodama, M. Noda and M. Okuyama: to be published in *Jpn. J. Appl. Phys.*, 2001
5. S. L. Miller and P. J. McWhorter, *J. Appl. Phys.* 72, 5999, 1992
6. E. Burstein and S. Lundqvist, *Tunneling Phenomena in Solids*. New York: PLENUM PRESS, 1969, Chap. 3, pp.23

High-Frequency Applications of Ferroelectrics

Mat. Res. Soc. Symp. Proc. Vol. 655 © 2001 Materials Research Society

Microstructural and Electrical Properties of La Doped $Ba_{1-x}Sr_xTiO_3$ Thin Films For Tunable Microwave Device Applications

M.W. Cole, P.C. Joshi, E. Ngo, C.W. Hubbard, U. Lee, M.H. Ervin
US Army Research Laboratory, Weapons and Materials Research Directorate
Aberdeen Proving Ground, MD 21005, U.S.A.

ABSTRACT

We have investigated the structural, compositional, interfacial, surface morphological and dielectric properties of $Ba_{0.6}Sr_{0.4}TiO_3$ solid solution thin films La doped from 0 to 10 mol%. The doped thin films were prepared by the metalorganic solution deposition technique using carboxylate-alkoxide precursors. After post-deposition annealing in oxygen ambient at 750 °C the films were characterized via x-ray diffraction, Auger electron microscopy, field emission scanning electron microscopy, and atomic force microscopy. The electrical measurements were achieved in the metal-insulator-metal (MIM) configuration with Pt as the top and bottom electrode. Our results demonstrated that La doping had a strong effect on the films microstructural, dielectric and insulating properties. Specifically, 1 mol% La doped BST films exhibited a lower dielectric constant, 283 and higher resistivity 31.4×10^{13} Ω-cm with respect to that of undoped BST. The loss tangent and tunability (at 100 kHz) of the 1 mol% La doped BST films were 0.019 and 21% (at E=300kV/cm) respectively.

INTRODUCTION

Electrical tunable ferroelectric thin film devices rely on the variation of a ferroelectric material's dielectric constant with application of an electric field [1-3]. $Ba_{1-x}Sr_xTiO_3$ (BST) is a promising ferroelectric material for tunable microwave device applications such as electronically tunable mixers, delay lines, filters and phase shifters. For BST to be employed for tunable device applications the dielectric and insulating properties must satisfy several critical requirements. These requirements include: (1) a low loss tangent over the range of operating dc bias voltages, (2) a large variation in the dielectric constant with applied dc bias, (3) for impedance matching purposes, the dielectric constant (ε_r) must be less than 500, and (4) the film must possess low leakage current (I_L) characteristics, (5) the film must be single phase with a dense microstructure and minimal defects, (6) the surface morphology must be smooth and crack free and (7) the film and substrate must be thermally stable as a function of both processing temperature and device operational environment [3, 4]. Pure (undoped) BST in thin film form offers tunabilities upward of 50% at bias voltages of less than 10 V, which is compatible with the voltage requirements of present semiconductor based systems. Unfortunately, the tradeoff for such high tunabilities are high loss tangents, that is, tan $\delta >> 0.02$. It is well documented that small concentrations of dopants can dramatically modify the properties of ferroelectric materials such as BST. In particular, Fe^{2+}, Fe^{3+}, Co^{2+}, Co^{3+}, Mn^{2+}, Mn^{3+}, Ni^{2+}, Mg^{2+}, Al^{2+}, Ga^{3+}, In^{3+}, Cr^{3+}, and Sc^{3+}, which can occupy the B sites of the ($A^{2+}B^{4+}O^{2-}{}_3$) perovskite structure, have been known to lower dielectric loss [3, 5-7]. The mechanism for this behavior centers on the thesis that ions with a charge less than 4^+ can substitute for Ti^{4+} and behave as electron acceptors. These acceptors prevent the reduction of Ti^{4+} to Ti^{3+} by neutralizing the donor action of the oxygen vacancies. Because the electrons resulting from the generation of oxygen vacancy can hop between different titanium ions and provide a mechanism for dielectric losses, the

compensation for the oxygen vacancy with the correct amount of acceptor dopants helps to lower the loss tangent. The goal of the present investigation is to determine the effects of La doping on the structural, microstructural, dielectric and insulating properties of $Ba_{0.6}Sr_{0.4}TiO_3$ thin films.

EXPERIMENTAL

Thin films were fabricated via the metalorganic solution deposition (MOSD) technique using barium acetate, strontium acetate, and titanium isopropoxide as precursors to form BST. Acetic acid and 2-methoxyethanol were used as solvents and lanthanum acetate was employed as the dopant at concentrations ranging from 1 to 10 mol%. The precursor films were spin coated onto Pt-coated silicon substrates. Particulates were removed from the solution by filtering through 0.2 µm syringe filters. Subsequent to coating, the films were pyrolized for 10 min. on a hot plate at 350 °C in order to evaporate solvents and organic addenda and form an inorganic film. The spin coat-pyrolization process was repeated until a film thickness of 150 nm was achieved. Post-deposition annealing was performed in oxygen ambient at 750 °C for 60 min. The films were characterized for structural, microstructural, compositional, surface morphological, dielectric and insulating properties. Specifically, x-ray diffraction (XRD), using a Rigaku diffractometer with CuKa radiation at 40 kV, was employed to assess film crystallinity, phase formation and film orientation. A Hitachi S4500 field emission scanning electron microscope (FESEM) was utilized to assess surface morphology, plan-view and cross-sectional grain formation and microstructure. Auger electron spectroscopy (AES) was employed to assess the elemental distribution within the film and across the film-Pt interface. The surface morphology of the films was analyzed with a Digital Instruments Nano Scope IIIa atomic force microscope (AFM) using tapping mode with amplitude modulation. The electrical measurements were conducted in the metal-insulator-metal (MIM) capacitor configuration. MIM capacitors were formed by sputter depositing 0.2 mm Pt dots with 0.5 mm spacings, through a shadow mask covering a 1 x 1 cm^2 area. Capacitance (C_p), dissipation factor (tan δ), and dielectric permitivity (ε_r) were measured with an HP 4192A impedance/gain analyzer. The films insulating properties, leakage current (I_L), were evaluated via I-V measurements using a HP 4140B semiconductor test system.

RESULTS AND DISCUSSION

Table I. Summary of dielectric and insulating properties for La doped BST films at 100 kHz.

La mol%	ε_r	tanδ	Tunability (%) (at 200 kV/cm)	ρ (x10^{13} Ω-cm) at 100 kV/cm)
0	450	> 0.02	28.1	0.04
1	283	0.019	12.1	31.4
5	204	0.019	3.49	31.4
10	200	0.030	1.2	1570

The dielectric and insulating properties of the 750 °C annealed 0-10 mol% La doped BST films at 100 kHz are summarized in table I. Table I clearly shows that the amount of La dopant

has a strong influence on the dielectric and insulating properties of the BST films. The dielectric constant, tan δ, tunability and leakage current (film resistivity increased) all decreased as the La concentration increased. The loss tangent value decreased from >0.02 for undoped BST to 0.019 for the 1 and 5 mol% La doped BST films. The dielectric response of the 1 mol% doped BST is shown in figure 1. The dielectric properties did not show any appreciable dispersion with measured frequency up to 1 MHz indicating good film quality and the absence of internal interfacial barriers. The measured small signal dielectric constant and loss factor at a frequency of 100 kHz were 283 and 0.019 respectively. The tunability of the capacitance (measured in terms of ΔC/Co, where ΔC is the change in capacitance relative to zero-bias capacitance Co) of the 1 mol% La doped film, increased with increase in the applied electric field (figure 2). Specifically, the tunability varied from 0 to 35% at applied electric fields of 0 to 500 kV/cm respectively. Considering the tradeoffs between tunability and the values of tan δ, dielectric constant and film resistivity, the 1 mol% La doped BST film possessed the best overall material properties for tunable device applications. However, in order to fully understand the properties discussed above the influence of the La concentration on the structural, microstructural interfacial and surface morphological properties must be evaluated and correlated with the films dielectric and insulating properties.

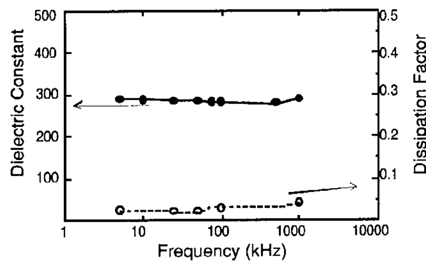

Figure 1. Dielectric constant and dissipation factor as a function of frequency for a 150 nm thick film annealed at 750 °C for 60 min.

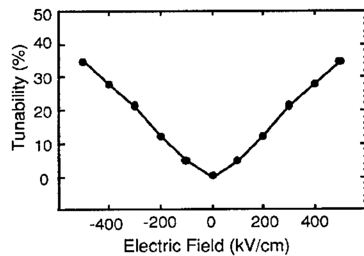

Figure 2. Tunability of $Ba_{0.6}Sr_{0.4}TiO_3$ thin films as a function of applied electric field.

X-ray diffraction was utilized to assess film crystallinity and to determine whether or not the films possessed a single phase structure. Figure 3 displays the x-ray diffraction patterns of the 750°C annealed BST films doped from 0 to 10 mol%. All films possessed a non-textured polycrystalline structure with no evidence of secondary phases. There was no apparent change in peak intensity resultant of the La doping. The full-width-half- maximum (FWHM) of the most intense diffraction peaks increased with increasing La content. This peak broadening is indicative of a decrease in grain size.

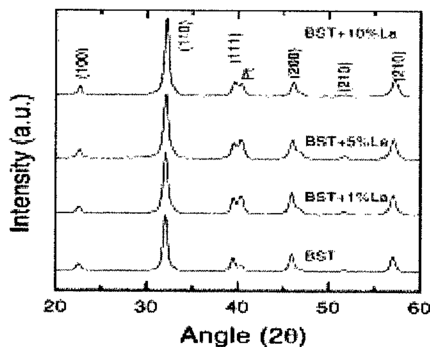

Figure 3. X-ray diffraction patterns of the La doped (0-10 mol%) $Ba_{0.6}Sr_{0.4}TiO_3$ films annealed at 750 °C for 60 min.

The surface morphology of the La doped films was smooth and crack free as determined by FESEM (not shown). Quantitative analysis of the film surfaces, via AFM (figure 4), determined the root mean square surface roughness, R_{rms}, to be less than 1.5 nm for all film compositions. Figure 4 clearly shows that both the undoped and doped films exhibited a dense microstructure which was significantly modified by the addition of La. Specifically, the undoped and 1 mol% La doped BST films exhibited a uniform microstructure with an average grain size of 60 nm and 50 nm respectively. The 5 and 10 mol% La doped films possessed a non-uniform grain structure with average grain sizes of 30 nm and 22 nm respectively. A non-uniform grain size-structure is indicative of either (1) multi-phased film or (2) immature film crystallinity, i.e. the film was not fully crystallized at the present annealing temperature/time. Since the x-ray diffraction measurements demonstrated that the 1, 5, and 10 mol% La films were single phase we suggest that the 5 and 10 mol% La doped BST films require a higher annealing temperature and/or longer annealing time in order to achieve a uniform grain size which is indicative of a fully developed crystalline microstructure.

The cross-sectional FESEM microstructural analysis of the undoped and La doped BST films are displayed in figure 5. The FESEM results show that the 1 mol% La doped film possessed a well crystallized, dense, void free microstructure composed of granular multi-grains randomly distributed throughout the film thickness. In contrast, the 5 and 10 mol% La doped films possessed an under developed microstructure with respect to the undoped and 1 mol% La doped films. This data confirms the AFM results. The FESEM image of the 1 mol% La doped film clearly delineates the film/Pt electrode structure. No amorphous layer or voiding was observed at the interface between the BST and the bottom electrode. This defect free, and structurally abrupt interface bodes well for the excellent mechanical integrity and good adhesion characteristics of the 1 mol% La doped BST film coated Si substrate. The AES depth profile of the 750° C annealed 1-10 mol% La doped BST films are displayed in figure 6. The AES depth

profiles revealed a sharp interface with no interdiffusion of constituent elements between the dielectric film and the Pt electrode. The depth profiles also revealed that each element component of the film possessed a uniform distribution from the film surface to the interface of the bottom Pt electrode substrate. These data substantiate the fact that the film and Platinized-silicon substrate maintain chemical and thermal stability at processing temperatures up to 750 °C (the annealing temperature). No impurities were observed in the AES profile, which without doubt, contributed to the films good dielectric and insulating properties.

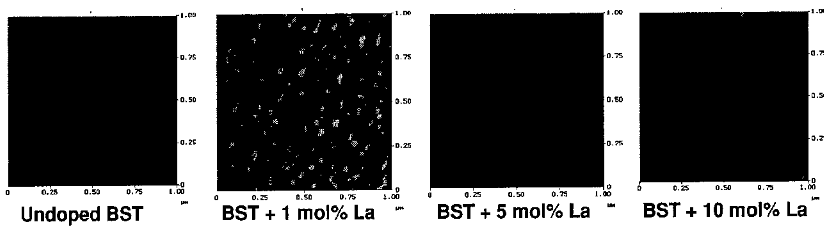

Figure 4. AFM micrographs of the undoped,1 mol%, 5 mol%, and 10 mol% La doped $Ba_{0.6}Sr_{0.4}TiO_3$ thin films.

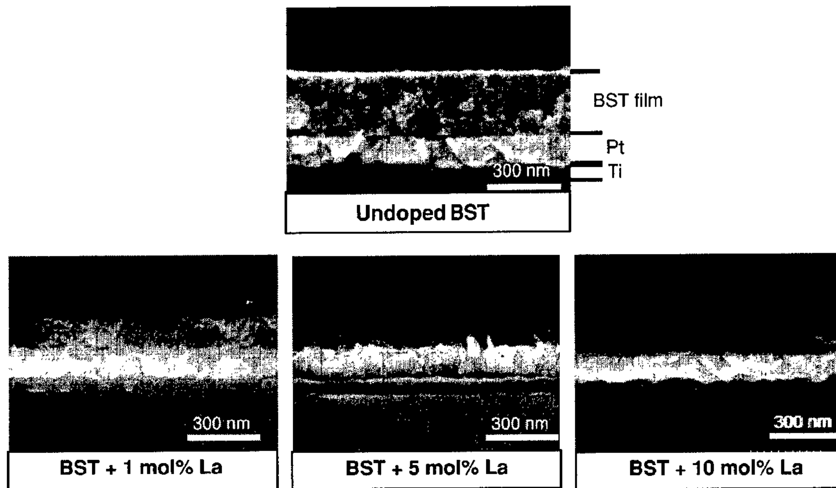

Figure 5. FESEM images of the undoped, 1 mol%, 5 mol% and 10 mol% La doped BST films.

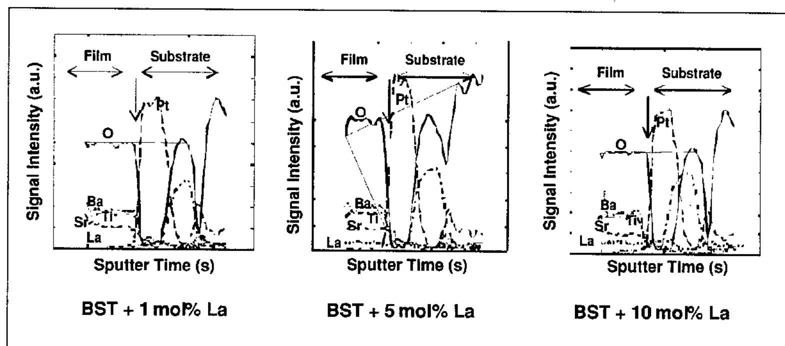

Figure 6. AES depth profiles of the 1 mol%, 5 mol% and 10 mol% La doped BST films.

CONCLUSIONS

This work has demonstrated that La doping has a strong influence on the material properties of BST thin films. We have achieved improved dielectric and insulating properties for 1 mol% La doped BST thin films. The measured values of dielectric constant, dissipation factor, tunability and resistivity of $Ba_{0.6}Sr_{0.4}TiO_3$ thin films doped with 1 mol% La were 283, 0.019, 12% at E=200kV/cm - 21% at E=300 kV/cm, and 31.4×10^{13} Ω-cm respectively. The 1 mol% La doped BST film was single phase, possessed a dense defect free microstructure with a thermally stable film-electrode interface, and smooth continuous surface morphology. Films doped at concentrations between 5-10 mol% possessed under developed microstructures suggesting that higher annealing temperatures and/or longer annealing times are required before the dielectric properties can be accurately assessed.

REFERENCES

1. L.A. Knauss, J.M. Pond, S.J. Horwitz, D.B. Chrisey, Appl. Phys. Lett., **69**, 25 (1992).
2. M.W. Cole, P.C. Joshi, M.H. Ervin, M.C. Wood, R.L. Pfeffer, Thin Solid Films, **374**, 34 (2000).
3. P.C. Joshi, M.W. Cole, Appl. Phys. Lett ., **77**, 289 (2000).
4. D. P. Patel, Radar Division, NavelResearch Laboratory, Washington DC, USA, private communication.
5. Y. Xu, Ferroelectric Materials and Their Applications, North Holland, New York, NY (1991)
6. U.N. Weston, J. Am. Ceramic Soc., **52**, 253 (1969).
7. V.K. Varadan, D.K. Ghodgaonkar, V.V. Varadan, Microwave J., **30**, 116 (1992).

Mat. Res. Soc. Symp. Proc. Vol. 655 © 2001 Materials Research Society

Experimental and Theoretical Investigation into the Dielectric Behaviour of Ferroelectric Thin Film Superlattices

J. M. Gregg, D. O'Neill, G. Catalan and R. M. Bowman
Condensed Matter Physics and Materials Science Division
School of Maths and Physics, Queen's University Belfast
Belfast BT7 1NN, U. K.

ABSTRACT

Pulsed laser deposition has been used to fabricate thin-film capacitor structures in which the dielectric layer is composed of a superlattice of $Ba_{0.8}Sr_{0.2}TiO_3$ and $Ba_{0.2}Sr_{0.8}TiO_3$. The properties of the capacitors were investigated as a function of superlattice periodicity. The dielectric constant was significantly enhanced, and temperature migration of the peak in dielectric constant as a function of frequency was observed, at stacking periodicities of a few unit cells. However, such 'relaxor-like' features were found to be associated with high dielectric loss. Analysis of the imaginary permittivity as a function of frequency showed that fine-scale superlattices conform to Maxwell-Wagner behaviour, indicating that the observed features may be an artefact of increased carrier mobility. Modelling showed that both dielectric enhancement and frequency relaxation could readily be reproduced by Maxwell-Wagner formalism.

INTRODUCTION

There is strong evidence that the physics of relaxor behaviour is intimately linked to nanoscale chemical heterogeneity [1- 4]. A number of investigations have used growth of thin film ceramic heterostructures to see whether artificial nanolayering of different ferroelectric materials can reproduce the beneficial properties of relaxors [5-11]. In many cases enhanced dielectric constants have been observed. Notably Erbil *et al.* [5] claimed a relative dielectric constant of 420,000 at 1kHz and at room temperature. Qu *et al.* [6] have also seen evidence that nanolayer heterostructures show the migration of T_m seen in relaxors, and nearly all work shows broad temperature dependence of dielectric response. However, there are serious inconsistencies in the body of research produced to date. The extent of dielectric enhancement varies dramatically, and is found to be a maximum at very different scales of heterostructure. Crucially, dielectric losses are not fully reported, or are high in much of the work. In an attempt to rationalise such inconsistencies the authors report from a study examining thin film capacitor structures in which the dielectric layer is a superlattice of $Ba_{0.8}Sr_{0.2}TiO_3$ and $Ba_{0.2}Sr_{0.8}TiO_3$.

EXPERIMENTAL DETAILS

Thin film capacitors were made by Pulsed Laser Deposition (PLD) as follows: $SrRuO_3$ lower electrodes were deposited onto single crystal {100} MgO substrates under 0.15mbar of oxygen with a substrate temperature of 775°C. $Ba_{0.8}Sr_{0.2}TiO_3$ / $Ba_{0.2}Sr_{0.8}TiO_3$ superlattices were then deposited under the same conditions, before cooling to 650°C for a 15 min post-deposition anneal under 900 mbar O_2. The total thickness of all the dielectric superlattices was maintained at 250 ± 15 nm. The specimen was then removed from the PLD system and two gold electrodes (~2 mm^2) were deposited by thermal evaporation through a hard mask. The structure works

effectively as two capacitors in series. Structural characterisation was performed using a Siemens D5000 x-ray diffractometer (XRD), and Tecnai F20 high-resolution transmission electron microscope with energy dispersive x-ray (EDX) analysis. Functional characterisation was performed using Hewlett-Packard LCR meters, with temperature variation effected using Lakeshore controllers and Oxford Instruments cryostats.

RESULTS AND DISCUSSION

Successful growth of the superlattice structures was established by the observation of satellite peaks in XRD (figure 1), and by direct imaging under cross-sectional transmission electron microscopy (figure 2). The layer periodicities within the superlattices were calculated from the XRD traces. Assuming that the deposition rates of $Ba_{0.8}Sr_{0.2}TiO_3$ and $Ba_{0.2}Sr_{0.8}TiO_3$ were the same individual layer thickness was half the superlattice periodicity.

The dielectric behaviour of the superlattices as a function of individual BST layer thickness is shown in figure 3. The form of the response is extremely similar to that published by Tabata *et al.* for $BaTiO_3$ / $SrTiO_3$ superlattices [7, 8]. In their work, a maximum in dielectric constant was also observed at individual dielectric layer thicknesses of 8-12 Å, and the background dielectric constant value of ~500 was enhanced by almost a factor of two to ~900 (compared to ~350 to ~800 in figure 3). Losses for individual layer thicknesses greater than 12 Å were also seen to be tan δ~0.05 as in our work. Losses for the fine multilayer structures associated with the dielectric peak were not presented by Tabata *et al.*.

Figure 4 shows the dielectric behaviour of the 8 Å (a) and 16 Å (b) superlattices as a function of temperature. A change from the relatively invariant behaviour typical of ferroelectric thin films in coarser superlattices, to behaviour strongly reminiscent of relaxors in fine superlattices can be seen. Fine-scale superlattices also demonstrate frequency behaviour that is qualitatively similar to that presented by Erbil *et al.* for $PbTiO_3$-$Pb_{1-x}La_xTiO_3$ heterostructures [5], with ε' increasing rapidly as frequency decreases. Such low frequency behaviour suggests that conduction mechanisms might play an important role. Results were therefore analysed in terms of the Maxwell-Wagner (MW) capacitor model [12, 13]. It can be shown that the MW capacitor yields real and imaginary parts of relative permittivity:

$$\varepsilon'(\omega) = \frac{1}{C_0(R_1 + R_2)} \frac{\tau_1 + \tau_2 - \tau + \omega^2 \tau_1 \tau_2 \tau}{1 + \omega^2 \tau^2} \qquad (1)$$

$$\varepsilon''(\omega) = \frac{1}{\omega C_0(R_1 + R_2)} \frac{1 - \omega^2 \tau_1 \tau_2 + \omega^2 \tau(\tau_1 + \tau_2)}{1 + \omega^2 \tau^2} \qquad (2)$$

where $\tau_1 = C_1R_1$, $\tau_2 = C_2R_2$, $\tau = \frac{\tau_1 R_2 + \tau_2 R_1}{R_1 + R_2}$, $C_0 = \varepsilon_0 \frac{A}{t}$, A = capacitor area, t = thickness; ω = frequency; subscripts 1 and 2 refer to superlattice components. By considering behaviour at zero and infinite frequency, equivalent expressions to (1) and (2) can be given in terms of ε_0 and ε_∞:

$$\varepsilon'(\omega) = \varepsilon_\infty + \frac{\varepsilon_0 - \varepsilon_\infty}{1 + \omega^2 \tau^2} \text{ and} \qquad (3)$$

$$\varepsilon''(\omega) = \frac{1}{\omega C_0(R_1 + R_2)} + \frac{(\varepsilon_0 - \varepsilon_\infty)\omega\tau}{1 + \omega^2 \tau^2} \qquad (4)$$

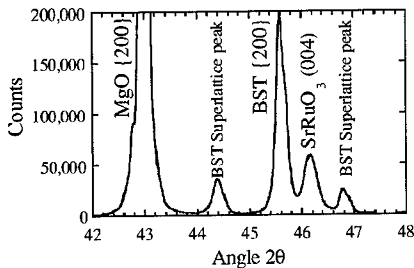

Figure 1. θ-2θ x-ray diffraction showing the appearance of superlattice satellite peaks around the BST {200} Bragg peak

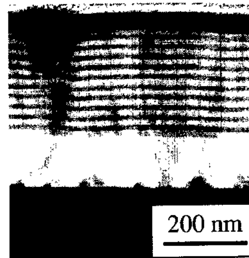

Figure 2. High angle annular dark field (HAADF) image (STEM mode) of a cross-section through a superlattice structure

Equation (3) is the same as that for Debye relaxation. However, the imaginary permittivity distinguishes between Debye and MW behaviour. In particular $\varepsilon'' \rightarrow 0$ as $\omega \rightarrow 0$ in a Debye system, whereas in a MW system $\varepsilon'' \rightarrow \infty$. Figure 5 shows ε" for superlattices as a function of frequency. Clearly, the behaviour of superlattices composed of individual BST layers greater than 8Å is significantly different from those of 8Å and 4Å. These finer superlattice structures show a tendency for ε" to increase with frequency decrease, indicating the onset of the MW effect. Figure 6 demonstrates that the frequency response for the finest scale superlattices can be directly modelled by a MW expression, and that a Debye expression cannot account for the low frequency behaviour.

The origin of the change in functional behaviour as individual layer thickness is reduced in the superlattice structures is not entirely clear. However, some insight was gained whenever the behaviour of the superlattices described above was compared to those in which delays were deliberately introduced between deposition of each successive layer in the superlattice stack. Figure 7 shows such a capacitor with individual layer thickness of 16Å. Clearly, dielectric enhancement and frequency relaxation have been introduced. The lack of such features in the

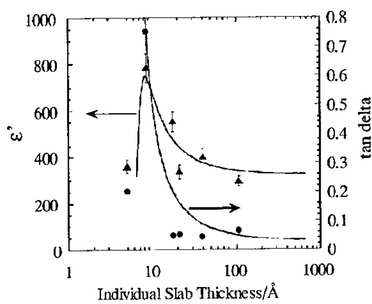

Figure 3. Dielectric constant and loss at room temperature and at 10kHz for BST superlattices as a function of individual layer thickness. Solid line represents fit from Maxwell-Wagner model.

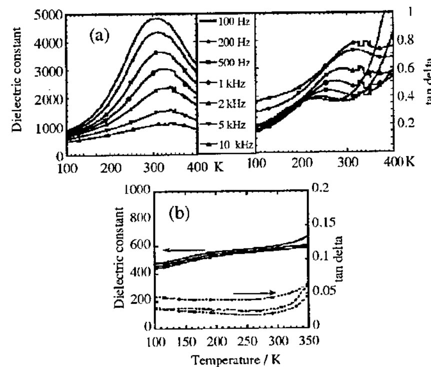

Figure 4. Dielectric behaviour of 8Å (a) and 16Å (b) superlattices with temperature and frequency

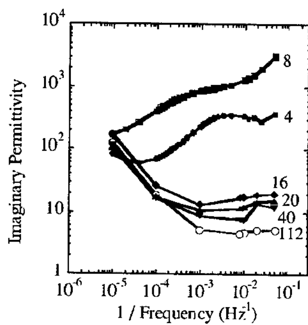

Figure 5. *Frequency dependence of the imaginary permittivity for BST superlattices. Number indices refer to individual layer thickness in Å*

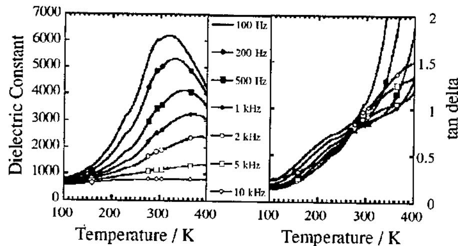

Figure 7. *The dielectric constant and loss for a 16Å slab thickness BST superlattice with delays introduced between the deposition of each layer.*

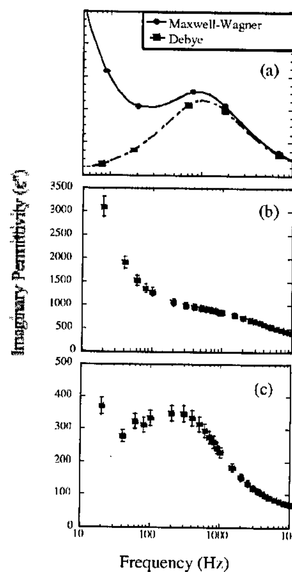

Figure 6. *Form of the imaginary permittivity response expected from both MW and Debye models (a) compared to that found in superlattices with individual BST layer thicknesses of (b) 8Å and (c) 4Å*

16Å superlattice without delays (figure 4) shows that absolute thickness of individual layers does not directly determine functional properties.

The top surfaces in individual layers in a capacitor with delayed deposition have been exposed to low pressures and high temperatures for long times in comparison to surfaces in superlattices without delays. Under such conditions surface modifications can be expected, their extent being dependent on the exposure time. In a given superlattice, the total extent of modification will also be proportional to the number of interfaces present. Hence, similar relative levels of surface-related modification in a superlattice capacitor can be achieved by either increasing exposure times or decreasing slab thickness. This is exemplified by the functional similarity between the 16Å slab thickness capacitor with delays (figure 7) and the 8Å slab thickness capacitor without delays (figure 4a).

Increased permittivities, and associated frequency relaxation features, were consistently found to be correlated with increased conductivities. Surface modifications must therefore be such that they reduce the resistivity of the interfacial material, resulting in an overall decrease of resistance across the capacitor. We can again invoke the MW series capacitor treatment given above, but with the effective superlattice structure now consisting of interfacial, semiconducting regions intercalated between bulk-like, insulating ferroelectric.

Taking equations (1) and (2), and performing the general substitutions: $R_j=\rho_j\, t_j/A$, $C_j=\varepsilon_j\, A/t_j$, where $j= i, b$ and where subscripts i and b refer to the interfacial-like and bulk-like layers respectively, the effective dielectric constant and loss can be expressed as a function of $t_i/\,t$ (relative thickness of interfacial zones), provided that the intrinsic dielectric constants and resistivities of the interfacial and bulk regions can be determined.

Typical measured values for single layer thin film BST were adopted for ε_b (~320 [14]), and it was also assumed that $\varepsilon_i=\varepsilon_b$, consistent with previous work [12]. ρ_i was varied and used as a fitting parameter, and in order that the results could be directly compared with experimental data, t_i was also varied. The results of the model were found to be relatively insensitive to ρ_b down to $\rho_b \sim 10^5$ Ω m. The measured functional response at 10kHz and room temperature for a series of superlattice capacitors in which no deliberate deposition delays were introduced are presented in figure 3, along with values predicted by the MW model with fitting parameters $\rho_i = 1500$ Ω m and $t_i = 6.5$Å. The figure shows that the MW model is capable of reproducing this behaviour. The scaling factor t_i yields a value close to 1 unit cell on either side of the interface, and a thickness ratio of low-resistivity interfacial material between 0.8 and 0.9 for the superlattices with maximum dielectric enhancement.

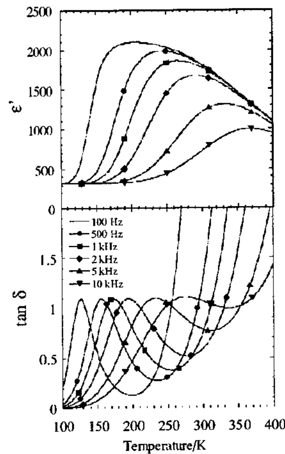

Figure 8. Dielectric constant and loss as a function of temperature and frequency predicted by the model for a capacitor with $t_i/t = 0.85$. Note the similarity with the capacitor behaviour in Figures 4 and 7.

In order to model ε' and tan δ as a function of temperature and frequency, the thermal dependencies of ε_i, ρ_i, ε_b and ρ_b have to be determined. Consistent with experimental results for thin films, ε_i and ε_b were assumed to be relatively temperature-independent. For the resistivities, a thermally-activated semiconducting behaviour was assumed:

$$\rho = \rho_0 \exp(\Delta / kT) \quad (5)$$

Where k is Boltzmann's constant, Δ is the activation energy and ρ_0 is deduced from the room temperature resistivity if Δ is known.

Assuming $1/R=\omega C_0\varepsilon''$[12], the activation energies were extracted from the imaginary permittivities as follows: figure 3 indicates that for the relaxor-like capacitors the thickness of the interfacial layer is considerably bigger than that of the bulk-like layer (t_i~0.8-0.9 t); at the same time, the resistivity of the interfacial layer is several orders of magnitude less than that of the bulk-like layer. This leads to the effective approximations $C_b >> C_s$ and $R_b >> R_s$. Using these approximations, and performing appropriate substitutions into equation (2), it follows that the activation energies corresponding to the bulk-like and interfacial-like layers can be directly extracted from the Arrhenius plots of ε'' for the lowest and highest measured frequencies [15]. The values corresponding to the capacitor in figure 7 are $\Delta_i \sim 0.08$ eV and $\Delta_b \sim 0.25$ eV. These activation energies were subsequently used to calculate $\rho_i(T)$ and $\rho_b(T)$ with equation (5).

Introducing the temperature-dependent resistances in (1) and (2) allows the expected ε' and tanδ as a function of temperature and frequency for a given capacitor to be plotted (figure 8). As can be seen, the qualitative similarity between the modelled dielectric behaviour and the experimental results is good.

CONCLUSIONS

Thin film capacitor structures with dielectric layers composed of superlattices of $Ba_{0.8}Sr_{0.2}TiO_3$ and $Ba_{0.2}Sr_{0.8}TiO_3$ were made by pulsed laser deposition. Although fine-scale superlattices showed dielectric behaviour reminiscent of relaxor electroceramics, analysis of the imaginary permittivity showed the likely dominant role of Maxwell-Wagner (MW) behaviour. It was suspected that such behaviour arose due to interfacial defect layers with decreased resistance. Adaptation of the MW model to include thermally dependent transport properties of interfacial and bulk layers in a superlattice configuration was found capable of reproducing the most important dielectric features experimentally observed, namely:

(i) a distinct peak in dielectric constant as a function of superlattice stacking periodicities;
(ii) giant permittivity with broad temperature dependence of dielectric peaks;
(iii) temperature migration of dielectric maxima as a function of frequency.

It therefore seems clear that the relaxor-like features seen in these superlattices are not indicative of the nanoscale-heterogeneity-induced superparaelectricity found in relaxor electroceramics. Further, similarity between these results and those obtained in previous studies suggests that MW behaviour cannot be ruled out of any of the published literature on dielectric properties of ferroelectric superlattices.

ACKNOWLEDGEMENTS

The authors acknowledge financial support from EPSRC and collaboration with AVX / Kyocera and FEI Philips in Eindhoven.

REFERENCES

[1] K. Park, L. Salamancariba, M. Wuttig, and D. Viehland, J. Mat Sci, **29**, 1284 (1994).
[2] N. de Mathan, J. Phys.: Condens. Matter **3**, 8159 (1991).
[3] N. Setter and L. E. Cross, J. Appl. Phys. **51**, 4356 (1980).
[4] Y. Yan, S. J. Pennycook, Z. Xu, and D. Viehland, Appl. Phys. Lett., **72**, 3145 (1998).
[5] A. Erbil, Y. Kim and R. A. Gerhardt, Phys. Rev. Lett., **77**, 1628 (1996).
[6] B. D. Qu, M. Evstigneev, D. J. Johnson and R. H. Prince, Appl. Phys. Lett., **72**, 1394 (1998).
[7] H. Tabata, H. Tanaka, T. Kawai, M. Okuyama, Jpn. J. Appl. Phys., **34**, 544 (1995).
[8] H. Tabata, H. Tanaka, and T. Kawai, Appl. Phys. Lett. **65**, 1970 (1994).
[9] Shaoping Li, J. A. Eastman, J. M. Vetrone, R. E. Newnham and L. E. Cross, Phil. Mag. B, **76**, 47 (1997).
[10] I. Kanno, S. Hayashi, R. Takayama and T. Hirao, Appl. Phys. Lett., **68**, 328 (1996).
[11] Y. Ohya, T. Ito, Y. Takahashi, Jpn. J. Appl. Phys. **33**, 5272 (1994).
[12] Volger, Progress in Semiconductors, **4**, 207 (1960).
[13] A. von Hippel, *Dielectrics and Waves*, Artech House, London, 1995
[14] D. Roy, S. B. Krupanidhi, Appl. Phys. Lett., **62**, 1056 (1993).
[15] R. Stumpe, D. Wagner, D. Bauerle, Phys. Stat. Sol., **75**, 143 (1983).

Mat. Res. Soc. Symp. Proc. Vol. 655 © 2001 Materials Research Society

Effect of Laser Energy and Laser Pulses on the Microstructure, Composition and Properties of Barium Strontium Titanate Thin Films Synthesized by Pulsed Laser Deposition

Costas G. Fountzoulas, J. D. Demaree and Steven H. McKnight
Weapons and Materials Research Directorate, Army Research Laboratory, APG, MD, 21005-5069.

ABSTRACT

Barium strontium titanate (BSTO) films were synthesized by the pulsed laser deposition technique (PLD) on silicon substrates at room temperature. The thin films were synthesized at ambient temperature and 30 mT oxygen partial pressure, with 300, 400 and 500 mJ/cm^2 laser fluence at 5, 10 and 20 pulses per second on silicon wafer substrates. All films were subsequently post-annealed at 750°C in an continuous oxygen stream. The microstructure, crystallinity and lattice constant of the BSTO films were studied with the aid of atomic force microscopy (FEM) and Glancing Angle X-ray Diffraction analysis (GAXRD). The hardness and modulus of elasticity of the films were studied with the aid of a nanohardness indenter. The film stoichiometry was determined with the aid of Rutherford Backscattering Spectrometry (RBS). The results of this research will be combined with the results of our previous work [1, 2] on the effect of substrate temperature and oxygen partial pressure on the microstructure and properties of the BSTO films in order to construct a structural zone model (SZM) of the BSTO films synthesized by PLD.

INTRODUCTION

Thin films of barium strontium titanate (BSTO) deposited by the pulsed laser deposition (PLD) technique exhibit excellent electronic properties including tunable dielectric constants and low electronic loss. The dielectric constant of the BSTO depends on the applied electric field. This variable dielectric constant results in a change in phase velocity in the device allowing it to be tuned, in real time, for a particular application. The dielectric requirements for a tunable BSTO thin film are (a) loss less than 0.01; (b) high tunability; (c) dielectric constant between 30 and 100; (d) low leakage current; and (e) good frequency and temperature stability of dielectric properties [1].

A tunable BSTO film must be single phase and crystalline. It must also have a smooth, defect free surface, uniform microstructure, and exhibit good thermal stability with the substrate. The microstructure of the film influences the electronic and mechanical properties (internal stresses and adhesion). These important factors affect the mechanical integrity and reliability of a device made of these thin films.

For several decades ferroelectric memory has attempted unsuccessfully to compete with semiconductor and magnetic memory. Niche markets have developed around the advantages of ferroelectric memory such as radiation hardness and non-volatility. Among the features holding back ferroelectric memory have been cost, fatigue, and large switching voltages. The use of epitaxial structures, and the metallization of the ferroelectric with oxides such as YBCO, La-Sr-Co-O, and Sr-Ru-O in place of Pt or Au has created structures with superior aging and low switching voltages. Thin film optical waveguides in ferroelectric oxides have traditionally been lossy and unsuitable as replacements for single crystals. In addition to a cost advantage,

epitaxial thin-film optical waveguides would have stronger mode confinement (due to a large difference in refractive index between cladding and ferroelectric) and could result in novel structures for applying electrodes and/or integrating monolithically with transistors or laser diodes [3]. Huang and Robson [4] and Schwyn Thöny at al [5] reported losses on the order of 1 dB/cm in $KNbO_3$ and $LiNbO_3$. Rou et al [6] and Fork et al [7] synthesized epitaxial $KNbO_3$ and $LiNbO_3$ on Si and GaAs substrates. Monolithic integration with light sources or as modulators would still pose a formidable task in terms of waveguide fabrication, optical coupling, and other fabrication requirements.

It has been also anticipated [2] that in the near future electronic structures based on the PLD technique will be used to monolithically combine well-developed semiconductor technology with the diverse physical properties of oxide systems. The commonly used semiconductor substrates have either cubic diamond or cubic zinc blende structures. The crystal structures of materials grown epitaxially on semiconductors are diverse and include the cubic fluorite, perovskite, rock salt, hausmannite and spinel structures A primary consideration in forming epitaxial compounds on any type of substrate is chemical reaction. Epitaxial growth on silicon is challenging due to the high reactivity of silicon with oxygen, especially at high substrate temperatures. The formation of even a thin amorphous silicon oxide layer before epitaxy is established would prevent epitaxy altogether. To circumvent the thermodynamic problem of substrate oxidation, it is possible to arrange a thermodynamically stable set of interfaces, for example McKee at al [8]. A second major consideration in forming epitaxial compounds on semiconductor substrates is the mismatch in thermal expansion coefficient [2]. Chrisley and Hubler [2] list various oxides epitaxially grown on silicon, their structures, crystallography, method of fabrication, lattice mismatch, and citation. $SrTiO_3$ an ABO_3 perovskite is a bilayer structure requiring initial growth of SrO layers prior to $SrTiO_3$ deposition in order to prevent interfacial reaction. $LiNbO_3$ which is z-axis oriented, has been grown on Si(111). The choice of Si(111) was motivated by the trigonal symmetry of lithium niobate.

We have initiated an investigation of the crystallinity, microstructure, mechanical and adhesive properties of a dielectric thin film of barium strontium titanium oxide (BSTO) deposited on silicon substrate by the pulsed laser deposition method (PLD) as a function of laser energy and repletion rate. This paper presents the initial results of this study of the properties of BSTO thin films as a function of oxygen partial pressure.

EXPERIMENTAL

The experimental apparatus consists of a pulsed laser deposition chamber equipped for optical diagnostics. The 248-nm output of an excimer laser (Lambda Physik, EMG 150 MSC) was directed through a 50-cm focal length lens and focused at 45° near the stoichiometric $Ba_{0.6}Sr_{0.4}TiO_3$ target (BSTO), which was mounted inside a stainless-steel chamber on a high-vacuum, rotatable holder. The details of this deposition technique are given elsewhere [9]. In this work thin films of BSTO were deposited by the PLD technique on 6 to 9 cm^2 (110) silicon substrates at room temperature, using 300, 400 and 500 mJ laser energy, at 5, 10 and 20 Hz repetition rate, and 30 mTorr partial oxygen pressures [1 mTorr = 1.33×10^{-4} Pa]. Prior to film synthesis the silicon substrates were degreased, cleaned for 5 minutes in warm (70-75 °C) methanol and ethanol baths and rinsed in warm (70-75 °C) distilled water for another 5 minutes. Subsequently the native oxide of the silicon substrate was removed in a dilute HF aqueous

solution. All films were annealed at 750°C for 45 minutes in a tube furnace in a continuous oxygen flow. Each deposition lasted for 30 min.

The microstructure of the films was observed by atomic force microscopy (AFM); the crystallinity of the films was determined by Glancing Angle X-ray Diffraction (GAXRD); the stoichiometry of the films was determined by Rutherford Back Scattering (RBS); and the Modulus of Elasticity (Young's Modulus) and the nanohardness of the films were determined with the aid of a nanoindenter.

The composition and thickness of the BSTO films was measured by Rutherford backscattering spectrometry (RBS), using a 2 MeV He^+ beam and a backscattering angle of 170 degrees, and the spectra were analyzed using the simulation program RUMP [10]. Because of the low scattering cross section of oxygen, there is a large amount of uncertainty in the oxygen composition determined, but the Ba:Sr:Ti ratios are much more precisely measured. Because of the film roughness, the RBS peaks show "tails" as well as bulk "ledges" corresponding to each element present, and this "tail-to-ledge" ratio can be considered a qualitative measure of the film roughness.

RESULTS AND DISCUSSION

Microstructure

The microstructure and morphology of the BSTO films, at various laser energies and repetition rates, was determined by optical microscopy and by AFM. All films observed by metallographic microscopy exhibited red and green elliptical striations, indicative of the thickness variation throughout the substrate, an inherent disadvantage of the PLD technique. After annealing the color of some films became white opaque or slightly yellow, which indicate the existence of the perovskite phase [11]. The surface of the films was relatively smooth on a macroscopic scale, as observed in the metallographic microscope, in spite of thermal grooving which occurred in all films. Thermal grooving occurs when a material is hot enough to generate considerable atomic migration. The groove forms where the grain boundary meets the surface in order to reduce the grain boundary area and hence free energy [12]. However, particulates, expelled parts of the target, were evident on the surface of the films. Figure 1 shows two dimensional microstructure of three BSTO films synthesized at 20 Hz repetition rate and at 300, 400 and 500 mJ/cm^2 laser energy fluence respectively. On the surface of both films clusters are

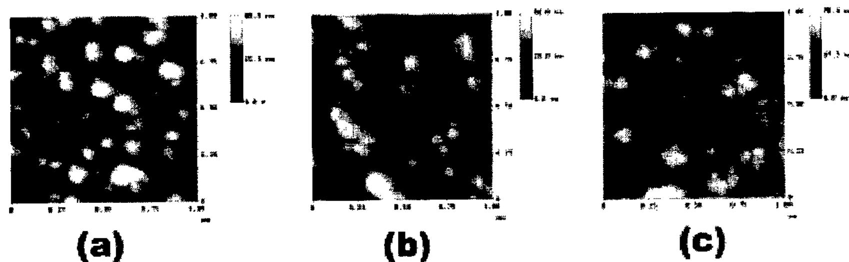

Figure 1. Atomic force microscopy of the BSTO film synthesized at 20 Hz repetition rate at (a) 300 mJ, (b) 400 mJ, and (c) 500 mJ laser energy.

found, which were composed of nano-sized grains in size of about 150 – 250 nm. The cluster density increases with increase total laser energy. The surface morphology of the films has a columnar structure as seen from the protrusion parts of grains. Figures 1b and 1c show a lot of rosettes, looking like a blooming flower or cauliflower, consisting of many small grains. The rosette density increases with total laser energy and film thickness. Furthermore, the rosette formation results in less complete substrate coverage which perhaps affects the nanohardness measurements.

RBS Results and Film Thickness

A typical RBS spectrum of the BSTO films is shown in Figure 2, along with a schematic model and simulated spectrum obtained using RUMP. For all BSTO coatings, before and after annealing, the Ba:Sr ratio was virtually identical to that of the PLD target (1.5). All of the films contained slightly less Ti than the expected ratio: Ti:(Ba+Sr) = 0.9. Since this is consistent across all films, and does not vary with laser energy or pulse rate, it is assumed that the original composition of the PLD target was slightly Ti-poor. The average composition of the film can be summarized as $Ba_{10.2}Sr_{6.8}Ti_{15}O_{68}$. The thickness of the as-deposited films seems to be a simple linear function of the total laser power deposited: Figure 3 shows the thickness plotted against the product of the laser pulse energy and the pulse rate.

Annealing the BSTO films resulted in both a decrease in oxygen content as well as a significant roughening of the films. All of the films contain much more oxygen than the expected 60 at%, especially in the as-deposited state. The fact that there is a significant decrease in the oxygen content of the films after annealing indicates that this oxygen might be loosely bound as water or some other unstable oxide, and that the films after annealing are probably the

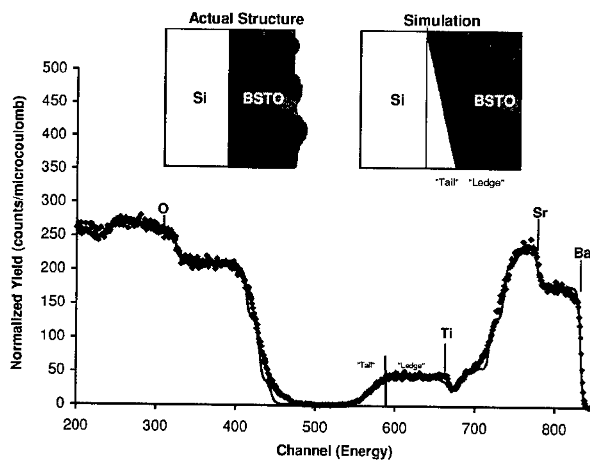

Figure 2. RBS spectrum of a typical BSTO film synthesized at 30 mTorr oxygen pressure, showing the elemental peaks and the "tails" indicative of film roughness.

same stoichiometric oxide as the PLD target. A qualitative estimate of film roughness generated by the RBS "tail-to-ledge" ratio is shown in Figure 4. The as deposited films all show some roughness, but the majority of the

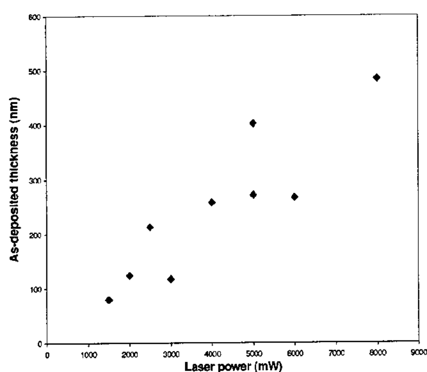

Figure 3 As-deposited film thickness as a function of laser power (laser energy x pulse rate).

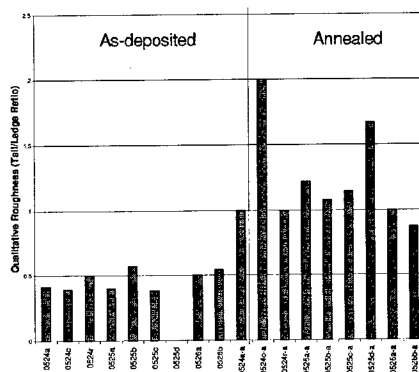

Figure 4 Film roughness as estimated by the RBS "tail to ledge" ratio.

material is in a continuous layer; after annealing, the film roughness is on the same order as the film thickness.

Glancing Angle X-ray Diffraction

The GAXRD analysis showed that all annealed films were crystalline for all deposition parameters. The unit cell of all annealed films belonged to the cubic system. The average lattice constant "a" is about 3.96 Å. The lattice constants of the BSTO films are shown in the Table I. This average lattice constant is in very good agreement with other published values [12].

Table I. Lattice constant (in nanometers) of the BSTO films as a function of the deposition parameters

	Pulse Rate (Hz)		
Energy (mJ)	***5***	***10***	***20***
300	0.392	0.395	0.396
400	0.390	0.399	0.397
500	0.395	0.397	0.397

Nanohardness and Modulus of Elasticity

Although it is recommended that the depth of nanohardness measurements be less than 10% of the total film thickness [13], the depth of these nanohardness measurements was 30% of the film thickness, because of the low thickness of some of the films. Because of this, it is expected that these measurements of the hardness were somewhat influenced by the substrate [13]. The nanohardness and the modulus of elasticity decrease as a function of the total laser energy (Table II). This may be attributed to the increased rosette density and smaller substrate coverage with increasing laser energy and repetition rate. The nanohardness and the modulus of elasticity of the amorphous BSTO film, before annealing, were 0.32 GPa and 30.8 GPa respectively.

Table II. Modulus of elasticity and nanohardness of the BSTO films as a function of laser energy and pulse rate

Modulus of elasticity (GPa)				Nanohardness (GPa)			
	Pulse Rate (Hz)				Pulse Rate (Hz)		
Energy (mJ)	***5***	***10***	***20***	**Energy (mJ)**	***5***	***10***	***20***
300	10.7	15.3	26.3	***300***	1.31	0.979	0.33
400	44.0	43.0	33.1	***400***	0.50	0.46	0.42
500	94.7	71.5	35.0	***500***	2.73	0.558	0.32

CONCLUSIONS

The crystallinity, surface morphology, stoichiometry, adhesion, modulus of elasticity and nanohardness of BSTO films synthesized on silicon substrates by the PLD technique were studied as a function of the laser energy and repetition rate. All films were crystalline after annealing at 750°C for 45 minutes, as shown by GAXRD analysis. The modulus of elasticity and nanohardness decreased with increased laser energy and repetition rate, while the roughness and the rosette density, resulting in smaller substrate coverage, decreased. The possibility of exchanging laser energy and repetition rate with deposition time may result in smoother films.

REFERENCES

1. C. G. Fountzoulas and S. Sengupta, Thin Films-Stresses and Mechanical Properties VII, *Mat. Res. Soc. Proc.* **505** (1998)
2. C.G. Fountzoulas, E.H. Ngo, C.W. Hubbard, P.C. Joshi, M.W. Cole, *Mat. Res. Soc. Proc* **603** (1999)
3. *Pulsed Laser Deposition of Thin Films*, ed. D. B. Chrisley and G. k. Hubler (John Wiley and Sons 1994)
4. L. S. Huang and T. Robson, *Proc. IFIF 91 3rd International Symposium on Integrated Ferroelectrics*, Colorado Springs, pp. 278-287 (1991)
5. Thöny Schwyn, S. H. W. Lehmann, and P. Günter, *Appl. Phys. Lett.* **61** (4) , pp. 373-375 (1992)
6. S. H. Rou, T. M. Graettinger, A. F. Chow, *Mat. Res. Soc. Proc.* **243**,pp. 81-91 (1992)
7. D. K. Fork, and G. B. Anderson, *Appl. Phys. Lett.* **63**(8), pp. 1029-1031 (1990)
8. R. A. McKee, F. J. Walker, and J. R. Conner, *Appl. Phys. Lett.* **59** (7), pp. 782-784 (1991)
9. J. Lee, R. Ramesh and V. G. Keramidas, *Mat. Res. Soc. Proc*, **361**, 67 (1995).
10. L. R. Doolittle, *Nucl. Instrum. Methods*, **B15**, 227 (1980)
11. K. D. Preston and G. H. Harting, *Appl. Phys. Lett.* **60** (23), 2831 (1992)
12. B. A. Baumert, L. H. Chang, A. T. Matsuda, T. L. Tsai, C. J. Tracy, D. J. Taylor, T. Otsuki, E Fujii, a. Hayashi and K. Suu, *J. Appl. Phys.*, **82**, (5), pp. 3558-3565 (1997)
13. G. M. Pharr, and W. C. Oliver, *MRS Bulletin* **17**, 28 (1992)

AUTHOR INDEX

Adenwalla, S., CC10.14
Agius, B., CC2.2
Akai, Takao, CC10.13
Alpay, S.P., CC8.8
Amorín, H., CC11.11
Andricacos, P.C., CC2.1
Andronov, A.N., CC7.7
Athavale, S.D., CC2.1
Ayguavives, F., CC2.2

Baeri, A., CC5.5
Baniecki, J.D., CC2.1, CC6.1
Bartels, Jörn, CC10.11
Baturin, I., CC10.8
Bausen, D., CC13.1
Bendersky, L.A., CC8.8
Bhaskar, S., CC4.7
Boettger, Ulrich, CC7.6
Bolten, Dierk, CC7.6, CC10.8
Bonnell, Dawn A., CC7.2
Bowman, R.M., CC3.2, CC11.8, CC13.2, CC14.9
Butenko, A.V., CC11.13

Cabral, Jr., C., CC2.1
Catalan, G., CC11.8, CC14.9
Cheng, Jian-Gong, CC11.10
Chikyo, Toyohiko, CC1.9
Cho, Yasuo, CC7.4
Chu, Fan, CC1.2
Chu, Jun-Hao, CC11.10
Chung, Ilsub, CC1.7
Cohen, Lester M., CC13.6
Cole, M.W., CC12.8, CC14.2
Condorelli, G.G., CC5.5
Corbett, M.H., CC11.8, CC13.2
Costrini, G., CC2.1

Das, Rasmi R., CC5.6, CC12.11
Davenport, Tom, CC1.2
Davis, C.C., CC8.9
Dehm, Christine, CC1.1
Deicher, Manfred, CC10.11
Demaree, J.D., CC14.10
Dietrich, Marc, CC10.11
Dixit, A., CC5.6
Dobal, P.S., CC4.7, CC5.6, CC12.11
Dong, Xiaomin, CC5.1

Ducharme, Stephen, CC10.14

Ehrhart, P., CC9.4
Ervin, M.H., CC14.2

Fè, Laura, CC9.1
Ferrater, Cesar, CC5.7
Fitsilis, F., CC9.4
Fonseca, Luis F., CC10.12
Fountzoulas, Costas G., CC14.10
Fox, Glen, CC1.2
Fragalà, I.L., CC5.5
Freitag, Kristian, CC10.11
Freundorfer, A.P., CC12.13
Fridkin, V.M., CC10.14
Fujimori, Yoshikazu, CC2.10
Fujimoto, Masayuki, CC10.13
Fujimura, Norifumi, CC3.11
Fujisaki, Yoshihisa, CC3.6
Fujisawa, H., CC1.10, CC10.4
Fujiwara, Norito, CC2.3
Funakubo, Hiroshi, CC1.9, CC4.6, CC10.13
Fundora, A., CC11.11

Ganpule, C.S., CC1.5
García-Cuenca, María V., CC5.7
Gerlach, G., CC7.7
Gonzalo, Julio A., CC10.12
Gregg, J.M., CC3.2, CC11.8, CC13.2, CC14.9
Grishin, Alex, CC11.5
Grossmann, Michael, CC7.6
Gruverman, A., CC8.5
Güell, Frank, CC5.7
Guerrero, Cesar, CC5.7
Guerrero, F., CC11.11
Guo, Shao-Ling, CC11.10

Haeni, J.H., CC7.8
Hammad, H., CC12.13
Han, Pengdi, CC7.5
Harnagea, C., CC5.3
Hartner, Walter, CC1.1
Hashimoto, Kazuhiko, CC11.9
Hesse, D., CC5.3
Higashi, Noriyuki, CC4.6
Honda, K., CC10.4

Hong, E., CC11.7
Hong, Ying, CC2.3
Horii, Sadayoshi, CC4.2
Horikawa, T., CC6.5, CC9.3
Horita, Susumu, CC4.2
Hsu, Sheng Teng, CC2.3, CC3.10
Huang, M.Q., CC11.12
Hubbard, C.W., CC12.8, CC14.2
Hugon, M.C., CC2.2
Hwang, Jay, CC6.6

Imura, Masaaki, CC13.7
Ishiwara, Hiroshi, CC3.6, CC13.9
Isobe, C., CC8.5
Isobe, Takeaki, CC13.9
Ito, Daisuke, CC3.11
Ito, Taichiro, CC3.11

Jia, C.L., CC9.4
Jin, H.Z., CC9.4
Joshi, P.C., CC12.8, CC14.2
Juergensen, H., CC9.4

Kakuno, Kousuke, CC3.11
Kalinin, Sergei V., CC7.2
Kasko, Igor, CC1.1
Katiyar, Ram S., CC4.7, CC5.6, CC12.11, CC12.14
Kato, Kazumi, CC12.12
Kawahara, T., CC6.5, CC9.3
Keur, W., CC13.1
Khartsev, S.I., CC11.5
Kiewitt, R., CC13.1
Kijima, Takeshi, CC3.6, CC13.9
Kim, Chang Jung, CC1.7
Kim, Hyeong Joon, CC3.7
Kim, Jin Woong, CC2.8
Kim, Jin Yong, CC3.7
Kim, Joon Hyeong, CC3.7
Kingon, A.I., CC2.2
Kirby, Paul, CC13.7
Kita, K., CC1.10
Klee, M., CC13.1
Kodama, Kazushi, CC13.10
Koh, Jung-Hyuk, CC11.5
Kohlstedt, H., CC2.5
Komuro, Eiju, CC13.7
Kosarev, A.I., CC7.7
Krupanidhi, S.B., CC12.11

Kubo, Yoshimi, CC2.7
Kuroiwa, T., CC6.5
Kwietniak, K.T., CC2.1
Kwon, O. Sung, CC2.8

Lai, P.T., CC11.12
Laibowitz, R.B., CC2.1, CC6.1
Lee, C.H., CC8.9
Lee, H.N., CC5.3
Lee, June Key, CC1.7
Lee, U., CC14.2
Lee, Yong Kyun, CC1.7
Letendu, F., CC2.2
Levin, R., CC11.13
Li, B., CC11.12
Li, G.Q., CC11.12
Li, Tingkai, CC3.10
Lian, J.J., CC2.1, CC6.1
Liang, H.Y., CC8.9
Limb, Y., CC2.1
Liu, Ran, CC7.5
Lockwood, G.R., CC13.6
Lohse, Oliver, CC7.6, CC10.8
Lok, P., CC13.1

Maa, Jer-shen, CC2.3
Majumder, S.B., CC4.7, CC12.14
Marqués, Manuel I., CC10.12
Martinez, A., CC12.14
Masuda, Atsushi, CC2.10
Matsumura, Hideki, CC2.10
Matsuno, S., CC6.5
Matsuura, Kaori, CC7.4
Mazure, Carlos, CC1.1
McKnight, Steven H., CC14.10
Melgarejo, R.E., CC5.6
Melngailis, J., CC1.5
Miki, Takeshi, CC12.12
Mikolajick, Thomas, CC1.1
Minamikawa, Toshiharu, CC2.10
Mitsuya, Masatoshi, CC10.13
Moert, Manfred, CC1.1
Morimoto, K., CC10.4
Morros, C., CC11.8
Mukaigawa, Tomonori, CC11.9
Mukherjee, B.K., CC13.6

Nagarajan, V., CC1.5, CC8.8, CC8.9
Nagel, Nicolas, CC1.1

Nakaiso, Toshiyuki, CC3.5, CC13.10
Nakamura, Takashi, CC2.10
Neumayer, D.A., CC2.1
Ngo, E., CC12.8, CC14.2
Nikolaeva, E., CC10.8
Nishi, Yuji, CC10.13
Nishizawa, Kaori, CC12.12
Niu, H., CC1.10, CC10.4
Noda, Minoru, CC3.5, CC11.9, CC13.10
Norga, G.J., CC9.1
Nukaga, Masanori, CC10.13

Odagawa, Hiroyuki, CC7.4
Ohnishi, Shigeo, CC2.3
Ohtani, S., CC10.4
Okuda, Norikazu, CC4.6
Okuyama, Masanori, CC3.5, CC11.9, CC13.10
Olding, T.R., CC13.6
O'Neill, D., CC14.9
Ono, Yoshi, CC2.3
Oomori, T., CC9.3
Otani, Seigen, CC2.6

Palto, S.P., CC10.14
Pan, X.Q., CC7.8
Pang, G., CC13.6
Park, Chanro, CC2.8
Parks, C., CC6.1
Perez, B., CC12.14
Pérez, W., CC5.6, CC12.11
Petrovsky, Vladimir, CC11.5
Petukhova, N.N., CC10.14
Pignolet, A., CC5.3
Pinnow, Cay-Uwe, CC1.1
Poplavko, Yu., CC7.7
Portelles, J., CC11.11
Poulsen, Matt, CC10.14

Ramesh, R., CC1.5, CC8.8, CC8.9
Ramos, Rafael, CC10.12
Regnery, S., CC9.4
Ren, W., CC13.6
Rodríguez, R.J., CC12.11
Roldán, José, CC5.7
Romero, Juan D., CC10.12
Roy, B., CC12.14
Roytburd, A.L., CC1.5, CC8.8

Saenger, K.L., CC2.1
Saiki, Atsushi, CC1.9
Saito, Keisuke, CC1.9, CC10.13
Sakai, Tomohiro, CC1.9
Samokhvalov, Vyacheslav, CC10.11
Sánchez, Florencio, CC5.7
Sandomirsky, V., CC11.13
Sato, T., CC6.5
Sayer, M., CC12.13, CC13.6
Schienle, F., CC9.4
Schlesinger, Y., CC11.13
Schlom, D.G., CC7.8
Schneider, St., CC2.5
Schumacher, M., CC9.4
Senz, S., CC5.3
Seol, Yeo Song, CC2.8
Shaw, T.M., CC6.1
Shibano, T., CC6.5, CC9.3
Shimakawa, Yuichi, CC2.7
Shimizu, M., CC1.10, CC10.4
Shishkin, E., CC10.8
Shur, V., CC10.8
Sinnamon, L.J., CC3.2
Siqueiros, J.M., CC11.11
Smolyaninov, I.I., CC8.9
Stanishevsky, A., CC1.5
Su, Qing-Xin, CC13.7
Suchaneck, G., CC7.7
Suzuki, Kazuyuki, CC12.12
Suzuki, Toshimasa, CC10.13

Takahashi, Mitsue, CC13.10
Takenaga, T., CC6.5
Tamura, Tetsuro, CC2.6
Tanaka, M., CC8.5
Tang, Jun, CC11.10
Tarutani, M., CC6.5, CC9.3
Tian, W., CC7.8
Tokumitsu, Eisuke, CC13.9
Tomar, M.S., CC5.6
Trolier-McKinstry, Susan, CC11.3, CC11.7

Ulrich, Bruce, CC3.10
Unterricker, Sepp, CC10.11

Varela, Manuel, CC5.7
Venet, M., CC11.11
Vickridge, I., CC2.2

Wang, Hua, CC5.1
Wang, Yunbo, CC5.1
Waser, Rainer, CC2.5, CC7.6, CC9.4, CC10.8
Watanabe, Takayuki, CC1.9
Whatmore, Roger, CC13.7
Williams, E.D., CC1.5
Wise, M.L., CC2.1
Wissen, D., CC13.1
Wolf, R., CC11.7

Xu, Huaping, CC11.9

Yamaji, Isao, CC10.13
Yamamuka, M., CC6.5, CC9.3
Yi, Insook, CC1.7
Ying, Hong, CC3.10
Yoneda, Y., CC6.5
Yonezawa, Yasuto, CC2.10
Yoon, Hee Koo, CC2.8
Yoshimura, Takeshi, CC11.3
Yu, Jun, CC5.1
Yudin, S.G., CC10.14

Zelonka, K., CC12.13
Zeng, S.H., CC11.12
Zhang, Fengyan, CC2.3
Zhang, Qi, CC13.7
Zhen, Wendong, CC2.3
Zhou, Q.F., CC11.7
Zhou, Wenli, CC5.1
Zhu, Hong, CC11.9
Zhu, Lili, CC5.1
Zhuang, Weiwei, CC2.3

SUBJECT INDEX

atomic force microscope, CC1.5

barium
  strontium titanate, CC6.1, CC11.9, CC11.10, CC12.8, CC12.13, CC14.10/DD6.10
  titanate, CC7.8, CC10.11, CC11.12
barriers, CC2.1
$(Bi,La)_4Ti_3O_{12}$, CC3.6
bi-layered compounds, CC5.6, CC12.11
bismuth-lanthanum titanate (BLT), CC3.7, CC13.9
$Bi_4Ti_3O_{12}$, CC5.1
BLSF, CC1.9
BST, CC6.5, CC9.3, CC9.4, CC12.13
  capacitors, CC6.6

$CaBi_2Ta_2O_9$ thin film, CC12.12
capacitor, CC2.8
$CaRuO_3$, CC4.6
catalytic chemical vapor deposition, CC2.10
chemical solution deposition, CC12.14
chlorine, CC2.5
complex oxide films, CC13.1
composites, CC13.6
contact potential difference, CC7.7
coupling, CC13.2
CVD, CC6.5, CC9.3

damage, CC2.8
dead-layers, CC3.2
degradation, CC2.7
devices, CC13.6
dielectric
  bolometer, CC11.9
  relaxation, CC7.6
diffusion barrier, CC2.2
domain structure, CC10.13

electric field effect, CC11.13
electrodes, CC2.1
electrophoretic deposition, CC12.8
endurance, CC1.2
epitaxial, CC1.9, CC4.2
  films, CC5.3
  growth, CC11.3
  structure, CC3.11
epitaxy, CC8.8
external electric field, CC10.11

fatigue, CC10.8
  behavior, CC12.12
FERAM, CC1.1, CC2.8
ferroelectric(s), CC2.3, CC2.6, CC3.10, CC10.12, CC11.5, CC13.9, CC14.9
  diodes, CC5.1
  films, CC8.5, CC8.8
  gate
    FET, CC13.10
    transistor, CC3.11
  materials, CC7.2
  polarization, CC7.4
  property, CC12.12
  PZT oxide, CC2.7
  thin film(s), CC5.3, CC8.9, CC12.11
filters, CC13.7
forming gas, CC6.1
FRAM, CC1.2

high
  resolution transmission electron microscopy, CC7.8
  temperature
    cathode, CC6.6
    electrode, CC2.3
    process, CC2.5
hydrothermal processing, CC12.13

imprint properties, CC2.6
integration of thin film capacitors, CC13.1
inverse piezoresponse, CC1.5
iridium, CC1.10, CC4.2
  oxide, CC1.10
Ir-Ta-O, CC2.3

kinetics, CC5.5

Langmuir-Blodgett deposition, CC10.14
laser ablation, CC5.6
lateral scaling, CC1.5

lead
zirconate titanate, CC5.7, CC7.6, CC7.7, CC10.4, CC13.6
zirconium titanate, CC13.7

Maxwell-Wagner, CC14.9
mechanism, CC9.3
metal-
ferroelectric-insulator-semiconductor (MFIS), CC3.5
organic-decomposition, CC11.9
MFIS-FET, CC3.6
microwave, CC14.2
MOCVD, CC1.9, CC1.10, CC3.7, CC3.10, CC4.6, CC5.5, CC9.4
multi-wafer reactor, CC9.4

Nd doped PZT thin film, CC12.14
nonvolatile memory, CC13.10
NSOM, CC8.9

^{18}O depth profile, CC2.2
one-transistor memory, CC3.10
orientation, CC9.1
overview, CC1.1
oxidation resistance, CC2.2

passivation, CC2.10
$Pb(Zr_{0.52}Ti_{0.48})O_3$, CC5.1
perturbed $\gamma\gamma$-angular correlations (PAC), CC10.11
phase transition, CC10.14
phonons, CC7.5
piezoelectric, CC11.7
thin films, CC11.3
piezoresponse, CC10.4, CC11.8
force microscopy, CC7.2
planar electrode, CC12.14
platinum, CC2.1, CC2.5
PLT thin films, CC4.7
PLZT, CC4.6
thin film, CC1.2
polarization switching, CC7.6
polydomain formation, CC8.8
Pt etching, CC6.6
pulse injection method, CC3.7
pulsed laser deposition (PLD), CC3.5, CC5.7, CC11.5, CC12.11, CC14.10
P(VDF-TrFE), CC10.14
pyroelectric, CC11.10
pyroelectricity, CC11.11
PZN-BT, CC11.8
PZT, CC1.7, CC9.1, CC11.8
thin film, CC7.4

radical nitrified Si_3N_4 film, CC3.6
Raman, CC7.5
scattering, CC4.7
relaxor, CC13.2
ferroelectric, CC11.3
retention, CC8.5
characteristics, CC13.10
Ru, CC6.5
ruthenium oxide, CC4.7

SBN ferroelectric ceramics, CC11.11
SBT, CC1.1, CC5.5
scanning
force microscopy, CC8.5
nonlinear dielectric microscopy, CC7.4
probe microscopy, CC7.2, CC10.4
second harmonic generation, CC8.9
self-polarization, CC7.7
sensitivity, CC11.12
series capacitor model, CC3.2
silicon nitride, CC2.10
silver niobate-tantalate, CC11.5
simple oxide films, CC13.1
size effects, CC10.12
sol-gel, CC1.7, CC9.1, CC11.7, CC11.10, CC13.9
-PZT, CC2.6
solid-state chemistry, CC2.7
space charge, CC6.1
$SrBi_2Ta_2O_9$, CC5.3, CC5.6, CC7.5
$Sr_2(Ta_{1-x}, Nb_x)_2O_7$ (STN), CC3.5
strain effect on spontaneous polarization, CC7.8
strontium bismuth tantalum oxide, CC10.13
superlattice, CC13.2, CC14.9

surface effects, CC10.12
switching, CC10.8

thermally stimulated depolarization
current (TSDC), CC11.11
thermoelectric, CC11.13
thick film, CC11.7
thickness dependence of dielectric
constant, CC3.2
thin film(s), CC5.7, CC10.8, CC11.12,
CC11.13, CC14.2, CC14.10
bulk acoustic resonator, CC13.7

tunable devices, CC14.2

ultra thin film, CC1.7

x-ray diffraction, CC10.13

$YMnO_3$, CC3.11

zirconium nitride, CC4.2